

JYU DISSERTATIONS 355

---

**Joel Kostensalo**

**Theoretical Calculations for Electron  
Spectra and Neutrino-Nucleus  
Scattering in Context of Reactor  
Antineutrino and Gallium Anomalies**

---



UNIVERSITY OF JYVÄSKYLÄ  
FACULTY OF MATHEMATICS  
AND SCIENCE

JYU DISSERTATIONS 355

---

Joel Kostensalo

**Theoretical Calculations for Electron  
Spectra and Neutrino-Nucleus Scattering  
in Context of Reactor Antineutrino  
and Gallium Anomalies**

Esitetään Jyväskylän yliopiston matemaattis-luonnontieteellisen tiedekunnan suostumuksella  
julkisesti tarkastettavaksi maaliskuun 5. päivänä 2021 kello 14.

Academic dissertation to be publicly discussed, by permission of  
the Faculty of Mathematics and Science of the University of Jyväskylä,  
on March 5, 2021, at 2 PM.



JYVÄSKYLÄN YLIOPISTO  
UNIVERSITY OF JYVÄSKYLÄ

JYVÄSKYLÄ 2021

Editors

Ilari Maasilta

Department of Physics, University of Jyväskylä

Päivi Vuorio

Open Science Centre, University of Jyväskylä

Copyright © 2021, by University of Jyväskylä

Permanent link to this publication: <http://urn.fi/URN:ISBN:978-951-39-8541-7>

ISBN 978-951-39-8541-7 (PDF)

URN:ISBN:978-951-39-8541-7

ISSN 2489-9003

# Preface

When I wrote the following publications, or rather the bulk of them, I dwelt in an ill-lit apartment on the shore of Lake Jyväsjärvi, living off various grants and odd teaching jobs during the years 2017–2020.

Financial support from Jenny and Antti Wihuri foundation is gratefully acknowledged. Financial assistance for travel from Magnus Ehrnroth foundation, University of Osaka, and University of Washington is also appreciated.

I want to thank my supervisor Prof. Jouni Suhonen for providing me with a myriad of research problems not limited to those covered in this thesis. His prolific generation of new ideas for research papers would be enough to offset even the most miserable of failure rates. I would also like to express my gratitude to Prof. Mihai Horoi and Prof. Gabriel Martínez-Pinedo for reviewing the manuscript and Prof. Jonathan Engel for agreeing to be the opponent on the day of the defense.

I would like to thank all the collaborators, especially Dr. Leendert Hayen, Prof. Nathal Severjins, Dr. Carlo Giunti, and Prof. Kai Zuber, discussions with whom have been immensely useful. Statistical advice from Dr. Santtu Tikka is greatly appreciated. The unofficial group meetings with Dr. Mikko Haaranen and Mr. Juhani Hyvärinen have also provided valuable input.

Finally, I would like to thank my wife Ada for suffering to bear witness to this, at times, Sisyphean task. It is obvious one must imagine Sisyphus happy.

Jyväskylä, January 2021  
Joel Kostensalo



# Abstract

This thesis consists of fourteen publications and an introductory part on rare beta decays and neutrino-nucleus scattering. The overarching theme of this work is to provide state-of-the-art theoretical calculations for statistical inferences related to the existence of eV-scale sterile neutrinos.

The first body of research relates to forbidden beta spectra and the reactor antineutrino anomaly. As a first application, the theoretical formalism is applied to several forbidden beta decays in order to study how adopting quenched values of the weak coupling constants  $g_A$  and  $g_V$  affects the shape of the electron spectrum. Next, the formalism is applied to the first-forbidden unique decays of argon isotopes  $^{39,42}\text{Ar}$  in order to produce high-precision spectra which could be utilized for modeling background radiation in rare-event searches. Following this, the mesonic enhancement of the  $\gamma_5$  matrix element, also known as the axial-charge matrix element, for decays between neutron-rich nuclei is studied in the  $A \approx 95$  and  $A \approx 135$  mass regions. These include transitions which play a role in reactor antineutrino experiments. The theoretical spectra are then compared with the experimental results of COBRA for  $^{113}\text{Cd}$  and EXO-200 for  $^{137}\text{Xe}$  in order to assess the quality of the theoretical predictions, and excellent agreement is found. The formalism is then applied to the 36 most important first-forbidden contributors to the cumulative  $\beta$ -spectrum from nuclear fission in order to reassess the nuclear structure uncertainties related to the reactor antineutrino anomaly. The nuclear structure uncertainties are found to be significantly larger than has been previously assumed.

The second body of research focuses on charged-current scattering reactions for neutrinos and nuclei, with special emphasis on the gallium anomaly. Firstly, new estimates for solar and supernova neutrino cross sections for scattering off  $^{40}\text{Ar}$  are derived. Next, a new estimate for the solar neutrino cross section of  $^{205}\text{Tl}$ , an excellent candidate for radiochemical experiments, is evaluated. The formalism is then applied to the case of  $^{71}\text{Ga}$  in order to re-evaluate the theoretical cross section and to investigate possible shortcomings of charge-exchange reactions as a means of evaluating cross sections in the context of

the gallium anomaly. The statistical significance of the gallium anomaly is found to be reduced by the new calculations.

# Tiivistelmä

Tämä väitöskirja koostuu neljästätoista artikkelista sekä harvinaisia beetahajoamis- ja neutriino-ydin-sirontaa käsittelevästä johdanto-osasta. Pyrkimyksenä on ollut laskea mahdollisimman tarkkoja teoreettisia arvioita steriilien neutriinoiden olemassaoloon liittyvien kokeellisten tulosten tulkintaa varten.

Työ koostuu kahdesta kokonaisuudesta, joista ensimmäinen liittyy kiellettyihin beetahajoamisiin ja reaktoriantineutriinoanomaliaan. Kiellettyjen siirtymien formalismin ensimmäisenä sovelluksena on tutkittu elektronispektrin herkkyyttä ydinrakennelaskuihin liittyville epävarmuuksille. Toisena sovelluskohteena ovat isotooppien  $^{39,42}\text{Ar}$  uniikit siirtymät, joiden elektronispektrit on laskettu pimeään aineen kokeissa esiintyvän taustasäteilyn poisrajaamista varten. Seuraavaksi on tarkasteltu aksiaalivarausmatriisielementin mesoninvaihtovirtoihin liittyvän voimistumisen vaikutusta reaktoriantineutriinoanomalian kannalta olennaisiin siirtymiin. Teoreettisten spektrien laatu varmistettiin vertaamalla tuloksia COBRA- ja EXO-200-mittauksiin. Tämän jälkeen formalismia on sovellettu kolmeen kymmeneenkuuteen reaktoriantineutriinoanomalian kannalta olennaisimpaan siirtymään ydinrakennelaskuihin liittyvien epävarmuuksien arvioimiseksi. Uudet laskut osoittavat, että teoreettisiin laskuihin liittyvät epävarmuudet ovat selvästi suurempia kuin aiemmissä tutkimuksissa on oletettu.

Toisen kokonaisuuden muodostavat neutriino-ydin-sirontaan liittyvät laskut ja galliumanomalian tarkastelu. Ensimmäiseksi neutriino-ydin-sirontalaskujen kohteeksi on otettu  $^{40}\text{Ar}$ , jolle on määritetty uudet teoreettiset arviot aurinko- ja supernovaneutriinoiden siroamistodennäköisyyksille. Seuraavana kohteena on ollut  $^{205}\text{Tl}$ , jota voitaisiin potentiaalisesti hyödyntää radiokeemiallisissa neutriinokokeissa. Lopuksi on laskettu uudet arviot ytimen  $^{71}\text{Ga}$  vaikutusalalle neutriinolähdekokeissa. Uudet teoreettiset laskut osoittavat, että keinotekoisin neutriinolähteisiin liittyvät vaikutusalat on saatettu aiemmin yliarvioida.

**Author** Joel Kostensalo  
Department of Physics  
University of Jyväskylä  
Finland

**Supervisor** Professor Jouni Suhonen  
Department of Physics  
University of Jyväskylä  
Finland

**Reviewers** Professor Mihai Horoi  
Department of Physics  
Central Michigan University  
United States of America

Professor Gabriel Martínez-Pinedo  
Institut für Kernphysik  
Technische Universität Darmstadt  
Germany

**Opponent** Professor Jonathan Engel  
Department of Physics and Astronomy  
University of North Carolina  
United States of America

# List of Publications

This thesis consists of an introductory part and of the following publications:

- [I] **Electron spectra in forbidden  $\beta$  decays and the quenching of the weak axial-vector coupling constant  $g_A$**   
J. Kostensalo, M. Haaranen and J. Suhonen, *Phys. Rev. C* 95, no.4 (2017) 044313.
- [II]  **$g_A$ -driven shapes of electron spectra of forbidden  $\beta$  decays in the nuclear shell model**  
J. Kostensalo and J. Suhonen, *Phys. Rev. C* 96, no.2 (2017) 024317.
- [III] **Spectral shapes of forbidden argon  $\beta$  decays as background component for rare-event searches**  
J. Kostensalo, J. Suhonen and K. Zuber, *Journal of Physics G: Nuclear and Particle Physics* 45, no.2 (2017) 025202.
- [IV] **Shell-model computed cross sections for charged-current scattering of astrophysical neutrinos off  $^{40}\text{Ar}$**   
J. Kostensalo, J. Suhonen and K. Zuber, *Phys. Rev. C* 97, no.3 (2018) 034309.
- [V] **Beta-spectrum shapes of forbidden decays**  
J. Kostensalo and J. Suhonen, *International Journal of Modern Physics A* 33, no.09 (2018) 1843008.
- [VI] **Mesonic enhancement of the weak axial charge and its effect on the half-lives and spectral shapes of first-forbidden  $J^+ \leftrightarrow J^-$  decays**  
J. Kostensalo and J. Suhonen, *Physics Letters B* 781 (2018) 480–484, ISSN: 0370-2693.
- [VII] **First-forbidden transitions in reactor antineutrino spectra**  
L. Hayen, J. Kostensalo, N. Severijns and J. Suhonen, *Phys. Rev. C* 99, no.3 (2019) 031301.

- [VIII] **First-forbidden transitions in the reactor anomaly**  
L. Hayen, J. Kostensalo, N. Severijns and J. Suhonen, *Phys. Rev. C* 100, no.5 (2019) 054323.
- [IX] **Quenching of  $g_A$  deduced from the beta-spectrum shape of  $^{113}\text{Cd}$  measured with the COBRA experiment**  
L. Bodenstern-Dresler et al., *Physics Letters B* 800 (2020) 135092, ISSN: 0370-2693.
- [X] **The gallium anomaly revisited**  
J. Kostensalo, J. Suhonen, C. Giunti and P.C. Srivastava, *Physics Letters B* 795 (2019) 542–547, ISSN: 0370-2693.
- [XI] **Anomalies and sterile neutrinos – Implications of new theoretical results**  
J. Kostensalo and J. Suhonen, *AIP Conference Proceedings* 2165, no.1 (2019) 020016.
- [XII] **Calculated solar-neutrino capture rate for a radiochemical  $^{205}\text{Tl}$ -based solar-neutrino detector**  
J. Kostensalo, J. Suhonen and K. Zuber, *Phys. Rev. C* 101, no.3 (2020) 031302.
- [XIII] **Second-forbidden nonunique  $\beta^-$  decays of  $^{24}\text{Na}$  and  $^{36}\text{Cl}$  assessed by the nuclear shell model**  
A. Kumar, P. C. Srivastava, J. Kostensalo and J. Suhonen, *Phys. Rev. C* 101, no.6 (2020) 064304.
- [XIV] **Measurement of the Spectral Shape of the  $\beta$ -Decay of  $^{137}\text{Xe}$  to the Ground State of  $^{137}\text{Cs}$  in EXO-200 and Comparison with Theory**  
S. Al Kharusi et al., *Phys. Rev. Lett.* 124, no.23 (2020) 232502.

The author performed all the theoretical beta decay and neutrino-nucleus scattering calculations for all the listed publications except [XIII] and wrote the original draft of the publications [I, II, III, IV, VI, X, XI, XII]. The author developed the novel analysis approach in [XIII] and made the analysis plan for this paper.

# Contents

<b>1</b>	<b>Introduction</b>	<b>1</b>
<b>2</b>	<b>Theoretical Framework</b>	<b>3</b>
2.1	Nuclear structure . . . . .	3
2.2	Forbidden beta decays . . . . .	9
2.3	Neutrino-nucleus scattering . . . . .	13
<b>3</b>	<b>Results and Discussion</b>	<b>17</b>
3.1	Forbidden decays and the spectral shape . . . . .	17
3.2	Neutrino-nucleus scattering . . . . .	27
<b>4</b>	<b>Summary</b>	<b>37</b>
	<b>References</b>	<b>39</b>

# Chapter 1

## Introduction

There are several long-standing problems associated with various neutrino-related experiments. Mismatches between theoretical predictions and experimental results have been reported by LSND [1, 2], GALLEX [3–5], and SAGE [6], as well as various reactor-based short baseline oscillation experiments [7, 8]. One proposed solution to these problems has been neutrino oscillation to a sterile neutrino flavor, which would not interact via the weak interaction [9]. However, some of the results contradict each other, favoring different models for such particles [10].

The so-called reactor antineutrino anomaly (RAA) [7, 8] refers to the missing antineutrino flux from nuclear reactors as predicted by theoretical models. In addition to the missing flux, the experimental and predicted spectral shapes differ from each other. The disagreement is usually described as a “5 MeV bump” or a spectral shoulder, and persists after years of intense research [11–14].

The theoretical determination of the antineutrino flux from reactors relies on the predicted shape of individual  $\beta$ -spectra from the various fission products. In the research articles by Huber and Mueller *et al.* [15, 16] the predicted spectral shapes for the involved beta decays were calculated using simplifying approximations, which could potentially lead to non-trivial systematic errors. The reason for making such approximations is the complicated formalism involving a myriad of form factors. A further complication in forsaking such approximations would have been that using the full formalism requires computationally burdensome nuclear structure calculations in order to evaluate the relevant nuclear matrix elements.

In the paper [17] by Mougeot, the experimentally-measured shape factors were found to deviate significantly from allowed shape factors. A significant mismatch between theoretical and experimental results was seen for most of the studied transitions including light, medium-heavy, and heavy nuclei.

The effects of this were considered within the context of the reactor anomaly by Sonzogni *et al.* in [18]. The corrections stemming from the forbidden decays have been discussed in e.g. [19, 20] but actual microscopic calculations for the individual beta spectra contributing to the cumulative spectrum have been previously done only for three different nuclei [21]. However, uncertainties related to these approximations cannot be reliably quantified without considering the nuclear structure related corrections to the individual spectra which contribute to the cumulative antineutrino spectrum. Another problem adding to this issue is the observation that for some forbidden transitions the spectral shape uncertainties can be extremely large [22, 23].

The incongruity regarding the source experiments with GALLEX and SAGE relates also to the missing neutrino flux. This so-called gallium anomaly was first noticed [24–27] when comparing the source experiment results of GALLEX and SAGE to cross sections estimated by Bahcall [28]. These cross sections are based on the reduced Gamow–Teller transition probabilities (BGTs) and their upper limits, which were measured using a charge-exchange reaction in the 1980’s [29, 30]. While the ground-state-to-ground-state cross section is quite reliably known, there are vast uncertainties related to the excited state contributions. A further complication in the case of scattering to the first excited state at 175 keV relates to tensor contributions in the charge-exchange reactions, making the reliable determination of the BGT-values needed for the cross-section calculation incredibly difficult [31]. Another possible way to estimate the cross section and the uncertainties related to it would be a large-scale microscopic calculation. Though a shell-model calculation was performed in [31], significant truncations had to be made in order to compensate for the limited computational capacity in 1998.

The research papers included in this thesis aim to address the reactor antineutrino and gallium anomalies by providing updated values for the theoretical estimates. In order to address the reactor antineutrino anomaly, the spectral shapes of forbidden beta decays, their uncertainties and their effective operators as a way to cope with limitations in the theoretical calculations are investigated. Though the formalism for forbidden beta decays has been established decades ago [32], its application to the transitions relevant to the reactor antineutrino anomaly has been limited, as the large-scale calculations performed in this work have not been computationally feasible. This thesis also provides a new large scale estimate for the  $^{71}\text{Ga}$  cross section relevant for addressing the gallium anomaly.

# Chapter 2

## Theoretical Framework

This chapter provides an overview of the theoretical formalism necessary to describe the phenomena studied in this work. The nuclear structure calculations are described in section 2.1, the theory of forbidden beta decays and their beta spectra in 2.2, and neutrino-nucleus scattering in section 2.3. The treatment of beta decays follows the formalism of Behrens and Bühring [32] and neutrino-nucleus scattering the Donnelly–Walecka formalism [33].

### 2.1 Nuclear structure

The nuclear structure calculations needed for the description of the weak interaction processes considered in this work have been carried out using two nuclear models. Most of the calculations have been done using the interacting nuclear shell model (see e.g. [34]) while some odd- $A$  nuclei have been described using the microscopic quasiparticle-phonon model (MQPM) [35, 36]. The shell-model calculations of this work rely on effective Hamiltonians which have been fitted to specific model spaces. The advantage of the shell model is its popularity, which has resulted in a wide variety of such effective Hamiltonians ready to use in shell-model programs, such as NuShellX@MSU [37]. However, the shell model is mostly limited to nuclei near closed shells. This can be mainly attributed to the combinatorial nature of the model, due to which the computational burden grows as a factorial function of the number of valence particles, which can make describing some open-shell nuclei computationally too burdensome even for the largest computer clusters. For such open-shell nuclei it is not feasible to use particle-hole descriptions, but transforming the problem to a quasiparticle picture will lift the vast majority of the computational burden. For even- $A$  nuclei such models as the quasiparticle Tamm–Dancoff approximation (QTDA) and the quasiparticle random-phase

approximation (QRPA) are based on on this approach [38]. However, the open shell nuclei described in this work tend to be odd- $A$ , so a model capable of describing such nuclei, such as the microscopic quasiparticle-phonon model described in the next section, is needed.

### 2.1.1 Microscopic quasiparticle-phonon model (MQPM)

The microscopic quasiparticle-phonon model (MQPM) is based on a mean-field approach, where the nuclear many-body problem is transformed from  $A$  strongly interacting particles to weakly interacting quasiparticles, i.e. linear combinations of holes and particles, in a mean field which is created by the other  $A - 1$  nucleons in the nucleus. The states in the odd- $A$  nucleus are combinations of one-quasiparticle states and QRPA-phonons (both calculated in the neighboring even-even reference nucleus) coupled with quasiparticles to create three-quasiparticle-states. The Hamiltonian for the  $A$  fermions can be written in the occupation-number representation as [38]

$$H = \sum_{\alpha} \epsilon_{\alpha} c_{\alpha}^{\dagger} c_{\alpha} + \frac{1}{4} \sum_{\alpha\beta\gamma\delta} \bar{v}_{\alpha\beta\gamma\delta} c_{\alpha}^{\dagger} c_{\beta}^{\dagger} c_{\delta} c_{\gamma}, \quad (2.1)$$

where  $\bar{v}_{\alpha\beta\gamma\delta} = \langle \alpha\beta | v | \gamma\delta \rangle - \langle \alpha\beta | v | \delta\gamma \rangle$  is the antisymmetrized two-body matrix element, and  $c_i^{\dagger}$  and  $c_i$  are the creation and annihilation operators of the Hartree–Fock quasiparticles. The following expressions are simplified by adopting the notation introduced by Baranger [39]. In this notation the Latin letter  $a$  denotes the principal, orbital, and total angular momenta ( $n_a, l_a, j_a$ ), while the Greek letter  $\alpha$  includes the magnetic quantum number  $m_{\alpha}$  in addition to  $a$ .

The building blocks of the MQPM states are obtained by the Bardeen–Cooper–Schrieffer (BCS) theory [40] and the quasiparticle random-phase approximation (QRPA) [39]. The ground state of the even-even reference nucleus is approximated using BCS theory. Employing a Bogoliubov–Valatin transformation [41, 42]

$$a_{\alpha}^{\dagger} = u_a c_{\alpha}^{\dagger} + v_a \tilde{c}_{\alpha}, \quad (2.2)$$

$$\tilde{a}_{\alpha} = u_a \tilde{c}_{\alpha} - v_a c_{\alpha}^{\dagger}, \quad (2.3)$$

where  $\tilde{a}_{\alpha}$  is the time-reversed BCS-quasiparticle annihilation operator and  $a_{\alpha}^{\dagger}$  is the BCS-quasiparticle creation operator, we get the occupation and

vacancy amplitudes  $v_a$  and  $u_a$ . Following the transformation the Hamiltonian operator in Eq. (2.1) can be expressed in the form

$$H = H_{11} + H_{22} + H_{40} + H_{04} + H_{31} + H_{13}. \quad (2.4)$$

The number of BCS creation and annihilation operators are denoted by the indices [43]. When the ground-state energy is minimized, the two-quasiparticle terms vanish, which is why there are no  $H_{20}$  or  $H_{02}$  in Eq. (2.4).

In order to reproduce the semi-empirical pairing gaps, the monopole matrix elements of the two-body interaction are scaled by the so-called pairing-strength parameters  $g_{\text{pair}}^{(n)}$  and  $g_{\text{pair}}^{(p)}$ . The proton pairing gap  $\Delta_p$  and the neutron pairing gap  $\Delta_n$ , which appear in the BCS equations (see formulation in e.g. [38]), can be estimated using the simple three-point formulas [44, 45]

$$\Delta_p(A, Z) = \frac{1}{4}(-1)^{Z+1}[S_p(A+1, Z+1) - 2S_p(A, Z) + S_p(A-1, Z-1)], \quad (2.5)$$

$$\Delta_n(A, Z) = \frac{1}{4}(-1)^{A-Z+1}[S_n(A+1, Z) - 2S_n(A, Z) + S_n(A-1, Z)], \quad (2.6)$$

where  $S_n$  is the energy needed to separate a single neutron from the nucleus and  $S_p$  is the separation energy for protons.

The  $H_{22}$ ,  $H_{40}$ , and  $H_{04}$  terms of the Hamiltonian (2.4) relate to two-quasiparticle excitations. These excitations are described using quasiparticle random-phase approximation (QRPA) phonons of the neighboring even-even reference nucleus given by the QRPA-phonon creation operator

$$Q_\omega^\dagger = \sum_{a \leq a'} [X_{aa'}^\omega A_{aa'}^\dagger(J_\omega M) - Y_{aa'}^\omega \tilde{A}_{aa'}(J_\omega M)], \quad (2.7)$$

where  $\omega$  denotes the angular momentum  $J_\omega$ , parity  $\pi_\omega$ , and the index  $k_\omega$  which denotes the enumeration of the state with respect to other states with the same spin and parity. The quantity  $A_{aa'}^\dagger(J_\omega M) = \sqrt{1 + \delta_{aa'}}(-1)^J / (1 + \delta_{aa'}) [a_a^\dagger a_{a'}^\dagger]_{J_\omega}$  is the two-quasiparticle creation operator, and  $\tilde{A}_{aa'}(J_\omega M) = \sqrt{1 + \delta_{aa'}}(-1)^J / (1 + \delta_{aa'}) [\tilde{a}_a \tilde{a}_{a'}]_{J_\omega}$  is the corresponding annihilation operator. The diagonalization of the QRPA-matrix (see e.g. [38]) gives the forward-going amplitude  $X$  and the backward-going amplitude  $Y$ .

The MQPM basis states are constructed from the BCS-based one-quasiparticle states and three-quasiparticle states obtained by coupling QRPA-phonons with quasiparticles. The MQPM creation operator for the states in the odd- $A$  nucleus is defined by [36]

$$\Gamma_i^\dagger(jm) = \sum_n C_n^i a_{n jm}^\dagger + \sum_{a\omega} D_{a\omega}^i [a_a^\dagger Q_\omega^\dagger]_{jm}, \quad (2.8)$$

where  $C_n^i$  and  $D_{a\omega}^i$  are the amplitudes given by the MQPM matrix equation. Using equations-of-motion method [46] one ends up with the generalized eigenvalue problem [35]

$$\begin{pmatrix} A & B \\ B^T & A' \end{pmatrix} \begin{pmatrix} C^i \\ D^i \end{pmatrix} = \Omega_i \begin{pmatrix} 1 & 0 \\ 0 & N \end{pmatrix} \begin{pmatrix} C^i \\ D^i \end{pmatrix}, \quad (2.9)$$

where the sub-matrices  $A$ ,  $A'$ , and  $B$  are the matrix elements (for explicit expressions see [36]) of  $H_{11}$ ,  $H_{22}$ , and  $H_{31}$  of equation (2.4), respectively.

The overlap between a three-quasiparticle state and a one-quasiparticle state is identically zero, which results in the overlap matrix on the right-hand side of (2.9) being block-diagonal. For the one-quasiparticle states the overlap matrix is diagonal while for the three-quasiparticle states the overlap matrix  $N$  is non-diagonal. The resulting eigenvalue problem is non-Hermitian, and the basis set is usually over-complete and non-orthogonal.

In order to solve the MQPM eigenvalue problem (2.9), it needs to first be converted from a non-Hermitian eigenvalue problem to a Hermitian one by transforming it to an orthogonal basis and then solved by using diagonalization. To begin with, the eigenvalues of the matrix  $N$  are solved from the equation

$$\sum_j N_{ij} u_j^{(k)} = n_k u_i^{(k)}. \quad (2.10)$$

The emerging eigenvectors are then written using  $|i\rangle = \Gamma_i^\dagger |\text{QRPA}\rangle$  as a basis, in the form [36]

$$|\tilde{k}\rangle = \frac{1}{\sqrt{n_k}} \sum_i u_i^{(k)} |i\rangle. \quad (2.11)$$

The set of states  $|\tilde{k}\rangle$  with non-zero  $n_k$  form is both complete and orthonormal. Using this new set of states as a basis the MQPM Eq. (2.9) can be expressed as a symmetric and real eigenvalue problem

$$\sum_l \langle \tilde{k} | H | \tilde{l} \rangle g_l^{(n)} = \lambda_n g_k^{(n)}, \quad (2.12)$$

where

$$\langle \tilde{k} | H | \tilde{l} \rangle = \frac{1}{\sqrt{n_k n_l}} \sum_{ij} u_i^{(k)*} \langle i | H | j \rangle u_j^{(l)}. \quad (2.13)$$

The MQPM-based excitation spectrum of the nucleus  $^{87}\text{Sr}$  is given in Fig. 2.1 together with the experimental spectrum taken from [47] as an example.

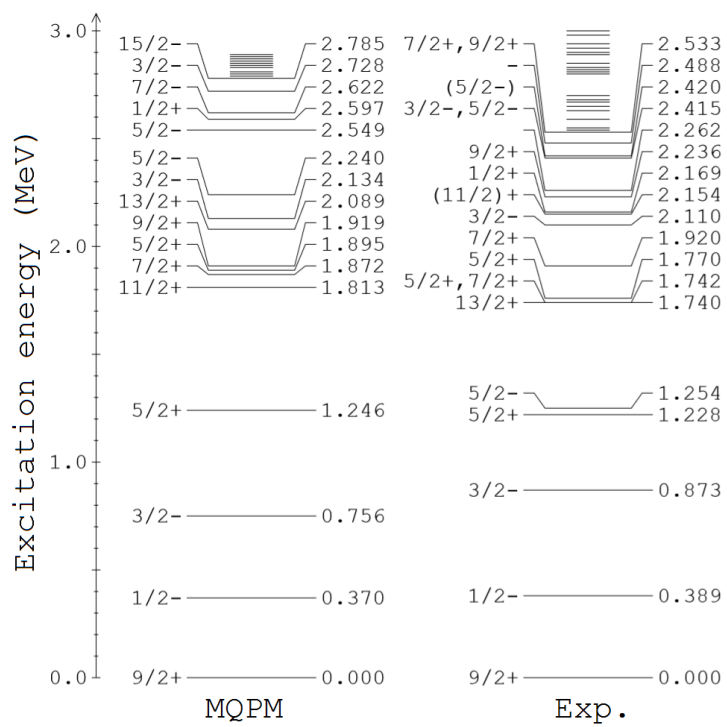


**Figure 2.1.** The experimental and MQPM-based theoretical excitation spectra for  $^{87}\text{Sr}$  (Originally published in [I]).

## 2.1.2 Model spaces and effective Hamiltonians

The shell-model calculations rely on effective Hamiltonians fitted for specific model spaces. For light nuclei, the model space usually consists of a single harmonic oscillator shell like the  $sd$ -shell or the  $fp$ -shell. For these limited model spaces a significant amount of experimental data is available and thus for these mass regions there are well-established Hamiltonians such as the USDB [48] for the  $sd$ -shell and GXPF1A [49, 50] for the  $fp$ -shell, which have been fitted to reproduce the excitation spectra and other observables.

The most important calculations in this work relate to beta decays of fission fragments and neutrino scattering off  $^{71}\text{Ga}$ . The fission fragments cluster around the mass numbers  $A \approx 95$  and  $A \approx 135$ . In order to describe first-forbidden transitions in the  $A \approx 95$  region, it would be preferable to include the proton orbitals  $0f-1p-0g_{9/2}$  and the neutron orbitals  $0g_{7/2}-1d-2s-0h_{11/2}$ . However, the computational burden for such a calculation would be beyond any modern machinery. For this reason, keeping the  $0f_{7/2}$  proton orbital full and the neutron orbitals  $0g_{7/2}$  and  $0h_{11/2}$  (which are above the  $1d$  and  $2s$  orbitals in this mass region) empty is necessary. In [51] multiple interactions were developed in slightly different model spaces to describe the decay of  $^{96}\text{Y}$ . In this work the interactions  $\text{glepn}$  and  $\text{glebpn}$  were used. The single-particle energies have been fitted specifically for the mass region while the two-body matrix elements have been generated from the G-matrix potential. The  $\text{glebpn}$  interaction is a bare G-matrix version, while  $\text{glepn}$  includes some manual adjustments. For the  $A \approx 135$  nuclei and the  $^{71}\text{Ga}$  case modern well-established Hamiltonians are available in model spaces including all the orbitals between the shell gaps.

The computational burden of MQPM calculations is substantially lower than that of the shell-model calculations, which permits the use of larger model spaces. In medium-heavy nuclei, a typical model space would include two major oscillator shells as well as the lowest orbitals from the next shell.

The single-particle states needed in the calculations of this work were calculated using a Coulomb-corrected Woods–Saxon potential with Bohr–Mottelson parametrization [52]. Minor modifications in the order of 1 MeV were done for some key orbitals based on the low-lying spectra of the odd- $A$  nuclei, since the lowest states are of dominantly one-quasiparticle type. The two-body matrix elements were generated from the Bonn one-boson-exchange potential applying  $G$ -matrix techniques [53]. The interaction matrix elements of the BCS-calculations were scaled to reproduce the phenomenological pairing gaps as described in section 2.1.1. Scaling constants were used in the QRPA-calculations for the multipoles  $0^+$ ,  $2^+$ , and  $4^+$  separately in order to reproduce the experimental excitation energies of states excluding known

two-quasiparticle states, which the MQPM is not able to describe.

While not a concern in the calculations regarding the anomalies, an obvious advantage of the MQPM approach over the shell model in relation to some of the transitions considered in this work is that pathological situations where some matrix elements are identically zero due to model-space restrictions do not emerge. However, the adjustments are done with the lowest states in mind, so the contributions from higher oscillator shells are unreliable at best. On the other hand, the MQPM could be used to estimate the magnitude of such matrix elements in the future.

## 2.2 Forbidden beta decays

Like the description of nuclear structure in section 2.1, the description of  $\beta$ -decay is complicated by the  $A$  strongly interacting fermions involved. In order to move forward with this problem, it is assumed that when the decay happens, the nucleus undergoing the decay interacts via the weak interaction only. The other  $A - 1$  nucleons are assumed to not be involved in the process. This simplification is referred to as the impulse approximation. In this approximation the leptonic and hadronic currents (the flow lines of the nucleons and emitted leptons) interact at a weak interaction vertex. The formalism presented here is for  $\beta^-$ -decays since these are the relevant decays for the reactor antineutrino anomaly. The formalism can be used for  $\beta^+$ -decays with some minor changes outlined in [32].

### 2.2.1 Renormalization of the axial-vector current

Due to the large mass of the vector boson  $W^-$  it propagates only a short distance compared to the size of the nucleus. The propagation distance is so short that the vertex can be thought of as being point-like with an effective coupling constant  $G_F$ , the Fermi constant. At the quark level the hadronic current can be described as a mixture of axial-vector and vector components [54–56]

$$J_H^\mu = \bar{u}(x)\gamma^\mu(1 - \gamma_5)d(x), \quad (2.14)$$

where  $\gamma^\mu$  and  $\gamma_5$  are the Dirac matrices. The strong interaction leads to some renormalization effects, which need to be considered when we move from quarks to nucleons. For protons ( $p$ ) and neutrons ( $n$ ) the hadronic current becomes [57]

$$J_H^\mu = \bar{p}(x)\gamma^\mu(g_V - g_A\gamma_5)n(x), \quad (2.15)$$

**Table 2.1.** Classification of forbidden beta decays based on the difference in parity  $\pi_i\pi_f$  and angular momentum  $\Delta J$  between the initial and final nuclei.  $K$  denotes the degree to which the transition is forbidden. Transitions for which  $\Delta J = K + 1$  are known as unique, while the rest of the decays are non-unique.

$K$	1	2	3	4	5
$\Delta J$	0,1,2	2,3	3,4	4,5	5,6
$\pi_i\pi_f$	-1	+1	-1	+1	-1

where  $g_V$  is the weak vector coupling constant and  $g_A$  is the weak axial-vector coupling constant. For a free nucleon the values  $g_V = 1.0$  and  $g_A = 1.27$  are given by the conserved vector-current hypothesis (CVC) and the partially conserved axial-vector-current hypothesis (PCAC) [58]. However, the value of  $g_A$  is affected by many-nucleon correlations within nuclear matter, so for calculations in nuclei consisting of multiple nucleons the use of the free nucleon values for the coupling constants might be problematic [38]. Especially when relying on nuclear structure calculations done in small model spaces, severe quenching of the axial-vector coupling constant seems to be necessary to reproduce experimental results [59]. In the phenomenological vector-minus-axial-vector theory ( $V - A$ ) of  $\beta$ -decay the Hamiltonian density can be written as

$$H_\beta(x) = -\frac{G_F}{\sqrt{2}}[\bar{p}(x)\gamma^\mu(g_V - g_A\gamma_5)n(x)\bar{e}(x)\gamma^\mu(1 - \gamma_5)\nu(x) + \text{h.c.}]. \quad (2.16)$$

## 2.2.2 Beta decay half-life and electron spectrum

In  $\beta^-$ -decay, the probability that the electron is emitted with energy (including rest mass) between  $W_e$  and  $W_e + dW_e$  is

$$P(W_e)dW_e = \frac{G_F}{(\hbar c)^6} \frac{1}{2\pi^3\hbar} C(W_e) \times p_e c W_e (W_0 - W_e)^2 F_0(Z, W_e) K(W_e) dW_e, \quad (2.17)$$

where  $Z$  is the proton number of the final nucleus,  $p_e$  is the momentum of the electron,  $F_0(Z, W_e)$  is the Fermi function,  $K(W_e)$  includes all the various corrections, such as finite-size corrections and atomic screening, and  $W_0$  is the end-point energy of the electron spectrum. The nuclear structure details are contained in the shape factor  $C(w_e)$ . Integrating over the possible kinetic energies gives the  $\beta$ -decay half-life, which is given by

$$t_{1/2} = \frac{\kappa}{\bar{C}}, \quad (2.18)$$

where  $\tilde{C}$  is the integrated shape function and the constant  $\kappa$  has the value [60]

$$\kappa = \frac{2\pi^3 \hbar^7 \ln 2}{m_e^5 c^4 (G_F \cos \theta_C)^2} = 6289 \text{ s}, \quad (2.19)$$

where  $\theta_C \approx 13.04^\circ$  is the Cabibbo angle. For describing  $\beta$ -decays it is convenient to work with units where  $m_e = 1$  by introducing unitless kinematic quantities  $w_0 = W_0/m_e c^2$ ,  $w_e = W_e/m_e c^2$ , and  $p = p_e c/(m_e c^2) = \sqrt{w_e^2 - 1}$ . The integrated shape factor in the denominator of Eq. (2.18) can be expressed in these quantities as

$$\tilde{C} = \int_1^{w_0} C(w_e) p w_e (w_0 - w_e)^2 F_0(Z, w_e) dw_e. \quad (2.20)$$

In Eq. (2.20) the kinematic factors are universal and the nuclear structure dependent part is included in  $C(w_e)$ .

The shape factor is obtained by doing a multipole expansion of the  $V - A$  hadronic current resulting in a complicated expression including momentum-dependent *form factors* which are then expanded as power series (see [32] for details). The shape factor can be then written as

$$C(w_e) = \sum_{k_e, k_\nu, K} \lambda_{k_e} \left[ M_K(k_e, k_\nu)^2 + m_K(k_e, k_\nu)^2 - \frac{2\gamma_{k_e} \mu_{k_e}}{k_e w_e} M_K(k_e, k_\nu) m_K(k_e, k_\nu) \right], \quad (2.21)$$

where  $k_\nu$  and  $k_e$  (with values 1,2,3,...) are related to the partial-wave expansion of the electron and neutrino wave functions,  $\mu_{k_e} \approx 1$ ,  $\gamma_{k_e} = \sqrt{k_e^2 - (\alpha Z)^2}$ , and  $\lambda_{k_e} = F_{k_e-1}(Z, w_e)/F_0(Z, w_e)$  is the Coulomb function and  $F_{k_e-1}(Z, w_e)$  is the so-called generalized Fermi function. The terms with a large change in angular momentum are heavily suppressed, and thus only the terms with  $k_e + k_\nu = K + 1$  and  $k_e + k_\nu = K + 2$  are relevant. The explicit expressions for the quantities  $m_K(k_e, k_\nu)$  and  $M_K(k_e, k_\nu)$  are listed in e.g. [32]. These expressions include several form factors along with various kinematic quantities.

The form factors are linked to *nuclear matrix elements*  $\mathcal{M}_{KLs}^{(N)}$  in the impulse approximation by

$$R^{LV} F_{KLs}^{(N)} = (-1)^{K-L} g_V^V \mathcal{M}_{KLs}^{(N)} \quad (2.22)$$

$$R^{LA} F_{KLs}^{(N)} = (-1)^{K-L+1} g_A^V \mathcal{M}_{KLs}^{(N)}, \quad (2.23)$$

**Table 2.2.** The leading-order matrix elements in  $K$ th forbidden decays. The matrix elements  ${}^A\mathcal{M}_{000}^{(0)}$  and  ${}^A\mathcal{M}_{011}^{(0)}$  are non-zero only for first-forbidden decays with  $\Delta J = 0$ . For unique transitions only the matrix element  ${}^A\mathcal{M}_{K+1,K,1}^{(0)}$  is non-zero simplifying the formalism greatly.

${}^A\mathcal{M}_{000}^{(0)}$	Axial-charge, enhanced by mesonic currents
${}^A\mathcal{M}_{011}^{(0)}$	–
${}^V\mathcal{M}_{K,K-1,1}^{(0)}$	Small relativistic NMEs, related to ${}^VM_{KK0}^{(0)}$ by CVC
${}^V\mathcal{M}_{KK0}^{(0)}$	–
${}^A\mathcal{M}_{KK1}^{(0)}$	Can cancel out with ${}^VM_{KK0}^{(0)}$ leading to different spectral shapes
${}^A\mathcal{M}_{K+1,K,1}^{(0)}$	Unique decay NME

where  $R$  is the nuclear radius, and the sign convention is the one used in e.g. [23]. The nuclear matrix elements can be evaluated using the relation

$${}^{V/A}\mathcal{M}_{KLS}^{(N)} = \frac{\sqrt{4\pi}}{\hat{J}_i} \sum_{pn} {}^{V/A}m_{KLS}^{(N)}(pn) (\Psi_f || [c_p^\dagger \tilde{c}_n]_K || \Psi_i), \quad (2.24)$$

where  ${}^{V/A}m_{KLS}^{(N)}(pn)$  is the single-particle matrix element corresponding to the proton orbital  $p$  and neutron orbital  $n$ , and  $(\Psi_f || [c_p^\dagger \tilde{c}_n]_K || \Psi_i)$  is the one-body transition density (OBTD), in which the nuclear structure information relevant for the transition is encoded. The choice of nuclear model enters the calculation through the evaluation of the OBTDs. For  $K$ th-forbidden beta decays the most important nuclear matrix elements are given in Table 2.2. In addition to these, there also appear multiple Coulomb-corrected versions of these matrix elements in the shape-factor expression as well. When next-to-leading-order terms are also included in the expressions, even more matrix elements are needed. However, these other matrix elements are suppressed by various small factors [23].

After combining some terms, the shape factor can be decomposed as

$$C(w_e) = g_V^2 C_V(w_e) + g_A^2 C_A(w_e) + g_V g_A C_{VA}(w_e). \quad (2.25)$$

It is well established that for weak interaction phenomena shortcomings in nuclear structure calculations can be corrected for to some degree by quenching the axial-vector coupling constant  $g_A$ . For forbidden spectra the ratio  $g_A/g_V$  affects the spectral shape, since the terms  $C_i(w_e)$  in Eq. (2.25) are all different functions of electron energy. However, the spectral shapes of pure rank-0 transitions, which are transitions between a  $0^+$  and a  $0^-$ -state, as well as unique transitions in the leading order, correspond to pure axial-vector transitions and thus do not depend on the coupling constants.

For transitions with  $\Delta J = 0$  the mesonic enhancement of the  $\gamma_5$  matrix element does play a role in determining the spectral shape. The enhancement is due to nuclear medium effects mediated by meson-exchange currents, as was first suggested in [61–63]. The  $\gamma_5$  matrix element is expected to be enhanced by 40–70% with respect to the value given by the impulse approximation. There are fundamental reasons for the enhancement, and the existence of the enhancement was first argued based on chiral-symmetry and soft-pion theorems [64, 65].

The spectral-shape dependence on the adopted ratio of  $g_A/g_V$  can be significant if the matrix elements  ${}^A\mathcal{M}_{KK1}^{(0)}$  and  ${}^V\mathcal{M}_{KK0}^{(0)}$  are roughly the same size and have opposite signs so that, depending on the ratio  $g_A/g_V$ , the cancellation can be close to perfect or less significant. When the cancellation is close to perfect, various small terms start dominating, resulting in a myriad of different spectral shapes.

## 2.3 Neutrino-nucleus scattering

In this section the streamlined version of the formalism related to calculating cross sections for charged-current neutrino-nucleus scattering is given. Further details of the formalism are given in e.g. [66, 67].

The main interest here are solar and other low-energy neutrinos which interact with nuclei, resulting in an emission of an electron

$$\nu_e + (A, Z) \rightarrow (A, Z + 1) + e^-, \quad (2.26)$$

where the final state can be either the ground state or an excited state in the final nucleus. For low-energy neutrinos ( $E_\nu < 50$  MeV) the neutrino energies are too low for the creation of lepton flavors  $\mu$  and  $\tau$ . The CC neutrino scattering is an inverse process to the electron capture in the daughter nucleus

$$(A, Z + 1) + e^- \rightarrow \nu_e + (A, Z). \quad (2.27)$$

Due to this symmetry, the ground-state-to-ground-state cross section can be related to the half-life of the  $(A, Z + 1)$ -nucleus. Thus, the ground-state-to-ground-state cross section is well known in cases where the electron capture proceeds to the ground state.

The four-momentum transfer in the transitions considered here is much smaller than the mass of the exchanged gauge boson  $W^\pm$ , that is,  $Q^2 = -q_\mu q^\mu \ll M_{W^\pm}^2$ . Therefore, scattering can be considered in the lowest order as a point-like vertex with a coupling constant  $G = G_F \cos(\theta_C)$ , analogously to the treatment of beta decays in the previous section. As in beta decay, the

matrix element of the effective Hamiltonian can be written as a product of the leptonic and hadronic currents

$$\langle f | H_{\text{eff}} | i \rangle = \frac{G}{\sqrt{2}} \int d^3 \mathbf{r} l_\mu e^{-\mathbf{q} \cdot \mathbf{r}} \langle f | \mathcal{J}^\mu(\mathbf{r}) | i \rangle, \quad (2.28)$$

where  $l_\mu = e^{\mathbf{q} \cdot \mathbf{r}} \langle l | j_\mu(r) | \nu \rangle$  and  $\mathcal{J}^\mu$  denotes the hadronic current [66].

When we assume that the initial and final nuclear states have well-defined spin-parities  $J_f^{\pi_f}$ , the double-differential cross section for the charged-current neutrino-nucleus scattering is given by [66, 68, 69]

$$\begin{aligned} \left[ \frac{d^2 \sigma_{i \rightarrow f}}{d\Omega dE_{\text{exc}}} \right] &= \frac{G^2 |\mathbf{k}_{e^-} | E_{e^-}}{\pi(2J_i + 1)} F(Z_f, E_{\mathbf{k}_{e^-}}) \\ &\times \left( \sum_{J \geq 0} \sigma_{\text{CL}}^J + \sum_{J \geq 1} \sigma_{\text{T}}^J \right), \end{aligned} \quad (2.29)$$

where  $E_{e^-}$  and  $\mathbf{k}_{e^-}$  are the energy and the three-momentum of the outgoing electron, respectively, and  $F(Z_f, E_{\mathbf{k}_{e^-}})$  is the Fermi function. The two quantities  $\sigma_{\text{CL}}^J$  and  $\sigma_{\text{T}}^J$  are the Coulomb-longitudinal and the transverse components where the Coulomb-longitudinal component is

$$\begin{aligned} \sigma_{\text{CL}}^J &= (1 + a \cos \theta) |(J_f | | \mathcal{M}_J(q) | | J_i \rangle|^2 \\ &\quad + (1 + a \cos \theta - 2b \sin^2 \theta) |(J_f | | \mathcal{L}_J(q) | | J_i \rangle|^2 \\ &\quad + \frac{E_{\mathbf{k}} - E_{\mathbf{k}'}}{q} (1 + a \cos \theta + c) \\ &\quad \times 2\text{Re}[(J_f | | \mathcal{M}_J(q) | | J_i \rangle)^* (J_f | | \mathcal{L}_J(q) | | J_i \rangle)], \end{aligned} \quad (2.30)$$

and the transverse component is

$$\begin{aligned} \sigma_{\text{T}}^J &= (1 - a \cos \theta + b \sin^2 \theta) \\ &\quad \times [|(J_f | | \mathcal{T}_J^{\text{mag}}(q) | | J_i \rangle|^2 + |(J_f | | \mathcal{T}_J^{\text{el}}(q) | | J_i \rangle|^2] \\ &\quad - \frac{E_{\mathbf{k}} - E_{\mathbf{k}'}}{q} (1 - a \cos \theta - c) \\ &\quad \times 2\text{Re}[(J_f | | \mathcal{T}_J^{\text{mag}}(q) | | J_i \rangle) (J_f | | \mathcal{T}_J^{\text{el}}(q) | | J_i \rangle)^*]. \end{aligned} \quad (2.31)$$

The quantities  $E_{\mathbf{k}}$  and  $E_{\mathbf{k}'}$  refer to the energies of the incoming and outgoing leptons. In Eqs. (2.30) and (2.31) the following shorthand notation is adopted:

$$a = \sqrt{1 - \frac{m_f^2}{E_{\mathbf{k}'^2}}}, \quad (2.32)$$

$$b = \frac{a^2 E_{\mathbf{k}} E_{\mathbf{k}'}}{q^2}, \quad (2.33)$$

$$c = \frac{n_f^2}{q E_{\mathbf{k}'}} \quad (2.34)$$

where  $m_f$  is the rest mass of the outgoing lepton (in this case an electron) and the magnitude of the three-momentum transfer  $q$  is given by

$$q = |\mathbf{q}| = \sqrt{(E_{\mathbf{k}} - aE_{\mathbf{k}'})^2 + 2aE_{\mathbf{k}}E_{\mathbf{k}'}(1 - \cos\theta)}. \quad (2.35)$$

The definitions of the operators  $\mathcal{T}_{JM}^{\text{el}}$ ,  $\mathcal{T}_{JM}^{\text{mag}}$ ,  $\mathcal{M}_{JM}$ , and  $\mathcal{L}_{JM}$  are given in [67]. As in beta decay, the operator contains axial-vector and vector components which include nuclear form factors  $F_{1,2}^{\text{V}}$  (vector),  $F^{\text{A}}$  (axial-vector), and  $F^{\text{P}}$  (pseudoscalar). Fermi and Gamow–Teller-type transitions, which proceed via the operators  $F^{\text{V}}(q)j_0(qr)\mathbf{1}$  and  $F^{\text{A}}(q)j_0(qr)\boldsymbol{\sigma}$  respectively, are dominant at energies considered in this work [66]. However, spin-dipole type transitions mediated by the operator  $F^{\text{A}}(q)[j_1(qr)\mathbf{Y}_1\boldsymbol{\sigma}]_{0-,1-,2-}$  also play a role for e.g. supernova neutrinos and cases where transitions to the low-lying states cannot proceed via a Fermi or a Gamow–Teller-type transition.

The final-state interactions can be taken into account with the modified effective-momentum approximation (MEMA) of [70], in which the effective momentum inside the nucleus is

$$k_{\text{eff}} = \sqrt{E_{\text{eff}} - m_e^2}, \quad (2.36)$$

where  $m_e$  is the electron mass and  $E_{\text{eff}}$  is defined as

$$E_{\text{eff}} = E_{\mathbf{k}'} - V_{\text{C}}(0). \quad (2.37)$$

The quantity  $V_{\text{C}}(0)$  denotes the Coulomb potential produced by the final-state nucleus at the origin. In the approximation the Fermi function is used for small values of  $k_{\text{eff}}$  but for large  $k_{\text{eff}}$  the Fermi function is omitted in Eq. (2.29) and the three-momentum and the energy of the outgoing lepton are replaced by  $k_{\text{eff}}$  and  $E_{\text{eff}}$ .



# Chapter 3

## Results and Discussion

The results from the publications are summarized in this chapter. In Section 3.1 the results regarding the shapes of beta spectra are presented. Firstly, theoretical results regarding the influence of the adopted  $g_A/g_V$ -ratio, mesonic enhancement of the axial-charge matrix element, and applying symmetries related to the conserved vector current hypothesis (CVC) on the spectral shape are discussed. Nuclear structure corrections in unique decays are also considered. The theoretical considerations are followed by comparisons between the predicted theoretical spectra and the experimental results from COBRA and EXO-200. Finally, the formalism is applied to the cumulative beta spectrum from fission products in order to study the implications to the reactor antineutrino anomaly.

In Section 3.2 the results regarding the neutrino-nucleus scattering calculations in the shell-model framework are presented. Firstly, the formalism is applied to the neutrino-nucleus scattering off  $^{40}\text{Ca}$  to reassess background in dark-matter experiments. Next, solar neutrino scattering off  $^{205}\text{Tl}$  is studied. The long half-life of the final nucleus  $^{205}\text{Pb}$  makes it a prime candidate for radiochemical experiments. Finally, calculations are presented for source experiments with  $^{51}\text{Cr}$  and  $^{37}\text{Ar}$  neutrinos scattering off  $^{71}\text{Ga}$ . The gallium anomaly and its statistical significance are reevaluated using the new theoretical estimates for the cross sections.

### 3.1 Forbidden decays and the spectral shape

High-precision description of forbidden beta decays has two important applications to new physics searches. Firstly, high-precision description of the spectral shape is needed in order to characterize background radiation in

rare-event searches, such as dark matter detection experiments. Secondly, detecting new physics in reactor experiments requires a good understanding of the antineutrino spectrum emitted from fission products as they  $\beta^-$ -decay towards stability. A large proportion of these decays are first-forbidden non-unique, and thus nuclear structure plays a crucial role in determining the spectral shape.

### 3.1.1 Weak coupling constants and the spectral shape

Quenching the value of the axial-vector coupling constant seems to be necessary for Gamow–Teller as well as first-forbidden unique decays in order to get a good agreement between experimental and theoretical half-lives [59]. For first-forbidden non-unique decays, quenching both the axial-vector coupling constant  $g_A$  and the vector coupling constant  $g_V$  has been used to account for core-polarization effects [71, 72]. However, it was first pointed out in [22] that the spectral shape can depend drastically on the ratio of the weak coupling constants used. Thus, for the prediction of spectral shapes it is crucial to understand whether both of the coupling constants need to be quenched the same amount, or whether the optimal renormalization differs for the two coupling constants. In addition, the renormalization could also depend on the particular transition and nuclear model involved.

The first papers regarding the  $g_A/g_V$ -dependence by Haaranen *et al.* [22, 23] limited the study to two transitions: the fourth-forbidden non-unique decays of  $^{113}\text{Cd}$  and  $^{115}\text{In}$ . These two transitions exhibited extreme dependence on the  $g_A/g_V$ -ratio. The dependence was also discovered to be largely independent of the adopted nuclear model.

As a first part of this thesis work, investigations were carried out in order to understand whether this type of dependence is common or not, and whether it is specific to fourth-forbidden decays. In the article [I] 26 transitions were investigated using the MQPM, and in [II] 16 transitions were studied in the shell model. The extreme  $g_A/g_V$ -dependence also manifested itself for some second-forbidden and third-forbidden transitions. In [V] the first-forbidden decay of  $^{210}\text{Bi}$  was discovered to also exhibit such  $g_A/g_V$ -dependence.

As an example of the results in [I, II] Fig. 3.1 shows the spectra of four transitions with both the MQPM and shell-model one-body transition densities. For all transitions the agreement between the MQPM and the shell model is quite remarkable, even though the half-life predictions seemed to be quite different (i.e. the absolute value of  $g_A$  and  $g_V$ ). Both the decay of  $^{99}\text{Tc}$  and the decay of  $^{137}\text{Cs}$  to the  $3/2^+$  ground state in barium are second-forbidden non-unique transitions, but only the  $^{99}\text{Tc}$  spectral shape depends remarkably on the coupling constants. A decay such as  $^{99}\text{Tc}$  would be a good candidate

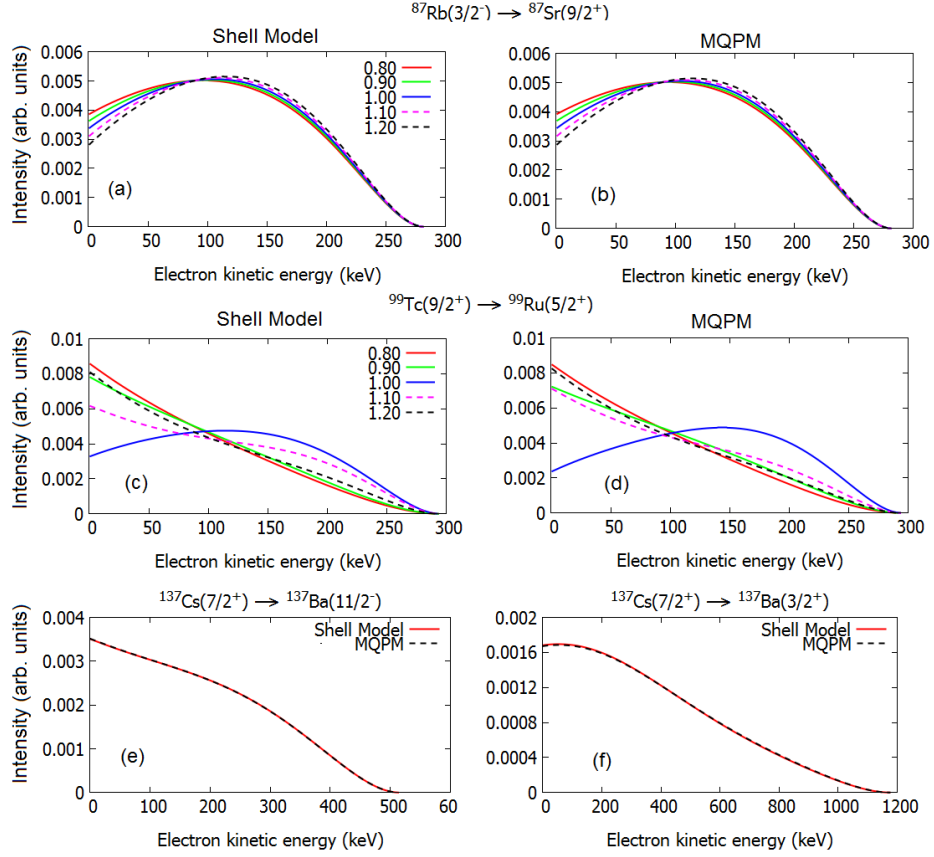


**Figure 3.1.** The shell-model and MQPM spectra for the ground-state-to-ground-state decays of  $^{87}\text{Rb}$ ,  $^{99}\text{Tc}$ , and  $^{137}\text{Cs}$ , and the decay of  $^{137}\text{Cs}$  to the isomeric  $11/2^-$  state in  $^{137}\text{Ba}$ . For  $^{87}\text{Rb}$  and  $^{99}\text{Tc}$  the color signifies the value of  $g_A/g_V$ . For  $^{137}\text{Cs}$  the spectra are  $g_A$ -independent (the variation is less than the line thickness), and the color signifies the microscopic model adopted (Originally published in [I]).

for the so-called spectrum-shape method [22], where the experimental and theoretical spectra are compared to probe the appropriate quenching factors for the nuclear model, which could then be used in predicting similar spectra with no experimental data. A transition such as the decay of  $^{137}\text{Cs}$  with  $g_A/g_V$ -dependence so small that it could not be seen with the resolution of Fig. 3.1, could be used to check the validity of the formalism. A poor match between the experimental and theoretical results would indicate that the shape-factor calculation needs to be done to a higher accuracy or that corrections, such as finite size and atomic exchange-effects, should be included to a higher precision.

### 3.1.2 Unique decays

The spectral shapes of unique decays are usually considered to be well understood, since in the first-order approximation the shape is determined purely by kinematics. However, when searching for rare events or evaluating anomalies, higher-order corrections come into play. In [III] the spectral shapes of  $^{39,42}\text{Ar}$  were calculated to estimate the magnitude of the nuclear structure corrections for background radiation in liquid-argon (LAr) experiments DarkSide-50 [73] and DEAP-3600 [74]. The low-energy end of the  $^{39}\text{Ar}$  electron spectrum shown in Fig. 3.2 is expected to be reduced by approximately 1 % due to next-to-leading-order corrections. The uncertainty related to the correction can be estimated by the difference in the MQPM and shell-model calculations and is of the order 0.5 %. Thus, signals of this magnitude could go unnoticed if the first-order approximation is used.

### 3.1.3 Mesonic enhancement in pseudoscalar transitions

The effects of the mesonic enhancement of the  $\gamma_5$  matrix element on the spectral shape of  $J^+ \leftrightarrow J^-$  decays was studied in [VI]. These transitions are major contributors to the cumulative beta spectrum from nuclear reactors. The mesonic enhancement is known to be approximately 40–100 % [61]. However, the exact amount is not well understood.

The half-life results from [VI] are listed in Tables 3.1 and 3.2. Based on the half-life considerations a reasonable half-life agreement can be found for any level of mesonic enhancement if the value of  $g_A$  is quenched enough. Based on these considerations there is no clear evidence for a single preferred value. Furthermore, the choice of the mesonic enhancement factor  $\epsilon_{\text{MEC}}$  can effect the shape of some spectra by several per cent as can be seen for  $^{93}\text{Y}$  in Fig. 3.3. The clear trend here is that larger values of mesonic enhancement require a larger quenching of  $g_A$ . From tables 3.1 and 3.2 one can also extrapolate

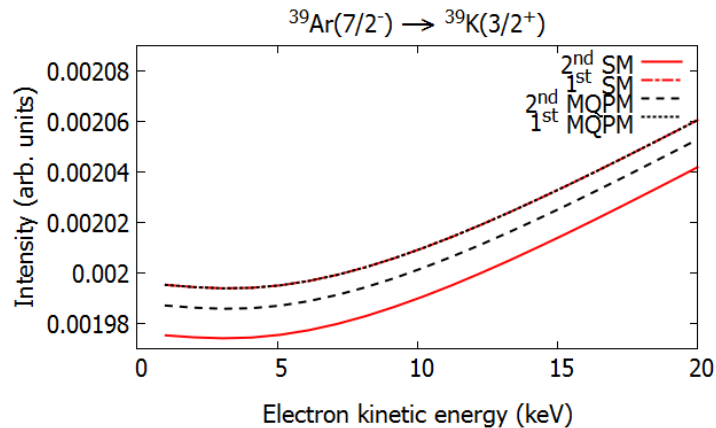


**Figure 3.2.** The electron spectrum of  $^{39}\text{Ar}$  in the low-energy range 0–20 MeV calculated using the nuclear shell model and the MQPM with just the first-order terms (1st) and with the second-order terms included (2nd). (Originally published in [III])

that there is a solution with  $\epsilon_{\text{MEC}} = 1.0$  and  $g_A \approx 1.0$ , which would agree with the experimental data.

**Table 3.1.** The shell-model based effective values of  $g_A$  for various levels of enhancement of the  $\int \gamma_5$  (axial-charge) for decays between nuclei with  $A=92$ –97. The initial nucleus is listed in the first column and the  $g_A$ -values needed to match the experimental half-life with  $g_V = 1.0$  are listed in columns 2–4 for different enhancement factors  $\epsilon_{\text{MEC}}$ . (Originally published in [VI])

Nucleus	$g_A$ (Hamiltonian glbepn)		
	$\epsilon_{\text{mec}}=1.40$	1.70	2.00
$^{92}\text{Rb}$	0.74(1)	0.62(1)	0.53(1)
$^{93}\text{Y}$	1.25(15)	1.03(17)	0.85(30)
$^{95}\text{Sr}$	0.88(4)	0.70(4)	0.58(3)
$^{96}\text{Y}$	0.96(1)	0.80(1)	0.69(1)
$^{97}\text{Y}$	0.85(15)	0.70(13)	0.59(12)
Average	$0.94 \pm 0.08$	$0.77 \pm 0.07$	$0.65 \pm 0.06$

### 3.1.4 Matrix element ratios and the conserved vector current hypothesis

For  $K^{\text{th}}$ -forbidden non-unique contributions, the two main vector form factors can be related to each other based on the conserved vector current hypothesis

**Table 3.2.** The shell-model based effective values of  $g_A$  for various levels of enhancement of the  $\int \gamma_5$  (axial-charge) for decays between nuclei with  $A=133$ – $139$ . The initial nucleus is listed in the first column and  $g_A$  needed to match the experimental half-life with  $g_V = 1.0$  are listed in columns 2–7 for different enhancement factors  $\epsilon_{\text{MEC}}$ . (Originally published in [VI])

Nucleus	$g_A$ (Hamil. jj56cdb)			$g_A$ (Hamil. jj56pnb)		
	$\epsilon_{\text{mec}}=1.40$	1.70	2.00	1.40	1.70	2.00
$^{133}\text{Sn}$	0.94(2)	0.80(2)	0.69(2)	0.94(2)	0.80(2)	0.69(2)
$^{134}\text{Sb}$	1.18(6)	0.99(5)	0.85(5)	0.85(4)	0.71(4)	0.62(3)
$^{135}\text{Te}$	0.86(2)	0.74(3)	0.65(2)	0.96(3)	0.84(3)	0.74(3)
$^{137}\text{Xe}$	0.74(2)	0.65(2)	0.58(2)	0.81(3)	0.71(2)	0.64(3)
$^{139}\text{Ba}$	0.68(1)	0.60(1)	0.54(1)	0.72(1)	0.64(1)	0.58(1)
$^{139}\text{Cs}$	1.15(3)	1.00(2)	0.88(2)	0.91(2)	0.79(2)	0.69(2)
Average	$0.93 \pm 0.08$	$0.87 \pm 0.06$	$0.70 \pm 0.06$	$0.87 \pm 0.04$	$0.75 \pm 0.03$	$0.66 \pm 0.03$

(CVC) by [32]

$$\begin{aligned}
{}^V F_{K,K-1,1} &= - \frac{1}{\sqrt{K(2K+1)}} \left[ (W_0 - M_n + M_p)R + \frac{6\alpha Z}{5} \right] {}^V F_{KK0} \\
&= - \frac{1}{\sqrt{K(2K+1)}} \Delta_{T,T-1} R {}^V F_{KK0},
\end{aligned} \tag{3.1}$$

where  $M_n - M_p$  is the mass difference of a neutron and a proton,  $Z$  the proton number of the daughter nucleus,  $\alpha \approx 1/137$  the fine-structure constant,  $R$  the nuclear radius,  $W_0$  the end-point energy, and  $\Delta_{T,T-1}$  the excitation energy of the isobaric analogue state (IAS). However, it should be noted that applying this formula in the impulse approximation is problematic. While agreement between the exact calculation and the impulse approximation can be reached in e.g. the independent-particle model, in more involved nuclear models (like the shell model), with residual interactions included, the formula cannot be applied as such [32].

For some model spaces and degrees of forbiddenness  $K$  the small matrix element  ${}^V \mathcal{M}_{K,K-1,1}$  is identically zero, which happens for example in the  $sd$ -shell for second-forbidden non-unique decays. In [XIII] a new effective method for dealing with this problem in cases where the half-life is known and the spectral shape is of interest was proposed. In this new method  $g_A$  is kept at a value which is in agreement with other transitions nearby. For shell-model calculations in the  $sd$ -model space a good choice is  $g_A = 1$  [59]. In the spirit of the CVC an unquenched value of  $g_V$  is used. The small matrix element is then adjusted until agreement with the experimental half-life is found. An example of the application of this method is presented in figure

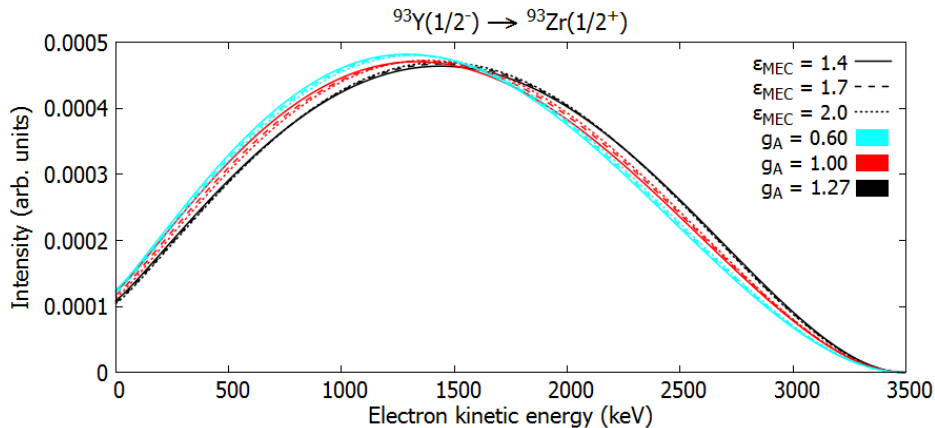


**Figure 3.3.** The shell-model based  $\beta$ -spectrum for  $^{93}\text{Y}$  obtained with the Hamiltonian glbepn. The color of the line denotes the effective value of  $g_A$  and the dash-coding signifies the mesonic enhancement  $\epsilon_{\text{MEC}}$ . (Originally published in [VI])

3.4. In this case leaving the matrix element  $^V\mathcal{M}_{211}$  as zero results in a major deviation from the experimental shape. Both the approximate expression (3.1) [75] and the new method are in good agreement with the experimental shape.

### 3.1.5 Comparison of theoretical and experimental spectra

In order to assess the quenching of the  $g_A/g_V$ -ratio in theoretical shell-model calculations for medium-heavy nuclei, a precision measurement of the decay of  $^{113}\text{Cd}$  was carried out with the COBRA-collaboration in [IX]. The experimental results and theoretical spectra for various values of the  $g_A/g_V$ -ratio are presented in Fig. 3.5. Best fit was found with  $g_A/g_V = 0.915 \pm 0.007$ , suggesting that a the quenching of  $g_A$  needs to be stronger than that of  $g_V$ .

Another comparison was done for  $^{137}\text{Xe}$  with the EXO-200-collaboration in [XIV]. The theoretical spectrum shape here is independent of the choice of  $g_A/g_V$  and  $\epsilon_{\text{MEC}}$  to about 1 % level. Thus, it makes for an excellent test for the validity of the application of the formalism, since the uncertainties in the theoretical prediction are tiny. The result of the comparison is shown in Fig. 3.6. The match is excellent, which is evidence of the good quality of the theoretical description.

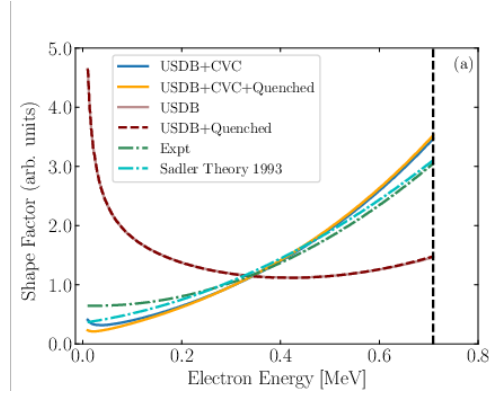


**Figure 3.4.** Comparison between the experimental and theoretical shape factors for the half-life based adjustments. The shape factor of Sadler is based in the approximate expression of Eq. (3.1) [75]. (Originally published in [XIII])

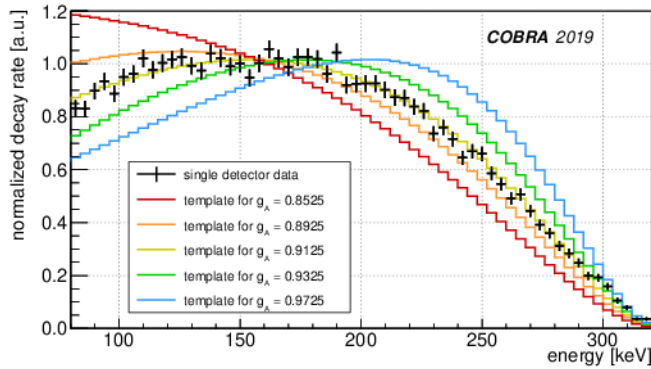


**Figure 3.5.** Comparison between a shell-model prediction and an experimental spectrum from one of the COBRA-detectors for  $^{113}\text{Cd}$ . (Originally published in [IX])

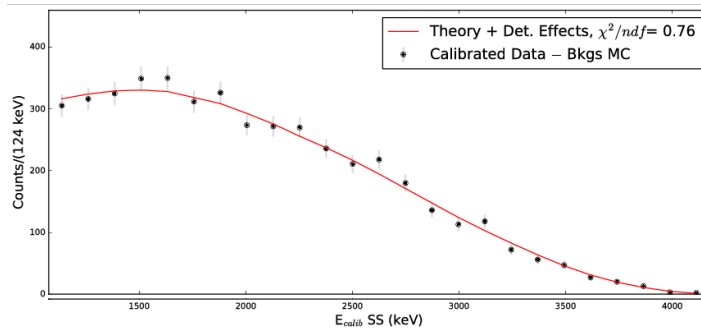


**Figure 3.6.** Comparison between theoretical and experimental electron spectra of  $^{137}\text{Xe}$ . (Originally published in [XIV])

### 3.1.6 Reactor antineutrino anomaly

Insights from the theoretical publications [I, II, III, VI] on spectral shapes were applied to the transitions relevant for the reactor antineutrino anomaly in [VII] and [VIII]. In total 36 first-forbidden transitions, listed in Table 3.3, were considered. The calculated shape factors are presented in Fig. 3.7. Most of the decays have shape factors which differ noticeably from the allowed shape, which corresponds to a straight line at unity. It also turns out that approximating the non-unique transitions as unique is an equally bad approximation. Therefore, previous estimates for the cumulative spectrum should be off as well. Based on the calculations there are some transitions with shape factors which very strongly deviate from the allowed one. For some decays, for example that of  $^{136}\text{Te}$ , the effective value of the  $g_A/g_V$ -ratio affects the shape, and thus the uncertainty related to this ratio must be considered.

#### Spectral shoulder and rate anomaly

In order to address the spectral shoulder, the spectral shape is considered with the overall normalization factor kept as a free parameter. In Fig. 3.8 the spectral shape changes related to different approximations are shown for three different nuclear reactors with slightly different fuel compositions.

Both the numerical and the parametrization-based approximations behave in a similar manner, with the deviation reaching a maximum of about 4 % with respect to the Huber–Mueller results. However, the total observed difference between the Huber–Muller and experimental results is twice the size of the theoretical deviation. Given the strongly-correlated nature of the theoretical errors with the nearby data points, the statistical significance of the spectral shoulder is decreased by the shell-model results. In the future, adding precise calculations for the allowed transitions contributing to the

**Table 3.3.** Dominant forbidden transitions above 4 MeV. Here  $Q_\beta$  is the ground-state-to-ground-state  $Q$ -value,  $E_{ex}$  the excitation energy of the daughter level, BR the branching ratio of the transition normalized to one decay, and FY is the cumulative fission yield of  $^{235}\text{U}$  from the ENDF database [76]. (Originally published in [VIII])

Nuclide	$Q_\beta$ (MeV)	$E_{ex}$ (MeV)	BR (%)	$J_i^\pi \rightarrow J_f^\pi$	FY (%)	$\Delta J$
$^{89}\text{Br}$	8.3	0	16	$3/2^- \rightarrow 3/2^+$	1.1	0
$^{90}\text{Rb}$	6.6	0	33	$0^- \rightarrow 0^+$	4.5	0
$^{91}\text{Kr}$	6.8	0.11	18	$5/2^+ \rightarrow 5/2^-$	3.5	0
$^{92}\text{Rb}$	8.1	0	95.2	$0^- \rightarrow 0^+$	4.8	0
$^{93}\text{Rb}$	7.5	0	35	$5/2^- \rightarrow 5/2^+$	3.5	0
$^{94}\text{Y}$	4.9	0.92	39.6	$2^- \rightarrow 2^+$	6.5	0
$^{95}\text{Rb}$	9.3	0.68	5.9	$5/2^- \rightarrow 5/2^+$	1.7	0
$^{95}\text{Sr}$	6.1	0	56	$1/2^+ \rightarrow 1/2^-$	5.3	0
$^{96}\text{Y}$	7.1	0	95.5	$0^- \rightarrow 0^+$	6.0	0
$^{97}\text{Y}$	6.8	0	40	$1/2^- \rightarrow 1/2^+$	4.9	0
$^{98}\text{Y}$	9.0	0	18	$0^- \rightarrow 0^+$	1.9	0
$^{133}\text{Sn}$	8.0	0	85	$7/2^- \rightarrow 7/2^+$	0.1	0
$^{135}\text{Te}$	5.9	0	62	$(7/2^-) \rightarrow 7/2^+$	3.3	0
$^{135}\text{Sb}$	8.1	0	47	$(7/2^+) \rightarrow (7/2^-)$	0.1	0
$^{136m}\text{I}$	7.5	1.89	71	$(6^-) \rightarrow 6^+$	1.3	0
$^{136m}\text{I}$	7.5	2.26	13.4	$(6^-) \rightarrow 6^+$	1.3	0
$^{137}\text{I}$	6.0	0	45.2	$7/2^+ \rightarrow 7/2^-$	3.1	0
$^{142}\text{Cs}$	7.3	0	56	$0^- \rightarrow 0^+$	2.7	0
$^{86}\text{Br}$	7.3	0	15	$(1^-) \rightarrow 0^+$	1.6	1
$^{86}\text{Br}$	7.3	1.6	13	$(1^-) \rightarrow 2^+$	1.6	1
$^{87}\text{Se}$	7.5	0	32	$3/2^+ \rightarrow 5/2^-$	0.8	1
$^{89}\text{Br}$	8.3	0.03	16	$3/2^- \rightarrow 5/2^+$	1.1	1
$^{91}\text{Kr}$	6.8	0	9	$5/2^+ \rightarrow 3/2^-$	3.4	1
$^{95}\text{Rb}^\dagger$	9.3	0.56	6.0	$5/2^- \rightarrow (7/2^+)$	1.7	1
$^{95}\text{Rb}$	9.3	0.68	5.9	$5/2^- \rightarrow 3/2^+$	1.7	1
$^{134m}\text{Sb}$	8.5	1.69	42	$(7^-) \rightarrow 6^+$	0.8	1
$^{134m}\text{Sb}$	8.5	2.40	54	$(7^-) \rightarrow (6^+)$	0.8	1
$^{136}\text{Te}$	5.1	0	8.7	$0^+ \rightarrow (1^-)$	3.7	1
$^{138}\text{I}$	8.0	0	26	$(1^-) \rightarrow 0^+$	1.5	1
$^{140}\text{Xe}$	4.0	0.08	8.7	$0^+ \rightarrow 1^-$	4.9	1
$^{140}\text{Cs}$	6.2	0	36	$1^- \rightarrow 0^+$	5.7	1
$^{143}\text{Cs}$	6.3	0	25	$3/2^+ \rightarrow 5/2^-$	1.5	1
$^{88}\text{Rb}$	5.3	0	76.5	$2^- \rightarrow 0^+$	3.6	2
$^{94}\text{Y}$	4.9	0	41	$2^- \rightarrow 0^+$	6.5	2
$^{95}\text{Rb}$	9.3	0	0.1	$5/2^- \rightarrow 1/2^+$	1.7	2
$^{139}\text{Xe}$	5.1	0	15	$3/2^- \rightarrow 7/2^+$	5.0	2

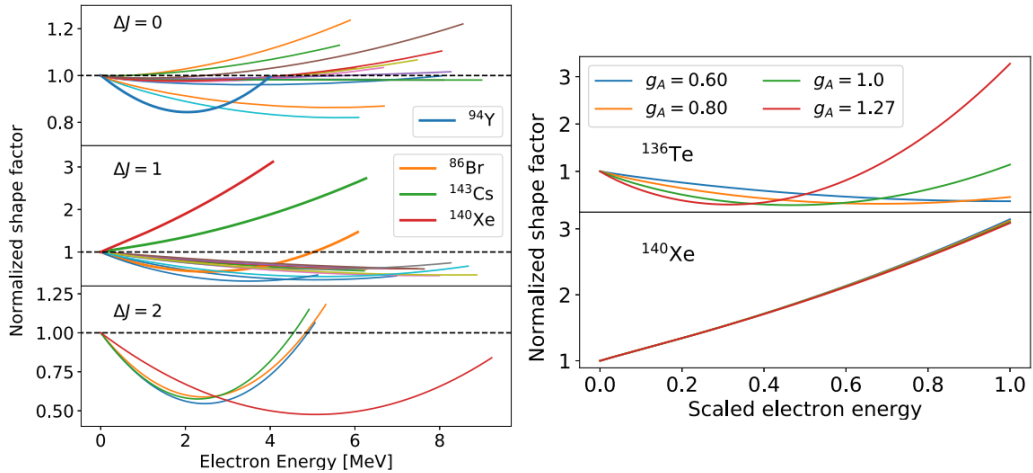


**Figure 3.7.** Left panel: shell-model-calculated shape factors for the 36 decays listed in Table 3.3 for each change in angular momentum  $\Delta J$ . The values  $g_A = 0.9$  and  $\epsilon_{\text{MEC}} = 1.4$  are assumed [VI, VII]. Right panel: shape factors for the previously considered  $^{136}\text{Te}$  (top) and  $^{140}\text{Xe}$  (bottom) for various values of  $g_A$ . (Originally published in [VIII])

5 MeV energy region might provide additional information regarding the spectral shoulder.

The additional uncertainty arising from the forbidden spectral shapes turns out to be significant compared to the sources of uncertainty considered in the previous analyses [15, 16]. This suggests that the theoretical uncertainties have been underestimated in analyses of the rate anomaly. The new calculations predict that the inverse-beta-decay rate should be 0.8(5)% higher for the three reactors considered here. When normalization uncertainties are included, the statistical significance remains unchanged as the estimate and the uncertainties increase in proportion (about 14%). From these results it is clear that the theoretical spectra need to be considered in their full complexity in order to make strong claims regarding the reactor antineutrino anomaly.

## 3.2 Neutrino-nucleus scattering

The second body of research in this thesis work is on neutrino-nucleus scattering, which provides an excellent probe to validate existing theories and to search for new phenomena related to neutrinos. In this thesis work neutrino-nucleus scattering off three isotopes,  $^{40}\text{Ar}$ ,  $^{71}\text{Ga}$ , and  $^{205}\text{Tl}$ , was considered. The reasons for studying these particular isotopes are manifold. For example, solar and supernova neutrino scattering off  $^{40}\text{Ar}$  are background in

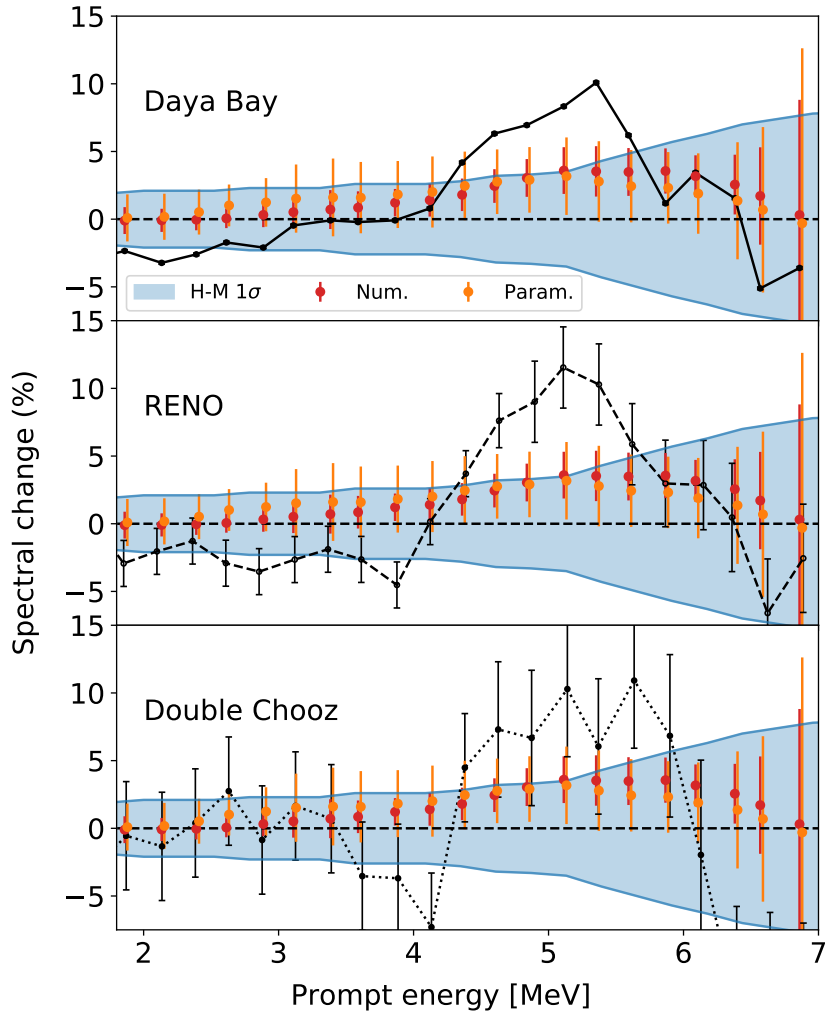


**Figure 3.8.** The expected shift in the spectral shape of three different reactors with the observed experimental results compared with the Huber–Mueller estimates. The red bars use the numerical shape factors and the orange bars include the parametrization of all forbidden decays. (Originally published in [VIII])

argon-based dark-matter searches.  $^{205}\text{Tl}$ , on the other hand, could be used to study the evolution of solar neutrino flux over millions of years through radiochemical investigations. The isotope  $^{71}\text{Ga}$  was used in the solar neutrino experiments GALLEX and SAGE, but deviations between theoretical predictions and experimental results in calibration experiments [3–6] need to be further investigated.

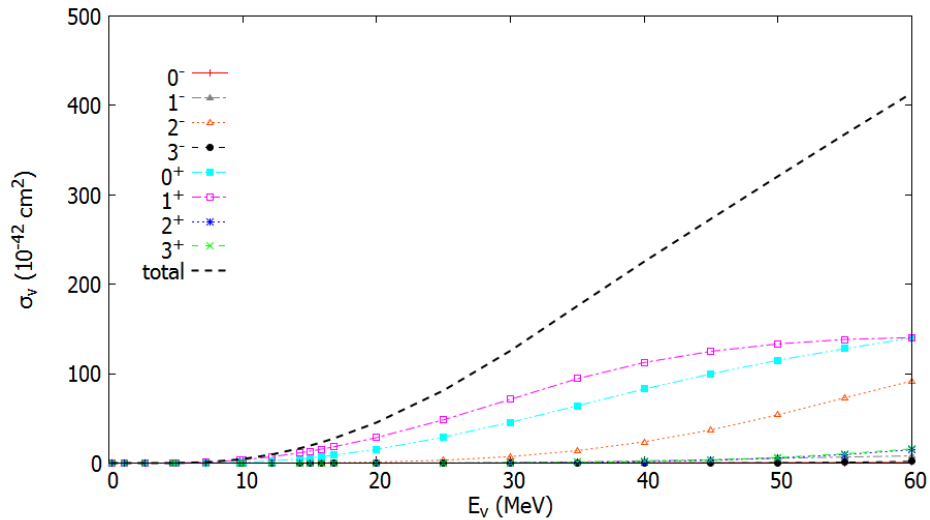


**Figure 3.9.** The scattering cross section for  $^{40}\text{Ar}(\nu, e^-)^{40}\text{K}$  as a function of neutrino energy for different multipoles. (Originally published in [IV])

### 3.2.1 Scattering off $^{40}\text{Ar}$

Dark matter could be potentially detected in an experiment in which a nucleus is hit by a dark-matter particle, and the recoil of the nucleus would be observed. One candidate nucleus for such an experiment is  $^{40}\text{Ar}$ , which is currently used in the large scale experiments DarkSide-50 [73] and DEAP-3600 [74].

The publication [IV] focused on cross-section determinations of  $^{40}\text{Ar}$  for neutrinos and antineutrinos with energies below 60 MeV. This energy region covers solar and supernova neutrinos as well as some atmospheric neutrinos. The discussion here is focused on neutrino reactions which dominate over the antineutrino ones. The reaction threshold for neutrino-nucleus scattering off  $^{40}\text{Ar}$  is 1.5044 MeV, and so the folded cross section is dominated by  $^8\text{B}$  neutrinos with small corrections coming from *hep* neutrinos and the high-energy end of CNO neutrinos. The flux of *hep* neutrinos is much smaller than that of the  $^8\text{B}$  neutrinos [77], and can thus be neglected in this context.

The cross section of the scattering  $^{40}\text{Ar}(\nu, e^-)^{40}\text{K}$  is given in Fig. 3.9 with multipole decomposition. The total cross section grows in a roughly quadratic way for low neutrino energies, but above 35 MeV the cross section seems to grow linearly. For the whole energy range considered here, the allowed transitions dominate, but the  $2^-$  transitions contribute in a non-trivial way above 30 MeV.

Above 50 MeV other multipoles play a role but the contributions are

relatively small, in the 1 % range. Based on the RPA-calculation performed in Ref. [78] the contribution of the multipole  $1^-$  should be similar to that of  $2^-$  below 60 MeV, which is not seen in the shell-model calculation. The linear energy dependency for energies above 35 MeV is an indication that the limited shell-model space is not able to predict the cross sections for the higher energies. However, the solar and supernova neutrino distributions considered here fall almost completely below 35 MeV.

For supernova neutrinos, the averaged cross section  $\langle\sigma\rangle$  can be calculated by folding the total cross section with the neutrino-energy distribution. Here we assume that supernova neutrinos follow a Fermi–Dirac distribution

$$F_{\text{FD}}(E_{\mathbf{k}}) = \frac{1}{F_2(\alpha_\nu)T_\nu} \frac{(E_{\mathbf{k}}/T_\nu)^2}{1 + \exp(E_{\mathbf{k}}/T_\nu - \alpha_\nu)}, \quad (3.2)$$

where  $\alpha_\nu$  is a pinching parameter and  $T_\nu$  is the effective neutrino temperature. The average neutrino energy can be related to the temperature and the pinching parameter by

$$\langle E_\nu \rangle / T_\nu = \frac{F_3(\alpha_\nu)}{F_2(\alpha_\nu)}, \quad (3.3)$$

where

$$F_k(\alpha_\nu) = \int \frac{x^k dx}{1 + \exp(x - \alpha_\nu)}. \quad (3.4)$$

In order to study the contributions from individual states, the normalized contributions are presented for the reaction  $^{40}\text{Ar}(\nu, e^-)^{40}\text{K}$  in Fig. 3.10. For solar neutrinos the cross section is dominated by the state  $1_3^+$  which accounts for half of the folded cross section. Other important states are  $1_6^+$ ,  $1_{10}^+$ ,  $1_{15}^+$ , and  $1_{17}^+$  and the IAS state  $0_2^+$ . For supernova neutrinos the results are similar, except that the domination of the state  $1_3^+$  is not as strong.

A ratio of 12.5 of supernova neutrinos to supernova antineutrinos was reported in Ref. [79] with no neutrino oscillations included and average neutrino energies of  $\langle E_\nu \rangle = 11$  MeV and  $\langle E_{\bar{\nu}} \rangle = 16$ . Taking the pinching parameter value  $\alpha = 0$  we find  $\sigma_\nu = 14.6 \times 10^{-42} \text{cm}^2$  and  $\sigma_{\bar{\nu}} = 887 \times 10^{-45} \text{cm}^2$ , assuming that the neutrino energies follow a Fermi–Dirac distribution. The shell-model-based ratio for neutrinos and antineutrinos is therefore 16.5, which is similar to the RPA-based result given of Ref. [79].

### 3.2.2 Scattering off $^{205}\text{Tl}$

Solar neutrinos are usually studied by real-time measurements (e.g. Super-Kamiokande, the Sudbury Neutrino Observatory (SNO), KamLAND, Borex-

**Table 3.4.** Parameter values for supernova neutrino energy distributions.  $\alpha$  is the pinching parameter,  $T$  is the effective neutrino temperature, and  $\langle E_{\nu_{e/x}} \rangle$  is the average neutrino energy. The values are from Ref. [80].

	$(\alpha_{\nu_e}, T_{\nu_e}, \langle E_{\nu_e} \rangle)$	$(\alpha_{\bar{\nu}_e}, T_{\bar{\nu}_e}, \langle E_{\bar{\nu}_e} \rangle)$	$(\alpha_{\nu_x}, T_{\nu_x}, \langle E_{\nu_x} \rangle)$	$(\alpha_{\bar{\nu}_x}, T_{\bar{\nu}_x}, \langle E_{\bar{\nu}_x} \rangle)$
(I)	(3.0, 2.88, 11.5)	(3.0, 3.41, 13.6)	(3.0, 4.08, 16.3)	(3.0, 4.08, 16.3)
(II)	(0.0, 3.65, 11.5)	(0.0, 4.32, 13.6)	(0.0, 5.17, 16.3)	(0.0, 5.17, 16.3)
(III)	(3.0, 2.88, 11.5)	(3.0, 3.41, 13.6)	(0.0, 5.17, 16.3)	(0.0, 5.17, 16.3)

ino) but an alternative method is to use radiochemical experiments. One promising nucleus for such an experiment would be  $^{205}\text{Tl}$ , since it has an extremely low threshold energy allowing for the capture of  $pp$ -neutrinos.

The dominant charged-current neutrino-nucleus reaction considered here is



where the final state is the low-lying excited state in  $^{205}\text{Pb}$  at 2.33 keV. In contrast the feeding to the  $5/2^-$  ground state of  $^{205}\text{Pb}$  is much smaller due to the change in angular momentum. The  $Q$ -value for the ground-state-to-ground-state transition is  $50.6 \pm 0.5$  keV [81], making it the lowest threshold among the candidates considered for radiochemical experiments. In addition to the low threshold the long half-life of  $1.73(7) \times 10^7$  yr of  $^{205}\text{Pb}$  [82] makes  $^{205}\text{Tl}$  a prime candidate for measuring the average solar neutrino flux over millions of years.

The neutrino-capture cross sections are extremely tiny, which is why expressing capture rates in solar neutrino units (SNU), defined as 1 SNU =  $10^{-36}$  capture / target atom / second makes sense. For the complete solar neutrino spectrum the capture rate in SNU is given by

$$R = 10^{36} \sum_i \int \sigma(E) \phi_i(E) dE, \quad (3.6)$$

where  $E$  is the neutrino energy,  $\phi_i(E)$  the differential neutrino spectra, and  $\sigma(E)$  is the neutrino-capture cross section. The differential neutrino spectra are given at a distance of 1 astronomical unit. All eight neutrino components from the CNO and  $pp$  cycles are included in the sum (3.6). The neutrino cross sections for each individual multipolarity are shown in Fig. 3.11.

The fluxes related to each neutrino component are based on the solar model BS05(OP) (see [77]). Ignoring neutrino survival probabilities the capture rates are 132.4 SNU with  $g_A = 1.00$  and 100.2 SNU with  $g_A = 0.75$ . The dominant contributions come from  $1^-$  and  $2^-$  transitions, which result in a non-trivial  $g_A$ -dependence of the cross section. Based on the paper [83] the

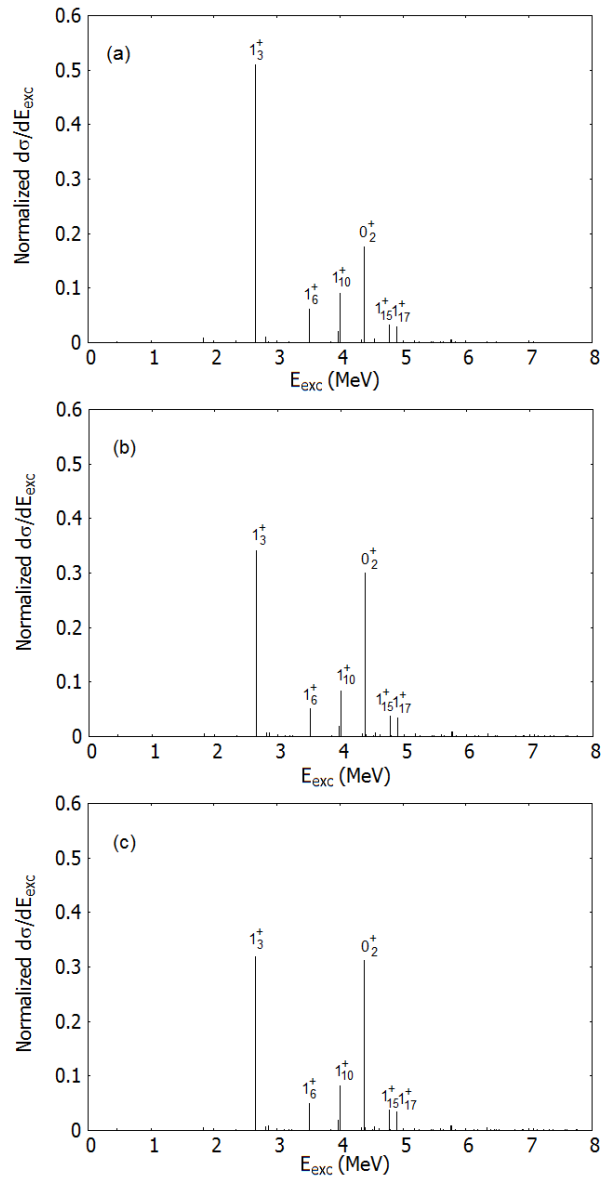


**Figure 3.10.** Contributions of individual states to the total cross section (normalized to unity). Panel (a) is folded with the  $^8\text{B}$  neutrino spectrum, panel (b) with Fermi–Dirac distribution with parametrization (I), and panel (c) with parametrization (II). (Originally published in [IV])

survival probabilities of 0.54 for the  $pp$ ,  $^7\text{Be}$ , and  $^{13}\text{N}$  neutrinos, and 0.50 for the  $\text{pep}$ ,  $^{15}\text{O}$ , and  $^{17}\text{F}$  neutrinos, and 0.36 for the  $^8\text{B}$  neutrinos, are adopted.

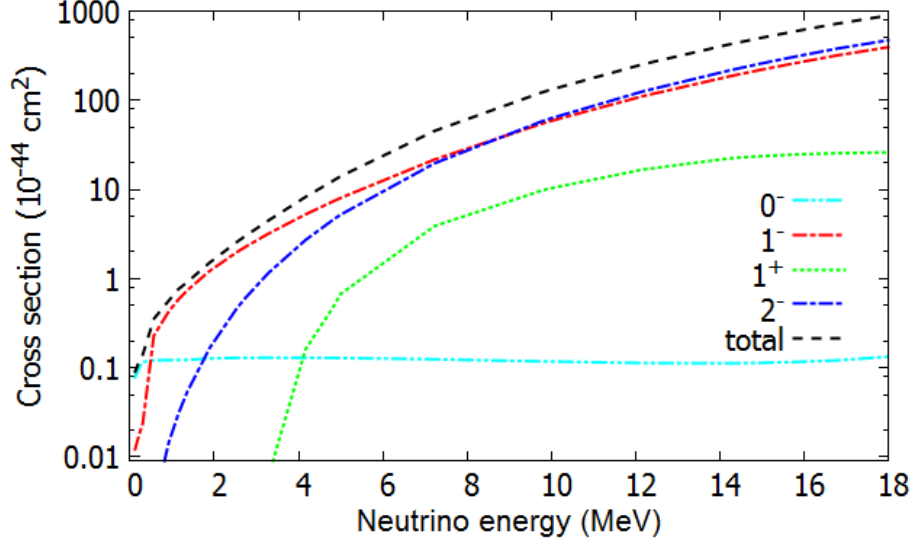


**Figure 3.11.** The cross section for CC neutrino-nucleus scattering off  $^{205}\text{Tl}$  for the leading transition multipoles assuming  $g_A = 1.00$ . (Originally published in [XII])

This results in the estimate

$$R(^{205}\text{Tl}) = 62.2 \pm 8.6 \text{ SNU} \quad (3.7)$$

for the solar neutrino capture rate for  $^{205}\text{Tl}$ .

### 3.2.3 Gallium anomaly

The so-called gallium anomaly was first noticed [24–27] when comparing the source-experiment results of GALLEX and SAGE to the cross sections of Bahcall [28] given in Table 3.8. These cross sections are based on the reduced Gamow–Teller matrix elements (BGTs) measured in 1985 utilizing a charge-exchange reaction ((p,n)-reaction) by Krofcheck *et al.* [29, 30], given in Table 3.9. The neutrino-nucleus scattering cross sections can be related to the BGT values (B1u for the first-forbidden unique decay) with the equation

$$\sigma = \sigma_{\text{gs}} \left( 1 + \xi_{5/2-} \frac{\text{BGT}_{5/2-}}{\text{BGT}_{\text{gs}}} + \xi_{3/2-} \frac{\text{BGT}_{3/2-}}{\text{BGT}_{\text{gs}}} + \xi_{5/2+} \frac{\text{B1u}_{5/2+}}{\text{BGT}_{\text{gs}}} \right), \quad (3.8)$$

with the phase-space coefficients [28] for  $^{51}\text{Cr}$  and  $^{37}\text{Ar}$  electron neutrinos given by

$$\xi_{5/2-}(^{51}\text{Cr}) = 0.663 \quad \xi_{3/2-}(^{51}\text{Cr}) = 0.221 \quad \xi_{5/2+}(^{51}\text{Cr}) = 0, \quad (3.9)$$

$$\xi_{5/2-}(^{37}\text{Ar}) = 0.691 \quad \xi_{3/2-}(^{37}\text{Ar}) = 0.262 \quad \xi_{5/2+}(^{37}\text{Ar}) = 0.200, \quad (3.10)$$

and [28]

$$\sigma_{\text{gs}}(^{51}\text{Cr}) = (5.53 \pm 0.01) \times 10^{-45} \text{ cm}^2, \quad (3.11)$$

$$\sigma_{\text{gs}}(^{37}\text{Ar}) = (6.62 \pm 0.01) \times 10^{-45} \text{ cm}^2. \quad (3.12)$$

Frekers *et al.* [84] made new measurements in 2011 for  $\text{BGT}_{5/2-}$  and  $\text{BGT}_{3/2-}$  which are listed in Table 3.9, with the charge-exchange reaction  $^{71}\text{Ga}(^3\text{He}, ^3\text{H})^{71}\text{Ge}$ .

A value for  $\text{BGT}_{5/2-}$  was measured and it turned out to be close to the upper limit given by Krofcheck *et al.* [29, 30]. However, the uncertainties related to this were large. For the other excited state  $\text{BGT}_{3/2-}$  Frekers *et al.* got a much larger value than Krofcheck *et al.*. If these Gamow–Teller strengths are considered to be reliable for the  $\nu_e$ - $^{71}\text{Ga}$  cross-section calculation as such, the statistical significance of the gallium anomaly would increase with respect to the Bahcall cross sections, with the new estimate for the anomaly at  $3.0\sigma$  (see Table 3.10).

In the article [X] the cross sections were calculated for the first time using the full model space  $0f_{5/2}, 1p, 0g_{9/2}$  for both neutrons and protons with the effective Hamiltonian JUN45 [85]. In addition to deriving new cross sections for source experiments, the reliability of charge-exchange reactions in determining the Gamow–Teller strengths for neutrino-nucleus scattering was examined. Especially the role of tensor contributions for  $l$ -forbidden decays is an important issue to consider. The shell-model GT and tensor matrix elements and reduced transition densities are given in Table 3.5. The cross-section results for individual excited states are given in tables 3.6 and 3.7 for  $^{51}\text{Cr}$  and  $^{37}\text{Ar}$  neutrinos respectively.

From Table 3.8 it can be seen that the new JUN45 shell-model-based cross sections are smaller than the previous estimates. With these cross sections one arrives at an anomaly of  $2.3\sigma$  which is a remarkable reduction. It should be noted that the estimation of the statistical significance uses some approximations (like assuming the systematic errors as independent), which result in a smaller  $p$ -value than a more sophisticated treatment would.

The gallium anomaly is one of the discrepancies between theoretical predictions and experimental results that have been viewed as a potential indication of mixing with a sterile neutrino flavor [87–89]. In a model with 3+1 neutrinos with an eV-scale sterile neutrino, the survival probability of an electron neutrino is

$$P_{\nu_e \rightarrow \nu_e}^{\text{SBL}} = 1 - 4|U_{e4}|^2 (1 - |U_{e4}|^2) \sin^2\left(\frac{\Delta m_{41}^2 L}{4E}\right), \quad (3.13)$$

where  $U$  is the unitary  $4 \times 4$  neutrino mixing matrix,  $E$  is the neutrino energy,  $L$  is the source-detector distance, and  $\Delta m_{41}^2 = m_4^2 - m_1^2$  is the squared-mass

**Table 3.5.** The matrix elements and reduced transition probabilities for  $^{71}\text{Ga}$  with tensor mixing parameter  $\delta = 0.097$ . (Originally published in [X])

State	$\langle f    O_{GT}    i \rangle$	$\langle f    O_{L=2}    i \rangle$	$\text{BGT}_{\beta}^{\text{SM}}$	$\text{BGT}_{(\text{p,n})}^{\text{SM}}$
$1/2_{\text{g.s.}}^{-}$	-0.795	0.465	0.158	0.141
$5/2_1^{-}$	0.144	-1.902	0.0052	0.0004
$3/2_1^{-}$	0.100	0.0482	0.0025	0.0027
$3/2_2^{-}$	0.430	-0.0014	0.0462	0.0462
$1/2_2^{-}$	-0.620	0.348	0.0958	0.0857

**Table 3.6.** Theoretical cross sections ( $\text{cm}^2$ ) for  $^{51}\text{Cr}$  neutrinos calculated using the Hamiltonian JUN45 [85]. (Originally published in [X])

State	$g_A = 0.955(6)$
$1/2_{\text{g.s.}}^{-}$	$5.53 \pm 0.07 \times 10^{-45}$
$5/2_1^{-}$	$1.21 \pm 0.61 \times 10^{-46}$
$9/2_1^{+}$	$\leq 10^{-56}$
$3/2_1^{-}$	$1.94 \pm 0.97 \times 10^{-47}$
total	$5.67 \pm 0.10 \times 10^{-45}$

**Table 3.7.** Theoretical cross sections ( $\text{cm}^2$ ) for  $^{37}\text{Ar}$  neutrinos calculated using the Hamiltonian JUN45 [85]. (Originally published in [X])

State	$g_A = 0.955(6)$
$1/2_{\text{g.s.}}^{-}$	$6.62 \pm 0.09 \times 10^{-45}$
$5/2_1^{-}$	$1.51 \pm 0.76 \times 10^{-46}$
$9/2_1^{+}$	$\leq 10^{-56}$
$3/2_1^{-}$	$2.79 \pm 1.40 \times 10^{-47}$
$5/2_1^{+}$	$5.91 \pm 2.96 \times 10^{-51}$
total	$6.80 \pm 0.12 \times 10^{-45}$

difference between a heavy, almost sterile,  $\nu_4$  with mass  $m_4 \sim 1$  eV and the standard three light neutrinos  $\nu_1$ ,  $\nu_2$ , and  $\nu_3$ , with respective masses  $m_1$ ,  $m_2$ , and  $m_3$  much smaller than 1 eV (hence,  $\Delta m_{41}^2 \simeq \Delta m_{42}^2 \simeq \Delta m_{43}^2$  in Eq. (3.13)).

Comparing the JUN45 shell-model calculations to NEOS and DANSS gives a goodness of fit of 16 % ( $\Delta\chi^2/\text{NDF} = 3.6/2$ ), which is a significant improvement over the value of 4 % reported in in Ref. [10] for the Frekers *et al.* cross sections.

**Table 3.8.** Cross sections ( $10^{-45} \text{ cm}^2$ ) for  $^{37}\text{Ar}$  and  $^{51}\text{Cr}$  neutrinos and the ratio to the estimates of Bahcall [28]. The cross sections have been evaluated with BGTs from Haxton [31, 86] (shell model), Frekers *et al.* [84, 86] (charge-exchange), and the JUN45 calculation (shell model). (Originally published in [X])

	$\sigma^{51\text{Cr}}$	$\sigma^{51\text{Cr}}/\sigma_{\text{B}}^{51\text{Cr}}$	$\sigma^{37\text{Ar}}$	$\sigma^{37\text{Ar}}/\sigma_{\text{B}}^{37\text{Ar}}$
Bahcall	$5.81 \pm 0.16$		$7.00 \pm 0.21$	
Haxton	$6.39 \pm 0.65$	$1.100 \pm 0.112$	$7.72 \pm 0.81$	$1.103 \pm 0.116$
Frekers	$5.92 \pm 0.11$	$1.019 \pm 0.019$	$7.15 \pm 0.14$	$1.021 \pm 0.020$
JUN45	$5.67 \pm 0.06$	$0.976 \pm 0.011$	$6.80 \pm 0.08$	$0.971 \pm 0.011$

**Table 3.9.** The reduced Gamow–Teller transition probabilities from Krofcheck *et al.* [29, 30], Haxton [31], Frekers *et al.* [84], and using the JUN45 calculation. (Originally published in [X])

Method		$\frac{\text{BGT}_{5/2-}}{\text{BGT}_{\text{gs}}}$	$\frac{\text{BGT}_{3/2-}}{\text{BGT}_{\text{gs}}}$	$\frac{\text{B}1\text{u}_{5/2+}}{\text{BGT}_{\text{gs}}}$
Krofcheck	$^{71}\text{Ga}(p, n)^{71}\text{Ge}$	$< 0.057$	$0.126 \pm 0.023$	
Haxton	Shell model	$0.19 \pm 0.18$		
Frekers	$^{71}\text{Ga}(^3\text{He}, ^3\text{H})^{71}\text{Ge}$	$0.040 \pm 0.031$	$0.207 \pm 0.016$	
JUN45	Shell model	$(3.30 \pm 1.66) \times 10^{-2}$	$(1.59 \pm 0.79) \times 10^{-2}$	$(4.46 \pm 2.24) \times 10^{-6}$

**Table 3.10.** The ratios of the experimental results and theoretical predictions for  $^{71}\text{Ge}$  event rates in the GALLEX and SAGE experiments and the statistical significance of the gallium anomaly. (Originally published in [X])

	GALLEX-1	GALLEX-2	SAGE-1	SAGE-2	Average	Anomaly
$R_{\text{Bahcall}}$	$0.95 \pm 0.11$	$0.81 \pm 0.11$	$0.95 \pm 0.12$	$0.79 \pm 0.08$	$0.85 \pm 0.06$	$2.6\sigma$
$R_{\text{Haxton}}$	$0.86 \pm 0.13$	$0.74 \pm 0.12$	$0.86 \pm 0.14$	$0.72 \pm 0.10$	$0.76 \pm 0.10$	$2.5\sigma$
$R_{\text{Frekers}}$	$0.93 \pm 0.11$	$0.79 \pm 0.11$	$0.93 \pm 0.12$	$0.77 \pm 0.08$	$0.84 \pm 0.05$	$3.0\sigma$
$R_{\text{JUN45}}$	$0.97 \pm 0.11$	$0.83 \pm 0.11$	$0.97 \pm 0.12$	$0.81 \pm 0.08$	$0.88 \pm 0.05$	$2.3\sigma$

# Chapter 4

## Summary

In this thesis forbidden beta decays and low-energy neutrino-nucleus scattering were studied in order to address theoretical uncertainties in spectral-shape predictions and scattering cross sections. Not only are reliable spectral shapes with robust uncertainty estimates needed to characterize background radiation in rare-event searches, but they also play a key role in the reactor antineutrino anomaly. Accurate estimates for neutrino-nucleus-scattering cross sections are needed in order to understand the solar neutrino flux. Reliable uncertainties for theoretical estimates are also crucial in order to make valid comparisons between theoretical and experimental results in neutrino-source experiments.

The first body of research in this thesis was on  $\beta$ -spectrum shapes in forbidden decays. The theoretical predictions for the spectral shapes of forbidden decays were found to depend heavily on the ratio of the adopted effective values of the weak coupling constants  $g_A$  and  $g_V$  for a plurality of decays, including first-forbidden non-unique decays. An experiment done for  $^{113}\text{Cd}$  in collaboration with COBRA shows that the appropriate ratio most likely differs from the free-nucleon ratio, and a value of roughly 0.9 should be used in the formalism and nuclear models used in this thesis. For first-forbidden  $\Delta J = 0$  transitions, uncertainties in the strength of mesonic enhancement of the axial-charge matrix element also propagate to the spectral shape. The application of the formalism to the first-forbidden decays was validated by comparing the theoretical predictions to the experimental spectrum of  $^{137}\text{Xe}$ .

The insights from the theoretical spectral shape calculations were applied to the 36 first-forbidden transitions with the largest contributions to the cumulative beta spectrum from nuclear reactors. Microscopic calculations were carried out in the shell-model formalism with wide ranges of values for the  $g_A/g_V$  ratio and the mesonic enhancement factor  $\epsilon_{\text{MEC}}$ . It was shown that an oversimplified estimation of the spectral shapes by allowed and

forbidden unique shape factors underestimates the theoretical uncertainties which are extremely important for the reactor antineutrino anomaly. Thus, precise description of the forbidden transitions is crucial for understanding the spectral shoulder and the rate anomaly.

The second body of research focused on low-energy neutrino-nucleus scattering off nuclei. New shell-model-based estimates of cross sections for scattering off  $^{40}\text{Ar}$  were found to be larger than the previous RPA-based results for low-energy neutrinos. This means that the background from  $^{40}\text{Ar}$  neutrino-nucleus scattering could be elevated from previous estimates in argon-based dark matter searches. New estimates for the solar neutrino cross section of  $^{205}\text{Tl}$  were also derived, in order to assess the feasibility of using the isotope in radiochemical neutrino detection experiments. A new estimate for the reaction rate is  $R(^{205}\text{Tl}) = 62.2 \pm 8.6$  SNU, which is much smaller than the previous theoretical cross sections.

Finally, the neutrino-nucleus formalism was applied to  $^{71}\text{Ga}$ , which was the detector material for the solar neutrino experiments GALLEX and SAGE. The possible missing neutrino flux in source experiments was addressed by deriving new theoretical estimates for scattering cross sections. The new estimates for the scattering cross sections decrease the gallium anomaly from  $3.0\sigma$  to about  $2.3\sigma$ . The new cross sections also agree with the reactor data from NEOS and DANSS much better, increasing the parameter goodness of fit from 4% to 16%. Therefore, the new cross sections both promote a model with no sterile neutrinos and, at the same time, help the models with sterile neutrinos fit the recent reactor data more consistently.

# References

- [1] C. Athanassopoulos et al., Results on  $\nu_\mu \rightarrow \nu_e$  Neutrino Oscillations from the LSND Experiment, *Phys. Rev. Lett.* 81, no.9 (1998) 1774–1777.
- [2] J. M. Conrad, W. C. Louis and M. H. Shaevitz, The LSND and MiniBooNE Oscillation Searches at High  $\Delta m^2$ , *Annual Review of Nuclear and Particle Science* 63, no.1 (2013) 45–67, eprint: <https://doi.org/10.1146/annurev-nucl-102711-094957>.
- [3] P. Anselmann et al., First results from the  $^{51}\text{Cr}$  neutrino source experiment with the GALLEX detector, *Physics Letters B* 342, no.1 (1995) 440–450, ISSN: 0370-2693.
- [4] W. Hampel et al., GALLEX solar neutrino observations: results for GALLEX IV, *Physics Letters B* 447, no.1 (1999) 127–133, ISSN: 0370-2693.
- [5] F. Kaether, W. Hampel, G. Heusser, J. Kiko and T. Kirsten, Re-analysis of the Gallex solar neutrino flux and source experiments, *Physics Letters B* 685, no.1 (2010) 47–54, ISSN: 0370-2693.
- [6] J. N. Abdurashitov et al., The Russian-American Gallium Experiment (SAGE) Cr Neutrino Source Measurement, *Phys. Rev. Lett.* 77, no.23 (1996) 4708–4711.
- [7] A. A. Aguilar-Arevalo et al., Significant Excess of Electronlike Events in the MiniBooNE Short-Baseline Neutrino Experiment, *Phys. Rev. Lett.* 121, no.22 (2018) 221801.
- [8] G. Mention et al., Reactor antineutrino anomaly, *Phys. Rev. D* 83, no.7 (2011) 073006.
- [9] Johnathon R. Jordan, Yonatan Kahn, Gordan Krnjaic, Matthew Moschella and Joshua Spitz, Severe Constraints on New Physics Explanations of the MiniBooNE Excess, *Phys. Rev. Lett.* 122, no.8 (2019) 081801.

- [10] S. Gariazzo, C. Giunti, M. Laveder and Y. F. Li, Model-independent  $\bar{\nu}_e$  short-baseline oscillations from reactor spectral ratios, *Physics Letters B* 782 (2018) 13–21, ISSN: 0370-2693.
- [11] A. C. Hayes et al., Possible origins and implications of the shoulder in reactor neutrino spectra, *Phys. Rev. D* 92, no.3 (2015) 033015.
- [12] P. Huber, NEOS Data and the Origin of the 5 MeV Bump in the Reactor Antineutrino Spectrum, *Phys. Rev. Lett.* 118, no.4 (2017) 042502.
- [13] F. P. An et al., Measurement of the Reactor Antineutrino Flux and Spectrum at Daya Bay, *Phys. Rev. Lett.* 116, no.6 (2016) 061801.
- [14] S. H. Seo et al., Spectral measurement of the electron antineutrino oscillation amplitude and frequency using 500 live days of RENO data, *Phys. Rev. D* 98, no.1 (2018) 012002.
- [15] P. Huber, Determination of antineutrino spectra from nuclear reactors, *Phys. Rev. C* 84, no.2 (2011) 024617.
- [16] Th. A. Mueller et al., Improved predictions of reactor antineutrino spectra, *Phys. Rev. C* 83, no.5 (2011) 054615.
- [17] X. Mougeot, Reliability of usual assumptions in the calculation of  $\beta$  and  $\nu$  spectra, *Phys. Rev. C* 91, no.5 (2015) 055504.
- [18] A. A. Sonzogni, E. A. McCutchan and A. C. Hayes, Dissecting Reactor Antineutrino Flux Calculations, *Phys. Rev. Lett.* 119, no.11 (2017) 112501.
- [19] A. C. Hayes, J. L. Friar, G. T. Garvey, Gerard Jungman and G. Jonkmans, Systematic Uncertainties in the Analysis of the Reactor Neutrino Anomaly, *Phys. Rev. Lett.* 112, no.20 (2014) 202501.
- [20] Y.-F. Li and D. Zhang, New realization of the conversion calculation for reactor antineutrino fluxes, *Phys. Rev. D* 100, no.5 (2019) 053005.
- [21] D.-L. Fang and B. A. Brown, Effect of first-forbidden decays on the shape of neutrino spectra, *Phys. Rev. C* 91, no.2 (2015) 025503.
- [22] M. Haaranen, P. C. Srivastava and J. Suhonen, Forbidden nonunique  $\beta$  decays and effective values of weak coupling constants, *Phys. Rev. C* 93, no.3 (2016) 034308.
- [23] M. Haaranen, J. Kotila and J. Suhonen, Spectrum-shape method and the next-to-leading-order terms of the  $\beta$ -decay shape factor, *Phys. Rev. C* 95 (2017) 024327.

- [24] J. N. Abdurashitov et al., Measurement of the response of a Ga solar neutrino experiment to neutrinos from a  $^{37}\text{Ar}$  source, *Phys. Rev. C* 73, no.4 (2006) 045805.
- [25] M. Laveder, Unbound Neutrino Roadmaps, *Nuclear Physics B – Proceedings Supplements* 168 (2007), Proceedings of the Neutrino Oscillation Workshop 344–346, ISSN: 0920-5632.
- [26] C. Giunti and M. Laveder, Short-baseline active-sterile neutrino oscillations?, *Modern Physics Letters A* 22, no.33 (2007) 2499–2509, eprint: <https://doi.org/10.1142/S0217732307025455>.
- [27] M. A. Acero, C. Giunti and M. Laveder, Limits on  $\nu_e$  and  $\bar{\nu}_e$  disappearance from Gallium and reactor experiments, *Phys. Rev. D* 78, no.7 (2008) 073009.
- [28] J. N. Bahcall, Gallium solar neutrino experiments: Absorption cross sections, neutrino spectra, and predicted event rates, *Phys. Rev. C* 56, no.6 (1997) 3391–3409.
- [29] D. Krofcheck et al., Gamow-Teller Strength Function in  $^{71}\text{Ge}$  via the  $(p, n)$  Reaction at Medium Energies, *Phys. Rev. Lett.* 55, no.10 (1985) 1051–1054.
- [30] D. Krofcheck, *PhD thesis*, 1987.
- [31] W. C. Haxton, Cross section uncertainties in the gallium neutrino source experiments, *Physics Letters B* 431, no.1 (1998) 110–118, ISSN: 0370-2693.
- [32] H. Behrens and W. Bühring, *Electron Radial Wave Functions and Nuclear Beta Decay*, Clarendon, Oxford, 1982.
- [33] J. S. O’Connell, T. W. Donnelly and J. D. Walecka, Semileptonic Weak Interactions with  $\text{C}^{12}$ , *Phys. Rev. C* 6, no.3 (1972) 719–733.
- [34] K. L. G. Heyde, *The Nuclear Shell Model*, Springer-Verlag Berlin Heidelberg, 1990.
- [35] J. Toivanen and J. Suhonen, Microscopic quasiparticle-phonon description of odd- $A$  Xe isotopes, *J. Phys. G.* 21 (1995) 1491–1497.
- [36] J. Toivanen and J. Suhonen, Microscopic quasiparticle-phonon description of odd-mass  $^{127-133}\text{Xe}$  isotopes and their  $\beta$  decay, *Phys. Rev. C* 57, no.3 (1998) 1237–1245.
- [37] B. A. Brown and W. D. M. Rae, The Shell-Model Code NuShellX@MSU, *Nuclear Data Sheets* 120 (2014) 115.

- [38] J. Suhonen, *From Nucleons to Nucleus: Concepts of Microscopic Nuclear Theory*, Springer, Berlin, 2007.
- [39] M. Baranger, Extension of the Shell Model for Heavy Spherical Nuclei, *Phys. Rev.* 120 (1960) 957.
- [40] A. Bohr, B. R. Mottelson and D. Pines, Possible Analogy between the Excitation Spectra of Nuclei and Those of the Superconducting Metallic State, *Phys. Rev.* 110 (1958) 936.
- [41] N. N. Bogoliubov, A new method in the theory of superconductivity, *Sov. Phys. JETP* 7 (1958) 41.
- [42] J. G. Valatin, Generalized Hartree-Fock Method, *Phys. Rev.* 122 (1961) 1012.
- [43] P. Ring and P. Schuck, *The Nuclear Many-Body Problem*, Springer, New York, 1980.
- [44] G. Audi and A. H. Vapstra, The 1993 Atomic mass evaluation, *Nucl. Phys. A* 565 (1993) 1.
- [45] G. Audi and A. H. Vapstra, The 1995 update to the atomic mass evaluation, *Nucl. Phys. A* 595 (1995) 409.
- [46] D. J. Rowe, *Nuclear Collective Motion*, Methuen London, 1970.
- [47] .
- [48] B. Alex Brown and W. A. Richter, New “USD” Hamiltonians for the *sd* shell, *Phys. Rev. C* 74 (3 2006) 034315.
- [49] M. Honma, T. Otsuka, B. A. Brown and T. Mizusaki, Effective interaction for pf-shell nuclei, *Phys. Rev. C* 65 (6 2002) 061301.
- [50] M. Honma, T. Otsuka, B. A. Brown and T. Mizusaki, Shell-model description of neutron-rich pf-shell nuclei with a new effective interaction GXPF1, *Eur. Phys. J. A.* 25 (2005) 499.
- [51] H. Mach et al., Meson-exchange enhancement of the first-forbidden  $^{96}\text{Y}^g(0^-) \rightarrow ^{96}\text{Zr}^g(0^+)$   $\beta$  transition:  $\beta$  decay of the low-spin isomer of  $^{96}\text{Y}$ , *Phys. Rev. C* 41 (1 1990) 226–242.
- [52] A. Bohr and B. R. Mottelson, *Nuclear Structure Vol. I*, W. A. Benjamin, New York, 1969.
- [53] K. Holinde, Two-nucleon forces and nuclear matter, *Physics Reports* 68, no.3 (1981), cited By 384 121–188.
- [54] R. P. Feynmann and M. Gell-Mann, Theory of the Fermi Interaction, *Phys. Rev.* 109 (1958) 193.

- [55] M. Gell-Mann, Test of the Nature of the Vector Interaction in  $\beta$  Decay, *Phys. Rev.* 111 (1958) 362.
- [56] W. R. Theis, A ranking of the single terms in weak interactions, *Z. Phys.* 150 (1958) 590.
- [57] K. Zuber, *Neutrino Physics*, Institute of Physics Publishing Ltd, 2004.
- [58] E. D. Commins, *Weak Interactions*, McGraw-Hill, New York, 2007.
- [59] J. T. Suhonen, Value of the Axial-Vector Coupling Strength in  $\beta$  and  $\beta\beta$  Decays: A Review, *Frontiers in Physics* 5 (2017) 55, ISSN: 2296-424X.
- [60] M. Tanabashi et al., Review of Particle Physics, *Phys. Rev. D* 98, no.3 (2018) 030001.
- [61] K. Kubodera, J. Delorme and M. Rho, Axial Currents in Nuclei, *Phys. Rev. Lett.* 40, no.12 (1978) 755–758.
- [62] P. A. M. Guichon, M. Giffon, J. Joseph, R. Laverriere and C. Samour, Exchange current corrections for partial capture rates of muons in nuclei, *Z.Phys. A* 285 (1978) 183–189.
- [63] P. A. M. Guichon, M. Giffon and C. Samour, Possible evidence for mesonic exchange correction in  $^{16}\text{N}(0^-) \leftarrow ^{16}\text{O}(0^+)$   $\beta$ -decay and  $\mu$ -capture reactions, *Physics Letters B* 74, no.1 (1978) 15–17, ISSN: 0370-2693.
- [64] I. S. Towner and F. C. Khanna, Role of 2p-2h states in weak  $0^+ \leftrightarrow 0^-$  transitions in  $A = 16$  nuclei, *Nuclear Physics A* 372, no.3 (1981) 331–348, ISSN: 0375-9474.
- [65] J. Delorme, Meson degrees of freedom in nuclei, *Nuclear Physics A* 374 (1982) 541–555, ISSN: 0375-9474.
- [66] E. Ydrefors and J. Suhonen, Charged-current neutrino-nucleus scattering off the even molybdenum isotopes, *Adv. High Energy Phys.* 2012 (2012) 373946.
- [67] J. D. Walecka, *Theoretical Nuclear and Subnuclear Physics*, Imperial College Press, London, 2004.
- [68] E. Kolbe, K. Langanke, G. Martínez-Pinedo and P. Vogel, Neutrino–nucleus reactions and nuclear structure, *Journal of Physics G: Nuclear and Particle Physics* 29, no.11 (2003) 2569.
- [69] E. Ydrefors and J. Suhonen, Charged-current neutrino-nucleus scattering off  $^{95,97}\text{Mo}$ , *Phys. Rev. C* 87, no.3 (2013) 034314.

- [70] J. Engel, Approximate treatment of lepton distortion in charged-current neutrino scattering from nuclei, *Phys. Rev. C* 57, no.4 (1998) 2004–2009.
- [71] E. K. Warburton and B. A. Brown, Appraisal of the Kuo-Herling shell-model interaction and application to  $A = 210$ – $212$  nuclei, *Phys. Rev. C* 43, no.2 (1991) 602–617.
- [72] Q. Zhi et al., Shell-model half-lives including first-forbidden contributions for  $r$ -process waiting-point nuclei, *Phys. Rev. C* 87, no.2 (2013) 025803.
- [73] P. Agnes et al., First results from the DarkSide-50 dark matter experiment at Laboratori Nazionali del Gran Sasso, *Physics Letters B* 743 (2015) 456–466, ISSN: 0370-2693.
- [74] P.-A. Amaudruz et al., First Results from the DEAP-3600 Dark Matter Search with Argon at SNOLAB, *Phys. Rev. Lett.* 121, no.7 (2018) 071801.
- [75] R. Sadler and H Behrens, Second-forbidden beta-decay and the effect of (V+A)-and S-interaction admixtures:  $^{36}\text{Cl}$ , *Z. Phys. A* 346 (1993) 25–33.
- [76] M. B. Chadwick et al., ENDF/B-VII.1 Nuclear Data for Science and Technology: Cross Sections, Covariances, Fission Product Yields and Decay Data, *Nuclear Data Sheets* 112, no.12 (2011), Special number on ENDF/B-VII.1 Library 2887–2996, ISSN: 0090-3752.
- [77] J. N. Bahcall, A. M. Serenelli and S. Basu, New Solar Opacities, Abundances, Helioseismology, and Neutrino Fluxes, *The Astrophysical Journal* 621, no.1 (2005) L85–L88.
- [78] M.-K. Cheoun, E. Ha and T. Kajino, Reactions on  $^{40}\text{Ar}$  involving solar neutrinos and neutrinos from core-collapsing supernovae, *Phys. Rev. C* 83, no.2 (2011) 028801.
- [79] I. Gil-Botella and A. Rubbia, Oscillation effects on supernova neutrino rates and spectra and detection of the shock breakout in a liquid argon TPC, *Journal of Cosmology and Astroparticle Physics* 2003, no.10 (2003) 009–009.
- [80] M. T. Keil, Georg G. Raffelt and H.-T. Janka, Monte Carlo Study of Supernova Neutrino Spectra Formation, *The Astrophysical Journal* 590, no.2 (2003) 971–991.
- [81] M. Wang et al., The AME2016 atomic mass evaluation (II). Tables, graphs and references, *Chinese Physics C* 41, no.3 (2017) 030003.

- [82] F. G. Kondev, Nuclear Data Sheets for  $A=205$ , *Nuclear Data Sheets* 101, no.4 (2004) 521–662, ISSN: 0090-3752.
- [83] M. Agostini et al., Comprehensive measurement of  $pp$ -chain solar neutrinos, *Nature* 562 (2018) 505–210.
- [84] D. Frekers et al., The  ${}^{71}\text{Ga}({}^3\text{He}, t)$  reaction and the low-energy neutrino response, *Physics Letters B* 706, no.2 (2011) 134–138, ISSN: 0370-2693.
- [85] M. Honma, T. Otsuka, T. Mizusaki and M. Hjorth-Jensen, New effective interaction for  $0f_{5/2}1p0g_{9/2}$ -shell nuclei, *Phys. Rev. C* 80, no.6 (2009) 064323.
- [86] C. Giunti, M. Laveder, Y. F. Li, Q. Y. Liu and H. W. Long, Update of short-baseline electron neutrino and antineutrino disappearance, *Phys. Rev. D* 86, no.11 (2012) 113014.
- [87] S. Gariazzo, C. Giunti, M. Laveder, Y. F. Li and E. M. Zavanin, Light sterile neutrinos, *Journal of Physics G: Nuclear and Particle Physics* 43, no.3 (2015) 033001.
- [88] C. Giunti and T. Lasserre, eV-Scale Sterile Neutrinos, *Annual Review of Nuclear and Particle Science* 69, no.1 (2019) 163–190, eprint: <https://doi.org/10.1146/annurev-nucl-101918-023755>.
- [89] S. Böser et al., Status of light sterile neutrino searches, *Progress in Particle and Nuclear Physics* 111 (2020) 103736, ISSN: 0146-6410.



## ORIGINAL PAPERS

### I

# ELECTRON SPECTRA IN FORBIDDEN $\beta$ DECAYS AND THE QUENCHING OF THE WEAK AXIAL-VECTOR COUPLING CONSTANT $g_A$

by

Kostensalo, J., Haaranen, M., & Suhonen, J. 2017

Physical Review C, 95 (4), 044313  
doi:10.1103/PhysRevC.95.044313

Reproduced with kind permission by American Physical Society.

## Electron spectra in forbidden $\beta$ decays and the quenching of the weak axial-vector coupling constant $g_A$

Joel Kostensalo,<sup>\*</sup> Mikko Haaranen, and Jouni Suhonen<sup>†</sup>

*Department of Physics, University of Jyväskylä, P.O. Box 35, FI-40014, Finland*

(Received 14 February 2017; published 12 April 2017)

Evolution of the electron spectra with the effective value of the weak axial-vector coupling constant  $g_A$  was followed for 26 first-, second-, third-, fourth- and fifth-forbidden  $\beta^-$  decays of odd- $A$  nuclei by calculating the involved nuclear matrix elements (NMEs) in the framework of the microscopic quasiparticle-phonon model (MQPM). The next-to-leading-order terms were included in the  $\beta$ -decay shape factor of the electron spectra. The spectrum shapes of third- and fourth-forbidden nonunique decays were found to depend strongly on the value of  $g_A$ , while first- and second-forbidden decays were mostly unaffected by the tuning of  $g_A$ . The  $g_A$ -driven evolution of the normalized  $\beta$  spectra was found to be quite universal, largely insensitive to the small changes in the nuclear mean field and the adopted residual many-body Hamiltonian producing the excitation spectra of the MQPM. This makes the comparison of experimental and theoretical electron spectra, coined “the spectrum-shape method” (SSM), a robust tool for extracting information on the effective values of the weak coupling constants. In this exploratory work two new experimentally interesting decays for the SSM treatment were discovered: the ground-state-to-ground-state decays of  $^{99}\text{Tc}$  and  $^{87}\text{Rb}$ . Comparing the experimental and theoretical spectra of these decays could shed light on the effective values of  $g_A$  and  $g_V$  for second- and third-forbidden nonunique decays. The measurable decay transitions of  $^{135}\text{Cs}$  and  $^{137}\text{Cs}$ , in turn, can be used to test the SSM in different many-body formalisms. The present work can also be considered as a (modest) step towards solving the  $g_A$  problem of the neutrinoless double beta decay.

DOI: 10.1103/PhysRevC.95.044313

### I. INTRODUCTION

The observation of the neutrinoless mode of double beta decay ( $0\nu\beta\beta$ ) would be groundbreaking since it would prove that the neutrino is its own antiparticle. The half-life of  $0\nu\beta\beta$  decay is proportional to the fourth power of the weak axial-vector coupling constant  $g_A$  [1,2], but it is not quite clear what value to use for it when calculating theoretical predictions for the decay rates [3,4]. Theoretical predictions for the half-lives are crucial when designing optimal experimental setups to detect  $0\nu\beta\beta$  events. In this context it is crucial to conceive complementary ways to address the  $g_A$  problem of  $0\nu\beta\beta$  decay. One alternative is the study of  $\beta$  decays, both allowed and forbidden, since experimental data is available to compare with the calculated physical observables. The related quenching of the computed nuclear matrix elements (NMEs) was addressed already for the allowed Gamow–Teller [4] and first-forbidden [3] transitions in medium-heavy even-mass nuclei. In the present work we extend these studies to first-, second-, third-, fourth- and fifth-forbidden  $\beta^-$  decays of odd-mass (odd- $A$ ) nuclei by studying the shape evolution of the associated electron spectra and by calculating the involved nuclear matrix elements (NMEs) in the framework of the microscopic quasiparticle-phonon model (MQPM). In this way we hope to shed light on the effective value of  $g_A$  in forbidden  $\beta$  transitions, which play also a prominent role in the virtual transitions mediating the  $0\nu\beta\beta$  decay.

The weak interaction is parity nonconserving, which is reflected in the fact that the hadronic current can be written as a mixture of vector and axial-vector components [5–7]. The weak coupling constants  $g_V$  and  $g_A$  appear in the theory of  $\beta$  decay as means to renormalize the hadronic current, when moving from the quark level to nucleons [8]. The conserved vector-current hypothesis (CVC) and the partially conserved axial-vector-current hypothesis (PCAC) of the standard model can be used to derive the free-nucleon values  $g_V = 1.00$  and  $g_A = 1.27$  [9]. In nuclear matter, however, the value of  $g_A$  is affected by many-nucleon correlations, and so in practical calculations a quenched effective value could give results which are closer to experimental results [10]. In the practical calculations the shortcomings in the treatment of the many-body quantum mechanics could also be absorbed into the value of  $g_A$  [11,12].

In earlier studies the effective value of the weak axial-vector coupling constant was probed by comparing the experimental half-lives of Gamow–Teller and first-forbidden unique decays to those predicted by the proton-neutron quasiparticle random-phase approximation (pnQRPA) [3,4,13–15]. These studies show consistently that a quenched value of  $g_A$  is needed to reproduce the experimental data. In Ref. [16] a systematic study of high-forbidden unique decays showed similar features as the earlier studies supporting the fact that a quenched effective value of  $g_A$  might need to be used for the high-forbidden decay branches as well.

In a recent study (see Ref. [17]) an interesting new feature was found regarding the weak coupling constants  $g_V$  and  $g_A$ . The shape of the electron spectra of the fourth-forbidden nonunique ground-state-to-ground-state  $\beta^-$  decays of  $^{113}\text{Cd}$  and  $^{115}\text{In}$  depend strongly on the value of  $g_V$  and  $g_A$  due to

<sup>\*</sup>joel.j.kostensalo@student.jyu.fi

<sup>†</sup>jouni.suhonen@phys.jyu.fi

TABLE I. Change in angular momentum  $\Delta J$  and parity  $\pi$  in a  $K$ th forbidden  $\beta$  decay. The decays with  $\Delta J = K$  (in the case of  $K = 1$  also  $\Delta J = 0$ ) are known as nonunique, while those with  $\Delta = K + 1$  are known as unique.

$K$	1	2	3	4	5
$\Delta J$	0,1,2	2,3	3,4	4,5	5,6
$\pi_i \pi_f$	-1	+1	-1	+1	-1

the complicated shape factor featuring vector, axial-vector, and mixed vector-axial-vector parts containing a number of different NMEs and phase-space factors. The shapes of the theoretical and experimental spectra can be compared to find the effective values of the coupling constants in a new method called the spectrum-shape method (SSM). The study [17] used two nuclear models; namely, the MQPM [18,19] and the nuclear shell model (NSM) [20–22]. When the computed electron spectra of  $^{113}\text{Cd}$  were compared with the experimental spectrum of Ref. [23], a close match was found by using the effective values  $g_A \approx 0.90$  and  $g_V = 1.0$  (equal to its CVC value!). This study was extended in Ref. [24] to include also the NMEs calculated within the microscopic interacting boson-fermion model (IBFM-2) [25,26]. The remarkable result of this study was that the three models MQPM, NSM, and IBFM-2 yielded a consistent result of  $g_A \approx 0.92$  by comparison with the experimental electron spectrum of Ref. [23]. This is the more surprising when considering the very different theory frameworks of the three models. The qualitative behavior of the MQPM, NSM, and IBFM-2 spectra was remarkably similar for both the  $^{113}\text{Cd}$  and  $^{115}\text{In}$  decays, suggesting that the details of the nuclear residual Hamiltonian and the many-body methods to solve the associated eigenvalue problem do not affect much the evolution of the electron spectra and thus the SSM itself. Based on this, it is reasonable to conjecture that just one of these models could be used to further explore new, potentially interesting  $\beta$  decays and their basic features.

In this paper we set out to find if the  $\beta$  spectra of other forbidden decays depend sensitively on the value of  $g_A$  using the MQPM, which can be relatively easily applied to a large number of odd- $A$  nuclei. We will explore unique and nonunique first- and second-forbidden decays and third-, fourth-, and fifth-forbidden nonunique decays. The identification of the degree of forbiddenness of a  $\beta$ -decay transition is presented in Table I. Most of these transitions and the associated electron spectra can be measured in the present and future low-background (underground) experiments. Some of the considered higher-forbidden transitions, with competing allowed transitions, cannot be easily measured. They were, however, included to better access the possible systematic features in transitions of increasing forbiddenness. As in Refs. [17] and [24] we take into account the next-to-leading-order terms in the shape factor, and so the spectra of unique-forbidden decays also depend on the axial-vector coupling constant in a nontrivial way. Based on the conclusions of Ref. [17], we adopt the CVC value  $g_V = 1.00$  in the calculations. In the analyzes we use the normalized electron spectra (the normalized spectra are also used when comparing with available experimental data)

for which the integrated area under the spectrum curve is unity. While the half-life is affected by the absolute values of the weak coupling constants, the normalized electron spectra depend only on the ratio  $g_A/g_V$ , so varying only  $g_A$  is sufficient.

The microscopic quasiparticle-phonon model is a fully microscopic model, which can be used to describe spherical and nearly spherical open-shell odd- $A$  nuclei. In the MQPM all three parts of the Hamiltonian, namely the quasiparticle, phonon, and quasiparticle-phonon terms are treated in an internally consistent way. The odd- $A$  nucleus is built from a basis of one- and three-quasiparticle states. The one-quasiparticle states are obtained by performing a BCS calculation for the neighboring even-even reference nucleus, and the three-quasiparticle states by coupling the BCS quasiparticles to the QRPA phonons of Ref. [18]. Finally, the residual Hamiltonian, which contains the interaction of the odd nucleon and the even-even reference nucleus, is diagonalized in the combined one- and three-quasiparticle basis [19].

This article is organized as follows: In Sec. II we give the theoretical background behind the MQPM and the  $\beta$  spectrum shape. In Sec. III we describe the application of the MQPM to the spectrum shape of forbidden  $\beta^-$  decays. In Sec. IV we present our results, and in Sec. V we draw the conclusions.

## II. THEORETICAL FORMALISM

In this section we give the theoretical background behind the nuclear model MQPM used in the calculations (see Sec. II A) and present the practical aspects of the theory of forbidden  $\beta^-$  decays and the shape of the electron spectra (see Sec. II B). The description of the MQPM summarizes the two original papers describing the model (see Refs. [18] and [19]). For a more complete description of the theory of  $\beta$  decays, see Ref. [27].

### A. Microscopic quasiparticle-phonon model

The starting point of the MQPM is a realistic  $A$ -fermion Hamiltonian consisting of the mean-field part and the residual-interaction part. In the occupation-number representation the Hamiltonian reads [10]

$$H = \sum_{\alpha} \epsilon_{\alpha} c_{\alpha}^{\dagger} c_{\alpha} + \frac{1}{4} \sum_{\alpha\beta\gamma\delta} \bar{v}_{\alpha\beta\gamma\delta} c_{\alpha}^{\dagger} c_{\beta}^{\dagger} c_{\gamma} c_{\delta}, \quad (1)$$

where  $c_i^{\dagger}$  and  $c_i$  are the creation and annihilation operators of the Hartree-Fock quasiparticles and  $\bar{v}_{\alpha\beta\gamma\delta} = \langle \alpha\beta | v | \gamma\delta \rangle - \langle \alpha\beta | v | \delta\gamma \rangle$  is the antisymmetrized two-body matrix element. Here we adopt the notation of Baranger [28], where the Roman letter  $a$  includes the single-particle quantum numbers  $n_a$  (principal),  $l_a$  (orbital angular momentum), and  $j_a$  (total angular momentum) and the Greek letter  $\alpha$ , the quantum numbers  $a$ , and the magnetic quantum number  $m_a$ .

The approximate ground state of the even-even reference nucleus is obtained by using BCS theory [29]. The occupation and vacancy amplitudes  $v_a$  and  $u_a$  emerge from the Bogoliubov-Valatin transformation [30,31],

$$a_{\alpha}^{\dagger} = u_{\alpha} c_{\alpha}^{\dagger} + v_{\alpha} \tilde{c}_{\alpha}, \quad (2)$$

$$\tilde{a}_{\alpha} = u_{\alpha} \tilde{c}_{\alpha} - v_{\alpha} c_{\alpha}^{\dagger}, \quad (3)$$

where  $a_\alpha^\dagger$  is the BCS quasiparticle creation operator and  $\tilde{a}_\alpha$  is the time-reversed BCS quasiparticle annihilation operator. After the Bogoliubov–Valatin transformation, the Hamiltonian of Eq. (1) can be written as

$$H = H_{11} + H_{22} + H_{40} + H_{04} + H_{31} + H_{13}, \quad (4)$$

where the indices correspond to the number of BCS creation and annihilation operators [32]. The terms  $H_{20}$  and  $H_{02}$  are missing from Eq. (4), since they vanish when minimizing the BCS ground-state energy.

When solving the BCS equations (see formulation in, e.g., Ref. [10]), the monopole matrix elements of the two-body interaction can be scaled by pairing-strength parameters  $g_{\text{pair}}^{(n)}$  and  $g_{\text{pair}}^{(p)}$  to reproduce the semi-empirical pairing gaps. The proton and neutron pairing gaps  $\Delta_p$  and  $\Delta_n$  needed for solving the BCS equations can be calculated by using the three-point formulas [33,34],

$$\begin{aligned} \Delta_p(A, Z) &= \frac{1}{4}(-1)^{Z+1}[S_p(A+1, Z+1) \\ &\quad - 2S_p(A, Z) + S_p(A-1, Z-1)], \\ \Delta_n(A, Z) &= \frac{1}{4}(-1)^{A-Z+1}[S_n(A+1, Z) \\ &\quad - 2S_n(A, Z) + S_n(A-1, Z)], \end{aligned} \quad (5)$$

where  $S_p$  is the proton separation energy and  $S_n$  the neutron separation energy.

Once the one-quasiparticle states have been calculated by using BCS theory, the next step is to consider two-quasiparticle excitations, i.e., treat the  $H_{22}$ ,  $H_{40}$ , and  $H_{04}$  terms of the Hamiltonian (4). In the MQPM, the two-quasiparticle excitations are the quasiparticle random-phase approximation (QRPA) [28] phonons of the even-even reference nucleus defined by the QRPA phonon-creation operator

$$Q_\omega^\dagger = \sum_{a \leq a'} [X_{aa'}^\omega A_{aa'}^\dagger(J_\omega M) - Y_{aa'}^\omega \tilde{A}_{aa'}(J_\omega M)], \quad (6)$$

where  $\omega$  denotes the angular momentum  $J_\omega$ , parity  $\pi_\omega$ , and the index  $k_\omega$  which identifies the different excitations with the same  $J$  and  $\pi$ . The quantity  $A_{aa'}^\dagger(J_\omega M) = (1 + \delta_{aa'})^{-1/2} [a_a^\dagger a_{a'}^\dagger]_{J_\omega}$  is the two-quasiparticle creation operator, and  $\tilde{A}_{aa'}(J_\omega M) = (1 + \delta_{aa'})^{-1/2} [\tilde{a}_a \tilde{a}_{a'}]_{J_\omega}$  is the corresponding annihilation operator. The forward- and backward-going amplitudes  $X$  and  $Y$  are solved by diagonalizing the QRPA matrix (see, e.g., Ref. [10]).

The basis states of the microscopic quasiparticle-phonon model are the one-quasiparticle states given by the BCS calculation and the three-quasiparticle states emerging from the coupling of QRPA phonons with BCS quasiparticles. The states of the odd- $A$  nucleus are created by the MQPM creation operator [19]

$$\Gamma_i^\dagger(jm) = \sum_n C_n^i a_{njm}^\dagger + \sum_{a\omega} D_{a\omega}^i [a_a^\dagger Q_\omega^\dagger]_{jm}, \quad (7)$$

where  $C_n^i$  and  $D_{a\omega}^i$  are the amplitudes determined by the MQPM matrix equation. The use of the equations-of-motion method [35] leads to the generalized eigenvalue problem [18]

$$\begin{pmatrix} A & B \\ B^T & A' \end{pmatrix} \begin{pmatrix} C^i \\ D^i \end{pmatrix} = \Omega_i \begin{pmatrix} 1 & 0 \\ 0 & N \end{pmatrix} \begin{pmatrix} C^i \\ D^i \end{pmatrix}, \quad (8)$$

where the submatrices  $A$ ,  $A'$ , and  $B$  are the matrix elements of  $H_{11}$ ,  $H_{22}$ , and  $H_{31}$  of equation (4), respectively. The explicit expressions for these submatrices are listed in Ref. [19]. The overlap between a one-quasiparticle state and a three-quasiparticle state is always zero leading to a block-diagonal structure of the overlap matrix on the right-hand side of Eq. (8). The overlaps between one-quasiparticle states lead to the unity matrix and the overlaps between three-quasiparticle states lead to the submatrix  $N$  of the overlap matrix. The appearance of the nondiagonal submatrix  $N$  in the overlap matrix leads, in turn, to a non-Hermitian eigenvalue problem in a nonorthogonal, often over-complete, basis set.

To solve the non-Hermitian eigenvalue problem of Eq. (8), we turn it into a Hermitian problem by writing it in a new orthogonal basis and diagonalizing it in the usual way. We start by solving the eigenvalue problem of the overlap matrix  $N$ , which reads

$$\sum_j N_{ij} u_j^{(k)} = n_k u_i^{(k)}. \quad (9)$$

The eigenvectors of  $N$  can be written in the basis  $|i\rangle = \Gamma_i^\dagger |\text{QRPA}\rangle$ , where  $|\text{QRPA}\rangle$  is the correlated ground state of the reference nucleus, as [19]

$$|\tilde{k}\rangle = \frac{1}{\sqrt{n_k}} \sum_i u_i^{(k)} |i\rangle. \quad (10)$$

The states  $|\tilde{k}\rangle$  with a nonzero eigenvalue  $n_k$  form an orthonormal complete set. In the orthonormal basis of Eq. (10) the MQPM matrix equation (8) can be written as a real and symmetric eigenvalue problem,

$$\sum_l \langle \tilde{k} | H | \tilde{l} \rangle g_l^{(n)} = \lambda_n g_k^{(n)}, \quad (11)$$

where

$$\langle \tilde{k} | H | \tilde{l} \rangle = \frac{1}{\sqrt{n_k n_l}} \sum_{ij} u_i^{(k)*} \langle i | H | j \rangle u_j^{(l)}. \quad (12)$$

The coefficients  $C_i^n$  of the MQPM matrix equation can be calculated from the coefficients  $g$  using the equation [19]

$$C_i^n = \sum_k \frac{1}{\sqrt{n_k}} g_k^{(n)} u_i^{(k)}. \quad (13)$$

As an example of the kind of excitation spectrum that the microscopic quasiparticle-phonon model produces, the experimental and MQPM spectra of  $^{87}\text{Sr}$  are presented in Fig. 1. The experimental spectrum was obtained from Ref. [36].

## B. $\beta$ spectrum shape

To simplify the description of the  $\beta^-$  decay, we assume that at the very moment of decay the decaying nucleus only interacts via the weak interaction, and the strong interaction with the  $A - 1$  other nucleons can be neglected. In this scheme, known as the impulse approximation, the flow lines of the nucleons, i.e., the hadronic current, and the flow lines of the emitted leptons, i.e., the leptonic current, interact at a weak-interaction vertex. Since the vector boson  $W^-$  has a large mass, and thus propagates only a short distance, the vertex

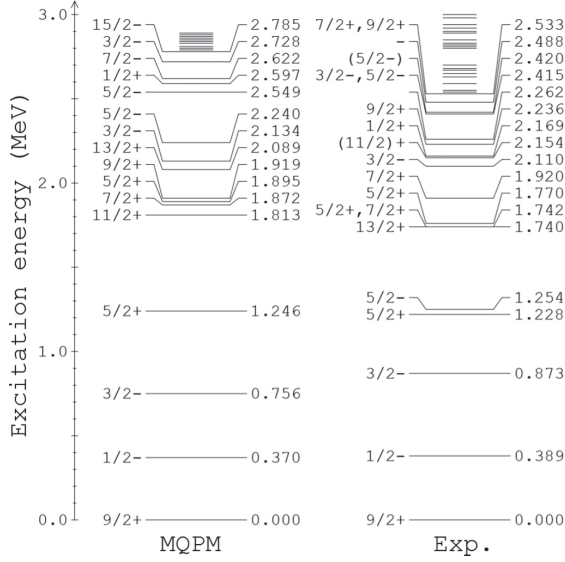


FIG. 1. Experimental and MQPM excitation spectra for the nucleus  $^{87}\text{Sr}$ .

can be considered to be point like with an effective coupling constant  $G_F$ , the Fermi constant. The weak interaction is parity nonconserving, which is reflected in the fact that the hadronic current can be written at the quark level as a mixture of vector and axial-vector components as [5–7]

$$J_H^\mu = \bar{u}(x)\gamma^\mu(1 - \gamma_5)d(x), \quad (14)$$

where  $\gamma^\mu$  and  $\gamma_5$  are the usual Dirac matrices. When moving from the quark level to the nucleon level, one must take into account renormalization effects of strong interactions. The hadronic current at the nucleon level (proton  $p$  and neutron  $n$ ) can then be written as [8]

$$J_H^\mu = \bar{p}(x)\gamma^\mu(g_V - g_A\gamma_5)n(x), \quad (15)$$

where  $g_V$  and  $g_A$  are the weak vector and axial-vector coupling constants, respectively. The conserved vector-current hypothesis (CVC) and the partially conserved axial-vector-current hypothesis (PCAC) of the standard model give the so-called bare nucleon values  $g_V = 1.0$  and  $g_A = 1.27$  [9]. In nuclear matter the value of  $g_A$  is affected by many-nucleon correlations, and so the bare nucleon value might not be the one to use in practical calculations [10].

In the impulse approximation the probability of the electron being emitted with kinetic energy between  $W_e$  and  $W_e + dW_e$  is

$$P(W_e)dW_e = \frac{G_F}{(\hbar c)^6} \frac{1}{2\pi^3\hbar} C(W_e)p_e c W_e (W_0 - W_e)^2 \times F_0(Z, W_e)dW_e, \quad (16)$$

where  $p_e$  is the momentum of the electron,  $Z$  is the proton number,  $F_0(Z, W_e)$  is the Fermi function, and  $W_0$  is the endpoint energy of the  $\beta$  spectrum. The shape factor  $C(w_e)$  encodes the nuclear-structure information.

The half-life of a  $\beta$  decay can be expressed as

$$t_{1/2} = \frac{\kappa}{\tilde{C}}, \quad (17)$$

where  $\tilde{C}$  is the integrated shape factor and  $\kappa$  is a constant with value [37]

$$\kappa = \frac{2\pi^3\hbar^7\ln 2}{m_e^5 c^4 (G_F \cos\theta_C)^2} = 6147 \text{ s}, \quad (18)$$

with  $\theta_C$  being the Cabibbo angle. For convenience, it is common to introduce unitless kinematic quantities  $w_e = W_e/m_e c^2$ ,  $w_0 = W_0/m_e c^2$ , and  $p = p_e c/(m_e c^2) = (w_e^2 - 1)^{1/2}$ . Using these quantities the integrated shape factor can be written as

$$\tilde{C} = \int_1^{w_0} C(w_e) p w_e (w_0 - w_e)^2 F_0(Z, w_e) dw_e. \quad (19)$$

In Eq. (19) the kinematic factors are universal and the shape factor  $C(w_e)$  has a complicated expression including both kinematic and nuclear form factors. The choice of nuclear model (in the case of this paper, MQPM) enters the picture when calculating the one-body transition densities [38] related to the NMEs of the shape factor. The details of the shape factor and the constitution of its NMEs can be found from Refs. [27] and [38]. As in the Refs. [17] and [24] we take into account the next-to-leading-order terms of the shape function (for details see Ref. [24]). In the commonly adopted leading-order approximation the shape of the electron spectrum of unique-forbidden decays does not depend on the NMEs and it is just scaled by  $g_A^2$ . When the next-order terms are taken into account, the shape factor of these decays depends on the computed NMEs and through this on  $g_A$  in a nontrivial way [24]. This means that, at least in theory, the SSM could be applied also to unique decays.

The shape factor  $C(w_e)$  can be decomposed into vector, axial-vector, and vector-axial-vector parts. In this decomposition the shape factor reads

$$C(w_e) = g_V^2 C_V(w_e) + g_A^2 C_A(w_e) + g_V g_A C_{VA}(w_e). \quad (20)$$

For the integrated shape factor we get the analogous expression

$$\tilde{C} = g_V^2 \tilde{C}_V + g_A^2 \tilde{C}_A + g_V g_A \tilde{C}_{VA}. \quad (21)$$

It should be noted that in Eq. (20) the shape factors  $C_i$  are functions of electron kinetic energy, while the integrated shape factors  $\tilde{C}_i$  in Eq. (21) are real numbers.

### III. NUMERICAL APPLICATION OF FORMALISM

The electron spectra of 26 forbidden  $\beta^-$  transitions were calculated for different values of the coupling constants  $g_A$  by using the NMEs produced by the MQPM model. The application of the MQPM model followed the same basic steps as the earlier studies regarding the fourth-forbidden nonunique ground-state-to-ground-state  $\beta^-$  decays of  $^{113}\text{Cd}$ ,  $^{115}\text{In}$  [17,24,38], and  $^{115}\text{Cd}$  [39], including the use of the Bonn one-boson exchange potential with  $G$ -matrix techniques [19].

The single-particle energies needed to solve the BCS equations were calculated by using the Coulomb-corrected

Woods–Saxon potential with the Bohr–Mottelson parametrization [40]. For the protons of the even-even reference nuclei the valence space spanned 10 single-particle states in the range  $0f_{7/2}–0h_{11/2}$ . This valence space was also used for the neutrons of the reference nuclei with  $A < 90$ , while for the heavier nuclei a larger valence space spanning the single-particle-orbitals  $0f_{5/2}–0i_{13/2}$  (15 single-particle states) was used.

The BCS one-quasiparticle spectra were tuned by adjusting manually some of the key single-particle energies computed by using the Woods–Saxon potential. This was done to get a closer match between the low-lying one-quasiparticle states and the measured experimental ones. The adjustments were kept minimal with some changes in the span of spin-orbit gap(s) close to the proton and/or neutron Fermi surfaces. The computed pairing gaps were adjusted to fit the empirical values by tuning the pairing strength parameters  $g_{\text{pair}}^p$  and  $g_{\text{pair}}^n$  for protons and neutrons, separately. The empirical values were calculated by using the three-point formulas (5) and the experimental separation energies given in Ref. [41]. The QRPA spectra of the reference nuclei were tuned by scaling the particle-hole matrix elements with the parameter  $g_{\text{ph}}$  in order to reproduce the excitation energy of the lowest state of a given multipolarity. In the MQPM calculations a 3.0 MeV cutoff energy was used for the QRPA phonons to decrease the formidable computational burden.

#### IV. RESULTS AND DISCUSSION

Below we present our results: the electron spectra of 26 forbidden  $\beta^-$  decays (Figs. 2–9) and their integrated shape factors (Table II). The electron spectra are discussed in Sec. IV A and the integrated shape factors in Sec. IV B.

##### A. Electron spectra and effective value of $g_A$

The electron spectra for the studied first-forbidden decays are presented in Figs. 2–4 for  $g_A = 0.80–1.20$  (the identification of the decay type is presented in Table I). Similar figures for second-, third-, fourth-, and fifth-forbidden decays are presented in Figs. 5–9.

For the nonunique decay of  $^{125}\text{Sb}$ , presented in Fig. 2(a), decreasing the value of  $g_A$  increases the intensity of electrons emitted with low energies (0–100 keV), while decreasing the intensity of electrons with energies 250–350 keV. The differences in the shapes of the spectra are however very small—nothing like the dramatic behavior observed for the fourth-forbidden decays of  $^{113}\text{Cd}$  and  $^{115}\text{In}$  in Refs. [17] and [24]. From the other first-forbidden decays very slight changes in the low-energy spectrum can be seen for the nonunique decays of  $^{141}\text{Ce}$  in Fig. 2(b) and  $^{169}\text{Er}$  in Fig. 3(a), as well as for the unique decay of  $^{79}\text{Se}$  below it in Fig. 3(b). For the other first-forbidden decays the  $\beta$  spectrum seems to be independent of the value of  $g_A$ . The slight variation in the spectrum of  $^{79}\text{Se}$  can only be seen when the next-to-leading-order terms of the shape factor are taken into account. In the lowest-order approximation the spectrum would be completely unaffected when  $g_A$  is varied. The variation is minimal, but on the other hand, it is also minimal for the nonunique first-forbidden decays.

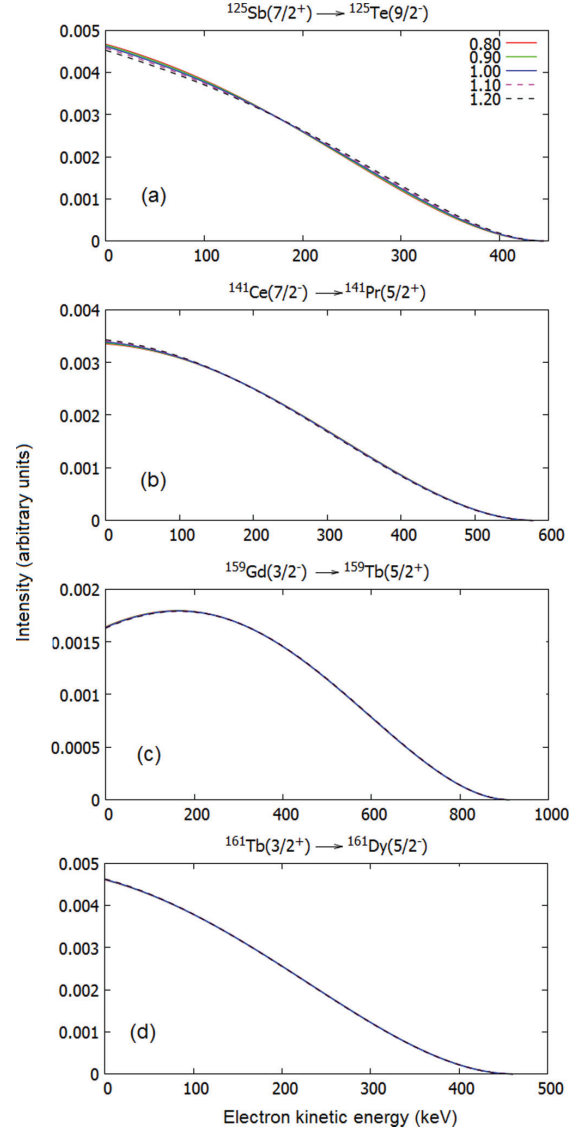


FIG. 2. The  $\beta$  spectra for first-forbidden nonunique  $\beta^-$  decays of the ground states of  $^{125}\text{Sb}$ ,  $^{141}\text{Ce}$ ,  $^{159}\text{Gd}$ , and  $^{161}\text{Tb}$ . The color coding represents the value of the weak axial-vector coupling constant  $g_A$ . For the vector coupling constant  $g_V$  the value 1.00 was adopted.

Another interesting feature for the first-forbidden decays is the remarkably similar shapes of the  $^{125}\text{Sb}$ ,  $^{141}\text{Ce}$ ,  $^{161}\text{Tb}$  [Figs. 2(a), 2(b), and 2(d)],  $^{169}\text{Er}$ ,  $^{79}\text{Se}$  [Figs. 3(a) and 3(b)], and  $^{107}\text{Pd}$  [Fig. 4(a)] spectra. For all of these the spectrum shape can be described as linearly decreasing with a slight downward bend at approximately 75% of the  $Q$  value. This is remarkable, since the  $Q$  values vary from a tiny 34.1(23) keV for  $^{107}\text{Pd}$  to a much larger 580.4(11) keV for  $^{141}\text{Ce}$  [36]. Another group of decays with very similar spectra are the first-forbidden unique

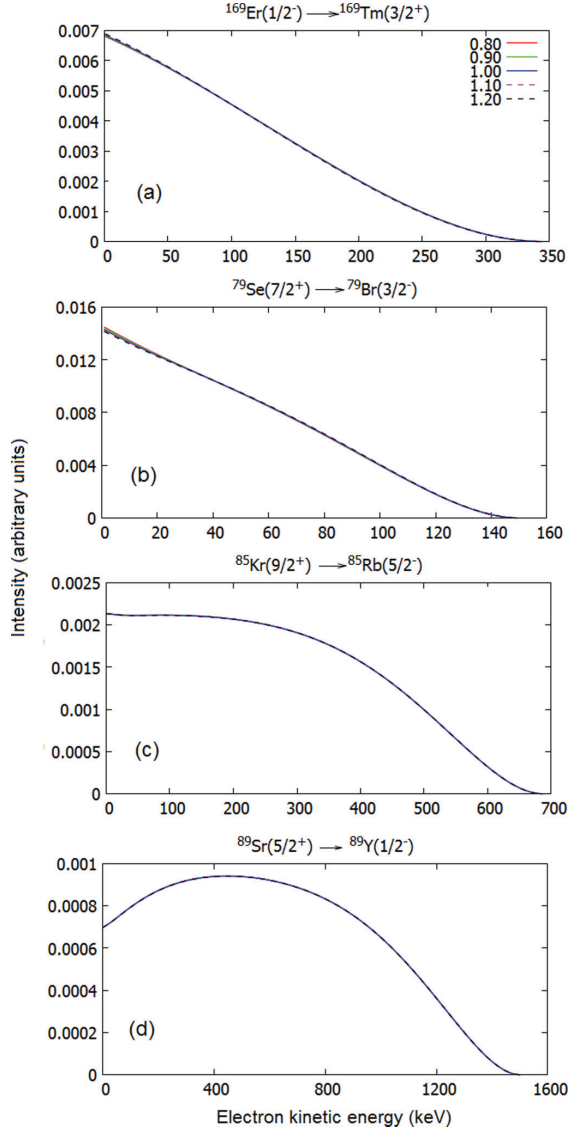


FIG. 3. The same as Fig. 2, but for the first-forbidden nonunique decay of  $^{169}\text{Er}$  and the unique decays of  $^{79}\text{Se}$ ,  $^{85}\text{Kr}$ , and  $^{89}\text{Sr}$ .

decay of  $^{125}\text{Sb}$  and  $^{137}\text{Cs}$  to the isomeric  $11/2^-$  states of the daughter nuclei presented in Figs. 4(b) and 4(c) and the second-forbidden unique decay of  $^{129}\text{I}$  shown in Fig. 5(a). Common to this group of decays is that the initial state has spin-parity  $7/2^+$ . For the decays of the first group no such obvious common feature is seen.

The electron spectra of second-forbidden decays shown in Fig. 5 differ from each other much more than the first-forbidden ones. In the case of the second-forbidden unique decay of  $^{129}\text{I}$  the next-to-leading-order terms of the shape factor do not make the beta spectrum, shown in Fig. 5(a),

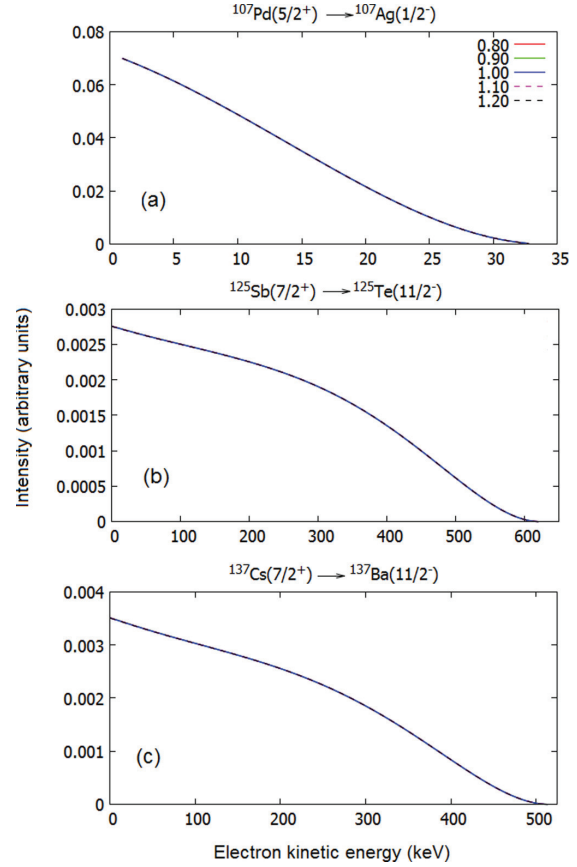


FIG. 4. The same as Fig. 2, but for the first-forbidden unique decays of  $^{107}\text{Pd}$ ,  $^{125}\text{Sb}$ , and  $^{137}\text{Cs}$ .

dependent on  $g_A$  in a noticeable way. Slight bending is seen for the nonunique decay of  $^{93}\text{Zr}$  [Fig. 5(b)], but the only second-forbidden transition showing heavy  $g_A$  dependence is the ground-state-to-ground-state decay of  $^{99}\text{Tc}$  presented in Fig. 5(c). The dependence is similar to that observed in Refs. [17,24] for  $^{113}\text{Cd}$  and  $^{115}\text{In}$ : when  $g_A \approx g_V$  a bell-shaped spectrum is produced, while otherwise the spectrum is monotonically decreasing. This decay is an excellent candidate for SSM. Comparison with experimental spectra could shed light on the effective value of  $g_A$  for second-forbidden nonunique transitions, and even second-forbidden  $\beta$  decays in general. The shape of  $^{135}\text{Cs}$  and  $^{137}\text{Cs}$  spectra on the other hand does not depend on the value of axial-vector coupling constant at all, as seen from Figs. 5(d) and 5(e). Decays such as the ground-state-to-ground-state decays of  $^{135,137}\text{Cs}$ , which are practically independent of  $g_A$ , are also experimentally important, since they could be used to check the accuracy of the theoretical spectra predicted by the MQPM as well as by other nuclear models, such as the nuclear shell model and the microscopic interacting boson-fermion model.

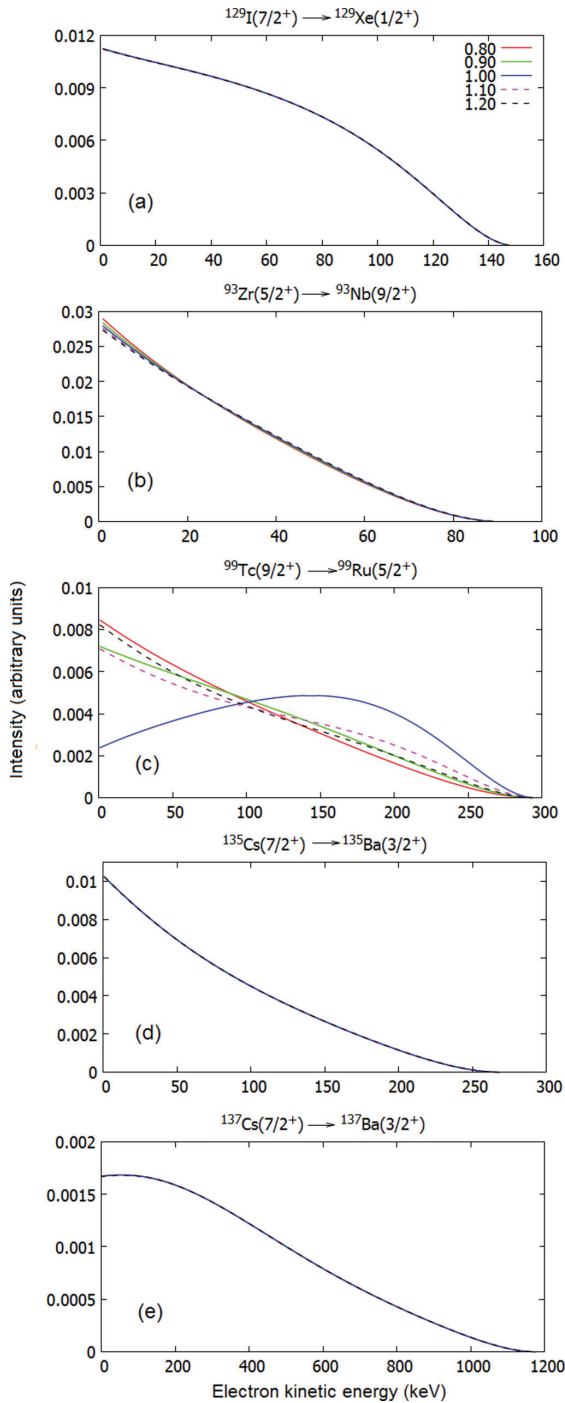


FIG. 5. The same as Fig. 2, but for the second-forbidden unique decay of  $^{129}\text{I}$  and the nonunique decays of  $^{93}\text{Zr}$ ,  $^{99}\text{Tc}$ ,  $^{135}\text{Cs}$ , and  $^{137}\text{Cs}$ .

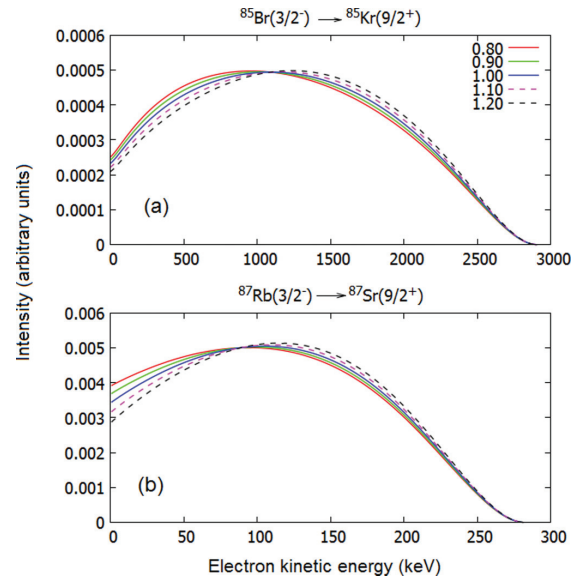


FIG. 6. The same as Fig. 2, but for the third-forbidden nonunique decays of  $^{85}\text{Br}$  and  $^{87}\text{Rb}$ .

While doing the MQPM calculation for the  $^{137}\text{Cs}$  decay, an important new feature of the  $\beta$  spectra was discovered. While the area under the curve depends significantly on the computed MQPM level scheme (e.g., the one shown in Fig. 1), the shape of the normalized (to unit area) electron spectrum does not. Even shifting the single-particle energies enough to change the ordering of energy levels in the odd- $A$  nucleus did not change the shape of the normalized spectrum at all. The other studied nuclei behave similarly, although for some of them slight changes in the electron spectrum were seen. At the mean-field level, moving arbitrarily the key single-particle orbitals at the proton and/or neutron Fermi surfaces by 0.5–1.5 MeV had very little effect. However, the shape is not completely independent of the computed level scheme, and large changes in it can deform the electron spectrum considerably. In terms of practical calculations it appears that getting the low end of the level scheme to reasonably agree with data, with the right ground-state spin-parity and few low-lying states near their experimental counterparts, is sufficient to produce an electron spectrum which is largely unaffected by further fine tuning. On the other hand, the theoretical half-life predictions can change by orders of magnitude when small changes to the single-particle energies are made, especially in cases where the even-even reference nucleus is (semi-)magic [16]. This stems from the sharp Fermi surface and vanishing pairing gap, making the BCS-approach sensitive to the details of the single-particle spectrum at the Fermi surface.

The results for third-forbidden nonunique ground-state-to-ground-state decays of  $^{85}\text{Br}$  and  $^{87}\text{Rb}$  are shown in Fig. 6. The shape factor depends on  $g_A$  in a very similar manner, even though the  $Q$  value for  $^{85}\text{Br}$  is tenfold larger than the one for  $^{87}\text{Rb}$ . Both of these decays are from a  $3/2^-$

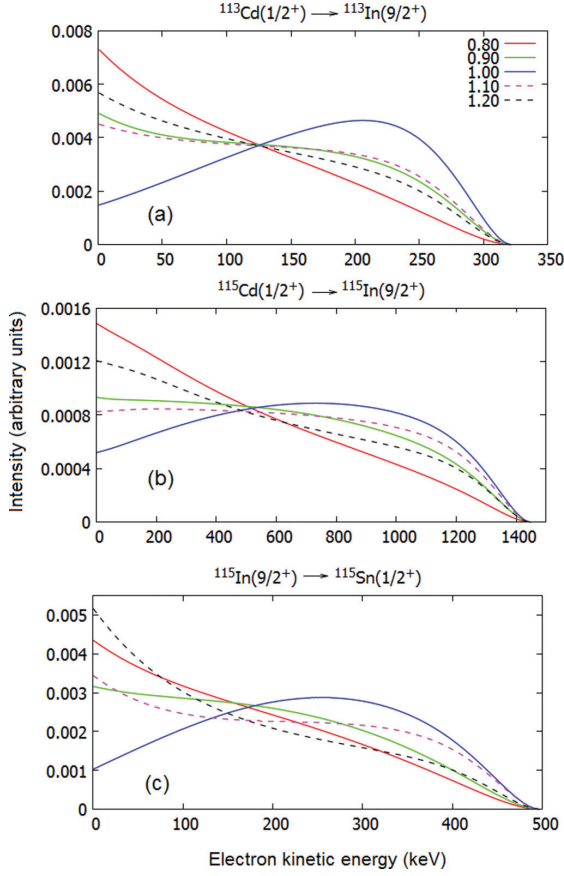


FIG. 7. The same as Fig. 2, but for the fourth-forbidden nonunique decays of  $^{113}\text{Cd}$ ,  $^{115}\text{Cd}$ , and  $^{115}\text{In}$ .

initial state to a  $9/2^+$  final state. The decay of  $^{87}\text{Rb}$  is experimentally measurable and thus another candidate for application of the spectrum-shape method. Unlike in the case of  $^{99}\text{Tc}$ , the dependence is fairly simple: when  $g_A$  decreases, the low-energy intensity increases, and the intensity at larger energies decreases.

The results for fourth-forbidden decays, all nonunique, are presented in Figs. 7 and 8. The transitions are split into two groups according to their basic features. The first one consists of the decays of  $^{113}\text{Cd}$ ,  $^{115}\text{Cd}$ , and  $^{115}\text{In}$  shown in Fig. 7. The transitions of  $^{113}\text{Cd}$  and  $^{115}\text{In}$  are experimentally measurable and have been studied extensively (see Refs. [17,24,38,42]). The spectra show a distinctive hump when  $g_A \approx g_V$ . Interestingly, the behavior is similar to that of  $^{99}\text{Tc}$  [see Fig. 5(c)]. These decays have one common feature: the  $9/2^+$  state is either the initial or final state. For  $^{113}\text{Cd}$  and  $^{115}\text{In}$  the effect of varying the weak axial-vector coupling constant is in line with the results of Ref. [24]. However, in the earlier study [17] the turning point of the MQPM spectrum of  $^{113}\text{Cd}$  was found to be at  $g_A \approx 0.9$  and for  $^{115}\text{In}$  at  $g_A \approx 0.95$ . It seems that the use of a larger model space for neutrons in this study and

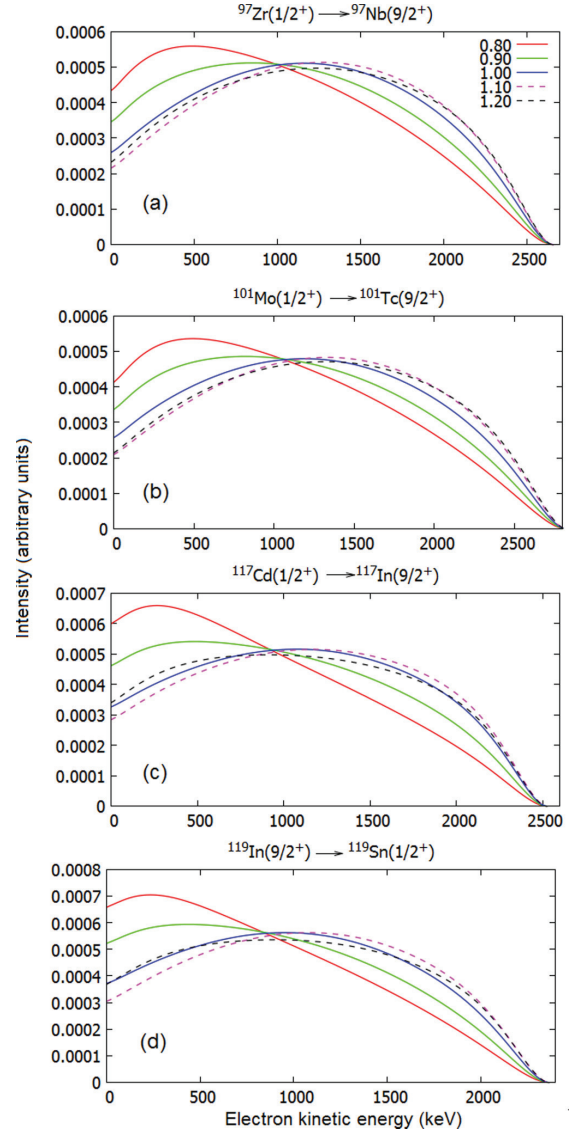


FIG. 8. The same as Fig. 2, but for the fourth-forbidden nonunique decays of  $^{97}\text{Zr}$ ,  $^{101}\text{Mo}$ ,  $^{117}\text{Cd}$ , and  $^{119}\text{In}$ .

in Ref. [24] has a notable effect on the shape of the electron spectrum. In Ref. [42] the electron spectra of these decays were calculated with the proton-neutron variant of MQPM with the free-nucleon values  $g_V = 1.0$  and  $g_A = 1.25$ . The shapes of the resulting spectra are nearly identical, which further supports the results of this paper.

To see whether the strong dependence of the shape factor on the weak coupling constants of the fourth-forbidden nonunique decays is limited to the three neighboring nuclei,  $^{113}\text{Cd}$ ,  $^{115}\text{Cd}$ , and  $^{115}\text{In}$ , four further fourth-forbidden nonunique ground-state-to-ground-state transitions were studied. These were the

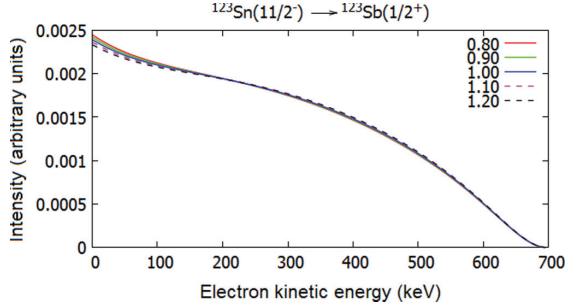


FIG. 9. The same as Fig. 2, but for the fifth-forbidden nonunique decay of  $^{123}\text{Sn}$ .

ground-state-to-ground-state  $\beta^-$  decays of  $^{97}\text{Zr}$ ,  $^{101}\text{Mo}$ ,  $^{117}\text{Cd}$ , and  $^{119}\text{Cd}$ , for which the spectra are presented in Fig. 8. These four decays also behave almost identically as functions of  $g_A$ . For these decays the spectrum shape is rather similar when  $g_A = 1.00$ – $1.20$ , but the shape changes radically when  $g_A$  is quenched below unity.

As shown thus far the dependence of the shape factor on the value of  $g_A$  seems to increase when the degree of forbiddenness grows. To test this hypothesis the fifth-forbidden decay of  $^{123}\text{Sn}$  to the lowest  $1/2^+$  excited state in  $^{123}\text{Sb}$  (see Fig. 9) was included in this study. This transition is not experimentally

measurable, but the theoretical results are important. As seen in the figure for this decay the spectrum shape does not depend on  $g_A$  in any significant way, thus invalidating the above-mentioned hypothesis. The sensitivity to  $g_A$  seems to connect more to the specific nuclear-structure details [like the almost magical involvement of a  $9/2^+$  state in all the SSM-sensitive nuclei of Figs. 7, 8, and 5(c)] rather than to the forbiddenness of the decay transition.

The observation that the  $\beta$  spectra of many transitions behave similarly is a strong indication that significant changes in the MQPM-predicted level schemes do not affect the shape evolution of the  $\beta$  spectra. Similar conclusions can be drawn from Ref. [24] where the three nuclear models, MQPM, NSM, and IBFM-2 were used to study  $^{113}\text{Cd}$  and  $^{115}\text{In}$  decays. An obvious conclusion drawn from this is that the SSM seems to be quite insensitive to the fine details of the nuclear Hamiltonian and the different approximations adopted to solve the related eigenvalue problem. This makes the SSM very robust, and thus a reliable tool for determining the effective value of  $g_A$ .

## B. Integrated shape factor $\tilde{C}$

In Refs. [17] and [24] it was noticed that for the decays of  $^{113}\text{Cd}$  and  $^{115}\text{In}$  the components  $\tilde{C}_V$ ,  $\tilde{C}_A$ , and  $\tilde{C}_{VA}$  of the decomposed integrated shape function  $\tilde{C}$  [see Eq. (21)] have much larger absolute values than  $\tilde{C}$ . The integrated shape function and its components are listed in Table II for each of the presently studied transitions.

TABLE II. Unitless integrated shape functions  $\tilde{C}$  of the studied transitions and their vector  $\tilde{C}_V$ , axial-vector  $\tilde{C}_A$ , and mixed components  $\tilde{C}_{VA}$ . For the total integrated shape factor  $\tilde{C}$  the values of the coupling constants were set to  $g_V = g_A = 1.0$ .

Transition	Type	$\tilde{C}_V$	$\tilde{C}_A$	$\tilde{C}_{VA}$	$\tilde{C}$
$^{125}\text{Sb}(7/2^+) \rightarrow ^{125}\text{Te}(9/2^-)$	1st non-uniq.	$1.524 \times 10^{-5}$	$4.734 \times 10^{-6}$	$-1.428 \times 10^{-5}$	$5.696 \times 10^{-6}$
$^{141}\text{Ce}(7/2^-) \rightarrow ^{141}\text{Pr}(5/2^+)$	1st non-uniq.	$1.906 \times 10^{-1}$	$2.944 \times 10^{-1}$	$-1.494 \times 10^{-1}$	$7.069 \times 10^{-2}$
$^{159}\text{Gd}(3/2^-) \rightarrow ^{159}\text{Tb}(5/2^+)$	1st non-uniq.	$9.439 \times 10^{-1}$	$2.436 \times 10^{-1}$	$9.563 \times 10^{-1}$	2.144
$^{161}\text{Tb}(3/2^+) \rightarrow ^{161}\text{Dy}(5/2^-)$	1st non-uniq.	$7.937 \times 10^{-3}$	$3.309 \times 10^{-4}$	$-3.223 \times 10^{-3}$	$5.045 \times 10^{-3}$
$^{169}\text{Er}(1/2^-) \rightarrow ^{169}\text{Tm}(3/2^+)$	1st non-uniq.	$1.833 \times 10^{-2}$	$3.097 \times 10^{-3}$	$-1.506 \times 10^{-2}$	$6.369 \times 10^{-3}$
$^{79}\text{Se}(7/2^+) \rightarrow ^{79}\text{Br}(3/2^-)$	1st unique	$2.224 \times 10^{-15}$	$1.161 \times 10^{-12}$	$6.105 \times 10^{-14}$	$1.224 \times 10^{-12}$
$^{85}\text{Kr}(9/2^+) \rightarrow ^{85}\text{Rb}(5/2^-)$	1st unique	$1.724 \times 10^{-10}$	$2.540 \times 10^{-5}$	$8.921 \times 10^{-8}$	$2.549 \times 10^{-5}$
$^{89}\text{Sr}(5/2^+) \rightarrow ^{89}\text{Y}(1/2^-)$	1st unique	$2.219 \times 10^{-16}$	$3.366 \times 10^{-11}$	$1.233 \times 10^{-13}$	$3.378 \times 10^{-11}$
$^{107}\text{Pd}(5/2^+) \rightarrow ^{107}\text{Ag}(1/2^-)$	1st unique	$8.332 \times 10^{-17}$	$1.472 \times 10^{-10}$	$6.432 \times 10^{-14}$	$1.473 \times 10^{-10}$
$^{125}\text{Sb}(7/2^+) \rightarrow ^{125}\text{Te}(11/2^-)$	1st unique	$1.600 \times 10^{-9}$	$1.397 \times 10^{-4}$	$6.427 \times 10^{-7}$	$1.404 \times 10^{-4}$
$^{137}\text{Cs}(7/2^+) \rightarrow ^{137}\text{Ba}(11/2^-)$	1st unique	$4.492 \times 10^{-9}$	$3.311 \times 10^{-4}$	$1.617 \times 10^{-6}$	$3.328 \times 10^{-4}$
$^{93}\text{Zr}(5/2^+) \rightarrow ^{93}\text{Nb}(9/2^+)$	2nd non-uniq.	$2.020 \times 10^{-16}$	$8.460 \times 10^{-15}$	$-2.191 \times 10^{-15}$	$6.471 \times 10^{-15}$
$^{99}\text{Tc}(9/2^+) \rightarrow ^{99}\text{Ru}(5/2^+)$	2nd non-uniq.	$4.342 \times 10^{-9}$	$4.386 \times 10^{-9}$	$-8.713 \times 10^{-9}$	$1.602 \times 10^{-11}$
$^{135}\text{Cs}(7/2^+) \rightarrow ^{135}\text{Ba}(3/2^+)$	2nd non-uniq.	$1.133 \times 10^{-8}$	$1.656 \times 10^{-8}$	$2.737 \times 10^{-8}$	$5.526 \times 10^{-8}$
$^{137}\text{Cs}(7/2^+) \rightarrow ^{137}\text{Ba}(3/2^+)$	2nd non-uniq.	$3.217 \times 10^{-5}$	$2.654 \times 10^{-5}$	$5.822 \times 10^{-5}$	$1.169 \times 10^{-4}$
$^{129}\text{I}(7/2^+) \rightarrow ^{129}\text{Xe}(1/2^+)$	2nd unique	$8.191 \times 10^{-22}$	$5.634 \times 10^{-17}$	$2.685 \times 10^{-19}$	$5.661 \times 10^{-17}$
$^{85}\text{Br}(3/2^-) \rightarrow ^{85}\text{Kr}(9/2^+)$	3rd non-uniq.	$1.597 \times 10^{-6}$	$3.022 \times 10^{-7}$	$-1.309 \times 10^{-6}$	$5.902 \times 10^{-7}$
$^{87}\text{Rb}(3/2^-) \rightarrow ^{87}\text{Sr}(9/2^+)$	3rd non-uniq.	$1.531 \times 10^{-13}$	$2.718 \times 10^{-14}$	$-1.264 \times 10^{-13}$	$5.387 \times 10^{-14}$
$^{97}\text{Zr}(1/2^+) \rightarrow ^{97}\text{Nb}(9/2^+)$	4th non-uniq.	$6.210 \times 10^{-11}$	$4.995 \times 10^{-11}$	$-1.055 \times 10^{-10}$	$6.588 \times 10^{-12}$
$^{101}\text{Mo}(1/2^+) \rightarrow ^{101}\text{Tc}(9/2^+)$	4th non-uniq.	$8.370 \times 10^{-11}$	$6.529 \times 10^{-11}$	$-1.399 \times 10^{-10}$	$9.131 \times 10^{-12}$
$^{113}\text{Cd}(1/2^+) \rightarrow ^{113}\text{In}(9/2^+)$	4th non-uniq.	$1.925 \times 10^{-19}$	$2.094 \times 10^{-19}$	$-4.002 \times 10^{-19}$	$1.385 \times 10^{-21}$
$^{115}\text{Cd}(1/2^+) \rightarrow ^{115}\text{In}(9/2^+)$	4th non-uniq.	$2.030 \times 10^{-14}$	$2.091 \times 10^{-14}$	$-4.059 \times 10^{-14}$	$6.238 \times 10^{-16}$
$^{115}\text{In}(9/2^+) \rightarrow ^{115}\text{Sn}(1/2^+)$	4th non-uniq.	$6.503 \times 10^{-18}$	$6.126 \times 10^{-18}$	$-1.256 \times 10^{-17}$	$6.492 \times 10^{-20}$
$^{117}\text{Cd}(1/2^+) \rightarrow ^{117}\text{In}(9/2^+)$	4th non-uniq.	$7.361 \times 10^{-12}$	$6.610 \times 10^{-12}$	$-1.342 \times 10^{-11}$	$5.545 \times 10^{-13}$
$^{119}\text{In}(9/2^+) \rightarrow ^{119}\text{Sn}(1/2^+)$	4th non-uniq.	$5.370 \times 10^{-12}$	$4.441 \times 10^{-12}$	$-9.441 \times 10^{-12}$	$3.708 \times 10^{-13}$
$^{123}\text{Sn}(11/2^-) \rightarrow ^{123}\text{Sb}(1/2^+)$	5th non-uniq.	$3.791 \times 10^{-28}$	$8.323 \times 10^{-30}$	$-9.932 \times 10^{-29}$	$2.881 \times 10^{-28}$

For all transitions the  $\tilde{C}_V$  and  $\tilde{C}_A$  components are positive, but the sign of  $\tilde{C}_{VA}$  varies. Although the next-to-leading-order terms are taken into account,  $\tilde{C}$  is dominated by the axial-vector component in the unique decays. The vector and vector-axial components add small positive corrections, which are about two orders of magnitude smaller than  $C_A$  at their largest. For the nonunique first-forbidden decays the largest contribution comes from  $\tilde{C}_V$ . The axial-vector component introduces a small positive correction, while the  $\tilde{C}_{VA}$  is negative, and has an absolute value of about 50%–90% of  $\tilde{C}_V$ . As an exception, the  $\tilde{C}_{VA}$  component is positive for  $^{159}\text{Gd}$ . The second-forbidden nonunique transitions on the other hand, have very different decompositions from each other. For  $^{93}\text{Zr}$  the axial-vector component dominates, and the negative correction of  $\tilde{C}_{VA}$  is about 25%. In the case of  $^{99}\text{Tc}$ ,  $\tilde{C}_V$  and  $\tilde{C}_A$  have almost identical values, while  $\tilde{C}_{VA}$  is twice as large and negative. The resulting total integrated shape function  $\tilde{C}$  is two orders of magnitude smaller than the absolute values of its components. For  $^{135}\text{Cs}$  and  $^{137}\text{Cs}$  the results are rather similar, but  $\tilde{C}_{VA}$  is positive. For the two third-forbidden nonunique decays the vector component dominates, the axial-vector component is small, and the absolute value of the negative  $\tilde{C}_{VA}$  is about 80% of the vector component. The fourth-forbidden decays are divided into the same groups as suggested by the electron spectra. The decomposition is similar to  $^{99}\text{Tc}$  for  $^{113}\text{Cd}$ ,  $^{115}\text{Cd}$ , and  $^{115}\text{In}$ . For the rest of the fourth-forbidden decays  $\tilde{C}_V$  dominates,  $\tilde{C}_A$  is about 20% smaller, and  $\tilde{C}_{VA}$  is negative and has an absolute value of slightly less than the sum of  $\tilde{C}_V$  and  $\tilde{C}_A$ . The resulting total integrated shape factor is one order of magnitude smaller than its components. For the fifth-forbidden transition of  $^{123}\text{Sn}$ ,  $\tilde{C}$  is dominated by  $\tilde{C}_V$ , and the corrections from other components are small.

## V. CONCLUSIONS

The sensitivity of the shapes of electron spectra for 26 forbidden  $\beta^-$  decays of odd- $A$  nuclei were studied by using the nuclear matrix elements derived from the microscopic quasiparticle-phonon model (MQPM) and by varying the value of the axial-vector coupling constant  $g_A$ . The next-to-leading-order terms were included in the corresponding  $\beta$ -decay shape factors. In the spectrum-shape method (SSM) the shapes of computed electron spectra can be compared with the measured ones to access the effective value of  $g_A$ . The shape of the computed electron spectrum was found to be unaffected by minor changes in the computed excitation spectra of the involved nuclei, implying stability against the variations of the details of the nuclear Hamiltonian. This is supported by the study [24] where three different nuclear Hamiltonians were used. The study of Ref. [24] suggests also that the SSM is

not very sensitive to the many-body framework used to solve the Hamiltonian-related eigenvalue problem since the three nuclear-structure models produced quite compatible SSM results despite their completely different theory frameworks. At the level of the mean field, in turn, in most cases moving the single-particle energies of the underlying mean field by as much as 1.5 MeV did not affect the normalized  $\beta$  spectra, even though the half-life was affected significantly. Furthermore, transitions of the same type (forbiddenness, uniqueness) in neighboring nuclei produce similar spectrum shapes regardless of the  $Q$  value. The above features make the SSM a much more robust method than just comparing the theoretical and experimental half-lives to extract the effective value of  $g_A$ .

The electron spectrum of the ground-state-to-ground-state decays of  $^{99}\text{Tc}$  and  $^{87}\text{Rb}$  depend significantly on the effective value of the axial-vector coupling constant  $g_A$ . Since these decays are experimentally measurable, they can be used to gain knowledge on the effective value of  $g_A$  in second- and third-forbidden nonunique beta decays by using the spectrum-shape method. The decays for which the spectrum shape does not depend on the values of the weak coupling constants, such as the transitions of  $^{135}\text{Cs}$  and  $^{137}\text{Cs}$ , could be used to test the accuracy of the theoretical spectra.

The shape factors of the third- and especially fourth-forbidden decays depend very sensitively on the value of the coupling constants. Besides the transitions in this study, there are no other medium-heavy odd- $A$  nuclei which have a third- or fourth-forbidden decay branch with a significant branching ratio. However, for example  $^{50}\text{V}$  decays via a fourth-forbidden nonunique transition and could be a candidate for SSM when a shell-model type of framework would be used to evaluate the needed wave functions.

In general, the decomposition of the integrated shape functions  $\tilde{C}$  into vector, axial-vector, and vector-axial-vector components is similar when the normalized  $\beta$  spectra resemble each other. However, the decompositions of the studied first- and third-forbidden nonunique decays are similar, with the exception of the one of  $^{159}\text{Gd}$ , but the normalized  $\beta$  spectra of these decays are nothing alike.

Finally, the information gained through SSM on the effective value of  $g_A$  in forbidden decay transitions could help in solving the  $g_A$  problem related to the neutrinoless double beta decay, which proceeds via virtual transitions, and largely via the forbidden ones.

## ACKNOWLEDGMENTS

This work has been partially supported by the Academy of Finland under the Finnish Centre of Excellence Programme 2012-2017 (Nuclear and Accelerator Based Programme at JYFL).

[1] J. Suhonen and O. Civitarese, *Phys. Rep.* **300**, 123 (1998).

[2] J. Maalampi and J. Suhonen, *Adv. High Energy Phys.* **2013**, 505874 (2013).

[3] H. Ejiri, N. Soukouti, and J. Suhonen, *Phys. Lett. B* **729**, 27 (2014).

[4] H. Ejiri and J. Suhonen, *J. Phys. G* **42**, 055201 (2015).

- [5] R. P. Feynmann and M. Gell-Mann, *Phys. Rev.* **109**, 193 (1958).  
[6] R. P. Feynmann and M. Gell-Mann, *Phys. Rev.* **111**, 362 (1958).  
[7] W. Theis, *Eur. Phys. J. A* **150**, 590 (1958).  
[8] K. Zuber, *Neutrino Physics* (Institute of Physics Publishing, Ltd., London, 2004).  
[9] E. D. Commins, *Weak Interactions* (McGraw-Hill, New York, 2007).  
[10] J. Suhonen, *From Nucleons to Nucleus: Concepts of Microscopic Nuclear Theory* (Springer, Berlin, 2007).  
[11] J. Suhonen and O. Civitarese, *Phys. Lett. B* **725**, 153 (2013).  
[12] J. Suhonen and O. Civitarese, *Nucl. Phys. A* **924**, 1 (2014).  
[13] P. Pirinen and J. Suhonen, *Phys. Rev. C* **91**, 054309 (2015).  
[14] D. S. Delion and J. Suhonen, *Europhys. Lett.* **107**, 52001 (2014).  
[15] F. F. Deppisch and J. Suhonen, *Phys. Rev. C* **94**, 055501 (2016).  
[16] J. Kostensalo and J. Suhonen, *Phys. Rev. C* **95**, 014322 (2017).  
[17] M. Haaranen, P. C. Srivastava, and J. Suhonen, *Phys. Rev. C* **93**, 034308 (2016).  
[18] J. Toivanen and J. Suhonen, *J. Phys. G* **21**, 1491 (1995).  
[19] J. Toivanen and J. Suhonen, *Phys. Rev. C* **57**, 1237 (1998).  
[20] B. H. Wildenthal, M. S. Curtin, and B. A. Brown, *Phys. Rev. C* **28**, 1343 (1983).  
[21] G. Martínez-Pinedo, A. Poves, E. Caurier, and A. P. Zuker, *Phys. Rev. C* **53**, R2602(R) (1996).  
[22] E. Caurier, F. Nowacki, and A. Poves, *Phys. Lett. B* **711**, 62 (2012).  
[23] P. Belli, R. Bernabei, N. Bukilic, F. Cappella, R. Cerulli, C. J. Dai, F. A. Danevich, J. R. de Laeter, A. Incicchitti, V. V. Kobychev, S. S. Nagorny, S. Nisi, F. Nozzoli, D. V. Poda, D. Prosperi, V. I. Tretyak, and S. S. Yurchenko, *Phys. Rev. C* **76**, 064603 (2007).  
[24] M. Haaranen, J. Kotila, and J. Suhonen, *Phys. Rev. C* **95**, 024327 (2017).  
[25] F. Iachello and A. Arima, *The Interacting Boson Model* (Cambridge University Press, Cambridge, 1987).  
[26] F. Iachello and P. V. Isacker, *The Interacting Boson-Fermion Model* (Cambridge University Press, USA, 1991).  
[27] H. Behrens and W. Bühring, *Electron Radial Wave Functions and Nuclear Beta Decay* (Clarendon, Oxford, 1982).  
[28] M. Baranger, *Phys. Rev.* **120**, 957 (1960).  
[29] A. Bohr, B. R. Mottelson, and D. Pines, *Phys. Rev.* **110**, 936 (1958).  
[30] N. N. Bogoliubov, *Sov. Phys. JETP* **34**, 41 (1958).  
[31] J. Valatin, *Phys. Rev.* **122**, 1012 (1961).  
[32] P. Ring and P. Schuck, *The Nuclear Many-Body Problem* (Springer, New York, 1980).  
[33] G. Audi and A. Vapstra, *Nucl. Phys. A* **565**, 1 (1993).  
[34] G. Audi and A. Vapstra, *Nucl. Phys. A* **595**, 409 (1995).  
[35] D. Rowe, *Nuclear Collective Motion* (Methuen, London, 1970).  
[36] National Nuclear Data Center, Brookhaven National Laboratory, [www.nndc.bnl.gov](http://www.nndc.bnl.gov).  
[37] J. C. Hardy, I. S. Towner, V. Koslowsky, E. Hagberg, and H. Schmeing, *Nucl. Phys. A* **509**, 429 (1990).  
[38] M. T. Mustonen, M. Aunola, and J. Suhonen, *Phys. Rev. C* **73**, 054301 (2006).  
[39] M. Haaranen and J. Suhonen, *Eur. Phys. J. A* **19**, 93 (2013).  
[40] A. Bohr and B. R. Mottelson, *Nuclear Structure* (Benjamin, New York, 1969), Vol. I.  
[41] G. Audi, F. G. Kondev, M. Wang, B. Pfeiffer, X. Sun, J. Blachot, and M. MacCormick, *Chin. Phys. C* **36**, 1157 (2012).  
[42] M. T. Mustonen and J. Suhonen, *Phys. Lett. B* **657**, 38 (2007).



## II

# **$g_A$ -DRIVEN SHAPES OF ELECTRON SPECTRA OF FORBIDDEN $\beta$ DECAYS IN THE NUCLEAR SHELL MODEL**

by

Kostensalo, J. and Suhonen, J. 2017

Physical Review C 96, 024317  
doi: 10.1103/PhysRevC.96.024317

Reproduced with kind permission by American Physical Society.

**$g_A$ -driven shapes of electron spectra of forbidden  $\beta$  decays in the nuclear shell model**

Joel Kostensalo\* and Jouni Suhonen†

*Department of Physics, University of Jyväskylä, P.O. Box 35, FI-40014, Finland*

(Received 10 May 2017; published 21 August 2017)

The evolution of the shape of the electron spectra of 16 forbidden  $\beta^-$  decays as a function of  $g_A$  was studied using the nuclear shell model in appropriate single-particle model spaces with established, well-tested nuclear Hamiltonians. The  $\beta$  spectra of  $^{94}\text{Nb}(6^+) \rightarrow ^{94}\text{Mo}(4^+)$  and  $^{98}\text{Tc}(6^+) \rightarrow ^{98}\text{Ru}(4^+)$  were found to depend strongly on  $g_A$ , which makes them excellent candidates for the determination of the effective value of  $g_A$  with the spectrum-shape method (SSM). A strong  $g_A$  dependence is also seen in the spectrum of  $^{96}\text{Zr}(0^+) \rightarrow ^{96}\text{Nb}(6^+)$ . This decay could be used for determining the quenching of  $g_A$  in sixth-forbidden decays in the future, when the measurement of the spectrum becomes experimentally feasible. The calculated shell-model electron spectra of the ground-state-to-ground-state decays of  $^{87}\text{Rb}$ ,  $^{99}\text{Tc}$ , and  $^{137}\text{Cs}$  and the decay of  $^{137}\text{Cs}$  to the isomeric  $11/2^-$  state in  $^{137}\text{Ba}$  were found to be in excellent agreement with the spectra previously calculated using the microscopic quasiparticle-phonon model. This is further evidence of the robust nature of the SSM observed in the previous studies.

DOI: 10.1103/PhysRevC.96.024317

**I. INTRODUCTION**

At the nuclear level  $\beta$  decay can be considered as a mutual interaction of the hadronic and leptonic currents mediated by a massive vector boson  $W^\pm$  [1]. The leptonic and hadronic currents can be expressed as a mixture of both vector and axial-vector components [2–4]. The weak vector and axial-vector coupling constants  $g_V$  and  $g_A$  enter the theory when the hadronic current is renormalized at the nucleon level [5]. The conserved vector-current hypothesis (CVC) and partially conserved axial-vector-current hypothesis (PCAC) yield the free-nucleon values  $g_V = 1.00$  and  $g_A = 1.27$  [6] but inside nuclear matter the value of  $g_A$  is affected by many-nucleon correlations and a quenched value might be needed to reproduce experimental data [1]. Precise information on the effective value of  $g_A$  is crucial when predicting half-lives of neutrinoless double beta decays since the half-lives are proportional to the fourth power of  $g_A$  [7,8].

The effective value of  $g_A$  has earlier been probed using a half-life comparison method, in which the predicted and experimental values are compared for different values of  $g_A$ . This has been done for Gamow-Teller and first-forbidden decays using nuclear matrix elements calculated with the proton-neutron quasiparticle random-phase approximation (pnQRPA) [9–13]. The half-life comparison method predicts that the value of  $g_A$  is quenched significantly in these transitions. Also in the old studies [14–17] of first-forbidden  $\beta$  decays, strong quenchings were predicted. In a recent shell-model study [18] of  $r$ -process waiting-point nuclei, a strong quenching of  $g_A$  was confirmed. The half-life comparison method could be used to find out if similar quenching of  $g_A$  is seen in highly forbidden unique beta decays by using the half-lives calculated in Ref. [19], once experimental data become available.

In Ref. [20] the spectrum-shape method (SSM) was introduced as a complementary way to study the effective

value of the weak coupling constants. In the SSM the shapes of computed and experimental (normalized) electron spectra are compared in order to find the ratio  $g_A/g_V$  for nonunique forbidden beta  $\beta^-$  decays, for which the shape factors depend on  $g_A/g_V$  in a very nontrivial way. In Ref. [21] the SSM was applied to the fourth-forbidden ground-state-to-ground-state transition of  $^{113}\text{Cd}$  using the microscopic quasiparticle-phonon model (MQPM) [22,23], the nuclear shell model (NSM) [24–26], the microscopic interacting boson-fermion model (IBFM-2) [27,28], and experimental spectrum of Ref. [29]. The closest match between the theoretical and experimental spectra was found when  $g_A/g_V \approx 0.92$  for all three nuclear models. The half-life comparison method, on the other hand, gave very different results when different nuclear models were used. In Ref. [30] it was noticed that the shape of the spectrum was largely unaffected by modest changes in the MQPM wave function, even though the predicted half-life was affected significantly. The observations of these previous studies suggest that the SSM is very robust, quite insensitive to the details of the adopted nuclear mean field and Hamiltonian. It is thus a reliable tool for probing the ratio  $g_A/g_V$ .

The  $g_A$ -driven evolution of the shapes of several experimentally measurable forbidden nonunique decay spectra in medium-heavy odd- $A$  nuclei was studied using the MQPM in Ref. [30]. Only four good candidates for the application of the spectrum-shape method have been found thus far. These are the ground-state-to-ground-state decays of  $^{87}\text{Rb}$ ,  $^{99}\text{Tc}$ ,  $^{113}\text{Cd}$ , and  $^{115}\text{In}$  [20,30]. In the present paper we set out to find potential new candidates for the application of the SSM in light to medium-heavy nuclei using the nuclear shell model. We also compare the NSM and MQPM  $\beta$  spectra of  $^{87}\text{Rb}$ ,  $^{99}\text{Tc}$ , and  $^{137}\text{Cs}$  to see if the model independence observed in Ref. [21] applies for these decays as well. The decays of  $^{137}\text{Cs}$  to the  $3/2^+$  ground state and the  $11/2^-$  isomeric state of  $^{137}\text{Ba}$  are particularly interesting for comparing the differences in the MQPM and NSM spectra, since the MQPM calculations predict a  $g_A$ -independent spectrum shape for these decays.

This article is organized as follows. In Sec. II we give the theoretical background behind the  $\beta$  spectrum shape. In

\*joel.kostensalo@student.jyu.fi

†jouni.suhonen@phys.jyu.fi

Sec. III we describe the application of the nuclear shell model to the spectrum shape of forbidden  $\beta^-$  decays. In Sec. IV we present our results and in Sec. V we draw the conclusions.

## II. THEORETICAL FORMALISM

We begin the description of the  $\beta^-$  decay by making the so-called impulse approximation, in which at the exact moment of decay the decaying nucleon only interacts via the weak interaction and the strong interaction with the other  $A - 1$  nucleons can be ignored. Since the vector boson  $W^-$  has a large mass and thus propagates only a short distance, the flow lines of the nucleons, i.e., the hadronic current, and the flow lines of the emitted leptons, i.e., the leptonic current, can be considered to interact at a pointlike weak-interaction vertex with an effective coupling constant  $G_F$ , the Fermi constant. The parity nonconserving nature of the weak interaction is reflected in the fact that the hadronic current can be written at the quark level (up  $u$  and down  $d$  quarks) as a mixture of vector and axial-vector components as [2–4]

$$J_H^\mu = \bar{u}(x)\gamma^\mu(1 - \gamma_5)d(x), \quad (1)$$

where  $\gamma^\mu$  are the usual Dirac matrices and  $\gamma_5 = i\gamma^0\gamma^1\gamma^2\gamma^3$ . Renormalization effects of strong interactions must be taken into account when moving from the quark level to the hadron level. The hadronic current at the nucleon level (neutron  $n$  and proton  $p$ ) can then be written as [5,6]

$$J_H^\mu = \bar{p}(x)\gamma^\mu(g_V - g_A\gamma_5)n(x), \quad (2)$$

where  $g_V$  and  $g_A$  are the weak vector and axial-vector coupling constants, respectively. The conserved vector-current hypothesis of the standard model (CVC) gives the free-nucleon value  $g_V = 1.0$  for the weak vector coupling constant and the partially conserved axial-vector-current hypothesis (PCAC) gives the free-nucleon value  $g_A = 1.27$  for the weak axial-vector coupling constant. Inside the nuclear matter the value of  $g_A$  is affected by many-nucleon correlations and so the free nucleon value might not be the one to use in practical calculations [6]. The present paper is a step towards solving the problem of what value to use for  $g_A$  inside finite nuclei.

In the impulse approximation the probability of the electron being emitted with kinetic energy between  $W_e$  and  $W_e + dW_e$  is

$$P(W_e)dW_e = \frac{G_F}{(\hbar c)^6} \frac{1}{2\pi^3\hbar} C(W_e) \times p_e c W_e (W_0 - W_e)^2 F_0(Z, W_e) dW_e, \quad (3)$$

where  $p_e$  is the momentum of the electron,  $Z$  is the proton number,  $F_0(Z, W_e)$  is the Fermi function, and  $W_0$  is the end-point energy of the  $\beta$  spectrum. The nuclear structure information is buried in the shape factor  $C(w_e)$ .

The half-life of a  $\beta$  decay can be written as

$$t_{1/2} = \frac{\kappa}{\tilde{C}}, \quad (4)$$

where  $\tilde{C}$  is the integrated shape factor and the constant  $\kappa$  has the value [31]

$$\kappa = \frac{2\pi^3\hbar^7 \ln 2}{m_e^5 c^4 (G_F \cos\theta_C)^2} = 6147 \text{ s}, \quad (5)$$

$\theta_C$  being the Cabibbo angle. In order to simplify the formalism it is usual to introduce unitless kinematic quantities  $w_e = W_e/m_e c^2$ ,  $w_0 = W_0/m_e c^2$ , and  $p = p_e c/(m_e c^2) = \sqrt{w_e^2 - 1}$ . With the unitless quantities the integrated shape factor can be expressed as

$$\tilde{C} = \int_1^{w_0} C(w_e) p w_e (w_0 - w_e)^2 F_0(Z, w_e) dw_e. \quad (6)$$

The shape factor  $C(w_e)$  of Eq. (6) contains complicated combinations of both (universal) kinematic factors and NMEs. In this paper we use the nuclear shell model to calculate the one-body transition densities related to the NMEs of the shape factor. The details of the shape factor and the constitution of its NMEs can be found from Refs. [32,33]. As in the previous SSM studies [20,21,30] we go beyond the earlier studies [32,33] and take into account the next-to-leading-order

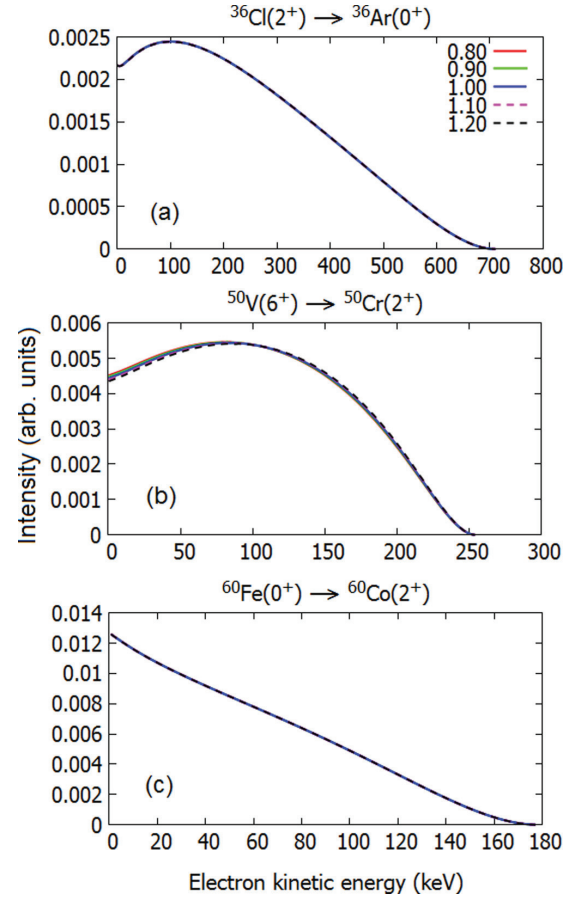


FIG. 1. Normalized electron spectra for the second-forbidden nonunique  $\beta^-$  decays of  $^{36}\text{Cl}$  [panel (a)] and  $^{60}\text{Fe}$  [panel (c)], and the fourth-forbidden nonunique decay of  $^{50}\text{V}$  [panel (b)]. The value  $g_V = 1.00$  was adopted and the color coding represents the value of  $g_A$ .

terms of the shape function. The details of the next-to-leading order shape factors are discussed in [21].

The shape factor  $C(w_e)$  can be decomposed into vector, axial-vector, and mixed vector-axial-vector parts. In this decomposition the shape factor is

$$C(w_e) = g_V^2 C_V(w_e) + g_A^2 C_A(w_e) + g_V g_A C_{VA}(w_e). \quad (7)$$

Integrating Eq. (7) over the electron kinetic energy, we get an analogous expression for the integrated shape factor

$$\tilde{C} = g_V^2 \tilde{C}_V + g_A^2 \tilde{C}_A + g_V g_A \tilde{C}_{VA}, \quad (8)$$

where the factors  $\tilde{C}_i$  in Eq. (8) are just constants, independent of the electron energy.

### III. ADOPTED MODEL SPACES AND NUCLEAR HAMILTONIANS

The electron spectra of 16 forbidden  $\beta^-$  transitions were calculated for different values of the coupling constant  $g_A$  using the nuclear matrix elements produced by the nuclear shell model. The calculations were done using the shell model code NuShellX@MSU [34], with appropriate model spaces and well established Hamiltonians chosen for each studied decay individually. No additional truncations, beyond those used in the original works, were introduced. The calculations were run on a desktop computer with a 3.3 GHz processor, so the computational burden had to be taken into account when choosing the model space.

The adopted model spaces and Hamiltonians are as follows. *sd shell*: for the calculation of the wave functions and one-body transition densities related to the decay  $^{36}\text{Cl}(2^+) \rightarrow ^{36}\text{Ar}(0^+)$  we adopted the  $0d-1s$  model space and the phenomenological USDB interaction [35]. *pf shell*: as in the earlier shell-model studies regarding the half-lives of the transitions  $^{48}\text{Ca}(0^+) \rightarrow ^{48}\text{Sc}(4^+, 5^+, 6^+)$  [36] and  $^{50}\text{V}(6^+) \rightarrow ^{50}\text{Cr}(2^+)$  [37], the  $0f-1p$  model space with the interaction GXPF1A [38,39] was used

to calculate the electron spectra of these decays. The GXPF1A interaction is very good at predicting the properties of *pf*-shell nuclei. However, since the computational burden increases dramatically when the number of particles approaches half of the maximum in the valence space, this interaction could not be used for the  $^{60}\text{Fe}(0^+) \rightarrow ^{60}\text{Co}(2^+)$  decay transition. Instead, a model space spanning the  $\pi 0f_{7/2}, \nu 1p_{3/2}, \nu 0f_{5/2}$ , and  $\nu 1p_{1/2}$  orbitals was adopted with the Horie-Ogawa interaction [40,41]. *pf $g_{9/2}$  shell*: the *jj44b* interaction developed by Brown and Lisetskiy for the  $0f_{5/2} - 1p - 0g_{9/2}$  model space (see endnote on Ref. [28] of [42]) was used for the calculation of the  $^{87}\text{Rb}(3/2^-) \rightarrow ^{87}\text{Sr}(9/2^+)$  transition. For the decays of the  $A = 94-99$  nuclei, the effective interaction of Gloeckner [43] in the model space spanning the  $\pi 1p_{1/2}, \pi 0g_{9/2}, \nu 2s_{1/2}$ , and  $2d_{5/2}$  was used. *sdgh $_{11/2}$  shell*: finally, for the decay transitions  $^{126}\text{Sn}(0^+) \rightarrow ^{126}\text{Sb}(2^+)$  and  $^{137}\text{Cs}(7/2^+) \rightarrow ^{137}\text{Ba}(11/2^-, 3/2^+)$  the Sn100pn interaction [44] in the  $0g_{7/2} 2s 1d0h_{11/2}$  model space was adopted.

### IV. RESULTS AND DISCUSSION

Below we present our results: the electron spectra of 16 forbidden  $\beta^-$  decays (Figs. 1–5) and their integrated shape factors (Table I). The electron spectra are discussed in Sec. IV A and the integrated shape factors in Sec. IV B.

#### A. Electron spectra and the effective value of $g_A$

The studied spectra fall into three groups.

*GROUP 1.* The first group, for which the spectra can be found in Figs. 1 and 2, consists of six transitions for which the SSM analysis has not been done prior to this study. These decays are potentially interesting for the practical application of the spectrum-shape method, since most of them are second-forbidden nonunique transitions with branching ratios above 90%. The only exception is the undetected fourth-forbidden  $\beta^-$  decay branch of  $^{50}\text{V}$ , for which the branching ratio has

TABLE I. Unitless integrated shape functions  $\tilde{C}$  of the studied transitions and their vector  $\tilde{C}_V$ , axial-vector  $\tilde{C}_A$ , and mixed components  $\tilde{C}_{VA}$ . For the total integrated shape factor  $\tilde{C}$  the values of the coupling constants were set to  $g_V = g_A = 1.0$ .

Transition	Type	$\tilde{C}_V$	$\tilde{C}_A$	$\tilde{C}_{VA}$	$\tilde{C}$
$^{137}\text{Cs}(7/2^+) \rightarrow ^{137}\text{Ba}(11/2^-)$	1st uniq.	$9.681 \times 10^{-11}$	$8.322 \times 10^{-6}$	$3.761 \times 10^{-8}$	$8.359 \times 10^{-6}$
$^{36}\text{Cl}(2^+) \rightarrow ^{36}\text{Ar}(0^+)$	2nd nonuniq.	$6.081 \times 10^{-9}$	$3.152 \times 10^{-10}$	$-2.746 \times 10^{-9}$	$3.650 \times 10^{-9}$
$^{60}\text{Fe}(0^+) \rightarrow ^{60}\text{Co}(2^+)$	2nd nonuniq.	$2.347 \times 10^{-13}$	$5.232 \times 10^{-11}$	$-7.000 \times 10^{-12}$	$4.556 \times 10^{-11}$
$^{94}\text{Nb}(6^+) \rightarrow ^{94}\text{Mo}(4^+)$	2nd nonuniq.	$1.598 \times 10^{-8}$	$1.469 \times 10^{-8}$	$-3.058 \times 10^{-8}$	$1.029 \times 10^{-10}$
$^{98}\text{Tc}(6^+) \rightarrow ^{98}\text{Ru}(4^+)$	2nd nonuniq.	$2.723 \times 10^{-8}$	$2.544 \times 10^{-8}$	$-5.254 \times 10^{-8}$	$1.207 \times 10^{-10}$
$^{99}\text{Tc}(9/2^+) \rightarrow ^{99}\text{Ru}(5/2^+)$	2nd nonuniq.	$2.240 \times 10^{-9}$	$2.130 \times 10^{-9}$	$-4.361 \times 10^{-9}$	$8.777 \times 10^{-12}$
$^{126}\text{Sn}(0^+) \rightarrow ^{126}\text{Sb}(2^+)$	2nd nonuniq.	$1.422 \times 10^{-8}$	$7.125 \times 10^{-9}$	$2.011 \times 10^{-8}$	$4.145 \times 10^{-8}$
$^{137}\text{Cs}(7/2^+) \rightarrow ^{137}\text{Ba}(3/2^+)$	2nd nonuniq.	$4.211 \times 10^{-6}$	$2.836 \times 10^{-6}$	$6.879 \times 10^{-6}$	$1.392 \times 10^{-5}$
$^{87}\text{Rb}(3/2^-) \rightarrow ^{87}\text{Sr}(9/2^+)$	3rd nonuniq.	$1.185 \times 10^{-13}$	$2.082 \times 10^{-14}$	$-9.734 \times 10^{-14}$	$4.202 \times 10^{-14}$
$^{48}\text{Ca}(0^+) \rightarrow ^{48}\text{Sc}(4^+)$	4th nonuniq.	$8.946 \times 10^{-28}$	$5.934 \times 10^{-29}$	$-4.606 \times 10^{-28}$	$4.934 \times 10^{-28}$
$^{50}\text{V}(6^+) \rightarrow ^{50}\text{Cr}(2^+)$	4th nonuniq.	$1.024 \times 10^{-23}$	$9.137 \times 10^{-25}$	$2.131 \times 10^{-24}$	$1.329 \times 10^{-23}$
$^{96}\text{Zr}(0^+) \rightarrow ^{96}\text{Nb}(4^+)$	4th nonuniq.	$3.176 \times 10^{-27}$	$3.170 \times 10^{-28}$	$-2.006 \times 10^{-27}$	$1.486 \times 10^{-27}$
$^{48}\text{Ca}(0^+) \rightarrow ^{48}\text{Sc}(5^+)$	4th uniq.	$2.577 \times 10^{-30}$	$3.931 \times 10^{-25}$	$1.334 \times 10^{-27}$	$3.945 \times 10^{-25}$
$^{96}\text{Zr}(0^+) \rightarrow ^{96}\text{Nb}(5^+)$	4th uniq.	$1.765 \times 10^{-29}$	$1.551 \times 10^{-24}$	$6.844 \times 10^{-27}$	$1.558 \times 10^{-24}$
$^{48}\text{Ca}(0^+) \rightarrow ^{48}\text{Sc}(6^+)$	6th nonuniq.	$1.124 \times 10^{-32}$	$3.498 \times 10^{-34}$	$3.947 \times 10^{-33}$	$1.554 \times 10^{-32}$
$^{96}\text{Zr}(0^+) \rightarrow ^{96}\text{Nb}(6^+)$	6th nonuniq.	$5.811 \times 10^{-33}$	$7.494 \times 10^{-33}$	$-1.318 \times 10^{-32}$	$1.234 \times 10^{-34}$

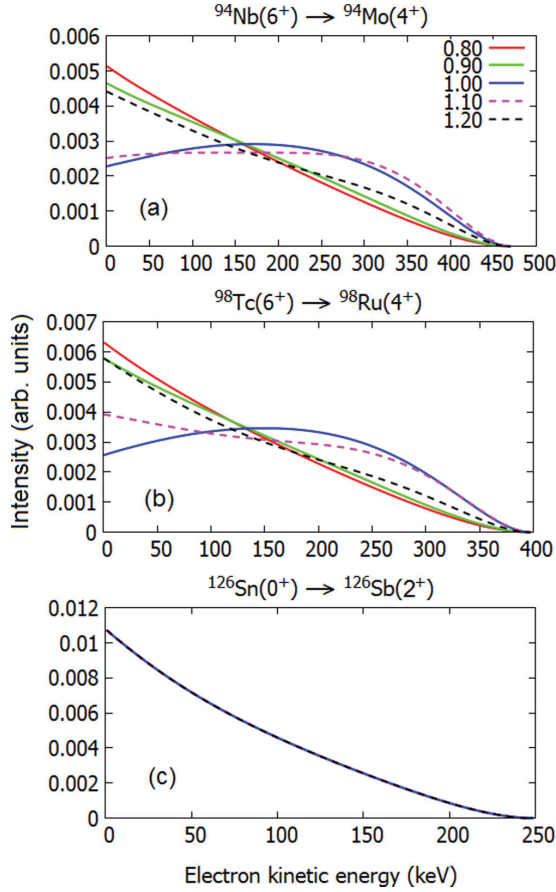


FIG. 2. Same as Fig. 1 but for the second-forbidden nonunique decays of  $^{94}\text{Nb}$  [panel (a)],  $^{98}\text{Tc}$  [panel (b)], and  $^{126}\text{Sn}$  [panel (c)].

been predicted to be  $\approx 2\%$  by a recent shell-model calculation [36]. An earlier study [30] of the  $g_A$ -driven evolution of the electron spectra of odd- $A$  nuclei demonstrated that the second and especially the fourth-forbidden nonunique  $\beta$ -decay spectra depend strongly on the effective value of the weak axial-vector coupling constant.

**GROUP 2.** The second group consists of the fourth-to-sixth-forbidden decays  $^{48}\text{Ca}(0^+) \rightarrow ^{48}\text{Sc}(4^+, 5^+, 6^+)$  and  $^{96}\text{Zr}(0^+) \rightarrow ^{96}\text{Nb}(4^+, 5^+, 6^+)$ , for which the beta spectra are presented in Figs. 3 and 4. The decays of  $^{48}\text{Ca}$  and  $^{96}\text{Zr}$  appear to be dominated by the two-neutrino double beta decay mode [36,45,46], so the study of these decays is somewhat challenging experimentally. However, they can shed light on whether the spectra of highly forbidden beta decays are  $g_A$  dependent or not.

**GROUP 3.** The third group consists of four decays:  $^{137}\text{Cs}(7/2^+) \rightarrow ^{137}\text{Ba}(11/2^-, 3/2^+)$ ,  $^{99}\text{Tc}(9/2^+) \rightarrow ^{99}\text{Ru}(5/2^+)$ , and  $^{87}\text{Rb}(3/2^-) \rightarrow ^{87}\text{Sr}(9/2^+)$ . The electron spectra of these decays was studied previously in [30] using the MQPM. The spectra of the  $^{137}\text{Cs}$  decays were found to

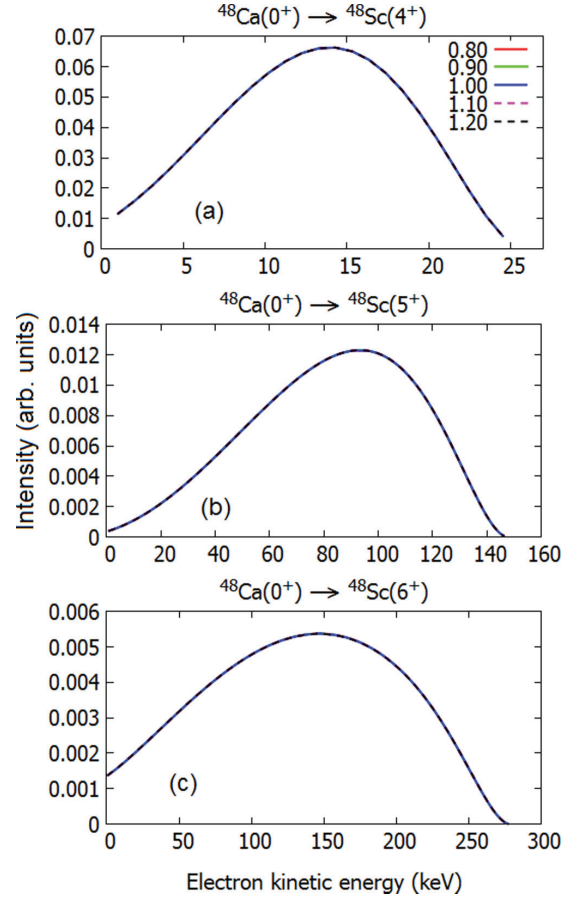


FIG. 3. Same as Fig. 1 but for the decays  $^{48}\text{Ca}(0^+) \rightarrow ^{48}\text{Sc}(4^+, 5^+, 6^+)$  [panels (a), (b), and (c)].

be independent of the value of  $g_A$ , while the dependence was significant for  $^{87}\text{Rb}$  and  $^{99}\text{Tc}$ . The shell-model and MQPM spectra of these decays are compared in order to see if the previously observed model independence of  $^{113}\text{Cd}$  and  $^{115}\text{In}$  spectra [21] holds also for these decays.

The spectra presented in Figs. 1 and 2 (GROUP 1) fall into two subgroups. The spectra of  $^{36}\text{Cl}$ ,  $^{50}\text{V}$ , and  $^{60}\text{Fe}$  [Fig. 1, panels (a), (b), and (c)], and  $^{126}\text{Sn}$  [Fig. 2, panel (c)] do not exhibit noticeable dependence on the value of the axial-vector coupling constant. This is very surprising since the decay of  $^{50}\text{V}$  is fourth forbidden, and all the seven studied fourth-forbidden decays in Ref. [30] depend heavily on  $g_A$ . The spectra of the second subgroup,  $^{94}\text{Nb}$  and  $^{98}\text{Tc}$  [Fig. 2, panels (a) and (b)], are significantly  $g_A$  dependent. The  $g_A$  driven evolution of the spectra is not only very similar for these two decays, but also nearly identical to the one of  $^{99}\text{Tc}$ , shown in Fig. 5, panel (c), even though the  $Q$  value of these decays varies between 300 keV and 450 keV. A similar grouping phenomenon was seen for several decays in [30]: for example the shapes of the spectra of fourth-forbidden

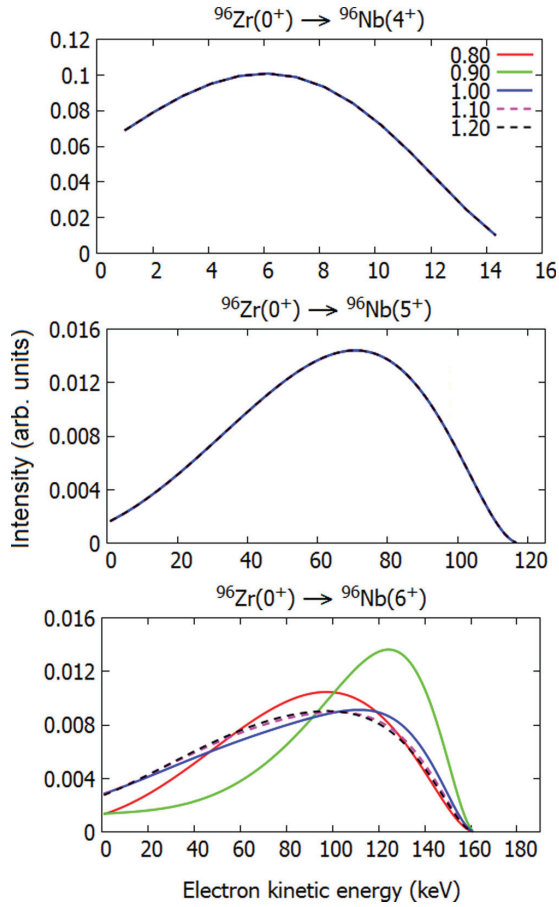


FIG. 4. Same as Fig. 1 but for the decays  $^{96}\text{Zr}(0^+) \rightarrow ^{96}\text{Nb}(4^+, 5^+, 6^+)$  [panels (a), (b), and (c)].

ground-state-to-ground-state  $\beta^-$  decays of  $^{97}\text{Zr}$ ,  $^{101}\text{Mo}$ ,  $^{117}\text{Cd}$ , and  $^{119}\text{In}$  have an almost identical  $g_A$  evolution.

Decays of GROUP 2,  $^{48}\text{Ca}(0^+) \rightarrow ^{48}\text{Sc}(4^+, 5^+, 6^+)$  and  $^{96}\text{Zr}(0^+) \rightarrow ^{96}\text{Nb}(4^+, 5^+, 6^+)$ , were studied in order to see if there appears some interesting systematic behavior. Since the shape of the spectra of fourth-forbidden nonunique decays of odd- $A$  nuclei depends on  $g_A$  in a significant way, it is interesting to see if this holds for the even- $A$  nuclei. Since the spectrum on  $^{50}\text{V}$  is largely independent of the values of the weak coupling constants, the dependence is not strong for at least some fourth-forbidden decays. The shape of the electron spectra of  $^{48}\text{Ca}(0^+) \rightarrow ^{48}\text{Sc}(4^+, 5^+, 6^+)$  and  $^{96}\text{Zr}(0^+) \rightarrow ^{96}\text{Nb}(4^+, 5^+)$  transitions is independent of  $g_A$ , as shown in Fig. 3, panels (a), (b), and (c) and in Fig. 4, panels (a) and (b), revealing a second exception,  $^{48}\text{Ca}(0^+) \rightarrow ^{48}\text{Sc}(4^+)$ , to the  $g_A$ -dependent fourth-forbidden nonunique decays. The sixth-forbidden decay  $^{96}\text{Zr}(0^+) \rightarrow ^{96}\text{Nb}(6^+)$  [Fig. 4, panel (c)], on the other hand, exhibits a strong  $g_A$  dependence. The evolution is very different from the one of the  $^{94}\text{Nb}$  and  $^{98}\text{Tc}$  [Fig. 2, panels (a) and (b)], and  $^{99}\text{Tc}$  [Fig. 5, panel (c)] studied

in the present paper and the fourth-forbidden ones studied in [30]. The branching ratio is, however, so small that the measurement of this spectrum is not currently within reach of experiments. It is somewhat striking that, from the 38 different forbidden decays studied in the present paper and in Ref. [30], strong  $g_A$  dependence is seen only in even-forbidden decays.

In Fig. 5 the shell-model and MQPM spectra of the experimentally interesting decays found in Ref. [30] are shown for comparison. For  $^{87}\text{Rb}$  [panels (a) and (b)], which is the best candidate for the determination of the quenching of  $g_A$  in third-forbidden decays, the MQPM and shell-model spectra are practically identical. For  $^{99}\text{Tc}$  [panels (c) and (d)] the evolution predicted by the two models is also similar, but in the range  $g_A = 0.9$ – $1.1$  there is some difference in the shape, leading to a potential small uncertainty in the value of  $g_A$  when comparing to the experimental spectrum, hopefully available in the (near) future. The two studied decays of  $^{137}\text{Cs}$  [panels (e) and (f)] were found to be  $g_A$  independent when using the MQPM model in Ref. [30]. The shell-model spectra calculated for these decays were not only also  $g_A$  independent, but overlap with the MQPM spectra perfectly. Measurements of these spectra would be very desirable, since they would shed light on the quality of the calculated spectra, independent of the chosen nuclear model.

### B. Integrated shape factor $\tilde{C}$

The integrated shape factors  $\tilde{C}$  and their decomposition to the components of Eq. (8) are presented in Table I. For all the studied decays the sign of the vector and axial-vector components is positive and the sign of the mixed vector-axial-vector component varies. For the second-forbidden nonunique decays of  $^{94}\text{Nb}$  and  $^{98,99}\text{Tc}$  which have very similar spectrum-shape evolution, the vector- and axial-vector components are roughly equal and the vector-axial-vector component is roughly twice as large, but with a negative sign. The resulting total integrated shape factor is two magnitudes smaller than its components. For the sixth-forbidden decay  $^{96}\text{Zr}(0^+) \rightarrow ^{96}\text{Nb}(6^+)$  the axial-vector component is 30% larger than the vector component and the vector-axial-vector component is again roughly the sum of the two other components and negative in sign.

For  $^{87}\text{Rb}$  the decomposition is similar to the case of the MQPM: the vector component  $\tilde{C}_V$  is the largest, the axial-vector component  $\tilde{C}_A$  is about 20% of  $\tilde{C}_V$ , and the vector-axial-vector component  $\tilde{C}_{VA}$  is the smallest and has a negative sign. However, the components and the total integrated shape factor are approximately 30% larger for the MQPM. In the case of  $^{99}\text{Tc}$  the difference is much larger and the MQPM results are roughly twice the shell model ones. For the two studied decays of  $^{137}\text{Cs}$  there is no  $g_A$  dependence. The decay to the isomeric  $11/2^-$  state is unique and thus (practically)  $g_A$  independent. On the other hand, the decay to the  $3/2^+$  ground state is nonunique but  $g_A$  independent since the three components of  $\tilde{C}$  have the same sign and no interference between the components occurs. For these two decays the normalized shell model and MQPM electron spectra overlap perfectly but the difference in  $\tilde{C}$  is considerable. Again, the relative fractional decomposition is almost identical for the two nuclear models, but the absolute

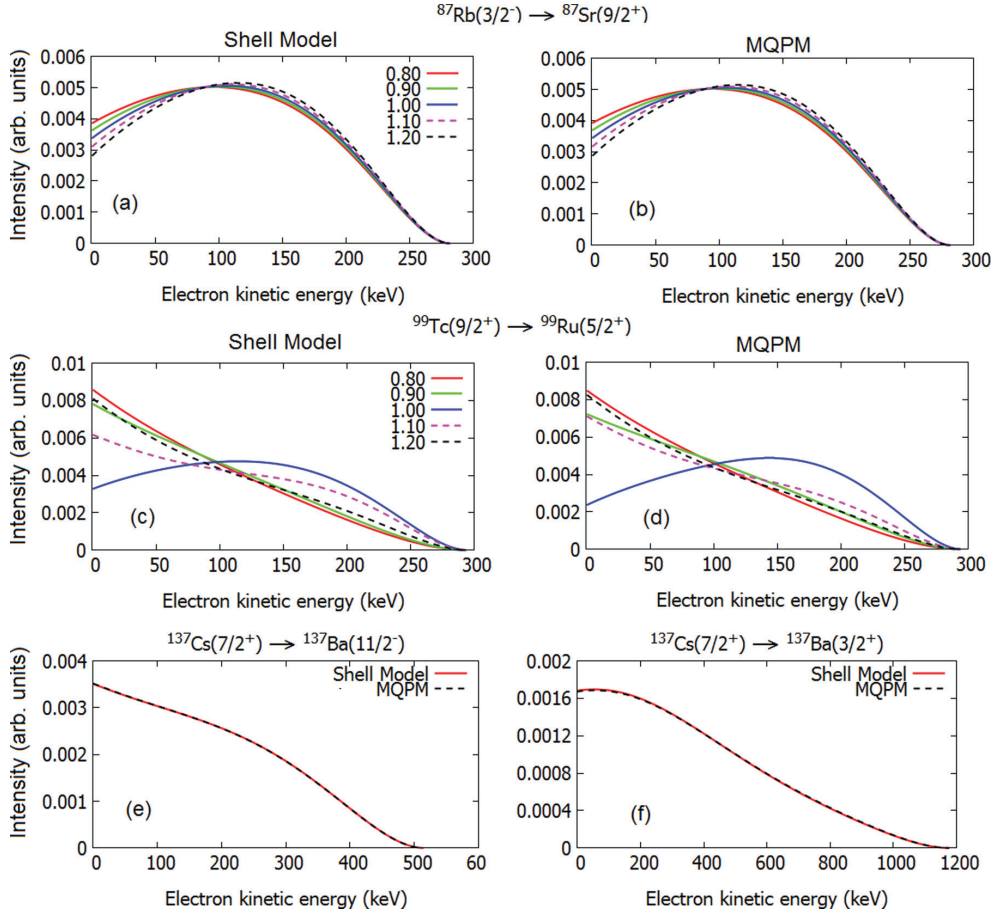


FIG. 5. Presently calculated shell-model spectra and the MQPM spectra, first published in Ref. [30], for the ground-state-to-ground-state decays of  $^{87}\text{Rb}$  [panels (a) and (b)],  $^{99}\text{Tc}$  [panels (c) and (d)], and  $^{137}\text{Cs}$  [panel (f)], and the decay of  $^{137}\text{Cs}$  to the isomeric  $11/2^-$  state in  $^{137}\text{Ba}$  [panel (e)]. The color coding in the spectra of  $^{87}\text{Rb}$  and  $^{99}\text{Tc}$  refers to the value of  $g_A$ . The shape of the electron spectra of the two  $^{137}\text{Cs}$  decays is  $g_A$  independent, and the color coding in these decays refers to the adopted nuclear model. The free-nucleon value  $g_V = 1.00$  was used in all calculations.

value of the MQPM  $\tilde{C}$  is 40-fold the shell model one for the decay to the  $11/2^-$  state, and 8-fold for the decay to the  $3/2^+$  state. Due to the  $\tilde{C}^{-1}$  dependence of the half-life, the half-lives predicted by the two models do not agree with each other at all. This is a strong indication that the spectrum-shape method is a more robust tool for determining the effective value of  $g_A$  than just a simple half-life comparison.

## V. CONCLUSIONS

The evolution of the electron-spectrum shapes of 16 forbidden  $\beta^-$  decays, driven by the value of the axial-vector coupling constant  $g_A$ , were studied using nuclear matrix elements derived from the nuclear shell model. Established and well-tested nuclear Hamiltonians were used in these investigations. In the  $\beta$ -decay shape factors the usually omitted next-to-leading-order terms were taken into account. The main

objective of the study was to find experimentally detectable transitions for which the shape of the electron spectra depends sensitively on the value of the weak coupling constants. Comparing the calculated and measured spectra the effective value of  $g_A$  can be extracted.

The electron spectra of  $^{94}\text{Nb}(6^+) \rightarrow ^{94}\text{Mo}(4^+)$  and  $^{98}\text{Tc}(6^+) \rightarrow ^{98}\text{Ru}(4^+)$  depend significantly on the effective value of  $g_A$  and these transitions are thus excellent new candidates for the spectrum-shape method (SSM). Both of these decays have almost a 100% branching ratio, and have been experimentally observed. The shell-model spectra of the previously found candidates, the ground-state-to-ground-state decays of  $^{87}\text{Rb}$  and  $^{99}\text{Tc}$ , agree well with the microscopic quasiparticle-phonon model predicted spectra of a previous study, which makes the experimental measurement of these spectra very desirable. The  $g_A$ -independent shell model and MQPM spectrum shapes of the

$^{137}\text{Cs}(7/2^+) \rightarrow ^{137}\text{Ba}(11/2^-, 3/2^+)$  transitions overlap perfectly. The measurement of these spectra would shed light on the quality of the calculated spectra.

The transitions for which a heavy  $g_A$  dependence has been recorded thus far are all even forbidden. Unlike in the case of the fourth-forbidden transitions in odd- $A$  nuclei studied in Ref. [30], which all showed a strong  $g_A$  dependence, such a dependence is not seen in the corresponding transitions in the studied even- $A$  nuclei. Thus far all the found transitions with a very strongly  $g_A$ -dependent spectrum shape are in the mass region  $A = 94\text{--}119$ . Most of the experimentally accessible forbidden nonunique transitions in odd- $A$  nuclei with  $A \leq 169$  and second or higher-forbidden nonunique transitions in even-

$A$  nuclei with  $A \leq 98$  have now been studied. The potential new candidates for the spectrum-shape method are heavier, and the study of these decays requires the adoption of some other nuclear model due to the large computational burden and the other problems with shell-model calculations for heavy deformed nuclei.

#### ACKNOWLEDGMENTS

This work has been partially supported by the Academy of Finland under the Finnish Centre of Excellence Programme 2012-2017 (Nuclear and Accelerator Based Programme at JYFL).

- 
- [1] J. Suhonen, *From Nucleons to Nucleus: Concepts of Microscopic Nuclear Theory* (Springer, Berlin, 2007).
  - [2] R. P. Feynmann and M. Gell-Mann, *Phys. Rev.* **109**, 193 (1958).
  - [3] R. P. Feynmann and M. Gell-Mann, *Phys. Rev.* **111**, 362 (1958).
  - [4] W. Theis, *Z. Phys.* **150**, 590 (1958).
  - [5] K. Zuber, *Neutrino Physics* (Institute of Physics Publishing Ltd., London, 2004).
  - [6] E. D. Commins, *Weak Interactions* (McGraw-Hill, New York, 2007).
  - [7] J. Suhonen and O. Civitarese, *Phys. Rep.* **300**, 123 (1998).
  - [8] J. Maalampi and J. Suhonen, *Adv. High Energy Phys.* **2013**, 505874 (2013).
  - [9] H. Ejiri and J. Suhonen, *J. Phys. G: Nucl. Part. Phys.* **42**, 055201 (2015).
  - [10] H. Ejiri, N. Soukouti, and J. Suhonen, *Phys. Lett. B* **729**, 27 (2014).
  - [11] P. Pirinen and J. Suhonen, *Phys. Rev. C* **91**, 054309 (2015).
  - [12] D. S. Delion and J. Suhonen, *Europhys. Lett.* **107**, 52001 (2014).
  - [13] F. F. Deppisch and J. Suhonen, *Phys. Rev. C* **94**, 055501 (2016).
  - [14] E. K. Warburton, *Phys. Rev. C* **42**, 2479 (1990).
  - [15] E. K. Warburton, *Phys. Rev. C* **44**, 233 (1991).
  - [16] E. K. Warburton, I. S. Towner, and B. A. Brown, *Phys. Rev. C* **49**, 824 (1994).
  - [17] E. K. Warburton and I. S. Towner, *Phys. Rep.* **242**, 103 (1994).
  - [18] Q. Zhi, E. Caurier, J. J. Cuenca-García, K. Langanke, G. Martínez-Pinedo, and K. Sieja, *Phys. Rev. C* **87**, 025803 (2013).
  - [19] J. Kostensalo and J. Suhonen, *Phys. Rev. C* **95**, 014322 (2017).
  - [20] M. Haaranen, P. C. Srivastava, and J. Suhonen, *Phys. Rev. C* **93**, 034308 (2016).
  - [21] M. Haaranen, J. Kotila, and J. Suhonen, *Phys. Rev. C* **95**, 024327 (2017).
  - [22] J. Toivanen and J. Suhonen, *J. Phys. G* **21**, 1491 (1995).
  - [23] J. Toivanen and J. Suhonen, *Phys. Rev. C* **57**, 1237 (1998).
  - [24] B. H. Wildenthal, M. S. Curtin, and B. A. Brown, *Phys. Rev. C* **28**, 1343 (1983).
  - [25] G. Martínez-Pinedo, A. Poves, E. Caurier, and A. P. Zuker, *Phys. Rev. C* **53**, R2602(R) (1996).
  - [26] E. Caurier, F. Nowacki, and A. Poves, *Phys. Lett. B* **711**, 62 (2012).
  - [27] F. Iachello and A. Arima, *The Interacting Boson Model* (Cambridge University Press, Cambridge, UK, 1987).
  - [28] F. Iachello and P. V. Isacker, *The Interacting Boson-Fermion Model* (Cambridge University Press, New York, 1991).
  - [29] P. Belli, R. Bernabei, N. Bukilic, F. Cappella, R. Cerulli, C. J. Dai, F. A. Danevich, J. R. de Laeter, A. Incicchitti, V. V. Kobychev, S. S. Nagorny, S. Nisi, F. Nozzoli, D. V. Poda, D. Prosperi, V. I. Tretyak, and S. S. Yurchenko, *Phys. Rev. C* **76**, 064603 (2007).
  - [30] J. Kostensalo, M. Haaranen, and J. Suhonen, *Phys. Rev. C* **95**, 044313 (2017).
  - [31] J. C. Hardy, I. S. Towner, V. Koslowsky, E. Hagberg, and H. Schmeing, *Nucl. Phys. A* **509**, 429 (1990).
  - [32] H. Behrens and W. Bühring, *Electron Radial Wave Functions and Nuclear Beta Decay* (Clarendon, Oxford, 1982).
  - [33] M. T. Mustonen, M. Aunola, and J. Suhonen, *Phys. Rev. C* **73**, 054301 (2006).
  - [34] B. A. Brown and W. D. M. Rae, *Nucl. Data Sheets* **120**, 115 (2014).
  - [35] B. A. Brown and W. A. Richter, *Phys. Rev. C* **74**, 034315 (2006).
  - [36] M. Haaranen, M. Horoi, and J. Suhonen, *Phys. Rev. C* **89**, 034315 (2014).
  - [37] M. Haaranen, P. C. Srivastava, J. Suhonen, and K. Zuber, *Phys. Rev. C* **90**, 044314 (2014).
  - [38] M. Honma, T. Otsuka, B. A. Brown, and T. Mizusaki, *Phys. Rev. C* **69**, 034335 (2004).
  - [39] M. Honma, T. Otsuka, B. A. Brown, and T. Mizusaki, *Eur. Phys. J. A* **25**, 499 (2005).
  - [40] H. Horie and K. Ogawa, *Prog. Theor. Phys.* **46**, 439 (1971).
  - [41] H. Horie and K. Ogawa, *Nucl. Phys. A* **216**, 407 (1973).
  - [42] B. Cheal, E. Mané, J. Billowes, M. L. Bissell, K. Blaum, B. A. Brown, F. C. Charlwood, K. T. Flanagan, D. H. Forest, C. Geppert, M. Honma, A. Jokinen, M. Kowalska, A. Krieger, J. Krämer, I. D. Moore, R. Neugart, G. Neyens, W. Nörtershäuser, M. Schug, H. H. Stroke, P. Vingerhoets, D. T. Yordanov, and M. Žáková, *Phys. Rev. Lett.* **104**, 252502 (2010).
  - [43] D. H. Gloeckner, *Nucl. Phys. A* **253**, 301 (1975).
  - [44] B. A. Brown, N. J. Stone, J. R. Stone, I. S. Towner, and M. Hjorth-Jensen, *Phys. Rev. C* **71**, 044317 (2005).
  - [45] H. Heiskanen, M. T. Mustonen, and J. Suhonen, *J. Phys. G: Nucl. Part. Phys.* **34**, 837 (2007).
  - [46] M. Alanssari, D. Frekers, T. Eronen, L. Canete, J. Dilling, M. Haaranen, J. Hakala, M. Holl, M. Jeřkovský, A. Jokinen, A. Kankainen, J. Koponen, A. J. Mayer, I. D. Moore, D. A. Nesterenko, I. Pohjalainen, P. Povinec, J. Reinikainen, S. Rinta-Antila, P. C. Srivastava, J. Suhonen, R. I. Thompson, A. Voss, and M. E. Wieser, *Phys. Rev. Lett.* **116**, 072501 (2016).



### III

## **SPECTRAL SHAPES OF FORBIDDEN ARGON $\beta$ DECAYS AS BACKGROUND COMPONENT FOR RARE-EVENT SEARCHES**

by

Kostensalo, J., Suhonen, J. and Zuber, K. 2017

Journal of Physics G:Nuclear and Particle Physics 45, no.2, 025202  
doi: 10.1088/1361-6471/aa958e

Reproduced with kind permission by IOP Publishing.

11 August 2017

# Spectral shapes of forbidden argon $\beta$ decays as background component for rare-event searches

**J. Kostensalo, J. Suhonen and K Zuber**

Department of Physics, University of Jyväskylä,  
P.O. Box 35, FI-40014 University of Jyväskylä, Finland

E-mail: [jouni.suhonen@phys.jyu.fi](mailto:jouni.suhonen@phys.jyu.fi)

Institut für Kern- und Teilchenphysik, Technische Universität Dresden,  
Zellescher Weg 19, 01069 Dresden, Germany

E-mail: [zuber@physik.tu-dresden.de](mailto:zuber@physik.tu-dresden.de)

**Abstract.** The spectral shape of the electrons from the two first-forbidden unique  $\beta^-$  decays of  $^{39}\text{Ar}$  and  $^{42}\text{Ar}$  were calculated for the first time to the next-to-leading order. Especially the spectral shape of the  $^{39}\text{Ar}$  decay can be used to characterise this background component for dark matter searches based on argon. Alternatively, due to the low thresholds of these experiments, the spectral shape can be investigated over a wide energy range with high statistics and thus allow a sensitive comparison with the theoretical predictions, in particular at low electron energies where the shape of the computed  $\beta$  spectrum has a slight dependence on the value of the weak axial-vector coupling constant.

## 1. Introduction

Liquid Argon (LAr) as a detection material is widely used in nuclear and particle physics with new applications coming in. The range covers calorimetry in high-energy-physics experiments at LHC all the way to large-scale low-background experiments for rare-event searches, especially dark matter. In addition, a 40 kiloton scale LArTPC detector is envisaged for the DUNE [1] long-baseline neutrino program. The GERDA experiment [2], searching for neutrino-less double beta decay using Ge-semiconductor detectors, is cooling its detectors with LAr, but uses it also for passive and active shield against backgrounds.

The focus of this paper is on the low-background section of the potential experiments, especially dark matter experiments, of which two ongoing LAr experiments are DEAP-3600 [3] and DarkSide-50 [4]. The question arises whether there are additional background contributions from the Ar itself. Indeed, Ar has three long-living nuclides,  $^{37}\text{Ar}$ ,  $^{39}\text{Ar}$  and  $^{42}\text{Ar}$ , which deserve some attention. First, there is the well-known  $^{37}\text{Ar}$  with a half-life of 35 days, which was the signal of the Homestake experiment for the radiochemical detection of solar neutrinos using a  $^{37}\text{Cl}$  detector [5]. This isotope decays via electron capture (EC) without emission of gamma rays, but it will produce X-ray lines below 10 keV. The isotope  $^{37}\text{Ar}$  might be produced by thermal neutron captures on  $^{36}\text{Ar}$ , but this nuclide has only a small abundance of 0.337 %. More severe contaminants are the long-living nuclides  $^{39}\text{Ar}$  and  $^{42}\text{Ar}$ , which we will discuss now in a bit more in detail.

The decay of both isotopes into the ground state of the corresponding daughter nucleus is characterised as first-forbidden unique  $\beta^-$ -decay:  $(\frac{7}{2}^+ \rightarrow \frac{3}{2}^-)$  for  $^{39}\text{Ar}$  and  $(0^+ \rightarrow 2^-)$  for  $^{42}\text{Ar}$ . The  $\beta$ -decay endpoints are given by  $565 \pm 5$  keV ( $^{39}\text{Ar}$ ) and  $599 \pm 6$  keV ( $^{42}\text{Ar}$ ), respectively [7]. The measured half-lives for  $^{39}\text{Ar}$  are  $265 \pm 30$  years [8] and  $269 \pm 3$  years [9]. Its content is on the level of 10 mBq/m<sup>3</sup> [14] and the specific activity was measured by the WARP experiment to be  $1.01 \pm 0.02 \pm 0.08$  Bq per kg of natural Ar [10]. The current accepted half-life for  $^{42}\text{Ar}$  is  $32.9 \pm 1.1$  years [9]. A recent study of the content of  $^{42}\text{Ar}$  in LAr was done in the GERDA collaboration [11] and its activity in the air was measured to be  $1.2_{-0.5}^{+0.3} \mu\text{Bq}/\text{m}^3$  [12].

There is an early measurement of the  $^{39}\text{Ar}$   $\beta$  spectrum [13] and the spectrum is also shown in [10] ‡. However, in neither reference the spectrum goes below 80 keV which is the interesting region for the dark-matter experiments. For  $^{42}\text{Ar}$  we could not find any measured or calculated spectrum.

In this paper we study the  $\beta$ -decay spectral shapes of the two isotopes  $^{39}\text{Ar}$  and  $^{42}\text{Ar}$ . We calculate the shapes using up to date nuclear models. In this way we plan to predict the expected  $\beta$ -spectrum shape for the Ar-based dark-matter experiments and, on the other hand, encourage the experimentalists to provide a spectrum which can be

‡ In [10], in its reference [5], a web site is given for a theoretical evaluation of the  $\beta$  spectrum. This web page, however, is permanently non-functional and the information about the  $^{39}\text{Ar}$   $\beta$  spectrum is no longer available.

compared with theory.

## 2. Calculation of the spectral shape of $^{39}\text{Ar}$ and $^{42}\text{Ar}$

In order to simplify the nuclear  $\beta^-$ -decay theory enough to allow us to do practical calculations we use the so-called impulse approximation in which at the exact moment of decay the decaying nucleon only feels the weak interaction [15]. The strong interaction with the remaining  $A - 1$  nucleons is ignored, and thus the pion exchange and other many-body effects are neglected. In the impulse approximation a neutron decays into a proton via emission of a massive  $W^-$  vector boson which in turn decays into an electron and an anti-neutrino. Due to the large mass of the  $W^-$  boson in comparison to the energy scale of the nuclear beta decay, the  $W^-$  boson couplings to the baryon and lepton vertices, with weak-interaction coupling strength  $g_W$ , can be approximated as a single effective interaction vertex with effective coupling strength  $G_F$ , the Fermi constant. When the decay process is described with the effective point-like interaction vertex, the probability of the electron being emitted with kinetic energy between  $W_e$  and  $W_e + dW_e$  is

$$P(W_e)dW_e = \frac{G_F}{(\hbar c)^6} \frac{1}{2\pi^3\hbar} C(W_e) \times p_e c W_e (W_0 - W_e)^2 F_0(Z, W_e) dW_e, \quad (1)$$

where  $p_e$  is the momentum of the electron,  $Z$  is the proton number,  $F_0(Z, W_e)$  is the Fermi function, and  $W_0$  is the end-point energy of the  $\beta$  spectrum. The nuclear-structure information is in the shape factor  $C(w_e)$ . Integrating Eq. (1) over the possible electron energies gives the total transition probability, and thus the half-life of the  $\beta^-$  decay.

The half-life of a  $\beta$  decay can be written as

$$t_{1/2} = \frac{\ln(2)}{\int_{m_e c^2}^{W_0} P(W_e) dW_e} := \frac{\kappa}{\tilde{C}}, \quad (2)$$

where  $\tilde{C}$  is the integrated shape factor and the constant  $\kappa$  has the value [16]

$$\kappa = \frac{2\pi^3 \hbar^7 \ln 2}{m_e^5 c^4 (G_F \cos \theta_C)^2} = 6147 \text{ s}, \quad (3)$$

$\theta_C$  being the Cabibbo angle. In order to simplify the formalism it is usual to introduce dimensionless kinematic quantities  $w_e = W_e/m_e c^2$ ,  $w_0 = W_0/m_e c^2$ , and  $p = p_e c/(m_e c^2) = \sqrt{w_e^2 - 1}$ . With the dimensionless quantities the integrated shape factor can be expressed as

$$\tilde{C} = \int_1^{w_0} C(w_e) p w_e (w_0 - w_e)^2 F_0(Z, w_e) dw_e. \quad (4)$$

The characteristics of the electron spectrum are encoded in the shape factor  $C(w_e)$ , which can be expressed as [17]

$$C(w_e) = \sum_{k_e, k_\nu, K} \lambda_{k_e} \left[ M_K(k_e, k_\nu)^2 + m_K(k_e, k_\nu)^2 - \frac{2\gamma_{k_e}}{k_e w_e} M_K(k_e, k_\nu) m_K(k_e, k_\nu) \right], \quad (5)$$

where  $k_e$  and  $k_\nu$  (both running through 1,2,3,...) emerge from the partial-wave expansion of the electron and neutrino wave functions,  $\gamma_{k_e} = \sqrt{k_e^2 - (\alpha Z)^2}$ , and  $\lambda_{k_e} = F_{k_e-1}(Z, w_e)/F_0(Z, w_e)$  is the Coulomb function where  $F_{k_e-1}(Z, w_e)$  is the generalized Fermi function. The largest contributions to the sum of Eq. (5) come from the terms with minimal angular-momentum transfer, so in the case of the unique forbidden decays studied in this work, we only consider the sum that satisfies the condition  $k_e + k_\nu = K + 2$ . The quantities  $M_K(k_e, k_\nu)$  and  $m_K(k_e, k_\nu)$  have lengthy expressions involving kinematic and nuclear form factors. The explicit expressions can be found from [17] (the expressions were also given in the recent article [18]). The form factors appearing in these expressions can be expanded as power series of  $qR/\hbar$  as

$$\mathcal{F}_{\text{KLS}}(q^2) = \sum_N \frac{(-1)^N (2L+1)!!}{(2N)!! (2L+2N+1)!!} (qR/\hbar)^{2N} \mathcal{F}_{\text{KLS}}^{(N)}, \quad (6)$$

where  $q = |p_e + p_\nu|$  and  $R$  is the nuclear radius. In practical calculations the quantities  $M_K(k_e, k_\nu)$  and  $m_K(k_e, k_\nu)$  are expanded as a power series of the quantities  $\eta_{1,2,3,4,5} = \alpha Z, p_e R/\hbar, qR/\hbar, m_e c R/\hbar,$  and  $W_e R/\hbar c$ .  $M_K(k_e, k_\nu)$  and  $m_K(k_e, k_\nu)$  consist of terms proportional to  $\prod_i \eta_i^{\alpha_i} \mathcal{F}_{\text{KLS}}$ , where  $\alpha_i = 0, 1, 2, 3, 4, 5$ . In the case of the unique decays the often used leading-order approximation takes into account only the  $(p_e R/\hbar)^{k_e-1} (qR/\hbar)^{k_\nu-1}$  term, while the here adopted next-to-leading-order treatment [18] takes into account also the  $(p_e R/\hbar)^{k_e-1} (qR/\hbar)^{k_\nu-1} \eta_j$  terms. The leading-order and next-to-leading-order expressions of the  $\beta$ -decay shape factor are discussed in detail in Ref. [18] for a more general framework including also the (more involved) non-unique forbidden decays.

In the impulse approximation the nuclear form factors can be replaced by nuclear matrix elements (NMEs) [17]. In the leading-order approximation there is only one NME contributing to the shape factor for the unique decays. Therefore, the spectrum-shape and the half-life are proportional to  $g_A^{-2}$ , where  $g_A$  is the weak axial-vector coupling constant. When the next-to-leading-order terms are taken into account, the number of contributing NMEs increases to five, with each NME carrying a prefactor  $g_A$  or  $g_V$  (weak vector coupling constant). As a result, the shape factor can be expressed as a decomposition

$$C(w_e) = g_V^2 C_V(w_e) + g_A^2 C_A(w_e) + g_V g_A C_{VA}(w_e). \quad (7)$$

In the here adopted next-to-leading-order theory the dependence on the weak coupling constants of the spectrum shape for the studied decays of Argon isotopes is, at least theoretically, non-trivial.

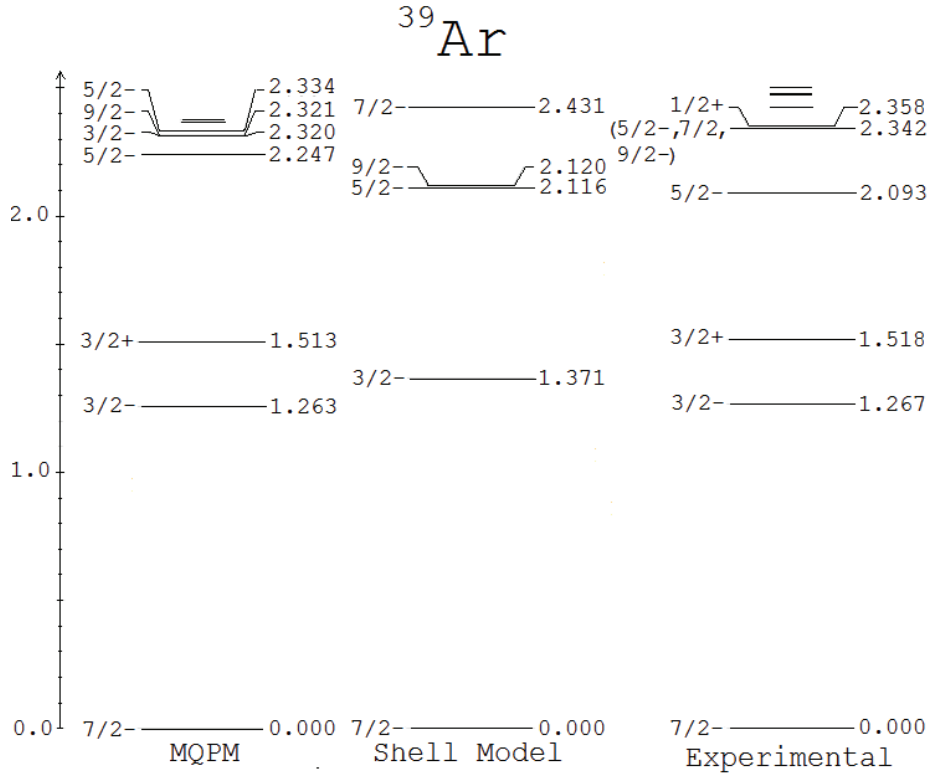


**Figure 1.** The excitation spectrum of  $^{39}\text{Ar}$  calculated using the MQPM and the shell model. The experimental excitation spectrum is from [19].

The choice of a nuclear model enters the picture when calculating the one-body transition densities (OBTDs) needed for the evaluation of the NMEs related to the transition. In this work the wave functions of the initial and final states were calculated using the microscopic quasiparticle-phonon model (MQPM) [20, 21] and the nuclear shell model. The MQPM is a fully microscopic model which can be used to describe spherical odd- $A$  nuclei, in the case of this work  $^{39}\text{Ar}$  and  $^{39}\text{K}$ . In the MQPM the states of the odd- $A$  nucleus are built from BCS (Bardeen-Cooper-Schrieffer) quasiparticles [15] and their couplings to QRPA phonons. The quasiparticles and phonons emerge from the calculations done on the neighboring even-even reference nucleus (here  $^{38}\text{Ar}$ ). The MQPM has previously been used in the calculations of forbidden beta-decay spectrum shapes in Refs. [18, 22, 23].

The practical application of the MQPM model follows the same basic steps as in the earlier studies (see Refs. [18, 21, 22, 23, 24, 25]) including the use of the Bonn one-boson-exchange potential with G-matrix techniques [21]. The single-particle energies, used to solve the BCS equations, were calculated using the Coulomb-corrected Woods-Saxon potential with the Bohr-Mottelson parametrization [26]. The valence space spanned the orbitals  $0s0p1s0d0f1p0g_{9/2}$ . The BCS one-quasiparticle spectra were tuned by adjusting manually some of the key single-particle energies to get a closer match between the low-lying one-quasiparticle states and the corresponding experimental ones. The empirical

pairing gaps, computed using the data from [6], were adjusted to fit the computed ones by tuning the pairing strength parameters  $g_{\text{pair}}^p$  and  $g_{\text{pair}}^n$  for protons and neutrons separately. In the MQPM calculations an extended cutoff energy of 6.0 MeV was used for the QRPA phonons instead of the 3.0-MeV cutoff energy used in Refs. [22, 23].

**Table 1.** Leading-order and next-to-leading-order nuclear matrix elements (NMEs) for the first-forbidden unique ground-state-to-ground-state decays of  $^{39}\text{Ar}$  and  $^{42}\text{Ar}$ . The Coulomb-corrected matrix elements are indicated by  $(k_e, m, n, \rho)$ . When only the leading-order terms are considered, the decay half-life depends only on the matrix element  $^A\mathcal{M}_{K+1\ K+1\ 1}^{(0)}$  greatly simplifying the calculation.

Transition	$^{39}\text{Ar} \rightarrow ^{39}\text{K}$		$^{42}\text{Ar} \rightarrow ^{42}\text{K}$
	MQPM	SM	SM
$^A\mathcal{M}_{K+1\ K\ 1}^{(0)}$	3.90427	-0.93180	1.41653
$^A\mathcal{M}_{K+1\ K+1\ 0}^{(0)}$	2.85202	-1.14637	1.43922
(1,1,1,1)	3.35235	-1.37438	1.70248
$^V\mathcal{M}_{K+1\ K+1\ 1}^{(0)}$	1.06393	-0.17889	0.23696
(1,1,1,1)	1.17718	-0.19971	0.25710

The shell-model OBTDs were calculated using the shell-model code NuShellX@MSU [27] with the effective interaction *sdpfnw* [28], tuned for the *1s0d0f1p* valence space. Since performing a shell-model calculation in the entire half-filled *1s0d0f1p* valence space would be impossible due to the extremely large dimensions of the shell-model Hamiltonian matrix, some controlled truncations were made. We limited the protons to the *sd*-shell, leaving the *fp*-shell empty, and forced a complete filling of the *sd*-shell for neutrons, leaving the entire *fp*-shell as the neutron valence space. These truncations are reasonable since we are only interested in the ground-state wave functions, to which configurations opening the neutron *sd*-shell and proton configurations with protons in the *fp*-shell have very small contributions due to the considerable energy gap between the two shells. The adopted shell-model Hamiltonian predicts correctly the spin-parities of the low-lying states in the studied nuclei. As an example, the energy spectra of  $^{39}\text{Ar}$ , predicted by the MQPM and shell model, are compared with the experimental spectrum [19] in Fig. 1. In the shell-model spectrum the positive-parity states are missing, since the odd neutron is restricted to the *fp*-shell.

The electron spectrum of the  $^{39}\text{Ar}$  decay is presented in Fig. 2. Here the next-to-leading-order terms are taken into account and the values  $g_V = g_A = 1$  were adopted for the weak coupling constants. The spectra were calculated also using the  $g_A/g_V$  ratios 0.8–1.2 but the spectra coincided perfectly, meaning that the possible dependence of the spectrum shape on the weak coupling constants is very weak. The spectra calculated using the shell model and the MQPM agree also extremely well, suggesting that the uncertainty related to the wave functions of the initial and final states is tiny. The difference between the two spectra is largest at the low-energy end, while at the high-

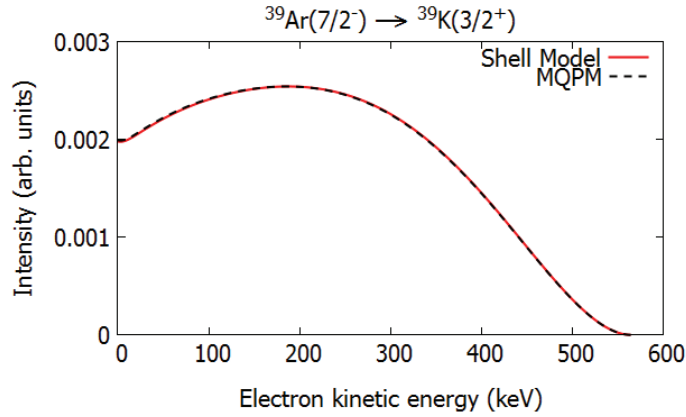


**Figure 2.** Electron spectrum of the ground-state-to-ground-state decay of  $^{39}\text{Ar}$  calculated using the MQPM and the shell model with the effective interaction  $\text{sdpfnw}$  [28]. The experimental excitation spectrum is from NNDC [19].

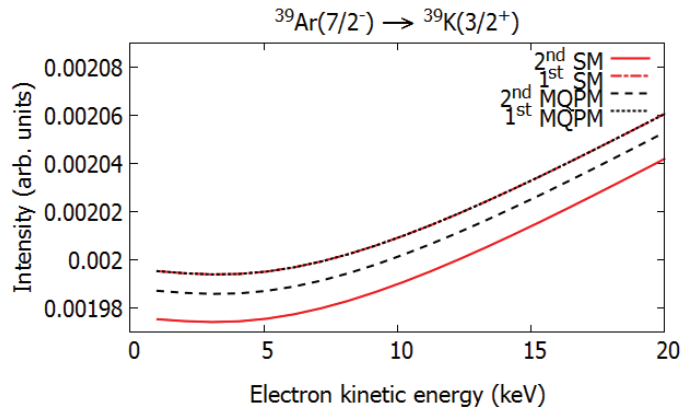


**Figure 3.** Zoom-in of the low-energy end of the electron spectrum of  $^{39}\text{Ar}$  calculated using the shell model (SM) and the microscopic quasiparticle-phonon model (MQPM) with leading-order (1st) and next-to-leading-order (2nd) terms of the shape factor  $C(w_e)$  included. The values  $g_A = g_V = 1.00$  were adopted. Note the range on the  $y$ -axis.

energy end the spectra coincide perfectly. In Fig. 3 a zoom-in of the low-energy part of the spectrum is presented, with the next-to-leading-order terms of the shape factor either included or neglected. The difference in the intensities predicted by the two models, with the next-to-leading-order terms included, is at most 0.5% of the intensity.

When the next-to-leading-order-terms are taken into account, the dependence of the shape-factor on the ratio  $g_A/g_V$  becomes non-trivial for the unique forbidden decays. The difference between the  $^{39}\text{Ar}$  spectra calculated using different values of  $g_A/g_V$  is largest at the low-energy end. The magnified low-energy shell-model electron spectrum is presented in Fig. 4. With larger quenching of  $g_A$ , the intensity of the low-energy electrons increase slightly, but the difference is negligible within the accuracy of practical

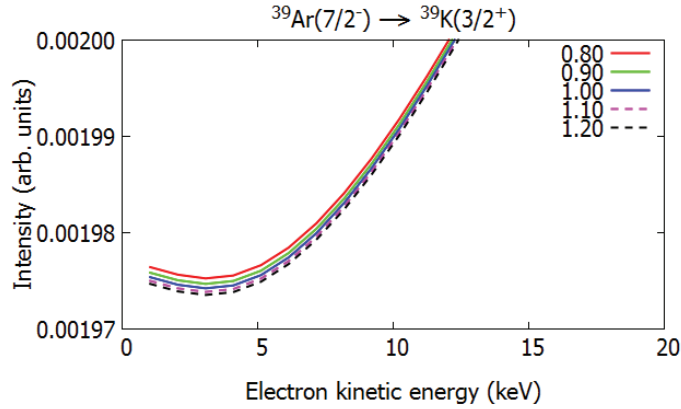


**Figure 4.** Zoom-in of the low-energy end of the electron spectrum of  $^{39}\text{Ar}$  calculated using the shell model. The color/dash coding refers to the ratio  $g_A/g_V$ . Note the range on the  $y$ -axis.

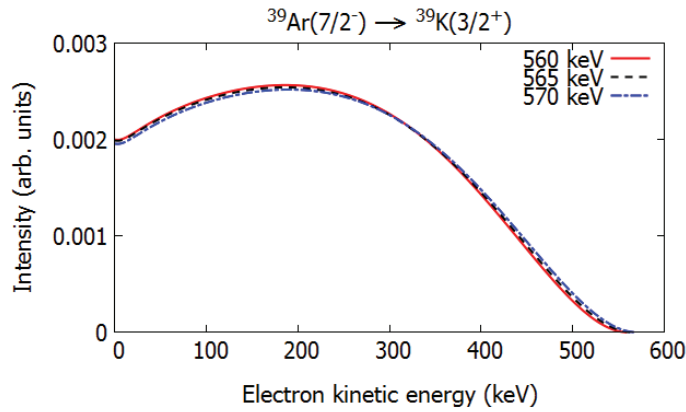


**Figure 5.** Electron spectrum of  $^{39}\text{Ar}$  calculated using the shell model and the experimental  $Q$ -value  $656 \pm 5$  keV [6]. The next-to-leading-order terms are included and the values  $g_A = g_V = 1.00$  were adopted.

measurements.

The final source of uncertainty of the spectrum shape is the uncertainty related to the  $Q$ -value. The current experimental  $Q$ -value of the  $^{39}\text{Ar}$  decay is  $565 \pm 5$  keV. The shell-model spectra with  $Q$ -values 560, 565, and 570 keV are plotted in Fig. 5. Here a small difference between the spectra can be seen without further magnification. The uncertainty related to the  $Q$ -value seems to be by far the largest contributor to the uncertainty in the theoretical spectrum-shape. The change in  $Q$ -value stretches the spectrum, but the overall shape does not change.

For the  $^{42}\text{Ar}$  ground-state-to-ground-state decay the MQPM cannot be applied. The uncertainties related to the wave functions were negligible in the case of  $^{39}\text{Ar}$ , as well as in the several other first-forbidden unique decays studied in Ref. [23], so the application of only one nuclear model should be sufficient. The electron spectrum is

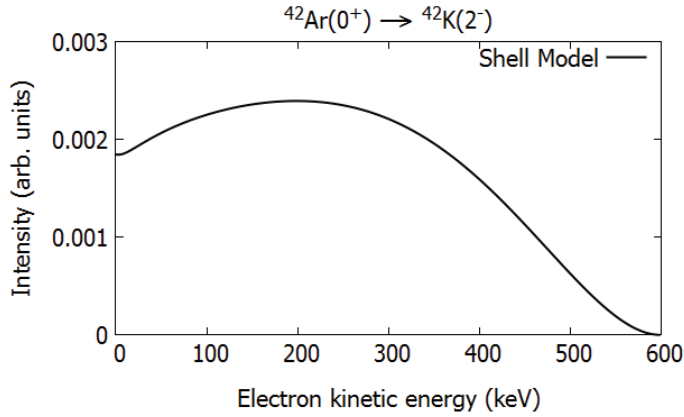


**Figure 6.** Electron spectrum of the ground-state-to-ground-state decay of  $^{42}\text{Ar}$  calculated using the shell model with the effective interaction *sdpfnw* [28]. The experimental excitation spectrum is from NNDC [19].

presented in Fig. 6. Again, there is no significant dependence on the values of  $g_A$  and  $g_V$ . For the decay of the  $^{42}\text{Ar}$  isotope the experimental uncertainty of the Q-value is at 6 keV, similar to that of the  $^{39}\text{Ar}$  isotope, and thus the uncertainty of the spectrum-shape is also of a similar magnitude.

### 3. Summary and conclusions

In this paper the  $\beta$  spectra of first-forbidden unique decays of  $^{39}\text{Ar}$  and  $^{42}\text{Ar}$  were calculated for the first time using a next-to-leading-order weak theory. The involved nuclear wave functions were computed by using the nuclear shell model and the microscopic quasiparticle-phonon model. The major uncertainty in studies of the spectral shapes is related to the uncertainty of the Q-value. Among the different calculations only very tiny differences could be observed at low energy of the  $\beta$  spectrum, depending on the value of the weak axial-vector coupling constant. This energy range can be studied in detail with the running or future LAr dark-matter detectors, as they are sensitive in this energy range. Our calculations indicate, however, that even this high sensitivity might not be enough to allow the exploration of the  $g_A/g_V$  ratio of the weak coupling constants. The higher-energy part of the  $\beta$  spectrum of  $^{39}\text{Ar}$  can already be seen in the released spectra of the GERDA experiment, but the lower-energy part might be disturbed due to dead-layer effects of the Ge detectors.

To summarise, the calculated  $\beta$  spectra can help to characterise the background contribution of the two studied isotopes for dark-matter searches based on LAr dark-matter detectors. On the other hand, these experiments can investigate the presently predicted spectral shape in detail as the expected decay rate, especially for  $^{39}\text{Ar}$ , is reasonably high in these detectors.

#### 4. Acknowledgement

This work was partly supported by the Academy of Finland under the Finnish Center of Excellence Program 2012-2017 (Nuclear and Accelerator Based Program at JYFL).

#### References

- [1] R. Acciarri et al., arXiv.1512.06148
- [2] K. H. Ackermann et al., *Euro. Phys. J. C* 2013 **73**, 2330
- [3] P. A. Amaudruz et al., *Nucl.Part.Phys.Proc.* 2016 **273 – 275**, 340
- [4] P. Agnes et al., *Phys. Lett. B* 2015 **743**, 456
- [5] B. T. Cleveland et al., *ApJ* 1998 **496**, 505
- [6] M. Wang et al., *Chin. Phys. C* 2012 **36**, 1603
- [7] M. Wang et al., *Chin. Phys. C* 2017 **41**, 030003
- [8] H. Zeldes et al., *Phys. Rev.* 1952 **86**, 811
- [9] R. W. Stoenner, O. A. Schaeffer, S. Katcoff, *Science* 1965 **148**, 1325
- [10] P. Benetti et al., *Nucl. Instrum. Methods A* 2007 **574**, 83
- [11] M. Agostini et al., *Euro. Phys. J. C* 2014 **74**, 2764
- [12] A. S. Barabash et al., *Nucl. Instrum. Methods A* 2016 **839**, 39
- [13] A. R. Brosi et al., *Phys. Rev.* 1950 **79**, 902
- [14] H. H. Loosli, *Earth Plan. Sci. Lett.* 1983 **63**, 51
- [15] J. Suhonen, *From Nucleons to Nucleus: Concepts in Microscopic Nuclear Theory*, Springer, Berlin (2007)
- [16] J. C. Hardy et al., *Nucl. Phys. A* 1990 **509**, 429
- [17] H. Behrens and W. Bühring, *Electron Radial Wave Functions and Nuclear Beta Decay*, Clarendon, Oxford (1982)
- [18] M. Haaranen et al., *Phys. Rev. C* 2017 **95**, 024327
- [19] National Nuclear Data Center, Brookhaven National Laboratory, [www.nndc.bnl.gov](http://www.nndc.bnl.gov)
- [20] J. Toivanen et al., *Journal of Physics G* 1995 **21**, 1491
- [21] J. Toivanen et al., *Phys. Rev. C* 1998 **57**, 1237
- [22] M. Haaranen et al., *Phys. Rev. C* 2016 **93**, 034308
- [23] J. Kostensalo et al., *Phys. Rev. C* 2017 **95**, 044313
- [24] M. T. Mustonen et al., *Phys. Rev. C* 2006 **73**, 054301
- [25] M. Haaranen et al., *Euro. Phys. J. A* 2013 **19**, 93
- [26] A. Bohr and B. R. Mottelson, *Nuclear Structure Vol I*, Benjamin, New York (1969)
- [27] B. A. Brown et al., *Nuclear Data Sheets* 2014 **120**, 115
- [28] S. Nummela et al., *Phys. Rev. C* 2001 **63**, 044316



## IV

# **SHELL-MODEL COMPUTED CROSS SECTIONS FOR CHARGED-CURRENT SCATTERING OF ASTROPHYSICAL NEUTRINOS OFF $^{40}\text{Ar}$ .**

by

Kostensalo, J., Suhonen, J., & Zuber, K. 2018

Physical Review C, 97 (3), 034309.  
doi:10.1103/PhysRevC.97.034309

Reproduced with kind permission by American Physical Society.

## Shell-model computed cross sections for charged-current scattering of astrophysical neutrinos off $^{40}\text{Ar}$

Joel Kostensalo\* and Jouni Suhonen†

University of Jyväskylä, Department of Physics, P.O. Box 35, FI-40014, Finland

K. Zuber‡

TU Dresden, Institute for Nuclear and Particle Physics, 01069 Dresden, Germany



(Received 3 October 2017; revised manuscript received 8 December 2017; published 6 March 2018)

Charged-current (anti)neutrino- $^{40}\text{Ar}$  cross sections for astrophysical neutrinos have been calculated. The initial and final nuclear states were calculated using the nuclear shell model. The folded solar-neutrino scattering cross section was found to be  $1.78(23) \times 10^{-42} \text{ cm}^2$ , which is higher than what the previous papers have reported. The contributions from the  $1^-$  and  $2^-$  multipoles were found to be significant at supernova-neutrino energies, confirming the random-phase approximation (RPA) result of a previous study. The effects of neutrino flavor conversions in dense stellar matter (matter oscillations) were found to enhance the neutrino-scattering cross sections significantly for both the normal and inverted mass hierarchies. For the antineutrino scattering, only a small difference between the nonoscillating and inverted-hierarchy cross sections was found, while the normal-hierarchy cross section was 2–3 times larger than that of the nonoscillating cross section, depending on the adopted parametrization of the Fermi-Dirac distribution. This property of the supernova-antineutrino signal could probably be used to distinguish between the two hierarchies in megaton LAr detectors.

DOI: [10.1103/PhysRevC.97.034309](https://doi.org/10.1103/PhysRevC.97.034309)

### I. INTRODUCTION

The standard model of particle physics is considered not to be the final theory of the Universe and its constituents. It does not provide a good candidate for dark matter and also the tiny asymmetry between matter and antimatter in the Universe is not understood, not to mention the origin of dark energy. The first point, dark matter, is massively tackled experimentally, as it is expected that such a dark-matter particle will collide with a nucleus, resulting in a measurable recoil energy of a few keV of the hit nucleus. As is known, cross sections are very small because they have not been observed yet; hence, large detectors with very little radioactive contamination (low background) have to be installed underground to provide the necessary sensitivity. One approach, among others, are large-scale noble gas detectors. One material is argon, which has an abundance of 99.6% of  $^{40}\text{Ar}$  and is currently used in the dark-matter experiments DEAP-3600 [1] and DarkSide-50 [2]. In addition, there are more applications of argon detectors in neutrino physics, one example being the 40-kiloton-scale LArTPC detector envisaged for the planned long-baseline experiment Deep Underground Neutrino Experiment (DUNE) [3]. Here, we would like to focus on cross-sectional determinations on  $^{40}\text{Ar}$  for astrophysical neutrinos, which would include solar and supernova neutrinos, neutrinos from the diffuse supernova-neutrino background, low-energy atmospheric neutrinos, or general astrophysical neutrinos with energies below 60 MeV.

The focus is on  $\nu_e$  and  $\bar{\nu}_e$  reactions. Starting with the electron neutrinos from the sun, the reaction (1) (see the following section) is possible. Given the fact that the reaction threshold between the mother nucleus  $^{40}\text{Ar}$  and the daughter nucleus  $^{40}\text{K}$  is 1.5044 MeV, only a fraction of the CNO neutrinos and the  $^8\text{B}$  neutrinos can be captured. The neutrino and antineutrino scatterings off  $^{40}\text{Ar}$  have previously been studied using the random-phase approximation (RPA) [4,5]. In Ref. [5], the importance of the scattering to the  $1^-$  and  $2^-$  final nuclear states was highlighted. The neutrino scattering  $^{40}\text{Ar}(\nu, e^-)^{40}\text{K}$  has been studied also using the nuclear shell model [6,7] but these investigations have been limited to Gamow-Teller (GT) and Fermi transitions. The shell-model calculations have been complicated by the large number of possible configurations for  $sd$ - $pf$  nuclei.

In Ref. [8], a new effective interaction was presented for the  $1s$ - $0d_{3/2}$ - $0f_{7/2}$ - $1p_{3/2}$  model space. This interaction was created to explain the isomeric shift in  $^{38}\text{K}^m$ . The model space for which the interaction is designed is significantly smaller than the entire  $sd$ - $pf$  model space. This allows for calculations without extra  $n\hbar\omega$  type truncations used in the previous shell-model calculations. In the present paper, we have managed to perform shell-model calculations for the neutrino and antineutrino scatterings off  $^{40}\text{Ar}$  for multipoles up to  $3^\pm$ . We give the averaged cross sections folded with both solar- and supernova-neutrino energy spectra, which are of interest from an experimental point of view. In the present paper, we also take into account the effects of neutrino flavor conversions in the dense stellar matter.

This article is organized as follows. In Sec. II, we give the theoretical background behind neutrino-nucleus scattering. In

\*joel.j.kostensalo@student.jyu.fi

†jouni.suhonen@phys.jyu.fi

‡zuber@physik.tu-dresden.de

Sec. III, we present our results for the total and averaged cross sections, and in Sec. IV, we draw the conclusions.

## II. THEORETICAL FORMALISM

In this work, we consider charged-current neutrino and antineutrino scattering off the nucleus  $^{40}\text{Ar}$ , i.e., the reactions

$$\nu_e + {}^{40}\text{Ar}(0^+)_{\text{g.s.}} \rightarrow {}^{40}\text{K} + e^- \quad (1)$$

and

$$\bar{\nu}_e + {}^{40}\text{Ar}(0^+)_{\text{g.s.}} \rightarrow {}^{40}\text{Cl} + e^+, \quad (2)$$

where the daughter nucleus can be in an excited state. At the energies considered in this work, the creation of the heavier lepton flavors,  $\mu$  and  $\tau$ , is not energetically possible.

For the solar and core-collapse supernova neutrinos, the four-momentum transfer is small compared to the mass of the exchanged gauge boson  $W^\pm$ , i.e.,  $Q^2 = -q_\mu q^\mu \ll M_{W^\pm}^2$ , where the transferred four-momentum is the difference in the momenta of the outgoing and incoming leptons (due to energy conservation also the difference of the momenta of the mother and daughter nuclei is small). Therefore, to a good approximation the scattering can be considered in the lowest order as a single effective vertex with a coupling constant  $G = G_F \cos(\theta_C)$ , where  $G_F$  is the Fermi constant and  $\theta_C \approx 13^\circ$  is the Cabibbo angle. The matrix element of this effective Hamiltonian can be written as

$$\langle f | H_{\text{eff}} | i \rangle = \frac{G}{\sqrt{2}} \int d^3\mathbf{r} l_\mu e^{-i\mathbf{q}\cdot\mathbf{r}} \langle f | \mathcal{J}^\mu(\mathbf{r}) | i \rangle, \quad (3)$$

where  $\mathcal{J}^\mu$  denotes the hadronic current and  $l_\mu = e^{i\mathbf{q}\cdot\mathbf{r}} \langle l | j_\mu(r) | \nu \rangle$  [9], where  $j_\mu$  is the leptonic current.

The initial nuclear state in the scatterings of Eqs. (1) and (2) is the  $J_i^{\pi_i} = 0^+$  ground state of  $^{40}\text{Ar}$ . We assume that the final nuclear states in  $^{40}\text{K}$  and  $^{40}\text{Cl}$  also have well-defined spin parities  $J_f^{\pi_f}$ . The double differential cross section for the charged-current (CC) (anti)neutrino-nucleus scattering is given by [9–11]

$$\left[ \frac{d^2\sigma_{i \rightarrow f}}{d\Omega dE_{\text{exc}}} \right] = \frac{G^2 |\mathbf{k}_{l^\mp}| E_{l^\mp}}{\pi(2J_i + 1)} F(\pm Z_f, E_{\mathbf{k}_{l^\mp}}) \times \left( \sum_{J \geq 0} \sigma_{\text{CL}}^J + \sum_{J \geq 1} \sigma_{\text{T}}^J \right), \quad (4)$$

where  $\mathbf{k}_{l^\mp}$  and  $E_{l^\mp}$  are the three-momentum and energy of the outgoing lepton ( $e^\mp$ ), respectively, and  $F(\pm Z_f, E_{\mathbf{k}_{l^\mp}})$  is the Fermi function which accounts roughly for the Coulomb interaction of the final-state lepton and nucleus. The Coulomb-longitudinal component  $\sigma_{\text{CL}}^J$  and the transverse component  $\sigma_{\text{T}}^J$  in Eq. (4) are defined as

$$\begin{aligned} \sigma_{\text{CL}}^J &= (1 + a \cos \theta) |(J_f || \mathcal{M}_J(q) || J_i)|^2 \\ &+ (1 + a \cos \theta - 2b \sin^2 \theta) |(J_f || \mathcal{L}_J(q) || J_i)|^2 \\ &+ \frac{E_{\mathbf{k}} - E_{\mathbf{k}'}}{q} (1 + a \cos \theta + c) \\ &\times 2\text{Re}[(J_f || \mathcal{M}_J(q) || J_i)^* (J_f || \mathcal{L}_J(q) || J_i)] \end{aligned} \quad (5)$$

and

$$\begin{aligned} \sigma_{\text{T}}^J &= (1 - a \cos \theta + b \sin^2 \theta) \\ &\times [ |(J_f || \mathcal{T}_J^{\text{mag}}(q) || J_i)|^2 + |(J_f || \mathcal{T}_J^{\text{el}}(q) || J_i)|^2 ] \\ &\mp \frac{E_{\mathbf{k}} - E_{\mathbf{k}'}}{q} (1 - a \cos \theta - c) \\ &\times 2\text{Re}[(J_f || \mathcal{T}_J^{\text{mag}}(q) || J_i) (J_f || \mathcal{T}_J^{\text{el}}(q) || J_i)^*]. \end{aligned} \quad (6)$$

Here  $E_{\mathbf{k}}$  and  $E_{\mathbf{k}'}$  refer to the energies of the incoming and outgoing leptons. The minus sign is used for the neutrino scattering and the plus sign is for the antineutrino scattering. The quantities  $a$ ,  $b$ , and  $c$  in Eqs. (5) and (6) are

$$a = \sqrt{1 - \frac{m_f^2}{E_{\mathbf{k}'^2}}}, \quad (7)$$

$$b = \frac{a^2 E_{\mathbf{k}} E_{\mathbf{k}'}}{q^2}, \quad (8)$$

$$c = \frac{n_f^2}{q E_{\mathbf{k}'}} \quad (9)$$

where the magnitude of three-momentum transfer  $q$  is given by

$$q = |\mathbf{q}| = \sqrt{(E_{\mathbf{k}} - a E_{\mathbf{k}'})^2 + 2a E_{\mathbf{k}} E_{\mathbf{k}'} (1 - \cos \theta)}. \quad (10)$$

The final-state interactions are treated in the modified effective-momentum approximation (MEMA) of Ref. [12]. There the effective momentum inside the nucleus is given by

$$k_{\text{eff}} = \sqrt{E_{\text{eff}} - m_e^2}, \quad (11)$$

where  $m_e$  is the electron mass and  $E_{\text{eff}}$  is defined as

$$E_{\text{eff}} = E_{\mathbf{k}'} - V_{\text{C}}(0). \quad (12)$$

The quantity  $V_{\text{C}}(0)$  is the value of the Coulomb potential produced by the final-state nucleus at the origin. According to MEMA, we use for small values of  $k_{\text{eff}}$  the Fermi function, whereas for the larger values of  $k_{\text{eff}}$  we omit the Fermi function in Eq. (4) and replace the energy and three-momentum of the outgoing lepton by the effective values  $k_{\text{eff}}$  and  $E_{\text{eff}}$ .

## III. RESULTS AND DISCUSSION

### A. Nuclear-structure calculations

The wave functions of the initial and final nuclear states, and the one-body transition densities (OBTDs), related to the transitions, were calculated using the nuclear shell model. The calculations were done using the shell-model code NUSHELLX@MSU [14] in the  $1s-0d_{3/2}-0f_{7/2}-1p_{3/2}$  valence space using the Hamiltonian ZBM2M [8]. In Ref. [8], the proton and neutron excitations across the  $N, Z = 20$  shell gap were found to be significant in the  $^{40}\text{Ca}$  region. Excitations across the shell gap are needed to produce the positive-parity states in  $^{40}\text{Cl}$  and  $^{40}\text{K}$  with  $J = 0, 1$ , which are the final nuclear states for the Fermi and Gamow-Teller type transitions. The contributions from these multipolarities dominate the (anti)neutrino-scattering cross sections at energies up to few tens of MeVs. In this work, we limit the considered final nuclear



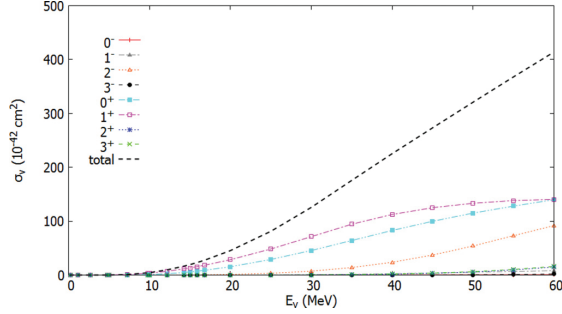


FIG. 3. Unfolded cross sections for the charged-current  $^{40}\text{Ar}(\nu, e^-)^{40}\text{K}$  scattering as functions of the energy of the incident neutrino.

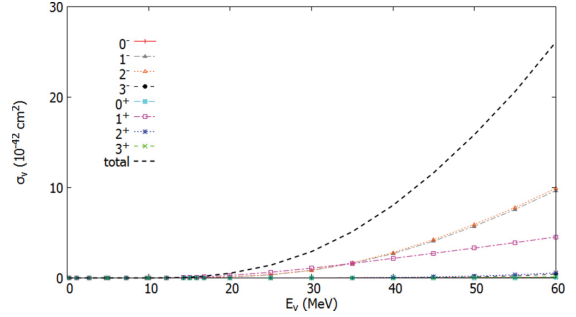


FIG. 4. Unfolded cross sections for the charged-current  $^{40}\text{Ar}(\bar{\nu}, e^+)^{40}\text{Cl}$  scattering as functions of the energy of the incident neutrino.

energies below 60 MeV. The present shell-model calculation, however, predicts the  $1^-$  contributions to be much lower.

For the antineutrino scattering  $^{40}\text{Ar}(\bar{\nu}, e^+)^{40}\text{Cl}$ , the unfolded cross sections are presented in Fig. 4 and Table II as functions of the antineutrino energy. The total cross section grows quadratically for energies up to 60 MeV. The total cross section for the antineutrino scattering is only 5% of the neutrino-scattering cross section for high energies and even less for the lower energies. This is partially explained by the 6-MeV-higher  $Q$  value for the  $\beta^-$  decay of  $^{40}\text{Cl}$  [17]. The GT transitions dominate for energies below 40 MeV but for higher energies the spin-dipole states ( $1^-$  and  $2^-$ ) are the major contributors. The Fermi transitions do not play a role since there is no isobaric analog state of  $^{40}\text{Ar}$  in  $^{40}\text{Cl}$ .

### C. Averaged solar-neutrino cross sections

From the experimental point of view, the interesting quantity is the averaged cross section  $\langle\sigma\rangle$  which is found by folding the total cross section with the appropriate neutrino energy profile, taking into account the reaction threshold 1.5044 MeV. For the solar neutrinos, we adopt a  $^8\text{B}$  profile. The differential cross section for the solar-neutrino reaction  $^{40}\text{Ar}(\nu, e^-)^{40}\text{K}$  as a function of excitation energy is presented in Fig. 5(a). The largest contribution in the shell-model calculation comes from the scattering to the third  $1^+$  state at 2659 keV. This corresponds to the experimentally observed  $J = 1$  state at 2730 keV. The

transition to the IAS state contributes only 40% of this. The other significant contributions come from the transition to the  $1_6^+$ ,  $1_{10}^+$ ,  $1_{15}^+$ , and  $1_{17}^+$  states.

For the solar neutrinos, the total computed cross section is  $1.777 \times 10^{-42} \text{ cm}^2$ , which is higher than the averaged cross sections  $1.15(7) \times 10^{-42} \text{ cm}^2$  of Ref. [6] and  $1.405 \times 10^{-42} \text{ cm}^2$  of Ref. [7]. The folded cross sections of the previous papers have considered only the GT and IAS transitions. Furthermore, in the previous shell-model calculations, the model space has been chosen as  $sd$ - $pf$  with only the  $(sd)^{-2}(pf)^2$  type of two-particle-two-hole excitations allowed.

## D. Averaged supernova-neutrino cross sections

### 1. Averaged cross sections without neutrino flavor conversions

The averaged cross section  $\langle\sigma\rangle$  for the supernova neutrinos we find by folding the total cross section with a Fermi-Dirac distribution

$$F_{\text{FD}}(E_{\mathbf{k}}) = \frac{1}{F_2(\alpha_{\nu})T_{\nu}} \frac{(E_{\mathbf{k}}/T_{\nu})^2}{1 + \exp(E_{\mathbf{k}}/T_{\nu} - \alpha_{\nu})}, \quad (13)$$

where  $T_{\nu}$  is the effective neutrino temperature and  $\alpha_{\nu}$  is the pinching parameter. If the temperature  $T_{\nu}$  and the value of the parameter  $\alpha_{\nu}$  are known, the average neutrino energy is given

TABLE I. Total unfolded cross sections for the neutrino-nucleus scattering  $^{40}\text{Ar}(\nu, e^-)^{40}\text{K}$  for different neutrino energies, decomposed into the contributing multipolarities. The cross sections are in the units  $10^{-42} \text{ cm}^2$  and the exponents are shown in parentheses.

$E_{\nu}$ [MeV]	Total	$0^+$	$0^-$	$1^+$	$1^-$	$2^+$	$2^-$	$3^+$	$3^-$
5.0	1.01(-1)	9.27(-9)	3.02(-5)	1.01(-1)	5.56(-7)	1.37(-7)	3.41(-4)	1.51(-7)	8.96(-11)
10.0	4.56(0)	8.45(-1)	3.25(-3)	3.68(0)	1.55(-3)	9.62(-5)	3.08(-2)	1.19(-4)	1.03(-7)
15.0	1.99(1)	5.85(0)	1.99(-2)	1.37(1)	2.12(-2)	2.34(-3)	2.29(-1)	2.70(-3)	6.93(-6)
20.0	4.68(1)	1.55(1)	5.29(-2)	2.98(1)	1.14(-1)	1.90(-2)	1.27(0)	2.09(-2)	1.36(-4)
25.0	8.43(1)	2.90(1)	1.01(-1)	5.10(1)	3.79(-1)	8.84(-2)	3.64(0)	9.50(-2)	1.24(-3)
30.0	1.31(2)	4.55(1)	1.66(-1)	7.55(1)	9.32(-1)	2.95(-1)	8.22(0)	3.12(-1)	6.99(-3)
40.0	2.38(2)	8.28(1)	3.41(-1)	1.20(2)	3.29(0)	1.78(-0)	2.71(1)	1.85(0)	9.37(-2)
50.0	3.42(2)	1.15(2)	5.72(-1)	1.43(2)	7.25(0)	6.46(0)	6.19(1)	6.57(0)	6.19(-1)
60.0	4.45(2)	1.39(2)	8.50(-1)	1.51(2)	1.13(1)	1.68(1)	1.05(2)	1.67(1)	2.62(0)

TABLE II. Total unfolded cross sections for the antineutrino-nucleus scattering  $^{40}\text{Ar}(\bar{\nu}, e^+)^{40}\text{Cl}$  for different antineutrino energies, decomposed into the contributing multipolarities. The cross sections are in the units  $10^{-42} \text{ cm}^2$  and the exponents are shown in parentheses.

$E_\nu$ [MeV]	Total	$0^+$	$0^-$	$1^+$	$1^-$	$2^+$	$2^-$	$3^+$	$3^-$
5.0									
10.0	1.29(-3)	6.58(-12)	2.73(-5)	8.31(-4)	1.96(-6)	1.10(-8)	4.25(-4)	1.01(-10)	2.52(-9)
15.0	1.17(-1)	3.80(-7)	3.02(-3)	8.05(-2)	1.42(-2)	1.64(-5)	1.90(-2)	4.74(-6)	1.44(-6)
20.0	6.10(-1)	1.11(-5)	1.13(-2)	3.76(-1)	1.07(-1)	3.25(-4)	1.15(-1)	9.19(-5)	3.55(-5)
25.0	1.61(0)	8.94(-5)	2.51(-2)	8.54(-1)	3.58(-1)	2.22(-3)	3.74(-1)	6.12(-4)	3.25(-4)
30.0	3.24(0)	4.02(-4)	4.44(-2)	1.46(0)	8.48(-1)	9.07(-3)	8.81(-1)	2.43(-3)	1.75(-3)
40.0	8.64(0)	3.32(-3)	9.93(-2)	2.82(0)	2.75(0)	6.61(-2)	2.86(0)	1.66(-2)	2.05(-2)
50.0	1.67(1)	1.42(-2)	1.76(-1)	4.17(0)	5.87(0)	2.58(-1)	6.06(0)	5.89(-2)	1.17(-1)
60.0	2.72(1)	4.14(-2)	2.72(-1)	5.56(0)	9.94(0)	6.93(-1)	1.01(1)	1.41(-1)	4.32(-1)

by the relation

$$\langle E_\nu \rangle / T_\nu = \frac{F_3(\alpha_\nu)}{F_2(\alpha_\nu)}, \quad (14)$$

where

$$F_k(\alpha_\nu) = \int \frac{x^k dx}{1 + \exp(x - \alpha_\nu)}. \quad (15)$$

The normalized differential cross sections for the reaction  $^{40}\text{Ar}(\nu, e^-)^{40}\text{K}$  as function of the excitation energy are presented in Figs. 5(b) and 5(c). The largest contribution comes from the scattering to the third  $1^+$  state and the transition to the IAS state, both contributing some 50% of the total. The other significant contributions come from the transition to the  $1_6^+$ ,  $1_{10}^+$ ,  $1_{15}^+$ , and  $1_{17}^+$  states, as in the case of the solar neutrinos. The differential cross sections for the reaction  $^{40}\text{Ar}(\bar{\nu}, e^+)^{40}\text{Cl}$  as function of the excitation energy are presented in Fig. 6. The largest contributors are the transitions to  $1_6^+$ ,  $2_{\text{g.s.}}^-$ , and  $1_6^-$  states. There are significant contributions coming also from the  $2_{2,4}^-$ ,  $1_4^-$ , and  $1_{1,2,8,12,19,28}^+$  states.

In Ref. [4], the ratio of the supernova neutrino and antineutrino cross sections was found to be approximately 12.5 with no flavor conversions included in a scenario with averaged energies  $\langle E_\nu \rangle = 11 \text{ MeV}$  and  $\langle E_{\bar{\nu}} \rangle = 16 \text{ MeV}$  respectively. Folding the cross sections of the present work using Fermi-Dirac distributions with these average energies and assuming  $\alpha = 0.0$ , we find that  $\sigma_\nu = 14.6 \times 10^{-42} \text{ cm}^2$  and  $\sigma_{\bar{\nu}} = 887 \times 10^{-45} \text{ cm}^2$  respectively. This gives a ratio of 16.5 for the neutrino and antineutrino cross sections, which is in good agreement with the RPA result of Ref. [4].

## 2. Effects of (anti)neutrino flavor conversions

Because of the large rest masses of both muon and  $\tau$  lepton, only electron-flavor (anti)neutrinos are detected in charged-current solar- and supernova-neutrino detection experiments. The energy profile of the (anti)neutrinos detected on Earth is, however, affected by (anti)neutrino flavor conversions (matter oscillations) which take place when the neutrinos propagate through the dense stellar matter [18]. We assume that the muon and  $\tau$ -neutrino energy profiles are identical, reducing the problem into a two-neutrino one. In the two-neutrino problem, we consider flavor changes  $\nu_x \rightarrow \nu_e$ , where  $\nu_x$  is a linear combination of muon and  $\tau$  neutrinos [19,20]. The energy profiles of electron neutrinos and antineutrinos reaching Earth

can be written as

$$F_{\nu_e}(E_{\mathbf{k}}) = p(E_{\mathbf{k}})F_{\nu_e}^0(E_{\mathbf{k}}) + [1 - p(E_{\mathbf{k}})]F_{\nu_x}^0(E_{\mathbf{k}}), \quad (16)$$

$$F_{\bar{\nu}_e}(E_{\mathbf{k}}) = \bar{p}(E_{\mathbf{k}})F_{\bar{\nu}_e}^0(E_{\mathbf{k}}) + [1 - \bar{p}(E_{\mathbf{k}})]F_{\bar{\nu}_x}^0(E_{\mathbf{k}}), \quad (17)$$

where  $p$  and  $\bar{p}$  are the survival probabilities of the electron neutrinos and antineutrinos respectively, and the quantities  $F_{\nu_e}^0(E_{\mathbf{k}})$  and  $F_{\bar{\nu}_e}^0(E_{\mathbf{k}})$  are the initial energy profiles of the neutrinos and antineutrinos.

For the survival probabilities  $p$  and  $\bar{p}$ , we use the values from Refs. [21,22]. For the normal mass hierarchy, the values are

$$p(E_{\mathbf{k}}) = 0, \quad (18)$$

$$\bar{p}(E_{\mathbf{k}}) = \begin{cases} \cos^2 \theta_{12}, & E_{\mathbf{k}} < \bar{E}_s, \\ 0, & E_{\mathbf{k}} > \bar{E}_s, \end{cases} \quad (19)$$

where  $\bar{E}_s = 18 \text{ MeV}$  [22]. For the inverted mass hierarchy, we use the probabilities

$$p(E_{\mathbf{k}}) = \begin{cases} \sin^2 \theta_{12}, & E_{\mathbf{k}} < \bar{E}_s, \\ 0, & E_{\mathbf{k}} > \bar{E}_s, \end{cases} \quad (20)$$

$$\bar{p}(E_{\mathbf{k}}) = \cos^2 \theta_{12}, \quad (21)$$

where  $\bar{E}_s = 7 \text{ MeV}$  [19]. For the normal hierarchy  $\sin^2 \theta_{12} = 0.306$  and for the inverted hierarchy  $\sin^2 \theta_{12} = 0.312$  [23].

For the calculations, we used three sets of parameters ( $\alpha$ ,  $T$ ,  $\langle E \rangle$ ) taken from Ref. [24]. The values of the parameters for neutrinos and antineutrinos are presented in Table III.

The folded cross sections for supernova neutrinos are listed in Table IV. The neutrino-scattering cross section is increased roughly three-fold when the neutrino flavor conversions are taken into account. There is little difference between the cross sections with normal and inverted mass hierarchies. For the antineutrino scattering with parameter sets (I) and (II), the inverted-hierarchy cross section is enhanced by 30% while the normal-hierarchy cross section is enhanced by roughly 100% relative to the nonoscillating case. For the parameter set (III), the inverted-hierarchy cross section is 67% larger than the nonoscillating one, while the normal-hierarchy one is almost three times larger than the nonoscillating one.

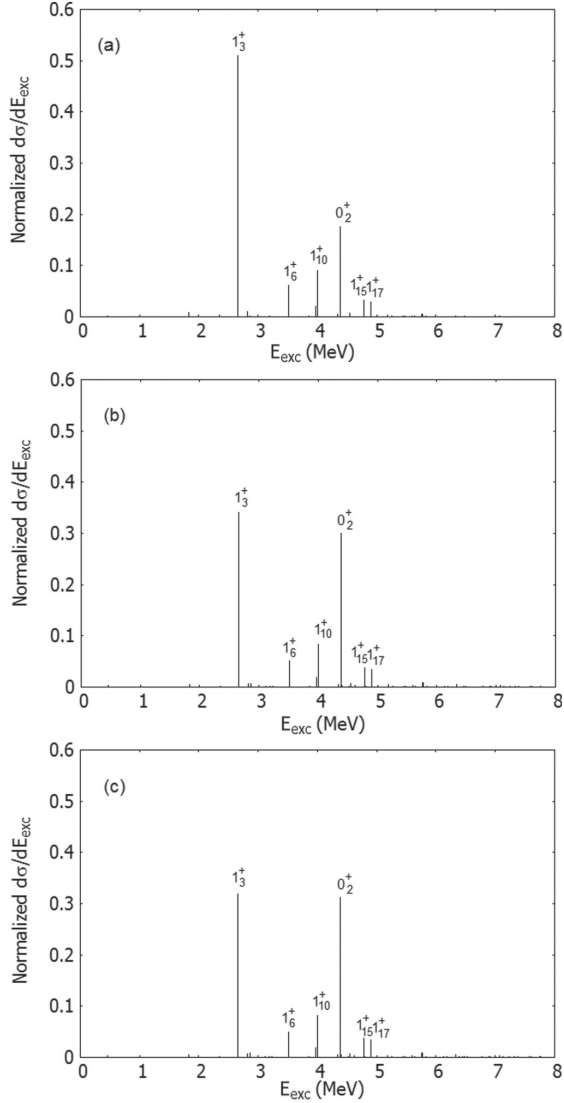


FIG. 5. Differential cross section for the CC supernova-neutrino scattering to final nuclear states at excitation energies  $E_{\text{exc}}$ . The total cross section is normalized to unity. Panel (a) is folded with the solar neutrino spectrum, panel (b) with Fermi-Dirac distribution with parametrization (I), and panel (c) with parametrization (II) (see Table III). Here the effects of flavor conversions are not included.

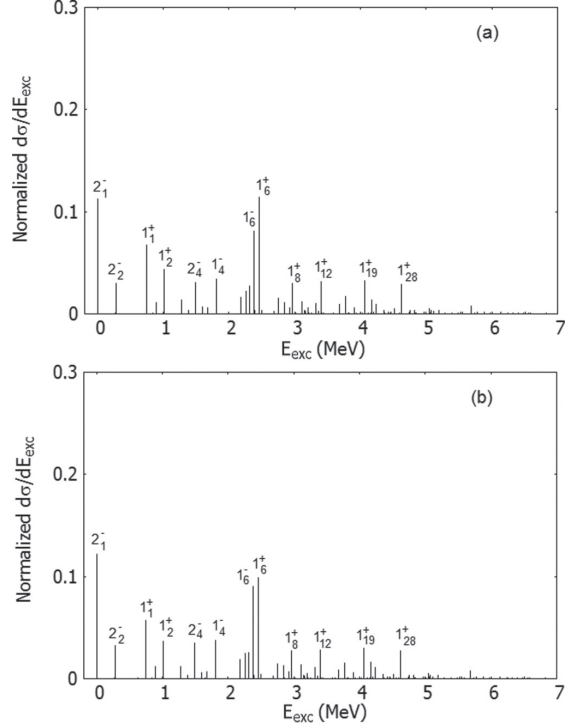


FIG. 6. Differential cross section for the CC supernova-antineutrino scattering to final nuclear states at excitation energies  $E_{\text{exc}}$ . The total cross section is normalized to unity. Panel (a) with Fermi-Dirac distribution with parametrization (I) and panel (b) with parametrization (II) (see Table III). Here the effects of flavor conversions are not included.

### E. Uncertainties

There are many sources of uncertainties for theoretical estimations of (anti)neutrino-nucleus scattering cross sections, which makes the estimation of the overall uncertainty difficult. In a previous shell-model study [6], the uncertainty was estimated by assuming that each GT strength has a statistical uncertainty of 10% since generally the uncertainties in the  $B(\text{GT})$  values are of the order 5–10% [25]. Because of the large number of states in the present study, such statistical uncertainties amount to less than 3%. For the supernova (anti)neutrinos, there are also uncertainties related to the distribution of neutrino energies, which cannot be accurately estimated. The actual supernova-neutrino spectrum is complex, and the details

TABLE III. Values of parameters  $\alpha$ ,  $T$ , and the average neutrino energy  $\langle E_{\nu_e/x} \rangle$  in MeV used for the supernova-neutrino calculations. The values are adopted from Ref. [24]. The index  $e$  refers to electron neutrinos and  $x = \mu, \tau$  to the nonelectron flavors.

	$(\alpha_{\nu_e}, T_{\nu_e}, \langle E_{\nu_e} \rangle)$	$(\alpha_{\bar{\nu}_e}, T_{\bar{\nu}_e}, \langle E_{\bar{\nu}_e} \rangle)$	$(\alpha_{\nu_x}, T_{\nu_x}, \langle E_{\nu_x} \rangle)$	$(\alpha_{\bar{\nu}_x}, T_{\bar{\nu}_x}, \langle E_{\bar{\nu}_x} \rangle)$
(I)	(3.0, 2.88, 11.5)	(3.0, 3.41, 13.6)	(3.0, 4.08, 16.3)	(3.0, 4.08, 16.3)
(II)	(0.0, 3.65, 11.5)	(0.0, 4.32, 13.6)	(0.0, 5.17, 16.3)	(0.0, 5.17, 16.3)
(III)	(3.0, 2.88, 11.5)	(3.0, 3.41, 13.6)	(0.0, 5.17, 16.3)	(0.0, 5.17, 16.3)

TABLE IV. Folded cross sections in units of  $\text{cm}^2$  for supernova neutrinos with the quenched value  $g_A = 1.00$ . The first column refers to the parameters of the Fermi-Dirac distribution given in Table III. In the second ( $\nu_e$ ) and fifth columns ( $\bar{\nu}_e$ ), cross sections for nonoscillating neutrinos are given, while the third, fourth, sixth, and seventh columns give the cross sections with matter oscillations included in the normal mass hierarchy (NH) and in the inverted mass hierarchy (IH).

Parameters	$\nu_e$	$\nu_{ex}^{\text{NH}}$	$\nu_{ex}^{\text{IH}}$	$\bar{\nu}_e$	$\bar{\nu}_{ex}^{\text{NH}}$	$\bar{\nu}_{ex}^{\text{IH}}$
(I)	$13.90 \times 10^{-42}$	$37.08 \times 10^{-42}$	$37.09 \times 10^{-42}$	$322.8 \times 10^{-45}$	$678.1 \times 10^{-45}$	$436.2 \times 10^{-45}$
(II)	$16.63 \times 10^{-42}$	$41.70 \times 10^{-42}$	$42.08 \times 10^{-42}$	$477.7 \times 10^{-45}$	$947.3 \times 10^{-45}$	$624.9 \times 10^{-45}$
(III)	$13.90 \times 10^{-42}$	$41.70 \times 10^{-42}$	$42.06 \times 10^{-42}$	$322.8 \times 10^{-45}$	$948.5 \times 10^{-45}$	$518.3 \times 10^{-45}$

of the spectrum are not well known. However, there are two potentially large sources of uncertainty which we can address. The first one is related to the value of the axial-vector coupling constant  $g_A$ , for which the correct effective value is not well understood. For the *sd* and *pf* shells half-life comparisons of GT transitions suggest a quenched value  $g_A \approx 1.00$  [26,27]. However, there are indications that for high-energy neutrinos the free-nucleon value  $g_A = 1.27$  should be used [16]. The effects of  $g_A$  are discussed in Sec. III E 1. The other potentially large source of systematic uncertainty is related to the limited valence space used in the calculations. Neutrinos with high energies excite states which are out of reach for valence spaces used in the shell-model calculations. The effect of the higher energy states on the folded cross sections are discussed in Sec. III E 2.

### 1. Value of $g_A$

Adopting the free-nucleon value  $g_A = 1.27$  instead of the quenched value increases the folded cross section for the solar-neutrino-nucleus scattering  $^{40}\text{Ar}(\nu, e^-)^{40}\text{K}$  to  $\sigma_\nu = 2.642 \times 10^{-42} \text{ cm}^2$ . However, for the solar neutrinos the quenched value  $g_A = 1.0$  is more appropriate, since the neutrino energies are lower. We assume the uncertainty related to this choice to be 5% (i.e.,  $g_A = 1.00(5)$ ), which includes most effective values obtained in previous shell-model studies in the *sd* and *pf* shells [26,28]. The 3% error related to the nuclear structure can be assumed to be uncorrelated with the error of  $g_A$ . With these assumptions, we end up with a cross section of  $1.78(23) \times 10^{-42} \text{ cm}^2$  for the solar-neutrino-nucleus scattering.

For the supernova (anti)neutrinos, the results are listed in Table V. Since the energies are several MeV higher than for the solar neutrinos, the appropriate effective value to be used for  $g_A$  is not so clear. It is best to consider the results of Table IV as lower limits and those of Table V as upper limits for the cross section. Since the GT transitions dominate the folded cross sections, the cross sections scale roughly  $\propto g_A^2$ . Because of this scaling, the ratios between the folded cross sections corresponding to the nonoscillating case, inverted mass hierarchy, and normal mass hierarchy are similar for both the free-nucleon and quenched values of  $g_A$ .

TABLE V. Same as Table IV but with the free nucleon value  $g_A = 1.27$  adopted for the axial-vector coupling constant.

Parameters	$\nu_e$	$\nu_{ex}^{\text{NH}}$	$\nu_{ex}^{\text{IH}}$	$\bar{\nu}_e$	$\bar{\nu}_{ex}^{\text{NH}}$	$\bar{\nu}_{ex}^{\text{IH}}$
(I)	$19.15 \times 10^{-42}$	$50.80 \times 10^{-42}$	$50.81 \times 10^{-42}$	$512.8 \times 10^{-45}$	$1077 \times 10^{-45}$	$693.1 \times 10^{-45}$
(II)	$23.03 \times 10^{-42}$	$56.83 \times 10^{-42}$	$56.87 \times 10^{-42}$	$759.1 \times 10^{-45}$	$1501 \times 10^{-45}$	$993.2 \times 10^{-45}$
(III)	$19.15 \times 10^{-42}$	$56.83 \times 10^{-42}$	$56.87 \times 10^{-42}$	$512.8 \times 10^{-45}$	$1506 \times 10^{-45}$	$823.7 \times 10^{-45}$

### 2. High-energy neutrinos

The shell-model computed supernova-neutrino-nucleus cross section for the reaction  $^{40}\text{Ar}(\nu, e^-)^{40}\text{K}$  is roughly proportional to  $E_\nu^2$  up to 35 MeV, as can be seen from Fig. 7. Beyond that, the shell model predicts roughly a linear energy dependence for the cross section. However, the QRPA result of Ref. [5] predicts larger cross sections and a rough proportionality to  $E_\nu^2$  for neutrino energies between 40 and 80 MeV. Since we expect the QRPA results be more reliable than the shell model ones for higher energies, we need to correct for the missing cross section for the high-energy neutrinos. The small cross sections for high-energy neutrinos stem from the use of a too limited valence space for neutrino scattering at these energies. However, the effects of this on the folded cross sections are expected to be rather modest, since the tail of the supernova-neutrino energy distribution above 35 MeV is quite small and dies out exponentially. The missing strength can be approximated by assuming that the cross section keeps growing proportional to  $E_\nu^2$  also for energies above 35 MeV in a way which reproduces the QRPA cross sections at the higher energies. In Fig. 7, the total cross section is plotted together with a quadratic fit function which intersects the origin and tangents the shell-model cross section at 35 MeV. The resulting fit function agrees with the QRPA results of Ref. [5] at high energies, giving roughly  $\sigma = 5 \times 10^{-40} \text{ cm}^2$  for 60 MeV and  $\sigma = 8 \times 10^{-40} \text{ cm}^2$  for 80 MeV. It should be stressed that the energy dependence of the neutrino cross section is not as trivial as  $E_\nu^2$ , but the fitted function can be used to estimate the effect of the missing high-energy states, since it reproduces the 60- to 80-MeV QRPA results well, as well as agreeing with the shell-model results for the 35- to 40-MeV energies. For the lower energies, the shell-model cross section should of course be used and not that of the fit.

One can estimate the effect of the missing total cross section beyond 40 MeV (this is where the quadratic fit function and the shell-model cross section start to depart from each other) on the folded cross sections. For this, we look at the proportion of neutrinos with energies above 40 MeV in the neutrino-energy profile. The proportion of these neutrinos is the largest for the

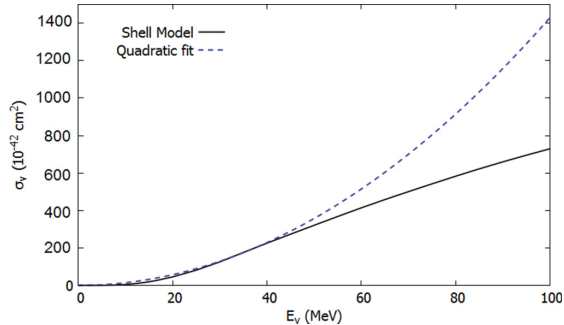


FIG. 7. The total shell-model cross section and a quadratic fit.

parameters ( $\alpha = 0, T = 5.17$ ) and it is 1.87%. It then turns out that calculating the folded cross section with the quadratic fit function above 35 MeV, instead of the shell-model one, actually increases the folded cross section by about 0.9%. For parameter sets with lower average energies, the effect is significantly reduced from this. For example, for ( $\alpha = 3, T = 2.88$ ) the increase is only about 0.01%. Therefore, the lack of computed strength beyond 35 MeV has no practical effect on the folded cross sections calculated in the present paper. However, the numbers of Table I are expected to be realistic only up to 40 MeV. As seen in Fig. 4, the roughly quadratic behavior of the total antineutrino cross section continues up to 60 MeV and thus the numbers in Table II should be reliable. Furthermore, one should point out that the most contribution to the folded cross sections, both for the solar as well as for the supernova neutrinos, comes from nuclear excitations at energies that are best described by the nuclear shell model. In this sense, the present results for the folded cross sections should be considered as the best on the market.

#### IV. CONCLUSIONS

In the present paper, we have calculated cross sections for the charged-current neutrino and antineutrino scatterings  $^{40}\text{Ar}(\nu, e^-)^{40}\text{K}$  and  $^{40}\text{Ar}(\bar{\nu}, e^+)^{40}\text{Cl}$  for astrophysical neutrinos with energies below 60 MeV, especially relevant for both solar and supernova neutrinos. The initial and final nuclear wave functions were calculated using the nuclear shell model. The effects of (anti)neutrino flavor conversions in dense stellar matter (matter oscillations) were also included.

While the previous shell-model calculations of cross sections have considered only Gamow-Teller and Fermi types of transitions, in the present paper we consider also transitions to the first  $100 0^\pm, 1^\pm, 2^\pm,$  and  $3^\pm$  states. Contributions from the spin-dipole states ( $1^-$  and  $2^-$ ) dominate the total unfolded antineutrino-scattering cross section for antineutrino energies above 40 MeV. Especially the lowest two  $2^-$  states and the

$6^{\text{th}} 1^-$  state give significant contributions to the cross section. For the total unfolded neutrino cross section, the transitions to  $2^-$  states in  $^{40}\text{K}$  becomes significant above 30 MeV of neutrino energy. It is therefore clear that the  $1^-$  and  $2^-$  multipolarities should not be omitted in the cross-sectional calculations.

For solar neutrinos, with a  $^8\text{B}$  distribution, the folded cross section was found to be  $\sigma_\nu = 1.78(23) \times 10^{-42} \text{ cm}^2$ . This cross section is higher than the folded cross sections  $1.15(7) \times 10^{-42} \text{ cm}^2$  [6] and  $1.405 \times 10^{-42} \text{ cm}^2$  [7] of previous theoretical papers, where only Fermi and Gamow-Teller transitions were taken into account.

We also computed the folded scattering cross sections for supernova (anti)neutrinos. To test the scope of our calculations, the cross sections were also folded with the supernova-neutrino spectra used in the RPA-based calculation of Ref. [4] with no matter oscillations included. The neutrino-antineutrino cross-sectional ratio was found to be 16.5, which is in a reasonable agreement with the ratio 12.5 reported in Ref. [4]. Though the limited valence space considered in the present paper is unable to account for giant resonances, the systematic uncertainty related to this propagates to the folded cross sections at the level of 1% or less, as verified by our analysis of the previous RPA results. Since the folded cross sections for both the solar and supernova neutrinos gather the relevant contributions from nuclear excitations best described by the nuclear shell model, the present results for the folded cross sections can be considered as the most accurate ones available thus far.

For supernova-neutrino scattering, the cross section is increased roughly threefold when the neutrino flavor conversions are taken into account. The results for normal and inverted mass hierarchies agreed with 1% accuracy for all three adopted Fermi-Dirac distribution parameter sets (see Table III). For parametrizations (I) and (II), the antineutrino-scattering cross sections in the inverted-hierarchy scenario were enhanced by 30–35% with respect to the nonoscillating ones, while for the parameter set (III) the inverted-hierarchy cross section was 67% larger. The normal-hierarchy cross section was roughly twice as large as the nonoscillating cross section for the first two parameter sets and three times larger for the parameter set (III). One can then speculate that the strong effects of the neutrino mass hierarchy on the supernova-antineutrino signal could be used to distinguish between the two hierarchies in megaton LAr detectors. On the other hand, if the hierarchy was known, one could learn about the flavor-conversion processes inside the supernovae.

#### ACKNOWLEDGMENT

This work has been partially supported by the Academy of Finland (Suomen Akatemia) under the Finnish Centre of Excellence Programme 2012–2017 (Nuclear and Accelerator Based Programme at JYFL).

- [1] P.-A. Amaudruz, M. Baldwin, M. Batygov, B. Beltran, C. E. Bina, D. Bishop, J. Bonatt, G. Boorman, M. G. Boulay, B. Broerman *et al.*, [arXiv:1707.08042](https://arxiv.org/abs/1707.08042).  
 [2] P. Agnes *et al.*, *Phys. Lett. B* **743**, 456 (2015).

- [3] R. Acciarri, M. A. Acero, M. Adamowski, C. Adams, P. Adamson, S. Adhikari, Z. Ahmad, C. H. Albright, T. Alion, E. Amador *et al.*, [arXiv:1512.06148](https://arxiv.org/abs/1512.06148).

- [4] I. Gil-Botella and A. Rubbia, *J. Cosmol. Astropart. Phys.* **2003**, 009 (2003).
- [5] M.-K. Cheoun, E. Ha, and T. Kajino, *Phys. Rev. C* **83**, 028801 (2011).
- [6] W. E. Ormand, P. M. Pizzochero, P. F. Bortignon, and R. A. Broglia, *Phys. Lett. B* **345**, 343 (1995).
- [7] T. Suzuki and M. Honma, *Phys. Rev. C* **87**, 014607 (2013).
- [8] M. L. Bissell, J. Papuga, H. Naïdja, K. Kreim, K. Blaum, M. De Rydt, R. F. Garcia Ruiz, H. Heylen, M. Kowalska, R. Neugart, G. Neyens, W. Nörtershäuser, F. Nowacki, M. M. Rajabali, R. Sanchez, K. Sieja, and D. T. Yordanov, *Phys. Rev. Lett.* **113**, 052502 (2014).
- [9] E. Ydrefors and J. Suhonen, *Adv. High Energy Phys.* **2012**, 373946 (2012).
- [10] E. Kolbe, K. Langanke, G. Martínez-Pinedo, and P. Vogel, *J. Phys. G: Nucl. Part. Phys.* **29**, 2569 (2003).
- [11] E. Ydrefors and J. Suhonen, *Phys. Rev. C* **87**, 034314 (2013).
- [12] J. Engel, *Phys. Rev. C* **57**, 2004 (1998).
- [13] National Nuclear Data Center, Brookhaven National Laboratory [www.nndc.bnl.gov]
- [14] B. A. Brown and W. D. M. Rae, *Nucl. Data Sheets* **120**, 115 (2014).
- [15] W. Almosly, B. G. Carlsson, J. Suhonen, J. Toivanen, and E. Ydrefors, *Phys. Rev. C* **94**, 044614 (2016).
- [16] T. Katori and M. Martini, *J. Phys. G: Nucl. Part. Phys.* **45**, 013001 (2018).
- [17] J. Chen, *Nucl. Data Sheets* **140**, 1 (2017).
- [18] B. Dasgupta, A. Dighe, G. G. Raffelt, and A. Y. Smirnov, *Phys. Rev. Lett.* **103**, 051105 (2009).
- [19] J. Gava and C. Volpe, *Phys. Rev. D* **78**, 083007 (2008).
- [20] A. B. Balantekin and G. M. Fuller, *Phys. Lett. B* **471**, 195 (1999).
- [21] G. G. Raffelt, *Prog. Part. Nucl. Phys.* **64**, 393 (2010).
- [22] G. Martínez-Pinedo, B. Ziebarth, T. Fischer, and K. Langanke, *Eur. Phys. J. A* **47**, 98 (2010).
- [23] K. Nakamura *et al.* (Particle Data Group), *J. Phys. G: Nucl. Part. Phys.* **37**, 075021 (2010).
- [24] M. T. Keil, G. G. Raffelt, and H.-T. Janka, *Astrophys. J.* **590**, 971 (2003).
- [25] B. A. Brown and B. H. Wildenthal, *At. Data Nucl. Data Tables* **33**, 347 (1985).
- [26] B. H. Wildenthal, M. S. Curtin, and B. A. Brown, *Phys. Rev. C* **28**, 1343 (1983).
- [27] G. Martínez-Pinedo, A. Poves, E. Caurier, and A. P. Zuker, *Phys. Rev. C* **53**, R2602(R) (1996).
- [28] T. Siiskonen, M. Hjorth-Jensen, and J. Suhonen, *Phys. Rev. C* **63**, 055501 (2001).



V

**BETA-SPECTRUM SHAPES OF FORBIDDEN  $\beta$  DECAYS**

by

Kostensalo, J., & Suhonen, J. 2018

International Journal of Modern Physics A, 33 (9), 1843008.  
doi:10.1142/S0217751X1843008X

Reproduced with kind permission by World Scientific Publishing.

## Beta-spectrum shapes of forbidden $\beta$ decays

Joel Kostensalo and Jouni Suhonen\*

*Department of Physics, University of Jyväskylä, P.O. Box 35,  
Jyväskylä, FI-40014, Finland  
\*jouni.suhonen@phys.jyu.fi*

Received 29 December 2017

Accepted 23 January 2018

Published 27 March 2018

The neutrinoless  $\beta\beta$  decay of atomic nuclei continues to attract fervent interest due to its potential to confirm the possible Majorana nature of the neutrino, and thus the nonconservation of the lepton number. At the same time, the direct dark matter experiments are looking for weakly interacting massive particles (WIMPs) through their scattering on nuclei. The neutrino-oscillation experiments on reactor antineutrinos base their analyses on speculations of  $\beta$ -spectrum shapes of nuclear decays, thus leading to the notorious “reactor antineutrino anomaly.” In all these experimental efforts, one encounters the problem of  $\beta$ -spectrum shapes of forbidden  $\beta$  decays, either as unwanted backgrounds or unknown components in the analyses of data. In this work, the problem of spectrum shapes is discussed and illustrated with a set of selected examples. The relation of the  $\beta$ -spectrum shapes to the problem of the effective value of the weak axial-vector coupling strength  $g_A$  and the enhancement of the axial-charge matrix element is also pointed out.

*Keywords:* Forbidden beta decays; beta spectrum shapes; double beta decay; direct dark matter search; reactor antineutrino anomaly; axial-vector coupling strength; axial-charge matrix element.

PACS numbers: 21.60.Cs, 21.60.Jz, 23.40.Bw, 23.40.Hc

### 1. Introduction

At the moment, the neutrinoless  $\beta\beta$  ( $0\nu\beta\beta$ ) decay is the only practical means of accessing the possible Majorana nature of the neutrino. In order to proceed, the decay requires the violation of lepton-number conservation and a nonzero neutrino mass. There are a host of different possible mechanisms which mediate the decay.<sup>1</sup> The  $0\nu\beta\beta$  decay is related to nuclear structure via the nuclear matrix elements (NMEs), calculated in many different theory frameworks (see the reviews in Refs. 2–5), e.g. the quasiparticle random-phase approximation.<sup>6–8</sup>

\*Corresponding author.

Due to its great potential to revolutionize the field of electroweak interactions, the  $0\nu\beta\beta$  has attracted and continues to attract intense experimental interest. The presently running  $0\nu\beta\beta$  experiments include AURORA, GERDA, NEMO-3, COBRA, CUORE, EXO and KamLAND-Zen.<sup>9–15</sup> The future experiments include Majorana, SuperNEMO, MOON, AMoRE, LUMINEU, CUPID, SNO+, NEXT and PandaX-III.<sup>16–24</sup> Some of these second-order processes compete with extremely retarded first-order processes, namely  $\beta$  decays in the  $^{48}\text{Ca}$ – $^{48}\text{Sc}$ – $^{48}\text{Ti}$  system<sup>25,26</sup> and in the  $^{96}\text{Zr}$ – $^{96}\text{Nb}$ – $^{96}\text{Mo}$  system.<sup>27,28</sup> Many of the listed experiments are based on liquid scintillators which have light nuclei as cosmogenic backgrounds. Also, very heavy nuclei like  $^{214}\text{Bi}$  can be a dangerous background in  $0\nu\beta\beta$  experiments.

At present, there are many candidates for the weakly interacting massive particles (WIMPs). Probably, the most popular one is the lightest supersymmetric particle (LSP).<sup>29–35</sup> The WIMPs are expected to be nonrelativistic and they can be detected by their scattering on atomic nuclei. There is a vast number of direct dark matter detection experiments with different target materials: XENON10, XENON100, XMASS, ZEPLIN, PANDA-X, LUX, CDMS, CoGENT, EDELWEISS, DAMA, KIMS, PICASSO, ADMX, CDEX, CRESST, DarkSide, DMTPC, DRIFT and SIMPLE.<sup>36–54</sup> Many of these experiments suffer from backgrounds produced by unknown  $\beta$ -spectrum shapes.

A further interesting application of the  $\beta$ -spectrum studies is the reactor antineutrino anomaly (RAA).<sup>55</sup> The antineutrino spectra in the nuclear reactors result from the long uranium and plutonium  $\alpha$  and  $\beta^-$  decay chains and the subsequent fission used as fuel to drive the energy production in the nuclear power plants. In RAA, the experimentally measured antineutrino flux is lower than what is expected from the  $\beta$  decays of the nuclear fission fragments deduced from nuclear data with some approximations.<sup>56</sup> The method of virtual  $\beta$  branches<sup>57–59</sup> has been used to aid in the process of collecting the cumulative  $\beta$  spectra responsible for the estimated theoretical antineutrino flux. The involved  $\beta$  decays go partly by forbidden transitions that cannot be assessed by the present nuclear data, but instead, could be calculated by the formalism introduced in Refs. 60 and 61. The measured flux is some 6(2)% lower, making this a rough  $3\sigma$  deviation.<sup>62</sup> Possible shortcomings of the used analysis methods have been pointed out in Ref. 63.

Beyond the half-life analyses (see, e.g. Refs. 64–68), the  $\beta$ -spectrum shapes can also be used to pin down the effective value of the weak axial-vector coupling strength  $g_A$  in forbidden nonunique  $\beta$  decays. In some  $\beta$ -decay transitions, the shape of the  $\beta$  spectrum is quite sensitive to the variations in the value of  $g_A$ . This feature can be utilized in determining the value of  $g_A$  for forbidden  $\beta$  transitions. This method is called the spectrum-shape method (SSM) and was introduced in Ref. 70. Further systematic studies using the SSM were performed in Refs. 61, 71 and 72. The status of the effective values of  $g_A$  in  $\beta$  and  $\beta\beta$  decays is summarized in Ref. 73 and the impact of the effective values of  $g_A$  on the sensitivities of the presently running and future  $\beta\beta$ -decay experiments has been discussed in Ref. 74. The SSM can also be used to study the enhancement in the axial-charge matrix element

(for an overview of the problem, see Ref. 73) for the first-forbidden nonunique  $J^+ \leftrightarrow J^-$  transitions.

## 2. Schematic Outline of the Theory

In the *allowed* nuclear  $\beta^-$  ( $\beta^+$ ) transitions, the emitted leptons, electron antineutrino and electron (electron neutrino and positron) carry away zero units of orbital angular momentum. The 0 or 1 units of change in the nuclear spin is compensated by the anti-alignment or alignment of the spins of the leptons. For the *forbidden*  $\beta$  decays, the emitted leptons carry away at least one unit of orbital angular momentum, and thus the decay amplitude is suppressed by a factor of  $qR \sim 0.01$  or its higher powers. Here,  $R \sim \text{few fm}$  is the nuclear radius and  $q \sim 1 \text{ MeV}$  is the momentum of the leptons. This means that the decay probability is suppressed by a huge factor (roughly by  $10^{-4}$ ) each time the forbiddenness increases by one unit.

### 2.1. Forbidden unique $\beta$ decays

The forbidden unique  $\beta$  transitions are the simplest ones that mediate  $\beta$  decays between nuclear states of (large) angular-momentum difference  $\Delta J$ . In particular, if one of the states is a  $0^+$  state, then for a  $K$ th forbidden ( $K = 1, 2, 3, \dots$ ) unique beta decay, the angular momentum of the other involved state is  $J = K + 1$ . At the same time, the parity changes in the odd-forbidden and remains the same in the even-forbidden decays.<sup>75</sup> The change in angular momentum and parity for different degrees of forbiddenness is presented in Table 1, and they obey the simple rule

$$(-1)^{\Delta J} \Delta\pi = -1 \quad (\text{forbidden unique decays}). \quad (1)$$

The theoretical half-lives  $t_{1/2}$  of  $K$ th forbidden unique  $\beta$  decays can be expressed in terms of reduced transition probabilities  $B_{Ku}$  and phase-space factors  $f_{Ku}$ . The  $B_{Ku}$  is given by the NME, which in turn is given by the single-particle NMEs and one-body transition densities. Then (for further details, see Ref. 75),

$$t_{1/2} = \frac{\kappa}{f_{Ku} B_{Ku}}; \quad B_{Ku} = \frac{g_A^2}{2J_i + 1} |M_{Ku}|^2, \quad (2)$$

where  $J_i$  is the angular momentum of the mother nucleus and  $\kappa$  is a constant with value<sup>76</sup>

$$\kappa = \frac{2\pi^3 \hbar^7 \ln 2}{m_e^5 c^4 (G_F \cos \theta_C)^2} = 6147 \text{ s} \quad (3)$$

Table 1. Change in angular momentum and parity in  $K$ th forbidden unique  $\beta$  decays with a  $0^+$  state as an initial or final nuclear state.

$K$	1	2	3	4	5	6	7
$\Delta J$	2	3	4	5	6	7	8
$\Delta\pi = \pi_i \pi_f$	-1	+1	-1	+1	-1	+1	-1

with  $G_F$  being the Fermi constant and  $\theta_C$  being the Cabibbo angle. The phase-space factor  $f_{Ku}$  for the  $K$ th forbidden unique  $\beta^\pm$  decay can be written as

$$f_{Ku} = \left(\frac{3}{4}\right)^K \frac{(2K)!!}{(2K+1)!!} \int_1^{w_0} C_{Ku}(w_e) p_e w_e (w_0 - w_e)^2 F_0(Z_f, w_e) dw_e, \quad (4)$$

where  $C_{Ku}$  is the shape factor for  $K$ th forbidden unique  $\beta$  decays which can be written as (see, e.g. Refs. 75 and 77)

$$C_{Ku}(w_e) = \sum_{k_e+k_\nu=K+2} \frac{\lambda_{k_e} p_e^{2(k_e-1)} (w_0 - w_e)^{2(k_\nu-1)}}{(2k_e-1)!(2k_\nu-1)!}, \quad (5)$$

where the indices  $k_e$  and  $k_\nu$  (both  $k = 1, 2, 3, \dots$ ) come from the partial-wave expansion of the electron ( $e$ ) and neutrino ( $\nu$ ) wave functions. Here,  $w_e$  is the total energy of the emitted electron/positron,  $p_e$  is the electron/positron momentum,  $Z_f$  is the charge number of the daughter nucleus and  $F_0(Z_f, w_e)$  is the Fermi function taking into account the Coulombic attraction/repulsion of the electron/positron and the daughter nucleus.<sup>a</sup> The factor  $\lambda_{k_e}$  contains the generalized Fermi function  $F_{k_e-1}$ <sup>78</sup> as the ratio

$$\lambda_{k_e} = \frac{F_{k_e-1}(Z_f, w_e)}{F_0(Z_f, w_e)}. \quad (6)$$

The integration is performed over the total (by electron rest mass) scaled energy of the emitted electron/positron,  $w_0$  being the endpoint energy, corresponding to the maximum electron/positron energy in a given transition.

The NME in (2) can be expressed as

$$M_{Ku} = \sum_{ab} M^{(Ku)}(ab) (\psi_f || [c_a^\dagger \tilde{c}_b]_{K+1} || \psi_i), \quad (7)$$

where the factors  $M^{(Ku)}(ab)$  are the single-particle matrix elements and the quantities  $(\psi_f || [c_a^\dagger \tilde{c}_b]_{K+1} || \psi_i)$  are the one-body transition densities with  $\psi_i$  being the initial-state wave function and  $\psi_f$  the final-state wave function. The operator  $c_a^\dagger$  is a creation operator for a nucleon in an orbital  $a$  and the operator  $\tilde{c}_a$  is the corresponding annihilation operator. The single-particle matrix elements are given (in the Biedenharn–Rose phase convention) by

$$M_{Ku}(ab) = \sqrt{4\pi} (a || r^K [Y_K \boldsymbol{\sigma}]_{K+1} i^K || b), \quad (8)$$

where  $Y_K$  is a spherical harmonic of rank  $K$ ,  $\boldsymbol{\sigma}$  a vector containing the Pauli matrices as its components,  $r$  the radial coordinate, and  $a$  and  $b$  stand for the single-particle orbital quantum numbers. The NME (8) is given explicitly in Ref. 75.

<sup>a</sup>For positron emission the change  $Z_f \rightarrow -Z_f$  has to be performed in  $F_0(Z_f, w_e)$  and  $F_{k_e-1}(Z_f, w_e)$ , Eq. (6).

## 2.2. Forbidden nonunique $\beta$ decays

In the forbidden nonunique  $\beta$  decay, the half-life can be given, analogously to (2), in the form

$$t_{1/2} = \frac{\kappa}{\tilde{C}}, \quad (9)$$

where  $\tilde{C}$  is the dimensionless integrated shape function, given by

$$\tilde{C} = \int_1^{w_0} C(w_e) p w_e (w_0 - w_e)^2 F_0(Z_f, w_e) dw_e, \quad (10)$$

with the notation explained in Subsec. 2.1. The general form of the shape factor of Eq. (10) is a sum

$$C(w_e) = \sum_{k_e, k_\nu, K} \lambda_{k_e} \left[ M_K(k_e, k_\nu)^2 + m_K(k_e, k_\nu)^2 - \frac{2\gamma_{k_e}}{k_e w_e} M_K(k_e, k_\nu) m_K(k_e, k_\nu) \right], \quad (11)$$

where the factor  $\lambda_{k_e}$  was given in (6) and  $Z_f$  is the charge number of the final nucleus. The indices  $k_e$  and  $k_\nu$  ( $k = 1, 2, 3, \dots$ ) are related to the partial-wave expansion of the electron ( $e$ ) and neutrino ( $\nu$ ) wave functions,  $K$  is the order of forbiddenness of the transition, and  $\gamma_{k_e} = \sqrt{k_e^2 - (\alpha Z_f)^2}$ ,  $\alpha \approx 1/137$  being the fine-structure constant. The nuclear-physics information is hidden in the factors  $M_K(k_e, k_\nu)$  and  $m_K(k_e, k_\nu)$ , which are complicated combinations of different NMEs and leptonic phase-space factors. For more information on the integrated shape function, see Refs. 78 and 79.

The shape factor  $C(w_e)$  (11) can be decomposed into vector, axial-vector and mixed vector-axial-vector parts in the form<sup>70</sup>

$$C(w_e) = g_V^2 C_V(w_e) + g_A^2 C_A(w_e) + g_V g_A C_{VA}(w_e). \quad (12)$$

The same is true for the shape function of the forbidden unique decays (5) when the so-called next-to-leading-order terms are added to the leading ones.<sup>61,70</sup> Integrating Eq. (12) over the electron kinetic energy, we obtain an analogous expression for the integrated shape function (10)

$$\tilde{C} = g_V^2 \tilde{C}_V + g_A^2 \tilde{C}_A + g_V g_A \tilde{C}_{VA}, \quad (13)$$

where the factors  $\tilde{C}_i$  in Eq. (13) are just constants, independent of the electron energy.

## 3. Contaminants in Rare-Event Searches

There is a long list of common background contaminants in dark matter and rare-event experiments.<sup>80</sup> Usually, the  $\beta$ -spectrum shapes of the corresponding  $\beta$  decays have not been measured or computed. Below, we give few examples of the  $\beta$  spectra that have also been measured, but quite long time ago (during the 50's). More such spectra will be presented elsewhere as a separate compilation.

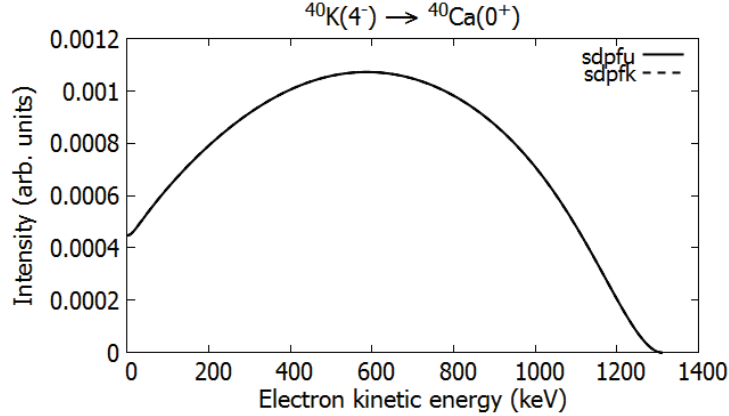


Fig. 1. Normalized  $\beta$  spectrum for the third-forbidden unique ground-state-to-ground-state  $\beta^-$  decay of  $^{40}\text{K}$  calculated by using two different shell-model interactions. The value  $g_V = 1.00$  was adopted in the calculations.

The long-lived potassium isotope  $^{40}\text{K}$  is a common pollutant in the environment and in many materials. In Fig. 1, the normalized electron spectrum (the superficial area is normalized to unity) for the  $\beta^-$  decay of  $^{40}\text{K}$  is presented. The dominant decay channel (89.28%) is the third-forbidden unique  $\beta^-$  decay to the ground state of  $^{40}\text{Ca}$ .<sup>81</sup> The electron spectra have been computed by using the interacting shell model (ISM) with two different effective interactions: sdpfu<sup>82</sup> and sdprk.<sup>83</sup> The wave functions were calculated by restricting the protons to the  $sd$  shell and neutrons to the  $sd_{7/2}$  valence space, thus permitting configuration mixing for the doubly magic nucleus  $^{40}\text{Ca}$ . An old measurement of the  $\beta$ -spectrum shape has been reported in Ref. 84.

The  $\beta^+$  decay of  $^{22}\text{Na}$  is a common pollutant in the Ge-based experiments.<sup>85</sup> In Fig. 2, the normalized positron spectrum for the second-forbidden unique ground-state-to-ground-state  $\beta^+$  decay of  $^{22}\text{Na}$  is depicted. The spectra have been calculated in the  $sd$  valence space using the ISM with three different interactions, namely usda, usdb and usde.<sup>86</sup> The  $Q$ -value of this decay is known quite accurately.<sup>87</sup> An old measurement of the  $\beta$  spectrum has been reported in Ref. 88.

The  $\beta^-$  decay of  $^{60}\text{Co}$  is a common pollutant in the environment and in Ge-based experiments.<sup>85</sup> In Fig. 3, the normalized electron spectra for the second-forbidden unique  $\beta^-$  decay of  $^{60}\text{Co}$  to the first  $2^+$  state in  $^{60}\text{Ni}$  are shown for five different values for  $g_A$ . The  $\beta$  spectra have been calculated by using the ISM with the Horie–Ogawa interaction.<sup>89,90</sup> Due to the large number of valence nucleons in the  $pf$  shell, the calculations were truncated to the proton- $0f_{7/2}$ -neutron- $1p_{0f_{5/2}}$  subspace. Though the dominant decay channel is the allowed decay to the first  $4^+$  state in  $^{60}\text{Ni}$ , there is a small branching (0.12%) to the first  $2^+$  state in  $^{60}\text{Ni}$ .<sup>91</sup> The decomposition (12) suggests that the spectrum shape could be  $g_A$ -dependent. It can be seen in the figure, however, that the next-to-leading-order corrections

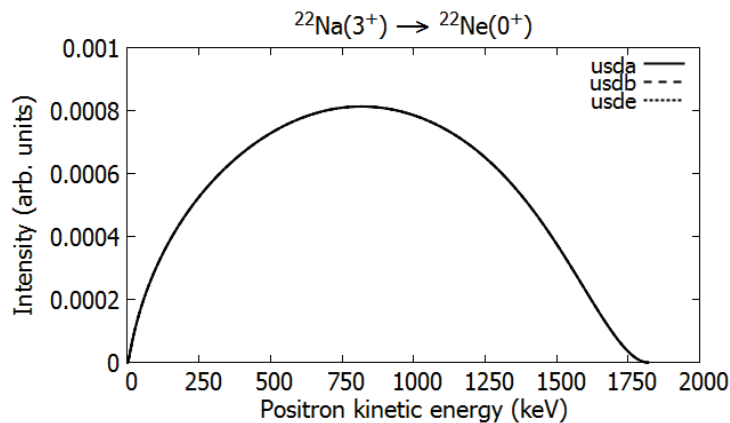


Fig. 2. Normalized  $\beta$  spectrum for the second-forbidden unique ground-state-to-ground-state  $\beta^+$  decay of  $^{22}\text{Na}$  calculated by using three different shell-model interactions. The value  $g_V = 1.00$  was adopted in the calculations.

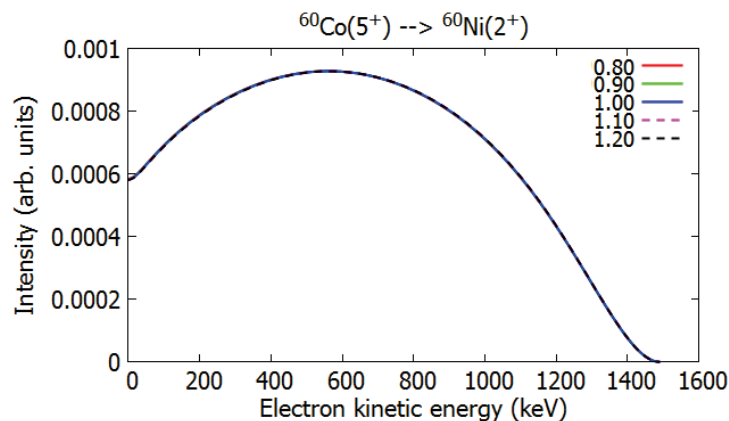


Fig. 3. (Color online) Normalized  $\beta$  spectra for the second-forbidden unique  $\beta^-$  decay of  $^{60}\text{Co}$  to the first  $2^+$  state in  $^{60}\text{Ni}$ . The value  $g_V = 1.00$  was adopted in the calculations and the color coding represents the different adopted values for  $g_A$ .

to the  $\beta$ -decay shape factor are not strong enough to make the spectrum shape  $g_A$ -dependent. An old measurement of the  $\beta$ -spectrum shape has been reported in Ref. 92.

#### 4. Reactor Antineutrino Anomaly

While the actual cumulative  $\beta$  spectra leading to the RAA and emerging from the decays of the fission fragments are numerous, not all of them contribute in equal amounts. Then, the cumulative  $\beta$  spectra can be nicely fit by just a quite limited number of virtual  $\beta$  spectra emerging from nonexistent fictional  $\beta$  branches.<sup>57–59</sup> A shortcoming of this procedure is that all the virtual branches are assumed to

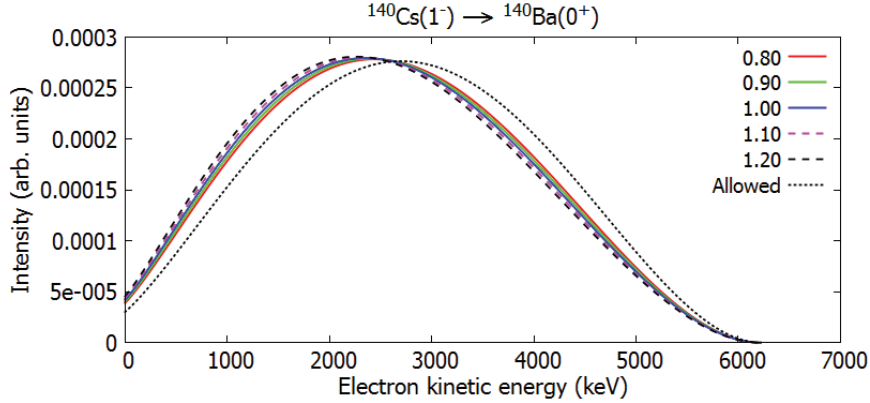


Fig. 4. (Color online) Normalized  $\beta$  spectrum for the first-forbidden nonunique ground-state-to-ground-state  $\beta^-$  decay of  $^{140}\text{Cs}$ . The value  $g_V = 1.00$  was adopted in the calculations and the color coding represents the different adopted values for  $g_A$ . The allowed spectrum shape is plotted for comparison.

be described by the allowed  $\beta$ -spectrum shapes. Also, adding information from the nuclear database is not accurate enough due to deficiencies in this information. Out of the several thousand  $\beta$  branches taking part in the cumulative  $\beta$  spectra, the majority are allowed Fermi and Gamow–Teller decays. Forbidden decays become increasingly unlikely with increasing degree of forbiddenness.

The most important  $\beta$  branches taking part in the cumulative  $\beta$  spectra of the RAA were identified in Ref. 93 and they include the first-forbidden decays of  $^{88}\text{Rb}$ ,  $^{90}\text{Rb}$ ,  $^{92}\text{Rb}$ ,  $^{95}\text{Sr}$ ,  $^{96}\text{Y}$ ,  $^{100}\text{Nb}$ ,  $^{135}\text{Te}$ ,  $^{140}\text{Cs}$  and  $^{142}\text{Cs}$  from the fission of  $^{235}\text{U}$ . The branchings of these decay transitions are between 33% and 96%. Here, as also in the analysis of Ref. 63, allowed  $\beta$  spectrum shapes were also assumed for the forbidden transitions, like the first-forbidden decays listed above. Thus, it is of paramount importance to compute the shapes of the  $\beta$  spectra associated to the above-listed key transitions and compare these spectra with the allowed shape to see the error made in the allowed approximation. The computation of the proper spectral shapes can be done by using the formalism of Subsecs. 2.1 and 2.2. An example of the application of the formalism is presented in Fig. 4 where the ISM-computed first-forbidden nonunique ground-state-to-ground-state  $\beta^-$  decay of  $^{140}\text{Cs}$  is depicted and compared with the allowed spectrum shape. The used interaction is `jj56pnb`<sup>69</sup> in the proton  $3s-2d-1g_{7/2}$  and neutron  $3p-2f-1h_{9/2}$  valence space. As can be seen, there is a notable deviation from the spectrum shape of an allowed transition with the same  $Q$ -value. In this case, there is also some dependence of the spectrum shape on the value of  $g_A$  and in other key transitions, this could be the case as well, as suggested by the decomposition (12). The effects stemming from the uncertainty in the value of  $g_A$  have also been neglected in the analyses of the RAA thus far.

## 5. Spectral Shapes and the Effective Value of $g_A$

In Ref. 70, it was found that the shapes of  $\beta$  spectra could be used to determine the values of the weak coupling strengths by comparing the computed spectrum with the measured one for forbidden nonunique  $\beta$  decays. This method was coined the SSM. In this study, the next-to-leading-order corrections to the  $\beta$ -decay shape factor were also included. In Ref. 70, the  $\beta$ -electron spectra were studied for the 4th-forbidden nonunique ground-state-to-ground-state  $\beta^-$  decay branches  $^{113}\text{Cd}(1/2^+) \rightarrow ^{113}\text{In}(9/2^+)$  and  $^{115}\text{In}(9/2^+) \rightarrow ^{115}\text{Sn}(1/2^+)$  using the microscopic quasiparticle-phonon model (MQPM)<sup>94</sup> and the ISM. It was verified by both nuclear models that the  $\beta$  spectrum shapes of both transitions are highly sensitive to the values of  $g_V$  and  $g_A$ , and hence the comparison of the calculated spectrum shape with the measured one opens a way to determine the values of these coupling strengths.<sup>b</sup> As a by-product, it was found that for all values of  $g_A$ , the best fits to data were obtained by using the canonical CVC value  $g_V = 1.0$  for the vector coupling strength. The work of Ref. 70 was extended to other nuclei and nuclear models in Refs. 61, 70–72. In these studies, it was found that the SSM is very robust, quite insensitive to the adopted mean field and nuclear model and its model Hamiltonian used to produce the wave functions of the participant initial and final nuclear states.

Examples of possible  $g_A$  dependencies are given in the previously discussed Fig. 4 and in Fig. 5 where the ISM-computed first-forbidden nonunique ground-state-to-ground-state  $\beta^-$  decays of  $^{207}\text{Tl}$  (top),  $^{210}\text{Bi}$  (middle) and  $^{214}\text{Bi}$  (bottom) are depicted. The wave functions related to the decay of  $^{207}\text{Tl}$  were calculated using the interaction khhe<sup>96</sup> in a valence space spanned by the proton orbitals  $0g_{7/2}$ ,  $1d$ ,  $2s$  and  $0h_{11/2}$ , and the neutron orbitals  $0h_{9/2}$ ,  $1f$ ,  $2p$  and  $0i_{13/2}$ . For the heavier nuclei,  $^{210}\text{Bi}$  and  $^{214}\text{Bi}$ , the interaction khpe<sup>96</sup> was adopted. For  $^{210}\text{Bi}$ , the valence space was spanned by the proton orbitals  $0h_{9/2}$ ,  $1f$ ,  $2p$  and  $0i_{13/2}$ , and neutron orbitals  $0i_{11/2}$ ,  $1g$  and  $2d_{5/2}$ . For  $^{214}\text{Bi}$ , excitations to the neutron  $2d - 3s$  orbitals were not allowed to reduce the formidable computational burden.

The  $\beta$ -spectrum shapes of  $^{207}\text{Tl}$  and  $^{214}\text{Bi}$  are only slightly  $g_A$ -dependent, but for  $^{210}\text{Bi}$ , the dependence is extremely strong. This makes  $^{210}\text{Bi}$  an excellent candidate for the application of the SSM. This is so far the only known first-forbidden  $\beta$  transition with a strong  $g_A$ -dependence. There is also an old  $\beta$ -spectrum measurement reported in Ref. 97. Other strongly  $g_A$ -dependent decay transitions are listed in Table 2. Table 2 summarizes the exploratory works of Refs. 61, 70–72 in terms of listing the studied  $\beta$ -decay transitions which are potentially measurable in rare-event experiments. Usually, only the nonunique forbidden  $\beta$ -decay transitions can be sensitive enough to  $g_A$  to be measured even when the next-to-leading-order terms are included in the  $\beta$ -decay shape factor.<sup>70</sup>

<sup>b</sup>This effect was overlooked in the earlier studies in Refs. 79 and 95.

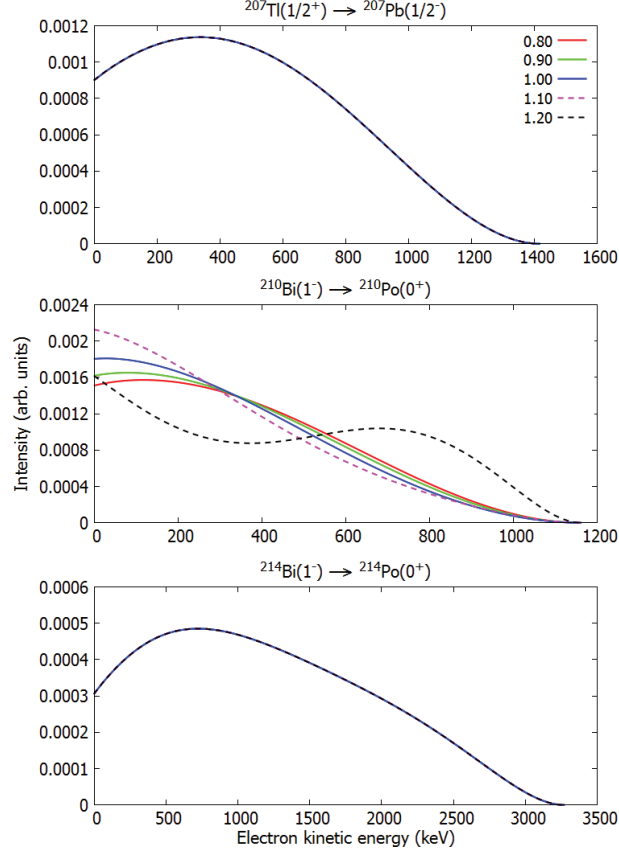


Fig. 5. (Color online) Normalized  $\beta$  spectra for the first-forbidden nonunique ground-state-to-ground-state  $\beta^-$  decays of  $^{207}\text{Tl}$  (top),  $^{210}\text{Bi}$  (middle) and  $^{214}\text{Bi}$  (bottom). The value  $g_V = 1.00$  was adopted in the calculations and the color coding represents the different adopted values for  $g_A$ .

Table 2. List of forbidden nonunique  $\beta^-$ -decay transitions and their sensitivity to the value of  $g_A$ . Here,  $J_i$  ( $J_f$ ) is the angular momentum of the initial (final) state,  $\pi_i$  ( $\pi_f$ ) the parity of the initial (final) state, and  $K$  the degree of forbiddenness. The initial state is always the ground state (gs, column 2) of the mother nucleus and the final state is either the ground state (gs) or the  $n_f$  :  $th$ ,  $n_f = 2, 3$ , excited state (column 3) of the daughter nucleus. The branchings to the indicated final states are practically 100% in all cases. Column 4 indicates the sensitivity to the value of  $g_A$ , and the last column lists the nuclear models which have been used (thus far) to compute the  $\beta$ -spectrum shape. Here, references to the original works are also given.

Transition	$J_i^{\pi_i}$ (gs)	$J_f^{\pi_f}$ ( $n_f$ )	$K$	Sensitivity	Nucl. model
$^{87}\text{Rb} \rightarrow ^{87}\text{Sr}$	$3/2^-$	$9/2^+$ (gs)	3	Moderate	MQPM, <sup>71</sup> ISM <sup>72</sup>
$^{94}\text{Nb} \rightarrow ^{94}\text{Mo}$	$6^+$	$4^+$ (2)	2	Strong	ISM <sup>72</sup>
$^{98}\text{Tc} \rightarrow ^{98}\text{Ru}$	$6^+$	$4^+$ (3)	2	Strong	ISM <sup>72</sup>
$^{99}\text{Tc} \rightarrow ^{99}\text{Ru}$	$9/2^+$	$5/2^+$ (gs)	2	Strong	MQPM, <sup>71</sup> ISM <sup>72</sup>
$^{113}\text{Cd} \rightarrow ^{113}\text{In}$	$1/2^+$	$9/2^+$ (gs)	4	Strong	MQPM, <sup>70,71</sup> ISM, <sup>70</sup> IBFM-2 <sup>61</sup>
$^{115}\text{In} \rightarrow ^{115}\text{Sn}$	$9/2^+$	$1/2^+$ (gs)	4	Strong	MQPM, <sup>70,71</sup> ISM, <sup>61</sup> IBFM-2 <sup>61</sup>
$^{210}\text{Bi} \rightarrow ^{210}\text{Po}$	$1^-$	$0^+$ (gs)	1	Strong	ISM (this work)

## 6. Enhancement of the Axial-Charge Matrix Element

The enhancement of the axial-charge NME  $\gamma_5$  due to nuclear medium effects in the form of meson-exchange current (MEC) was first suggested nearly four decades ago.<sup>98–100</sup> An enhancement of 40–70% over the impulse-approximation value was predicted based on chiral-symmetry arguments and soft-pion theorems. This enhancement seems fundamental in nature and insensitive to nuclear-structure aspects.<sup>101,102</sup> Systematic shell-model studies of the  $\gamma_5$  matrix elements in the  $A \approx 16$ ,  $A \approx 40$ , and  $A \approx 208$  regions indicated enhancements of 60–100%.<sup>103–105</sup> In Ref. 106, the exceptionally large enhancement of the  $\gamma_5$  NME in heavy nuclei, witnessed in the shell-model studies of Warburton,<sup>105</sup> was reproduced by introducing an effective Lagrangian incorporating approximate chiral and scale invariance of the QCD.

The  $\gamma_5$  NME is one of the two rank-zero matrix elements contributing to first-forbidden  $\Delta J = 0$ ,  $J^+ \leftrightarrow J^-$ , transitions. It plays quite an important role in the decay rates of many of these transitions. Therefore, a significant enhancement of this matrix element can also affect the shapes of the corresponding beta spectra.

For our discussion, we adopt the expansion of Behrens and Bühring,<sup>78</sup> where in the leading order, the nonrelativistic reduction produces two NMEs that mediate  $J^+ \leftrightarrow J^-$  type of decay transitions, see Ref. 61. These NMEs correspond to the operators

$$g_A(\gamma_5) \boldsymbol{\sigma} \cdot \mathbf{p}_e, \quad (14)$$

$$g_A \boldsymbol{\sigma} \cdot \mathbf{r}, \quad (15)$$

where  $\mathbf{r}$  is the radial coordinate,  $\mathbf{p}_e$  is the electron momentum and  $\boldsymbol{\sigma}$  contains the Pauli matrices. Here, the enhancement of the  $\gamma_5$  NME ( $\boldsymbol{\sigma} \cdot \mathbf{p}_e$  in the nonrelativistic reduction) is included in the coupling strength by

$$g_A(\gamma_5) = (1 + \varepsilon_{\text{MEC}})g_A, \quad (16)$$

where the enhancement  $\varepsilon_{\text{MEC}}$  stems from MEC. In this work, we include also the next-to-leading-order terms in the Behrens–Bühring expansion.<sup>78</sup> The atomic screening effects and radiative corrections are also included in the shape factor. Details of the formalism can be found in Ref. 61.

Our ISM calculations were performed in the following valence spaces: For the decay of  $^{95}\text{Sr}$ , a model space including the proton orbitals  $0f_{5/2}$ ,  $1p_{3/2}$ ,  $1p_{1/2}$  and  $0g_{9/2}$ , and the neutron orbitals  $1d_{5/2}$ ,  $1d_{3/2}$  and  $0s_{1/2}$  was used together with the interaction *glbepn*.<sup>107</sup> The interaction *glbepn* is a bare G-matrix interaction which also has an adjusted version *glepn*, where two-body matrix elements from Gloeckner<sup>108</sup> and Ji and Wildenthal<sup>109</sup> have been adopted. The decay of  $^{135}\text{Te}$  was calculated using a model space spanned by the proton orbitals  $0g_{7/2}$ ,  $1d_{5/2}$ ,  $1d_{3/2}$ ,  $2s_{1/2}$  and  $0h_{11/2}$ , and the neutron orbitals  $0h_{9/2}$ ,  $1f_{7/2}$ ,  $1f_{5/2}$ ,  $2p_{3/2}$ ,  $2p_{1/2}$  and  $0i_{13/2}$  with the effective interactions *jj56pnb*.<sup>110</sup>

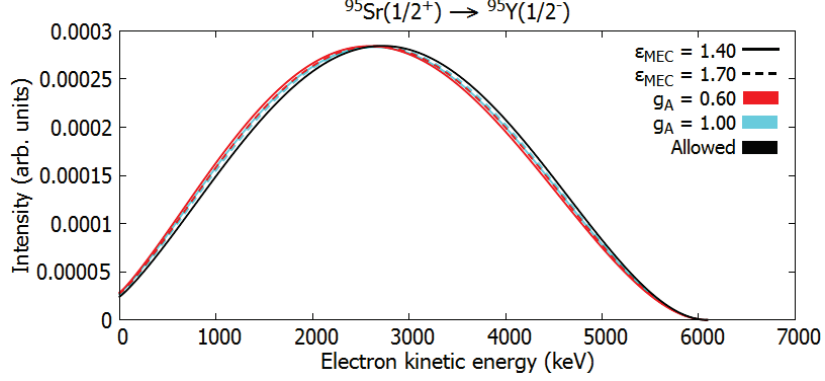


Fig. 6. (Color online) Normalized  $\beta$  spectra for the first-forbidden nonunique ground-state-to-ground-state  $\beta^-$  decay of  $^{95}\text{Sr}$ . The value  $g_V = 1.00$  was adopted in the calculations and the color coding represents the different adopted values for  $g_A$  and the enhancement ( $\epsilon_{\text{MEC}}$ ) of the axial charge.

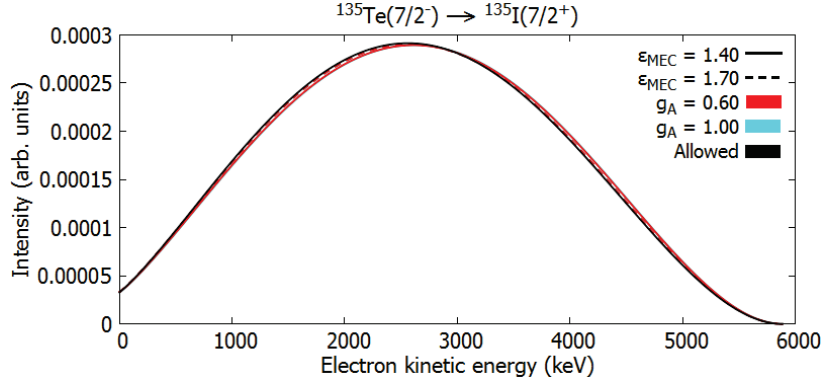


Fig. 7. (Color online) Normalized  $\beta$  spectra for the first-forbidden nonunique ground-state-to-ground-state  $\beta^-$  decay of  $^{135}\text{Te}$ . The value  $g_V = 1.00$  was adopted in the calculations and the color coding represents the different adopted values for  $g_A$  and the enhancement ( $\epsilon_{\text{MEC}}$ ) of the axial charge.

Examples of possible  $g_A$  and  $g_A(\gamma_5)$  dependencies of  $\beta$  spectra are given in Figs. 6 and 7 where the ISM-computed first-forbidden nonunique ground-state-to-ground-state  $\beta^-$  decays of  $^{95}\text{Sr}$  and  $^{135}\text{Te}$  are depicted. It is seen that neither the effective value of  $g_A$  nor the enhancement (16) of  $g_A(\gamma_5)$  affects the spectrum shape in an easily measurable way. Hence, in these cases, the comparison with the experimental half-lives is the only way to pin down the amount of enhancement (16), and its possible mass dependence, in the axial-charge NME. Only a further exploratory work could tell if there are nuclear transitions where the  $\beta$  spectra are sensitive to the value of  $g_A(\gamma_5)$ . It should also be borne in mind that the spectrum shapes of  $J^+ \leftrightarrow J^-$  transitions play an important role in the investigations of the validity of the RAA.

## 7. Conclusions

In this paper, the electron-spectrum shapes are discussed for  $\beta$ -decay transitions that are important as contaminants in rare-event searches, as integral ingredients in the RAA and sensitive to the effective value of the weak axial-vector coupling constant  $g_A$  and the weak axial charge. Quite little is known experimentally about  $\beta$ -spectrum shapes, in particular for the forbidden  $\beta$  decays. This is why theoretical calculations can assist in the identification of dangerous backgrounds in rare-event searches. Allowed  $\beta$ -spectrum shapes are assumed in the analyses related to the RAA and calculations of the spectrum shapes for the involved key forbidden  $\beta$  decays can shed more light to the confidence level of the anomaly. In a promising new method, the SSM, the comparison of the computed and measured  $\beta$  spectra for forbidden nonunique  $\beta$  decays helps in pinning down the effective value of  $g_A$ . The robustness of the method is based on the observations that the computed spectra are relatively insensitive to the adopted mean-field, nuclear models and model Hamiltonians. The SSM can also be used to pin down the amount of enhancement in the axial-charge matrix element for the first-forbidden nonunique  $J^+ \leftrightarrow J^-$  transitions. Further exploratory theoretical work has to be done in the future and measurements of electron spectra for the found potentially interesting key nonunique  $\beta$  transitions are strongly encouraged.

## Acknowledgments

This work has been partially supported by the Academy of Finland under the Finnish Center of Excellence Programme 2012–2017 (Nuclear and Accelerator-Based Programme at JYFL).

## References

1. J. D. Vergados, H. Ejiri and F. Šimkovic, *Int. J. Mod. Phys. E* **25**, 1630007 (2016).
2. J. Suhonen and O. Civitarese, *Phys. Rep.* **300**, 123 (1998).
3. J. Suhonen and O. Civitarese, *J. Phys. G: Nucl. Part. Phys.* **39**, 085105 (2012).
4. J. Suhonen and O. Civitarese, *J. Phys. G: Nucl. Part. Phys.* **39**, 124005 (2012).
5. J. Engel and J. Menéndez, *Rep. Prog. Phys.* **80**, 046301 (2017).
6. J. Maalampi and J. Suhonen, *Adv. High Energy Phys.* **2013**, 505874 (2013).
7. J. Hyvärinen and J. Suhonen, *Phys. Rev. C* **91**, 024613 (2015).
8. J. Hyvärinen and J. Suhonen, *Phys. Rev. C* **93**, 064306 (2016).
9. AURORA Collab. (O. G. Polischuk *et al.*), *AIP Conf. Proc.* **1894**, 020018 (2017).
10. GERDA Collab. (M. Agostini *et al.*), *Nature* **544**, 47 (2017).
11. NEMO-3 Collab. (R. Arnold *et al.*), *Phys. Rev. D* **95**, 012007 (2017).
12. COBRA Collab. (J. Ebert *et al.*), *Phys. Rev. C* **94**, 024603 (2016).
13. CUORE Collab. (C. Alduino *et al.*), *Eur. Phys. J. C* **77**, 532 (2017).
14. EXO-200 Collab. (J. B. Albert *et al.*), *Nature* **510**, 229 (2014).
15. KamLAND-Zen Collab. (A. Gando *et al.*), *Phys. Rev. Lett.* **117**, 082503 (2016).
16. MAJORANA Collab. (V. E. Guiseppe *et al.*), *AIP Conf. Proc.* **1894**, 020010 (2017).
17. SuperNEMO Collab. (D. Waters *et al.*), *J. Phys. Conf. Ser.* **888**, 012033 (2017).
18. MOON Collab. (S. Y. Young *et al.*), *PoS ICRC2017*, 1056 (2017).

19. AMoRE Collab. (H. Park *et al.*), *AIP Conf. Proc.* **1686**, 020016 (2015).
20. LUMINEU Collab. (T. B. Becker *et al.*), *Astropart. Phys.* **72**, 38 (2016).
21. CUPID Collab. (G. Wang *et al.*), arXiv:1504.03599 [physics.ins-det].
22. SNO+ Collab. (S. Andringa *et al.*), *Adv. High Energy Phys.* **2016**, 6194250 (2016).
23. NEXT-100 Collab. (J. Martin-Albo *et al.*), *J. High Energy Phys.* **1605**, 159 (2016).
24. PandaX-III Collab. (X. Chen *et al.*), *Sci. China Phys. Mech. Astron.* **60**, 061011 (2017).
25. M. Aunola, J. Suhonen and T. Siiskonen, *Europhys. Lett.* **46**, 577 (1999).
26. M. Haaranen, M. Horoi and J. Suhonen, *Phys. Rev. C* **89**, 034315 (2014).
27. H. Heiskanen, M. T. Mustonen and J. Suhonen, *J. Phys. G: Nucl. Part. Phys.* **34**, 837 (2007).
28. M. Alanssari *et al.*, *Phys. Rev. Lett.* **116**, 072501 (2016).
29. J. Ellis and R. Flores, *Phys. Lett. B* **263**, 259 (1991).
30. J. Ellis and L. Roszkowski, *Phys. Lett. B* **283**, 252 (1992).
31. J. Ellis and R. Flores, *Phys. Lett. B* **300**, 175 (1993).
32. V. A. Bednyakov, H. Klapdor-Kleingrothaus and S. Kovalenko, *Phys. Lett. B* **329**, 5 (1994).
33. R. Arnowitt and P. Nath, *Phys. Rev. Lett.* **74**, 4592 (1995).
34. R. Arnowitt and P. Nath, *Phys. Rev. D* **54**, 2374 (1996).
35. A. Bottino *et al.*, *Phys. Lett. B* **402**, 113 (1997).
36. XENON10 Collab. (J. Angle *et al.*), *Phys. Rev. Lett.* **107**, 051301 (2011).
37. XENON100 Collab. (E. Aprile *et al.*), *Phys. Rev. Lett.* **107**, 131302 (2011).
38. XMASS Collab. (K. Abe *et al.*), *Phys. Lett. B* **759**, 272 (2016).
39. ZEPLIN Collab. (C. Ghag *et al.*), *Astropart. Phys.* **35**, 76 (2011).
40. PANDAX Collab. (T. Andi *et al.*), *Phys. Rev. D* **93**, 122009 (2016).
41. LUX Collab. (D. S. Akerib *et al.*), *Phys. Rev. Lett.* **116**, 161301 (2016).
42. CDMS Collab. (R. Agnese *et al.*), *Phys. Rev. D* **95**, 082002 (2017).
43. CoGENT Collab. (C. Aalseth *et al.*), *Phys. Rev. Lett.* **106**, 131301 (2011).
44. EDELWEISS Collab. (K. Eitel *et al.*), *Phys. Procedia* **61**, 61 (2015).
45. DAMA Collab. (R. Bernabei *et al.*), *Eur. Phys. J. C* **73**, 2648 (2013).
46. KIMS Collab. (H. S. Lee *et al.*), *Phys. Rev. D* **90**, 052006 (2014).
47. PICASSO Collab. (S. Archambault *et al.*), *Phys. Lett. B* **711**, 153 (2012).
48. ADMX Collab. (S. J. Asztalos *et al.*), *Phys. Rev. Lett.* **104**, 141301 (2010).
49. CDEX Collab. (Q. Yue *et al.*), *Phys. Rev. D* **90**, 091701(R) (2014).
50. CRESST Collab. (G. Angloher *et al.*), *Eur. Phys. J. C* **74**, 3184 (2014).
51. DarkSide Collab. (P. Agnes *et al.*), *Phys. Lett. B* **743**, 456 (2014).
52. DMTPC Collab. (S. Ahlen *et al.*), *Phys. Lett. B* **695**, 124 (2011).
53. DRIFT Collab. (E. Daw *et al.*), *Astropart. Phys.* **35**, 397 (2012).
54. SIMPLE Collab. (M. Felizardo *et al.*), *Phys. Rev. Lett.* **108**, 201302 (2012).
55. C. Buck, A. P. Collin, J. Haser and M. Lindner, *Phys. Lett. B* **765**, 159 (2017).
56. T. A. Mueller *et al.*, *Phys. Rev. C* **83**, 054615 (2011).
57. K. Schreckenbach, G. Colvin, W. Gelletly and F. Von Feilitzsch, *Phys. Lett. B* **160**, 325 (1985).
58. A. A. Hahn *et al.*, *Phys. Lett. B* **218**, 365 (1989).
59. N. Haag, A. Gütlein, M. Hofmann, L. Oberauer, W. Potzel and K. Schreckenbach, *Phys. Rev. Lett.* **112**, 122501 (2014).
60. E. Ydrefors, M. T. Mustonen and J. Suhonen, *Nucl. Phys. A* **842**, 33 (2010).
61. M. Haaranen, J. Kotila and J. Suhonen, *Phys. Rev. C* **95**, 024327 (2017).
62. F. P. An *et al.*, *Phys. Rev. Lett.* **118**, 251801 (2017).

63. A. C. Hayes, J. L. Friar, G. T. Garvey, G. Jungman and G. Jonkmans, *Phys. Rev. Lett.* **112**, 202501 (2014).
64. H. Ejiri, N. Soukouti and J. Suhonen, *Phys. Lett. B* **729**, 27 (2014).
65. H. Ejiri and J. Suhonen, *J. Phys. G: Nucl. Part. Phys.* **42**, 055201 (2015).
66. P. Pirinen and J. Suhonen, *Phys. Rev. C* **91**, 054309 (2015).
67. F. F. Deppisch and J. Suhonen, *Phys. Rev. C* **94**, 055501 (2016).
68. J. Kostensalo and J. Suhonen, *Phys. Rev. C* **95**, 014322 (2017).
69. J. M. Allmond *et al.*, *Phys. Rev. C* **90**, 014322 (2014).
70. M. Haaranen, P. C. Srivastava and J. Suhonen, *Phys. Rev. C* **93**, 034308 (2016).
71. J. Kostensalo, M. Haaranen and J. Suhonen, *Phys. Rev. C* **95**, 044313 (2017).
72. J. Kostensalo and J. Suhonen, *Phys. Rev. C* **96**, 024317 (2017).
73. J. Suhonen, *Front. Phys.* **5**, 55 (2017).
74. J. Suhonen, *Phys. Rev. C* **96**, 055501 (2017).
75. J. Suhonen, *From Nucleons to Nucleus: Concepts of Microscopic Nuclear Theory* (Springer, Berlin, 2007).
76. J. C. Hardy, I. S. Towner, V. Koslowsky, E. Hagberg and H. Schmeig, *Nucl. Phys. A* **509**, 429 (1990).
77. N. B. Gove and M. J. Martin, *Nucl. Data Tables* **10**, 205 (1971).
78. H. Behrens and W. Bühring, *Electron Radial Wave Functions and Nuclear Beta-Decay* (Clarendon Press, Oxford, 1982).
79. M. T. Mustonen, M. Aunola and J. Suhonen, *Phys. Rev. C* **73**, 054301 (2006).
80. V. I. Tretyak, *AIP Conf. Proc.* **1894**, 020026 (2017).
81. J. Chen, *Nucl. Data Sheets* **140**, 1 (2017).
82. F. Nowacki and A. Poves, *Phys. Rev. C* **79**, 014310 (2009).
83. K. Kaneko, Y. Sun, T. Mizusaki and M. Hasegawa, *Phys. Rev. C* **83**, 014320 (2011).
84. W. H. Kelly, G. B. Beard and R. A. Peters, *Nucl. Phys.* **11**, 492 (1959).
85. W.-Z. Wei, D.-M. Mei and C. Zhang, arXiv:1706.05324 [nucl-ex].
86. B. A. Brown and W. A. Richter, *Phys. Rev. C* **74**, 034315 (2006).
87. M. S. Basunia, *Nucl. Data Sheets* **127**, 69 (2015).
88. B. T. Wright, *Phys. Rev.* **90**, 159 (1953).
89. H. Horie and K. Ogawa, *Prog. Theor. Phys.* **46**, 349 (1971).
90. H. Horie and K. Ogawa, *Nucl. Phys. A* **216**, 407 (1973).
91. E. Browne and J. Tuli, *Nucl. Data Sheets* **114**, 1849 (2013).
92. G. L. Keister and F. H. Schmidt, *Phys. Rev.* **93**, 140 (1954).
93. A. A. Sonzogni, T. D. Johnson and E. A. McCutchan, *Phys. Rev. C* **91**, 011301(R) (2015).
94. J. Toivanen and J. Suhonen, *Phys. Rev. C* **57**, 1237 (1998).
95. M. T. Mustonen and J. Suhonen, *Phys. Lett. B* **657**, 38 (2007).
96. E. K. Warburton and B. A. Brown, *Phys. Rev. C* **43**, 602 (1991).
97. H. Daniel, *Nucl. Phys.* **31**, 293 (1962).
98. K. Kubodera, J. Delorme and M. Rho, *Phys. Rev. Lett.* **40**, 755 (1978).
99. P. Guichon, M. Giffon, J. Joseph, R. Laverriere and C. Samour, *Z. Phys. A* **285**, 183 (1978).
100. P. Guichon, M. Giffon and C. Samour, *Phys. Lett. B* **74**, 15 (1978).
101. I. S. Towner and F. C. Khanna, *Nucl. Phys. A* **372**, 331 (1981).
102. J. Delorme, *Nucl. Phys. A* **374**, 541c (1982).
103. E. K. Warburton, I. S. Towner and B. A. Brown, *Phys. Rev. C* **49**, 824 (1994).
104. E. K. Warburton, J. A. Becker, B. A. Brown and D. J. Millener, *Ann. Phys.* **187**, 471 (1988).

*J. Kostensalo & J. Suhonen*

105. E. K. Warburton, *Phys. Rev. C* **44**, 233 (1991).
106. K. Kubodera and M. Rho, *Phys. Rev. Lett.* **67**, 3479 (1991).
107. H. Mach, E. K. Warburton, R. L. Gill, R. F. Casten, J. A. Becker, B. A. Brown and J. A. Wigner, *Phys. Rev. C* **41**, 226 (1991).
108. D. H. Gloeckner, *Nucl. Phys. A* **253**, 301 (1975).
109. X. Ji and B. H. Wildenthal, *Phys. Rev. C* **37**, 1256 (1988).
110. B. A. Brown, unpublished.



## VI

### **MESONIC ENHANCEMENT OF THE WEAK AXIAL CHARGE AND ITS EFFECT ON THE HALF-LIVES AND SPECTRAL SHAPES OF FIRST-FORBIDDEN $J^+\leftrightarrow J^-$ DECAYS**

by

Kostensalo, J., & Suhonen, J. 2018

Physics Letters B, 781, 480-484.  
doi:10.1016/j.physletb.2018.02.053

Reproduced with kind permission by Elsevier.



Contents lists available at ScienceDirect

Physics Letters B

www.elsevier.com/locate/physletb



# Mesonic enhancement of the weak axial charge and its effect on the half-lives and spectral shapes of first-forbidden $J^+ \leftrightarrow J^-$ decays



Joel Kostensalo\*, Jouni Suhonen

University of Jyväskylä, Department of Physics, P. O. Box 35, FI-40014, Finland

## ARTICLE INFO

## Article history:

Received 8 November 2017  
 Accepted 21 February 2018  
 Available online 26 February 2018  
 Editor: W. Haxton

## Keywords:

Meson-exchange currents  
 Weak interactions  
 Nuclear medium effects  
 Forbidden beta decays  
 Spectral shape

## ABSTRACT

The effects of the enhancement of the axial-charge matrix element  $\gamma_5$  were studied in medium heavy and heavy nuclei for first-forbidden  $J^+ \leftrightarrow J^-$  decay transitions using the nuclear shell model. Noticeable dependence on the enhancement  $\epsilon_{\text{MEC}}$  of the axial-charge matrix element, as well as on the value of the axial-vector coupling constant  $g_A$  was found in the spectral shapes of  $^{93}\text{Y}$ ,  $^{95}\text{Sr}$ , and  $^{97}\text{Y}$ . The importance of the spectrum of  $^{138}\text{Cs}$  in the determination of  $g_A$  is discussed. Half-life analyses in the  $A \approx 95$  and  $A \approx 135$  regions were done, and consistent results  $g_A \approx 0.90, 0.75$ , and  $0.65$ , corresponding to the three enhancement scenarios  $\epsilon_{\text{MEC}} = 1.4, 1.7$ , and  $2.0$ , were obtained. Connection to the reactor-antineutrino anomaly is pointed out.

© 2018 The Authors. Published by Elsevier B.V. This is an open access article under the CC BY license (<http://creativecommons.org/licenses/by/4.0/>). Funded by SCOAP<sup>3</sup>.

The enhancement of the axial-charge nuclear matrix element (NME)  $\gamma_5$  due to nuclear medium effects in the form of meson-exchange currents was first suggested nearly four decades ago [1–3]. An enhancement of 40–70% over the impulse-approximation value was predicted based on chiral-symmetry arguments and soft-pion theorems. This enhancement is fundamental in nature and insensitive to nuclear-structure aspects [4,5]. Systematic shell-model studies of the  $\gamma_5$  matrix elements in the  $A \approx 16$ ,  $A \approx 40$ , and  $A \approx 208$  regions indicated enhancements of 60–100% [6–8]. In [9] the exceptionally large enhancement of the  $\gamma_5$  NME in heavy nuclei, witnessed in the shell-model studies of Warburton [8], was reproduced by introducing an effective Lagrangian incorporating approximate chiral and scale invariance of the QCD.

The non-trivial dependence of the spectral shapes of the fourth-forbidden non-unique decays of  $^{113}\text{Cd}$  and  $^{115}\text{In}$  on the effective value of the axial-vector coupling constant  $g_A$  was first pointed out in Ref. [10]. A new method, coined the spectrum-shape method (SSM), where theoretical and experimental spectra are compared was proposed as a complementary way to the half-life comparison method for extraction of the effective value of  $g_A$ . Further investigations in [11] and [12] found that several other non-unique decays exhibit a similar dependence. It was also pointed out in [11–13] that the spectral shapes of many studied decays are prac-

tically indifferent to the fine details of the wave functions, making the spectrum-shape method a potentially much more robust tool than the often used half-life method.

Since the  $\gamma_5$  NME is one of the two rank-zero matrix elements contributing to first-forbidden  $\Delta J = 0$  transitions it plays quite an important role in the decay rates of many of these transitions. Therefore, a significant enhancement of this matrix element can also affect the shapes of the corresponding beta spectra. In the present Letter we investigate the impact of the  $\gamma_5$  enhancement on half-lives and shapes of beta spectra for several first-forbidden  $J^+ \leftrightarrow J^-$  decay transitions in the  $A \approx 95$ ,  $A \approx 135$ , and  $A \approx 208$  regions. Decays with beta spectra which have a significant dependence on the enhancement of the axial-charge matrix element could potentially be used to extract the enhancement in a similar way to the extraction of the effective value of  $g_A$ . The importance of the consideration of the meson-exchange-current effects on beta spectra used in the reactor-antineutrino analyses and for characterization of the background radiation in rare-event searches is also pointed out.

The half-life of a forbidden non-unique beta decay can be written as

$$t_{1/2} = \kappa / \tilde{C}, \quad (1)$$

where  $\kappa = 6147 \text{ s}$  [14] and  $\tilde{C}$  is the dimensionless integrated shape function, given by

\* Corresponding author.

E-mail address: joel.kostensalo@student.jyu.fi (J. Kostensalo).

$$\tilde{C} = \int_1^{w_0} C(w_e) p w_e (w_0 - w_e)^2 F_0(Z, w_e) dw_e. \quad (2)$$

The shape factor  $C(w_e)$  of Eq. (2) contains complicated combinations of both (universal) kinematic factors and nuclear form factors. The nuclear form factors can be related to the corresponding NMEs using the impulse approximation. For the first-forbidden non-unique decays with  $J_i = J_f$ , considered in this work, the relevant NMEs are those of the transition operators denoted here by  $\mathcal{O}(0^-)$ ,  $\mathcal{O}(1^-)$ , and  $\mathcal{O}(2^-)$ . We adopt the expansion of Behrens and Bühring [15], where in the leading order in the non-relativistic reduction there are six matrix elements corresponding to the operators

$$\mathcal{O}(0^-) : g_A(\boldsymbol{\sigma} \cdot \mathbf{p}_e), \quad g_A(\boldsymbol{\sigma} \cdot \mathbf{r}) \quad (3)$$

$$\mathcal{O}(1^-) : g_V \mathbf{p}_e, \quad g_A(\boldsymbol{\sigma} \times \mathbf{r}), \quad g_V \mathbf{r} \quad (4)$$

$$\mathcal{O}(2^-) : g_A[\boldsymbol{\sigma} \mathbf{r}]_2, \quad (5)$$

where  $\mathbf{r}$  is the radial coordinate and  $\mathbf{p}_e$  is the electron momentum. In this work the enhancement factor of the  $\gamma_5$  NME ( $\boldsymbol{\sigma} \cdot \mathbf{p}_e$  in the non-relativistic limit) is denoted by  $\epsilon_{\text{MEC}}$ . In addition to these six NMEs, there are three NMEs corresponding to the operators  $g_A(\boldsymbol{\sigma} \cdot \mathbf{r})$ ,  $g_A(\boldsymbol{\sigma} \times \mathbf{r})$ , and  $g_V \mathbf{r}$  with the Coulomb factor  $\mathcal{I}(1, 1, 1, 1; r)$  included in the radial integral. The Coulomb factor is given by [15]

$$\frac{2}{3} \mathcal{I}(1, 1, 1, 1; r) = \begin{cases} 1 - \frac{1}{5} \frac{r}{R}, & 0 < r < R \\ \frac{R}{r} - \frac{1}{5} \left(\frac{R}{r}\right)^3, & r > R, \end{cases} \quad (6)$$

where  $R$  is the nuclear radius. In this work we include also the next-to-leading-order terms in the Behrens–Bühring expansion [15], which increases the number of NMEs involved in transitions up to 21. The NMEs involved in the transitions can be evaluated using the relation

$${}^{V/A} \mathcal{M}_{KLS}^{(N)}(k_e, m, n, \rho) = \frac{\sqrt{4\pi}}{J_i} \sum_{pn} {}^{V/A} m_{KLS}^{(N)}(pn)(k_e, m, n, \rho) (\Psi_f || [c_p^\dagger c_n]_K || \Psi_i), \quad (7)$$

where  ${}^{V/A} m_{KLS}^{(N)}(pn)(k_e, m, n, \rho)$  is the single-particle matrix element, and  $(\Psi_f || [c_p^\dagger c_n]_K || \Psi_i)$  is the one-body transition density (OBTD), which contains the nuclear-structure information. The atomic screening effects and radiative corrections are also included in the shape factor. The details of the scope of the formalism can be found from Ref. [13].

In the present work the electron spectra of 16 first-forbidden  $\Delta J = 0$   $\beta^-$  transitions were calculated using the NMEs produced by the use of the nuclear shell model. The spectra were calculated using nine different scenarios including all combinations of  $\epsilon_{\text{MEC}} = 1.40, 1.70, 2.00$  corresponding to 40%, 70% and 100% enhancements of the axial-charge matrix element and  $g_A = 0.6, 1.00$ , and 1.27 corresponding to the heavily quenched, quenched, and free-nucleon values of the axial-vector coupling constant. The nuclear-structure calculations were done using the shell-model code NuShellX@MSU [16], with appropriate model spaces and Hamiltonians chosen for the three mass regions separately.

For the decay transitions in the mass range  $A = 92$ –97 a model space including the proton orbitals  $0f_{5/2}, 1p_{3/2}, 1p_{1/2}$ , and  $0g_{9/2}$  and the neutron orbitals  $1d_{5/2}, 1d_{3/2}$ , and  $0s_{1/2}$  were used together with the interaction glbepn [17]. The interaction glbepn is a bare G-matrix interaction which has an adjusted version glepn, where

**Table 1**

Decays considered in this study. The references used for the half-lives and branching ratios are given in the fourth column.

Transition	$t_{1/2}$	BR(%)	Ref.
${}^{92}\text{Rb}(0_{g.s.}^-) \rightarrow {}^{92}\text{Sr}(0_{g.s.}^+)$	4.492(20) s	95.2(7)	[23]
${}^{93}\text{Y}(1/2_{g.s.}^-) \rightarrow {}^{93}\text{Zr}(1/2_1^+)$	10.18(8) h	2.7(5)	[24]
${}^{95}\text{Sr}(1/2_{g.s.}^+) \rightarrow {}^{95}\text{Y}(1/2_{g.s.}^-)$	23.90(14) s	55.7(25)	[25]
${}^{96}\text{Y}(0_{g.s.}^-) \rightarrow {}^{96}\text{Zr}(0_{g.s.}^+)$	5.34(5) s	95.5(5)	[26]
${}^{97}\text{Y}(1/2_{g.s.}^+) \rightarrow {}^{97}\text{Zr}(1/2_{g.s.}^-)$	3.75(3) s	40(10)	[27]
${}^{133}\text{Sn}(7/2_{g.s.}^-) \rightarrow {}^{133}\text{Sb}(7/2_{g.s.}^+)$	1.46(3) s	85(3)	[28]
${}^{134}\text{Sb}(0_{g.s.}^-) \rightarrow {}^{134}\text{Te}(0_{g.s.}^+)$	0.78(6) s	97.6(5)	[29]
${}^{135}\text{Te}(7/2_{g.s.}^-) \rightarrow {}^{135}\text{I}(7/2_{g.s.}^+)$	19.0(2) s	62(3)	[30]
${}^{137}\text{Xe}(7/2_{g.s.}^-) \rightarrow {}^{137}\text{Cs}(7/2_{g.s.}^+)$	3.818(13) min	67(3)	[31]
${}^{138}\text{Cs}(3_{g.s.}^-) \rightarrow {}^{138}\text{Ba}(3_1^+)$	32.5(2) min	44.0(10)	[32]
${}^{139}\text{Ba}(7/2_{g.s.}^-) \rightarrow {}^{139}\text{La}(7/2_{g.s.}^+)$	83.06(28) min	70.0(3)	[33]
${}^{139}\text{Cs}(7/2_{g.s.}^+) \rightarrow {}^{139}\text{Ba}(7/2_{g.s.}^-)$	9.27(5) min	85(3)	[33]
${}^{142}\text{Pr}(2_{g.s.}^-) \rightarrow {}^{142}\text{Nd}(2_1^+)$	19.12(4) h	3.7(5)	[34]
${}^{143}\text{Pr}(7/2_{g.s.}^+) \rightarrow {}^{143}\text{Nd}(7/2_{g.s.}^-)$	13.57(2) d	100	[35]
${}^{211}\text{Pb}(9/2^+) \rightarrow {}^{211}\text{Bi}(9/2^-)$	36.1(2) min	91.32(12)	[36]
${}^{213}\text{Bi}(9/2^-) \rightarrow {}^{213}\text{Po}(9/2^+)$	45.61(6) min	65.9(4)	[37]

two-body matrix elements from Gloeckner [18] and Ji and Wildenthal [19] have been adopted. The half-lives calculated using the interactions glbepn and glepn agreed for  ${}^{96}\text{Y}$  to 2%, but for example for  ${}^{93}\text{Y}$  the modified interaction was unable to reproduce the experimental half-life with any physically meaningful value of  $g_A$  and  $\epsilon_{\text{MEC}}$ . The bare G-matrix interaction, on the other hand, was able to reproduce the experimental half-lives, ranging from less than a second to several days. Therefore the half-life analysis was done using this interaction. The decay transitions in the mass range  $A = 133$ –139 were calculated using a model space spanned by the proton orbitals  $0g_{7/2}, 1d_{5/2}, 1d_{3/2}, 2s_{1/2}$ , and  $0h_{11/2}$  and the neutron orbitals  $0h_{9/2}, 1f_{7/2}, 1f_{5/2}, 2p_{3/2}, 2p_{1/2}$ , and  $0i_{13/2}$  with the effective interactions jj56pnb [20] and jj56cdb [21]. For the decays of  ${}^{142}\text{Pr}$  and  ${}^{143}\text{Pr}$  the dimensions of the problem were so large that truncations became necessary, and no nucleons were allowed on the  $\pi 0h_{11/2}$  and  $\nu 0i_{13/2}$  orbitals. This decay was not included in the half-life analysis since rather severe truncations were used. For the  $A = 211$ –213 nuclei the model space consisted of the proton orbitals  $0h_{9/2}, 1f_{7/2}, 1f_{5/2}, 2p_{3/2}, 2p_{1/2}$ , and  $0i_{13/2}$  and the neutron orbitals  $0i_{11/2}, 1g_{9/2}, 1g_{7/2}, 2d_{5/2}, 2d_{3/2}, 3s_{1/2}$ , and  $0j_{15/2}$  with the corresponding Hamiltonian khpe [22]. Half-lives of the decays in the  $A \approx 95$  and  $A \approx 135$  regions were also calculated and compared with the experimental data. The effects of the mesonic enhancement on the half-lives of the first-forbidden decays in the  ${}^{208}\text{Pb}$  region have been studied in detail in Ref. [8] and thus we refer to these results for the half-life part. However, the beta spectra of these decays have not been previously published.

The transitions studied in this work, the corresponding branching ratios, and the half-lives of the mother nuclei are listed in Table 1. In Table 2 are given the values of  $g_A$  needed to reproduce the experimental half-life with  $\epsilon_{\text{MEC}} = 1.4, 1.7$ , and 2.0 for decay transitions in the mass range  $A = 91$ –97. The uncertainties in the obtained  $g_A$  values stem from the uncertainty in the branching ratio and the half-life, and is given by the standard deviation  $\sigma/\sqrt{N}$ . The uncertainty coming from the nuclear-structure calculations is at least of the same order as the largest half-life errors, so the total uncertainty is of the order of 30% uniformly for all the decays.

The results for decays in the  $A \approx 95$  region are listed in Table 2. When an enhancement of 40% for the axial-charge matrix element is assumed, an effective value close to unity is obtained

**Table 2**

Effective values of the coupling constant  $g_A$  for different scenarios of the enhancement of the time-like axial-vector matrix element  $\int \gamma_5$  for decay transitions in the mass range  $A = 92$ – $97$ . The mother nuclei are listed in the first column and the values of  $g_A$  which reproduce the experimental half-life are given in columns 2–4 for each value of  $\epsilon_{\text{MEC}}$  separately. The CVC value  $g_V = 1.00$  was adopted in the analysis. The error in  $g_A$  comes from the uncertainty in the branching ratio and the half-life, given by the standard deviation  $\sigma/\sqrt{N}$ .

Nucleus	$g_A$ with glbepn interaction		
	$\epsilon_{\text{mec}} = 1.4$	1.7	2.0
$^{92}\text{Rb}$	0.74(1)	0.62(1)	0.53(1)
$^{93}\text{Y}$	1.25(15)	1.03(17)	0.85(30)
$^{95}\text{Sr}$	0.88(4)	0.70(4)	0.58(3)
$^{96}\text{Y}$	0.96(1)	0.80(1)	0.69(1)
$^{97}\text{Y}$	0.85(15)	0.70(13)	0.59(12)
Average	$0.94 \pm 0.08$	$0.77 \pm 0.07$	$0.65 \pm 0.06$

for the axial-vector coupling constant  $g_A$ . For larger  $\epsilon_{\text{MEC}}$  a more quenched value of  $g_A$  is required to reproduce the experimental half-lives. A previous direct calculation by Kirchbach and Reinhardt [38] for the enhancement factor resulted in  $\epsilon_{\text{MEC}} = 45\%$ . This would correspond to  $g_A \approx 0.90$ . The  $g_A$  values obtained for the 40% enhancement of the  $\gamma_5$  matrix element are in line with previous shell-model results for Gamow–Teller decays in light and medium-heavy nuclei [39–41]. This is also in line with the result  $g_A = 0.92$  for the fourth-forbidden decay of  $^{113}\text{Cd}$  obtained using the spectrum-shape method with three different nuclear models [13].

For the  $A \approx 135$  region the results for the effective values of  $g_A$  can be found from Table 3. The general trend is similar as for the  $A \approx 95$  nuclei for both interactions: For larger enhancements of the axial-charge matrix element smaller values of  $g_A$  are needed to reproduce the experimental half-lives. The more recent jj56pnb interaction gives  $g_A = 0.87 \pm 0.04$  when  $\epsilon_{\text{MEC}} = 1.4$  is assumed. The result obtained using the interaction jj56cdb is in agreement with this result within error limits. For enhancement of 70% the jj56pnb agrees excellently with the result for  $A \approx 95$  nuclei with  $g_A = 0.75 \pm 3$ . The jj56cdb result, on the other hand, is noticeably higher with  $g_A = 0.87 \pm 0.06$ . For  $\epsilon_{\text{MEC}} = 2.0$  the shell-model results  $0.70 \pm 0.06$  and  $0.66 \pm 0.03$  for the  $A \approx 135$  region are in harmony. This is in an astonishingly good agreement with the  $A \approx 95$  result  $g_A = 0.65 \pm 0.06$ . This suggests that the proper effective value of  $g_A$  is the same for both the  $A \approx 95$  and  $A \approx 135$  regions. Our calculations suggest that an effective value of  $g_A$  below unity should be used also for first-forbidden non-unique decays with  $\Delta J = 0$ .

Instead of studying the effective value of  $g_A$  as a function of  $\epsilon_{\text{MEC}}$ , we can of course turn this the other way around. Previous systematic studies in the  $A \approx 16$  [6] and  $A \approx 208$  [8] regions have resulted in enhancement factors  $1.61 \pm 0.03$  and  $2.01 \pm 0.05$  respectively. In addition, separate studies for  $^{50}\text{K}$  [6] and  $^{96}\text{Y}$  [17] yielded the enhancement factors 1.52 and  $1.75 \pm 0.30$ . Calculating

**Table 3**

Same as Table 2 for decay transitions in the mass range  $A = 133$ – $139$  calculated using the Hamiltonians based on the jj56cdb and jj56pnb two-body interactions.

Nucleus	$g_A(\gamma_5)$ with jj56cdb int.			$g_A$ with jj56pnb int.		
	$\epsilon_{\text{mec}} = 1.4$	1.7	2.0	1.4	1.7	2.0
$^{133}\text{Sn}$	0.94(2)	0.80(2)	0.69(2)	0.94(2)	0.80(2)	0.69(2)
$^{134}\text{Sb}$	1.18(6)	0.99(5)	0.85(5)	0.85(4)	0.71(4)	0.62(3)
$^{135}\text{Te}$	0.86(2)	0.74(3)	0.65(2)	0.96(3)	0.84(3)	0.74(3)
$^{137}\text{Xe}$	0.74(2)	0.65(2)	0.58(2)	0.81(3)	0.71(2)	0.64(3)
$^{139}\text{Ba}$	0.68(1)	0.60(1)	0.54(1)	0.72(1)	0.64(1)	0.58(1)
$^{139}\text{Cs}$	1.15(3)	1.00(2)	0.88(2)	0.91(2)	0.79(2)	0.69(2)
Average	$0.93 \pm 0.08$	$0.87 \pm 0.06$	$0.70 \pm 0.06$	$0.87 \pm 0.04$	$0.75 \pm 0.03$	$0.66 \pm 0.03$

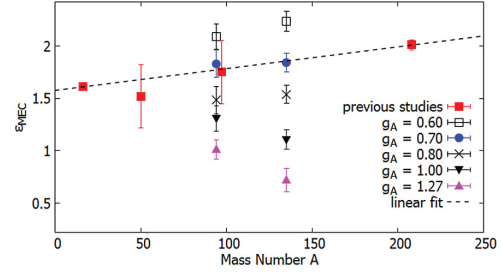


**Fig. 1.** The obtained enhancements  $\epsilon_{\text{MEC}}$  of the previous studies and the present study as a function of the mass number  $A$ . The red squares represent the previous systematic studies done in the  $A \approx 16$  and  $A \approx 208$  regions and the separate studies done for  $^{50}\text{K}$  and  $^{96}\text{Y}$ . The other points represent the results of this study for different effective values of  $g_A$ . The linear fit is an error weighted fit, where the results of the previous studies and the previous study with  $g_A = 0.70$  are used. (For interpretation of the colors in the figure(s), the reader is referred to the web version of this article.)

$\epsilon_{\text{MEC}}$  for different set values of  $g_A$  in the  $A \approx 95$  and  $A \approx 135$  regions and comparing to the previous results allows us to see how the mesonic enhancement behaves as a function of mass number in different scenarios. The results are presented in Fig. 1. For  $^{50}\text{K}$  the error is assumed to be 0.30 as it is for  $^{96}\text{Y}$ . When the free nucleon value 1.27 is adopted, no mesonic enhancement is obtained for  $A \approx 95$  and for  $A \approx 135$  quenching of the axial-charge matrix element is needed to reproduce the experimental half-lives. For the unity value of the axial-vector coupling constant the results are rather similar: an enhancement of only 0–20%. When  $g_A = 0.70$  is adopted, a clear linear trend is seen. A fit to the data gives the relation

$$\epsilon_{\text{MEC}} = 1.576 + 2.08 \times 10^{-3} A. \quad (8)$$

For an even heavily quenched value,  $g_A = 0.60$ , an enhancement factor well above 2.0 is required to reproduce the experimental half-lives, which is not in line with the previous results. The scenario with  $g_A = 0.80$ , on the other hand, would result in enhancements  $1.48 \pm 0.13$  and  $1.54 \pm 0.09$  for the 95 and 135 regions respectively. Based on previous results this kind of scenario is also possible. The general trend in this case would not be linearly increasing, but roughly constant in the medium-heavy region.

In addition to the half-lives the shapes of the electron spectra and their dependence on  $g_A$  and  $\epsilon_{\text{MEC}}$  were studied. The most interesting spectra are shown in Figs. 2–5. The spectrum related to the decay of  $^{93}\text{Y}$  to the first  $1/2^+$  state in  $^{93}\text{Zr}$  is presented in Fig. 2. Not only is there a clear dependence on the effective value of the axial-vector coupling constant  $g_A$ , there is also a noticeable dependence on the value of  $\epsilon_{\text{MEC}}$ . The spectra calculated for each scenario of the effective value of  $g_A$  are clearly distinct for any chosen  $\epsilon_{\text{MEC}}$ . However, for example the combinations

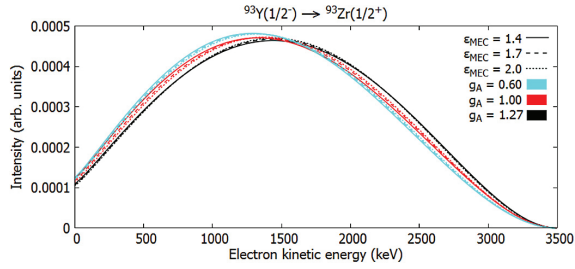


Fig. 2. Electron spectra of  $^{93}\text{Y}$  calculated with the interaction *glbepn*. The color coding signifies the value of  $g_A$  and the dash coding the value of the mesonic enhancement  $\epsilon_{\text{MEC}}$ .

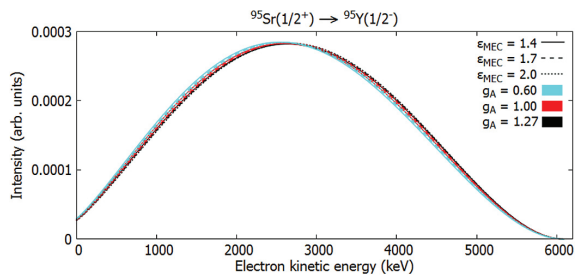


Fig. 3. Same as Fig. 2 for the decay of  $^{95}\text{Sr}$ .

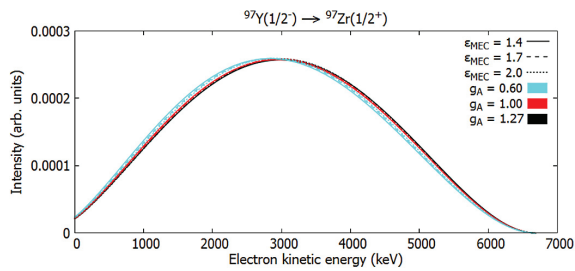


Fig. 4. Same as Fig. 2 for the decay of  $^{97}\text{Y}$ .

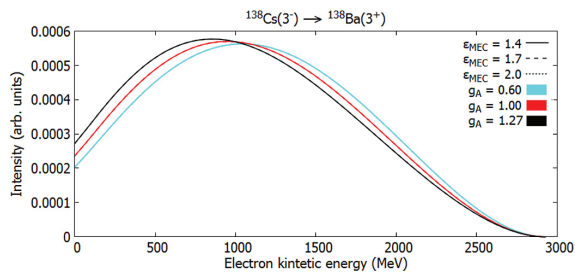


Fig. 5. Same as Fig. 2 for the decay of  $^{138}\text{Cs}$  calculated with the *jj56pnb* interaction.

$(g_A, \epsilon_{\text{MEC}}) = (1.0, 1.4)$  and  $(g_A, \epsilon_{\text{MEC}}) = (0.6, 2.0)$  produce spectra which are significantly closer. This is also consistent with the half-life results, where both combinations  $(g_A, \epsilon_{\text{MEC}}) \approx (0.95, 1.4)$  and  $(g_A, \epsilon_{\text{MEC}}) \approx (0.65, 2.0)$  reproduced the experimental half-lives. The branching ratio of this transition is  $2.7 \pm 5$  (see Table 1), so in principal this spectrum could be measured experimentally. A high-precision measurement of this spectrum would be desir-

able, since it could be used to confirm the need to use quenched  $g_A$  values below unity for forbidden  $\Delta J$  transitions.

Noticeable dependence on the used  $g_A$  and  $\epsilon_{\text{MEC}}$  combinations can also be seen in the spectra of  $^{95}\text{Sr}$  and  $^{97}\text{Y}$  presented in Figs. 3 and 4. Though the dependence is smaller than in  $^{93}\text{Y}$ , it is very important due to the contribution of the  $^{95}\text{Sr}$  spectrum to the cumulative beta spectrum used in reactor-antineutrino analyses [42]. Another important contributor is  $^{135}\text{Te}$ . The dependence of the spectral shape of  $^{135}\text{Te}$  is roughly half of that of  $^{95}\text{Sr}$ , and is not presented here. However, these small effects are crucial when considering the significance of the reactor-antineutrino anomaly.

In addition to the decays considered in the half-life analysis, five more transitions were studied. The decay of  $^{138}\text{Cs}$  was excluded from the half-life analysis, since the dependence of the half-life on the value of  $\epsilon_{\text{MEC}}$  was practically non-existent, and thus a meaningful extraction of  $g_A$  with different values of  $\epsilon_{\text{MEC}}$  was impossible. Naturally, the spectral shape of  $^{138}\text{Cs}$  is also independent on the enhancement factor. The electron spectrum of  $^{138}\text{Cs}$  calculated using different values of  $g_A$  is shown in Fig. 5. For this transition the dependence is significant enough that the extraction of the effective value of  $g_A$  using the spectrum-shape method is feasible to at least an accuracy of 0.1–0.2. This would be enough to see whether the value of  $g_A$  is close to unity (implying  $\epsilon_{\text{MEC}} \approx 1.4$ ), close to 0.6 (implying  $\epsilon_{\text{MEC}} \approx 2.0$ ), or something between. The branching ratio for this decay is  $44.0 \pm 10$  and the  $Q$ -value is close to 3 MeV which makes an accurate measurement of the spectrum shape possible, since the experimentally problematic low-energy part of the beta spectrum is a relatively small portion in comparison with beta decays which have a  $Q$ -value of a few hundred keV.

The decays of  $^{142}\text{Pr}$  and  $^{143}\text{Pr}$  were also calculated to see if any significant dependence on either  $g_A$  and  $\epsilon_{\text{MEC}}$  is present. For these decays, as well as for the decays of  $^{211}\text{Pb}$  and  $^{213}\text{Bi}$ , the dependencies turned out to be smaller than for example the dependence for  $^{95}\text{Sr}$  and  $^{97}\text{Y}$ . Due to the rather severe truncations used for the Pr isotopes these decays were not included in the half-life analyses.

In this Letter the significant impact of the enhancement of the axial-charge matrix element on the half-lives and spectral shapes of first-forbidden  $J^+ \leftrightarrow J^-$  decay transitions was pointed out. Half-life analyses were carried out in the  $A \approx 95$  and  $A \approx 135$  mass regions, extracting effective values of  $g_A$  corresponding to different scenarios of the enhancement of the axial-charge matrix element, characterized by the enhancement factor  $\epsilon_{\text{MEC}}$ . In both regions the effective values  $g_A \approx 0.90, 0.75$ , and  $0.65$  corresponded to the enhancement scenarios  $\epsilon_{\text{MEC}} = 1.4, 1.7$ , and  $2.0$ . On the flip side, a linear dependence of  $\epsilon_{\text{MEC}}$  on the mass number was found when  $g_A = 0.70$  was adopted. The dependence of the beta-spectrum shape of the transition  $^{93}\text{Y}(1/2^-_{\text{g.s.}}) \rightarrow ^{93}\text{Zr}(1/2^+)$  on both  $g_A$  and  $\epsilon_{\text{MEC}}$  was pointed out. Similar but less significant dependencies were also recorded in the decays of  $^{95}\text{Sr}$  and  $^{97}\text{Y}$ . The spectrum related to the  $\beta^-$  decay of  $^{138}\text{Cs}$  was found to be significantly  $g_A$  dependent, while simultaneously being independent of  $\epsilon_{\text{MEC}}$ . This opens up the possibility for the determination of a proper effective value of  $g_A$  in the  $A \approx 135$  region for first-forbidden decays using the spectrum-shape method. This value of  $g_A$  would also imply an appropriate value of  $\epsilon_{\text{MEC}}$  in medium-heavy nuclei. Accurate values of the weak couplings are needed in order to produce accurate spectra to be used in the reactor-antineutrino analyses as well as analyses of the backgrounds in rare-event searches.

## References

- [1] K. Kubodera, J. Delorme, M. Rho, *Phys. Rev. Lett.* 40 (1978) 755.
- [2] P. Guichon, M. Giffon, J. Joseph, R. Laverriere, C. Samour, *Z. Phys. A* 285 (1978) 183.

- [3] P. Guichon, M. Giffon, C. Samour, *Phys. Lett. B* 74 (1978) 15.  
[4] I.S. Towner, F.C. Khanna, *Nucl. Phys. A* 372 (1981) 331.  
[5] J. Delorme, *Nucl. Phys. A* 374 (1982) 541c.  
[6] E.K. Warburton, I.S. Towner, B.A. Brown, *Phys. Rev. C* 49 (1994) 824.  
[7] E.K. Warburton, J.A. Becker, B.A. Brown, D.J. Millener, *Ann. Phys.* 187 (1988) 471.  
[8] E.K. Warburton, *Phys. Rev. C* 44 (1991) 233.  
[9] K. Kubodera, M. Rho, *Phys. Rev. Lett.* 67 (1991) 3479.  
[10] M. Haaranen, P.C. Srivastava, J. Suhonen, *Phys. Rev. C* 93 (2017) 034308.  
[11] J. Kostensalo, M. Haaranen, J. Suhonen, *Phys. Rev. C* 95 (2017) 044313.  
[12] J. Kostensalo, J. Suhonen, *Phys. Rev. C* 96 (2017) 024317.  
[13] M. Haaranen, J. Kotila, J. Suhonen, *Phys. Rev. C* 95 (2017) 024327.  
[14] J.C. Hardy, I.S. Towner, V. Koslowsky, E. Hagberg, H. Schmeig, *Nucl. Phys. A* 509 (1990) 429.  
[15] H. Behrens, W. Bühring, *Electron Radial Wave Functions and Nuclear Beta-decay*, Clarendon Press, Oxford, 1982.  
[16] B.A. Brown, W.D.M. Rae, *Nucl. Data Sheets* 120 (2014) 115.  
[17] H. Mach, E.K. Warburton, R.L. Gill, R.F. Casten, J.A. Becker, B.A. Brown, J.A. Wigner, *Phys. Rev. C* 41 (1991) 226.  
[18] D.H. Gloeckner, *Nucl. Phys. A* 253 (1975) 301.  
[19] X. Ji, B.H. Wildenthal, *Phys. Rev. C* 37 (1988) 1256.  
[20] B.A. Brown, unpublished.  
[21] B.A. Brown, N.J. Stone, J.R. Stone, I.S. Towner, M. Hjorth-Jensen, *Phys. Rev. C* 71 (2005) 044317.  
[22] E.K. Warburton, B.A. Brown, *Phys. Rev. C* 43 (1991) 602.  
[23] C.M. Baglin, *Nucl. Data Sheets* 113 (2012) 2187.  
[24] C.M. Baglin, *Nucl. Data Sheets* 112 (2011) 1163.  
[25] S.K. Basu, G. Mukherjee, A.A. Sonzogni, *Nucl. Data Sheets* 111 (2010) 2555.  
[26] D. Abriola, A.A. Sonzogni, *Nucl. Data Sheets* 109 (2008) 2501.  
[27] N. Nica, *Nucl. Data Sheets* 111 (2010) 525.  
[28] Y. Khazov, A. Rodionov, F.G. Kondev, *Nucl. Data Sheets* 112 (2011) 855.  
[29] A.A. Sonzogni, *Nucl. Data Sheets* 103 (2004) 1.  
[30] B. Singh, A.A. Rodionov, Y.L. Khazov, *Nucl. Data Sheets* 109 (2008) 517.  
[31] E. Browne, J.K. Tuli, *Nucl. Data Sheets* 108 (2007) 2173.  
[32] J. Chen, *Nucl. Data Sheets* 146 (2017) 1.  
[33] P.K. Joshi, B. Singh, S. Singh, *Nucl. Data Sheets* 138 (2016) 1.  
[34] T.D. Johnson, D. Symochko, M. Fadil, J.K. Tuli, *Nucl. Data Sheets* 112 (2011) 1949.  
[35] E. Browne, J.K. Tuli, *Nucl. Data Sheets* 113 (2012) 715.  
[36] E.A. Mccutchan, C.M. Baglin, O. Gorbachenko, N. Todorovic, *Nucl. Data Sheets* 114 (2013) 661.  
[37] M.S. Basunia, *Nucl. Data Sheets* 108 (2007) 633.  
[38] M. Kirchbach, H. Reinhardt, *Phys. Lett. B* 208 (1988) 79.  
[39] W.T. Chou, E.K. Warburton, B.A. Brown, *Phys. Rev. C* 47 (1993) 163.  
[40] B.H. Wildenthal, M.S. Curtin, B.A. Brown, *Phys. Rev. C* 28 (1983) 1343.  
[41] T. Siiskonen, M. Hjorth-Jensen, J. Suhonen, *Phys. Rev. C* 63 (2001) 055501.  
[42] C. Buck, A.P. Collin, J. Haser, M. Lindner, *Phys. Lett. B* 765 (2017) 159.



## VII

### FIRST-FORBIDDEN TRANSITIONS IN REACTOR ANTINEUTRINO SPECTRA

by

Hayen, L., Kostensalo, J., Severijns, N., & Suhonen, J. 2019

Physical Review C, 99 (3), 031301(R).  
doi:10.1103/physrevc.99.031301

Reproduced with kind permission by American Physical Society.

**First-forbidden transitions in reactor antineutrino spectra**L. Hayen,<sup>1,\*</sup> J. Kostensalo,<sup>2</sup> N. Severijns,<sup>1</sup> and J. Suhonen<sup>2</sup><sup>1</sup>*Instituut voor Kern- en Stralingsfysica, KU Leuven, Celestijnenlaan 200D, B-3001 Leuven, Belgium*<sup>2</sup>*Department of Physics, University of Jyväskylä, P.O. Box 35, FI-40014 University of Jyväskylä, Finland*

(Received 31 May 2018; revised manuscript received 21 December 2018; published 6 March 2019)

We study the dominant forbidden transitions in the antineutrino spectra of the fission actinides from 4 MeV onward using the nuclear shell model. Through explicit calculation of the shape factor, we show the expected changes in cumulative electron and antineutrino spectra. Relative to the allowed approximation this results in a minor decrease of electron spectra above 4 MeV, whereas an increase of several percent is observed in antineutrino spectra. We show that forbidden transitions dominate the spectral flux for most of the experimentally accessible range. Based on the shell model calculations we attempt a parametrization of forbidden transitions and propose a spectral correction for all first-forbidden transitions. We enforce correspondence with the Institut Laue-Langevin data set using a summation+conversion approach. When compared against modern reactor neutrino experiments, the resultant spectral change is observed to be of comparable magnitude and shape as the reported spectral shoulder.

DOI: [10.1103/PhysRevC.99.031301](https://doi.org/10.1103/PhysRevC.99.031301)

For the past years, neutrino physics has seen a flurry of interest in the so-called reactor anomaly [1–3], a 6% deficit in the experimentally observed antineutrino count rate relative to theoretical predictions. Together with more long-standing anomalies (reported by LSND [4,5] and GALLEX [6] collaborations), much theoretical interest has gone toward the possibility of one or more eV-scale sterile neutrinos [7,8]. Motivated by these findings, several dedicated experiments worldwide are directly looking for an oscillation pattern at very short baselines, meaning results are independent of theoretical calculations. The explored parameter space is, however, inspired by theoretical estimates. Many experiments are in the process of data taking and have published preliminary results [9–14]. So far, all of these exclude the best theoretical fit value [8] with  $\geq 2\sigma$ , so a better understanding and control of the theoretical estimate remains an important goal.

With the availability of precision antineutrino spectra, all modern long baseline reactor neutrino experiments have additionally observed a spectral disagreement with respect to theoretical predictions between 4 and 6 MeV [15–17]. Up to now, this so-called shoulder has remained unexplained, and several possibilities have been proposed for its solution [18–22]. The role of (first-)forbidden transitions in both the anomaly and shoulder has so far received limited study, either in parametrized [23] or microscopic treatments [24]. Based on the behavior of pseudoscalar ( $\Delta J^\pi = 0^-$ ) transitions the forbidden influence has been estimated as negligible [20], despite their flux dominance in the region of interest [25]. Here we investigate the influence of first-forbidden  $\beta$  decays by calculating the shape factor of the dominant transitions in

the region of interest using the nuclear shell model, and show its far-reaching consequences.

We use the formalism of Behrens and Bühring [26] to describe the spectral shape, taking into account finite-size and Coulomb corrections at all levels. We write the  $\beta$  spectrum as

$$\frac{dN}{dW} = pW(W - W_0)^2 F(Z, W) C(Z, W) K(Z, W), \quad (1)$$

where  $W = E/m_e c^2 + 1$  is the total  $\beta$  energy,  $p = \sqrt{W^2 - 1}$  the momentum,  $W_0$  the spectral endpoint, and  $Z$  the proton number of the daughter. Additionally,  $F(Z, W)$  is the Fermi function,  $C(Z, W)$  the shape factor, and  $K(Z, W)$  additional higher-order effects [27]. In previous analyses [3,28] forbidden transitions were approximated as allowed, either using  $C = 1$  or including a linear weak magnetism correction so that  $dC/dW = 0.67\% \text{ MeV}^{-1}$ . In the so-called Huber-Mueller (H-M) case, all forbidden transitions were assumed to have a unique shape [2]. We compare our findings against the allowed approximation, and comment on the H-M approximation.

We write the generalized unique forbidden shape factor of order  $L$  as [29]

$$C_U = \sum_{k=1}^L \lambda_k \frac{p^{2(k-1)} q^{2(L-k)}}{(2k-1)! [2(L-k)+1]}, \quad (2)$$

and for illustrative purposes we write the first-forbidden pseudoscalar and pseudovector shape factors using their dominant parts as

$$C_{0^-} = 1 + \frac{2R}{3W} b + \mathcal{O}(\alpha Z R, W_0 R^2), \quad (3)$$

$$C_{1^-} = 1 + aW + \mu_1 \gamma \frac{b}{W} + cW^2, \quad (4)$$

\*leendert.hayen@kuleuven.be

TABLE I. Dominant forbidden transitions above 4 MeV. Here  $Q_\beta$  is the ground-state to ground-state  $Q$  value,  $E_{ex}$  the excitation energy of the daughter level, BR the branching ratio of the transition normalized to one decay, and FY the cumulative fission yield of  $^{235}\text{U}$  from the ENDF database [48].

Nuclide	$Q_\beta$ (MeV)	$E_{ex}$ (MeV)	BR (%)	$J_i^\pi \rightarrow J_f^\pi$	FY (%)	$\Delta J$
$^{89}\text{Br}$	8.3	0	16	$3/2^- \rightarrow 3/2^+$	1.1	0
$^{90}\text{Rb}$	6.6	0	33	$0^- \rightarrow 0^+$	4.5	0
$^{91}\text{Kr}$	6.8	0.11	18	$5/2^+ \rightarrow 5/2^-$	3.5	0
$^{92}\text{Rb}$	8.1	0	95.2	$0^- \rightarrow 0^+$	4.8	0
$^{93}\text{Rb}$	7.5	0	35	$5/2^- \rightarrow 5/2^+$	3.5	0
$^{94}\text{Y}$	4.9	0.92	39.6	$2^- \rightarrow 2^+$	6.5	0
$^{95}\text{Sr}$	6.1	0	56	$1/2^+ \rightarrow 1/2^-$	5.3	0
$^{96}\text{Y}$	7.1	0	95.5	$0^- \rightarrow 0^+$	6.0	0
$^{97}\text{Y}$	6.8	0	40	$1/2^- \rightarrow 1/2^+$	4.9	0
$^{98}\text{Y}$	9.0	0	18	$0^- \rightarrow 0^+$	1.9	0
$^{133}\text{Sn}$	8.0	0	85	$7/2^- \rightarrow 7/2^+$	0.1	0
$^{135}\text{Te}$	5.9	0	62	$(7/2^-) \rightarrow 7/2^+$	3.3	0
$^{136m}\text{I}$	7.5	1.89	71	$(6^-) \rightarrow 6^+$	1.3	0
$^{136m}\text{I}$	7.5	2.26	13.4	$(6^-) \rightarrow 6^+$	1.3	0
$^{137}\text{I}$	6.0	0	45.2	$7/2^+ \rightarrow 7/2^-$	3.1	0
$^{142}\text{Cs}$	7.3	0	56	$0^- \rightarrow 0^+$	2.7	0
$^{86}\text{Br}$	7.3	0	15	$(1^-) \rightarrow 0^+$	1.6	1
$^{86}\text{Br}$	7.3	1.6	13	$(1^-) \rightarrow 2^+$	1.6	1
$^{87}\text{Se}$	7.5	0	32	$3/2^+ \rightarrow 5/2^-$	0.8	1
$^{89}\text{Br}$	8.3	0.03	16	$3/2^- \rightarrow 5/2^+$	1.1	1
$^{91}\text{Kr}$	6.8	0	9	$5/2^+ \rightarrow 3/2^-$	3.4	1
$^{134m}\text{Sb}$	8.5	1.69	42	$(7^-) \rightarrow 6^+$	0.8	1
$^{134m}\text{Sb}$	8.5	2.40	54	$(7^-) \rightarrow (6^+)$	0.8	1
$^{138}\text{I}$	8.0	0	26	$(1^-) \rightarrow 0^+$	1.5	1
$^{140}\text{Cs}$	6.2	0	36	$1^- \rightarrow 0^+$	5.7	1
$^{88}\text{Rb}$	5.3	0	76.5	$2^- \rightarrow 0^+$	3.6	2
$^{94}\text{Y}$	4.9	0	41	$2^- \rightarrow 0^+$	6.5	2
$^{95}\text{Rb}$	9.2	0	0.1	$5/2^- \rightarrow 1/2^+$	0.8	2
$^{139}\text{Xe}$	5.1	0	15	$3/2^- \rightarrow 7/2^+$	5.0	2

where  $R$  is the nuclear radius,  $\alpha$  is the fine-structure constant,  $\gamma = \sqrt{1 - (\alpha Z)^2}$ ,  $q = W_0 - W$  is the (anti)neutrino momentum, and  $\lambda_k$  is a Coulomb correction function. Here  $a$ ,  $b$ , and  $c$  are (complex) combinations of nuclear matrix elements, corresponding to powers of  $W$  +1, -1, and +2. Note that we have not used the simplified expressions of Eqs. (3) and (4), but rather used the complete formulation as can be found, e.g., in Ref. [30]. As such, we additionally take into account finite-size effects and Coulomb corrections to the nuclear matrix elements. As cancellations can occur in the main matrix elements, the latter can eventually dominate the shape factor. The importance of these corrections cannot be understated, in particular for the high masses of the actinide fission fragments [31].

Based on the compilation in Ref. [25] we have selected 29 forbidden transitions, listed in Table I. All transitions have a  $\beta$  spectrum endpoint above 4 MeV, meaning that all contribute to the observed spectral shoulder. Using the experimental results obtained at the Institut Laue-Langevin (ILL) [32–36], the selected transitions correspond to at least 50% of the

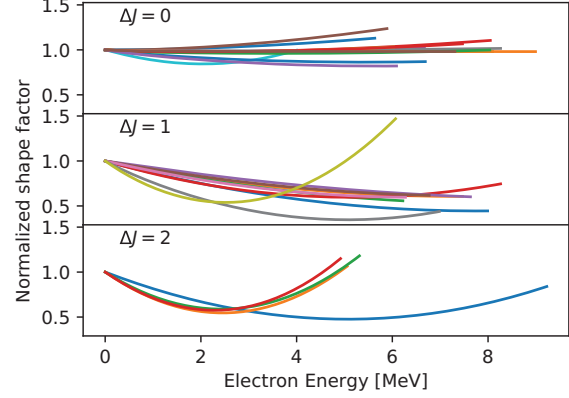


FIG. 1. Calculated shape factors  $C$  vs electron kinetic energy, categorized according to the spin-parity change of the transition. For allowed transitions  $C \approx 1$ . Each shape factor was normalized to its value at  $E = 0$ . Results correspond to  $g_A = 0.9$  and  $\epsilon_{\text{MEC}} = 1.4$ , where applicable [31,42]. Two cases stand out:  $^{94}\text{Y}$  ( $2^- \rightarrow 2^+$ ) and  $^{86}\text{Br}$  ( $1^- \rightarrow 2^+$ ). Both contain strong admixtures of  $\Delta J = 2$  operators, since both  $2^+$  final states identify as vibrational excitations of the  $0^+$  ground state.

cumulative electron flux in the region of interest (2–8 MeV), and exceed 65% at 6 MeV for all fission actinides [31]. The shell model calculations were performed using the shell model code NUSHELLX@MSU [37]. For nuclei with  $A < 100$  the effective interaction  $\text{glepn}$  [38] was adopted in a full model space consisting of the proton orbitals  $0f_{5/2}-1p-0g_{9/2}$  and the neutron orbitals  $1d-2s$ . The  $^{86}\text{Br}$  and  $^{89}\text{Br}$  cases were calculated using the interaction  $\text{jj45pna}$  [39,40], in the full model space spanned by the proton orbitals  $0f_{5/2}-1p-0g_{9/2}$  and the neutron orbitals  $0g_{7/2}-2s-1d-0h_{11/2}$ . For the nuclei with  $A = 133$ –142 the Hamiltonian  $\text{jj56pnb}$  [41] was used in the full model space spanned by the proton orbitals  $0g_{7/2}-1d-2s-0h_{11/2}$  and neutron orbitals  $0h_{9/2}-1f-2p-0i_{13/2}$  for  $A < 139$ , while for the heavier nuclei the proton orbital  $0h_{11/2}$  and the neutron orbital  $0i_{13/2}$  were kept empty due to the enormous dimensions of a full model space calculation. Uncertainties due to  $g_A$  quenching and meson exchange currents (MECs) in pseudoscalar transitions in the fission fragment region have been reported [31,42–46], and will be briefly commented upon further in this work.

We have separately used the ENSDF [47] and ENDF [48] decay libraries. While the former suffers from multiple cases of the pandemonium effect [49], the latter has been corrected to obtain improved agreement with experimental reactor data [50,51]. Unless mentioned explicitly, the results below are obtained using the ENDF/B-VIII.0 decay library with spin-parity information from ENSDF. Transitions with unknown spin change are assumed allowed and unknown branching ratios are distributed equally from the remaining intensity [31].

Figure 1 shows the calculated shape factors categorized according to the change in spin-parity. Clearly almost all shape factors deviate significantly from unity. The spin change

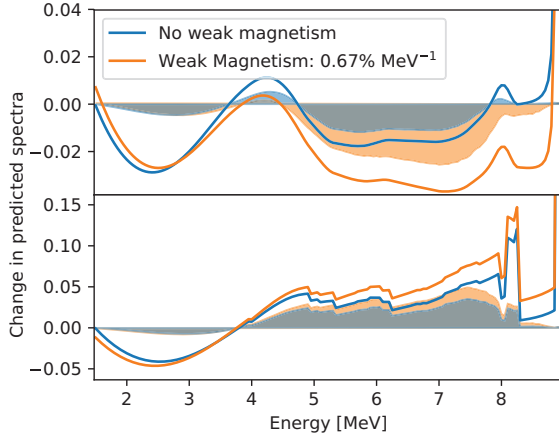


FIG. 2. Top panel: Change in the predicted electron spectra of the considered transitions compared to the allowed approximation with an optional weak magnetism correction. Bottom panel: Change in the predicted antineutrino spectrum compared to the allowed approximation. Shaded areas correspond to the results multiplied by the total spectral contribution compared to experimental flux results. The energy axis refers to the kinetic energy of the electron (top) and antineutrino (bottom).

is a good predictor of the calculated shape factor, with the exception of pseudoscalar,  $\Delta J^\pi = 0^-$ , transitions. From Eq. (3) its behavior should be trivial with  $|bR| \sim 10^{-2}$ , yet large variations appear. Many of these transitions connect initial and final states with spins larger than zero, meaning additional  $\Delta J = 1, 2$  operators contribute non-negligibly. As such, in many cases the energy dependence is dominated by higher-order operators. Even though results appear to scatter around unity, the limited number of contributing branches forbids simple statistical averaging arguments.

Using the fission yields of the ENDF database [48], Fig. 2 shows the change of both electron and antineutrino spectra compared to the allowed approximation with an optional weak magnetism correction. Compared to the weak magnetism correction typically used [2,3], electron spectra see a modest 2% decrease in the 4 to 8 MeV region. Cumulative antineutrino spectra, on the other hand, see a change of up to 5% in the same region. The parabolic behavior below 4 MeV is almost entirely attributable to first-forbidden unique decays (see Fig. 1).

While a significant fraction of the spectral change occurs because of pseudovector ( $\Delta J^\pi = 1^-$ ) transitions, inspection of Fig. 1 should make it clear that even pseudoscalar transitions carry significant deviations from unity. Previous arguments for its neglect [20] have used  $^{92}\text{Rb}$  and  $^{96}\text{Y}$  as examples for their predictions, even though many important pseudoscalar transitions are not pure  $0^- \rightarrow 0^+$  decays (see Fig. 1).

The results presented in Fig. 2 depend on the value used for the weak magnetism correction in the allowed approximation. In the formalism by Holstein [52] its electron spectral

dependence is written as

$$\left(\frac{dN}{dW}\right)^{\text{wm}} \propto \frac{4b}{3Mc} \left(W - \frac{W_0}{2} - \frac{1}{2W}\right), \quad (5)$$

where  $b$  and  $c$  are the weak magnetism and Gamow-Teller form factors, respectively, and  $M$  is the nuclear mass, omitting phase-space factors and additional correction factors [27]. Above a few MeV then, its energy dependence is approximately linear leading to the behavior observed in Fig. 2. Evaluation of this ratio of form factors can happen through a combination of the conserved vector current hypothesis (rendering  $b$ ) and the  $ft$  value (rendering  $c$ ), or having to rely on many-particle quantum calculations such as the nuclear shell model. The former is only possible for decays occurring within isospin multiplets and is limited to nuclei where  $N \sim Z$  [53]. Previous analyses have taken this approach [3] and used results extracted from mass  $A \leq 28$  systems with the assumption that they are equally valid at high masses, leading to  $dC/dW = 0.67\% \text{ MeV}^{-1}$  quoted above [2,3]. When one cannot rely on symmetries, one must attempt to calculate these by introducing the impulse approximation. Here, the nuclear current is treated as a sum of noninteracting nucleon currents and the form factor ratio reduces to

$$\frac{b}{Ac} = \frac{1}{g_A} \left( g_M + g_V \frac{\mathcal{M}_L}{\mathcal{M}_{\text{GT}}} \right) \quad (6)$$

where  $g_M = 4.706$  and  $\mathcal{M}_L, \mathcal{M}_{\text{GT}}$  are the orbital and Gamow-Teller matrix elements [52]. An extensive study [54] performed in the fission fragment region found large variations in  $\mathcal{M}_L/\mathcal{M}_{\text{GT}}$  compared to simple approximations, but concluded that the latter is sufficiently precise for the considered allowed transitions. An additional uncertainty lies in the evaluation of  $g_A$ , as nuclear models typically require (heavily) quenched values compared to the free-nucleon value [45]. Also in several shape factors reported here a dependence on  $g_A$  is present. While our nuclear shell model results converge around  $g_A^{\text{eff}} \simeq 0.9$  [31,42–44], all shape factors have been calculated within both a fully correlated and uncorrelated window for  $g_A \in [0.7, 1.27]$ , taking the extremal values per bin as a  $1\sigma$  uncertainty [31]. Weak magnetism effects in allowed transitions are, however, calculated according to the benchmark analyses [2,3], which allows us to clearly separate the effect of forbidden transitions and directly compare against previously published results.

While several compilations have been produced in the past [25,55], forbidden decays have typically been pushed to the background as they only make up about 30% of the total number of transitions contributing to the total flux. Many of the large-endpoint transitions are, however, of forbidden nature due to the parity change of proton and neutron orbitals in the neutron-rich fission fragments. States of equal parity typically reside at excitation energies of several MeV with fragmented branching ratios, thereby pushing them out of the region of interest. To clarify these concerns, Fig. 3 shows the constituents of the summed full  $^{235}\text{U}$  spectrum. It is immediately clear that allowed transitions, contrary to simple estimates, contribute less than 50% in the entire experimentally interesting region. In the observed shoulder, in particular, forbidden transitions constitute more than 60% of the total electron flux. The

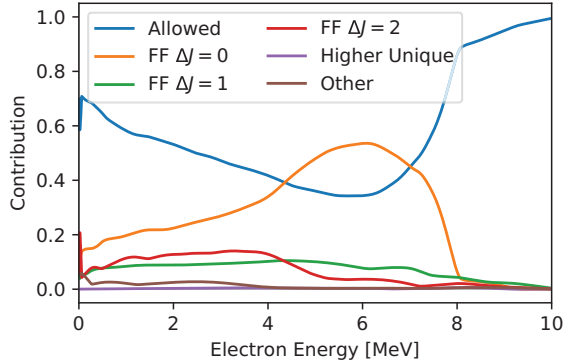


FIG. 3. Constituents of the summed  $^{235}\text{U}$  electron spectrum using the ENDF database [48]. Here FF stands for first-forbidden and Other for non-unique transitions with  $\Delta J \geq 2$ . Behavior past 10 MeV is dominated by a low number of branches. Using decay information from ENSDF (not shown here) these features are strongly amplified, with the contribution of allowed decays reaching a minimum below 20% around 5 MeV [31].

majority of these are pseudoscalar transitions, which in a pure  $0^- \leftrightarrow 0^+$  transition show minimal deviation from an allowed equivalent. As shown above, however, this situation is not typical and subject to large higher-order contributions. Contributions from  $\Delta J = 1, 2$  first-forbidden decays remain relatively constant throughout the entire spectrum up to 7 MeV, making up around 20%. Given their strongly deviating shape factor as shown in Fig. 1, their influence cannot be neglected.

In light of these results and the relatively uniform behavior of the shape factors as calculated by the nuclear shell model, we attempt a simple parametrization. While the shape factor of pure pseudoscalar transitions [Eq. (3)] is simple enough, the influence of higher-order operators prevents a physically insightful function description. As such, we simply fit the obtained shape factors with a general description as in Eq. (4) and analogously for pseudovector transitions. The shape factor of unique forbidden decays [Eq. (2)] describes observed spectra within a few percent, which is sufficient for our purpose.

The parametrization then functions as follows [31]. Each of the non-unique shape factors calculated by the nuclear shell model is fit using functions described above. For each spin change ( $\Delta J = 0, 1$ ), one obtains distributions of fit parameters. Their spread is dominated by differences between transitions rather than individual uncertainties arising from  $g_A$  and  $\epsilon_{\text{MEC}}$  ambiguity. Due to limited statistics, we use Gaussian kernel smoothing [56] where we manually set the bandwidth to  $h = 2$ . Our choice results in fit parameter distributions with conservative uncertainties where all shape factors of Fig. 1 are contained within a  $< 2\sigma$  window. Full spectra are then calculated in a Monte Carlo fashion, where for each non-unique first-forbidden transition, fit parameters are obtained from the correlated parameter ensemble, with the exception of the transitions numerically calculated in this work. Repeating this procedure many times results in a translation of the

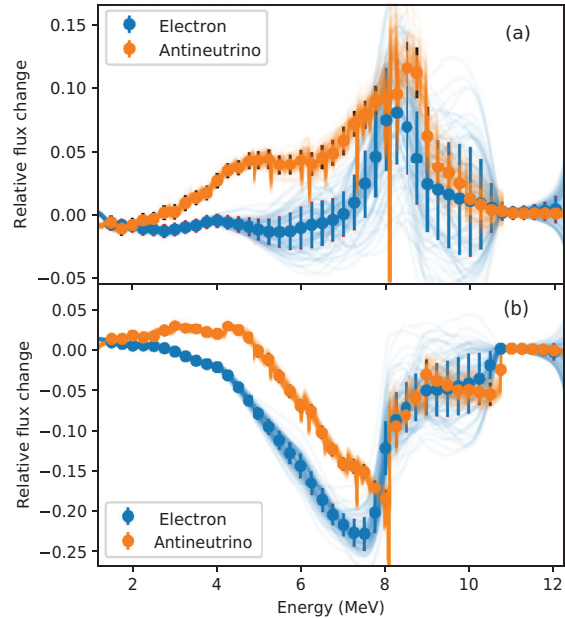


FIG. 4. Spectral change for electron and antineutrino cumulative spectra in the pure summation approach using the forbidden parametrization. The energy axis shows the kinetic energy of the electron and antineutrino. Top panel: Comparison against the allowed transition with a weak magnetism term. Bottom panel: Comparison against treating all forbidden decays as unique. Uncertainties result from a Monte Carlo calculation of 100 samples, together with a theory uncertainty of 1% from the uncertainty in the axial vector coupling constant  $g_A$  and pseudoscalar mesonic enhancement [31].

parametrization uncertainty into a spectral uncertainty. The additional spectrum shape corrections in Eq. (1) are calculated using Ref. [57].

Figure 4 shows the spectral change and associated uncertainty for  $^{235}\text{U}$  in the summation approach using 100 samples. We have made the comparison against the allowed approximation and against the Huber-Mueller method where all forbidden decays are treated as unique. We discuss both in turn.

As shown in Fig. 2, spectral changes to the electron cumulative spectrum are limited relative to the allowed approximation. The change in the antineutrino cumulative spectrum, on the other hand, shows significant deviations in the entire region of interest. Differences reach 5% in the 5–6 MeV region, showing an increase of the predicted neutrino flux relative to the allowed approximation. The uncertainty shown is an uncorrelated combination of a theory uncertainty of 1% due to the quenching of  $g_A$  and mesonic corrections [31,42] and the Monte Carlo uncertainty. Compared to treating all forbidden decays as unique, on the other hand, significant deviations in both electron and antineutrino cumulative spectra are observed. Considering the large differences in shape (shown in Fig. 1) this is hardly surprising. This will be

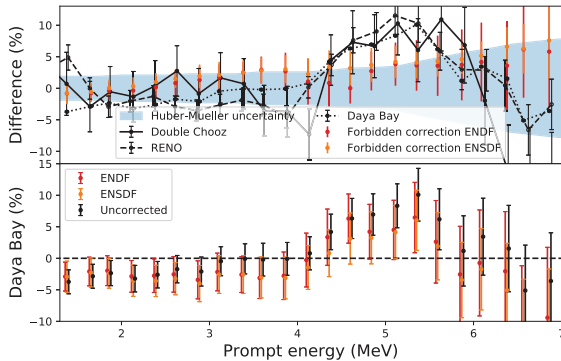


FIG. 5. Top panel: Normalized spectral ratios for three modern experiments relative to the Huber-Mueller predictions [2], and the normalized forbidden spectrum correction described in this work using ENDF and ENSDF decay libraries. The prompt energy of the positron emerging from the inverse  $\beta$  decay is related to the antineutrino energy via  $E_{\text{prompt}} \approx E_{\nu} - 0.782$  MeV. Bottom panel: Difference between Daya Bay spectral data and different theoretical models. Error bars are calculated using experimental, H-M, and forbidden uncertainties and are assumed uncorrelated. Here Uncorrected is relative to the H-M estimate shown in the top panel, and ENDF and ENSDF are the new results.

the subject of further research with relation to the reactor normalization anomaly.

The starting point of the usual anomaly and spectral shoulder analysis is congruity with the ILL data. To guarantee this agreement, we employ a mixed summation+conversion method as in Ref. [2]. Differences in calculated electron spectra from the summation component using our different approximations are then compensated by the conversion part of the procedure. Aside from  $^{235}\text{U}$  and  $^{238}\text{U}$ , however, summation predictions overestimate the experimental ILL data. For the  $^{239,241}\text{Pu}$  isotopes, then, the reference electron spectra are set to the summation calculation in the allowed approximation. As the implementation of forbidden transitions lowers the expected electron flux (see Fig. 2), this introduced deficit can be recovered analogously with the conversion procedure [31]. The agreement with calculated and reference electron spectra is better than 1% up to 7 MeV, after which the uncertainty in the calculated antineutrino spectra is linearly

increased with the observed discrepancy in electron spectra. By enforcing equivalence between electron spectra in our different approaches, the resultant antineutrino spectral changes can be directly compared to the experimentally observed shoulder.

Figure 5 shows the spectral ratios of Daya Bay [15], RENO [17], and Double Chooz [16] data relative to the Huber-Mueller prediction with the uncertainty of the latter. Additionally, we show the correction from forbidden transitions as described above using a normalized spectrum between 2 and 8 MeV using the Daya Bay reactor composition [58], as is done for the experimental results. Further, we show the discrepancy of the Daya Bay spectral data with respect to our new calculations. The partial mitigation of the spectral shoulder and increased uncertainties arising from the treatment of first-forbidden transitions hint at a reduction in the statistical significance. The original spectral shoulder appears now to be compatible with theoretical estimates seeing how nearly all points agree within  $1\sigma$ . Strong bin-to-bin correlations are present, however, to be discussed in a follow-up work [31].

In summary, we have for the first time performed microscopic calculations of the dominant forbidden transitions in the electron and antineutrino reactor spectra above 4 MeV. Through the use of a complete theoretical formalism, Coulomb corrections were taken into account at the appropriate level and shape factors strongly deviating from the usual allowed approximation were found. Using fission yield information, large changes were observed in the antineutrino spectrum. It was shown that despite being limited in number, forbidden transitions are the dominant component of the electron flux between 2 and 7 MeV. Based on the uniform behavior in the calculated shape factors, a parametrization of non-unique first-forbidden transitions was attempted. Using Monte Carlo methods, a spectral correction was obtained for all first-forbidden and higher uniquely forbidden transitions with an associated uncertainty. When compared to spectral discrepancies reported by all modern reactor neutrino experiments, the correction was shown to be of similar shape and magnitude. Taking these results at face value, a large portion of the reactor shoulder appears to be mitigated. Due to increased theoretical uncertainties arising from an improved treatment of first-forbidden transitions, the remaining spectral differences are of decreased statistical significance. Therefore, forbidden decays are not only non-negligible, but also an essential ingredient in the understanding of reactor antineutrino spectra and they merit additional research.

- [1] G. Mention, M. Fechner, T. Lasserre, T. A. Mueller, D. Lhuillier, M. Cribier, and A. Letourneau, *Phys. Rev. D* **83**, 073006 (2011).
- [2] T. A. Mueller, D. Lhuillier, M. Fallot, A. Letourneau, S. Cormon, M. Fechner, L. Giot, T. Lasserre, J. Martino, G. Mention, A. Porta, and F. Yermia, *Phys. Rev. C* **83**, 054615 (2011).
- [3] P. Huber, *Phys. Rev. C* **84**, 24617 (2011), **85**, 029901(E) (2012).
- [4] C. Athanassopoulos *et al.* (LSND Collaboration), *Phys. Rev. Lett.* **81**, 1774 (1998).

- [5] J. M. Conrad, W. C. Louis, and M. H. Shaevitz, *Annu. Rev. Nucl. Part. Sci.* **63**, 45 (2013).
- [6] F. Kaether, W. Hampel, G. Heusser, J. Kiko, and T. Kirsten, *Phys. Lett. B* **685**, 47 (2010).
- [7] K. N. Abazajian *et al.*, [arXiv:1204.5379](https://arxiv.org/abs/1204.5379).
- [8] S. Gariazzo, C. Giunti, M. Laveder, Y. F. Li, and E. M. Zavanin, *J. Phys. G: Nucl. Part. Phys.* **43**, 033001 (2015).
- [9] Y. J. Ko *et al.* (NEOS Collaboration), *Phys. Rev. Lett.* **118**, 121802 (2017).

- [10] J. Ashenfelter *et al.* (PROSPECT Collaboration), *Phys. Rev. Lett.* **121**, 251802 (2018).
- [11] I. Alekseev *et al.* (DANSS Collaboration), *Phys. Lett. B* **787**, 56 (2018).
- [12] H. Almazán *et al.* (STEREO Collaboration), *Phys. Rev. Lett.* **121**, 161801 (2018).
- [13] A. P. Serebrov *et al.* (Neutrino-4 Collaboration), *arXiv:1805.10561*.
- [14] Y. Abreu *et al.* (SoLid Collaboration), *J. Instrum.* (2017) P04024.
- [15] F. P. An *et al.* (Daya Bay Collaboration), *Phys. Rev. Lett.* **116**, 061801 (2016).
- [16] Y. Abe *et al.* (Double Chooz Collaboration), *J. High Energy Phys.* **10** (2014) 086.
- [17] S. H. Seo *et al.* (RENO Collaboration), *Phys. Rev. D* **98**, 012002 (2018).
- [18] G. Mention, M. Vivier, J. Gaffiot, T. Lasserre, A. Letourneau, and T. Materna, *Phys. Lett. B* **773**, 307 (2017).
- [19] A. C. Hayes and P. Vogel, *Annu. Rev. Nucl. Part. Sci.* **66**, 219 (2016).
- [20] A. C. Hayes, J. L. Friar, G. T. Garvey, D. Ibeling, G. Jungman, T. Kawano, and R. W. Mills, *Phys. Rev. D* **92**, 033015 (2015).
- [21] P. Huber, *Phys. Rev. Lett.* **118**, 042502 (2017).
- [22] C. Buck, A. P. Collin, J. Haser, and M. Lindner, *Phys. Lett. B* **765**, 159 (2017).
- [23] A. C. Hayes, J. L. Friar, G. T. Garvey, G. Jungman, and G. Jonkmans, *Phys. Rev. Lett.* **112**, 202501 (2014).
- [24] D.-L. Fang and B. A. Brown, *Phys. Rev. C* **91**, 025503 (2015).
- [25] A. A. Sonzogni, T. D. Johnson, and E. A. McCutchan, *Phys. Rev. C* **91**, 011301 (2015).
- [26] H. Behrens and W. Bühring, *Electron Radial Wave Functions and Nuclear Beta-Decay* (Clarendon Press, Oxford, 1982).
- [27] L. Hayen, N. Severijns, K. Bodek, D. Rozpedzik, and X. Mougeot, *Rev. Mod. Phys.* **90**, 015008 (2018).
- [28] D. A. Dwyer and T. J. Langford, *Phys. Rev. Lett.* **114**, 012502 (2015).
- [29] H. Behrens and J. Jänecke, *Landolt-Börnstein Tables, Gruppe I, Band 4* (Springer, Berlin, 1969).
- [30] H. Behrens and W. Bühring, *Nucl. Phys. A* **162**, 111 (1971).
- [31] L. Hayen, J. Kostensalo, N. Severijns, and J. Suhonen (unpublished).
- [32] K. Schreckenbach, H. Faust, F. von Feilitzsch, A. Hahn, K. Hawerkamp, and J. Vuilleumier, *Phys. Lett. B* **99**, 251 (1981).
- [33] F. V. Feilitzsch, A. Hahn, and K. Schreckenbach, *Phys. Lett. B* **118**, 162 (1982).
- [34] K. Schreckenbach, G. Colvin, W. Gelletly, and F. Von Feilitzsch, *Phys. Lett. B* **160**, 325 (1985).
- [35] A. A. Hahn, K. Schreckenbach, W. Gelletly, F. von Feilitzsch, G. Colvin, and B. Krusche, *Phys. Lett. B* **218**, 365 (1989).
- [36] N. Haag, W. Gelletly, F. von Feilitzsch, L. Oberauer, W. Potzel, K. Schreckenbach, and A. A. Sonzogni, *arXiv:1405.3501*.
- [37] B. A. Brown and W. D. M. Rae, *Nucl. Data Sheets* **120**, 115 (2014).
- [38] H. Mach, E. K. Warburton, R. L. Gill, R. F. Casten, J. A. Becker, B. A. Brown, and J. A. Winger, *Phys. Rev. C* **41**, 226 (1990).
- [39] R. Machleidt, *Phys. Rev. C* **63**, 024001 (2001).
- [40] S. Lalkovski *et al.*, *Phys. Rev. C* **87**, 034308 (2013).
- [41] B. A. Brown (unpublished).
- [42] J. Kostensalo and J. Suhonen, *Phys. Lett. B* **781**, 480 (2018).
- [43] J. Kostensalo, M. Haaranen, and J. Suhonen, *Phys. Rev. C* **95**, 044313 (2017).
- [44] M. Haaranen, J. Kotila, and J. Suhonen, *Phys. Rev. C* **95**, 024327 (2017).
- [45] J. Suhonen, *Front. Phys.* **5**, 55 (2017).
- [46] L. Bodenstern-Dresler *et al.* (COBRA Collaboration), *arXiv:1806.02254*.
- [47] “Evaluated nuclear structure data file”, <https://www.nndc.bnl.gov/ensdf/> (2018).
- [48] M. Chadwick *et al.*, *Nucl. Data Sheets* **112**, 2887 (2011).
- [49] J. C. Hardy, L. C. Carraz, B. Jonson, and P. G. Hansen, *Phys. Lett. B* **71**, 307 (1977).
- [50] I. Gauld, M. Pigni, and G. Ilas, *Nucl. Data Sheets* **120**, 33 (2014).
- [51] E. Mendoza, F. Álvarez-Velarde, V. Bécáres, D. Cano-Ott, E. González-Romero, T. Martínez, and D. Villamarín, *Nucl. Instrum. Methods Phys. Res. Sect. A* **870**, 60 (2017).
- [52] B. Holstein, *Rev. Mod. Phys.* **46**, 789 (1974).
- [53] N. Severijns, L. Hayen, and I. Towner (unpublished).
- [54] X. B. Wang and A. C. Hayes, *Phys. Rev. C* **95**, 064313 (2017).
- [55] A. C. Hayes, G. Jungman, E. A. McCutchan, A. A. Sonzogni, G. T. Garvey, and X. B. Wang, *Phys. Rev. Lett.* **120**, 022503 (2018).
- [56] D. W. Scott, *Multivariate Density Estimation: Theory, Practice, and Visualization* (Wiley, New York, 1992).
- [57] L. Hayen and N. Severijns, *arXiv:1803.00525*.
- [58] F. P. An *et al.* (Daya Bay Collaboration), *Phys. Rev. Lett.* **108**, 171803 (2012).



## VIII

### FIRST-FORBIDDEN TRANSITIONS IN THE REACTOR ANOMALY

by

Hayen, L., Kostensalo, J., Severijns, N., Suhonen, J. 2019

Physical Review C, 100 (5), 054323.  
DOI: 10.1103/PhysRevC.100.054323

Reproduced with kind permission by American Physical Society.

**First-forbidden transitions in the reactor anomaly**L. Hayen <sup>1,\*</sup>, J. Kostensalo <sup>2</sup>, N. Severijns <sup>1</sup> and J. Suhonen <sup>2</sup><sup>1</sup>*Instituut voor Kern- en Stralingsfysica, KU Leuven, Celestijnenlaan 200D, B-3001 Leuven, Belgium*<sup>2</sup>*Department of Physics, University of Jyväskylä, P.O. Box 35, FI-40014 University of Jyväskylä, Finland*

(Received 22 August 2019; published 20 November 2019)

We describe here microscopic calculations performed on the dominant forbidden transitions in reactor antineutrino spectra above 4 MeV using the nuclear shell model. By taking into account Coulomb corrections in the most complete way, we calculate the shape factor with the highest fidelity and show strong deviations from allowed approximations and previously published results. Despite small differences in the *ab initio* electron cumulative spectra, large differences on the order of several percent are found in the antineutrino spectra. Based on the behavior of the numerically calculated shape factors we propose a parametrization of forbidden spectra. Using Monte Carlo techniques we derive an estimated spectral correction and uncertainty due to forbidden transitions. We establish the dominance and importance of forbidden transitions in both the reactor anomaly and spectral shoulder analysis with their respective uncertainties. Based on these results, we conclude that a correct treatment of forbidden transitions is indispensable in both the normalization anomaly and spectral shoulder.

DOI: [10.1103/PhysRevC.100.054323](https://doi.org/10.1103/PhysRevC.100.054323)**I. INTRODUCTION**

The field associated with short baseline reactor neutrinos has seen tremendous activity in recent years. Faced both with long-standing issues (LNSD [1,2] and GALLEX & SAGE [3,4] collaborations) and more recently the reactor antineutrino anomaly (RAA) [5,6], phenomenology proposes the existence of sterile neutrinos in an effort to solve these issues [7,8]. Besides the normalization anomaly, a spectral disagreement commonly referred to as the “5-MeV bump” remains after several years of intense work [9–13]. Due to the magnitude of the problem in several regards, nuclear theory is pushing the boundaries in getting to grips with theoretical predictions and uncertainties [14].

A central element in the theoretical determination of the antineutrino flux is the theoretical shape of individual  $\beta$  spectra. The original treatments by Huber and Mueller *et al.* [15,16] introduced strong approximations in their treatments of forbidden transitions. Using a sample of experimentally measured shape factors, significant deviations from allowed shape factors were observed throughout the nuclear chart for the majority of forbidden transitions [17], which were considered within the reactor anomaly by Sonzogni *et al.* [18]. In the years following the Huber and Mueller reports, the influence of forbidden transitions has, however, been discussed mostly in general terms [19,20], with microscopic calculations performed only on three nuclei [21]. While both of these studies showed a significant influence on the final result within the context of the RAA, its calculational difficulty presents a serious challenge for a more complete analysis.

Following our earlier work [22], we discuss here the result of a shell model calculation of the dominant forbidden transitions above 4 MeV. This work represents both a more thorough explanation and discussion of our earlier work and an extension as more data were included and more sophisticated methods employed. We start off in Sec. II by revisiting the used formalism, and describe both the included corrections in this work and the breakdown of approximations made in the literature. We review the proper expressions for allowed shape factors and discuss several terms which are missing in previous descriptions and note their significance. In Sec. III we describe our selection and treatment of nuclear databases. We go on to describe the direct results of these calculations in Secs. IV and VII B 1, including an estimate of its uncertainties. We compare our findings to common approximations found in the literature and find strongly diverging results, which we interpret as the breakdown of approximations in the formalism of Sec. II. Further, in Sec. VI we attempt an expansion of the numerical results in a statistical fashion and perform improved summation calculations. Finally, in Sec. VIII we report on the consequences on both the reactor normalization anomaly and the spectral shoulder for the current generation of reactor antineutrino experiments.

**II.  $\beta$  DECAY FORMALISM**

The treatment of (forbidden)  $\beta$  decays is a complex task, compounded by the large proton number of the fission fragments of interest. Its final description is an interplay between kinematic, nuclear, and Coulomb terms with significant potential for cancellations. This leads to a wide variety of potential spectrum shapes and it serves one well to go back to the starting point of the  $\beta$  decay description. Our discussion here will be relatively extensive since no such overview is currently present in the literature surrounding the RAA, even though

\*Corresponding author: [lmhayen@ncsu.edu](mailto:lmhayen@ncsu.edu); present address: Department of Physics, North Carolina State University, Raleigh, North Carolina 27695, USA; Triangle Universities Nuclear Laboratory, Durham, North Carolina 27708, USA.

a correct analysis hinges critically on a correct assessment of all intricacies and moving parts. In the case of forbidden decays this fact is amplified, as will become clear in later sections. All results are written in units natural for  $\beta$  decay, i.e.,  $\hbar = c = m_e = 1$ , unless explicitly mentioned.

Employing the usual Fermi contact interaction, the correct generalization of the tree-level transition matrix element in the presence of electromagnetic effects is given by [23,24]

$$\begin{aligned} \mathcal{M}_{fi} = & \int d^3r \bar{\phi}_e(\vec{r}, \vec{p}_e) \gamma^\mu (1 + \gamma^5) v(\vec{p}_v) \\ & \times \int \frac{d^3s}{(2\pi)^3} e^{i\vec{s}\cdot\vec{r}} \frac{1}{2} [ \langle f(\vec{p}_f + \vec{p}_e - \vec{s}) | V_\mu + A_\mu | i(\vec{p}_i) \rangle \\ & + \langle f(\vec{p}_f) | V_\mu + A_\mu | i(\vec{p}_i - \vec{p}_e + \vec{s}) \rangle ], \end{aligned} \quad (1)$$

where  $\bar{\phi}_e$  is the solution to the Dirac equation in the static Coulomb potential of the final state and  $V_\mu + A_\mu$  is the usual weak interaction current. Equation (1) reveals two important, intertwined contributions: (i) nuclear structure effects encoded in the weak interaction current in the inner integral; (ii) Coulomb influences represented by the outer integral through the use of the electron wave function in the static Coulomb potential of the final state.

Direct consequences of this form are a renormalization of the matrix element from extraction of the electron density at the origin,<sup>1</sup>  $|\phi_e(0, \vec{p}_e)|^2$ , resulting in the usual Fermi function. The electron continuum wave function varies significantly within the nuclear volume, however, so that its radial dependence couples directly to that of the nuclear weak interaction current. Besides the Fermi function then, the traditional nuclear structure terms can be modified significantly for higher  $Z$  through the convolution with the electron continuum wave function. We will discuss the influence of both of these separately.

Combining Eq. (1) with the available phase space, the  $\beta$  spectrum shape is traditionally written as

$$\begin{aligned} \frac{dN}{dW} = & \frac{G_V^2 V_{ud}^2}{2\pi^3} pW(W - W_0)^2 \\ & \times F(Z, W)C(Z, W)K(Z, W) \end{aligned} \quad (2)$$

with  $W = E_{kin}/m_e c^2 + 1$  the total electron energy in units of its rest mass,  $W_0$  the spectral end point,  $p = \sqrt{W^2 - 1}$  the electron momentum in units of  $m_e c$ ,  $Z$  the atomic number of the final state,  $F(Z, W)$  the well-known Fermi function,  $C(Z, W)$  the so-called shape factor, and  $K(Z, W)$  higher-order correction terms [25]. All nuclear structure information resides in the shape factor  $C$ , which depends primarily on the degree of forbiddenness of the decay. The Fermi function and higher-order corrections are known to a sufficient level [14,25], making the shape factor  $C$  the primary target in this work.

<sup>1</sup>Rigorously, it corresponds to the extraction of the large components of the  $j = 1/2$  ( $s_{1/2}$  and  $p_{1/2}$ ) wave functions at the origin. Small components, higher- $j$  components, radial dependence, etc., are commonly noted by “finite size corrections” which appear later in this work and are extensively discussed elsewhere [25].

One can generally write the shape factor as [26,27]

$$\begin{aligned} C(Z, W) = & \sum_{k_e, k_v, K} \lambda_{k_e} \left\{ M_K^2(k_e, k_v) + m_K^2(k_e, k_v) \right. \\ & \left. - \frac{2\mu_{k_e} \gamma_{k_e}}{k_e W} M_K(k_e, k_v) m_K(k_e, k_v) \right\}, \end{aligned} \quad (3)$$

where

$$\lambda_{k_e} = \frac{\alpha_{-k_e}^2 + \alpha_{+k_e}^2}{\alpha_{-1}^2 + \alpha_{+1}^2}, \quad (4)$$

$$\mu_{k_e} = \frac{\alpha_{-k_e}^2 - \alpha_{+k_e}^2}{\alpha_{-k_e}^2 + \alpha_{+k_e}^2} \frac{k_e W}{\gamma_{k_e}} \quad (5)$$

are Coulomb functions depending on the so-called Coulomb amplitudes  $\alpha_\kappa$ , which encode the value of the electron wave function at the origin. The integers  $k_e, k_v$  are defined as  $|k_{e,v}|$  where  $k_{e,v}$  is related to the angular momenta in the usual way.<sup>2</sup> Contributions from different  $k_{e,v}$  come from the expansion of the lepton wave functions in spherical waves. The integer  $K$  corresponds to the multipolarity of the relevant nuclear current, and must form a vector triangle with  $j_e$  and  $j_v$  as well as with the nuclear spins  $J_i$  and  $J_f$ . We have then  $|J_i - J_f| \leq K \leq J_i + J_f$  from the nuclear vector triangle. Finally,  $M_K(k_e, k_v)$  and  $m_K(k_e, k_v)$  contain the convolution of leptonic wave functions and nuclear structure information encoded as form factors. Appropriately, the capital letter contribution contains the dominant terms, so that typically one neglects the second term in Eq. (3).

In conclusion then, the shape factor  $C$  as defined in Eqs. (2) and (3) depends on three things: (i) the spin change of the transitions and the corresponding appearance of kinematical factors ( $W, p$ ) and form factors; (ii) finite size corrections proportional to  $R^n$  resulting from the integration over the nuclear volume; (iii) Coulomb corrections proportional to  $(\alpha Z)^n$  resulting from the expansion of the electron wave function. The final shape factor will be a combination of all three with various cross terms.

### A. Nuclear structure

In contrast to their nomenclature, so-called forbidden transitions correspond to  $\beta$  decays for which the main Fermi and Gamow-Teller matrix elements are identically zero due to spin-parity requirements or internal nuclear structure. As a consequence, their decays are perpetuated by matrix elements that are typically strongly suppressed and are consequently heavily dependent on nuclear structure effects and prone to accidental cancellations.

We briefly review a scheme to systematically classify their behavior, the so-called *elementary particle treatment*. This entails that initial and final nuclear states are treated as fundamental particles and all interaction dynamics is encoded through form factors which obey angular momentum conservation  $F(q^2)$ , with  $q$  the momentum transfer between initial

<sup>2</sup>Here  $\kappa$  is the eigenvalue of the operator  $K = \beta(\sigma L + 1)$ , such that  $k = |\kappa| = j + \frac{1}{2}$ ,  $\kappa = -l - 1$  if  $l = j + \frac{1}{2}$ , and  $\kappa = l$  if  $l = j - \frac{1}{2}$ .

and final nuclear states. It shines in the case of nuclear decays because of the (near-)spherical symmetry of the system at hand and the smallness of the momentum transfer with respect to the nuclear mass. The latter means that we are usually only concerned with the form factors near zero momentum transfer,  $F(0) \equiv F$ . The former implies that through conservation of angular momentum one can construct a multipole decomposition of both the nuclear and leptonic currents in terms of (vector) spherical harmonics for the timelike (spacelike) component. In the Behrens-Bühhing formalism that we follow here [27], this allows one to label the nuclear structure form factors using three numbers:  $K$ ,  $L$ , and  $s$ , being the total and orbital angular momentum of the nuclear current and its timelike (0) or spacelike (1) nature, respectively. The form factors are denoted by  ${}^{V/A}F_{KLS}$ . The three quantum numbers form a vector triangle, and the parity requirement can be summarized as

$$\begin{aligned} \pi_i \pi_f &= (-)^{L+s} && \text{vector contributions} \\ \pi_i \pi_f &= (-)^{L+s+1} && \text{axial vector contributions,} \end{aligned} \quad (6)$$

where  $\pi$  is the parity of initial and final nuclear state. Conservation of angular momentum then limits the number of contributing form factors for a specific transition with spin-parity change  $\Delta J^\pi$ .

In this work we focus on first-forbidden  $\beta$  transitions, i.e.,  $\Delta J = 0, 1, 2$  and  $\pi_i \pi_f = -1$ . To first order this limits the number of form factors to 6. In order to proceed with an actual calculation, each of these must be translated into nuclear matrix elements,  ${}^{V/A}\mathcal{M}_{KLS}$ . This is commonly done by introducing the impulse approximation, in which all nucleons inside a nucleus are treated as independent particles in a mean-field potential. This neglects multiparticle correlations and meson exchange effects, the effects of which are put in manually through effective interactions in the usual shell-model fashion [28,29]. We briefly report on the expected shape factors for different  $\Delta J$ .

For a pure pseudoscalar transition ( $0^+ \leftrightarrow 0^-$ ) only two form factors contribute. It is dominated by  ${}^A F_{000}$  which translates into the traditional pseudoscalar matrix element  ${}^A \mathcal{M}_{000} = -g_A \int \gamma_5$ , and receives first-order corrections from  ${}^A F_{011} \rightarrow {}^A \mathcal{M}_{011} = -g_A \int i(\boldsymbol{\sigma} \cdot \mathbf{r})/R$ . Here  $R$  is the nuclear radius and is  $\mathcal{O}(10^{-2})$  in our units. The shape factor can then be written as

$$C_{0^-} \propto 1 + \frac{2R}{3W} b + \mathcal{O}(\alpha ZR, W_0 R^2) \quad (7)$$

after extraction of the main matrix element. Here  $b = {}^A \mathcal{M}_{011}^{(0)}/{}^A \mathcal{M}_{000}^{(0)} \sim \mathcal{O}(-1)$  and  $\alpha$  is the fine-structure constant.

Moving on to a pure pseudovector transition ( $1^{+(-)} \leftrightarrow 0^{-(+)}$ ), three matrix elements contribute significantly and it is *a priori* not possible to establish a hierarchy leading to an analog of Eq. (7). Instead, we write

$$C_{1^-} \propto 1 + aW + \mu_1 \gamma_1 \frac{b}{W} + cW^2, \quad (8)$$

inspired by the general form of Eq. (3), where  $a, b, c$  are free parameters.

In the case of unique forbidden decays, only one form factor contributes to first order and Eq. (3) simplifies significantly, so that one is left with

$$C_U \propto \sum_{k=1}^L \lambda_k \frac{p^{2(k-1)} q^{2(L-k)}}{(2k-1)! [2(L-k)+1]!}, \quad (9)$$

after extraction of the prefactor, where  $L$  is the maximum angular momentum change.

## B. Coulomb corrections

The shape factor of Eq. (3) is a result of the convolution of the leptonic and nucleonic wave functions written in Eq. (1). The change due to the leptonic wave function  $\phi_e$  resulting from the Coulomb interaction can be seen as (i) a renormalization at the origin, and (ii) a modified radial behavior inside the nuclear volume. We discuss both in turn.

### 1. Static Coulomb renormalization

As noted at the start of this section, one traditionally extracts the large components of the  $j = 1/2$  electron wave function at the origin, denoted by  $\alpha_\kappa$  in the Behrens-Bühhing formalism. Here  $\kappa$  takes the values  $-1$  ( $s_{1/2}$ ) or  $+1$  ( $p_{1/2}$ ) so that the Fermi function is defined as

$$F_0(Z, W) = \frac{\alpha_{-1}^2 + \alpha_{+1}^2}{2p^2}. \quad (10)$$

Corrections from the small components or higher- $j$  components then introduce the  $\mu_{k_e}$  [Eq. (5)] and  $\lambda_{k_e}$  [Eq. (4)] functions, respectively. In the region of interest, it is safe to set  $\mu_{k_e}$  to unity [30] so that we focus our attention instead on  $\lambda_{k_e}$ . For a point-charge nucleus, it can be written as [27]

$$\lambda_k = \frac{F_{k-1}}{F_0} \frac{k + \gamma_k}{k(1 + \gamma_1)}, \quad (11)$$

where  $k = |\kappa|$ , and

$$\gamma_k = \sqrt{k^2 - (\alpha Z)^2} \quad (12)$$

is the generalized  $\gamma$  parameter,

$$\begin{aligned} F_{k-1} &= [k(2k-1)!!]^2 4^k (2pR)^{2(\gamma_k-k)} \exp(\pi y) \\ &\times [|\Gamma(\gamma_k + iy)|/\Gamma(1 + 2\gamma_k)]^2 \end{aligned} \quad (13)$$

is the generalized Fermi function, and

$$y = \frac{\alpha ZW}{p}. \quad (14)$$

While its influence is negligible in allowed decays except for extreme cases, it features quite prominently in forbidden transitions. The value of  $\lambda_2$ , for example, can exceed 10 for very low momenta and does not converge to unity at large momenta like the Fermi function [30]. We explicitly discuss its influence in the following section in the context of unique decays.

### 2. Coulombic convolution distortion

Beyond the renormalization of the electron wave function at the origin, the radial behavior near the nucleus becomes

modified due to the Coulomb potential. As the potential grows deeper with increasing  $Z$ , the electron density is greatly increased within the nuclear volume, so that the shape of the nuclear charge density also plays a role. One expands the electron wave function in terms of  $(m_e R)^a$ ,  $(WR)^b$ , and  $(\alpha Z)^c$ , where the details of the Coulomb potential are encoded in functions<sup>3</sup>  $I(k_e, m, n, \rho)$ . Following the result of Eq. (1) this requires a generalization of the nuclear form factors and matrix elements according to the following notation:

$$\mathcal{M}_{KLS}^{(n)} \longrightarrow \mathcal{M}_{KLS}^{(n)}(k_e, m, n, \rho), \quad (15)$$

where now

$$\mathcal{M}_{KLS}^{(n)}(k_e, m, n, \rho) = \int dr r^2 \phi_f(r) O_{KLS}^{(n)} \times I(k_e, m, n, \rho; r) \phi_i(r), \quad (16)$$

where  $O_{KLS}^{(n)}$  is the relevant operator and  $\phi_{i,f}$  represent initial and final nuclear wave functions. The Coulomb shape functions,  $I(k_e, m, n, \rho; r)$ , are tabulated in [26] and depend on the charge distribution of the nucleus. Terms with large values for  $m$ ,  $n$ , or  $\rho$  are typically strongly suppressed, resulting in rather slight modifications of the main matrix elements. The modified matrix elements enter the shape factor of Eq. (3), however, accompanied by factors of  $\alpha Z$  and  $W_0 R$  resulting from the electron Coulomb-corrected wave function expansion. As such, the additional terms for nuclei in the fission fragment region are highly non-negligible. In the case of cancellation effects, these Coulomb terms can even become the dominant contributions for the shape factor.

### C. Breakdown of usual approximations

Some general remarks are essential at this point in order to both understand previous approximations and their breakdown, discussed below.

(i) Equation (7) was derived assuming a *pure* pseudoscalar transition. Many  $\Delta J^\pi = 0^-$  transitions occur, however, between higher-spin partners meaning higher-order matrix elements can equally contribute. This can significantly change the energy dependence. Analogously, pseudovector contributions can contain contributions from  $\Delta J = 2$  matrix elements.

(ii) Neglecting the electron mass and Coulomb interaction, Eq. (9) is symmetric when interchanging electron and antineutrino energies. This has been used as an argument to neglect forbidden transitions within the context of the RAA [15,16]. This argument is invalid, however, for nonunique transitions [Eqs. (7) and (8)] which occur more frequently than anticipated as we shall see in Sec. VI. Additionally, we will show explicitly that Coulomb corrections significantly distort the shape factor, breaking the purported symmetry, even for unique transitions.

We discuss the breakdown of the usual approximations both for nonunique transitions and unique transitions, which typically occur for different reasons.

<sup>3</sup>Here  $m = a + b + c$  represents the total power of  $mR$ ,  $WR$ , and  $\alpha Z$ ,  $n = b + c$  is the total power of  $WR$  and  $\alpha Z$ , and  $\rho$  is the power of  $\alpha Z$ . One has trivially that  $I(k_e, m, n, 0) = 1$ .

### I. Nonunique forbidden transitions: $\xi$ approximation

In general the shape factor for nonunique decays is governed by four to six matrix elements for pseudovector and pseudoscalar transitions, respectively. It has long been known, however, that only certain linear combinations appear. Some of these contain the so-called Coulomb energy,  $\alpha Z/R \equiv 2\xi$ , its large magnitude making it useful as an expansion parameter.<sup>4</sup> In the so-called  $\xi$  approximation, one retains the shape factor only to order  $\xi^2$  [31,32]. The particular benefit of this approximation is that it leaves the shape factor mostly energy independent, as all kinematical terms contain lower powers of  $\xi$ . This leaves all quantities (such as the spectrum shape, the  $\beta$ - $\gamma$  correlation, etc.) equal to the results of allowed transitions up to order  $1/\xi \sim 10\%$ . Based on the general formulation of Eq. (8), it is a valid approximation when

$$2\xi = \frac{\alpha Z}{R} \gg W_0, \quad (17)$$

where  $W_0$  is the end point of the transition. For the relevant fission fragments, however, this approximation is of questionable worth in the experimentally accessible regime. Using typical values for  $Z$  encountered in a nuclear reactor one obtains rather  $\alpha Z/2R \sim W_0$  for end-point energies of a few MeV. Substantial changes are expected to occur based on this breakdown alone. It is well known, however, that even though Eq. (17) might hold, the  $\xi$  approximation can fail [33]. This is either due to cancellation effects, or through selection rules originating from the underlying nuclear structure and collective behavior. This has been demonstrated explicitly in Ref. [17] where a large sample of experimentally measured shape factors were compared to an allowed approximation. Besides the unique forbidden transitions (discussed in the next section), the majority of nonunique forbidden  $\beta$  transitions showed a shape factor significantly deviating from unity. We will demonstrate several examples of this occurrence in our discussion of the numerical results in Sec. IV.

### 2. Unique transitions: Coulomb functions

Unique transitions have a particular simplicity as only one matrix element contributes to first order. Its shape factor for first-forbidden transitions is simply

$$C_{2-} \propto p_\nu + \lambda_2 p_e^2, \quad (18)$$

where  $p_\nu = W_0 - W$  is the antineutrino momentum. As mentioned before,  $\lambda_2$  [Eq. (4)] is a Coulomb function of order unity. On the percent level precision, however, setting it to unity is unsatisfactory for the region of interest for the RAA. This was also touched upon in Ref. [17]. As an example, we consider the change in the spectrum shape due to the influence of these Coulomb functions on first and second unique forbidden decays. We consider a fictional transition in the region of interest, with  $Z = 50$  and end-point energy  $E_0 = 6$  MeV. The relative change in spectral shapes can be seen in Fig. 1, where we normalize the shape factor to unity at the start of the spectrum. Here we included, in addition, the results when

<sup>4</sup>Remember that in our choice of units  $R \sim \mathcal{O}(0.01)$ .

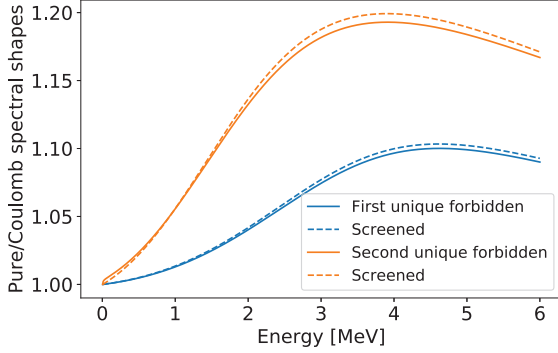


FIG. 1. Change in the unique forbidden spectral shape when using the appropriate  $\lambda_k$  Coulomb functions instead of approximating them as unity for a  $\beta$  transition with  $Z = 50$  and  $E_0 = 6$  MeV. Full lines represent unscreened ratios, while dashed lines represent the screened ratios for the different  $\lambda_k$ .

introducing screening corrections to the Coulomb functions as described in Ref. [34].

As can be observed, besides the clear deviation from allowed shapes in the parabolic expression of Eq. (18), setting  $\lambda_2$  to unity introduces additional discrepancies rising to 10–20%. The increased numerical effort in including screening corrections is not expected to contribute substantially in cumulative  $\beta$  spectra and will be omitted for the remainder of this work.

#### D. On allowed shape factors

Several different expressions have been utilized for allowed shape factors throughout the literature within the context of the reactor antineutrino anomaly. As the results presented in this work depend not only on the shape factor of forbidden transitions but equally on its ratio to that of allowed transitions, we briefly review previous expressions and point out their deficiencies.

In general, the shape factor is constructed in the rather opaque way of Eq. (3). A particular advantage of allowed transitions, however, is their dominance of a single matrix element which simplifies its form dramatically. Compared to the main Fermi or Gamow-Teller matrix elements, corrections are usually on the order of only a few percent. This motivates one to write down the shape factor in its most crude form,

$$C \approx 1. \quad (19)$$

Within the context of the RAA, the original works by Mueller *et al.* [16] and Huber [15] have gone beyond Eq. (19) to varying degrees. While important differences appear for the “regular” finite size corrections [Eqs. (8) and (9) in Ref. [15] and Eq. (8) in Ref. [16]], the correction due to induced currents is similar, and only takes into account a weak magnetism correction term:

$$1 + \delta_{\text{wm}} = 1 + \frac{4}{3M_n} \frac{b}{Ac} W, \quad (20)$$

where  $M_n \approx 1830$  is the nucleon mass in our units,  $A$  is the nuclear mass number, and  $b/c$  is the ratio of weak magnetism and Gamow-Teller form factors in the well-known Holstein formalism [35]. In impulse approximation the latter simplifies to

$$\frac{b}{Ac} = \frac{1}{g_A} \left( g_M + g_V \frac{M_L}{M_{\text{GT}}} \right). \quad (21)$$

Here  $g_A = 1.27$  is the axial vector coupling constant,  $g_M = 4.706$  is the weak magnetism coupling constant,  $M_L = \langle f | \tau^\pm \vec{l} | i \rangle$  is the orbital angular momentum matrix element, and  $M_{\text{GT}}$  is the main Gamow-Teller matrix element. When proton and neutron Fermi surfaces are strongly separated, the ratio  $M_L/M_{\text{GT}}$  is usually approximated as  $-1/2$  [36], so that  $b/Ac \approx 4.2/g_A$ . In previous analyses [15,16], a constant value was taken so that  $dN/dE = 0.67\% \text{ MeV}^{-1}$ , extracted from an analysis of mirror decays for low masses. While large-scale calculations show significant variation around this value [36], we choose to use this value so that effects from forbidden decays can be cleanly separated.

The above expressions correspond to rather strong approximations. In fact, comparing to the full expressions [e.g., Eqs. (106a)–(106d) in Ref. [25]], several differences appear which require some pause. Starting with the weak magnetism correction, we note that  $\delta_{\text{wm}}$  should be written more completely:

$$\delta_{\text{wm}} = \frac{4}{3M_n} \frac{b}{Ac} \left( W - \frac{1}{2W} - \frac{W_0}{2} - \frac{3}{5} \frac{\alpha Z}{R} \right). \quad (22)$$

The last two terms are energy independent but serve to renormalize the shape factor. The second term is energy dependent and of opposite sign to the leading term. Its influence is most important in the low energy range, where in the context of the RAA it is unconstrained by the ILL data set. As with any low energy effect, however, it shows up throughout the entire antineutrino spectrum and collectively changes the integrated antineutrino flux.

Further, in the case of allowed transitions the weak magnetism correction is not the only effect due to induced currents, as also the induced tensor term is nonzero for a general Gamow-Teller transition. One then requires an additional term which so far has never been taken into account:

$$\delta_{\text{it}} = \frac{1}{3M_n} \frac{d}{Ac} \left( W_0 + \frac{6}{5} \frac{\alpha Z}{R} - \frac{1}{W} \right). \quad (23)$$

In general,  $d/Ac$  is only identically zero for transitions within an isospin multiplet such as the mirror decays that were used for the weak magnetism correction by Huber [15]. For all remaining Gamow-Teller decays, however,  $d/Ac$  is generally of comparable magnitude as  $b/Ac$  and can easily exceed it by a factor ( $\sim 5$ ) on a case-by-case basis.

Finally, allowed decays obtain corrections from another form factor with a similar structure as several finite size correction terms. In the Holstein formalism [35], it is related to the induced pseudoscalar contribution  $h(q^2)$ . Writing only the dominant term within the context of the RAA, the main terms

are modified through the appearance of a  $\Lambda'$  contribution [25],

$$\delta_{\text{fs}} \approx (\Lambda' - 1) \left[ \frac{21}{35} \alpha ZWR + \frac{4}{9} (W - W_0) WR^2 \right], \quad (24)$$

where

$$\Lambda' = \frac{\sqrt{2} \mathcal{M}_{121}}{3 \mathcal{M}_{101}} \quad (25)$$

is of order unity and can vary substantially on a case-by-case basis. This  $\Lambda'$  contribution has so far never been taken into account. As such, the finite size corrections applied regularly in the RAA community [compare, e.g., Eq. (24) with Eq. (9) of [15]] can easily vanish or even change sign.

It should be clear by now that the shape factors used for allowed decays in the RAA analysis suffer from missing terms and an uncertain evaluation of the terms it does include. The effect on the anomaly itself and its uncertainty estimation will depend critically on a more careful evaluation and is the topic of ongoing research.

In order to investigate the effect of the calculated forbidden shape factors presented here, we compare our results against, respectively, Eq. (19) and including only the weak magnetism correction as in Eq. (20). This corresponds, approximately, to setting  $\Lambda'$  equal to 0 and 1, respectively, for  $Z \sim 50$ . The effects of Eqs. (22)–(24) are commented upon later and will be investigated in a future work.

### III. DATA SELECTION AND HANDLING

The success of the summation approach hinges on the quality of the nuclear databases for fission yields and decay information [16,37]. This is particularly true for our discussion here, as the impact of first-forbidden transitions depends critically on the knowledge of nuclear level schemes with well-determined spin parities and branching ratios. As such, we briefly discuss our selection and treatment of database information in the context of our later results in Secs. IV B, V, and VI.

#### A. Database selection

In terms of decay data, there are several evaluated public databases available. Of these, the Evaluated Nuclear Structure Data File (ENSDF) database is well known but recent total absorption gamma spectroscopy (TAGS) [38–43] measurements have identified several discrepancies regarding branching ratios and level density. Previous measurements suffered from the so-called pandemonium effect [44], where due to the rapidly decreasing efficiency of germanium detectors for high  $\gamma$  energies deexcitations from highly excited states were missed, thereby overestimating  $\beta$  branching ratios to low-lying states. This problem was apparent also in the context of the reactor anomaly in the significant overestimation of the flux in the high energy part [16,37].

As a consequence, the absolute predictions of the electron and antineutrino flux based on the ENSDF library are highly flawed. We have taken several measures here to mitigate this effect. The first lies in a required correspondence with the Schreckenbach cumulative electron spectra measured at the

ILL [45–47]. Additionally, we present our results as a relative difference between the allowed approximation and our more sophisticated approach. Finally, we choose instead to use a tuned version of the ENSDF library instead. As such, we have opted here for the ENDF/B-VIII.0 (ENDF) decay data library [48]. In the latest version, several TAGS results were already incorporated. Additionally, consistency with reactor decay heat and a multitude of additional sources is checked [49]. We do not, however, include the theoretically calculated  $\beta$  spectra that are provided with the library, as these are based on gross theory which does not agree well with recent TAGS measurements.

For the purpose of this work we are particularly interested in the spin parities of nuclear levels. As such, we have made a combination of ENDF and ENSDF data in the following manner: Nuclear level energies and branching ratios are taken from ENDF and when a match is found with the ENSDF data we use the spin-parity information of the latter. This is because in ENDF,  $\beta$  transitions are labeled explicitly only in the case of unique (forbidden) decays. In this way we benefit from pandemonium-corrected data but maintain nuclear level information.

For the fission yields we have used cumulative yields of the JEFF3.3 database [50], which are to be preferred over those of ENDF [51]. This is different compared to our previous work [22], where the latter were used. For consistency, we report our results using both JEFF3.3 and ENDF fission yields together with the decay data of the latter as elaborated upon above. While differences arise for individual isotopes [9], overall differences within the context of this work are minimal.

#### B. Data treatment

The nuclear databases are known to be incomplete for some regions of the nuclear chart. For some isotopes no (full) level schemes or branching ratios are known. If a particular isotope is populated in the fission process but contains incomplete or no data at all, we employ the so-called  $Q_\beta$  approximation. The latter consists of filling the remaining  $\beta$  branching by dividing it equally among a number of transitions. In the usual case, three branches are artificially created with end points at  $\{Q, 2Q/3, Q/3\}$  where  $Q$  is the  $Q$  value of the  $\beta$  decay. In the case of the ENDF Decay Database, certain isotopes do not contain “discrete” information of transitions to specific final states but instead contain continuous spectrum data [52–54]. Within the context of reactor antineutrinos this poses a challenge for its inversion. We will treat this point more extensively in Sec. VII A.

When combining ENDF decay data with ENSDF level information, we assume the transition to be allowed if spin-parity determinations are incomplete or uncertain if the reported possibilities allow for it. Besides this, no information is replaced from the ENDF decay database.

### IV. SHAPE FACTOR CALCULATION

We proceed with the explicit calculation of a large sample of first-forbidden (non)unique transitions using the nuclear

shell model. Based on the discussion in Sec. II C we expect significant changes in the spectral shapes due to the breakdown of the usual approximations in the region of interest. Note that in the numerical results presented here, no approximations were made in the description of the shape factor, such as presented in Eqs. (7)–(9).

### A. Selected transitions

In the high energy region of the spectrum, i.e., larger than 4 MeV, the electron flux can be largely described using a limited number of  $\beta$  branches. These have been compiled by Sonzogni *et al.* [55], and in the following years several of these isotopes have been investigated using total absorption gamma spectroscopy (TAGS) [38–43]. This has for many isotopes resulted in a correction of branching ratios to high-lying states which had previously eluded due to the pandemonium effect [44]. Inspired by the compilation of Ref. [55], we calculated 36 dominant forbidden transitions with the nuclear shell model, all of which are first forbidden. Note that we have included here more transitions than the 29 that were included in our previously published work [22]. A summary of their properties is shown in Table I. A large fraction of these are so-called pseudoscalar  $\Delta J^\pi = 0^-$  transitions. Additionally, the initial and final states are either ground states or low-lying states, for which we can expect the nuclear shell model to perform adequately.

### B. Flux coverage

The transitions of Table I were selected for their large contribution to the total cumulative flux based on the compilation by Sonzogni *et al.* [55]. In order to obtain a full spectrum shape for each transition, we combine the shape factor formalism of the previous section with the additional corrections to the  $\beta$  spectrum shape [25,56] to form the full  $\beta$  spectrum of Eq. (2). Summing the individual contributions of each of the transitions weighted by its fission yield and branching ratio discussed in Sec. III, we obtain a partial cumulative forbidden spectrum. Figure 2 shows the contribution of the latter relative to the measured spectra at the ILL for  $^{235}\text{U}$  [47].

By including only 36 transitions, we reach 40% of the total flux in the entire region between 4 and 7 MeV, while the maximum contribution exceeds 50% around 6 MeV. Comparing with the results compiled by Sonzogni *et al.* [55] we find that inclusion of the dominant allowed  $\beta$  spectra brings the total cumulative flux upwards of 80% in this region. In conclusion, within the region of interest the chosen sample of transitions corresponds to a significant fraction of the total flux and our explicit calculation of their shape factor significantly influences the spectrum shape in this region.

### C. Nuclear shell model

The shape factor for each of the transitions was calculated in the formalism by Behrens and Bühring using the nuclear shell model. No approximations were made concerning the formulation of the shape factors, so that the only dominant uncertainty comes from the shell model calculation of the nuclear matrix elements. These calculations were performed

TABLE I. Dominant forbidden transitions above 4 MeV. Here  $Q_\beta$  is the ground-state to ground-state  $Q$  value,  $E_{ex}$  the excitation energy of the daughter level, BR the branching ratio of the transition normalized to one decay and FY the cumulative fission yield of  $^{235}\text{U}$  from the ENDF database [53]. Transitions with small fission yields shown here contribute substantially more for  $^{238}\text{U}$  and  $^{241}\text{Pu}$ .

Nuclide	$Q_\beta$ (MeV)	$E_{ex}$ (MeV)	BR (%)	$J_i^\pi \rightarrow J_f^\pi$	FY (%)	$\Delta J$
$^{89}\text{Br}$	8.3	0	16	$3/2^- \rightarrow 3/2^+$	1.1	0
$^{90}\text{Rb}$	6.6	0	33	$0^- \rightarrow 0^+$	4.5	0
$^{91}\text{Kr}$	6.8	0.11	18	$5/2^+ \rightarrow 5/2^-$	3.5	0
$^{92}\text{Rb}$	8.1	0	95.2	$0^- \rightarrow 0^+$	4.8	0
$^{93}\text{Rb}$	7.5	0	35	$5/2^- \rightarrow 5/2^+$	3.5	0
$^{94}\text{Y}$	4.9	0.92	39.6	$2^- \rightarrow 2^+$	6.5	0
$^{95}\text{Rb}^a$	9.3	0.68	5.9	$5/2^- \rightarrow 5/2^+$	1.7	0
$^{95}\text{Sr}$	6.1	0	56	$1/2^+ \rightarrow 1/2^-$	5.3	0
$^{96}\text{Y}$	7.1	0	95.5	$0^- \rightarrow 0^+$	6.0	0
$^{97}\text{Y}$	6.8	0	40	$1/2^- \rightarrow 1/2^+$	4.9	0
$^{98}\text{Y}$	9.0	0	18	$0^- \rightarrow 0^+$	1.9	0
$^{133}\text{Sn}$	8.0	0	85	$7/2^- \rightarrow 7/2^+$	0.1	0
$^{135}\text{Te}$	5.9	0	62	$(7/2^-) \rightarrow 7/2^+$	3.3	0
$^{135}\text{Sb}$	8.1	0	47	$(7/2^+) \rightarrow (7/2^-)$	0.1	0
$^{136m}\text{I}$	7.5	1.89	71	$(6^-) \rightarrow 6^+$	1.3	0
$^{136m}\text{I}$	7.5	2.26	13.4	$(6^-) \rightarrow 6^+$	1.3	0
$^{137}\text{I}$	6.0	0	45.2	$7/2^+ \rightarrow 7/2^-$	3.1	0
$^{142}\text{Cs}$	7.3	0	56	$0^- \rightarrow 0^+$	2.7	0
$^{86}\text{Br}$	7.3	0	15	$(1^-) \rightarrow 0^+$	1.6	1
$^{86}\text{Br}$	7.3	1.6	13	$(1^-) \rightarrow 2^+$	1.6	1
$^{87}\text{Se}$	7.5	0	32	$3/2^+ \rightarrow 5/2^-$	0.8	1
$^{89}\text{Br}$	8.3	0.03	16	$3/2^- \rightarrow 5/2^+$	1.1	1
$^{91}\text{Kr}$	6.8	0	9	$5/2^+ \rightarrow 3/2^-$	3.4	1
$^{95}\text{Rb}^a$	9.3	0.56	6.0	$5/2^- \rightarrow (7/2^+)$	1.7	1
$^{95}\text{Rb}$	9.3	0.68	5.9	$5/2^- \rightarrow 3/2^+$	1.7	1
$^{134m}\text{Sb}$	8.5	1.69	42	$(7^-) \rightarrow 6^+$	0.8	1
$^{134m}\text{Sb}$	8.5	2.40	54	$(7^-) \rightarrow (6^+)$	0.8	1
$^{136}\text{Te}$	5.1	0	8.7	$0^+ \rightarrow (1^-)$	3.7	1
$^{138}\text{I}$	8.0	0	26	$(1^-) \rightarrow 0^+$	1.5	1
$^{140}\text{Xe}$	4.0	0.08	8.7	$0^+ \rightarrow 1^-$	4.9	1
$^{140}\text{Cs}$	6.2	0	36	$1^- \rightarrow 0^+$	5.7	1
$^{143}\text{Cs}$	6.3	0	25	$3/2^+ \rightarrow 5/2^-$	1.5	1
$^{88}\text{Rb}$	5.3	0	76.5	$2^- \rightarrow 0^+$	3.6	2
$^{94}\text{Y}$	4.9	0	41	$2^- \rightarrow 0^+$	6.5	2
$^{95}\text{Rb}$	9.3	0	0.1	$5/2^- \rightarrow 1/2^+$	1.7	2
$^{139}\text{Xe}$	5.1	0	15	$3/2^- \rightarrow 7/2^+$	5.0	2

<sup>a</sup>The spin-parity designation is uncertain, and shape factors were calculated for both options. Due to small branching ratios, the effect on the cumulative spectrum is negligible.

using the shell model code NUSHELLX@MSU [57]. For nuclei with  $A < 100$  the effective interaction  $\text{g1epn}$  [58] was adopted in a full model space consisting of the proton orbitals  $0f_{5/2} - 1p - 0g_{9/2}$  and the neutron orbitals  $1d - 2s$ . The  $^{86}\text{Br}$  and  $^{89}\text{Br}$  cases were calculated using the interaction  $\text{jj45pna}$  [59,60], in the full model space spanned by the proton orbitals  $0f_{5/2} - 1p - 0g_{9/2}$  and the neutron orbitals  $0g_{7/2} - 2s - 1d - 0h_{11/2}$ . For the nuclei with  $A = 133-142$  the Hamiltonian  $\text{jj56pnb}$  [61] was used in the full model space spanned by the proton orbitals  $0g_{7/2} - 1d - 2s - 0h_{11/2}$

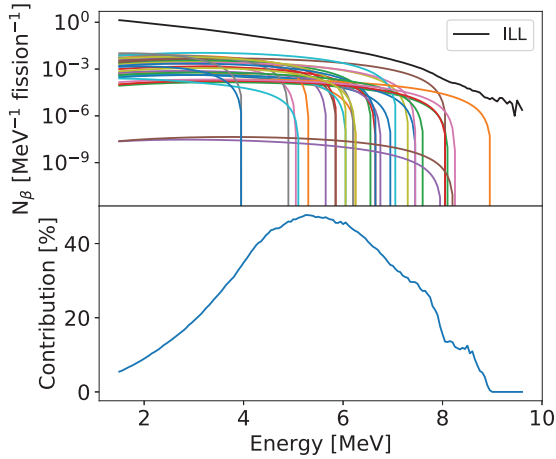


FIG. 2. Contributions of individual  $\beta$  transitions listed in Table I and calculated as explained in the text and a comparison to the measured cumulative spectra measured at ILL for  $^{235}\text{U}$ . The upper panel shows the individual  $\beta$  spectra, while the bottom panel shows the cumulative contribution of all calculated forbidden transitions relative to the ILL flux. The chosen transitions exceed 50% of the flux around 6 MeV.

and neutron orbitals  $0h_{9/2} - 1f - 2p - 0i_{13/2}$  for  $A < 139$ , while for the heavier nuclei the proton orbital  $0h_{11/2}$  and the neutron orbital  $0i_{13/2}$  were kept empty due to the enormous dimensions of a full model space calculation.

The choice of a proper model space and Hamiltonian is crucial for meaningful shell model calculations. The region around  $A \approx 95$  is especially challenging, since taking full harmonic oscillator shells is currently not possible due to the enormous computational burden as well as a lack of a well tested Hamiltonian. Since a shell model Hamiltonian is fitted for a particular model space, it is always preferable to use a small enough model space to make the problem computationally reasonable without resorting to additional truncation of the model space. The model space chosen here for  $A \approx 95$  is small enough so that additional truncation of the model space is not necessary. In addition, this Hamiltonian is the natural choice for the reason that it was originally developed to describe one of the most important contributors to the cumulative beta spectrum here, namely the decay of  $^{96}\text{Y}$  [58]. In principle all the decays with  $A < 100$  can be described using the interaction  $g_{1e}pn$  but moving further away from  $^{96}\text{Y}$  the description of the nuclear structure starts to get more problematic. In the case of this study the lighter cases  $^{86}\text{Br}$  and  $^{89}\text{Br}$  turned out to be rather poorly described by this Hamiltonian, which is why the larger model space associated with the interaction  $jj45pna$  was used. It should be pointed out that agreement with the experimental half-life was also not reached with this interaction.

As is typical in the nuclear shell model a renormalization of fundamental coupling constants was used to account for meson exchange current and core polarization effects. For simple Gamow-Teller transitions the value of the axial charge

coupling constant is changed to an effective value below  $g_A = 1.27$ . Also for the forbidden beta decays considered here, a quenching of the coupling constant  $g_A$  is necessary [62]. In the case of a pseudoscalar transition there is another nuance, as here the transition is dominated by the  $^A\mathcal{M}_{000}^{(0)}$  nuclear matrix element, better known as the axial charge or  $\gamma_5$  relativistic operator. Meson exchange current effects are known to be particularly strong for this operator, resulting in a well-known enhancement of this operator, which we denote here by  $\epsilon_{\text{MEC}}$ . For the pseudoscalar transitions, excluding the few problematic cases such as the bromide decays as well as the heavier cases where truncations are necessary, the experimental half-lives are reproduced with reasonable values of  $g_A$  and  $\epsilon_{\text{MEC}}$ . For example choices such as  $g_A = 0.9$  and  $\epsilon_{\text{MEC}} = 1.4$  or  $g_A = 0.75$  and  $\epsilon_{\text{MEC}} = 1.7$  give a good fit. For the pure  $\Delta J = 1$  transitions both  $g_A$  and  $g_V$  need to be quenched in order to reproduce the experimental half-lives. This is a well-known issue which is usually attributed to core-polarization effects and is in line with previous research [62]. The excellent agreement using the experimental data with the usual assumptions is strong evidence that our calculations are indeed accurate for the majority of the decays, especially the most important ones. Uncertainties due to  $g_A$  quenching and meson exchange currents (MECs) in pseudoscalar transitions in the fission fragment region have been previously reported on [22,62–66], and will be discussed in the total uncertainty estimation of Sec. V B.

#### D. Numerical results

Taking the information of Table I with the formalism of Sec. II, we calculate the numerical shape factors using a uniformly charged sphere for the charge density and nuclear wave functions from the nuclear shell model as described above. The results are shown in Fig. 3, categorized according to the spin change in the transition.

Almost all calculated shape factors deviate significantly from unity, including the pseudoscalar transitions. From Eq. (7) the behavior of the latter should be trivial as  $|bR| \sim 10^{-2}$ , in an apparent contradiction. Many of these transitions connect initial and final states with spins larger than zero, meaning additional  $\Delta J = 1, 2$  operators contribute. As such, in many cases the energy dependence is dominated by higher-order operators as is evident from the curves. This was already touched upon in Sec. II C. Additionally, because the  $\xi$  approximation is not expected to hold for transitions with larger end points, this energy dependence is not suppressed. The pseudoscalar transition with the lowest end-point energy,  $^{94}\text{Y} [2^-]$  to the first excited state of  $^{94}\text{Zr} [2^+]$ , is of particular interest. Despite a reasonable argument in favor of the validity of the  $\xi$  approximation [Eq. (17)], the calculated shape factor shows a strong parabolic behavior reminiscent of a unique transition. Upon inspection of the level scheme of  $^{94}\text{Zr}$ , the first excited state can be interpreted as a consequence of collective behavior of the nucleus in terms of a dipole vibration. Interpreted in the spherical shell model with explicit vibrational degrees of freedom, the nuclear wave function can be decomposed into a combination of Slater determinants and a vibrational wave function [67]. Neglecting higher-order

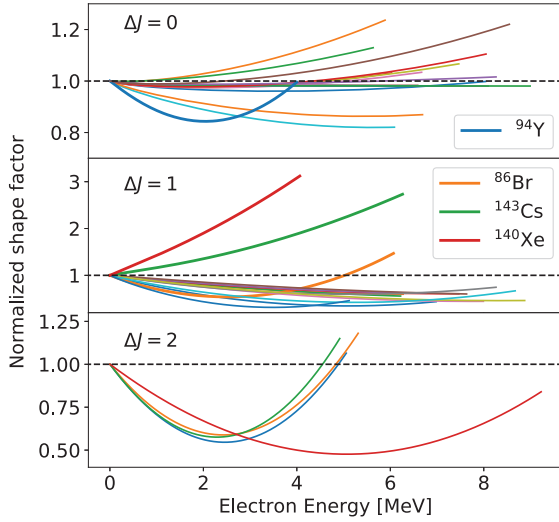


FIG. 3. Calculated shape factors  $C$  for the 36 first-forbidden transitions in Table 1 versus electron kinetic energy, categorized according to the spin-parity change of the transition. For allowed transitions  $C \approx 1$ , represented by the black dotted line. Each shape factor was normalized to its value at  $E = 0$ . Results correspond to  $g_A = 0.9$  and  $\epsilon_{\text{MEC}} = 1.4$ , where applicable [22,63]. Note the difference in scales on the y axis. A few cases stand out and have been highlighted. These are discussed in the text.

corrections, the former is the same as that of the  $0^+$  ground state. The  $\beta$  decay operator acts only on the Slater determinants, so that the nature of the transition—and as a consequence the shape factor—resembles that of the ground-state ( $^{94}\text{Y}[2^-]$ ) to ground-state ( $^{94}\text{Zr}[0^+]$ ) unique  $\beta$  decay. Residual interactions contaminate the vibrational wave functions, so that the change in vibrational states causes only a slowdown in the decay rate. This is an excellent example of the failure of the  $\xi$  approximation due to the so-called selection rule effect [33].

The pseudovector transitions show drastic deviations from unity for all studied transitions. For all transitions  $\xi \sim W_0$ , so that deviations are not wholly unexpected. Due to the nature of the fission process, almost all populated nuclei are heavily neutron rich so that protons and neutrons reside in different major shells interpreted in the shell model. As a consequence, proton and neutron Fermi surfaces usually lie in regions of opposite parity so that many different possibilities arise for a parity-changing transition including  $\Delta J = 2$ .

We discuss some cases that stand out from the pack. In the case of the  $\beta$  transition of  $^{86}\text{Br}$  [ $1^-$ ] to the first excited state of  $^{86}\text{Kr}$  [ $2^+$ ] the  $\Delta J = 2$  contribution is clearly seen to be dominant. While the excited state in  $^{86}\text{Kr}$  at 1.5 MeV is possibly a good vibrational candidate, the higher-order band structure is not visible. The numerical results hint at a cancellation effect in the additional first-order matrix elements. Besides this, both  $^{140}\text{Xe}$  and  $^{143}\text{Cs}$  show strongly diverging shape factors compared to all others calculated. This will have important consequences in the parametrization described in

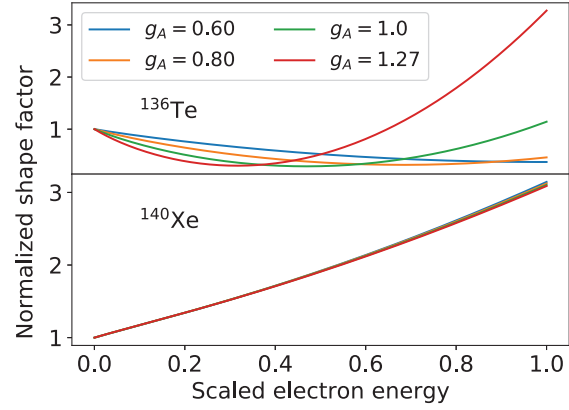


FIG. 4. Numerical shape factors calculated with the nuclear shell model for the first-forbidden pseudovector transitions in  $^{136}\text{Te}$  (top) and  $^{140}\text{Xe}$  (bottom) for different values of the axial vector coupling constant. Comparison with the results by Fang and Brown [21] are favorable for  $^{140}\text{Xe}$ , whereas for  $^{136}\text{Te}$  a slope with opposite sign is found for an equivalent value of  $g_A$ .

Sec. VI. It is not intuitively clear here why this occurs, as their results are particularly sensitive to cancellations. This can occur both due to nuclear structure considerations and contributions of various single-particle transitions of opposite sign, but also due to Coulomb effects. In the latter case, some matrix elements occur accompanied with factors of  $\alpha Z$ , so that changing the proton number has significant consequences. Because of this, even smaller matrix elements can end up dominating the shape factor due to cancellations between the main matrix elements. Regardless, all of these reasons are examples of an additional breakdown of the  $\xi$  approximation.

Corrections to the unique shape factors are typically observed to be on the few percent level or lower when taking into account the appropriate Coulomb corrections factors as discussed in Sec. II C. Our numerical results confirm these findings in the studied transitions.

### E. Comparison with existing literature

As mentioned in the previous section, the chosen values for effective coupling constants  $g_A$  and  $\epsilon_{\text{MEC}}$  reproduce experimental half-lives nicely [68]. In addition to these, there are data that we can compare our calculations to. While there has been a limited amount of study on the effect of forbidden transitions within the context of the reactor anomaly and shoulder [9,18,19,21,55], so far, there has only been a microscopic study on two nuclei [21]:  $^{136}\text{Te}$  and  $^{140}\text{Xe}$ . As both of these are even-even nuclei, investigated decays occur from the  $0^+$  ground state so that their first-forbidden transitions correspond to “pure” transitions. In Ref. [21], only  $^{136}\text{Te}$  was studied both in the shell model and the quasiparticle random phase approximation (QRPA), while  $^{140}\text{Xe}$  was computed only using the latter due to computational constraints [69]. Here we have calculated transitions from both nuclei in the nuclear shell model using the jj56b model space. Figure 4

shows the calculated shape factors for different values of effective  $g_A$  used.

The shape factor of  $^{140}\text{Xe}$  is almost insensitive to the choice of  $g_A$  and agrees well with the results by Fang and Brown [21]. The calculation for  $^{136}\text{Te}$ , on the other hand, shows a strong dependence on the effective value of  $g_A$ , in particular in connection with a quadratic component. However, when trying to replicate the shape factor of  $^{136}\text{Te}$  using the same Hamiltonian as reported in Ref. [17], we find a different slope. Interestingly, we can reproduce their results when manually changing the phase convention of either the single-particle matrix elements or one-body transition densities between Condon-Shotley (prevalent in shell model calculations) and Biedenharn-Rose (typical in QRPA codes) conventions. Additionally, we found that the shape factor is heavily dependent on the ratio  $g_A/g_V$ , the proper value of which is not well established for every Hamiltonian. In the original work, a value of  $g_{A,\text{eff}} = 0.5 g_A$  was used. Since also  $g_V$  was quenched by the same amount, however, their ratio remains unchanged even though the half-life is naturally reproduced.

## V. SPECTRAL CHANGES

Any spectral changes that occur from inclusion of our numerically calculated forbidden shape factors depend on the allowed shape factor that it is compared to. Following the discussion in Sec. IID, we look at the difference in the spectral shapes of both electron and antineutrino spectra using both  $C = 1$  [Eq. (19)] and the simplified weak magnetism correction of Eq. (20).

### A. Results

We compare the effects of the forbidden shape factors taking into account the relative weights of the different transitions. Three different partial cumulative forbidden spectra are constructed using the forbidden shape factors of the previous section, the allowed approximation  $C = 1$ , and the weak magnetism correction of Eq. (20). Results for the ratio of forbidden to allowed calculations are shown for  $^{235}\text{U}$  in Fig. 5 for both electron and antineutrino spectra. Shaded areas correspond to the partial spectral ratios weighted by the contribution of our included transitions to the total flux, as reported in Fig. 2, to estimate the effective change to the full spectrum.

Starting with relative changes in the electron spectrum, several quantitative features become immediately apparent. The first is the parabolic behavior at energies below 4 MeV, which originates from the unique forbidden transitions which dominate our transition selection (see also Fig. 3). Second is the lowering of the predicted electron flux in the higher energy window, for which the downward slope of the shape factors of the calculated pseudovector transitions are mainly responsible. Further, the strong increase at the highest energies is dominated by very few—or even a single—branch, for which strong deviations are expected near the end of the spectrum based on the results of Fig. 3. Finally, the tilt in the comparison between  $C = 1$  and the weak magnetism correction comes from the positive linear slope in Eq. (20).

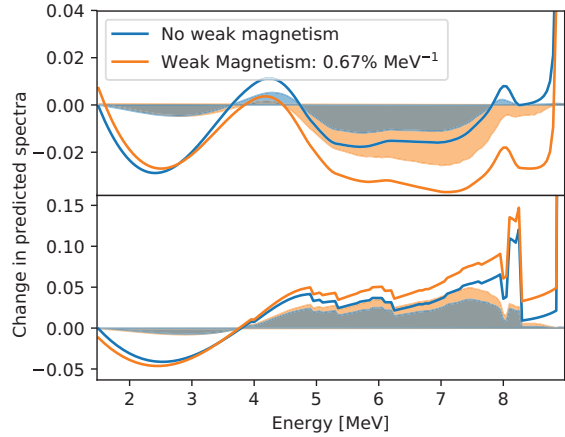


FIG. 5. Top panel: Change in the predicted partial electron spectra of the considered transitions compared to the allowed approximation and with an optional weak magnetism correction. Bottom panel: Change in the predicted antineutrino spectrum compared to the allowed approximation. Shaded areas correspond to the results multiplied by the total spectral contribution compared to experimental flux results (Fig. 2). The energy axis refers to the kinetic energy of the electron (top) and antineutrino (bottom). All results are calculated using  $g_A = 0.9$  and  $\epsilon_{\text{MEC}} = 1.4$ , for which good agreement was found with experimental lifetimes.

Quantitatively, clear changes are visible compared to the simple allowed approximation, and a general shift in predictions of roughly  $-2\%$  is observed when comparing against the results obtained with a simple weak magnetism term. Due to the limited selection of the calculated transitions, contributions to the total flux swiftly recede to zero outside of the bump energy window, thereby quenching spectral changes.

The antineutrino spectra in the bottom panel of Fig. 5 show several interesting features when compared to those of the electron. The fine structure in the spectrum is the consequence of the Fermi function, which lifts the  $\beta$  spectrum shape above zero for near-vanishing electron energy. Besides this, the most interesting result resides in the magnitude of the induced discrepancies compared to that in the electron spectrum. For the antineutrino spectrum, a significant enhancement of the expected antineutrino flux is observed above 4 MeV. Weighted results show enhancements of over 5% around 6 and 7 MeV, whereas changes are limited to 2% in the equivalent electron window. The reason for this resides in the steep decrease of the total flux for increasing energy. A downward sloping shape factor such as those in Fig. 3 pushes more of the flux to lower electron energies. The change to the total cumulative spectrum is minimal, however, due to the absolute magnitude of the spectrum being orders of magnitude larger at lower energies. The opposite goes for the antineutrino spectrum, resulting in stronger discrepancies. The downward trend below 4 MeV is mitigated due to the limited contribution of the considered forbidden spectra to the total flux.

### B. Uncertainty estimation

A trustworthy determination of the uncertainty of all sources included in the calculation is of paramount importance. On the other hand, estimation of theory uncertainties within nuclear structure calculations presents a tremendous challenge. Recently, some efforts have been made in the  $sd$  shell, where a Bayesian analysis translated experimental and fit uncertainties into final uncertainties in nuclear matrix elements [70]. Given the large model space and number of fit parameters, this procedure is not currently possible for our transitions of interest. As such, here we vary the available parameters used in tuning shell model results to obtain agreement with experimental lifetimes. In the most general case this corresponds to a modification of the axial coupling constant  $g_A$ , whereas for the pseudoscalar transitions meson exchange currents strongly modify the so-called axial charge [63]. In order to take into account this effect, we additionally vary  $g_A$  for pseudoscalar operators, which we note by  $\epsilon_{\text{MEC}}$ .

The results shown in Fig. 5 were obtained for  $g_A = 0.9$  and  $\epsilon_{\text{MEC}} = 1.4$ , for which good agreement was reached with experimental lifetimes for almost all transitions [22,63]. In order to get a measure for the uncertainty on our results, we vary the coupling constants within a window as described below. This is done because for many isotopes the experimental half-life is the only quantity to which one can compare. When quenching both  $g_V$  and  $g_A$  (as was done by Fang and Brown [21]), a degeneracy appears in their ratio as the experimental half-life can always be obtained after suitable quenching. For the axial vector coupling constant four different values were used, setting  $g_A/g_V \in \{0.7, 0.9, 1.0, 1.27\}$ . The meson exchange corrections to the axial charge were picked from the interval  $\epsilon_{\text{MEC}} \in \{1.4, 1.7, 2.0\}$ .

There is, however, no unique way of choosing effective couplings for all transitions together. As a consequence, we choose the uncertainty to be the maximum of the deviation between fully correlated and random choices of  $g_A$  and  $\epsilon_{\text{MEC}}$  for all transitions. We do so only for the partial cumulative spectrum, as this is the only relevant theoretical input despite potential large differences in individual shape factors.

Figure 6 shows the spread in the relative change of the partial cumulative electron and antineutrino spectra for both allowed approximations as before. In both cases the largest uncertainty appears in the higher end of the spectrum. The origin of this can mainly be traced back to the pseudovector transitions, where the slope of the shape factor is usually a combination of  $\Delta J = 1$  and  $\Delta J = 2$  operators with different  $g_A$  dependence. These effects are limited to higher ends of the spectrum due to the selected transitions and their respective end points. The lower energy regions are mainly dominated by unique forbidden transitions, for which any deviations from Eq. (9) are already constrained to the percent level. The majority of the uncertainty comes from varying  $g_A$ . Effects from varying  $\epsilon_{\text{MEC}}$  are only relevant for pseudoscalar transitions and are found to be subdominant. The reason for this can intuitively be understood, as it concerns changes to the  $\Delta J = 0$  operators which have limited energy dependence [Eq. (7)]. A similar conclusion is reached for the antineutrino partial spectrum. Even so, the total uncertainty in the latter is

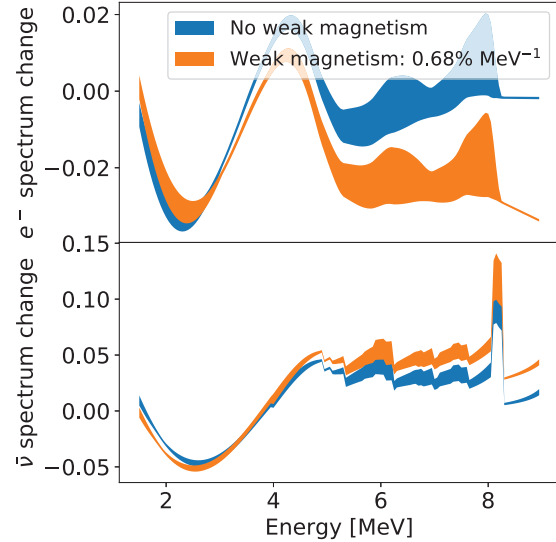


FIG. 6. Top (bottom): Uncertainty in the relative change in the prediction of the electron (antineutrino) spectra when calculating the transitions using forbidden spectral shapes instead of simple allowed shapes using different values of  $g_A$  and  $\epsilon_{\text{MEC}}$  for the former (see text). The filled regions show the maximal deviations in results. A large part of this uncertainty comes from setting the axial vector coupling to the free nucleon value of  $g_A = 1.27$ .

about a factor 2 larger, putting the theory error at around 1%, before multiplication with the forbidden flux contribution of Fig. 2.

The results of Fig. 6 represent a bound rather than a confidence interval in the statistical sense. For the purpose of the discussion, however, we will treat the variation around the central value as a  $1\sigma$  uncertainty. We shall see that this is not the dominant uncertainty when we generalize the approach of first-forbidden transitions for a more complete discussion in Sec. VI. This is expanded upon in the Appendix.

## VI. IMPROVED FORBIDDEN TRANSITION TREATMENT

Over the past several years, a lot of attention has gone towards an *ab initio* treatment of the electron and antineutrino spectra, fueled by a strong experimental effort in TAGS measurements (e.g., [39]). Despite a significant number of uncertainties in nuclear databases, it provides an independent analysis path with a much more fine-grained control. Additionally, it is the only method available that can predict the electron and antineutrino spectra below 1.8 MeV with reasonable accuracy. Up to now, the treatment of nonunique forbidden transitions has proceeded by either approximating it as an allowed decay [15], or as the shape of an  $n - 1$  unique forbidden decay for forbiddenness  $n$  [16]. In the case of first-forbidden decays, these are of course the same approximation. Based on the results of the previous section and the discussion of Sec. II C, the validity of these approximations appear unwarranted.

TABLE II. Breakdown of the number of  $\beta$  branches participating in the  $^{235}\text{U}$  electron flux. An arbitrary cut was made where the fission yield must be larger than  $1 \times 10^{-6}$ , bringing the total number to 8219. Exact numbers are not of importance, as several intermediate steps are required as described, e.g., in Sec. III.

	Nonunique	Unique	Total
Allowed	3049	2648	5697 (69%)
1st forbidden	1593	515	2108 (26%)
2nd forbidden	235	97	332 (4%)
3rd forbidden	52	12	64 (0.8%)
Other	33	11	44 (0.5%)

It is the question of this section to investigate the possibility of generalizing the information of the previous section and apply it to the remainder of (nonunique) forbidden decays present in the database. Before we embark on this journey, however, it is worthwhile to look at the structure of the electron and antineutrino flux. In doing so, we investigate the relative importance of forbidden transitions on the total flux. Following this, we attempt a parametrization of the results found in Sec. IV. Finally, we discuss how to use this information of the parametrization to obtain an uncertainty from the treatment of forbidden decays using Monte Carlo techniques.

#### A. Forbidden flux coverage

We investigate the composition of the cumulative electron spectrum. Table II shows the breakdown of the contributing  $\beta$  branches following the fission of  $^{235}\text{U}$ .

As is well known by now, around 30% of the transitions are forbidden. While several compilations have been made of the dominating branches or the number required to reach a certain flux [55], a closer look at the underlying structure of the spectrum has been absent. In order to obtain a more realistic picture, the results of Table II must be adjusted to account for the branching ratio and fission yield of each transition. Figure 7 shows the contributions of the various types of decays in the summed electron spectrum for  $^{235}\text{U}$  as a function of  $\beta$  energy.

It is clear that the dominion of allowed spectra based on only their number is overestimated. Keeping in mind the inverse beta decay threshold at 1.8 MeV and steep decrease in flux after 8 MeV, this conclusion becomes all the more relevant. In the 4–8-MeV region in particular, a clear dominance of forbidden spectra can be seen. This corresponds to the same region as the so-called bump or shoulder in the antineutrino spectra.

Expected consequences for differences in cumulative spectrum shapes can be superficially deduced from the results of Sec. IV. While typically spectra for  $\Delta J^\pi = 0^-$  closely correspond to equivalent allowed spectra, Fig. 3 shows that significant variations can occur as higher-order operators often also contribute. Interesting to note is how the contribution of  $\Delta J^\pi = 1^-$  transitions is reasonably constant around 15% throughout the entire spectrum. As these decays in particular bring about a large change in predicted electron and

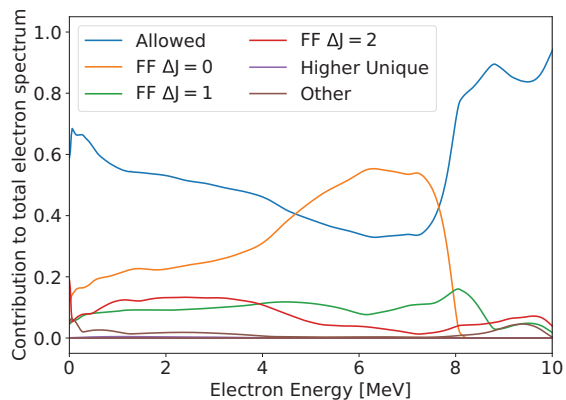


FIG. 7. Overview of the spectral composition of the cumulative electron fluxes of  $^{235}\text{U}$ , calculated assuming allowed shape factors. It's clear that, despite weight in numbers, the contribution of allowed decays is greatly diminished in most of the region of interest. Above the inverse beta decay threshold at 1.8 MeV and below 8.5 MeV—precisely the experimental range of the ILL campaigns—the cumulative spectrum is dominated by forbidden decays.

antineutrino spectra (see Fig. 3), significant changes can be expected over the full range. Higher unique forbidden transitions for which shape factors can be very well calculated turn out to be negligible over the full range. Higher nonunique decays are equally insignificant over the full range.

There is an interesting structure in Fig. 7, which can at least superficially be understood from an intuitive nuclear physics point of view. The majority of neutron-rich fission fragments that are populated have  $Q$  values around 4–8 MeV. Many of the transitions contributing in this window in Fig. 7 correspond then to decays from initial ground states to final ground states or low-lying excited states. Due to the large proton-neutron asymmetry, these typically reside in adjacent major orbital shells. Most of these orbitals have opposite parity, so that ground state to ground state transitions are automatically forbidden. As a consequence, these are dominant in the flux in the 4–8-MeV window. Using the usual Woods-Saxon orbital properties as a reference, the structure within first-forbidden transitions can additionally be understood. As nuclei decay towards the line of stability, the  $Q$  value decreases as the proton-neutron asymmetry lessens. Valence protons then populate the  $\pi g_{9/2}$  orbital, whereas valence neutrons drop into  $\nu d_{5/2}$  and  $\nu g_{7/2}$  orbitals. One expects then a rise in unique first-forbidden ( $\nu d_{5/2} \rightarrow \pi p_{1/2}$ ) and allowed ( $\nu g_{7/2} \rightarrow \pi g_{9/2}$ ) decays, which is reflected in Fig. 7. Transitions to excited states complicate this picture significantly for higher excitation energies, and here we run into the limits of our simple picture. Similarly, the behavior at high energies is dominated by very few branches from isotopes with very high  $Q$  values. For many of the latter, spin parities are unknown, meaning their  $\beta$  branches are simply approximated to be allowed.

### B. Parametrization procedure

From the results of Fig. 7, it is clear that the influence of forbidden transitions is non-negligible throughout the entire experimentally accessible spectrum. While the dominant contributions come from pseudoscalar transitions for which the shape factors resemble those of allowed decays, a significant contribution comes from higher forbidden decays with strikingly different shape factors. Additionally, from Fig. 3 it can be gleaned that shape factors within the same  $\Delta J$  category are reasonably similar, warranting a parametrization. It is with this observation in mind that we attempt to construct an effective correction to the spectra of both electron and antineutrino taking into account the underlying forbidden structure. Due to the larger sample of numerical shape factors presented here compared to our previous work, the parametrization procedure has evolved to better reflect the internal structure of the shape factor distribution. For completeness then, we outline both the procedure used in the previous work [22] and its current state.

#### 1. Parametrized forbidden shape factors

The expected shape factor contribution from pseudoscalar operators is approximately equal to unity [see, e.g., Eq. (7)], so that nearly all of the deviations observed in Fig. 3 arise from higher-order operators contributing to the  $J^\pi \rightarrow J'^\pi$  transition. Depending on the sign of these contributions one arrives at a positive or negative slope. As the number of terms contributing to the general shape factor is so large, combined with a near-statistical spread of the deviations from unity, we make no attempt at a *smart* parametrization and simply fit each of the shape factors according to

$$C = 1 + aW + b/W + cW^2, \quad (26)$$

inspired by the general form of the shape factor [Eq. (3)].

The behavior of the  $\Delta J^\pi = 1^-$  shape factors is more uniform as can be deduced from Fig. 3. As these operators now also carry a significant energy dependence, any energy-dependent change is not any more dominated by the influence of higher-order operators as it was for the pseudoscalar case. For nearly all transitions calculated, only two nuclear matrix elements contribute significantly: the time component of the first moment of the vector current,  $^V\mathcal{M}_{110}$ , and the space component of the first moment of the axial vector current,  $^A\mathcal{M}_{111}$ . While these are usually of similar magnitude, the possibility for cancellations stands in the way of a more insightful parametrization. The procedure is then analogous to that of the pseudoscalar transition, where we similarly fit all shape factors according to Eq. (26). Finally, the unique forbidden decays are well understood, with a shape factor that is approximately equal to that of Eq. (9). This result was obtained assuming the presence of only the dominant nuclear form factors, and deviations occur only at the percent level. As this will not appreciatively influence the final uncertainty, we simply assume the approximate unique forbidden shape factor of Eq. (9).

Here we distinguish between the approaches followed for our previous work [22] and the current status. We discuss both in turn.

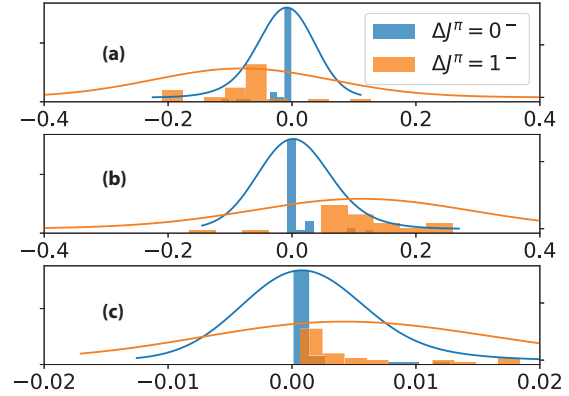


FIG. 8. Distribution of fit parameters  $a$ ,  $b$ , and  $c$  [Eq. (26)] from the numerical results of Sec. IV for pseudoscalar and pseudovector transitions. Full lines represent an expectation of the underlying distribution using Gaussian kernel density estimation. This corresponds to the old approach used in Ref. [22].

*Old.* After fitting all numerically calculated nonunique first-forbidden shape factors using Eq. (26), one obtains distributions of fit parameters for each  $\Delta J$ , including correlations between the fit parameters. Results are shown in Fig. 8 for the fit parameters with an average correlation matrix

$$\rho = \begin{pmatrix} 1 & -0.62 & -0.98 \\ -0.62 & 1 & 0.55 \\ -0.98 & 0.55 & 1 \end{pmatrix}. \quad (27)$$

Interestingly, the latter is almost identical for  $\Delta J = 0$  or  $1$  despite strong differences in the magnitude of the effect. Here all shape factors were included for the full range of  $g_A$  and  $\epsilon_{\text{MEC}}$ . This way, both the uncertainty due to effective coupling constants and spread in calculated shape factors contributes to our effective knowledge of first-forbidden shape factors.

We apply one additional step to obtain a useful distribution to eventually sample from. By employing Gaussian kernel density estimation [71], one obtains a parameter probability density function. Doing so eliminates all knowledge one might have about the particular transition other than its degree of forbiddenness, so that this parametrization rather becomes a quantification of uncertainty due to nonunique first-forbidden transitions in the electron and antineutrino spectra.

In performing this parametrization there is some freedom, hidden in the bandwidth estimate of the Gaussian kernel density estimation. While several rule-of-thumb bandwidth estimators exist in the literature, these are known to perform poorly for non-Gaussian or heavy-tail distributions. As such, we determine the bandwidth manually through comparison of the quantiles in the parametrized shape factors and the numerically calculated ones. By requiring all explicitly calculated shape factors to fall within  $2\sigma$  of the procedural set, one arrives at a bandwidth of  $h = 2$ . Using rule-of-thumb estimators such as “Silverman” or “Scott” [71], one finds much lower values for  $h \approx 0.6$  and poor agreement with numerical results.

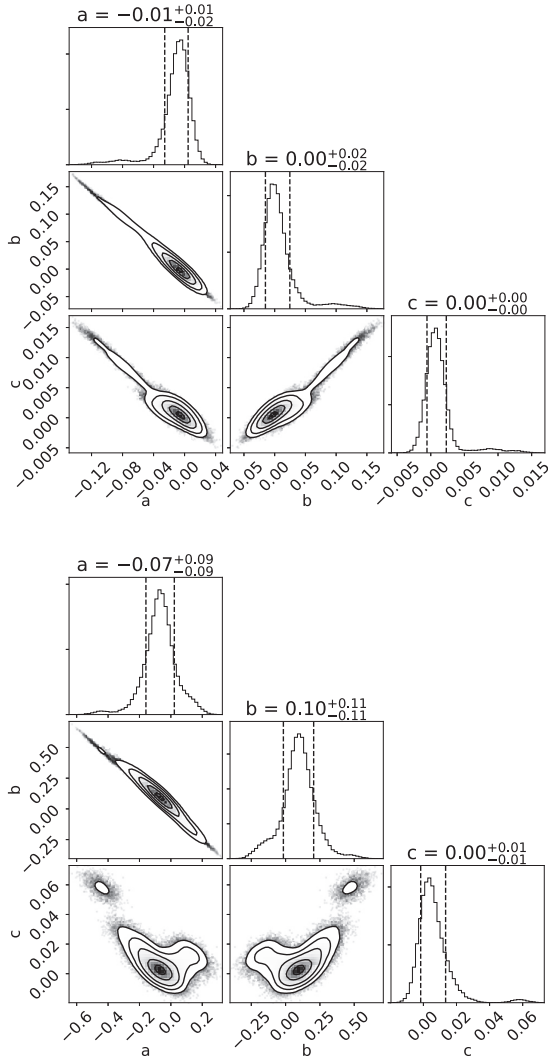


FIG. 9. Distribution of fit parameters  $a$ ,  $b$ , and  $c$  [Eq. (26)] and their correlation projections from the numerical results of Sec. IV for pseudoscalar (top) and pseudovector (bottom) transitions. The appearance of heavy tails and multimodal distributions show the need for the improvement. Plots were made using Ref. [72].

*New.* Due to the inclusion of additional shape factors presented in Sec. IV, the old procedure discussed above is not optimal. One of the main reasons for this lies in the appearance of shape factors with large positive slopes (see Fig. 3) for  $\Delta J = 1$ . Fit parameter distributions as shown in Fig. 8 become multimodal and substantial tails appear. As such, rather than approximating each parameter distribution individually as a single Gaussian related via an average correlation matrix [Eq. (27)], we take into account all correlations without compromise. Figure 9 shows the results for both

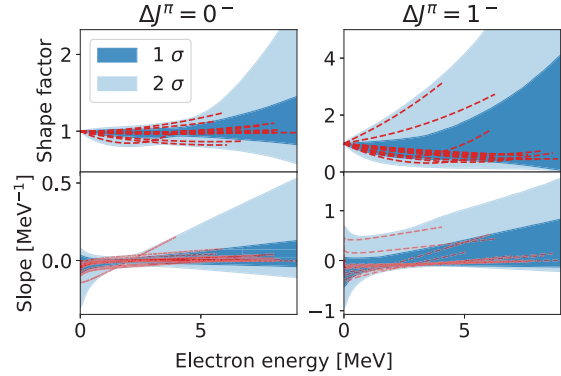


FIG. 10. Assessment of the quality of parametrized shape factors through a comparison with the numerically calculated shapes of Sec. IV. The top rows shows the normalized shape factors, whereas the bottom row shows the slope. The left (right) column shows these for pseudoscalar (pseudovector). Intervals corresponding to 68% and 95% quantiles are shown as  $1\sigma$  and  $2\sigma$ , respectively. Numerical shape factors are plotted using  $g_A = 0.9$  and  $\epsilon_{\text{MEC}} = 1.4$  where appropriate, as above.

pseudoscalar and pseudovector transitions after application of Gaussian kernel density estimation using the Scott bandwidth estimator.

Both the appearance of heavy tails and multimodal distributions can clearly be seen, showing the necessity of the new approach. Using the results of Fig. 3 some of the influences of the new shape factors on the parameter distribution can clearly be discerned. Using this information, one can now produce samples stochastically drawn from this three-dimensional probability distribution. This can be done either using Markov chain Monte Carlo techniques or using the properties of Gaussian functions when applying Gaussian kernel density smoothing. Here, we have opted for the latter due to its computational simplicity.

In order to gauge how well the parametrization performs, we compare a generated ensemble against the numerical calculations of Sec. IV, shown in Fig. 10. As we are mainly interested in the energy dependence, we additionally plot the first derivative.

Excellent agreement is obtained for both  $\Delta J = 0$  and  $\Delta J = 1$ , for the normalized shape factors as well as their first derivatives. The large range of possible shape factors for high end points, however, is related to the substantial variation in the quadratic component. In the pseudoscalar case this is, for example, because of transitions such as  $^{94}\text{Y}$ , where a strong quadratic component arises from a contribution of a  $\Delta J = 2$  operator despite it being a pseudoscalar transition. In the case of pseudovector transitions, large ranges are obtained due to the appearance of both positive and negative slope shape factors. Using the old approach, it is not possible to achieve a good agreement as in Fig. 10 without drastically increasing the width of the Gaussian kernels, voiding the original intent.

In using a simple polynomial fit for all shape factors, however, the distinctions between the origin of the different

kinematic terms are not made. This means, for example, that the quadratic component can be overestimated outside of the end-point range for which the fit was made. Taking  $^{94}\text{Y}$  as an example once more, its parabolic behavior arises mainly from the  $\Delta J = 2$  operator, which will give rise to a parabolic shape no matter the end point. Due to the “blind” fit of Eq. (26), however, such behavior is not recognized and only the large quadratic component is recorded. Due to the limited number of data points we choose not to go further in this, and keep in mind that uncertainties could be too conservative in the high energy range.

As with any parametrization, its quality is only as good as the input data on which it is based. Following the discussion of Sec. IV B, we argue that our selected transitions correspond to a representative sample of forbidden transitions within the region of interest. The parametrization proposed here thus corresponds to a generalization of our knowledge and our lack of it that we perceive to be realistic.

### 2. Monte Carlo procedure

The jump to a generalized summation calculation taking into account all first-forbidden transitions is now straightforward. The summation calculations proceed as normal, with the exception of forbidden transitions. Here, the spin-parity change is determined and the corresponding approximate shape factor is taken as described in the previous section, with the exception of the transitions described in Sec. IV. The nuclear-structure dependent change from the approximate shape factor is then assigned randomly according to the distribution of fit parameters as described above. Repeating the procedure many times results in a translation of the uncertainty of the shape factors into a spectral uncertainty. This uncertainty will become most apparent in regions where few branches contribute.

Based on the behavior of the categorized shape factors of Fig. 3, we expect the deviations from pseudoscalar transitions to average out within an individual calculation in regions where many branches contribute. Sampling  $\Delta J = 1^-$  shape factors as observed, we expect a decrease in the predicted electron flux at high energies and opposite for the antineutrino flux. Unique forbidden decays, finally, decrease both electron and antineutrino predictions in its central range, while providing only small increases at very low energies and their corresponding end points. This fact becomes increasingly strong for higher degrees of forbiddenness.

Note that a single summation calculation like this samples the probability distributions roughly 1600 times (see Table II). In the results discussed below, 100 Monte Carlo calculations then correspond to a sampling of the parametrized probability distributions of 160 000 times.

## VII. UPDATED SUMMATION CALCULATIONS

We combine all information from the foregoing sections into a comprehensive spectral analysis. As it forms the only experimental data available, we commence the discussion with a comparison to the ILL data set [47]. We move on to the spectral changes induced due to the enhanced treatment of

forbidden transitions in the summation approach and continue to the uncertainty estimate. Finally, we discuss our results within the context of the reactor spectral bump and the flux anomaly.

### A. ILL spectral reconstruction

Many authors have treated both summation and virtual branch methods in relation to the ILL data set [6,9,15,16,73]. While progress on the latter has been limited, improved summation calculations are made possible through an intensive research program employing total absorption gamma spectroscopy (e.g., [39]). Many cases troubled by pandemonium [44] have been resolved, and very recently state-of-the-art calculations have achieved a correspondence with the ILL data set at the few percent level through intricate connections between a vast array of databases [74]. In this work we employ a simpler approach to clearly identify the impact of nonunique forbidden transitions on the antineutrino spectrum.

Considering the identified problems with pandemonium in the ENSDF and related databases, we outlined three ways of mitigating this issue with the publicly available nuclear databases in Sec. III. Here we explicitly demonstrate the first, i.e., correspondence with the Schreckenbach cumulative electron spectral measurements. We enforce such a correspondence for both the allowed approximation and our more sophisticated results, so that we may check relative differences in the antineutrino spectrum as our second point. Finally, we choose to work here with a combination of the ENDF and ENSDF decay libraries, using the branching ratios of the former and spin parities of the latter. This will be denoted as “ENDF+ENSDF.”

Additionally, we return to the point of “continuous” data within the ENDF database for certain isotopes. This is often the case for isotopes far away from stability with relatively high  $Q$  values [53]. Its influence will then mainly be felt in the upper half ( $>5$  MeV) of electron and antineutrino spectra. A proper spectral inversion relies on knowledge of the underlying structure, however, so that it is essentially a miniature form of the more general spectral inversion. Due to the degeneracy in input theoretical shapes [19] and the enormous amount of fitting parameters, we choose not to attempt individual conversions and use instead only the transitions for which discrete information is available (ENDF Discrete). Introducing instead the  $Q_\beta$  approximation (Sec. III), poor agreement is obtained with the ILL data set with a significant overestimate of the total flux at energies higher than 5 MeV. A summary is presented in Fig. 11.

As discussed previously, the omission of isotopes with continuous spectra (be they experimentally or theoretically obtained [53,54]) manifests itself as a deficit with respect to the ILL data sets mainly at higher energies. Additionally, beyond 7.5 MeV,  $^{235}\text{U}$  shows telltale signs of pandemonium corruption. As this lies outside of the region of interest and is well under control through the inclusion of TAGS data, we instead move on with the ENDF+ENSDF discrete data set (ENDF Discrete in Fig. 11).

In order to obtain correspondence with the ILL data sets, we extend the analysis using a composite approach. Here,

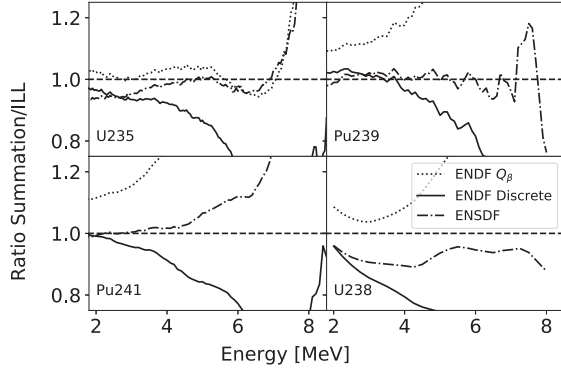


FIG. 11. Comparison of different ways of combining the nuclear databases and the resulting agreement with the ILL experimental electron spectra. We use the JEFF3.3 database for fission yield, and the decay library of the ENDF database (see Sec. III). Here ENDF Discrete takes into account only transitions for which discrete level data was present.

we fit the residual electron flux between the ENDF+ENSDF data set and the experimental data using a limited number of virtual branches. These are then explicitly inverted for the antineutrino spectrum. A summary is shown in Fig. 12. Good agreement is obtained for all fission actinides, with remaining residuals on the percent level. The fine structure that remains is a consequence of the summation part and cannot be adequately compensated for using virtual branches. Since these are limited to the region beyond 7.5 MeV, these will be of no consequence to our final result.

### B. Spectral shape changes

All the pieces are now in play to commence a final comparison of our results to those found in the literature. Throughout this work we have discussed various approximations made in

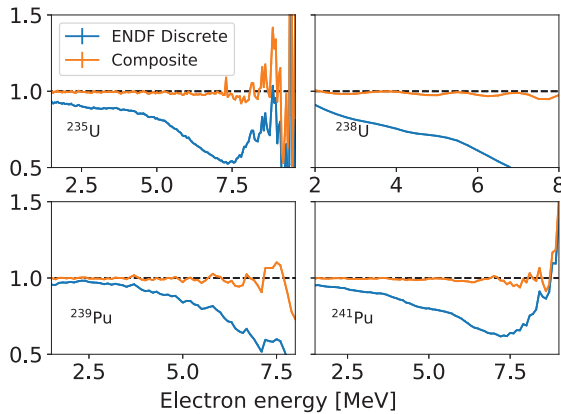


FIG. 12. Comparison of the summation and composite approach when using only discrete spectral information from the ENDF database as a foundation. For all four isotopes, less than eight virtual branches were used to obtain percent-level agreement in the composite approach.

earlier works (Secs. IIC and IID) and effects of including additional corrections in our description of individual and cumulative spectra. Here, we will discuss the influence of these various effects on the cumulative electron and antineutrino spectra.

Throughout this section and the next, we will compare three different approaches to calculating the composite spectra: (i) treating first-forbidden transitions using the 36 calculated shape factors of Sec. IV, with and without parametrized results for the remaining forbidden branches; (ii) treating those forbidden transitions as allowed with  $C = 1$  [Eq. (19)]; (iii) treating those transitions using the weak magnetism correction of  $0.67\% \text{ MeV}^{-1}$  [Eq. (20)]. We will report our result as the relative differences between these approaches, i.e., the difference between (i) and (ii), and (i) and (iii). Note that in each of these three approaches the summation contribution to the total electron flux will vary. As a consequence, the same applies for the virtual branch contribution in order to force correspondence with the ILL dataset. For the virtual branches, we allow the average  $Z$  value to change within the uncertainties of the fit [15], and randomize the end-point energy of each virtual branch within the bin size. This results in a statistical uncertainty due to the conversion procedure, which contributes to the final spectral uncertainty reported in the Appendix.

#### 1. Numerical shape factors

The central result of this work is the direct effect of including the numerically calculated shape factors of Sec. IV into the summation and composite calculations. For the former, the results were already demonstrated in Fig. 5, where the shaded areas correspond to the total difference in both electron and antineutrino spectra.

The remarkable finding is that the electron spectra can experience relatively minor changes of 2% and lower, while the antineutrino spectrum can increase by up to 5% in the same energy range. This is a coalescence of the steep decrease in magnitude of the cumulative electron flux and the composition profile of the flux as shown in Fig. 7. A downward sloping shape factor for a forbidden transition pushes electrons towards lower energies, but the relative change in the cumulative electron flux remains minor due to the flux being several orders of magnitude larger there. Any quadratic or energy-inverse component in the shape factor will enforce this result, as its effects are spread throughout the entire antineutrino spectrum due to the varying end points of the transitions. This is the central element common to all of our results.

Figure 13 shows the difference between cumulative electron spectra in the different approximations using the composite approach. Up to at least 7.5 MeV no statistically significant differences appear, meaning that our composite approach is able to fit successfully to the ILL spectra both when assuming the transitions of Table I to be allowed and when using the forbidden shape factors. This procedure is successful within the percent level up to  $\sim 7$  MeV. We take into account the remaining residuals in a so-called bias uncertainty, which is reported in the Appendix.

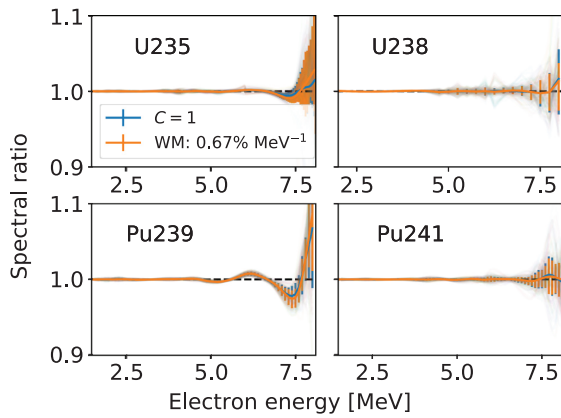


FIG. 13. Relative change in the cumulative electron spectra in the composite approach when treating the transitions in Table I as allowed and forbidden. The good agreement over the full range guarantees a good match to the ILL data set for all four actinides. Residuals from unity are taken into account as a bias uncertainty reported on in the Appendix.

The good agreement of the electron spectra in the three different approaches is a necessary requirement for a clean interpretation of the results in the antineutrino spectrum, which are shown in Fig. 14.

As anticipated (see Fig. 5), a similar pattern arises where significant changes occur in the antineutrino spectrum while the electron flux remains relatively unchanged. In performing the composite approach the latter is fixed, so that the decrease in the electron spectrum is compensated for through the virtual branches. This has then the effect that the change in the antineutrino spectrum change is even greater, and is approximately equal to the sum of the differences of antineutrino and

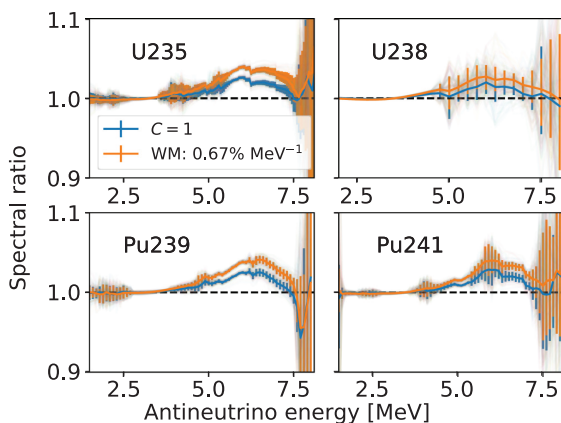


FIG. 14. Relative change to the cumulative antineutrino spectra in the composite approach when treating the transitions in Table I as allowed and forbidden. A bump appears between 4 and 7 MeV, with a magnitude of up to 4.5%.

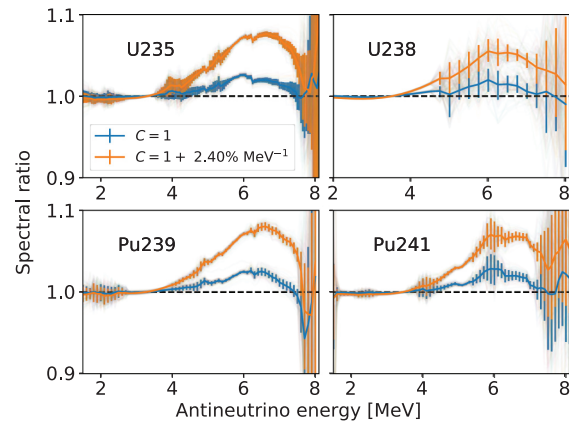


FIG. 15. Relative change to the cumulative antineutrino spectra in the composite approach when comparing against a trivial allowed shape factor and one with a slope roughly four times the weak magnetism correction. The magnitude of the induced bump reaches over 8.5%.

electron flux in Fig. 5. As a consequence, a bump appears in the 4–7-MeV range with a magnitude of up to 4.5% when comparing against the weak magnetism correction of Eq. (20). When comparing against setting  $C$  equal to unity the effect is less pronounced and the bump magnitude reaches only 2.5%.

Due to their similar proton-to-neutron ratio, the fission fragment distributions are very similar for  $^{235}\text{U}$  and  $^{239}\text{Pu}$ , leading to near-identical results. For  $^{241}\text{Pu}$ , on the other hand, additional substructure is visible around 6 MeV. This appears to be an accidental combination of circumstances in the shape factor results and fission yield distributions.

In the original work by Huber [15] it was noted that the chosen value for the weak magnetism correction had a strong influence on the final results of the reactor normalization anomaly. Further, it was estimated that an increase by a factor of 4 would be sufficient to eliminate the anomaly entirely. While a larger-scale study done specifically on weak magnetism found no such variations [36], from our discussion in Sec. IID it is clear that such a slope difference can arise from a variety of other terms which were up to now forgotten. Additionally, we found above that the amplitude of the bump arising from a proper treatment of forbidden transitions depends on the magnitude of the slope in the allowed shape factor. Figure 15 shows the same results as above, but instead using an allowed shape factor with a slope that is four times larger than the weak magnetism correction used in the original analysis.

Unsurprisingly, the magnitude of the bump is larger than when compared to the normal weak magnetism correction and now reaches up to 8.5% for all isotopes besides  $^{238}\text{U}$ . Interestingly, the magnitude of the correction now becomes very similar to that which is observed experimentally. It appears then that through a combination of proper treatment of forbidden transitions and a change in average slope of allowed transitions as discussed in Sec. IID, both the normalization

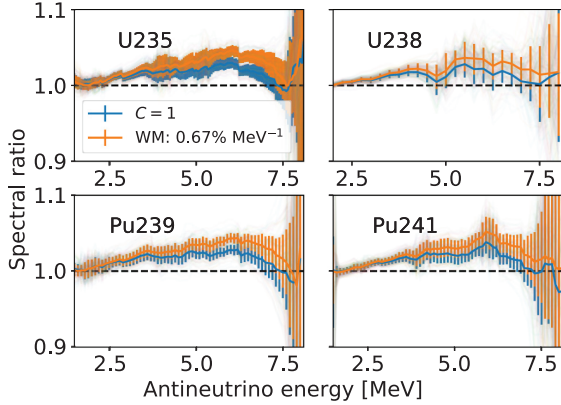


FIG. 16. Relative change to the cumulative antineutrino spectra in the composite approach when treating the transitions in Table I as allowed and forbidden and using the parametrization as described in Sec. VI for the remaining forbidden branches. Statistics are based on 100 Monte Carlo cycles. Uncertainties are a combination of the virtual branch procedure (see Fig. 14) and the parametrization.

anomaly and the spectral shoulder can be solved at the same time.

## 2. Including parametrized forbidden shape factors

Following the discussion of Sec. VI, we go one step further and use the parametrization derived there to look at the additional effects of including all other known forbidden transitions in a stochastic way. Since the explicitly calculated transitions already constitute a significant part of the total flux (see Fig. 2), and forbidden transitions take up about 60% of the flux in the region of interest (see Fig. 7), the inclusion of the parametrized shape factors will mainly affect the spectral uncertainty rather than the magnitude. As before, the agreement with the ILL electron flux is required in our composite approach. While this succeeds, the uncertainty quickly grows to 10% above 8 MeV due to the large range of parametrized shape factors at very high energies. For the purposes investigated here, however, this is sufficient. In Fig. 16 we show the result of the calculation of 100 Monte Carlo samples.

The most apparent change compared to Fig. 14 lies in the region between 2 and 4 MeV. According to the parametrization results, an increase in the theoretical flux is predicted over the whole range, which gives rise to a much wider shoulder. Whether this is a true verifiable feature or a limitation of our parametrization remains to be seen. In this region, the explicitly calculated transitions correspond to only 10–35% of the total flux, even though according to Fig. 7 about 50% of the flux must originate from forbidden transitions. Unique transitions occur more prominently here, which could partially explain this increase.

The uncertainties arising from the parametrization procedure are substantially larger than those from the conversion procedure of the spectrum residuals as discussed in the previous section. Depending on the isotope,  $1\sigma$  uncertainties range from 1.5% to 3% around the 6-MeV range and quickly

TABLE III. Difference in the integral and IBD flux compared to the Huber-Mueller results when using only the numerical shape factors as described in Secs. IV and VII B 1. Positive numbers indicate a larger calculated flux. Uncertainties quoted come only from the procedure explained here.

	$^{235}\text{U}$	$^{238}\text{U}$	$^{239}\text{Pu}$	$^{241}\text{Pu}$
$\phi$	0.2(2)	0.4(5)	0.2(2)	0.3(2)
$R_{\text{IBD}}$	0.8(5)	2.3(10)	0.7(5)	0.7(6)

grow to more than 10% at 8 MeV. These uncertainties must be added on top of those already present in the original procedure [15,16], as well as those originating from the uncertainty in the explicitly calculated shape factors of Sec. IV. This will be discussed in more detail in the Appendix.

## C. Integrated flux changes

In the previous section we have summarized the changes to the total cumulative electron and antineutrino spectra. We will now use the same results to look at the change in the integrated cumulative and inverse  $\beta$  decay (IBD) flux. For the cross section of the latter we use the expressions given by Refs. [14,75–77]. The strong energy dependence of the cross section forms a small counterweight against the steep decrease of the antineutrino flux. As a consequence, the change in theoretically predicted flux of Figs. 14–16 will leave an imprint. In Table III we show the difference in antineutrino and IBD flux with respect to the Huber-Mueller predictions.

As the antineutrino flux is dominated by its behavior at low energies, relative changes to the Huber-Mueller model are minimal for all isotopes and correspond to a  $1\sigma$  shift away from zero. The uncertainties are dominated by the changes to  $g_A$  in the description of the shape factors as we consider them to be fully correlated across bins and isotopes, meaning deviations remain at the  $1\sigma$  level even for different fuel compositions.

The IBD rate, on the other hand, picks up significant contributions from the expected increase in the bump region. The total effect is limited, however, to below one percent for the main contributors and constitutes a  $\sim 1.5\sigma$  effect.

Table IV shows an overview of the change in total flux and IBD rate for the different possibilities of constructing a forbidden-corrected spectrum. All results are relative to including only the numerical shape factors of Sec. IV.

As before, flux changes are minimal and within  $1\sigma$  uncertainty when including only the numerical shape factors. Differences are larger for higher values of the slope as the latter decreases the antineutrino spectrum yield. When including the parametrized shape factors both the central value and uncertainty increase significantly. Due to the increase in the expected flux starting at 3 MeV in the parametrized setup, flux changes exceed one percent and correspond to roughly a  $\sim 2\sigma$  effect. IBD rates, likewise, increase significantly as do the uncertainties. As with the effects of  $g_A$  quenching before, the large uncertainty arises mainly from the bin-to-bin correlation for the parametrized shape factors.

TABLE IV. Integrated flux and IBD rate change due to the inclusion of forbidden transition shape factors for the different fission actinides. Here slope is the slope of the shape factor of allowed decays which are to be compared against (see Sec. IID). Note that these are relative changes with respect to the improved treatment of forbidden transitions. For absolute changes with respect to the Huber-Mueller, one can take the difference with the results of Table III.

Slope	$\phi$				$R_{\text{IBD}}$			
	Numerical		Parametrized		Numerical		Parametrized	
	0%	0.67%	0%	0.67%	0%	0.67%	0%	0.67%
$^{235}\text{U}$	0.0(2)	0.2(2)	0.8(7)	1.5(7)	0.6(4)	1.0(6)	1.7(12)	2.4(12)
$^{238}\text{U}$	0.1(6)	0.2(6)	0.9(11)	1.6(11)	0.4(10)	0.7(10)	1.3(18)	1.9(18)
$^{239}\text{Pu}$	0.1(3)	0.2(3)	1.3(8)	1.6(8)	0.6(5)	0.9(6)	1.7(13)	2.4(13)
$^{241}\text{Pu}$	0.1(3)	0.1(3)	1.2(8)	1.4(8)	0.5(5)	0.9(7)	1.8(14)	2.3(14)

### VIII. REACTOR SPECTRUM CHANGES

Up to now we have discussed changes in spectral features of individual fission isotopes, in particular for  $^{235}\text{U}$ . Depending on the type of reactor, the other three actinides contribute substantially to the total flux. In general, the flux from a nuclear reactor with thermal power  $W_{\text{th}}$  can be given as

$$S(E_\nu) = \frac{W_{\text{th}}}{\sum_i R_i e_i} \sum_i R_i S_i(E_\nu), \quad (28)$$

where  $e_i$  is the energy released per fission by an actinide  $i$ ,  $R_i$  is the fractional contribution of each actinide, and  $S_i(E_\nu)$  is the corresponding antineutrino spectrum. Modern reactor experiments such as Daya Bay [78], RENO [79] and Double Chooz [12] all have different configurations of the fractional contributions  $R_i$ . All three experiments have, however, published results showing a bump in the 4–6-MeV region of the prompt positron energy ( $E_{\text{prompt}} \approx E_\nu - 0.782$  MeV) spectrum relative to the Huber-Mueller theoretical predictions. It is currently unclear which isotope(s) contribute primarily to the spectral shoulder or normalization anomaly. Here we have used previously published values for the fuel composition of the three experiments, listed in Table V.

The main difference regarding total flux in these experiments is the contribution of  $^{238}\text{U}$ , as it provides the hardest antineutrino spectrum of the four fission actinides. An investigation of the fuel dependency of the results presented here will be a topic of further research.

#### A. Spectral shoulder

In order to study the effect of the spectral shoulder, we focus only on the shape and leave the overall normalization a free parameter. Figure 17 shows the spectral shape changes

TABLE V. Reactor fuel composition in the three modern reactor antineutrino experiments.

Reactor	$^{235}\text{U}$	$^{238}\text{U}$	$^{239}\text{Pu}$	$^{241}\text{Pu}$
Daya Bay	0.586	0.076	0.288	0.05
RENO	0.62	0.12	0.21	0.05
Double Chooz	0.496	0.087	0.351	0.066

for the different reactors under the different approximations and treatments.

Both numerical only and parametrized versions behave very similarly, despite the latter typically obtaining a larger deviation in absolute magnitude. This is due to the normalization requirement which pushes the results of the latter

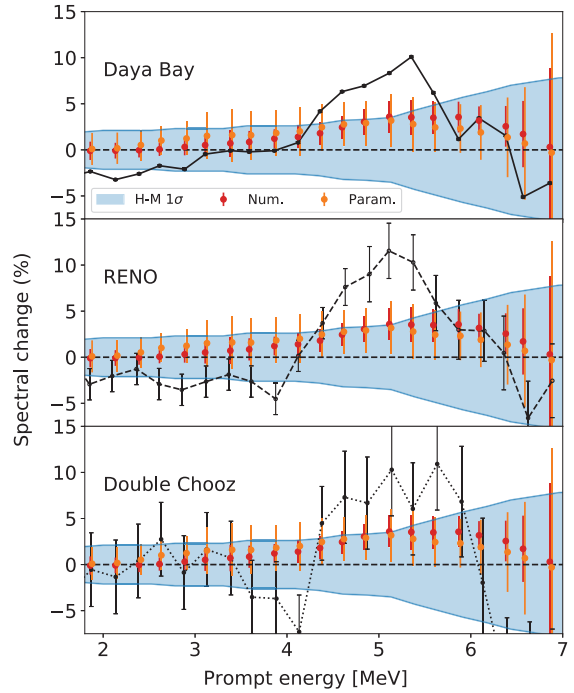


FIG. 17. Comparison of the expected spectrum change due to forbidden transitions for the different reactors, together with the observed discrepancies of experimental data relative to the Huber-Mueller results. Here “Num.” stands for including only the shape factors of Sec. IV and “Param.” includes a parametrization of all other forbidden transitions as discussed in Sec. VI. Both results are relative to an allowed shape with a weak magnetism correction of  $0.67\% \text{ MeV}^{-1}$ .

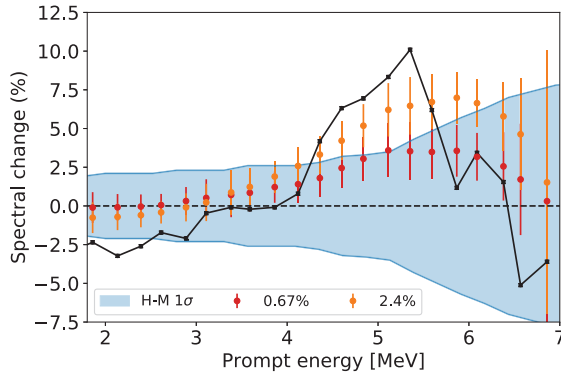


FIG. 18. Comparison of the Daya Bay shape discrepancy with the change due to the forbidden shape factors of Sec. IV when compared to two different slopes of the allowed approximation: 0.67% and 2.4%, as discussed in Secs. IID and VII B 1.

down. Both reach a magnitude of about 4% relative to the Huber-Mueller predictions. This corresponds to slightly less than half of the total effect observed by all three modern experiments. Combined with the increased correlated uncertainty on every data point, the statistical significance of the spectral shoulder is strongly mitigated. Due to the similarity of the effect for the two main fission actinides,  $^{235}\text{U}$  and  $^{239}\text{Pu}$ , small changes in the fuel composition of Table V do not appreciatively change the result due to forbidden transitions.

This effect shown in Fig. 17 is smaller than our previously reported findings [22]. Both our former and current results agree with each other within the uncertainties, however. The reason for this lies in part in the extended parametrization procedure discussed in Sec. VI. Due to the inclusion of additional shape factors and the “blind” fit of Eq. (26), the range for pseudoscalar and pseudovector shape factors is now substantially larger (see Fig. 10), particularly for higher end points. As such, a significant number of parametrized shape factors occur with a positive slope, despite only 2 out of 36 explicitly calculated shape factors showing such a behavior. As discussed above and in Sec. VI, this is possibly a limitation of our current approach. Despite this, the spread in sampled shape factors and corresponding uncertainty in the cumulative antineutrino spectra remains of particular interest as it is a quantitative estimate of the true uncertainty of previous procedures due to the neglect of forbidden shape factors. Specifically, compared to the uncertainty estimates in Tables VII–X by Huber [15], those arising from the parametrization (see Appendix) are larger or of similar size of the systematic effects presented there. We will elaborate upon this in the next section.

We have discussed in Sec. VII B 1 how an increase in the average slope of allowed transitions could combine with the results presented here to solve both the rate anomaly and the spectral shoulder at the same time. In Sec. IID we have proposed how such an increase in the slope could arise. In Fig. 18 we show the spectral shape change due to the

forbidden shape factors of Sec. IV relative to an allowed shape factor with a slope of  $2.4\% \text{ MeV}^{-1}$ .

As mentioned above, the magnitude of the deviation is now comparable to what is observed in the modern reactor experiments. A more elaborate investigation of the precise behavior of individual shape factors for the dominant allowed transitions will be able to shed more light on this. This is under current investigation.

### B. Rate anomaly

Despite forbidden transitions introducing several percent deviations in the spectrum, its effect on the integrated flux and IBD rate is limited as shown in Tables III and IV, due to the rapid decrease in antineutrino flux towards higher energies. As discussed above, however, the additional uncertainty arising from this process is significant or even dominant relative to the other systematic effects taken into account in the original analyses [15,16]. Additionally, due to the procedure used here several of the sources of uncertainty are fully correlated between bins *and* isotopes. As a consequence, the uncertainty due to forbidden transitions can be significant even when compared to the statistical and normalization uncertainties due to the experimental electron data. As such, the difference in shape factors for forbidden transitions and the resulting spectral changes point towards an underestimation of the theoretical uncertainty on the reactor rate anomaly.

Due to our simplified treatment of the databases in our composite approach (see Secs. III and VII A), we will comment here only on relative changes due to the inclusion of forbidden transitions. Due to the similarity in fuel composition of the different reactors (Table V), and the agreement in spectral changes among the main fission actinides presented here (Fig. 14), our conclusions on the rate anomaly will be the same for all three reactors.

According to the Huber-Mueller model [6,15,16] one found the following cross-section shifts for the four fission actinides: 3.7%, 4.2%, 4.7%, and 9.8% for  $^{235}\text{U}$ ,  $^{239}\text{Pu}$ ,  $^{241}\text{Pu}$ , and  $^{238}\text{U}$ , respectively. Following the reactor fuel composition, each contributes almost equally to generate a net 3–4% total shift. If we limit ourselves to the results of Table III where we used only the explicitly calculated shape factors of Sec. IV, we see that each fission actinide has an increase in the theoretical prediction of the integrated flux of less than 10% with an increased uncertainty of  $\sim 5\%$ . The IBD rate, on the other hand, is predicted to increase by  $\sim 15\text{--}25\%$  compared to the original analysis with a doubled uncertainty. Relative to the rate uncertainties quoted by Huber [15], however, this constitutes an increase of  $\sim 10\%$  of uncertainty correlated between isotopes. When combining this with the spectral normalization uncertainty common to all isotopes originating from the ILL data set (see Tables VII–X in Ref. [15]), the model uncertainty on the rate anomaly is enlarged by only 4% even though the disagreement shifts by +14%.

Using instead the parametrized results together with the numerical shape factors of Sec. IV, both the shift and uncertainty increase dramatically as shown in Table IV. Due to the increase of the predicted flux between 2 and 4 MeV, where the IBD flux reaches a maximum, the total shift corresponds to

2.3(13)%. Relative to the Huber predictions, this corresponds to an increase in the isotope shift of around 60% even though the uncertainty increases only by 30%. For the total rate anomaly this corresponds to a shift of almost 40% even though the uncertainty increases only by 13%.

Due to the limitations in the parametrization discussed above, one could argue using only the 36 explicitly calculated shape factors of Table I, but consider the uncertainty due to the parametrization of nonunique forbidden shape factors to represent a good estimate of the uncertainty due to the neglect of all others present in the database. In this case, we combine the central value shifts of Table III with the uncertainties for the parametrized calculations of Table IV. This then corresponds to an increase of the IBD rate by 0.8(13)% for every reactor. Once again combining this with the normalization uncertainties common to all isotopes, this leaves the significance of the rate anomaly unchanged as both central value and uncertainty shift by  $\sim 14\%$ .

## IX. CONCLUSION

We have, for the first time, calculated a significant number of dominant forbidden  $\beta$  transitions above 4 MeV using the nuclear shell model. As anticipated, a large fraction of these show strongly deviating shape factors from the allowed approximation. Even for pseudoscalar transitions, i.e.,  $\Delta J = 0^-$ , where shape factors are reasonably distributed around the allowed form, the limited number of contributing branches result in a net shift in the calculated electron and antineutrino spectra. This observation is strongly augmented by the results from transitions with  $\Delta J = 1^-, 2^-$ , as their shape factors are strongly divergent from the allowed approximation. A direct consequence of the inclusion of these results on the cumulative spectrum shapes is a net decrease of the predicted summation electron spectra by 1–2% in the region between 5 and 7 MeV, depending on what weak magnetism correction is used to compare against. A similar increase on the order of 4–5% is observed in the corresponding antineutrino spectra in the region between 4.5 and 7.5 MeV. We have investigated the uncertainty of these results by changing the renormalization of the axial vector coupling constant and axial charge, where appropriate, and found them to be on the order of 0.5%. The addition of an estimated *theoretical* uncertainty resulting from nuclear structure calculations is unprecedented in this mass range and within the context of the reactor anomaly.

In addition to the precise calculations described here, we have shown that the contribution of allowed  $\beta$  spectra to the electron and antineutrino flux dip (significantly) below 50% over most of experimentally accessible range. This occurs through a combination of fission yields and branching ratios favoring forbidden spectra. This dominion of forbidden spectra is particularly apparent in the region of the spectral shoulder, which motivated us in an attempt to generalize the contribution due to forbidden spectra. In this spirit, we have attempted a parametrization of effec-

tive nonunique first-forbidden shape factors according to the spin change  $\Delta J$ . Rather than assume an allowed shape, for each branch we now sample from a distribution of spectral shape based on the numerical results described above. While this parametrization has limitations due to the neglect of underlying nuclear structure considerations, the spectral uncertainty arising from it is comparable to or larger than the main systematic uncertainties in the Huber-Mueller model.

We have combined these results with the fuel compositions of the Daya Bay, RENO, and Double Chooz experiments and interpreted our results in terms of the observed spectral shoulder and rate anomaly. For the former, we find a spectral distortion very similar in shape as to what is observed experimentally, albeit with a lower magnitude. Due to the similarity of the spectral changes of the different actinides and relatively minor changes in fuel composition, our results are the same for all three experiments. For the rate anomaly, we show that our results increase the expected theoretical flux to varying degree depending on whether or not the parametrization results are taken into account. Using only the explicitly calculated shape factors, we find an increase in the expected IBD rate of 0.8(5)%. Using a proposed parametrization, this increase rises to 2.3(13)%. When combining the central value from the explicitly calculated shape factors with the uncertainty of the parametrization, the statistical significance of the rate anomaly remains unaltered.

Further, we have proposed that an increase in the average slope of allowed shape factors can yield a solution to both the rate anomaly and the spectral shoulder when combined with the results presented here. We have provided theoretical arguments and indications for why this could be the case. This is currently under investigation.

Finally, the arguments presented here regarding an oversimplified evaluation of allowed shape factors and the change in calculated electron and antineutrino flux using state of the art nuclear structure calculations point towards an underestimate of the theoretical uncertainties which lies at the heart of the reactor anomaly. As a consequence, it is clear that a proper understanding of forbidden shape factors is invaluable in the understanding of both the reactor anomaly and spectral bump.

## ACKNOWLEDGMENTS

One of the authors (L.H.) would like to thank M. Fallot and A. Sonzogni for constructive discussion. This work has been partly funded by the Belgian Federal Science Policy Office, under Contract No. IUAP EP/12-c, and the Fund for Scientific Research Flanders (FWO). This work has been partially supported by the Academy of Finland under Academy Project No. 318043. J.K. acknowledges the financial support from the Jenny and Antti Wihuri Foundation.

## APPENDIX: FLUX CHANGES AND UNCERTAINTIES

Tables VI–IX found below present a breakdown of all effects contributing to the final uncertainty of the relative spectrum changes we have described in this paper. We do this for all four fission actinides, and make a distinction between the ‘Numerical’ results using only the explicitly calculated shape factors of Sec. V, and the extended results using a parametrization for the remaining forbidden transitions.

TABLE VI. Results for the  $^{235}\text{U}$  spectrum. The errors in column 4 are completely uncorrelated, while those of column 5–7 are completely correlated. Column 4 is the statistical uncertainty in the conversion procedure resulting from the spread in virtual branch end points and average  $Z$  values. The bias uncertainty is the difference from unity in the agreement between the electron cumulative spectra in the different approaches. Column 5 represents the uncertainty due to  $g_A$  quenching as discussed in Sec. V B. Columns 4–6 contribute to the total uncertainty for the numerical approach. The parametrized results receive additional uncertainty from the parametrization procedure, listed in column 7.

$E_\nu$ (MeV)	Value		$1\sigma$ errors					
	$\delta N$ num. (%)	$\delta N$ param. (%)	Conv. (%)	Bias (%)	$g_A$ (%)	Param. (%)	Total num. (%)	Total param. (%)
2.0	0.1	0.4	0.3	0.0	0.1	+0.7 -0.5	0.1	+0.7 -0.5
2.25	-0.6	0.7	0.4	0.0	0.2	+1.0 -0.8	0.5	+1.1 -0.9
2.5	0.0	0.7	0.2	0.0	0.2	+0.3 -0.4	0.2	+0.4 -0.5
2.75	-0.1	1.2	0.0	0.0	0.3	+0.5 -0.5	0.3	0.6
3.0	-0.1	1.1	0.0	0.0	0.3	+0.5 -0.4	0.3	+0.6 -0.5
3.25	0.0	1.6	0.0	0.0	0.3	+0.5 -0.4	0.3	+0.6 -0.5
3.5	0.1	2.1	0.0	0.0	0.2	+0.4 -0.4	0.2	0.4
3.75	0.5	2.0	0.6	0.0	0.2	+0.5 -0.7	0.6	+0.8 -0.9
4.0	0.7	2.9	0.8	0.0	0.5	+1.3 -1.4	0.9	+1.6 -1.7
4.25	0.8	2.3	0.9	0.0	0.4	+1.3 -1.4	1.0	+1.6 -1.7
4.5	0.9	2.5	0.3	0.0	0.3	+1.3 -1.0	0.4	+1.3 -1.1
4.75	1.5	2.7	0.6	0.0	0.2	+0.9 -1.0	0.6	+1.1 -1.2
5.0	1.3	2.6	0.6	0.0	0.1	+1.0 -1.2	0.6	+1.2 -1.3
5.25	2.1	3.6	0.4	0.0	0.3	+1.0 -0.7	0.5	+1.1 -0.9
5.5	2.9	3.5	0.3	0.0	0.5	+0.8 -0.7	0.6	+1.0 -0.9
5.75	3.4	3.9	0.2	0.0	0.7	+0.8 -0.8	0.7	1.1
6.0	3.9	4.2	0.2	0.0	1.0	+0.9 -0.9	1.0	1.4
6.25	3.2	3.2	0.3	0.2	0.4	+0.8 -0.7	0.6	+1.0 -0.9
6.5	3.6	3.4	0.4	0.2	0.5	+0.9 -0.8	0.7	1.1
6.75	3.5	3.0	0.4	0.2	0.7	+1.0 -1.0	0.9	1.3
7.0	2.9	2.5	0.6	0.1	0.6	+1.4 -1.2	0.7	+1.6 -1.4
7.25	2.5	2.2	0.9	0.6	0.7	+2.3 -1.6	1.7	+2.8 -2.3
7.50	0.6	0.6	2.0	1.3	0.7	+3.7 -2.6	3.4	+5.0 -4.3
7.75	0.7	1.0	6.3	3.6	0.4	+4.1 -5.3	9.9	+10.7 -11.2
8.0	-1.0	-4.0	19.0	5.5	0.6	+11.0 -9.1	22.1	+24.7 -23.9

TABLE VII. Results for the  $^{238}\text{U}$  spectrum. The errors in column 4 are completely uncorrelated, while those of column 5–7 are completely correlated.

$E_\nu$ (MeV)	Value		$1\sigma$ errors					
	$\delta N$ num. (%)	$\delta N$ param. (%)	Conv. (%)	Bias (%)	$g_A$ (%)	Param. (%)	Total num. (%)	Total param. (%)
2.0	-0.1	0.1	0.0	0.1	0.5	+0.1 -0.1	0.5	+0.5 -0.5
2.25	-0.1	0.4	0.0	0.0	0.2	+0.1 -0.1	0.2	+0.2 -0.2
2.5	-0.2	0.5	0.0	0.0	0.4	+0.1 -0.2	0.4	+0.4 -0.4
2.75	-0.2	0.8	0.0	0.0	0.4	+0.2 -0.2	0.4	+0.4 -0.4
3.0	-0.2	0.8	0.0	0.0	0.4	+0.3 -0.3	0.4	+0.5 -0.5
3.25	0.1	1.2	0.0	0.0	0.5	+0.4 -0.4	0.5	+0.6 -0.6
3.5	0.0	1.6	0.1	0.0	0.6	+0.4 -0.4	0.6	+0.7 -0.7
3.75	0.2	1.7	0.1	0.0	0.6	+0.5 -0.4	0.6	+0.8 -0.7

TABLE VII. (Continued.)

$E_\nu$ (MeV)	Value		$1\sigma$ errors					
	$\delta N$ num. (%)	$\delta N$ param. (%)	Conv. (%)	Bias (%)	$g_A$ (%)	Param. (%)	Total num. (%)	Total param. (%)
4.0	0.4	2.2	0.1	0.1	0.7	+0.6 -0.4	0.7	+0.9 -0.8
4.25	0.6	2.3	0.1	0.1	0.7	+0.8 -0.6	0.7	+1.0 -0.9
4.5	0.9	2.0	0.1	0.0	0.5	+1.0 -0.7	0.5	+1.1 -0.9
4.75	1.5	1.6	0.4	0.2	0.4	+1.3 -0.6	0.6	+1.4 -0.8
5.0	0.0	1.9	2.0	0.0	0.3	+2.0 -1.9	2.0	+2.8 -2.8
5.25	1.3	3.2	1.2	0.1	0.2	+1.4 -1.3	1.2	+1.9 -1.8
5.5	2.6	4.3	1.7	0.0	0.4	+1.7 -1.5	1.7	+2.4 -2.3
5.75	2.8	3.6	1.3	0.2	0.6	+2.6 -2.8	1.4	+3.0 -3.2
6.0	2.0	3.0	2.3	0.2	0.9	+2.2 -2.5	2.5	+3.3 -3.5
6.25	1.5	3.0	2.4	0.2	0.5	+1.0 -1.0	2.5	+2.7 -2.7
6.5	2.3	3.4	1.6	0.0	0.6	+1.0 -1.3	1.7	+2.0 -2.1
6.75	2.1	2.9	1.1	0.2	0.8	+1.2 -1.5	1.4	+1.8 -2.0
7.0	1.5	1.6	0.8	0.2	0.3	+2.0 -1.5	0.9	+2.2 -1.7
7.25	2.3	1.6	2.2	0.1	0.3	+2.8 -2.9	2.2	+3.6 -3.7
7.50	-0.4	-0.2	5.1	0.3	0.1	+5.2 -2.6	5.1	+7.3 -5.7
7.75	1.3	2.3	5.3	0.3	0.3	+5.4 -6.4	5.3	+7.6 -8.3
8.0	-1.7	2.2	5.9	0.6	0.3	+6.7 -4.2	5.9	+9.0 -7.3

TABLE VIII. Results for the  $^{239}\text{Pu}$  spectrum. The errors in column 4 are completely uncorrelated, while those of column 5–7 are completely correlated.

$E_\nu$ (MeV)	Value		$1\sigma$ errors					
	$\delta N$ num. (%)	$\delta N$ param. (%)	Conv. (%)	Bias (%)	$g_A$ (%)	Param. (%)	Total num. (%)	Total param. (%)
2.0	-0.8	0.7	0.6	0.1	0.3	+0.8 -1.0	0.7	+1.0 -1.2
2.25	0.0	0.3	0.8	0.0	0.4	+1.2 -0.8	0.9	+1.5 -1.2
2.5	-0.3	1.6	0.7	0.0	0.4	+0.9 -1.0	0.8	+1.2 -1.3
2.75	-0.1	1.3	0.1	0.0	0.3	+0.7 -0.6	0.3	+0.8 -0.7
3.0	-0.1	1.4	0.1	0.0	0.3	+0.8 -0.5	0.3	+0.9 -0.6
3.25	0.0	1.9	0.1	0.0	0.2	+0.7 -0.6	0.2	+0.7 -0.6
3.5	0.1	2.7	0.0	0.0	0.2	+0.7 -0.6	0.2	+0.7 -0.6
3.75	0.4	2.9	0.0	0.1	0.2	+0.7 -0.6	0.2	+0.7 -0.6
4.0	0.6	2.7	0.1	0.1	0.4	+1.2 -1.4	0.4	+1.3 -1.5
4.25	0.9	3.2	0.2	0.0	0.3	+0.9 -0.9	0.4	+1.0 -1.0
4.5	1.0	3.3	0.3	0.0	0.2	+0.7 -0.9	0.4	+0.8 -1.0
4.75	1.5	3.9	0.5	0.1	0.2	+0.8 -1.0	0.5	+1.0 -1.1
5.0	1.9	4.0	0.2	0.3	0.3	+0.7 -0.9	0.5	+0.8 -1.0
5.25	2.2	4.4	0.1	0.3	0.5	+0.8 -0.8	0.6	+1.0 -1.0
5.5	2.5	4.2	0.1	0.1	0.7	+0.7 -0.7	0.7	+1.0 -1.0
5.75	3.2	4.5	0.1	0.2	0.8	+0.6 -0.6	0.8	+1.0 -1.0
6.0	3.9	4.7	0.1	0.7	1.1	+0.7 -0.5	1.3	+1.5 -1.4
6.25	4.2	3.7	0.3	0.7	1.1	+0.8 -0.7	1.3	+1.6 -1.5
6.5	4.2	3.7	0.4	0.4	0.4	+0.7 -0.8	0.7	+1.0 -1.0
6.75	3.9	3.4	0.7	0.1	0.5	+0.9 -0.8	0.9	+1.2 -1.2
7.0	3.0	3.0	0.5	1.0	0.4	+1.2 -1.1	1.2	+1.7 -1.6
7.25	2.4	2.5	0.3	2.0	0.5	+2.0 -1.6	2.1	+2.9 -2.6
7.50	1.1	2.0	0.7	2.5	0.6	+3.6 -2.7	2.7	+4.5 -3.8
7.75	-1.1	-1.4	7.3	0.0	0.4	+8.1 -7.1	7.3	+10.9 -10.2
8.0	-2.2	7.6	16.1	9.5	0.5	+20.1 -14.8	18.7	+27.5 -23.8

TABLE IX. Results for the  $^{241}\text{Pu}$  spectrum. The errors in column 4 are completely uncorrelated, while those of column 5–7 are completely correlated.

$E_\nu$ (MeV)	Value		$1\sigma$ errors					
	$\delta N$ num. (%)	$\delta N$ param. (%)	Conv. (%)	Bias (%)	$g_A$ (%)	Param. (%)	Total num. (%)	Total param. (%)
2.0	-0.1	0.4	0.1	0.0	0.3	+0.2 -0.2	0.3	+0.4 -0.4
2.25	-0.2	0.6	0.4	0.0	0.3	+0.3 -0.3	0.5	+0.6 -0.6
2.5	-0.2	0.8	0.4	0.0	0.4	+0.5 -0.4	0.6	+0.8 -0.7
2.75	-0.1	1.1	0.8	0.0	0.4	+0.3 -0.3	0.9	+0.9 -0.9
3.0	-0.1	1.2	0.1	0.0	0.4	+0.2 -0.2	0.4	+0.5 -0.5
3.25	-0.1	1.5	0.1	0.0	0.5	+0.5 -0.2	0.5	+0.5 -0.5
3.5	0.0	1.8	0.0	0.0	0.5	+0.3 -0.2	0.5	+0.6 -0.5
3.75	0.2	1.8	0.1	0.1	0.5	+0.4 -0.6	0.5	+0.7 -0.8
4.0	0.0	1.5	1.0	0.0	0.6	+0.6 -0.5	1.2	+1.3 -1.3
4.25	0.6	2.0	0.4	0.1	0.5	+1.0 -1.0	0.7	+1.2 -1.2
4.5	1.0	2.0	0.2	0.1	0.4	+1.4 -1.1	0.5	+1.5 -1.2
4.75	1.4	2.3	0.1	0.0	0.3	+1.6 -1.3	0.3	+1.6 -1.3
5.0	1.6	2.4	0.1	0.1	0.3	+1.3 -1.4	0.3	+1.3 -1.4
5.25	1.8	2.7	0.2	0.1	0.5	+1.0 -1.1	0.5	+1.1 -1.2
5.5	2.5	3.6	0.5	0.0	0.7	+0.7 -0.7	0.9	+1.1 -1.1
5.75	3.6	4.9	0.3	0.0	0.9	+1.3 -1.1	0.9	+1.6 -1.5
6.0	4.3	5.1	0.9	0.1	1.3	+2.0 -2.0	1.6	+2.6 -2.6
6.25	3.9	3.7	0.9	0.1	1.4	+1.4 -1.4	1.7	+2.2 -2.2
6.5	3.6	3.9	0.5	0.1	0.6	+1.2 -1.1	0.8	+1.4 -1.4
6.75	3.5	3.5	0.5	0.0	0.9	+1.4 -1.1	1.0	+1.7 -1.5
7.0	2.6	2.4	0.4	0.3	0.3	+2.0 -1.4	0.6	+2.1 -1.5
7.25	1.8	1.1	0.5	0.3	0.4	+3.1 -3.3	0.7	+3.2 -3.4
7.50	0.8	-0.2	3.6	0.5	0.4	+4.2 -4.3	3.7	+5.6 -5.7
7.75	2.2	5.0	5.1	0.5	0.2	+7.5 -7.9	5.1	+9.1 -9.4
8.0	4.6	0.3	4.0	0.5	0.3	+10.5 -9.7	4.0	+11.3 -10.5

- [1] C. Athanassopoulos *et al.* (LSND Collaboration), *Phys. Rev. Lett.* **81**, 1774 (1998).
- [2] J. M. Conrad, W. C. Louis, and M. H. Shaevitz, *Annu. Rev. Nucl. Part. Sci.* **63**, 45 (2013).
- [3] F. Kaether, W. Hampel, G. Heusser, J. Kiko, and T. Kirsten, *Phys. Lett. B* **685**, 47 (2010).
- [4] J. N. Abdurashitov *et al.* (The SAGE Collaboration), *Phys. Rev. C* **59**, 2246 (1999).
- [5] A. A. Aguilar-Arevalo, B. C. Brown, L. Bugel, G. Cheng, J. M. Conrad, R. L. Cooper, R. Dharmapalan, A. Diaz, Z. Djurcic, D. A. Finley, R. Ford, F. G. Garcia, G. T. Garvey, J. Grange, E.-C. Huang, W. Huelsnitz, C. Ignarra, R. A. Johnson, G. Karagiorgi, T. Katori *et al.*, *Phys. Rev. Lett.* **121**, 221801 (2018).
- [6] G. Mention, M. Fechner, T. Lasserre, T. A. Mueller, D. Lhuillier, M. Cribier, and A. Letourneau, *Phys. Rev. D* **83**, 073006 (2011).
- [7] K. N. Abazajian, M. A. Acero, S. K. Agarwalla, A. A. Aguilar-Arevalo, C. H. Albright, S. Antusch, C. A. Argüelles, A. B. Balantekin, G. Barenboim, V. Barger, P. Bernardini, F. Bezrukov, O. E. Bjalde, S. A. Bogacz, N. S. Bowden, A. Boyarsky, A. Bravar, D. B. Berguno, S. J. Brice, A. D. Bross *et al.*, [arXiv:1204.5379](https://arxiv.org/abs/1204.5379).
- [8] J. R. Jordan, Y. Kahn, G. Krnjaic, M. Moschella, and J. Spitz, *Phys. Rev. Lett.* **122**, 081801 (2019).
- [9] A. C. Hayes, J. L. Friar, G. T. Garvey, D. Ibeling, G. Jungman, T. Kawano, and R. W. Mills, *Phys. Rev. D* **92**, 033015 (2015).
- [10] P. Huber, *Phys. Rev. Lett.* **118**, 042502 (2017).
- [11] F. P. An, A. B. Balantekin, H. R. Band, M. Bishai, S. Blyth, I. Butorov, D. Cao, G. F. Cao, J. Cao, W. R. Cen, Y. L. Chan, J. F. Chang, L. C. Chang, Y. Chang, H. S. Chen, Q. Y. Chen, S. M. Chen, Y. X. Chen, Y. X. Chen, J. H. Cheng *et al.*, *Phys. Rev. Lett.* **116**, 061801 (2016).
- [12] Y. Abe, J. C. dos Anjos, J. C. Barriere, E. Baussan, I. Bekman, M. Bergevin, T. J. C. Bezerra, L. Bezrukov, E. Blucher, C. Buck, J. Busenitz, A. Cabrera, E. Caden, L. Camilleri, R. Carr, M. Cerrada, P.-J. Chang, E. Chauveau, P. Chimenti, A. P. Collin *et al.*, *J. High Energy Phys.* **10** (2014) 086; **02**, 074(E) (2015).
- [13] S. H. Seo, W. Q. Choi, H. Seo, J. H. Choi, Y. Choi, H. I. Jang, J. S. Jang, K. K. Joo, B. R. Kim, H. S. Kim, J. Y. Kim, S. B. Kim, S. Y. Kim, W. Kim, E. Kwon, D. H. Lee, Y. C. Lee, I. T. Lim, M. Y. Pac, I. G. Park, J. S. Park, R. G. Park, Y. G. Seon, C. D. Shin, J. H. Yang, J. Y. Yang, I. S. Yeo, and I. Yu, *Phys. Rev. D* **98**, 012002 (2018).

- [14] A. C. Hayes and P. Vogel, *Annu. Rev. Nucl. Part. Sci.* **66**, 219 (2016).
- [15] P. Huber, *Phys. Rev. C* **84**, 024617 (2011); **85**, 029901(E) (2012).
- [16] T. A. Mueller, D. Lhuillier, M. Fallot, A. Letourneau, S. Cormon, M. Fechner, L. Giot, T. Lasserre, J. Martino, G. Mention, A. Porta, and F. Yermia, *Phys. Rev. C* **83**, 054615 (2011).
- [17] X. Mougeot, *Phys. Rev. C* **91**, 055504 (2015).
- [18] A. A. Sonzogni, E. A. McCutchan, and A. C. Hayes, *Phys. Rev. Lett.* **119**, 112501 (2017).
- [19] A. C. Hayes, J. L. Friar, G. T. Garvey, G. Jungman, and G. Jonkmans, *Phys. Rev. Lett.* **112**, 202501 (2014).
- [20] Y.-F. Li and D. Zhang, *Phys. Rev. D* **100**, 053005 (2019).
- [21] D.-L. Fang and B. A. Brown, *Phys. Rev. C* **91**, 025503 (2015); **93**, 049903(E) (2016).
- [22] L. Hayen, J. Kostensalo, N. Severijns, and J. Suhonen, *Phys. Rev. C* **99**, 031301(R) (2019).
- [23] B. Stech and L. Schülke, *Z. Phys.* **179**, 314 (1964).
- [24] B. R. Holstein, *Phys. Rev. C* **19**, 1544 (1979).
- [25] L. Hayen, N. Severijns, K. Bodek, D. Rozpedzik, and X. Mougeot, *Rev. Mod. Phys.* **90**, 015008 (2018).
- [26] H. Behrens and W. Bühring, *Nucl. Phys. A* **162**, 111 (1971).
- [27] H. Behrens and W. Bühring, *Electron Radial Wave Functions and Nuclear Beta-decay* (Clarendon, Oxford, 1982).
- [28] E. K. Warburton and I. S. Towner, *Phys. Rep.* **242**, 103 (1994).
- [29] P. Baumann, M. Bounajma, F. Didierjean, A. Huck, A. Knipper, M. Ramdhane, G. Walter, G. Marguier, C. Richard-Serre, and B. Brown, *Phys. Rev. C* **58**, 1970 (1998).
- [30] H. Behrens and J. Jänecke, *Landolt-Börnstein Tables, Gruppe I, Band 4* (Springer, New York, 1969).
- [31] M. Morita and R. S. Morita, *Phys. Rev.* **109**, 2048 (1958).
- [32] H. F. Schopper, *Weak Interactions and Nuclear Beta Decay* (North-Holland, Amsterdam, 1966).
- [33] T. Kotani, *Phys. Rev.* **114**, 795 (1959).
- [34] W. Bühring, *Nucl. Phys. A* **430**, 1 (1984).
- [35] B. Holstein, *Rev. Mod. Phys.* **46**, 789 (1974).
- [36] X. B. Wang and A. C. Hayes, *Phys. Rev. C* **95**, 064313 (2017).
- [37] M. Fallot, S. Cormon, M. Estienne, A. Algora, V. M. Bui, A. Cucoanes, M. Elmimr, L. Giot, D. Jordan, J. Martino, A. Onillon, A. Porta, G. Pronost, A. Remoto, J. L. Taín, F. Yermia, and A.-A. Zakari-Issoufou, *Phys. Rev. Lett.* **109**, 202504 (2012).
- [38] A. Algora, D. Jordan, J. L. Taín, B. Rubio, J. Agramunt, A. B. Perez-Cerdan, F. Molina, L. Caballero, E. Nácher, A. Krasznahorkay, M. D. Hunyadi, J. Gulyás, A. Vitéz, M. Csatlós, L. Csige, J. Äystö, H. Penttilä, I. D. Moore, T. Eronen, A. Jokinen *et al.*, *Phys. Rev. Lett.* **105**, 202501 (2010).
- [39] A.-A. Zakari-Issoufou, M. Fallot, A. Porta, A. Algora, J. L. Taín, E. Valencia, S. Rice, V. Bui, S. Cormon, M. Estienne, J. Agramunt, J. Äystö, M. Bowry, J. A. Briz, R. Caballero-Folch, D. Cano-Ott, A. Cucoanes, V. V. Elomaa, T. Eronen, E. Estevez *et al.*, *Phys. Rev. Lett.* **115**, 102503 (2015).
- [40] S. Rice, A. Algora, J. L. Taín, E. Valencia, J. Agramunt, B. Rubio, W. Gelletly, P. H. Regan, A.-A. Zakari-Issoufou, M. Fallot, A. Porta, J. Rissanen, T. Eronen, J. Äystö, L. Batist, M. Bowry, V. M. Bui, R. Caballero-Folch, D. Cano-Ott, V.-V. Elomaa *et al.*, *Phys. Rev. C* **96**, 014320 (2017).
- [41] B. C. Rasco *et al.*, *Phys. Rev. Lett.* **117**, 092501 (2016).
- [42] A. Fijałkowska *et al.*, *Phys. Rev. Lett.* **119**, 052503 (2017).
- [43] B. C. Rasco *et al.*, *Phys. Rev. C* **95**, 054328 (2017).
- [44] J. C. Hardy, L. C. Carraz, B. Jonson, and P. G. Hansen, *Phys. Lett. B* **71**, 307 (1977).
- [45] K. Schreckenbach, H. Faust, F. von Feilitzsch, A. Hahn, K. Hawerkamp, and J. Vuilleumier, *Phys. Lett. B* **99**, 251 (1981).
- [46] K. Schreckenbach, G. Colvin, W. Gelletly, and F. Von Feilitzsch, *Phys. Lett. B* **160**, 325 (1985).
- [47] N. Haag, W. Gelletly, F. von Feilitzsch, L. Oberauer, W. Potzel, K. Schreckenbach, and A. A. Sonzogni, [arXiv:1405.3501](https://arxiv.org/abs/1405.3501).
- [48] P. Navratil, M. Dunn, M. Sin, I. Sirakov, G. Nобре, R. Wright, B. Sleaford, C. Bates, J. Conlin, A. Koning, V. Pronyaev, F. Brown, J. Lestone, D. Neudecker, M. Herman, S. Kopecky, T. Gaines, P. Romano, E. Soukhovitskii, A. Sonzogni *et al.*, *Nucl. Data Sheets* **148**, 1 (2018).
- [49] S. C. Van der Marck, *Nucl. Data Sheets* **113**, 2935 (2012).
- [50] M. Kellett, O. Bersillon, and R. Mills, Technical Report JEFF 20, 2009.
- [51] M. Fallot and A. Sonzogni (private communication).
- [52] M. Herman and A. Trkov, Brookhaven National Laboratory Technical Report No. BNL-90365-2009, Rev. 1, 2010.
- [53] M. Chadwick, M. Herman, P. Obložinský, M. Dunn, Y. Danon, A. Kahler, D. Smith, B. Pritychenko, G. Arbanas, R. Arcilla, R. Brewer, D. Brown, R. Capote, A. Carlson, Y. Cho, H. Derrien, K. Guber, G. Hale, S. Hoblit, S. Holloway *et al.*, *Nucl. Data Sheets* **112**, 2887 (2011).
- [54] T. Kawano, P. Möller, and W. B. Wilson, *Phys. Rev. C* **78**, 054601 (2008).
- [55] A. A. Sonzogni, T. D. Johnson, and E. A. McCutchan, *Phys. Rev. C* **91**, 011301(R) (2015).
- [56] L. Hayen and N. Severijns, *Comput. Phys. Commun.* **240**, 152 (2019).
- [57] B. A. Brown and W. D. M. Rae, *Nucl. Data Sheets* **120**, 115 (2014).
- [58] H. Mach, E. K. Warburton, R. L. Gill, R. F. Casten, J. A. Becker, B. A. Brown, and J. A. Winger, *Phys. Rev. C* **41**, 226 (1990).
- [59] R. Machleidt, *Phys. Rev. C* **63**, 024001 (2001).
- [60] S. Lalkovski, A. M. Bruce, A. Jungclaus, M. Górska, M. Pfützner, L. Cáceres, F. Naqvi, S. Pietri, Z. Podolyák, G. S. Simpson, K. Andgren, P. Bednarczyk, T. Beck, J. Benlliure, G. Benzoni, E. Casarejos, B. Cederwall, F. C. L. Crespi, J. J. Cuenca-García, I. J. Cullen *et al.*, *Phys. Rev. C* **87**, 034308 (2013).
- [61] B. A. Brown (unpublished).
- [62] J. Suhonen, *Front. Phys.* **5**, 55 (2017).
- [63] J. Kostensalo and J. Suhonen, *Phys. Lett. B* **781**, 480 (2018).
- [64] J. Kostensalo, M. Haaranen, and J. Suhonen, *Phys. Rev. C* **95**, 044313 (2017).
- [65] M. Haaranen, J. Kotila, and J. Suhonen, *Phys. Rev. C* **95**, 024327 (2017).
- [66] L. Bodenstern-Dresler, Y. Chu, D. Gehre, C. Gößling, A. Heimbald, C. Herrmann, R. Hodak, J. Kostensalo, K. Kröninger, J. Küttler, C. Nitsch, T. Quante, E. Rukhadze, I. Stekl, J. Suhonen, J. Tebrügge, R. Temminghoff, J. Volkmer, S. Zatschler, and K. Zuber, *Phys. Lett. B* (2019), doi: [10.1016/j.physletb.2019.135092](https://doi.org/10.1016/j.physletb.2019.135092).
- [67] J. P. Davidson, *Collective Models of the Nucleus* (Academic, New York, London, 1968).
- [68] J. Suhonen and J. Kostensalo, *Front. Phys.* **7**, 29 (2019).
- [69] D.-L. Fang (private communication).

- [70] T. Yoshida, T. Tachibana, S. Okumura, and S. Chiba, *Phys. Rev. C* **98**, 041303(R) (2018).
- [71] D. W. Scott, *Multivariate Density Estimation: Theory, Practice, and Visualization* (John Wiley & Sons, New York, 1992).
- [72] D. Foreman-Mackey, *J. Open Source Software* **1**, 24 (2016).
- [73] D. A. Dwyer and T. J. Langford, *Phys. Rev. Lett.* **114**, 012502 (2015).
- [74] M. Estienne, M. Falot, A. Algora, J. Briz-Monago, V. M. Bui, S. Cormon, W. Gelletly, L. Giot, V. Guadilla, D. Jordan, L. Le Meur, A. Porta, S. Rice, B. Rubio, J. L. Tañ, E. Valencia, and A.-A. Zakari-Issoufou, *Phys. Rev. Lett.* **123**, 022502 (2019).
- [75] P. Vogel and J. F. Beacom, *Phys. Rev. D* **60**, 053003 (1999).
- [76] A. Strumia and F. Vissani, *Phys. Lett. B* **564**, 42 (2003).
- [77] A. Kurylov, M. J. Ramsey-Musolf, and P. Vogel, *Phys. Rev. C* **67**, 035502 (2003).
- [78] F. P. An, J. Z. Bai, A. B. Balantekin, H. R. Band, D. Beavis, W. Beriguete, M. Bishai, S. Blyth, K. Boddy, R. L. Brown, B. Cai, G. F. Cao, J. Cao, R. Carr, W. T. Chan, J. F. Chang, Y. Chang, C. Chasman, H. S. Chen, H. Y. Chen *et al.*, *Phys. Rev. Lett.* **108**, 171803 (2012).
- [79] J. K. Ahn, S. Chebotaryov, J. H. Choi, S. Choi, W. Choi, Y. Choi, H. I. Jang, J. S. Jang, E. J. Jeon, I. S. Jeong, K. K. Joo, B. C. R. Kim, B. C. R. Kim, H. S. Kim, J. Y. Kim, S. H. B. Y. Kim, S. H. B. Y. Kim, S. H. B. Y. Kim, W. Kim, Y. D. Kim *et al.*, *Phys. Rev. Lett.* **108**, 191802 (2012).



## IX

# QUENCHING OF $g_A$ DEDUCED FROM THE BETA-SPECTRUM SHAPE OF $^{113}\text{Cd}$ MEASURED WITH THE COBRA EXPERIMENT

by

L. Bodenstein-Dresler et al. 2020

Physics Letters B, 800, 135092.  
doi: 10.1016/j.physletb.2019.135092

Reproduced with kind permission by Elsevier.



# Quenching of $g_A$ deduced from the $\beta$ -spectrum shape of $^{113}\text{Cd}$ measured with the COBRA experiment



COBRA collaboration

Lucas Bodenstein-Dresler<sup>a</sup>, Yingjie Chu<sup>b</sup>, Daniel Gehre<sup>b</sup>, Claus Gößling<sup>a</sup>, Arne Heimbold<sup>b</sup>, Christian Herrmann<sup>a</sup>, Rastislav Hodak<sup>c</sup>, Joel Kostensalo<sup>d</sup>, Kevin Kröninger<sup>a</sup>, Julia Küttler<sup>b</sup>, Christian Nitsch<sup>a</sup>, Thomas Quante<sup>a</sup>, Ekaterina Rukhadze<sup>c</sup>, Ivan Stekl<sup>c</sup>, Jouni Suhonen<sup>d</sup>, Jan Tebrügge<sup>a</sup>, Robert Temminghoff<sup>a</sup>, Juliane Volkmer<sup>b</sup>, Stefan Zatschler<sup>b,\*</sup>, Kai Zuber<sup>b</sup>

<sup>a</sup> TU Dortmund, Lehrstuhl für Experimentelle Physik IV, Otto-Hahn-Str. 4a, 44221 Dortmund, Germany

<sup>b</sup> TU Dresden, Institut für Kern- und Teilchenphysik, Zellescher Weg 19, 01069 Dresden, Germany

<sup>c</sup> CTU Prague, Institute of Experimental and Applied Physics, CZ-11000 Prague, Czech Republic

<sup>d</sup> University of Jyväskylä, Department of Physics, P.O. Box 35, FI-40014, Finland

## ARTICLE INFO

### Article history:

Received 29 May 2019

Received in revised form 20 September 2019

2019

Accepted 7 November 2019

Available online 12 November 2019

Editor: D.F. Geesaman

### Keywords:

$^{113}\text{Cd}$  beta-decay

Axial-vector coupling

$g_A$  quenching

Spectrum-shape method

CdZnTe

COBRA

## ABSTRACT

A dedicated study of the quenching of the weak axial-vector coupling strength  $g_A$  in nuclear processes has been performed by the COBRA collaboration. This investigation is driven by nuclear model calculations which show that the  $\beta$ -spectrum shape of the fourfold forbidden non-unique decay of  $^{113}\text{Cd}$  strongly depends on the effective value of  $g_A$ . Using an array of CdZnTe semiconductor detectors, 45 independent  $^{113}\text{Cd}$  spectra were obtained and interpreted in the context of three nuclear models. The resulting effective mean values are  $\bar{g}_A(\text{ISM}) = 0.915 \pm 0.007$ ,  $\bar{g}_A(\text{MQPM}) = 0.911 \pm 0.013$  and  $\bar{g}_A(\text{IBFM-2}) = 0.955 \pm 0.022$ . These values agree well within the determined uncertainties and deviate significantly from the free value of  $g_A$ . This can be seen as a first step towards answering the long-standing question regarding quenching effects related to  $g_A$  in low-energy nuclear processes.

© 2019 The Author. Published by Elsevier B.V. This is an open access article under the CC BY license (<http://creativecommons.org/licenses/by/4.0/>). Funded by SCOAP<sup>3</sup>.

## 1. Introduction

The potential quenching of the weak axial-vector coupling strength  $g_A$  in nuclei is of general interest, e.g. in nuclear astrophysics, rare single  $\beta$ -decays as well as double  $\beta$ -decays. The predicted rate for neutrinoless double beta ( $0\nu\beta\beta$ ) decay, in particular in the case of light Majorana neutrino exchange, depends strongly on the numerical value of  $g_A$  through the leading Gamow-Teller part of the  $0\nu\beta\beta$  nuclear matrix element (NME). A wide set of nuclear-theory frameworks has been adopted to calculate the value of this NME [1–5] but the associated quenching of  $g_A$

has not been addressed quantitatively. The effective value of  $g_A$  can be considerably quenched at least in low-energy processes such as single  $\beta$ -decays and two-neutrino double beta ( $2\nu\beta\beta$ ) decays [6–14]. This quenching can strongly affect the sensitivity of the presently running  $0\nu\beta\beta$ -experiments [15] including GERDA [16] and the MAJORANA DEMONSTRATOR [17] ( $^{76}\text{Ge}$ ), NEMO-3 [18–21] ( $^{82}\text{Se}$ ,  $^{96}\text{Zr}$ ,  $^{100}\text{Mo}$ ,  $^{116}\text{Cd}$ ), COBRA [22] ( $^{116}\text{Cd}$ ), CUORE [23] ( $^{130}\text{Te}$ ), EXO-200 [24] and KamLAND-Zen [25] ( $^{136}\text{Xe}$ ) and future projects such as LEGEND [26] ( $^{76}\text{Ge}$ ), SuperNEMO [27], AMoRE [28] and LUMINEU [29] ( $^{100}\text{Mo}$ ), MOON [30] ( $^{82}\text{Se}$ ,  $^{100}\text{Mo}$ ), AURORA [31] ( $^{116}\text{Cd}$ ), SNO+ [32] and CUPID [33] ( $^{130}\text{Te}$ ), NEXT-100 [34] as well as nEXO [35] and PandaX-III [36] ( $^{136}\text{Xe}$ ). Since  $0\nu\beta\beta$ -decay is a high-momentum exchange process of  $\sim 100$  MeV it is not clear how the results obtained for the quenching of  $g_A$

\* Corresponding author.

E-mail address: [stefan.zatschler@tu-dresden.de](mailto:stefan.zatschler@tu-dresden.de) (S. Zatschler).

<https://doi.org/10.1016/j.physletb.2019.135092>

0370-2693/© 2019 The Author. Published by Elsevier B.V. This is an open access article under the CC BY license (<http://creativecommons.org/licenses/by/4.0/>). Funded by SCOAP<sup>3</sup>.

in the low-momentum exchange single  $\beta$ -decays and  $2\nu\beta\beta$ -decays can be translated to  $0\nu\beta\beta$ -decay. Nevertheless, the conversion from the potentially measured  $0\nu\beta\beta$ -decay half-lives into a Majorana neutrino mass has a strong  $g_A$  dependence due to the involved Gamow-Teller NME. This is why it is important to study the quenching of  $g_A$  in as many ways as possible, even in low-energy processes, like single  $\beta$ -decays. The quenching of  $g_A$  at low energies has several different sources: Non-nucleonic degrees of freedom (e.g. delta resonances) and giant multipole resonances (like the Gamow-Teller giant resonance) removing transition strength from low excitation energies. Further sources of quenching (or sometimes enhancement, see [37]) are nuclear processes beyond the impulse approximation (in-medium meson-exchange or two-body weak currents) and deficiencies in the handling of the nuclear many-body problem (too small single-particle valence spaces, lacking many-body configurations, omission of three-body nucleon-nucleon interactions, etc.). Different methods have been introduced to quantify the quenching effect in decay processes of low momentum exchange (see the review [38]). One method recently proposed exploits the dependence of the  $\beta$ -spectrum shape of highly-forbidden non-unique decays on  $g_A$ . This approach will be introduced in the following.

### 1.1. The spectrum-shape method

In Ref. [39] it was proposed that the shapes of  $\beta$ -electron spectra could be used to determine the values of the weak coupling strengths by comparing the shape of the computed spectrum with the measured one for forbidden non-unique  $\beta$ -decays. This method was coined the spectrum-shape method (SSM) and its potential in determining the values of the weak coupling strengths  $g_V$  (vector part) and  $g_A$  (axial-vector part) is based on the complexity of the  $\beta$ -electron spectra. The corresponding  $\beta$ -decay shape factor  $C(w_e)$ ,  $w_e$  being the total energy of the emitted electron ( $\beta^-$ -decay) or positron ( $\beta^+$ -decay) in units of  $m_e$ , is an involved combination of different NMEs and phase-space factors [40] and can be decomposed [39] into vector, axial-vector and mixed vector-axial-vector parts in the form

$$C(w_e) = g_A^2 \left[ C_A(w_e) + \frac{g_V}{g_A} C_{VA}(w_e) + \left( \frac{g_V}{g_A} \right)^2 C_V(w_e) \right]. \quad (1)$$

In Ref. [39] also the next-to-leading-order corrections to  $C(w_e)$  were included. In the same reference it was noticed that the  $\beta$ -spectrum shape for the fourfold forbidden non-unique ( $\Delta J^\pi = 4^+$ ) ground-state-to-ground-state  $\beta^-$ -decay branch  $^{113}\text{Cd}(1/2^+) \rightarrow ^{113}\text{In}(9/2^+)$  is highly sensitive to the ratio  $g_V/g_A$  in Eqn. (1), and hence a comparison of the calculated spectra with the one measured by e.g. Belli et al. [41] could open a way to determine the value of this ratio. In Ref. [39] the theoretical electron spectra were computed by using the microscopic quasiparticle-phonon model (MQPM) [42] and the interacting shell model (ISM). This work was extended in [43] to include a comparison with the results of a third nuclear model, the microscopic interacting boson-fermion model (IBFM-2) [44]. The studies [39,43] were continued by the works [45] and [46] where the evolution of the  $\beta$ -spectra with changing value of  $g_V/g_A$  was followed for a number of highly-forbidden  $\beta^-$ -decays of odd- $A$  nuclei (MQPM and ISM calculations) and even- $A$  nuclei (ISM calculations).

There are also some potential uncertainties related to the SSM. One problem is the delicate balance of the vector, axial-vector and mixed vector-axial-vector parts in Eqn. (1) in the range where the SSM is most sensitive to the ratio  $g_V/g_A$ . At this point one has to

rely on results which require cancellations at a sub-percent level (see the review [38]). On the other hand, this point of cancellation seems to be similar for different nuclear models and quite insensitive to the parameters of the adopted model Hamiltonians and the details of the underlying mean field. Nevertheless, quantification of the associated uncertainties is non-trivial and here we estimate the systematic uncertainty in the extracted values of  $g_A$  (assuming vector-current conservation,  $g_V = 1$ ) by using three different nuclear-model frameworks (ISM, MQPM, IBFM-2) in our computations. One particular problem of the present calculations is that the used nuclear models cannot predict the half-life of  $^{113}\text{Cd}$  and the electron spectral shape for consistent values of  $g_A$  and  $g_V$ . This was already pointed out in Ref. [39] and further elaborated in Ref. [43]. The reason for this could be associated with the deficiencies of the adopted nuclear Hamiltonians in the presently discussed nuclear mass region  $A \sim 110$  and/or a need for a more nuanced treatment of the effective renormalization of the weak coupling constants, separately for different transition multipoles, like done in the context of first-forbidden non-unique transitions (see the examples in the review [38]). One has also to bear in mind that the half-life depends on the values of both  $g_A$  and  $g_V$  whereas the normalized spectrum shape depends only on the ratio of them. Thus the SSM can be used to fix the ratio  $g_V/g_A$  whereas the half-life can be used to fix the absolute value of e.g.  $g_A$ .

### 1.2. Previous studies on $^{113}\text{Cd}$

The fourfold forbidden non-unique  $\beta$ -decay of  $^{113}\text{Cd}$  was studied before using different experimental techniques. The main focus was to determine its  $Q$ -value and half-life. Among them are low-background experiments using  $\text{CdWO}_4$  scintillator crystals and  $\text{CdZnTe}$  semiconductor detectors like the COBRA experiment [51]. A summary of the most recent studies is given in Table 1. The most precise half-life measurement was achieved with a  $\text{CdWO}_4$  scintillator in 2007 [41]. The same  $\text{CdWO}_4$  crystal was already used ten years before in a similar study [48].  $\text{CdWO}_4$  scintillators reach typically lower thresholds, but feature a worse energy resolution compared to  $\text{CdZnTe}$  solid state detectors as used for COBRA. Additionally, the  $^{113}\text{Cd}$   $\beta$ -decay was investigated with early predecessors of the current COBRA demonstrator [49,50]. The latter study resulted in a half-life of  $(8.00 \pm 0.11 \text{ (stat.)} \pm 0.24 \text{ (syst.)}) \times 10^{15}$  years and a  $Q$ -value of  $322.2 \pm 0.3 \text{ (stat.)} \pm 0.9 \text{ (syst.) keV}$ . It is noteworthy that this  $Q$ -value is in perfect agreement with the accepted AME2016 value of  $Q_\beta = 323.83 \pm 0.27 \text{ keV}$  [47] while it is several 10 keV off for Ref. [41]. The other studies listed in Table 1 do not include an experimentally determined  $Q$ -value.

In addition, first attempts to describe the  $\beta$ -spectrum shape with conventional shape factors were pursued. All previous studies assumed that the  $^{113}\text{Cd}$   $\beta$ -decay can be described approximately with a shape factor corresponding to a threefold forbidden unique decay ( $\Delta J^\pi = 4^-$ ). This is a clear oversimplification probably due to the lack of accurate calculations at that time. Furthermore, the extracted shape factors are inconclusive as pointed out in Ref. [41] and [50]. The authors of Ref. [41] already mentioned that there is a discrepancy between the assumed polynomial fit and the experimental spectrum above 250 keV, if the  $Q$ -value is fixed to the accepted value quoted above. Nowadays, there is no justification to assume such an oversimplified parametrization. Instead, the present work is based on the SSM using calculations of the full expression for transitions with  $\Delta J^\pi = 4^+$ .

More recently, the COBRA collaboration used the  $^{113}\text{Cd}$   $\beta$ -decay to investigate the demonstrator's detector stability by monitoring the average decay rate over the time scale of several years [52].

**Table 1**

Summary of the most important previous  $^{113}\text{Cd}$  studies. Listed are the detection threshold  $E_{\text{th}}$ , the isotopic exposure for  $^{113}\text{Cd}$ , the energy resolution quoted as FWHM at the accepted AME2016  $Q$ -value [47], the signal-to-background ratio as well as the experimentally determined half-life  $T_{1/2}$ . Statistical and systematic uncertainties were added in quadrature, if quoted separately.

Detector material	$E_{\text{th}}$ / keV	isotop. exp. / kg d	FWHM / keV	S/B ratio	$T_{1/2}$ / $10^{15}$ yrs	Ref., year
CdWO <sub>4</sub> , 454 g	44	0.31	~49	~50	$7.7 \pm 0.3$	[48], 1996
CdZnTe, 3×5.9 g	100	0.05	~43	~8	$8.2^{+0.3}_{-1.0}$	[49], 2005
CdWO <sub>4</sub> , 434 g	28	1.90	~47	~56	$8.04 \pm 0.05$	[41], 2007
CdZnTe, 11×6.5 g	110	0.38	~20	~9	$8.00 \pm 0.26$	[50], 2009
CdZnTe, 45×6.0 g	84	2.89	~18	~47	–	present work

Such a continuous data-taking was not achieved in any experiment dedicated to the study of long-lived  $\beta$ -decays before. The analysis threshold for this particular study was  $\sim 170$  keV, which is comparatively high. It was chosen to ensure that the stability study is representative for the whole energy range interesting for  $\beta\beta$ -decay searches with COBRA excluding noise near the detection threshold. On the other hand, this drastically limits the available  $^{113}\text{Cd}$  energy range. Following this study, modifications on the hardware and software level were made to optimize the demonstrator setup for a dedicated low-threshold run with the aim to investigate the  $^{113}\text{Cd}$   $\beta$ -electron spectrum shape with high precision.

In this article we present the results of a dedicated  $^{113}\text{Cd}$  measurement campaign with the COBRA demonstrator. This study features the best signal-to-background ratio of all previous CdZnTe analyses, high statistics, a good energy resolution and moderate thresholds while providing 45 independent  $\beta$ -spectra of the transition  $^{113}\text{Cd}(1/2^+) \rightarrow ^{113}\text{In}(9/2^+)$ . The data will be used to evaluate quenching effects of  $g_A$  in the context of the three nuclear models (ISM, MQPM, IBFM-2) using the SSM as introduced in section 1.1.

## 2. Experimental setup

The COBRA collaboration searches for  $\beta\beta$ -decays with room temperature CdZnTe (CZT) semiconductor detectors. As  $0\nu\beta\beta$ -decay is expected to be an extremely rare process, the experiment is located at the Italian Laboratori Nazionali del Gran Sasso (LNGS), which is shielded against cosmic rays by 1400 m of rock. Currently, it comprises 64 coplanar-grid (CPG) detectors arranged in four layers of  $4 \times 4$  crystals. This stage of the experiment is referred to as the COBRA demonstrator [53]. Each crystal has a size of about  $1 \times 1 \times 1$  cm<sup>3</sup> and a mass of about 6.0 g. All of them are coated with a clear encapsulation known to be radio-pure. In previous iterations of the experiment it was found that the formerly used encapsulation lacquer contained intrinsic contaminations on the order of 1 Bq/kg for the long-lived radio-nuclides  $^{238}\text{U}$ ,  $^{232}\text{Th}$  and  $^{40}\text{K}$ . The new encapsulation lacquer has been investigated with ICP-MS at the LNGS, which confirmed the improved radio-purity with determined specific activities on the order of 1 mBq/kg for  $^{238}\text{U}$  and  $^{232}\text{Th}$  and about 10 mBq/kg for  $^{40}\text{K}$ . The four layers are framed by polyoxymethylene holders which are installed in a support structure made of electroformed copper. The inner housing is surrounded by 5 cm of electroformed copper, followed by 5 cm of ultra-low activity lead ( $< 3$  Bq/kg of  $^{210}\text{Pb}$ ) and 15 cm of standard lead. Additionally, the inner part is enclosed in an air-tight sealed box of polycarbonate, which is constantly flushed with evaporated nitrogen to suppress radon-induced background. Outside the inner housing the first stage of the read-out electronics is located. The complete setup is enclosed by a construction of iron sheets with a thickness of 2 mm, which acts as a shield against electromagnetic interferences. The last part of the shielding is a layer of 7 cm bor-

rated polyethylene with 2.7 wt.% of boron to effectively suppress the external neutron flux.

Charge-sensitive pre-amplifiers integrate the current pulses induced by particle interactions with the sensitive detector volume and convert the single-ended detector pulses into differential signals in order to minimize electronic noise during transmission. After linear amplification, the pulse shapes are digitized using 100 MHz flash analog-to-digital converters (FADCs) with a sample length of 10  $\mu\text{s}$ . Each FADC has eight input channels allowing for the read-out of four CPG detectors with two anode signals each. The clock speed and potential offset of the individual FADCs are corrected with the help of artificial pulses injected by a generator into the data acquisition chain. These are processed like real detector signals and provide well-defined synchronization points for an offline synchronization of the data. After this it is possible to identify and reject multi-detector hits for single detector analyses. The achievable accuracy of the time synchronization is about 0.1 ms. Additional key instruments in background suppression for COBRA are the reconstruction of the so-called interaction depth [54] and the use of pulse-shape discrimination techniques [55,56]. The interaction depth  $z$  is referred to as the normalized distance between the anode grid ( $z = 0$ ) and the planar cathode ( $z = 1$ ).

## 3. Data-taking and event selection

### 3.1. Run preparation

In preparation of a dedicated  $^{113}\text{Cd}$  run, the potential of optimizing the COBRA demonstrator towards minimum threshold operation was studied in detail. One major improvement was achieved by exchanging the coolant in the cooling system of the pre-amplifier stage, which allows operation at lower temperatures. The direct cooling of the first stage of the electronics dramatically reduces the thermal component of the signal noise while at the same time the detector performance benefits from an ambient temperature slightly below room temperature. The temperature inside the inner shield of the experiment is monitored by several sensors at different positions. In agreement with previous studies on CPG-CZT detectors [57] an optimal temperature was found to be around 9° C. The crystals themselves are not cooled directly, but through convection and radiation cooling they are kept at the same temperature as the surrounding shielding components. For each temperature set the optimal trigger threshold for every channel had to be determined after reaching the thermal equilibrium. This was done by monitoring the average trigger rate on a daily basis and adjusting the individual thresholds accordingly. While accomplishing this optimization, the worst-performing detector channels were switched off to prevent potential sources of electromagnetic interferences and crosstalk. The COBRA demonstrator was then calibrated at the point of best performance and the dedicated

$^{113}\text{Cd}$  data-taking period was started. It lasted from Jul.'17 until Feb.'18. During this period, the individual trigger thresholds  $E_{\text{th}}$  were mostly kept at the same level resulting in an average of  $\bar{E}_{\text{th}} = 83.9 \pm 14.8$  keV considering the average energy resolution in terms of FWHM at this energy. It should be noted that this is not the minimum amount of energy  $E_0$  that can be measured by the detectors, but includes a correction function  $f_{\text{cor}}(z)$  depending on the interaction depth  $z$  to ensure that the spectrum shape is not distorted by the event reconstruction (see Ref. [54]).

$$E_{\text{th}} = E_0 \cdot f_{\text{cor}}(z), \quad \text{with } f_{\text{cor}}(0) \approx 1.6. \quad (2)$$

Furthermore, an analysis threshold  $\tilde{E}_{\text{th}}$  is introduced by modifying Eqn. (2) to  $\tilde{E}_{\text{th}} = E_{\text{th}} + 8$  keV as will be motivated in section 4.2. Such a careful and conservative threshold correction is not discussed in the previous studies summarized in Table 1. The individual detector thresholds  $E_{\text{th}}$  range from 44 keV to 124 keV, whereas the 18 best detectors were operated below or around 70 keV and only the four worst-performing at 124 keV. For comparison, the threshold quoted in Ref. [41] using a  $\text{CdWO}_4$  scintillator can be referred to as  $28 \pm 14$  keV considering the given energy resolution. This is not far away from what has been achieved in the present study, where in addition a much higher number of detector channels could be used.

### 3.2. Detector calibration and characterization

The energy calibration of each detector was done using the radio-nuclides  $^{22}\text{Na}$ ,  $^{152}\text{Eu}$  and  $^{228}\text{Th}$  providing  $\gamma$ -lines in the range from 121.8 keV to 2614.5 keV. Each line was fitted with a Gaussian plus a polynomial function to take into account the underlying Compton continuum. The calibration is done by a linear fit of the peak position in channel numbers versus the known  $\gamma$ -line energy. Using the fit results, the energy resolution quoted as full-width at half-maximum (FWHM) can be parametrized for each detector separately as

$$\text{FWHM}(E) = \sqrt{p_0 + p_1 \cdot E + p_2 \cdot E^2}, \quad p_i > 0. \quad (3)$$

The parameter  $p_0$  is independent of the deposited energy and accounts for a constant contribution from noise. The second term scales with  $\sqrt{E}$  and is motivated by the Poisson fluctuations of the charge carrier production while the third term is a rather small correction for detector effects. With the parametrization given in Eqn. (3) the achieved mean relative resolution  $\text{FWHM}(E)/E$  ranges from  $12.5 \pm 0.6\%$  at 121.8 keV to  $1.7 \pm 0.1\%$  at 2614.5 keV including the uncertainty on the mean. The spread of the  $\text{FWHM}(E)/E$  distribution can be expressed by the according standard deviations of 4.0% (121.8 keV) and 0.7% (2614.5 keV).

### 3.3. Detector pool selection

To ensure stable operation during the dedicated  $^{113}\text{Cd}$  run, data with only a subset of the 64 installed detectors was collected. Three detectors were known to suffer from problems with the data acquisition electronics and unreliable contacting. Those were switched off from the very beginning. In addition, twelve detectors, that had to be operated with a threshold higher than 200 keV, were switched off subsequently during the setup optimization. Four additional detectors showed an altered performance comparing the results of calibration measurements during the  $^{113}\text{Cd}$  run.

The data of those were excluded from the final spectrum shape analysis. In the end, 45 out of 49 operated detectors qualified for the analysis with an average exposure of 1.10 kg d per detector. Two detectors were partly disabled and feature a reduced exposure of 0.29 kg d and 0.79 kg d, respectively. Using the natural abundance of  $^{113}\text{Cd}$  of 12.225% [58] in combination with the molar mass fraction of cadmium in the detector material, referred to as  $\text{Cd}_{0.9}\text{Zn}_{0.1}\text{Te}$ , it follows that the  $^{113}\text{Cd}$  isotopic exposure makes up for 5.84% of the total exposure. The combined isotopic exposure of all selected detectors adds up to 2.89 kg d.

### 3.4. Event selection

The standard COBRA selection cuts are used in the  $^{113}\text{Cd}$  analysis (see [59] for reference). Firstly, coincidences between all operational detectors are rejected, which is possible after synchronizing the 16 FADC clocks. The coincidence time window used to declare two events as simultaneous is set to 0.1 ms. The experiment's timing accuracy is about a factor of 30 better than achieved in previous studies (e.g. Ref. [41], 3.16 ms), which minimizes the loss of events due to random coincidences caused by potential  $^{113}\text{Cd}$  decays in different source crystals. The next stage consists of a set of data-cleaning cuts (DCCs) to remove distorted and unphysical events. The validity of those cuts was checked with a special run, where all channels of the same FADC were read out, if the trigger condition was fulfilled for a single channel. The triggered event trace was then rejected and only the remaining baseline pulses were analyzed. Those pulses were treated as a proxy for noise-only signals. It was found that  $99.8 \pm 0.1\%$  of the untriggered events are rejected by the DCCs while there is no significant variation between single channels. The signal acceptance of the DCCs is sufficiently constant over the  $^{113}\text{Cd}$  energy range and has been determined to  $87.5 \pm 0.6\%$ . After applying the DCCs the remaining events of the noise-only data are limited to energies  $< 40$  keV, which is well below the anticipated analysis threshold. Part of the DCCs is also a mild cut on the interaction depth  $z$  to remove near-anode reconstruction artifacts. The interaction depth is further restricted to remove events with an unphysically high  $z$ . The depth selection is optimized for each detector individually and covers, for the majority, the range  $0.2 < z \leq 0.97$ . No further pulse-shape discrimination cuts are necessary since the  $^{113}\text{Cd}$  decay is by far the strongest signal for COBRA at low energies.

### 3.5. Background description

Above the  $^{113}\text{Cd}$   $Q$ -value, the measured count rate drops by at least two orders of magnitude. Compared to the previous COBRA study [50], this is an improvement of about one order magnitude. The maximum count rate for the combined  $^{113}\text{Cd}$  spectrum of all detectors (see Fig. 1) is about 175 cts/(kg keV d) at 150 keV and drops sharply to below 1.5 cts/(kg keV d) at 400 keV. The background decreases exponentially for higher energies and is studied up to  $\sim 10$  MeV.

Previous  $\text{CdWO}_4$  studies limited the background study to much lower energies, e.g. in Ref. [41] for a first background run up to 1.7 MeV and for the  $^{113}\text{Cd}$  data-taking to 0.6 MeV. In the high-energy region two  $\alpha$ -decay peaks are present originating from  $^{190}\text{Pt}$  ( $Q_\alpha = 3.2$  MeV) and  $^{210}\text{Po}$  ( $Q_\alpha = 5.4$  MeV). Platinum is part of the electrode metalization while  $^{210}\text{Po}$  is a daughter nucleus of the radon decay chain. Both event populations are removed completely by a cut on the interaction depth due to their localized origin on the cathode side (see e.g. Ref. [22], Fig. 2). Nonetheless, surface contaminations with radio-nuclides, especially from the radon decay chain, are found to be the dominating source

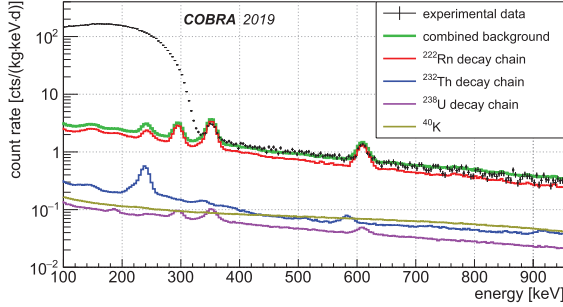


**Fig. 1.** Combined data of all detectors compared to the MC background prediction for the  $^{113}\text{Cd}$  energy range. Considered are the  $^{222}\text{Rn}$ ,  $^{232}\text{Th}$  and  $^{238}\text{U}$  decay chains as well as  $^{40}\text{K}$  with different origins of the primary decays.

of background for the search for  $0\nu\beta\beta$ -decay. In the most recent  $0\nu\beta\beta$ -decay search of COBRA, the background index for the  $^{116}\text{Cd}$  ( $Q_{\beta\beta} = 2.8$  MeV) region of interest (ROI) is quoted as 2.7 cts/(kgkeVyr) [59]. The background in this energy range is expected to be dominated by  $\alpha$ -decays on the lateral surfaces. The  $\alpha$ -particles have to pass through the encapsulation lacquer of about 20  $\mu\text{m}$  thickness before they can deposit energy in the sensitive detector volume. Because of the inhomogeneity of the lacquer, the according  $\alpha$ -spectrum is strongly deteriorated without a noticeable peak position. Near the  $^{113}\text{Cd}$  ROI there are only two prominent  $\gamma$ -lines visible in the combined spectrum of all detectors. These lines originate from the decays of  $^{214}\text{Pb}$  (351.9 keV) and  $^{214}\text{Bi}$  (609.3 keV) as short-living  $^{222}\text{Rn}$  daughters and correspond to the dominant de-excitation processes. In Dec.'17 there was a short period without nitrogen flushing of the inner shield of the experiment contributing to the overall radon exposure. Nevertheless, the effect on the spectrum shape is completely negligible since the  $\gamma$ -lines only produce weak Compton continua. The background contribution to the  $^{113}\text{Cd}$  region is estimated with a Monte Carlo (MC) simulation based on GEANT4 [60] using the shielding physics list, which is recommended for low-background experiments. The background projection considers the  $^{222}\text{Rn}$  decay chain within the gas layer of the geometry and near-detector contaminants from the  $^{238}\text{U}$  and  $^{232}\text{Th}$  decay chains as well as  $^{40}\text{K}$ . Impurities of the primordial radio-nuclides can only contribute marginally to the background due to the observed absence of characteristic prompt  $\gamma$ -lines, such as the de-excitation lines of  $^{208}\text{Tl}$  at 583.2 keV and 2614.5 keV. The signal-to-background ratio can be calculated as the integral over the  $^{113}\text{Cd}$  ROI, defined by the average threshold of  $\bar{E}_{\text{th}} = 83.9$  keV and the  $Q$ -value, for the experimental data and MC prediction. This leads to  $S/B \approx 46.8$ , which is comparable to former  $\text{CdWO}_4$  studies and about a factor of five better than previous COBRA studies (see Table 1). It should be noted that the background composition for the dedicated  $^{113}\text{Cd}$  run is different compared to the latest  $0\nu\beta\beta$ -decay analysis using data of the same setup from Oct.'11 to Sept.'16 [59]. There is no indication for the previously observed annihilation line at 511 keV or the  $^{40}\text{K}$   $\gamma$ -line at 1460.8 keV. One reason for this is that no pulse-shape discrimination cuts are used in the present analysis because the efficiency of those is rather poor at low energies. Furthermore, there is no sign for a contribution of the  $^{113\text{m}}\text{Cd}$   $\beta$ -decay ( $Q_{\beta} = 585.7$  keV,  $T_{1/2} = 14.1$  yr) as considered in Ref. [41]. Since the detectors have been underground at the LNGS since at least 3.5 years (installation of first detectors in Sept.'11, finalized setup since Nov.'13), short-lived cosmogenics affecting the low-energy region decayed away.

The ratio of the integrals over the  $^{113}\text{Cd}$  ROI and the total combined spectrum is 99.84%, indicating again the overwhelming dominance of the  $^{113}\text{Cd}$  decay for COBRA.

## 4. Analysis

### 4.1. Preparation of templates

The measured  $\beta$ -spectra are compared to sets of  $^{113}\text{Cd}$  template spectra calculated in different nuclear models in dependence on  $g_A$ . The calculations have been carried out for  $g_A \in [0.8, 1.3]$  in 0.01 steps with an energy binning of about 1 keV. The upper bound of this range is motivated by the free value of the axial-vector coupling  $g_A^{\text{free}} = 1.276(4)$  [61]. In order to compare the data for arbitrary  $g_A$  values in the given range of the original templates, so-called *splines* are used to interpolate the bin content between different values of  $g_A$  for each energy bin. In contrast to a conventional parameter fit, no optimization process is involved since a spline is uniquely defined as a set of polynomial functions over a range of points  $(x_n, y_n)$ , referred to as *knots*, and a set of boundary conditions. Per definition the original templates forming the knots are contained in the spline. For the spline construction, the *TSpline3* class of the ROOT [62] software package is used, which utilizes polynomials of grade three. For the comparison with the data, the finite energy resolution and the electron detection efficiency have to be taken into account. This is done by folding the templates with the detector-specific energy resolution and the energy dependent detector response function  $\varepsilon_{\text{det}}(E)$ . The latter is determined via a MC simulation assuming an average  $xy$ -dimension of 10.2 mm and a height of 10.0 mm to model the cubic  $\text{CdZnTe}$  crystals. It utilizes mono-energetic electrons of starting energies  $E_i$ , which are homogeneously distributed over the complete volume, and comprises  $10^6$  electrons for  $E_i \in [4, 340]$  keV in steps of 4 keV. The resulting response matrix also takes into account partial energy loss of the electrons and is used to extract  $\varepsilon_{\text{det}}(E)$  in form of a polynomial. The small deviations observed for the  $xy$ -dimension of individual crystals are treated as a systematic uncertainty (see section 4.4). Nevertheless, these variations are expected to have a rather small effect since the intrinsic detection efficiency  $\varepsilon_{\text{int}}$  for such low energies is very high. At the  $Q$ -value of  $^{113}\text{Cd}$  it can be quoted as  $\varepsilon_{\text{int}}(Q_{\beta}) = 97.7\%$  assuming the average crystal size. For lower energies the efficiency is continuously increasing.

Ref. [41] used a simplified approach to correct for the efficiency of their  $\text{CdWO}_4$  scintillator setup and introduced an energy independent scaling factor of  $\varepsilon = 99.97\%$ . This might affect the spectrum shape at low energies.

Finally, each convolved template spectrum is normalized by the integral over the accessible energy range depending on the threshold of each individual detector.

### 4.2. Spectrum shape comparison

As the individual detector thresholds had to be adjusted slightly over the run time of the  $^{113}\text{Cd}$  data-taking, it is necessary to normalize each energy bin of the experimental spectra with its corresponding exposure. The bin width is set to 4 keV, which is a compromise between a large number of bins  $N$  – beneficial for the anticipated  $\chi^2$  test to compare the spectrum shapes – and the assigned bin uncertainties arising from the number of entries per bin. The fixed binning requires to remove the lowest bin of each spectrum, because  $E_{\text{th}}$  is not necessarily a multiple of 4 keV. Additionally, as a conservative approach to address that some noise contribution might still be leaking into the  $^{113}\text{Cd}$  spectra for cer-

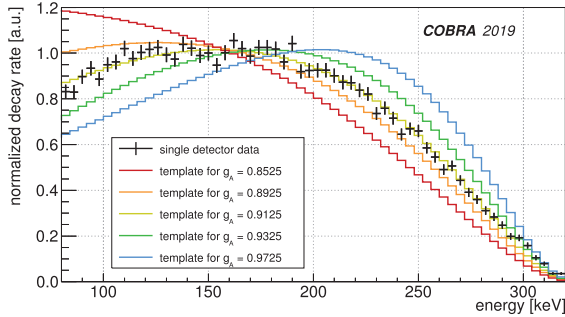


**Fig. 2.** Comparison of five interpolated, normalized template spectra based on the ISM calculations for the  $^{113}\text{Cd}$   $\beta$ -electron distribution and one COBRA single detector spectrum.

tain periods where the thresholds had to be increased along with a potential signal loss due to the DCC efficiency, the analysis threshold is set to  $\bar{E}_{\text{th}} = E_{\text{th}} + 8$  keV. This also increases the average threshold  $\bar{E}_{\text{th}}$  to 91.9 keV. Following, the experimental spectra are normalized to unity as well.

In contrast to this conservative approach, Ref. [41] used a finer binning, while their resolution is at least two times worse. The noise influence was corrected using a pulse-shape discrimination technique along with the deduced signal efficiency, which was estimated from calibration data, but no further threshold was introduced in this study.

Using the experimental values  $m_i$  of the energy bins  $i$  to  $N$  with Poisson uncertainties  $\sigma_i$  and the corresponding prediction  $t_i$  based on the template calculated for a certain  $g_A$ , the quantity  $\chi^2$  is derived as

$$\chi^2 = \sum_{i=1}^N \left( \frac{m_i - t_i}{\sigma_i} \right)^2. \quad (4)$$

A comparison between one of the single detector measurements and a subset of interpolated  $^{113}\text{Cd}$  ISM templates is illustrated in Fig. 2. For the same detector the reduced  $\chi^2_{\text{red}}(g_A) = \chi^2(g_A)/(N-1)$  in the given  $g_A$  range is shown in Fig. 3 for the three nuclear model calculations. This procedure is repeated for all 45 independent detector spectra to extract the best match  $g_A$  value from the minimum of the  $\chi^2_{\text{red}}(g_A)$  curve with a parabola fit for each of the models. The uncertainty on every best match  $g_A$  is derived from the minimum  $\chi^2 + 1$  as  $1\sigma$  deviation. Additionally, the analysis is performed for the combination of the individual spectra using average values to convolve the templates. A compilation of all the experimental spectra with the final threshold  $\bar{E}_{\text{th}}$  can be found in the appendix (see Fig. A.7–A.11).

#### 4.3. Results

The resulting distributions of the best match  $g_A$  values for the 45 independent measurements and the three nuclear models considered are shown in Fig. 4. While the ISM and MQPM results are tightly distributed around a common mean value, the IBFM-2 distribution is much wider. This is due to the fact that the latter model is less sensitive to  $g_A$  as can also be seen in the  $\chi^2_{\text{red}}(g_A)$  curve in Fig. 3.

From those single detector results a weighted mean using the  $\chi^2 + 1$  deviation can be constructed to extract an average  $\bar{g}_A$  for

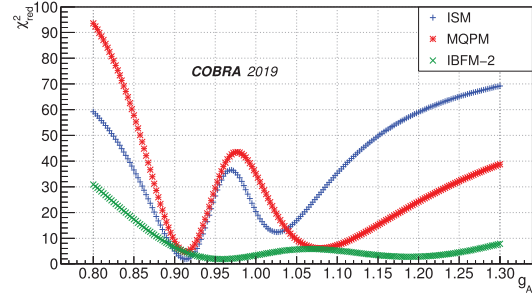


**Fig. 3.**  $\chi^2_{\text{red}}(g_A)$  curve for the spectrum shape comparison of one COBRA single detector spectrum and the interpolated templates provided by the ISM, MQPM and IBFM-2. The shape of the  $\chi^2_{\text{red}}(g_A)$  curves presented here is representative for the complete detector ensemble and the combined spectrum.

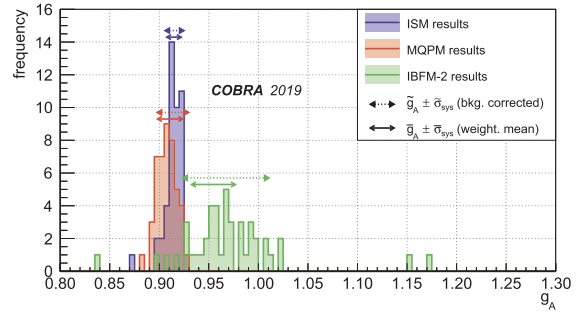


**Fig. 4.** Distribution of the 45 best match  $g_A$  values for the ISM, MQPM and IBFM-2. Additionally, the weighted mean  $\bar{g}_A \pm \bar{\sigma}_{\text{sys}}$  as well as the result of the spectrum shape comparison for the combined spectrum  $\bar{g}_A \pm \bar{\sigma}_{\text{sys}}$  including the background correction are highlighted.

each model. The statistical uncertainty  $\bar{\sigma}_{\text{stat}}$  on  $\bar{g}_A$  turns out to be negligibly small considering the systematics  $\bar{\sigma}_{\text{sys}}$  as done in section 4.4. They are on the order of  $\bar{\sigma}_{\text{stat}} \sim 2 \cdot 10^{-4}$  for ISM and MQPM and a factor of four higher for IBFM-2, respectively. The extracted weighted means including the dominant systematic uncertainties yield the following results

$$\bar{g}_A(\text{ISM}) = 0.915 \pm 0.007, \quad (5)$$

$$\bar{g}_A(\text{MQPM}) = 0.911 \pm 0.013, \quad (6)$$

$$\bar{g}_A(\text{IBFM-2}) = 0.955 \pm 0.022. \quad (7)$$

These values are in perfect agreement with the results obtained for the combined spectrum, where the MC prediction as presented in section 3.5 is used to correct for the underlying background (see Fig. 4). For the single detector analysis the background model is not used explicitly, but it enters as systematic uncertainty as discussed in the next section.

#### 4.4. Systematic uncertainties

The systematic uncertainties are determined after fixing all input parameters of the spectrum shape analysis. They are evaluated separately by modifying one considered parameter within

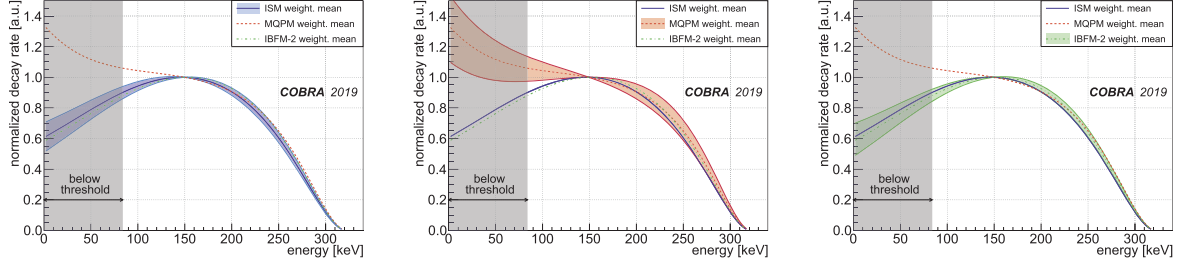


Fig. 5. Allowed spectrum range for the  $^{113}\text{Cd}$   $\beta$ -decay according to the ISM (left), MQPM (middle) and IBFM-2 (right) templates interpolated for the determined  $\bar{g}_A \pm \bar{\sigma}_{\text{sys}}$  including the experimental uncertainties. For comparison, the template corresponding to the weighted mean is shown for the respective other models.

**Table 2**  
Summary of systematic uncertainties.

Parameter	Uncertainty [%]		
	ISM	MQPM	IBFM-2
efficiency $\varepsilon(E)$	0.010	0.011	0.033
resolution FWHM( $E$ )	0.060	0.032	0.226
energy calibration	0.751	0.796	2.130
threshold	0.131	1.120	0.714
z-cut selection	0.120	0.192	0.457
template interpolation	0.002	0.002	0.001
$\chi^2_{\text{red}}$ fit range	0.102	0.058	0.034
background modeling	0.042	0.016	0.068
total	0.798	1.389	2.306

conservative limits while the other parameters are fixed to their default values in the analysis. The modulus of the difference between the altered and the default  $g_A$  result is then taken as a measure for the systematic uncertainty. The total systematic uncertainty for each model is obtained as the square root of the sum of squared uncertainties. A summary of the systematics is given in Table 2.

The effect of the efficiency scaling is studied by changing the crystal size in the MC simulation to the minimum and maximum physical  $xy$ -dimensions of the selected detectors. The systematic differences are then added in quadrature. To evaluate the influence of the resolution smearing, the FWHM( $E$ ) is fixed to the worst and best resolution curve. Following, the spectrum shape analysis is repeated with fixed FWHM( $E$ ) and the systematic differences are again added in quadrature. The influence of a misaligned energy calibration is studied by shifting the experimental data according to the uncertainty of the calibration and add the systematic differences in quadrature. An average peak shift of  $\pm 1.3$  keV was found for the 238.6 keV line of the combined  $^{228}\text{Th}$  calibration, allowing to neglect the uncertainty on the accepted  $^{113}\text{Cd}$   $Q$ -value quoted in section 1.2. It turns out that the calibration uncertainty is one of the dominating contributions. Increasing the analysis threshold for all detectors to at least 120 keV, which is more than two FWHM on average, is taken as a measure for systematic effects due to the threshold optimization and individual values. The effect is different for the nuclear models and ensues from the change of the predicted shape at low energies for MQPM compared to the other two models and the weaker  $g_A$  dependence of the IBFM-2 calculations. The systematic uncertainty of the z-cut selection is evaluated by slicing each detector in two disjunct depth ranges to perform the analysis for both slices independently. The systematic differences are again added in quadrature. The accuracy of the spline interpo-

lation is evaluated by removing the template that is the closest to the best match  $g_A$  from the given ensemble and determining the difference between the reduced and the full spline result. This is a conservative approach since the removed template is part of the final spline. The influence of the fit range to extract the minimum of  $\chi^2_{\text{red}}(g_A)$  is taken into account as another systematic uncertainty. Finally, the effect of neglecting the average background model in the single detector analysis is inferred from the analysis results of the combined spectrum with and without background subtraction. As expected from the superb  $S/B$  ratio, the effect is only marginal, which justifies the procedure.

Additional systematics as considered in previous studies (e.g. [41,50]), like the exact amount of  $^{113}\text{Cd}$  in the crystals, potential dead layer effects or a varying composition of CdZnTe due to the complex crystal growth, do not have an influence on the spectrum shape analysis. Those effects are only important for extracting the total decay rate, which is needed to determine the decay's half-life.

In total, the systematic uncertainties add up to values on the percent level and agree well with the observed spread of the  $g_A$  distributions as seen in Fig. 4. Furthermore, the single detector results are consistent with the analysis results of the combined spectrum, which yields about 30% higher uncertainties.

#### 4.5. Discussion

The average  $g_A$  values in combination with the determined experimental uncertainties can be used to illustrate the allowed spectrum range for the  $^{113}\text{Cd}$   $\beta$ -decay using the matching interpolated templates without incorporating detector effects such as finite energy resolution and efficiency (see Fig. 5).

While the spectral shape is very similar for the ISM and IBFM-2, the trend at low energies is contrary for the MQPM prediction. Nonetheless, the spectral shapes seem to be in good agreement for energies above 100 keV for all three models. Even though the IBFM-2 is associated with the highest experimental uncertainty, a comparable allowed spectrum range is achieved due to the fact that the model is less sensitive to  $g_A$ . Fig. 6 shows the minimum  $\chi^2_{\text{red}}$  distributions corresponding to the 45 best match  $g_A$  values. Again, the results based on the ISM and IBFM-2 calculations are very similar. The average values  $\bar{\chi}^2_{\text{red}}(\text{ISM}) = 1.57 \pm 0.08$ ,  $\bar{\chi}^2_{\text{red}}(\text{MQPM}) = 3.27 \pm 0.28$  and  $\bar{\chi}^2_{\text{red}}(\text{IBFM-2}) = 1.62 \pm 0.10$  considering the uncertainty of the mean of the distributions, indicate that there is less agreement between the MQPM prediction and the experimentally observed spectrum shape than for ISM and IBFM-2. This is why there is a slight preference for the ISM prediction due to the tightly distributed single detector results, the assigned

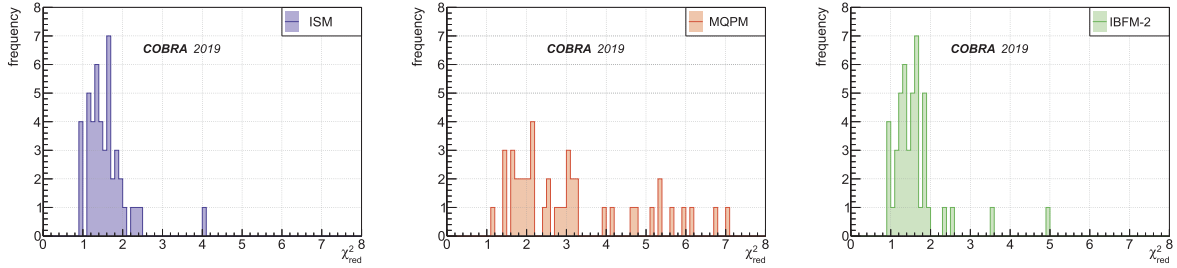


Fig. 6. Distribution of the minimum  $\chi^2_{\text{red}}$  values of the 45 best match  $g_A$  values for the single detector spectrum shape comparison.

systematic uncertainty and the pleasing minimum  $\chi^2_{\text{red}}$  distribution.

## 5. Conclusion

The spectrum shape of the fourfold forbidden non-unique  $\beta$ -decay of  $^{113}\text{Cd}$  has been investigated with 45 CdZnTe detectors and an average analysis threshold of 91.9 keV. The data set corresponds to an isotopic exposure of 2.89 kgd. Each individual  $^{113}\text{Cd}$   $\beta$ -spectrum was evaluated in the context of three nuclear models to extract average values of the effective axial-vector coupling  $g_A$ . The data support the idea that  $g_A$  is quenched in the low-momentum-exchange  $\beta$ -decay of  $^{113}\text{Cd}$  independently of the underlying nuclear model. Nevertheless, the low-energy region

needs to be explored further to distinguish the contrary behavior of the spectrum shape predicted by the different models.

## Acknowledgements

We thank the LNGS for the continuous support of the COBRA experiment, and the AMANDA collaboration, especially R. Wischniewski, for providing us with their FADCs. COBRA is supported by the German Research Foundation DFG (ZU123/3 and GO1133/1) and by the Ministry of Education, Youth and Sports of the Czech Republic with contract no. CZ.02.1.01/0.0/0.0/16\_013/0001733. Additionally, support from the Academy of Finland under the project no. 318043 and from the Jenny and Antti Wihuri Foundation is acknowledged.

## Appendix A. Single detector spectra

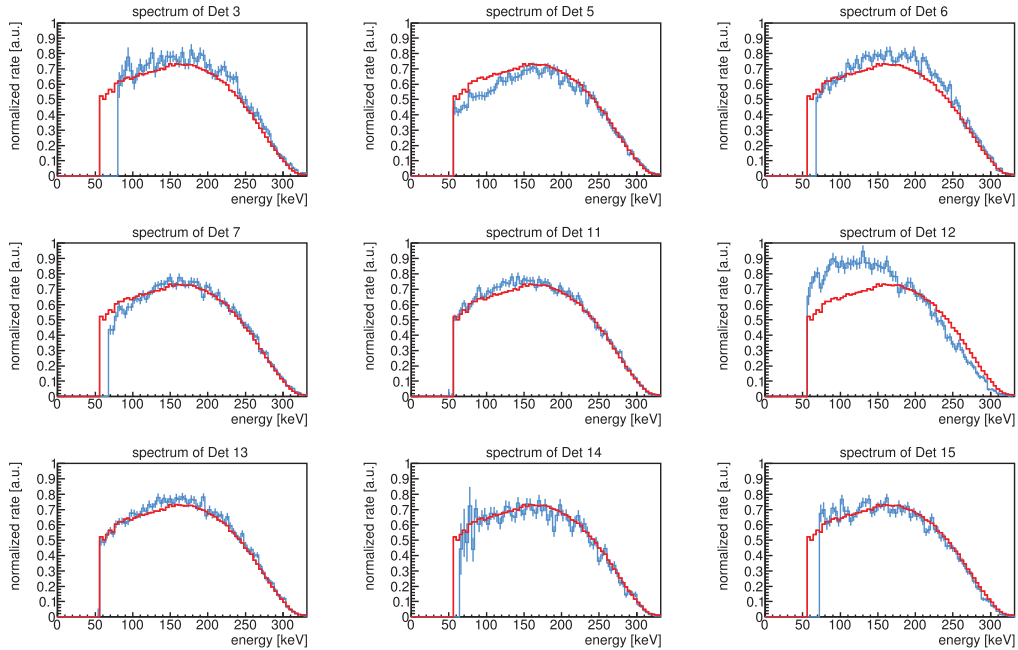
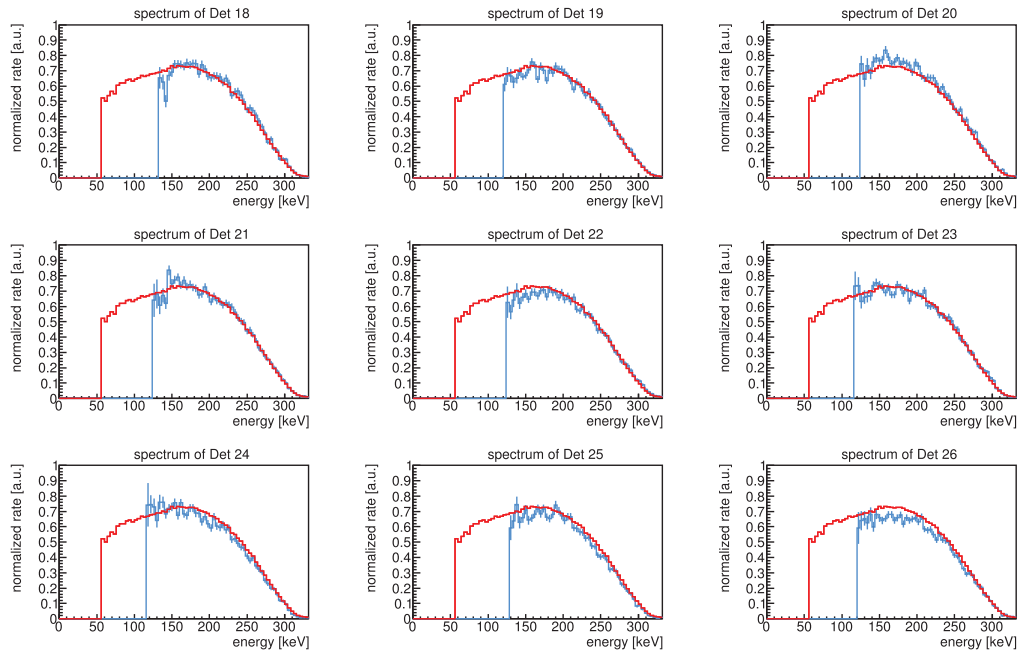
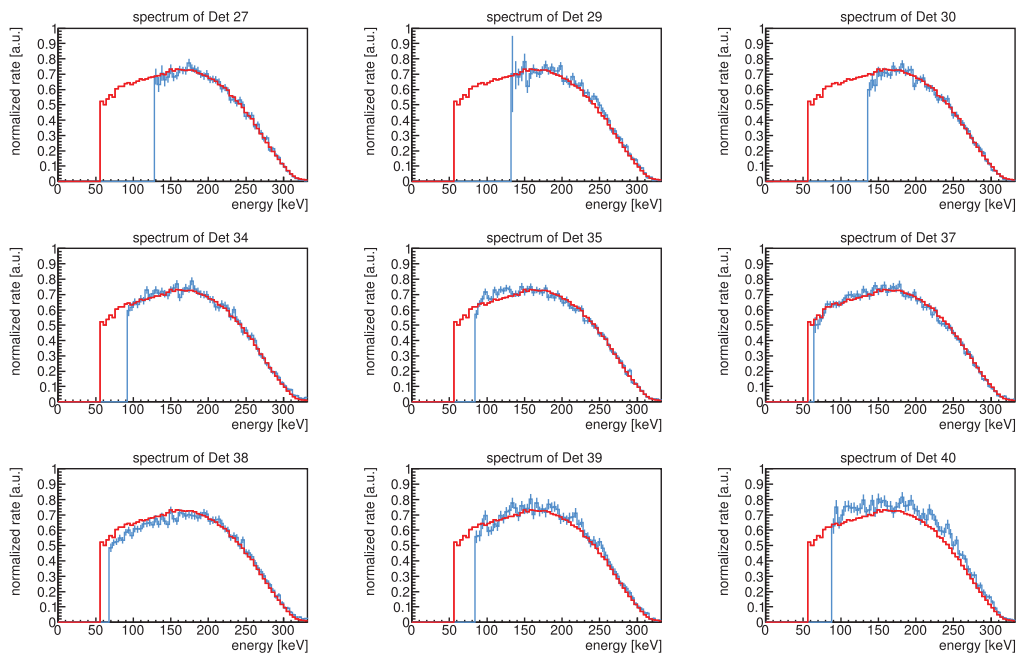


Fig. A.7. Compilation of the experimental  $^{113}\text{Cd}$  spectra measured with the COBRA demonstrator (Det3 – Det15). Each spectrum is normalized by the integral from the respective threshold to the  $Q$ -value of  $^{113}\text{Cd}$ . The combination of all detectors is shown for comparison (red solid histogram).



**Fig. A.8.** Compilation of the experimental  $^{113}\text{Cd}$  spectra measured with the COBRA demonstrator (Det18 – Det26). Each spectrum is normalized by the integral from the respective threshold to the Q-value of  $^{113}\text{Cd}$ . The combination of all detectors is shown for comparison (red solid histogram).



**Fig. A.9.** Compilation of the experimental  $^{113}\text{Cd}$  spectra measured with the COBRA demonstrator (Det27 – Det40). Each spectrum is normalized by the integral from the respective threshold to the Q-value of  $^{113}\text{Cd}$ . The combination of all detectors is shown for comparison (red solid histogram).

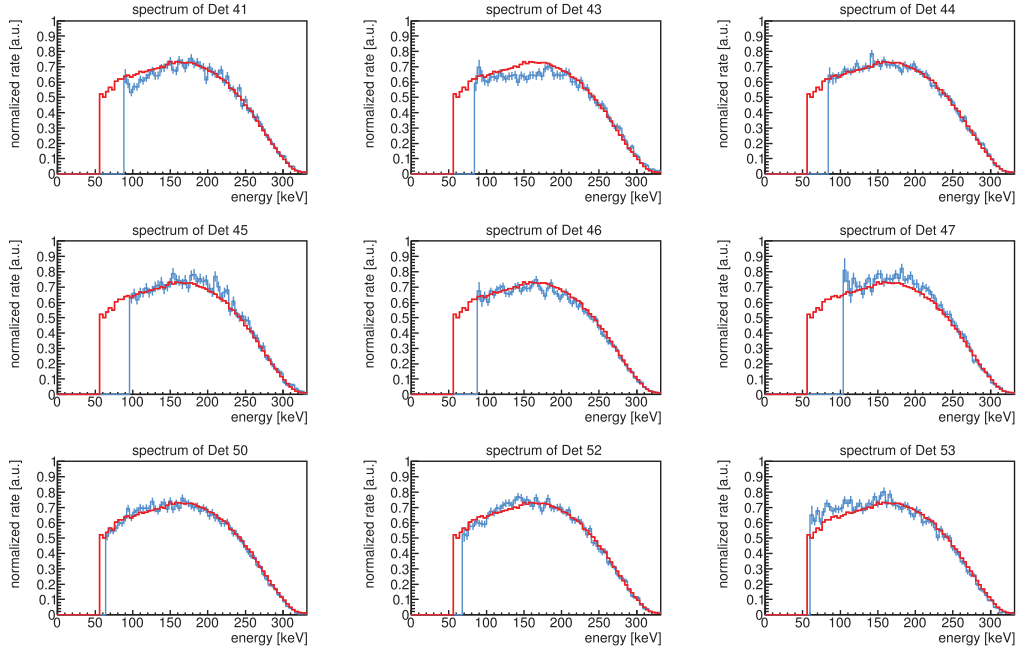


**Fig. A.10.** Compilation of the experimental  $^{113}\text{Cd}$  spectra measured with the COBRA demonstrator (Det41 – Det53). Each spectrum is normalized by the integral from the respective threshold to the  $Q$ -value of  $^{113}\text{Cd}$ . The combination of all detectors is shown for comparison (red solid histogram).

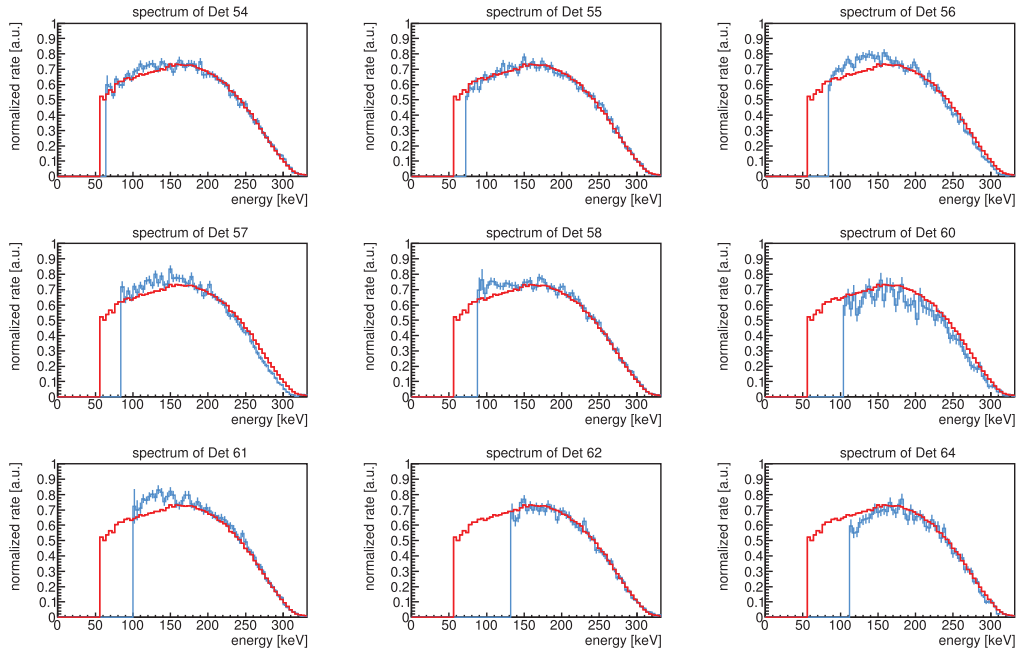


**Fig. A.11.** Compilation of the experimental  $^{113}\text{Cd}$  spectra measured with the COBRA demonstrator (Det54 – Det64). Each spectrum is normalized by the integral from the respective threshold to the  $Q$ -value of  $^{113}\text{Cd}$ . The combination of all detectors is shown for comparison (red solid histogram).

## References

- [1] J. Suhonen, O. Civitarese, *Phys. Rep.* 300 (3) (1998) 123–214.
- [2] J. Suhonen, O. Civitarese, *J. Phys. G* 39 (8) (2012) 085105.
- [3] J. Suhonen, O. Civitarese, *J. Phys. G* 39 (12) (2012) 124005.
- [4] J. Engel, J. Menéndez, *Rep. Prog. Phys.* 80 (4) (2017) 046301.
- [5] H. Ejiri, J. Suhonen, K. Zuber, *Phys. Rep.* 797 (2019) 1–102.
- [6] A. Juodagalvis, D.J. Dean, *Phys. Rev. C* 72 (Aug 2005) 024306.
- [7] A. Faessler, G.L. Fogli, E. Lisi, V. Rodin, A.M. Rotunno, F. Šimkovic, *J. Phys. G* 35 (7) (2008) 075104.
- [8] E. Caurier, F. Nowacki, A. Poves, *Phys. Lett. B* 711 (1) (2012) 62–64.
- [9] J. Suhonen, O. Civitarese, *Phys. Lett. B* 725 (1) (2013) 153–157.
- [10] J. Suhonen, O. Civitarese, *Nucl. Phys. A* 924 (2014) 1–23.
- [11] H. Ejiri, N. Soukouti, J. Suhonen, *Phys. Lett. B* 729 (2014) 27–32.
- [12] H. Ejiri, J. Suhonen, *J. Phys. G* 42 (5) (2015) 055201.
- [13] P. Pirinen, J. Suhonen, *Phys. Rev. C* 91 (May 2015) 054309.
- [14] F.F. Deppisch, J. Suhonen, *Phys. Rev. C* 94 (Nov 2016) 055501.
- [15] J. Suhonen, *Phys. Rev. C* 96 (Nov 2017) 055501.
- [16] M. Agostini, et al., GERDA collaboration, *Phys. Rev. Lett.* 120 (Mar 2018) 132503.
- [17] C.E. Aalseth, et al., Majorana collaboration, *Phys. Rev. Lett.* 120 (Mar 2018) 132502.
- [18] R. Arnold, et al., NEMO-3 collaboration, *JETP Lett.* 80 (6) (Sep 2004) 377–381.
- [19] J. Argyriades, et al., NEMO-3 collaboration, *Nucl. Phys. A* 847 (3) (2010) 168–179.
- [20] R. Arnold, et al., NEMO-3 collaboration, *Phys. Rev. D* 92 (Oct 2015) 072011.
- [21] R. Arnold, et al., NEMO-3 collaboration, *Phys. Rev. D* 95 (Jan 2017) 012007.
- [22] S. Zatschler, COBRA collaboration, *AIP Conf. Proc.* 1686 (1) (2015) 020027.
- [23] C. Alduino, et al., CUORE collaboration, *Phys. Rev. Lett.* 120 (Mar 2018) 132501.
- [24] J.B. Albert, et al., EXO-200 collaboration, *Phys. Rev. Lett.* 120 (Feb 2018) 072701.
- [25] A. Gando, et al., KamLAND-Zen collaboration, *Phys. Rev. Lett.* 117 (Aug 2016) 082503.
- [26] N. Abgrall, et al., LEGEND collaboration, *AIP Conf. Proc.* 1894 (1) (2017) 020027.
- [27] R. Hodák, SuperNEMO collaboration, *AIP Conf. Proc.* 1686 (1) (2015) 020012.
- [28] H. Park, AMoRE collaboration, *AIP Conf. Proc.* 1686 (1) (2015) 020016.
- [29] T.B. Bekker, et al., LUMINEU collaboration, *Astropart. Phys.* 72 (2016) 38–45.
- [30] K. Fushimi, et al., MOON collaboration, *J. Phys. Conf. Ser.* 203 (1) (2010) 012064.
- [31] A.S. Barabash, et al., AURORA collaboration, *Phys. Rev. D* 98 (Nov 2018) 092007.
- [32] S. Andringa, et al., SNO+ collaboration, *Adv. High Energy Phys.* 2016 (2016) 6194250.
- [33] D.R. Artusa, et al., CUPID collaboration, *Phys. Lett. B* 767 (2017) 321–329.
- [34] J. Martín-Albo, et al., NEXT collaboration, *J. High Energy Phys.* 2016 (5) (May 2016) 159.
- [35] J.B. Albert, et al., nEXO collaboration, *Phys. Rev. C* 97 (Jun 2018) 065503.
- [36] X. Chen, et al., PandaX-III collaboration, *Sci. China, Phys. Mech. Astron.* 60 (6) (Apr 2017) 061011.
- [37] J. Kostensalo, J. Suhonen, *Phys. Lett. B* 781 (1) (2018) 480–484.
- [38] J. Suhonen, *Front. Phys.* 55 (2017).
- [39] M. Haaranen, P.C. Srivastava, J. Suhonen, *Phys. Rev. C* 93 (Mar 2016) 034308.
- [40] M.T. Mustonen, M. Aunola, J. Suhonen, *Phys. Rev. C* 73 (May 2006) 054301.
- [41] P. Belli, et al., *Phys. Rev. C* 76 (Dec 2007) 064603.
- [42] J. Toivanen, J. Suhonen, *Phys. Rev. C* 57 (Mar 1998) 1237–1245.
- [43] M. Haaranen, J. Kotila, J. Suhonen, *Phys. Rev. C* 95 (Feb 2017) 024327.
- [44] F. Iachello, P. van Isacker, *The Interacting Boson-Fermion Model*, Cambridge Monographs on Mathematical Physics, Cambridge University Press, 1991.
- [45] J. Kostensalo, M. Haaranen, J. Suhonen, *Phys. Rev. C* 95 (Apr 2017) 044313.
- [46] J. Kostensalo, J. Suhonen, *Phys. Rev. C* 96 (Aug 2017) 024317.
- [47] M. Wang, et al., *Chin. Phys. C* 41 (3) (2017) 030003.
- [48] F.A. Danevich, et al., *Phys. At. Nucl.* 59 (1996) 1–5.
- [49] C. Gößling, et al., COBRA collaboration, *Phys. Rev. C* 72 (Dec 2005) 064328.
- [50] J.V. Dawson, et al., COBRA collaboration, *Nucl. Phys. A* 818 (3) (2009) 264–278.
- [51] K. Zuber, *Phys. Lett. B* 519 (1) (2001) 1–7.
- [52] J. Ebert, et al., COBRA collaboration, *Nucl. Instrum. Methods A* 821 (2016) 109–115.
- [53] J. Ebert, et al., COBRA collaboration, *Nucl. Instrum. Methods A* 807 (2016) 114–120.
- [54] M. Fritts, J. Durst, T. Göpfert, T. Wester, K. Zuber, *Nucl. Instrum. Methods A* 708 (2013) 1–6.
- [55] M. Fritts, et al., COBRA collaboration, *Nucl. Instrum. Methods A* 749 (2014) 27–34.
- [56] S. Zatschler, in: *IEEE NSS, MIC and RTSD proceedings*, 2016, pp. 1–5.
- [57] J.V. Dawson, et al., COBRA collaboration, *Nucl. Instrum. Methods A* 599 (2) (2009) 209–214.
- [58] J. Meija, T. Coplen, M. Berglund, et al., *Pure Appl. Chem.* 88 (3) (2013) 265–291.
- [59] J. Ebert, et al., COBRA collaboration, *Phys. Rev. C* 94 (Aug 2016) 024603.
- [60] J. Allison, et al., *Nucl. Instrum. Methods A* 835 (2016) 186–225. Release 10.0.p04.
- [61] J. Liu, et al., UCNA collaboration, *Phys. Rev. Lett.* 105 (Nov 2010) 219903.
- [62] R. Brun, F. Rademakers, *Nucl. Instrum. Methods A* 389 (1) (1997) 81–86. Release 6.12/04 – 2017-12-13.



**X**

**THE GALLIUM ANOMALY REVISITED**

by

Kostensalo, J., Suhonen, J., Giunti, C., Srivastava, P. C. 2019

Physics Letters B, 795, 542-547.  
DOI: 10.1016/j.physletb.2019.06.057

Reproduced with kind permission by Elsevier.



## The gallium anomaly revisited

J. Kostensalo<sup>a,\*</sup>, J. Suhonen<sup>a</sup>, C. Giunti<sup>b</sup>, P.C. Srivastava<sup>c</sup><sup>a</sup> University of Jyväskylä, Department of Physics, P.O. Box 35, FI-40014, Finland<sup>b</sup> INFN, Sezione di Torino, Via P. Giuria 1, I-10125 Torino, Italy<sup>c</sup> Department of Physics, Indian Institute of Technology, Roorkee 247667, India

## ARTICLE INFO

## Article history:

Received 26 June 2019

Accepted 27 June 2019

Available online 2 July 2019

Editor: W. Haxton

## Keywords:

Gallium anomaly

Charged-current cross-sections

Nuclear shell model

Neutrino-nucleus interactions

## ABSTRACT

The gallium anomaly, i.e. the missing electron-neutrino flux from  $^{37}\text{Ar}$  and  $^{51}\text{Cr}$  electron-capture decays as measured by the GALLEX and SAGE solar-neutrino detectors, has been among us already for about two decades. We present here a new estimate of the significance of this anomaly based on cross-section calculations using nuclear shell-model wave functions obtained by exploiting recently developed two-nucleon interactions. The gallium anomaly of the GALLEX and SAGE experiments is found to be smaller than that obtained in previous evaluations, decreasing the significance from  $3.0\sigma$  to  $2.3\sigma$ . This result is compatible with the recent indication in favor of short-baseline  $\bar{\nu}_e$  disappearance due to small active-sterile neutrino mixing obtained from the combined analysis of the data of the NEOS and DANSS reactor experiments.

© 2019 Published by Elsevier B.V. This is an open access article under the CC BY license (<http://creativecommons.org/licenses/by/4.0/>). Funded by SCOAP<sup>3</sup>.

## 1. Introduction

Gallium-based solar-neutrino experiments, GALLEX [1–3] and SAGE [4], were designed to detect  $pp$  neutrinos from the sun. These two experiments are unique in having been tested for their detection efficiency by  $^{37}\text{Ar}$  and  $^{51}\text{Cr}$  radioactive sources. These sources emit discrete-energy electron neutrinos ( $E_\nu < 1$  MeV) based on their decay via nuclear electron capture (EC). Detection of these neutrinos is achieved through the charged-current neutrino-nucleus scattering reaction

$$\nu_e + {}^{71}\text{Ga}(3/2^-)_{\text{g.s.}} \rightarrow {}^{71}\text{Ge}(J^\pi) + e^- \quad (1)$$

to the lowest four (flux from the  $^{51}\text{Cr}$  source) or five (flux from the  $^{37}\text{Ar}$  source) nuclear states in  $^{71}\text{Ge}$ . In this article we discuss also the analogous reaction

$$\nu_e + {}^{69}\text{Ga}(3/2^-)_{\text{g.s.}} \rightarrow {}^{69}\text{Ge}(J^\pi) + e^- \quad (2)$$

in order to test our calculated shell-model wave functions more comprehensively.

The scattering of  $^{37}\text{Ar}$  and  $^{51}\text{Cr}$  neutrinos off  $^{71}\text{Ga}$  leads mainly to the ground state and the excited states at 175 keV and 500

keV in  $^{71}\text{Ge}$ . The scattering cross sections for the mentioned three low-lying states can be estimated by using the data from charge-exchange reactions [5] or by using a microscopic nuclear model, like the nuclear shell model [6]. In both cases it has been found that the estimated cross sections are larger than the ones measured by the GALLEX [1–3] and SAGE [4] experiments. The measured neutrino capture rates (cross sections) are  $0.87 \pm 0.05$  of the rates based on the cross-section estimates by Bahcall [6]. The related model calculations and analyses based on them have been discussed in [7–9]. It should be noted that the response to the ground state is known from the electron-capture  $ft$  value of  $^{71}\text{Ge}$ . The discrepancy between the measured and theoretical capture rates constitutes the so-called “gallium anomaly”.

One of the explanations to the gallium anomaly is associated with the oscillation of the electron neutrinos to a sterile neutrino in eV mass scale [7,9]. The same scheme could also explain the so-called “reactor-antineutrino anomaly” [10–12], discussed, e.g. in [9]. Searches for the sterile neutrinos are under progress in several laboratories. However, it should be remarked here that there is no accepted sterile neutrino model to explain the experimental anomalies consistently, and also alternative solutions to the reactor-antineutrino anomaly have been proposed, like the proper inclusion of first-forbidden  $\beta$ -decay branches in the construction of the cumulative antineutrino spectra [13].

\* Corresponding author.

E-mail address: joel.j.kostensalo@student.jyu.fi (J. Kostensalo).

## 2. Neutrino-nucleus scattering formalism

We now summarize the main points of the formalism for calculating cross sections for charged-current neutrino-nucleus scattering. Details of the formalism can be found from [14,15].

For the low-energy ( $E_\nu < 1$  MeV)  $^{37}\text{Ar}$  and  $^{51}\text{Cr}$  neutrinos considered in this work the creation of the two heavier lepton flavors,  $\mu$  and  $\tau$ , is not energetically possible. At these low energies the four-momentum transfer is small compared to the mass of the exchanged gauge boson  $W^\pm$ , that is,  $Q^2 = -q_\mu q^\mu \ll M_{W^\pm}^2$ . Therefore, to a good approximation the scattering can be considered in the lowest order as a single effective vertex with a coupling constant  $G = G_F \cos(\theta_C)$ , where  $G_F$  is the Fermi constant and  $\theta_C \approx 13^\circ$  is the Cabibbo angle. The matrix element of this effective Hamiltonian can be written as

$$\langle f | H_{\text{eff}} | i \rangle = \frac{G}{\sqrt{2}} \int d^3\mathbf{r} l_\mu e^{-i\mathbf{q}\cdot\mathbf{r}} \langle f | \mathcal{J}^\mu(\mathbf{r}) | i \rangle, \quad (3)$$

where  $\mathcal{J}^\mu$  denotes the hadronic current and  $l_\mu = e^{i\mathbf{q}\cdot\mathbf{r}} \langle l | j_\mu(r) | \nu \rangle$  [14].

The initial nuclear state in the scatterings of Eqs. (1) and (2) is the  $J_i^{\pi_i} = 3/2^-$  ground state of  $^{69,71}\text{Ga}$ . Assuming that the final nuclear states in  $^{69,71}\text{Ge}$  also have well defined spin-parities  $J_f^{\pi_f}$ , the double differential cross section for the charged-current (CC) neutrino-nucleus scattering is given by [14,16,17]

$$\left[ \frac{d^2\sigma_{i \rightarrow f}}{d\Omega dE_{\text{exc}}} \right] = \frac{G^2 |\mathbf{k}_l| E_l}{\pi (2J_i + 1)} F(Z_f, E_l) \left( \sum_{J \geq 0} \sigma_{\text{CL}}^J + \sum_{J \geq 1} \sigma_{\text{T}}^J \right), \quad (4)$$

where  $\mathbf{k}_l$  and  $E_l$  are the three-momentum and energy of the outgoing lepton, respectively, and  $F(Z_f, E_l)$  is the Fermi function which accounts for the Coulomb interaction of the low-energy final-state lepton and the residual nucleus [18]. Here  $\sigma_{\text{CL}}^J$  is the Coulomb-longitudinal component and  $\sigma_{\text{T}}^J$  is the transverse component. Detailed formulas for these can be found in Ref. [15]. The operators contain vector and axial-vector pieces, which depend on the four-momentum-transfer-dependent nuclear form factors  $F_{1,2}^V$  (vector),  $F^A$  (axial-vector), and  $F^P$  (pseudoscalar). At low neutrino energies the cross section is dominated by Fermi and Gamow-Teller type of transitions which proceed via the operators  $F^V(q) j_0(qr) \mathbf{1}$  and  $F^A(q) j_0(qr) \boldsymbol{\sigma}$  respectively [14]. There are also small contributions from spin-dipole type transitions mediated by the operator  $F^A(q) [j_1(qr) \mathbf{Y}_1 \boldsymbol{\sigma}]_{0-,1-,2-}$ .

## 3. Results of nuclear-structure calculations

The nuclear wave functions and one-body transition densities (OBTDs) (see e.g. [19]) were calculated in the interacting nuclear shell model using the computer code NuShellX@MSU [20]. The calculations were done in a model space consisting of the proton and neutron orbitals  $0f_{5/2}$ ,  $1p$ , and  $0g_{9/2}$  with the effective Hamiltonian JUN45 [21]. The low-energy excitation spectra of  $^{71}\text{Ga}$  and  $^{71}\text{Ge}$ , of interest in this work, are presented in Figs. 1 and 2, respectively (see also Honma et al. [21] for the 1–3 MeV range in  $^{71}\text{Ge}$ ). For both cases the ground-state spin-parity is correctly predicted:  $3/2^-$  for  $^{71}\text{Ga}$  and  $1/2^-$  for  $^{71}\text{Ge}$ . The energies of the first two excited states in  $^{71}\text{Ga}$  agree well with the experimental spectrum but the ordering of the  $5/2^-$  and  $1/2^-$  states is reversed. The second  $3/2^-$  state is also higher than the experimental one, with energy 882 keV compared to the experimental energy 511 keV. For  $^{71}\text{Ge}$  the ordering of the first four states, including the negative parity states which we are actually interested in, agree with the experimental data. The qualitative features of the computed

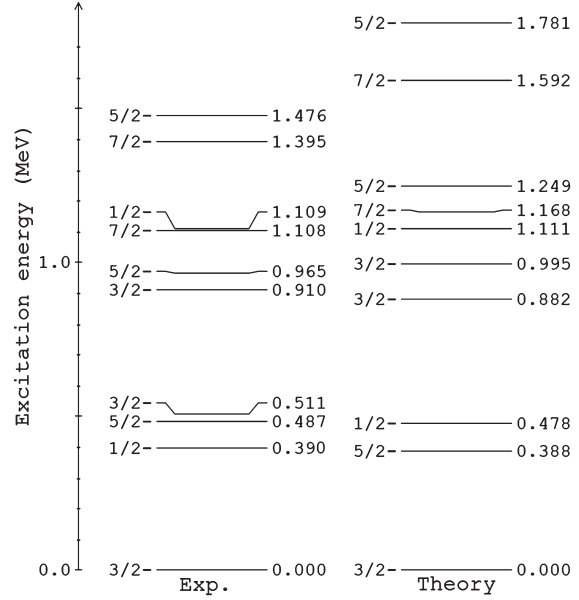


Fig. 1. Experimental and theoretical low-lying energy spectra of  $^{71}\text{Ga}$ .

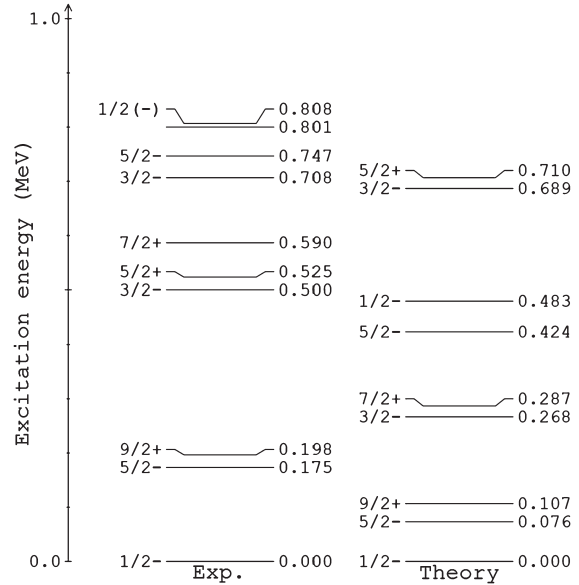


Fig. 2. Experimental and theoretical low-lying energy spectra of  $^{71}\text{Ge}$ .

low-energy spectrum are also very similar to the experimental one, with the gap between the  $5/2^-$  and  $9/2^+$  states being much narrower than the gap between the ground state and the first excited state as well as the gap between the  $9/2^+$  and  $3/2^-$  states. However, the shell-model-calculated energies of the excited states are a bit lower than the experimentally determined states, with the 175 keV state predicted at 76 keV and the 500 keV state predicted at 268 keV.

The electromagnetic properties are also pretty well predicted (see the original article of Honma et al. [21] for details). For the

**Table 1**  
Results for  $^{71}\text{Ga}$  with  $\delta = 0.097$  in Eq. (5).

State	$\langle f    O_{GT}    i \rangle$	$\langle f    O_{L=2}    i \rangle$	$\text{BGT}_{\beta}^{\text{SM}}$	$\text{BGT}_{(p,n)}^{\text{SM}}$
$1/2_{g.s.}^{-}$	-0.795	0.465	0.158	0.141
$5/2_{1}^{-}$	0.144	-1.902	0.0052	0.0004
$3/2_{1}^{-}$	0.100	0.0482	0.0025	0.0027
$3/2_{2}^{-}$	0.430	-0.0014	0.0462	0.0462
$1/2_{2}^{-}$	-0.620	0.348	0.0958	0.0857

ground state of  $^{71}\text{Ga}$  the theoretical electric quadrupole moment is  $+0.155 eb$  [21] (with effective charges  $e_p = 1.5$ ,  $e_n = 0.5$ ) while the experimental one is  $+0.1040(8) eb$  [22]. For the  $9/2^{+}$  state in  $^{71}\text{Ge}$  the theoretical value  $-0.339 eb$  seems to agree perfectly with the experimental value  $0.34(5) eb$  [23], however, the sign has not been experimentally determined. The magnetic dipole moments of the low-lying states are excellently predicted. With the  $g$  factors  $g_l = g_l^{(\text{free})}$  and  $g_s = 0.7g_s^{(\text{free})}$  the magnetic dipole moment of the  $^{71}\text{Ga}$  ground state is predicted to be  $+2.188 \mu_N$  which is in good agreement with the experimental value  $+2.56227(2) \mu_N$  [22]. For the  $1/2^{-}$ ,  $5/2^{-}$ , and  $9/2^{+}$  states in  $^{71}\text{Ge}$  the magnetic moments are  $+0.438 \mu_N$ ,  $+1.060 \mu_N$ ,  $-1.014 \mu_N$ , while the experimental ones are  $+0.547(5) \mu_N$  [24],  $+1.018(10) \mu_N$  [25], and  $-1.0413(7) \mu_N$  [23], respectively.

The calculations were also done for  $^{69}\text{Ge}$  and  $^{69}\text{Ga}$ . In this case the shell model reproduced the experimental data even better. The first three states in  $^{69}\text{Ge}$  were predicted with the correct spin parities  $5/2^{-}$ ,  $1/2^{-}$ , and  $3/2^{-}$ . The shell model energies 0 keV, 98 keV, and 189 keV agree well with the experimental energies 0 keV, 87 keV and 233 keV. Also the electromagnetic properties are well reproduced in this case [21].

For the calculation of the cross sections we use recently measured  $Q$  values and branching ratios from [26] and the same  $L/K$  capture ratios as well as atomic overlap corrections as Bahcall in his analysis [6]. The neutrino energies adopted here are for  $^{51}\text{Cr}$  751.82 keV (9.37%), 746.99 keV (80.70%), 431.74 keV (1.033%), and 426.91 keV (8.890%). For  $^{37}\text{Ar}$  the energies we use are 813.60 keV (90.2%) and 811.05 keV (9.8%).

#### 4. Results for BGT values

The neutrino-nucleus scattering cross sections are proportional to the  $\beta$ -decay BGT values, which could be, in principle, extracted from  $\beta$ -decay half-lives. This procedure gives us accurately the ground-state-to-ground-state BGT value, but it is not implementable for the BGTs of the excited states. Therefore, other techniques, such as performing charge-exchange reactions, must be utilized. However, this technique can be problematic for some transitions due to the significant tensor contributions, as was shown to be the case for the  $(p, n)$  reaction leading to the first excited state in  $^{71}\text{Ga}$  by Haxton [8]. In this case, there is a significant cancellation between the Gamow-Teller (GT) and tensor (T) matrix elements. The interference between the GT and T NMEs is described by the linear combination

$$\langle f || O_{(p,n)} || i \rangle = \langle f || O_{GT} || i \rangle + \delta \langle f || O_{L=2} || i \rangle, \quad (5)$$

where  $i$  ( $f$ ) is the initial (final) nuclear state and  $\delta$  is the mixing parameter.

The calculated GT and T matrix elements are listed in Tables 1 and 2. For  $^{71}\text{Ga}$  the matrix elements for the scattering to the  $3/2_{2}^{-}$  and  $1/2_{2}^{-}$  states are also included for comparison with the available charge-exchange data. As predicted by Haxton [8], the GT and T contributions cancel significantly for  $5/2_{1}^{-}$ . For the  $3/2_{1}^{-}$  state the contributions are constructive. Interestingly, the GT and

**Table 2**  
The results for  $^{69}\text{Ga}$  with  $\delta = 0.097$  in Eq. (5).

State	$\langle f    O_{GT}    i \rangle$	$\langle f    O_{L=2}    i \rangle$	$\text{BGT}_{\beta}^{\text{SM}}$	$\text{BGT}_{(p,n)}^{\text{SM}}$
$5/2_{g.s.}^{-}$	-0.0139	-1.180	$4.802 \times 10^{-5}$	$4.117 \times 10^{-3}$
$1/2_{1}^{-}$	-0.592	0.238	0.0876	0.0809
$3/2_{1}^{-}$	0.0298	0.422	$2.220 \times 10^{-4}$	$1.251 \times 10^{-3}$

T contributions counteract each other also for the ground-state-to-ground-state transition, meaning that a  $(p, n)$  reaction would underestimate the BGT value. This is significant regarding the validity of the BGT values reported by Frekers et al. [5,27], since these tensor contributions are ignored. This leads to an underestimation of the ground-state-to-ground-state BGT value and, since this is adjusted to the one extracted from  $\beta$  decay, to an overestimation of the BGT values to the excited states. It should be noted that the value  $\delta = 0.097$  used here, as well as in the work of Haxton, has been obtained by fitting  $\beta$  transitions in the  $p$ -shell [8]. However, uncertainties related to this choice are hard to quantify. A reasonable estimate might be  $0.05 < \delta < 0.15$ , meaning that the overestimation in the ground-state BGT is somewhere between 10% and 40%. It should be emphasized that this alone is not enough to explain the discrepancy between the shell-model calculations and charge-exchange results, since the ratio  $\text{BGT}_{500}/\text{BGT}_{g.s.}$  is  $0.207 \pm 0.016$  according to the charge-exchange experiment [27], while the shell model predicts a ratio as low as 0.019.

In [5] the projectile, target and relative angular-momentum transfers [ $J_{\text{projectile}}$   $J_{\text{target}}$   $J_{\text{relative}}$ ] were measured in the  $^{71}\text{Ga}(^3\text{He}, ^3\text{H})^{71}\text{Ge}$  charge-exchange reaction. One possible explanation for the remaining difference between the shell-model calculations and charge-exchange results relates to the extraction of the [110] component of the angular-momentum transfers at  $0^\circ$ , which corresponds to the GT and T contributions. This was done in [5] by fitting various angular-distribution functions, with different [ $J_{\text{projectile}}$   $J_{\text{target}}$   $J_{\text{relative}}$ ] combinations, to the experimental angular distribution. However, in the calculation of the distributions shell-model OBTDs calculated in the  $fp$ -space using the Hamiltonian GXPF1a [28,29] were used. This Hamiltonian does not seem to be the best choice here: it for example predicts the level ordering of  $^{71}\text{Ge}$  as  $5/2^{-}$  ground state,  $1/2^{-}$  at 388 keV, and  $3/2^{-}$  at 1496 keV, which does not agree at all with the experimental spectrum. The one-body transition densities turn out to be off as well. To replicate the experimental half-life of  $^{71}\text{Ge}$  one would need to adopt  $g_A \approx 0.6$  and the ratios  $\text{BGT}_{175}/\text{BGT}_{g.s.}$  and  $\text{BGT}_{500}/\text{BGT}_{g.s.}$  are predicted as 0.0025 and 0.695 respectively, which is not at all consistent with the final experimental values. Frekers et al. report the [110] component at  $0^\circ$  to be 92% for the ground state and 87% for the second excited state. It cannot be easily estimated how much and which way the use of these OBTDs effects the fits and thus the percentages. In a scenario where the ground-state [110] component is underestimated and/or the 500 keV-state [110] component is overestimated, we would also have another source of systematic overestimation of the ratio  $\text{BGT}_{500}/\text{BGT}_{g.s.}$ . For example if the true [110] components for the ground state and the  $3/2_{2}^{-}$  state would be 95% and 70% instead and  $\delta = 0.15$ , we would get roughly a 70% overestimate for the BGT ratio.

What comes to the transitions to the  $1/2_{2}^{-}$  and  $3/2_{2}^{-}$  states, the shell model is in agreement with the charge-exchange results in that the transition to the  $1/2_{2}^{-}$  state is the second strongest after the ground-state-to-ground-state transition. However, the transition to  $3/2_{2}^{-}$  is predicted to be significantly stronger than the one to the  $3/2_{1}^{-}$  state, while the results of Frekers et al. [27] would imply this to be the weakest of the transitions. The shell model predicts qualitatively correctly that the ground-state-to-ground-state scattering has a much lower cross section for  $^{69}\text{Ga}$  than for  $^{71}\text{Ga}$ ,

**Table 3**  
Cross-section results for the  $^{51}\text{Cr}$  neutrinos with JUN45 interaction. The cross sections are in units  $\text{cm}^2$ .

State	$g_A = 0.955(6)$
$1/2_{e.s.}^-$	$5.53 \pm 0.07 \times 10^{-45}$
$5/2_1^+$	$1.21 \pm 0.61 \times 10^{-46}$
$9/2_1^+$	$\leq 10^{-56}$
$3/2_1^-$	$1.94 \pm 0.97 \times 10^{-47}$
total	$5.67 \pm 0.10 \times 10^{-45}$

**Table 4**  
Cross-section results for the  $^{37}\text{Ar}$  neutrinos with JUN45 interaction. The cross sections are in units  $\text{cm}^2$ .

State	$g_A = 0.955(6)$
$1/2_{e.s.}^-$	$6.62 \pm 0.09 \times 10^{-45}$
$5/2_1^+$	$1.51 \pm 0.76 \times 10^{-46}$
$9/2_1^+$	$\leq 10^{-56}$
$3/2_1^-$	$2.79 \pm 1.40 \times 10^{-47}$
$5/2_1^+$	$5.91 \pm 2.96 \times 10^{-51}$
total	$6.80 \pm 0.12 \times 10^{-45}$

**Table 5**  
Gallium cross sections (in units of  $10^{-45} \text{cm}^2$ ) for  $^{51}\text{Cr}$  and  $^{37}\text{Ar}$  neutrinos and their ratios with the central value of the corresponding Bahcall cross section [35] in the first line. The other lines give the cross sections corresponding to the BGT's of Haxton [8,9], Frekers et al. [5,9], and the JUN45 calculation presented in this paper.

	$\sigma^{51\text{Cr}}$	$\sigma^{51\text{Cr}}/\sigma_B^{51\text{Cr}}$	$\sigma^{37\text{Ar}}$	$\sigma^{37\text{Ar}}/\sigma_B^{37\text{Ar}}$
Bahcall	$5.81 \pm 0.16$		$7.00 \pm 0.21$	
Haxton	$6.39 \pm 0.65$	$1.100 \pm 0.112$	$7.72 \pm 0.81$	$1.103 \pm 0.116$
Frekers	$5.92 \pm 0.11$	$1.019 \pm 0.019$	$7.15 \pm 0.14$	$1.021 \pm 0.020$
JUN45	$5.67 \pm 0.06$	$0.976 \pm 0.011$	$6.80 \pm 0.08$	$0.971 \pm 0.011$

but the ratio  $\approx 3 \times 10^{-4}$  seems to be off from the experimental value  $\approx 0.02$ . The inability of the shell model to predict very low BGT values is due to the fact that there are cancellations of single-particle matrix elements of roughly the same size, resulting in large numerical inaccuracies. However, this is not a problem for the larger BGT values where theoretical uncertainties are usually about 10% [30]. On the other hand, the BGT values for the excited states in  $^{71}\text{Ge}$  are rather small, but there should not be any problems with the numerical inaccuracies as large cancellations are not present. Here we adopt a very conservative 50% uncertainty for these transitions in order to avoid overstatements regarding the significance of the gallium anomaly.

### 5. Results for scattering cross sections

The cross sections for the  $^{51}\text{Cr}$  and  $^{37}\text{Ar}$  neutrinos scattering off  $^{71}\text{Ge}$  are given in Tables 3 and 4. The contributions of the excited states are about 2.5(1.3)%. The contributions of the positive-parity states are about  $10^{-4}\%$  and thus the fact that these were left out from the previous analyses does not affect the reliability of their conclusions.

### 6. Reassessment of the gallium anomaly

The gallium anomaly was originally discovered [31–34] using the Bahcall cross sections [35] reported in the first line of Table 5, that have been obtained using the BGT's measured in 1985 in the  $(p, n)$  experiment of Krofcheck et al. [36,37] (see Table I of Ref. [35]), listed in the first line of Table 6. The cross sections of  $^{51}\text{Cr}$  and  $^{37}\text{Ar}$  electron neutrinos can be calculated from the Gamow-Teller strengths through

$$\sigma = \sigma_{\text{gs}} \left( 1 + \xi_{5/2-} \frac{\text{BGT}_{5/2-}}{\text{BGT}_{\text{gs}}} + \xi_{3/2-} \frac{\text{BGT}_{3/2-}}{\text{BGT}_{\text{gs}}} + \xi_{5/2+} \frac{\text{BGT}_{5/2+}}{\text{BGT}_{\text{gs}}} \right), \quad (6)$$

with the phase-space coefficients [35]

$$\begin{aligned} \xi_{5/2-} (^{51}\text{Cr}) &= 0.663 & \xi_{3/2-} (^{51}\text{Cr}) &= 0.221 \\ \xi_{5/2+} (^{51}\text{Cr}) &= 0, \end{aligned} \quad (7)$$

$$\begin{aligned} \xi_{5/2-} (^{37}\text{Ar}) &= 0.691 & \xi_{3/2-} (^{37}\text{Ar}) &= 0.262 \\ \xi_{5/2+} (^{37}\text{Ar}) &= 0.200 \end{aligned} \quad (8)$$

and [35]

$$\sigma_{\text{gs}} (^{51}\text{Cr}) = (5.53 \pm 0.01) \times 10^{-45} \text{cm}^2, \quad (9)$$

$$\sigma_{\text{gs}} (^{37}\text{Ar}) = (6.62 \pm 0.01) \times 10^{-45} \text{cm}^2. \quad (10)$$

The first line in Table 7 gives the ratios of measured and expected  $^{71}\text{Ge}$  event rates in the four radioactive source experiments and their correlated average obtained using the Bahcall cross section, which led to a  $2.6\sigma$  gallium anomaly.

In 1998 Haxton [8] published a shell model calculation of  $\text{BGT}_{5/2-}$  that gave the relatively large value in the second line of Table 6, albeit with a very large uncertainty. The cross sections obtained with the Haxton  $\text{BGT}_{5/2-}$  and the Krofcheck et al. measurement of  $\text{BGT}_{3/2-}$  are listed in the second line of Table 5. As one can see from Table 7 the larger uncertainties of the Haxton cross sections lead to a slight decrease of the gallium anomaly from the Bahcall  $2.6\sigma$  to  $2.5\sigma$ , in spite of the larger Haxton cross sections.

In 2011 Frekers et al. [5] published the measurements of  $\text{BGT}_{5/2-}$  and  $\text{BGT}_{3/2-}$  in the third line of Table 6, obtained with  $^{71}\text{Ge}(^3\text{He}, ^3\text{H})^{71}\text{Ge}$  scattering. They found a finite value of  $\text{BGT}_{5/2-}$ , albeit with a large uncertainty, which is compatible with the upper limit of Krofcheck et al. [36,37]. On the other hand, the Frekers et al. value of  $\text{BGT}_{3/2-}$  is about  $2.9\sigma$  larger than that of Krofcheck et al. If one considers these Gamow-Teller strengths as applicable to the  $\nu_e$ - $^{71}\text{Ge}$  cross section without corrections due to the tensor contributions (that would require a theoretical calculation), there is a significant increase of the  $^{51}\text{Cr}$  and  $^{37}\text{Ar}$  neutrino cross sections with respect to the Bahcall cross sections and an increase of the gallium anomaly to  $3.0\sigma$ , as shown in Table 7.

From Table 5 one can also see that our JUN45 shell-model calculation of the Gamow-Teller strengths, listed in the fourth row of Table 6, gives cross sections that are smaller than the previous ones. As a result, the gallium anomaly decreases to  $2.3\sigma$ , as shown in Table 7.

The gallium anomaly has been considered as one of the indications in favor of short-baseline neutrino oscillations due to active-sterile neutrino mixing (see the reviews in Refs. [38–41]). In the framework of the  $3 + 1$  mixing scheme, which is the simplest one that extends the standard three-neutrino mixing with the addition of a sterile neutrino at the eV mass scale, the survival probability of electron neutrinos and antineutrinos<sup>1</sup> in short-baseline experiments is given by

$$P_{\nu_e \rightarrow \nu_e}^{\text{SBL}(-)} = 1 - 4|U_{e4}|^2 (1 - |U_{e4}|^2) \sin^2 \left( \frac{\Delta m_{41}^2 L}{4E} \right), \quad (11)$$

where  $L$  is the source-detector distance,  $E$  is the neutrino energy,  $U$  is the unitary  $4 \times 4$  neutrino mixing matrix, and  $\Delta m_{41}^2 = m_4^2 - m_1^2$

<sup>1</sup> In general, CPT invariance implies the equality of the survival probability of neutrinos and antineutrinos of each flavor (see, for example, Ref. [42]).

**Table 6**

Values of the Gamow-Teller strengths of the transitions from the ground state of  $^{71}\text{Ga}$  to the relevant excited states of  $^{71}\text{Ge}$  relative to the Gamow-Teller strength of the transitions to the ground state of  $^{71}\text{Ge}$  obtained by Krofcheck et al. [36,37], Haxton [8], Frekers et al. [5], and with the JUN45 calculation presented in this paper.

Method	$\frac{\text{BGT}_{5/2-}}{\text{BGT}_{\text{gs}}}$	$\frac{\text{BGT}_{3/2-}}{\text{BGT}_{\text{gs}}}$	$\frac{\text{BGT}_{5/2+}}{\text{BGT}_{\text{gs}}}$
Krofcheck $^{71}\text{Ga}(p, n)^{71}\text{Ge}$	$< 0.057$	$0.126 \pm 0.023$	
Haxton Shell Model	$0.19 \pm 0.18$		
Frekers $^{71}\text{Ga}(^3\text{He}, ^3\text{H})^{71}\text{Ge}$	$0.040 \pm 0.031$	$0.207 \pm 0.016$	
JUN45 Shell Model	$(3.30 \pm 1.66) \times 10^{-2}$	$(1.59 \pm 0.79) \times 10^{-2}$	$(4.46 \pm 2.24) \times 10^{-6}$

**Table 7**

Ratios of measured and expected  $^{71}\text{Ge}$  event rates in the four radioactive source experiments, their correlated average, and the statistical significance of the gallium anomaly obtained with the cross sections in Table 5.

	GALLEX-1	GALLEX-2	SAGE-1	SAGE-2	Average	Anomaly
$R_{\text{Bahcall}}$	$0.95 \pm 0.11$	$0.81 \pm 0.11$	$0.95 \pm 0.12$	$0.79 \pm 0.08$	$0.85 \pm 0.06$	$2.6\sigma$
$R_{\text{Haxton}}$	$0.86 \pm 0.13$	$0.74 \pm 0.12$	$0.86 \pm 0.14$	$0.72 \pm 0.10$	$0.76 \pm 0.10$	$2.5\sigma$
$R_{\text{Frekers}}$	$0.93 \pm 0.11$	$0.79 \pm 0.11$	$0.93 \pm 0.12$	$0.77 \pm 0.08$	$0.84 \pm 0.05$	$3.0\sigma$
$R_{\text{JUN45}}$	$0.97 \pm 0.11$	$0.83 \pm 0.11$	$0.97 \pm 0.12$	$0.81 \pm 0.08$	$0.88 \pm 0.05$	$2.3\sigma$

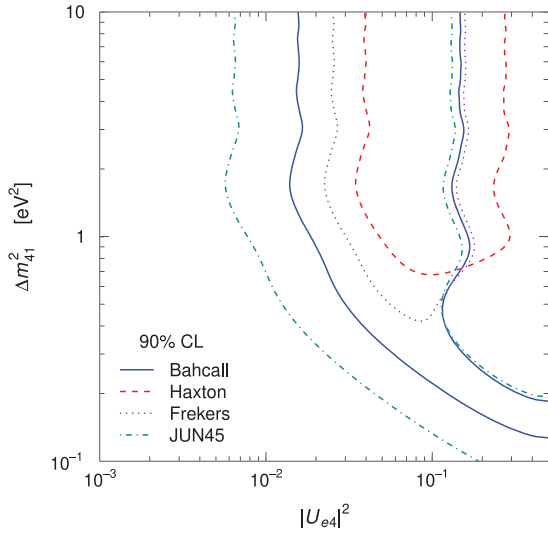


**Fig. 3.** Comparison of the 90% allowed regions in the  $|U_{e4}|^2 - \Delta m_{41}^2$  plane obtained with the cross sections in Table 5. The Bahcall and JUN45 allowed regions are between the two corresponding curves. The Haxton and Frekers allowed regions are enclosed by the corresponding curves, without an upper limit on  $\Delta m_{41}^2$ .

$m_1^2$  is the squared-mass difference between a heavy, almost sterile,  $\nu_4$  with mass  $m_4 \sim 1$  eV and the standard three light neutrinos  $\nu_1$ ,  $\nu_2$ , and  $\nu_3$  with respective masses  $m_1$ ,  $m_2$ , and  $m_3$  much smaller than 1 eV (hence,  $\Delta m_{41}^2 \simeq \Delta m_{42}^2 \simeq \Delta m_{43}^2$  in Eq. (11)).

Fig. 3 shows the differences of the 90% allowed regions in the  $|U_{e4}|^2 - \Delta m_{41}^2$  plane obtained from the gallium data with the four cross sections in Table 5. One can see that the Haxton and Frekers cross sections give a relatively large gallium anomaly, with preferred regions at  $0.03 \lesssim |U_{e4}|^2 \lesssim 0.2$  and  $\Delta m_{41}^2 \gtrsim 0.5 - 0.7$  eV<sup>2</sup>. The Bahcall cross sections allow lower values of  $|U_{e4}|^2$  and  $\Delta m_{41}^2$ , and our JUN45 shell model calculation allows still lower values, as low as  $|U_{e4}|^2 \gtrsim 0.007$  for  $\Delta m_{41}^2 \gtrsim 1$  eV<sup>2</sup>.

The indication in favor of short-baseline  $\nu_e$  disappearance due to active-sterile mixing is at the level of  $1.9$  ( $\Delta\chi^2 = 5.7$  with 2 degrees of freedom with respect to the absence of oscillations). This

value must be compared with the 2.2, 2.7, and 2.6 levels obtained with the Bahcall, Haxton, and Frekers cross sections, respectively.

It is also interesting to compare our results for the gallium anomaly with the recent indication in favor of short-baseline electron neutrino and antineutrino disappearance [43,44] obtained from the combined analysis of the data of the NEOS [45] and DANSS [46] reactor experiments. This indication is independent of our knowledge of the reactor antineutrino fluxes, because it is obtained from comparisons of the detection energy spectra at different distances from the reactor source. Hence, it depends only on the experimental uncertainties, not on the theoretical uncertainties of the neutrino rates and spectra that are widely considered to be larger than those estimated before the discovery of the mysterious 5 MeV bump (see, for example, Ref. [47]).

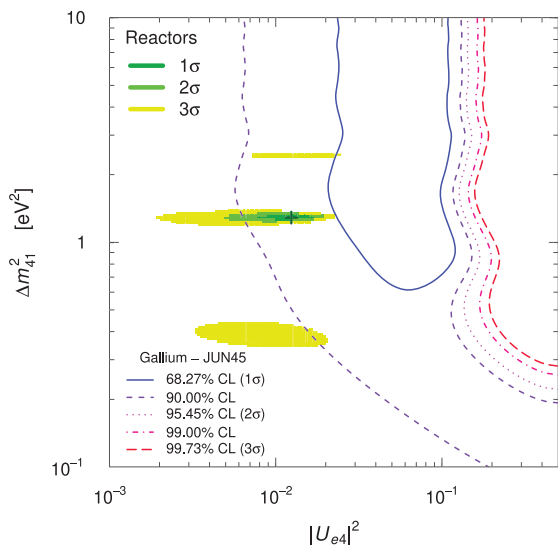
A comparison of the results for the gallium anomaly obtained with our JUN45 shell-model calculation with the NEOS and DANSS indications in favor of short-baseline oscillations is interesting because the comparison presented in Ref. [43], where the Frekers cross sections have been used, indicated an incompatibility of the  $2\sigma$  allowed regions, with a tension quantified by a parameter goodness of fit of 4%.

Fig. 4 shows the comparison of the allowed regions in the  $|U_{e4}|^2 - \Delta m_{41}^2$  plane obtained with our JUN45 shell model for different confidence levels with the regions obtained from the combined analysis of the data of the NEOS and DANSS reactor experiments, to which we have added the more recent data of the PROSPECT [48] reactor experiment that excludes large values of  $|U_{e4}|^2$  for  $0.7 \lesssim \Delta m_{41}^2 \lesssim 7$  eV<sup>2</sup>. One can see that there is an overlap of the 90% CL allowed regions, indicating a reasonable agreement between the gallium anomaly and the reactor data. The corresponding parameter goodness of fit is a favorable 16% ( $\Delta\chi^2/\text{NDF} = 3.6/2$ ).

## 7. Conclusions

In this Letter we presented the results from large-scale shell-model calculations regarding the scattering of  $^{37}\text{Ar}$  and  $^{51}\text{Cr}$  neutrinos off the  $^{69,71}\text{Ga}$  isotopes. The new theoretical estimates for the  $^{71}\text{Ga}$  cross sections are  $6.80 \pm 0.12 \times 10^{-45}$  cm<sup>2</sup> and  $5.67 \pm 0.10 \times 10^{-45}$  cm<sup>2</sup> respectively which are 2.5–3.0% lower than the previous predictions.

According to our JUN45 shell-model calculation of the cross sections of the interaction of  $\nu_e$ 's produced by  $^{51}\text{Cr}$  and  $^{37}\text{Ar}$  radioactive sources with  $^{71}\text{Ga}$ , the gallium anomaly related to the



**Fig. 4.** Comparison of the allowed regions in the  $|U_{e4}|^2 - \Delta m_{41}^2$  plane obtained from the Gallium data with the JUN45 cross sections and the allowed regions obtained from the analysis of the data of the NEOS, DANSS and PROSPECT reactor experiments.

GALLEX and SAGE experiments is weaker than that obtained in previous evaluations, decreasing the significance from  $3.0\sigma$  to  $2.3\sigma$ . Our result is compatible with the recent indication in favor of short-baseline  $\bar{\nu}_e$  disappearance due to small active-sterile neutrino mixing obtained from the combined analysis of the data of the NEOS and DANSS reactor experiments.

The possible sources for the difference between the new theoretical cross sections and those predicted by charge-exchange reactions were examined. It is pointed out that the cross section of the scattering to the 500 keV  $3/2^-$  state in  $^{71}\text{Ge}$  is most likely overestimated in the charge-exchange reaction due to a particular combination of destructive and constructive interferences between Gamow-Teller and tensor contributions.

#### Acknowledgements

This work has been partially supported by the Academy of Finland under the Academy project no. 318043. J.K. acknowledges the financial support from Jenny and Antti Wihuri Foundation. We would like to thank Prof. K. Zuber for his suggestion to tackle this topic and Prof. H. Ejiri for enlightening discussions.

#### References

[1] P. Anselmann, et al., *Phys. Lett. B* 342 (1995) 440.

[2] W. Hampel, et al., *Phys. Lett. B* 420 (1998) 114.  
 [3] F. Kaether, W. Hampel, G. Heusser, J. Kiko, T. Kirsten, *Phys. Lett. B* 685 (2010) 47.  
 [4] J.N. Abdurashitov, et al., *Phys. Rev. Lett.* 77 (1996) 4708; J.N. Abdurashitov, et al., *Phys. Rev. C* 59 (1999) 2246; J.N. Abdurashitov, et al., *Phys. Rev. C* 73 (2006) 045805; J.N. Abdurashitov, et al., *Phys. Rev. C* 80 (2009) 015807.  
 [5] D. Frekers, et al., *Phys. Lett. B* 706 (2011) 134.  
 [6] J.N. Bahcall, *Phys. Rev. C* 56 (1997) 3391.  
 [7] C. Giunti, M. Laveder, *Phys. Rev. C* 83 (2011) 065504.  
 [8] W.C. Haxton, *Phys. Lett. B* 431 (1998) 110, arXiv:nucl-th/9804011.  
 [9] C. Giunti, et al., *Phys. Rev. D* 86 (2012) 113014, arXiv:1210.5715.  
 [10] T.A. Mueller, et al., *Phys. Rev. C* 83 (2011) 054615, arXiv:1101.2663.  
 [11] G. Mention, et al., *Phys. Rev. D* 83 (2011) 073006, arXiv:1101.2755.  
 [12] P. Huber, *Phys. Rev. C* 84 (2011) 024617, arXiv:1106.0687.  
 [13] L. Hayen, J. Kostensalo, N. Severijns, J. Suhonen, *Phys. Rev. C* 99 (2019) 031301(R).  
 [14] E. Ydrefors, J. Suhonen, *Adv. High Energy Phys.* 2012 (2012) 373946.  
 [15] J.D. Walecka, *Theoretical Nuclear and Subnuclear Physics*, 2nd ed., Imperial College Press, London, 2004.  
 [16] E. Kolbe, K. Langanke, G. Martínez-Pinedo, P. Vogel, *J. Phys. G, Nucl. Part. Phys.* 29 (2003) 2569.  
 [17] E. Ydrefors, J. Suhonen, *Phys. Rev. C* 87 (2013) 034314.  
 [18] J. Engel, *Phys. Rev. C* 57 (1998) 2004.  
 [19] J. Suhonen, *From Nucleons to Nucleus: Concepts of Microscopic Nuclear Theory*, Springer, Berlin, 2007.  
 [20] B.A. Brown, W. Rae, *Nucl. Data Sheets* 120 (2014) 115.  
 [21] M. Honma, T. Otsuka, T. Mizusaki, M. Hjorth-Jensen, *Phys. Rev. C* 80 (2009) 064323.  
 [22] M. Pernpointner, P. Schwerdtfeger, *Chem. Phys. Lett.* 295 (1998) 347.  
 [23] H. Bertschat, J. Christiansen, H.-E. Mahnke, E. Recknagel, G. Schatz, R. Sielemann, W. Witthuhn, *Nucl. Phys. A* 150 (1970) 282.  
 [24] W.J. Childs, L.S. Goodman, *Phys. Rev.* 141 (1966) 141.  
 [25] J. Morgenstern, J. Schmidt, G. Flügge, H. Schmidt, *Phys. Lett. B* 27 (1968) 370.  
 [26] National Nuclear Data Center, Brookhaven National Laboratory, [www.nndc.bnl.gov](http://www.nndc.bnl.gov).  
 [27] D. Frekers, et al., *Phys. Rev. C* 91 (2015) 034608.  
 [28] M. Honma, T. Otsuka, B.A. Brown, T. Mizusaki, *Phys. Rev. C* 69 (2004) 034335.  
 [29] M. Honma, T. Otsuka, B.A. Brown, T. Mizusaki, *Eur. Phys. J. A* 25 (2005) 499.  
 [30] B.A. Brown, B. Wildenthal, *At. Data Nucl. Data Tables* 33 (1985) 347.  
 [31] SAGE, J.N. Abdurashitov, et al., *Phys. Rev. C* 73 (2006) 045805, arXiv:nucl-ex/0512041.  
 [32] M. Laveder, *Nucl. Phys., Proc. Suppl.* 168 (2007) 344.  
 [33] C. Giunti, M. Laveder, *Mod. Phys. Lett. A* 22 (2007) 2499, arXiv:hep-ph/0610352.  
 [34] M.A. Acero, C. Giunti, M. Laveder, *Phys. Rev. D* 78 (2008) 073009, arXiv:0711.4222.  
 [35] J.N. Bahcall, *Phys. Rev. C* 56 (1997) 3391, arXiv:hep-ph/9710491.  
 [36] D. Krofcheck, et al., *Phys. Rev. Lett.* 55 (1985) 1051.  
 [37] D. Krofcheck, PhD Thesis, Ohio State University, 1987.  
 [38] S. Gariazzo, et al., *J. Phys. G* 43 (2016) 033001, arXiv:1507.08204.  
 [39] C. Giunti, T. Lasserre, arXiv:1901.08330.  
 [40] A. Diaz, et al., arXiv:1906.00045.  
 [41] S. Boser, et al., arXiv:1906.01739.  
 [42] C. Giunti, C.W. Kim, *Fundamentals of Neutrino Physics and Astrophysics*, Oxford University Press, Oxford, UK, 2007.  
 [43] S. Gariazzo, et al., *Phys. Lett. B* 782 (2018) 13, arXiv:1801.06467.  
 [44] M. Dentler, et al., *J. High Energy Phys.* 1808 (2018) 010, arXiv:1803.10661.  
 [45] NEOS, Y. Ko, et al., *Phys. Rev. Lett.* 118 (2017) 121802, arXiv:1610.05134.  
 [46] DANSS, I. Alekseev, et al., *Phys. Lett. B* 787 (2018) 56, arXiv:1804.04046.  
 [47] A.C. Hayes, P. Vogel, *Annu. Rev. Nucl. Part. Sci.* 66 (2016) 219, arXiv:1605.02047.  
 [48] PROSPECT, J. Ashenfelter, et al., *Phys. Rev. Lett.* 121 (2018) 251802, arXiv:1806.02784.



# XI

## **ANOMALIES AND STERILE NEUTRINOS : IMPLICATIONS OF NEW THEORETICAL RESULTS**

by

Kostensalo, J. & Suhonen, J. 2019

AIP Conference Proceedings, 2165  
doi: 10.1063/1.5130977

Reproduced with kind permission by American Institute of Physics.

# Anomalies and Sterile Neutrinos – Implications of New Theoretical Results

Joel Kostensalo<sup>a)</sup> and Jouni Suhonen

*University of Jyväskylä,  
Department of Physics,  
P.O. Box 35,  
FI-40014,  
Finland.*

a)joel.j.kostensalo@student.jyu.fi

## Abstract.

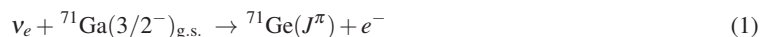
The reactor antineutrino and the gallium anomalies have been long unexplained. Possible explanations for both of these anomalies include new physics, such as the existence of one or more eV-scale sterile neutrino. However, the previous theoretical calculations, which do not replicate the experimental results, rely on many simplifying approximations. We have performed shell model calculations in order to gain insights into these issues. In the reactor-antineutrino analysis the beta decays contributing to the cumulative electron spectrum are usually assumed to have allowed spectral shapes. However, many of these decays are actually first-forbidden. Moreover, these decays dominate the experimentally observable region. Based on the recent results, the use of this allowed approximation can at least partially explain the so called reactor antineutrino anomaly. Our new large-scale shell model calculations regarding the neutrino-nucleus scattering cross section off  $^{71}\text{Ga}$  decreases the gap between theory and the experimental results of GALLEX and SAGE experiments. Conflict between charge-exchange BGTs and the neutrino-nucleus cross sections can to some extent be explained by destructive interference between Gamow-Teller and tensor contributions.

## INTRODUCTION

The reactor antineutrino and the gallium anomalies have been long unexplained. Possible explanations for both of these anomalies include new physics, such as the existence of one or more eV-scale sterile neutrino [1]. Both of these anomalies refer to small discrepancies between theoretical predictions and experimental results. However, the previous theoretical calculations rely on many simplifying approximations [2, 3]. The uncertainties related to these choices is hard to quantify, and thus a reasonable way to proceed is to do new theoretical calculations which do not rely on these approximations.

Reactor antineutrino anomaly refers to the observed 6% deficit in detected antineutrino flux with respect to the theoretical predictions [4, 5, 6]. In addition, precision antineutrino spectra in the 4–6 MeV region seem to show some disagreement in the spectral shape [7, 8, 9]. This bump, or spectral shoulder, has so far been unexplained. The problem with the previous theoretical analyses is all the decays contributing to the cumulative spectra are assumed to be either allowed or forbidden unique decays. However, in the region of interest, 4–6 MeV, the cumulative spectrum is actually dominated by non-unique forbidden decays [10], which can have spectral shapes that are quite different from the allowed and unique decays. In order to treat these decays properly we have performed calculations of these spectral shapes employing the interacting shell model.

The so-called gallium anomaly relates to the findings of the solar neutrino detectors GALLEX [11, 12, 13] and SAGE [14]. The detection efficiency of these detectors was tested using  $^{37}\text{Ar}$  and  $^{51}\text{Cr}$  radioactive sources. These sources emit discrete-energy electron neutrinos ( $E_\nu < 1$  MeV) as they decay via electron capture(EC). The detection of neutrinos is based on the charged-current neutrino-nucleus scattering reaction



to the lowest four (flux from the  $^{51}\text{Cr}$  source) or five (flux from the  $^{37}\text{Ar}$  source) nuclear states in  $^{71}\text{Ge}$ . Gallium anomaly refers to the fact that the experimental total neutrino-nucleus cross section as measured by the GALLEX and SAGE experiments is lower than the theoretical predictions, such as the one given by Bahcall [2]. The issue with the cross-section calculation relates to the use of results from charge-exchange reaction experiments. In order to address these issues, we have performed shell model calculations which give us important insights to the issue.

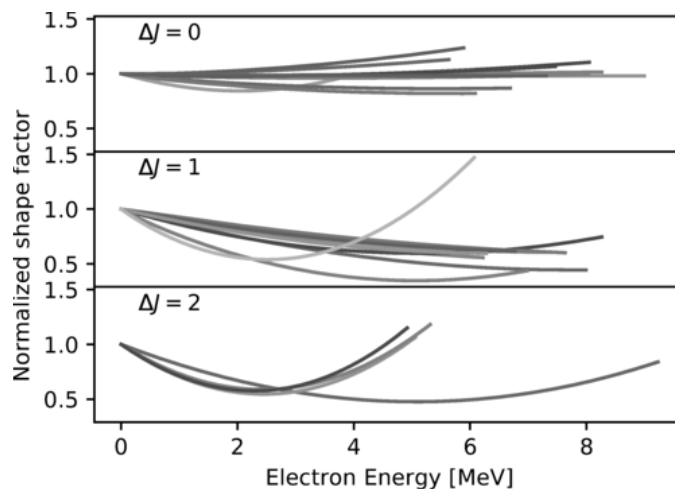


**FIGURE 1.** The shell model calculated shape factors  $C$  as a function of the electron kinetic energy, categorized according the spin-parity change of the transition. For allowed transitions  $C = 1$ , i.e. the shape factor is constant. Each shape factor was normalized to its value at electron kinetic energy 0 MeV. Results correspond to  $g_A = 0.9$  and  $\epsilon_{\text{MEC}} = 1.4$  (the latter is meaningful only for  $\Delta J = 0$  decays).

## REACTOR ANTINEUTRINO ANOMALY

The shape factor for forbidden non-unique beta decays is complicated and depends on the nuclear structure of the initial and final nuclear states which we describe here using the nuclear shell model. We considered in our analysis 29 of the most contributing forbidden decays (see details [3]). The shell model calculations were performed using the computer code NUSHELLX@MSU [15]. For nuclei with  $A < 100$  the effective interaction  $glepn$  [16] was adopted in a full model space consisting of the proton orbitals  $0f_{5/2}-1p-0g_{9/2}$  and the neutron orbitals  $1d-2s$ . The problematic lighter cases  $^{86}\text{Br}$  and  $^{89}\text{Br}$  were calculated using the interaction  $jj45pna$  [17, 18], in the full model space spanned by the proton orbitals  $0f_{5/2}-1p-0g_{9/2}$  and the neutron orbitals  $0g_{7/2}-2s-1d-0h_{11/2}$ . For the nuclei with  $A = 133-142$  the Hamiltonian  $jj56pnb$  [19] was used in the full model space spanned by the proton orbitals  $0g_{7/2}-2s-1d-0h_{11/2}$  and neutron orbitals  $0h_{9/2}-1f-2p-0i_{13/2}$  for  $A < 139$ , while for the heavier nuclei the proton orbital  $0h_{11/2}$  and the neutron orbital  $0i_{13/2}$  were kept empty in order to reduce the computational burden to manageable levels.

The results from the calculations are presented in Fig. 1. It is clear that the allowed approximation is not a good description for almost all the decays. Interestingly, the unique approximation turns out to be even worse for the dominant contributions which are of  $\Delta J = 0, 1$  type. When these shape factors are included in reactor antineutrino flux analysis, we see that the uncertainties related to the neutrino flux in the region 4–6 MeV are significantly increased, thus lowering the statistical significance of the reactor antineutrino anomaly. We also see a mitigation of the spectral shoulder. As a conclusion we can say that the forbidden beta decays must be taken into account with out using heavy approximations in order to make strong statements regarding the reactor anomaly.

## GALLIUM ANOMALY

The most referenced theoretical calculations for the full  $^{71}\text{Ga}$  cross section have been based on the reduced Gamow-Teller transition densities (BGTs) extracted from charge-exchange reactions [2, 20]. In order to get another estimate of this cross section we performed a large-scale shell model calculation for the BGT-values. The Hamiltonian we adopted was JUN45 [21] in the full  $0f_{5/2}-1p-0g_{9/2}$  model space for both protons and neutrons. The reason for this choice was the Hamiltonian's ability to reproduce well nuclear observables such as the energy spectra, magnetic dipole moments, electric quadrupole moments as well as the  $\beta$ -decay half-life of  $^{71}\text{Ge}$ . With these wave functions we get

the neutrino-nucleus cross sections

$$(5.67 \pm 0.10) \times \text{cm}^2 \quad ({}^{51}\text{Cr source}), \quad (2)$$

$$(6.80 \pm 0.12) \times \text{cm}^2 \quad ({}^{37}\text{Ar source}). \quad (3)$$

These cross sections are 2.5–3% lower than those reported by Bahcall [2], which is enough to reduce the statistical significance of the gallium anomaly from  $3\sigma$  to  $2.3\sigma$ . However, the disagreement with the shell model results and the charge-exchange reactions must be still addressed. One well known problem with the charge-exchange reactions are  $L = 2$  tensor contributions, which cannot be removed from the data by fitting angular distributions corresponding to different angular momentum combinations of the target and the projectile (the removing of the other components might not be trivial either since large-scale shell model calculations are usually involved). The interference between the Gamow-Teller (GT) and  $L = 2$  tensor (T) NMEs can be described by the linear combination

$$\langle f || O_{(p,n)} || i \rangle = \langle f || O_{\text{GT}} || i \rangle + \delta \langle f || O_{L=2} || i \rangle, \quad (4)$$

where  $i$  ( $f$ ) is the initial (final) nuclear state and  $\delta$  is the mixing parameter, which is usually considered to be about 0.1 [22]. The results for the nuclear matrix elements are shown in Table I. The large destructive interference for the  $5/2^-$  state is well known [22], making the charge-exchange reaction method problematic for scattering to the  $5/2^-$  state. For the ground state the interference is destructive while for the  $3/2^-$  state it is constructive. This means that the ratio  $\text{BGT}_{5/2^-}/\text{BGT}_{\text{g.s.}}$ , which the charge-exchange reaction analysis uses to determine cross-section for the scattering to the  $3/2^-$  state is systematically overestimated (see details [23]). However, this alone is not enough to explain the difference as it stands but it is a step towards explaining the charge-exchange results and ultimately the gallium anomaly.

**TABLE I.** Results for  ${}^{71}\text{Ga}$  with  $\delta = 0.097$  in Eq. (4).

State	$\langle f    O_{\text{GT}}    i \rangle$	$\langle f    O_{L=2}    i \rangle$	$\text{BGT}_{\beta}^{\text{SM}}$	$\text{BGT}_{(p,n)}^{\text{SM}}$
$1/2_{\text{g.s.}}^-$	-0.795	0.465	0.158	0.141
$5/2_1^-$	0.144	-1.902	0.0052	0.0004
$3/2_1^-$	0.100	0.0482	0.0025	0.0027

## ACKNOWLEDGMENTS

This work has been partially supported by the Academy of Finland under the Academy project no. 318043. J. K. acknowledges the financial support from Jenny and Antti Wihuri Foundation.

## REFERENCES

1. S. Gariazzo, C. Giunti, M. Laveder, Y. F. Li, and E. M. Zavanin, *J. Phys. G: Nucl. Part. Phys.* **43**, 033001 (2015).
2. J. N. Bahcall *Phys. Rev. C* **56**, 3391 (1997).
3. L. Hayen, J. Kostensalo, N. Severijns, and J. Suhonen *Phys. Rev. C* **99**, 031301(R) (2019).
4. G. Mention, M. Fechner, T. Lasserre, T. A. Mueller, D. Lhuillier, M. Cribier, and A. Letourneau, *Phys. Rev. D* **83**, 073006 (2011).
5. T. A. Mueller et al., *Phys. Rev. C* **83**, 054615 (2011).
6. P. Huber, *Phys. Rev. C* **84**, 024617 (2011).
7. F. P. An et al., *Phys. Rev. Lett.* **116**, 061801 (2016).
8. Y. Abe et al., *J. High Energy Phys.* **2014**, 86 (2014).
9. S. H. Seo et al., *Phys. Rev. D* **98**, 012002 (2018).
10. M. Chadwick et al. *Nucl. Data Sheets* **112**, 2887 (2011).
11. P. Anselmann et al., *Phys. Lett. B* **342** (1995) 440.
12. W. Hampel et al., *Phys. Lett. B* **420** (1998) 114.
13. F. Kaether, W. Hampel, G. Heusser, J. Kiko, and T. Kirsten, *Phys. Lett. B* **685** (2010) 47.
14. J.N. Abdurashitov et al., *Phys. Rev. Lett.* **77** (1996) 4708 ; *Phys. Rev. C* **59** (1999) 2246 ; *Phys. Rev. C* **73** (2006) 045805 ; *Phys. Rev. C* **80** (2009) 015807.
15. B. A. Brown and W. D. M. Rae, *Nucl. Data Sheets* **120**, 115 (2014).

16. H. Mach, E. K. Warburton, R. L. Gill, R. F. Casten, J. A. Becker, B. A. Brown, and J. A. Winger, *Phys. Rev. C* 41, 226 (1990).
17. R. Machleidt, *Phys. Rev. C* 63, 024001 (2001).
18. S. Lalkovskiet al., *Phys. Rev. C* 87, 034308 (2013).
19. B. A. Brown, Unpublished (2012).
20. D. Frekers et al., *Phys. Lett. B* 706 (2011) 134.
21. M. Honma, T. Otsuka, T. Mizusaki, M. Hjorth-Jensen, *Phys. Rev. C* 80 (2009) 064323.
22. W.C. Haxton, *Phys. Lett. B* 431, 110 (1998).
23. J. Kostensalo, J. Suhonen. C. Giunti, and P.C. Srivastava, *Phys. Lett. B* (accepted), arXiv:1906.10980 [nucl-th].



## XII

# CALCULATED SOLAR-NEUTRINO CAPTURE RATE FOR A RADIOCHEMICAL $^{205}\text{Tl}$ -BASED SOLAR-NEUTRINO DETECTOR

by

Kostensalo, J., Suhonen, J., Zuber, K. 2020

Physical Review C, 101 (3), 031302(R).  
DOI: 10.1103/PhysRevC.101.031302

Reproduced with kind permission by American Physical Society.

Calculated solar-neutrino capture rate for a radiochemical  $^{205}\text{Tl}$ -based solar-neutrino detectorJoel Kostensalo<sup>\*</sup> and Jouni Suhonen<sup>†</sup>

University of Jyväskylä, Department of Physics, P.O. Box 35, FI-40014, Finland

K. Zuber<sup>‡</sup>

Institute for Nuclear and Particle Physics, TU Dresden, 01069 Dresden, Germany

 (Received 19 December 2019; revised manuscript received 22 January 2020; accepted 19 February 2020; published 4 March 2020)

Radiochemical experiments for low-energy solar-neutrino detection have been making headlines by exploiting the isotopes  $^{37}\text{Cl}$  and  $^{71}\text{Ga}$ . Such a very low-threshold measurement of this type can also be performed using  $^{205}\text{Tl}$ , which has been considered for decades for this purpose. A unique feature of this detector nucleus is the integration in the solar-neutrino flux over  $10^6$  of years owing to its long-living daughter  $^{205}\text{Pb}$ . In this Rapid Communication, we have calculated for the first time the cross section for the charged-current solar-neutrino scattering off  $^{205}\text{Tl}$ . Taking into account the solar-model-predicted neutrino fluxes and the electron-neutrino survival probabilities, a solar-neutrino capture rate of  $62.2 \pm 8.6$  solar-neutrino units is determined, a value significantly smaller than in previous estimates.

DOI: 10.1103/PhysRevC.101.031302

*Introduction.* Neutrinos play a key role in several aspects of astroparticles and nuclear physics [1]. From the astrophysical point of view, solar neutrinos can be monitored in real-time measurements which allows to study neutrino properties, stellar structure, and evolution. To date, real-time monitoring of various neutrino chain reactions has been performed by the super-Kamiokande, the Sudbury Neutrino Observatory, KamLAND, and especially Borexino. Borexino was able to perform a common global fit of all the observed reactions of  $pp$ ,  $pep$ ,  $^7\text{Be}$ , and  $^8\text{B}$  in one detector [2].

An alternative method to the above-mentioned ones, used by the first solar-neutrino experiments, are the radio-chemical observations. These experiments employ the charged-current neutrino-nucleus scattering reaction,

$$\nu_e + (A, Z) \rightarrow e^- + (A, Z + 1) \quad (1)$$

for solar-neutrino detection. This reaction has been used in the pioneering Homestake experiment using  $^{37}\text{Cl}$  as the detector material [3], and, in this experiment, a deficit with respect to expectation was found. First measurements of the fundamental  $pp$  neutrinos were based on  $^{71}\text{Ga}$  (GALLEX, GNO, and SAGE). Several other nuclides, with different reaction thresholds, have been considered for more refined overall spectral analyses [4]. A very interesting candidate of this type is  $^{205}\text{Tl}$ , which has a very low threshold for solar neutrinos.

*The  $^{205}\text{Tl}$  reaction.* The dominant charged-current neutrino-nucleus reaction under discussion is

$$^{205}\text{Tl}(1/2^+) + \nu_e \rightarrow ^{205}\text{Pb}(1/2^-) + e^-, \quad (2)$$

which feeds the first excited state of  $^{205}\text{Pb}$  at 2.33 keV and is of first-forbidden nonunique type [5]. Only a tiny portion of the feeding goes to the  $5/2^-$  ground state of  $^{205}\text{Pb}$ , the corresponding transition being first-forbidden unique [5,6]. According to the current atomic mass evaluation [7], the  $Q$  value is given by  $50.6 \pm 0.5$  keV, which is so far the lowest threshold among radiochemical approaches for solar-neutrino detection. This results in a total threshold of about 53 keV for the transition (2). Furthermore, a unique feature of this reaction is the possibility for long-term monitoring of the average solar-neutrino flux and, hence, the mean solar luminosity over the past  $4.31 \times 10^6$  yr due to the long half-life of  $1.73(7) \times 10^7$  yr of  $^{205}\text{Pb}$  [8]. Hence, such a measurement could shed light on the long-term stability of the Sun and, therefore, on the stability of stars, in general [4].

The first studies of the Tl experiment were performed by Refs. [9–12] which later became the LOREX experiment [13,14]. Although several experimental aspects have already been addressed or have been worked on, the major remaining uncertainty is the cross section for this reaction. Hence, it is essential to get a reliable estimate of this cross section and this Rapid Communication reports on the calculation of this important quantity using current state-of-the-art techniques.

*Calculation of the  $^{205}\text{Tl}$  cross section.* The calculations for the neutrino-nucleus cross section are based on the O'Connell *et al.* [15] and Donnelly and Peccei [16] method for the treatment of semileptonic processes in nuclei. Details of the formalism as it is applied here can be found from Ref. [17]. A streamlined version has also been given in the recent papers [18,19].

The nuclear-structure calculations were performed in the shell-model framework using the shell-model code NUSHELLX@MSU [20] with the Hamiltonian *khhe* [21] in

<sup>\*</sup>joel.j.kostensalo@student.jyu.fi<sup>†</sup>jouni.t.suhonen@jyu.fi<sup>‡</sup>zuber@physik.tu-dresden.de

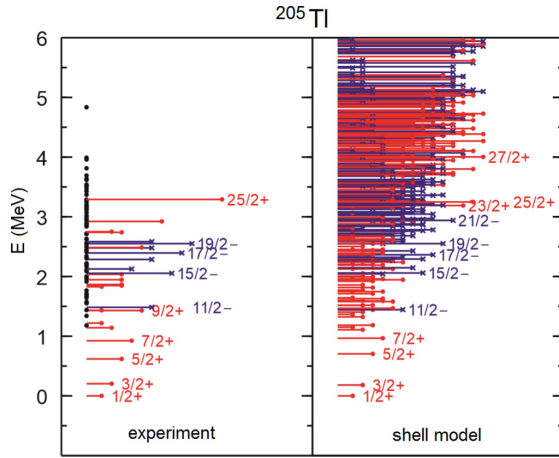


FIG. 1. Experimental and shell-model excitation spectra for  $^{205}\text{Tl}$ . Each horizontal bar represents a nuclear state, and its length is proportional to the angular momentum of the state.

the complete valence space spanned by the proton orbitals  $0g_{7/2}$ ,  $1d$ ,  $2s$ , and  $0h_{11/2}$ , and the neutron orbitals  $0h_{9/2}$ ,  $1f$ ,  $2p$ , and  $0i_{13/2}$ . As can be seen from Figs. 1 and 2, the energy spectra of the relevant nuclei are reproduced astonishingly well. The nucleus  $^{205}\text{Pb}$  decays via the  $^{205}\text{Pb}(5/2^-) \rightarrow ^{205}\text{Tl}(1/2^+)$  ground-state-to-ground-state  $\beta$  transition, and the corresponding half-life can be reproduced when  $g_A = 0.75$  is adopted as the effective axial-vector coupling. This result is consistent with the previous calculations for  $\beta$  decays in heavy nuclei [22]. However, as shown in Fig. 3 for the computed scattering cross section, the leading contributions come from the  $0^-$ ,  $1^-$ , and  $2^-$  multipole transitions. At the zero-momentum-transfer limit, these correspond

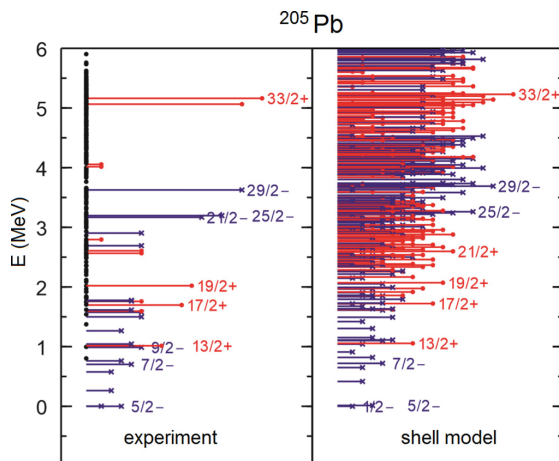


FIG. 2. Experimental and shell-model excitation spectra for  $^{205}\text{Pb}$ . Each horizontal bar represents a nuclear state, and its length is proportional to the angular momentum of the state.

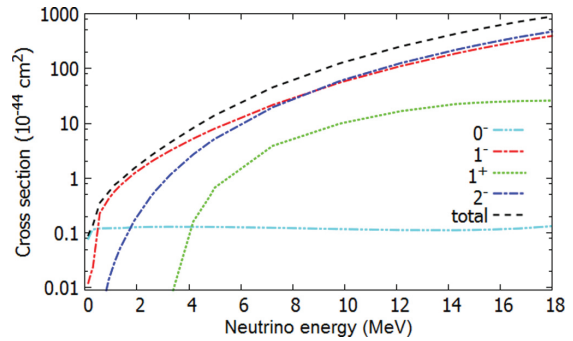


FIG. 3. Capture cross section for neutrino capture on  $^{205}\text{Tl}$  as function of neutrino energy for the leading transition multipoles with  $g_A = 1.00$ .

to the spin-dipole type of  $\beta$  transitions discussed extensively, e.g., in Refs. [23–25]. In the nuclear mass regions relevant to the above decay transition, which is a tensor transition, the effective values  $g_A \approx 0.90$  [23] and  $g_A \approx 0.5$  [25] have been obtained. Thus, the presently obtained effective value resides in the middle of these values. Furthermore, in the works [23–25], values of  $g_A \approx 0.38$ – $0.97$  were obtained for the  $1^-$  type of spin-dipole transitions, and values of  $g_A \approx 0.66$ – $0.92$  were obtained for the  $0^-$  type of spin-dipole transitions. This means that there is a lot of variation in the obtained values of the effective  $g_A$  for the spin-dipole type of  $\beta$  transitions. It is also not so clear how these values propagate to values of  $g_A$  for finite momentum transfers involved in the neutrino-nucleus scattering. Based on the above, we have taken the conservative approach and estimate the uncertainties related to nuclear structure by considering here the range of  $g_A = 0.75$ – $1.00$  for all transitions: a range which covers a reasonable range of values adopted in the above works and other large-scale shell-model calculations.

Since the exact energy of the low-lying states plays a significant role in determining the cross section for neutrinos with low energies, such as  $pp$  neutrinos, the energies of the dominating low-lying states were adjusted to their experimental values. The energy-adjusted states were the lowest two  $1/2^-$  states and the lowest three  $3/2^-$  and  $1/2^+$  states. Based on the ordering of the levels in the shell-model calculation, the state at 803 keV was taken to be  $1/2^-$  and the state at 996 keV was taken to be  $3/2^-$ .

The contributions by multipolarity of the transition operators are shown in Fig. 3 and by individual states in Fig. 4. The ground state of  $^{205}\text{Tl}$  has the spin-parity  $1/2^+$  so that the Gamow-Teller type of transitions ( $1^+$  transition multipole) are possible only to  $1/2^+$  and  $3/2^+$  states in  $^{205}\text{Pb}$ . There are only three known  $1/2^+$  states in  $^{205}\text{Pb}$  at 2795, 4016, and 4055 keV and no known  $3/2^+$  states. Gamow-Teller transitions are, therefore, available only for  $^8\text{B}$  and  $^7\text{He}$  neutrinos, which happen to have relatively low fluxes in the standard solar models [26]. For these higher-energy neutrinos, the  $1/2^+$  state at 4016 keV gives a noticeable contribution. However, the numerous low-lying negative-parity states still dominate even at the higher neutrino energies as the transitions to the low-lying

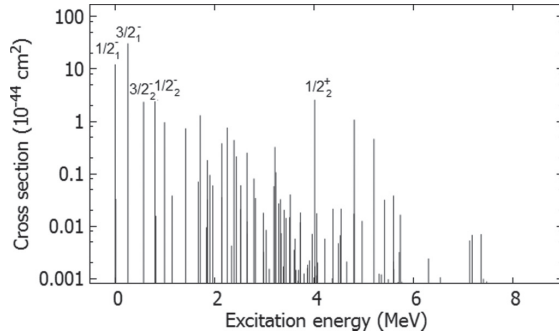


FIG. 4. Contributions of the individual states to the  ${}^8\text{B}$  neutrino cross section with  $g_A = 1.00$ . The horizontal axis gives the excitation energy in  ${}^{205}\text{Pb}$ .

states have a significant energy advantage. Due to this lack of positive-parity states with small angular momenta, the cross section is dominated by the spin-dipole type of forbidden transitions which render the total cross section smaller than expected from energy arguments alone.

The energy dependence of the scattering cross section for different transition multipoles is highly nontrivial, which is exemplified by the behavior of the  $0^-$  multipole. Based on our calculations, there is a significant contribution to this multipole from the transition to the first  $1/2^-$  state, but the other states contribute very little. Due to the first  $1/2^-$  contribution the cross section for the  $0^-$  multipole rises qualitatively in a similar way as that for the other multipoles up to about 0.4 MeV in neutrino energy but is mostly flat in the 0.5–15-MeV range. The reason for the flatness is due to the fact that the cross section is proportional to  $p_e E_e F(Z)$  (see, e.g., Ref. [27]), where  $p_e$  is the momentum of the outgoing electron,  $E_e$  is the total energy of the electron, and  $F(Z)$  is the Fermi function taking into account the final-state Coulomb interaction. The Fermi function is very large for the low energies, which is counterbalanced by the small  $p_e$  and  $E_e$ . For higher neutrino energies (which are not of interest here), we end up with the product  $p_e E_e$  dominating, leading to an approximately quadratic energy dependence of the cross section. For the other transition multipoles, there are a large number of important low-energy nuclear final states to scatter to, which is why the corresponding cross sections grow much faster at the low neutrino energies.

*Reaction rates in solar-neutrino units.* Owing to the small cross section of low-energy neutrino-nucleus interactions, it is convenient to present the neutrino-capture rate in the solar-neutrino units (SNU), given as 1 SNU =  $10^{-36}$  capture reactions per target atom per second. Then, the neutrino-capture rate  $R$  is described by

$$R = 10^{36} \sum_i \int \sigma(E) \phi_i(E) dE, \quad (3)$$

where  $E$ ,  $\sigma(E)$ , and  $\phi_i(E)$  are the neutrino energy, the neutrino-capture cross section (see the previous section), and the differential neutrino spectra. The latter are given at a distance of 1 AU. The sum in Eq. (3) includes all eight neutrino components from the  $pp$  and carbon nitrogen oxygen cycles.

For the calculation of solar-neutrino capture rates, the fluxes of the solar model BS05(OP) were adopted (see Table 2 in Ref. [26]) with the neutrino spectrum shapes available on Bahcall's website [28]. With these spectra and fluxes, we get for the capture rate 100.2 SNU with  $g_A = 0.75$  and 132.4 SNU with  $g_A = 1.00$  when the survival probability of electron neutrinos is not taken into account. Since the majority of the cross section comes from  $1^-$  and  $2^-$  types of transitions, the  $g_A$  dependence is not the trivial  $g_A^2$  as both the vector and the axial-vector components contribute. With the electron-neutrino survival probability of 0.54 for the  $pp$ ,  ${}^7\text{Be}$ , and  ${}^{13}\text{N}$  neutrinos, and 0.50 for the  $pep$ ,  ${}^{15}\text{O}$ , and  ${}^{17}\text{F}$  neutrinos, and 0.36 for the  ${}^8\text{B}$  neutrinos [29], we end up with a result of

$$R({}^{205}\text{Tl}) = 62.2 \pm 8.6 \text{ SNU} \quad (4)$$

for the capture rate.

*Summary and conclusions.* Given the revived interest in solar-neutrino detection using  ${}^{205}\text{Tl}$  due to its very small energy threshold, we have performed a large-scale shell-model calculation to find out the cross section for the conversion of  ${}^{205}\text{Tl}$  to  ${}^{205}\text{Pb}$ . Combined with the neutrino fluxes predicted by established solar models and taking into account the survival probabilities of electron neutrinos, the capture rate turns out to be  $62.2 \pm 8.6$  SNU. This capture rate is significantly smaller than estimated by previous estimations.

*Acknowledgments.* The authors would like to thank Dr. Y. Litvinov for bringing this issue to our attention. This work has been partially supported by the Academy of Finland under Academy Project No. 318043. J.K. acknowledges financial support from the Jenny and Antti Wihuri Foundation.

- [1] H. Ejiri, J. Suhonen, and K. Zuber, *Phys. Rep.* **797**, 1 (2019).
- [2] G. M. Agostini *et al.*, *Phys. Rev. D* **100**, 082004 (2018).
- [3] B. T. Cleveland *et al.*, *Astrophys. J.* **496**, 505 (1998).
- [4] J. N. Bahcall, *Neutrino Astrophysics* (Cambridge University Press, Cambridge, UK, 1989).
- [5] J. Kostensalo and J. Suhonen, *Phys. Lett. B* **781**, 480 (2018).
- [6] J. Suhonen, *From Nucleons to Nucleus: Concepts of Microscopic Nuclear Theory* (Springer, Berlin, 2007).
- [7] M. Wang, G. Audi, F. G. Kondev, W. J. Huang, S. Naimi, and X. Xu, *Chin. Phys. C* **41**, 030003 (2017).

- [8] F. G. Kondev, *Nucl. Data Sheets* **101**, 521 (2004).
- [9] S. M. Freedman *et al.*, *Science* **193**, 1117 (1976).
- [10] S. M. Freedman *et al.*, *Nucl. Instrum. Methods Phys. Res., Sect. A* **271**, 267 (1988).
- [11] P. Kienle, *Nucl. Instrum. Methods Phys. Res., Sect. A* **271**, 277 (1988).
- [12] W. Henning and D. Schuell, *Nucl. Instrum. Methods Phys. Res., Sect. A* **271**, 324 (1988).
- [13] M. K. Pavicevic, *Nucl. Instrum. Methods Phys. Res., Sect. A* **271**, 287 (1988).

- [14] M. K. Pavićević *et al.*, *Adv. High Energy Phys.* **2012**, 274614 (2012).
- [15] J. S. O'Connell, T. W. Donnelly, and J. D. Walecka, *Phys. Rev. C* **6**, 719 (1972).
- [16] T. W. Donnelly and R. D. Peccei, *Phys. Rep.* **50**, 1 (1979).
- [17] E. Ydrefors and J. Suhonen, *Adv. High Energy Phys.* **2012**, 373946 (2012).
- [18] J. Kostensalo, J. Suhonen, and K. Zuber, *Phys. Rev. C* **97**, 034309 (2018).
- [19] J. Kostensalo, J. Suhonen, C. Giunti, and P. C. Srivastava, *Phys. Lett. B* **795**, 542 (2019).
- [20] B. A. Brown and W. D. M. Rae, *Nucl. Data Sheets* **120**, 115 (2014).
- [21] E. K. Warburton and B. A. Brown, *Phys. Rev. C* **43**, 602 (1991).
- [22] J. Suhonen, *Front. Phys.* **5**, 55 (2017).
- [23] E. K. Warburton, *Phys. Rev. C* **42**, 2479 (1990).
- [24] E. K. Warburton, *Phys. Rev. C* **44**, 233 (1991).
- [25] Q. Zhi, E. Caurier, J. J. Cuenca-García, K. Langanke, G. Martínez-Pinedo, and K. Sieja, *Phys. Rev. C* **87**, 025803 (2013).
- [26] J. N. Bahcall *et al.*, *Astrophys. J., Lett.* **621**, L85 (2005).
- [27] H. Ejiri and S. R. Elliott, *Phys. Rev. C* **89**, 055501 (2014).
- [28] J. N. Bahcall, Software and data for solar neutrino research [<http://www.sns.ias.edu/jnb/>]
- [29] M. Agostini *et al.* (The Borexino Collaboration), *Nature (London)* **562**, 505 (2018).



## XIII

### SECOND-FORBIDDEN NONUNIQUE $\beta^-$ DECAYS OF $^{24}\text{Na}$ AND $^{36}\text{Cl}$ ASSESSED BY THE NUCLEAR SHELL MODEL

by

Kumar, A., Srivastava, P. C., Kostensalo, J., Suhonen, J. 2020

Physical Review C, 101 (6), 064304.  
DOI: 10.1103/PhysRevC.101.064304

Reproduced with kind permission by American Physical Society.

## Second-forbidden nonunique $\beta^-$ decays of $^{24}\text{Na}$ and $^{36}\text{Cl}$ assessed by the nuclear shell model

Anil Kumar <sup>1,\*</sup>, Praveen C. Srivastava <sup>1,†</sup>, Joel Kostensalo <sup>2,‡</sup>, and Jouni Suhonen <sup>2,§</sup>

<sup>1</sup>Department of Physics, Indian Institute of Technology Roorkee, Roorkee 247 667, India

<sup>2</sup>University of Jyväskylä, Department of Physics, P.O. Box 35 (YFL), FI-40014, University of Jyväskylä, Finland



(Received 15 April 2020; accepted 22 May 2020; published 8 June 2020)

We have performed a systematic study of the  $\log ft$  values, shape factors, and electron spectra for the second-forbidden nonunique  $\beta^-$  decays of  $^{24}\text{Na}(4^+) \rightarrow ^{24}\text{Mg}(2^+)$  and  $^{36}\text{Cl}(2^+) \rightarrow ^{36}\text{Ar}(0^+)$  transitions under the framework of the nuclear shell model. We have performed the shell model calculations in the  $sd$  model space, using more recent microscopic effective interactions such as Daejeon16, chiral N3LO, and JISP16. These interactions are derived from the no-core shell model wave functions using Okubo-Lee-Suzuki transformation. For comparison, we have also shown the results obtain from the phenomenological USDB interaction. To test the predictive power of these interactions first we have computed low-lying energy spectra of parent and daughter nuclei involved in these transitions. The computed results for energy spectra, nuclear matrix elements,  $\log ft$  values, shape factors, electron spectra, and decomposition of the integrated shape factor are reported and compare with the available experimental data.

DOI: [10.1103/PhysRevC.101.064304](https://doi.org/10.1103/PhysRevC.101.064304)

### I. INTRODUCTION

$\beta$  decay plays an important role in astrophysics, e.g., for the  $r$  process [1]. In the nuclear chart, there are selected candidates for double- $\beta$  decays, but on the other hand there are several potential candidates known for forbidden  $\beta$  decay. Out of these, only around 27 possible candidates of second-forbidden nonunique  $\beta$  decay are observed, as reported in Ref. [2]. Recently, a new candidate was observed corresponding to second-forbidden nonunique decay of  $^{20}\text{F}(2^+) \rightarrow ^{20}\text{Ne}(0^+)$  from ground-state-to-ground-state transition [3–5]. This study could change our understanding of the fate of intermediate-mass stars. A comprehensive review on the theoretical and experimental status of single- and double- $\beta$  decay was recently reported in Ref. [6].

In  $\beta$  decay, based on the value of angular momentum ( $l$ ) we can characterize any decay as allowed or forbidden. The  $l = 0$  decays are called “allowed” while the  $l > 0$  decays are called “forbidden.” Further, we can divide decays as forbidden unique (FU) and forbidden nonunique (FNU). In the case of FU, the total angular momentum  $K = l + 1$ , whereas in FNU decay  $K = l$ . The  $\beta$  decay half-life of the fourth-forbidden nonunique decay of  $^{50}\text{V}$  using the nuclear shell model is reported in Ref. [7]. The fourth-forbidden nonunique ground-state-to-ground-state  $\beta^-$  decay branches of  $^{113}\text{Cd}$  and  $^{115}\text{In}$  using the microscopic quasiparticle-phonon model and the nuclear shell model are reported in Refs. [8,9]. Also in these references the half-life method [8] and spectrum-shape

method (SSM) [9] are reported to extract the value of axial-vector coupling constant  $g_A$ .

Studies of forbidden  $\beta$  decay using the nuclear shell model with phenomenological interactions are available in the literature. With the recent progress in the *ab initio* approaches for nuclear structure study, it is highly desirable to see how these interactions are able to predict nuclear observables such as forbidden  $\beta$  decay. Recently, shell model results for allowed  $\beta$  decay properties of  $sd$ ,  $fp$ , and  $fp_g$  shell nuclei were reported by us in Refs. [10–13].

In the present work, our aim is to study second-forbidden nonunique  $\beta^-$  transitions of  $^{24}\text{Na}(4^+) \rightarrow ^{24}\text{Mg}(2^+)$  and  $^{36}\text{Cl}(2^+) \rightarrow ^{36}\text{Ar}(0^+)$  using *ab initio* interactions.  $\beta$ -decay transitions in these nuclei have been calculated and compared with the available experimental data to test the quality of the *ab initio* interaction wave functions. A theoretical attempt has been made in the past to calculate the  $\beta$  decay transition observable of  $^{36}\text{Cl}$  [14]. However, no theoretical estimate is found in the literature for the  $\beta$  decay of  $^{24}\text{Na}$  and also no experimental shape factors and electron spectra are found in the literature. Thus, our theoretical predictions for the  $\beta$  decay of  $^{24}\text{Na}$  are useful for the future experiments. In this work, we have computed the  $\log ft$  values, shape factors, and electron spectra of these branches. We have constrained the relativistic nuclear matrix element based on conserved vector current (CVC) theory and tested the role of this matrix element in the shape factors and electron spectra. In order to test our computed wave functions, first we computed the low-lying energy spectra of  $^{24}\text{Na}$ ,  $^{24}\text{Mg}$ ,  $^{36}\text{Cl}$ , and  $^{36}\text{Ar}$  and compared them with the available experimental energy spectra [15].

This article is organized as follows. In Sec. II we give a short overview of the theoretical formalism for the  $\beta^-$  decay and details about microscopic effective interactions. Results and discussions corresponding to low-lying energy spectra,

\*akumar5@ph.iitr.ac.in

†Corresponding author: praveen.srivastava@ph.iitr.ac.in

‡joel.j.kostensalo@student.jyu.fi

§jouni.t.suhonen@jyu.fi

nuclear matrix elements,  $\log ft$  values, shape factors, electron spectra, and decomposition of the integrated shape factors are reported in Sec. III. Finally, in Sec. IV we draw the conclusions.

## II. THEORETICAL FORMALISM

In Sec. II A we discuss the theory of forbidden  $\beta^-$  decay and the shape of the electron spectra. Section II B give the details about the valence space and microscopic effective interactions used in the present work.

### A. $\beta$ decay theory

The full details of formalism for both allowed and forbidden types of the  $\beta$  decay are available in the literature by Behrens and Bühring [16] (see also Ref. [17]). The generalized framework of the forbidden nonunique  $\beta$  decay theory is available in Refs. [9,18,19]. When the  $\beta$  decay process is described as a pointlike interaction vertex with an effective Fermi coupling constant  $G_F$ , the probability of the electron emission in the kinetic energy interval  $W_e$  and  $W_e + dW_e$  is expressed as

$$P(W_e)dW_e = \frac{G_F^2}{(\hbar c)^6} \frac{1}{2\pi^3\hbar} C(W_e) \times p_e c W_e (W_0 - W_e)^2 F_0(Z, W_e) dW_e. \quad (1)$$

Where the  $C(W_e)$  is the shape factor containing the nuclear structure information, and  $W_0$  is the endpoint energy of the  $\beta$  spectrum. The factor  $F_0(Z, W_e)$  is the Fermi function, which takes into account Coulombic interaction between the daughter nucleus and  $\beta$  particle, and  $Z$  is the proton number of the final nucleus. Furthermore,  $p_e$  and  $W_e$  are the momentum and energy of the emitted electron, respectively.

The partial half-life of the  $\beta$  decay is expressed as

$$t_{1/2} = \frac{\ln(2)}{\int_{m_e c^2}^{W_0} P(W_e) dW_e}, \quad (2)$$

where  $m_e$  is the mass of the electron. For convenience, Eq. (2) can be expressed in the form

$$t_{1/2} = \frac{\kappa}{\tilde{C}}, \quad (3)$$

where  $\tilde{C}$  is the unitless integrated shape factor, and the constant  $\kappa$  has the value

$$\kappa = \frac{2\pi^3 \hbar^7 \ln(2)}{m_e^5 c^4 (G_F \cos \theta_C)^2} = 6147 \text{ s}, \quad (4)$$

where  $\theta_C$  is the Cabibbo angle and the usual dimensionless kinematics quantities are defined as  $w_0 = W_0/m_e c^2$ ,  $w_e = W_e/m_e c^2$ , and  $p = p_e c/m_e c^2 = \sqrt{(w_e^2 - 1)}$ . Then the dimensionless integrated shape factor  $\tilde{C}$  can be expressed as

$$\tilde{C} = \int_1^{w_0} C(w_e) p w_e (w_0 - w_e)^2 F_0(Z, w_e) d w_e. \quad (5)$$

The comparative half-life, or the  $ft$  value, is obtained by multiplying the partial half-life with the following dimensionless

integrated Fermi function:

$$f_0 = \int_1^{w_0} p w_e (w_0 - w_e)^2 F_0(Z, w_e) d w_e, \quad (6)$$

but  $ft$  values are usually large, so they are normally expressed in term of “ $\log ft$ ” values [20]. The  $\log ft$  value is defined as

$$\log ft = \log_{10}(f_0 t_{1/2} [\text{s}]). \quad (7)$$

The shape factor  $C(w_e)$  in Eq. (5) for pure Gamow-Teller transition is defined as

$$C(w_e) = \frac{g_A^2}{2J_i + 1} |\mathcal{M}_{\text{GT}}|^2, \quad (8)$$

where the  $J_i$  is the angular momentum of the initial state,  $g_A$  is the axial-vector coupling constant, and the  $\mathcal{M}_{\text{GT}}$  is the Gamow-Teller nuclear matrix element [20], which is defined as

$$\begin{aligned} \mathcal{M}_{\text{GT}} &\equiv (\xi_f J_f \| \sigma \| \xi_i J_i) \\ &= \sum_{pn} \mathcal{M}_{\text{GT}}(pn) (\xi_f J_f \| [c_p^\dagger \tilde{c}_n]_1 \| \xi_i J_i), \end{aligned} \quad (9)$$

where  $\mathcal{M}_{\text{GT}}(pn)$  are the single-particle matrix elements (SPMEs). In case of forbidden nonunique  $\beta$  decay, the form of the shape factor  $C(w_e)$  in Eq. (5) is defined as

$$\begin{aligned} C(w_e) &= \sum_{k_e, k_v, K} \lambda_{k_e} \left[ M_K(k_e, k_v)^2 + m_K(k_e, k_v)^2 \right. \\ &\quad \left. - \frac{2\gamma_{k_e}}{k_e w_e} M_K(k_e, k_v) m_K(k_e, k_v) \right], \end{aligned} \quad (10)$$

where the indices  $k_e$  and  $k_v$  ( $k_e, k_v = 1, 2, 3, \dots$ ) are positive integers, which are emerging from the partial-wave expansion of the lepton wave functions and  $K$  is the order of forbiddenness of the transition. The nuclear structure information is contained in the quantities  $M_K(k_e, k_v)$  and  $m_K(k_e, k_v)$ , which are complicated combinations of different nuclear matrix elements (NMEs) and leptonic phase-space factors. The factor  $\lambda_{k_e}$  is the Coulomb function and is expressed as

$$\lambda_{k_e} = \frac{F_{k_e-1}(Z, w_e)}{F_0(Z, w_e)}, \quad (11)$$

where  $F_{k_e-1}(Z, w_e)$  is the generalized Fermi function [9,18], which is expressed as

$$\begin{aligned} F_{k_e-1}(Z, w_e) &= 4^{k_e-1} (2k_e)(k_e + \gamma_{k_e}) [(2k_e - 1)!!]^2 e^{\pi y} \\ &\quad \times \left( \frac{2p_e R}{\hbar} \right)^{2(\gamma_{k_e} - k_e)} \left( \frac{|\Gamma(\gamma_{k_e} + iy)|}{\Gamma(1 + 2\gamma_{k_e})} \right)^2. \end{aligned} \quad (12)$$

The auxiliary quantities are defined as  $\gamma_{k_e} = [k_e^2 - (\alpha Z)^2]^{1/2}$  and  $y = (\alpha Z w_e / p_e c)$ , where  $\alpha = 1/137$  is the fine structure constant.

The nuclear matrix elements (NMEs) are given by

$$\begin{aligned} &{}^{V/A} \mathcal{M}_{KLS}^{(N)}(pn)(k_e, m, n, \rho) \\ &= \frac{1}{\sqrt{2J_i + 1}} \sum_{pn} {}^{V/A} m_{KLS}^{(N)}(pn)(k_e, m, n, \rho) (\psi_f \| [c_p^\dagger \tilde{c}_n] \| \psi_i). \end{aligned} \quad (13)$$

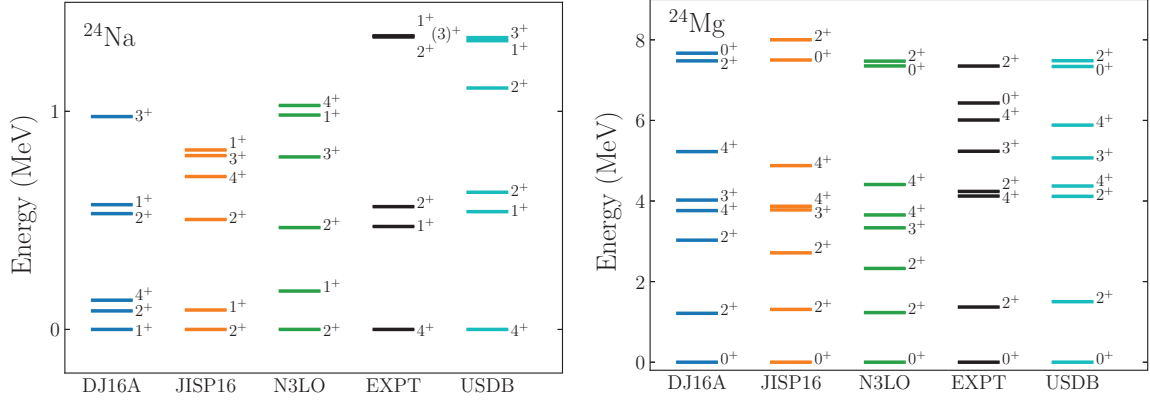


FIG. 1. Comparison of calculated and experimental [15] low-lying energy spectra for positive parity states of  $^{24}\text{Na}$  and  $^{24}\text{Mg}$  from microscopic and USDB interactions.

The nuclear matrix elements are divided in two parts: the first part  ${}^{V/A}m_{KLS}^{(N)}(pn)(k_e, m, n, \rho)$  is called the single-particle matrix element and the second part  $(\psi_f \| [c_p^\dagger \tilde{c}_n] \| \psi_i)$  is the reduced one-body transition density (OBTD) between the initial ( $i$ ) and final ( $f$ ) nuclear states. The single-particle matrix elements characterize the properties of the transition operators, so they are the same for all nuclear models. But the OBTDs are nuclear model dependent. In the present work the SPMEs are calculated using harmonic-oscillator wave functions (see Refs. [9,18]). The summation of Eq. (13) runs over the proton ( $p$ ) and neutron ( $n$ ) single-particle states.

The shape factor  $C(w_e)$  (10) can be decomposed into vector, axial-vector, and mixed vector-axial-vector components [8,9,21–23] in the form

$$C(w_e) = g_V^2 C_V(w_e) + g_A^2 C_A(w_e) + g_V g_A C_{VA}(w_e). \quad (14)$$

After the integration of Eq. (14) with respect to electron kinetic energy, we get an expression analogous to Eq. (5) for the integrated shape function  $\tilde{C}$ :

$$\tilde{C} = g_V^2 \tilde{C}_V + g_A^2 \tilde{C}_A + g_V g_A \tilde{C}_{VA}. \quad (15)$$

In Eq. (14) the shape factors  $C_i$  are functions of the electron kinetic energy, while the integrated shape factors  $\tilde{C}_i$  in Eq. (15) are just constant numbers.

## B. ADOPTED MODEL SPACE AND HAMILTONIANS

In the present work shell model calculations for the low-lying energy spectra,  $\log ft$  values, shape factors, and electron spectra of the  $\beta^-$  decay branches of  $^{24}\text{Na}$  and  $^{36}\text{Cl}$  were performed in the  $sd$  model space. In this framework we have calculated the OBTDs related to the NMEs of the shape factor. For the  $sd$  model space, we have used the three microscopic effective interactions DJ16A [24], JISP16 [25], and N3LO [25]. These interactions are obtained from the no-core shell model (NCSM) wave functions via the Okubo-Lee-Suzuki (OLS) unitary transformation [26–28]. We have also compared our results with the phenomenological USDB effective interaction [29]. The interaction “DJ16” [24] is obtained from

the Daejeon16  $NN$  potential [30]. After the monopole modification of DJ16, the interaction is labeled as “DJ16A” [24]. In this work, we have used the DJ16A interaction for further calculations. The OBTDs for NMEs were computed by the shell model code NUSHELLX [31]. For the evaluation of the many-body matrix elements, we have used the single-particle matrix element expression given in Ref. [16]. In our shell model calculations, we have used the single-particle matrix elements in the Condon-Shortley [32] phase convention.

## III. RESULTS AND DISCUSSION

In this section we present our calculated results of low-lying energy spectra, nuclear matrix elements,  $\log ft$  values, shape factors, electron spectra, and decomposition of the integrated shape factors for the second-forbidden nonunique  $\beta^-$  transitions of  $^{24}\text{Na}(4^+) \rightarrow ^{24}\text{Mg}(2^+)$  and  $^{36}\text{Cl}(2^+) \rightarrow ^{36}\text{Ar}(0^+)$ .

Previously, the  $\log ft$  values and shape factors of the second-forbidden  $\beta$  decay of  $^{36}\text{Cl}$  [14] have been reported by applying two different nuclear models: with pure  $1d_{3/2} \rightarrow 1d_{3/2}$  transitions and using the shell model with  $sd$  shell configuration space.

Recently, much progress has been achieved in developing modern effective interactions for the shell model calculations. Thus we have revisited the calculation for  $^{36}\text{Cl}$  and also for the first time for  $^{24}\text{Na}$  with recently developed microscopic (DJ16A, N3LO, and JISP16) and phenomenological (USDB) interactions in the  $sd$  model space. Our results for  $^{24}\text{Na}$  will be useful when compared with upcoming experimental data.

Below we have presented low-lying energy spectra (Figs. 1 and 2), nuclear matrix elements (Tables I and III),  $\log ft$  values (Table II and IV), shape factors, and electron spectra (Figs. 3 and 4). The low-lying energy spectra are discussed in Sec. III A. The  $\beta$  decay nuclear matrix elements and  $\log ft$  values are discussed in Sec. III B. Results of the shape factors and electron spectra are presented in Sec. III C. Decomposition of the integrated shape factor are discussed in Sec. III D.

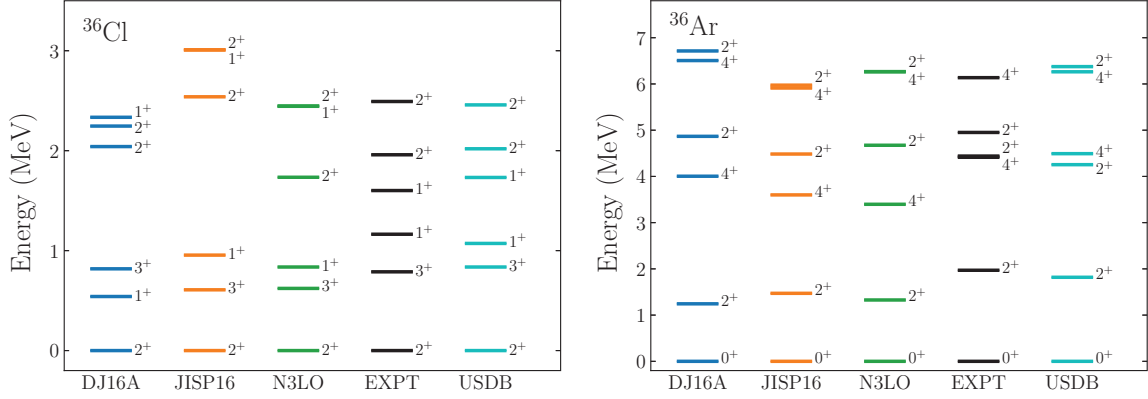


FIG. 2. Comparison of calculated and experimental [15] low-lying energy spectra for positive parity states of  $^{36}\text{Cl}$  and  $^{36}\text{Ar}$  from microscopic and USDB interactions.

### A. Low-lying energy spectra

In Fig. 1, we show the low-lying energy spectra of  $^{24}\text{Na}$  and  $^{24}\text{Mg}$ . In the case of  $^{24}\text{Na}$ , the ground state (g.s.)  $4^+$  is correctly reproduced by USDB interaction, while the other microscopic effective interactions N3LO and JISP16 give  $2^+$  as a g.s., and DJ16A predicts the g.s. as  $1^+$ . The low-energy spectrum of the well known  $sd$ -shell rotor nucleus  $^{24}\text{Mg}$  is already shown in Ref. [24] for all the interactions that we have used in the present work. For  $^{24}\text{Mg}$ , the  $0^+_{g.s.}$  and  $2^+_1$  are relatively well described by all the interactions. The computed  $2^+_1$  state is obtained at 1.213, 1.310, 1.231, and 1.502 MeV corresponding to DJ16A, JISP16, N3LO, and USDB, respectively, while the corresponding experimental value is 1.369 MeV. The theoretical low-lying energy spectra of  $^{36}\text{Cl}$  and  $^{36}\text{Ar}$  are shown in Fig. 2 in comparison with the experimental data. The g.s. is correctly reproduced by the microscopic (DJ16A, JISP16, and N3LO) and USDB interactions for  $^{36}\text{Cl}$  and  $^{36}\text{Ar}$ . For  $^{36}\text{Cl}$ , the order of  $3^+_1$  and  $1^+_1$  states is correctly reproduced from the JISP16, N3LO, and USDB interactions as in the experimental data, while the DJ16A interaction inverts the order of these states. In the case of  $^{36}\text{Ar}$ , the calculated  $2^+_1$  state values from the DJ16A, JISP16, N3LO, and USDB interactions are close to the experimental data. So, in general, the comparison of the computed low-lying energy levels shows good agreement with the experimental data for  $^{24}\text{Na}$ ,  $^{36}\text{Cl}$ , and  $^{36}\text{Ar}$ . In the present work we have taken  $Q$  values from the experimental data [15] for further calculations listed in Tables II and IV.

TABLE I. Calculated Gamow-Teller matrix elements of the allowed  $\beta^-$  decays from the g.s. ( $4^+$ ) of  $^{24}\text{Na}$  to the excited states in  $^{24}\text{Mg}$  from microscopic and USDB effective interactions.

Transitions	$\mathcal{M}_{\text{GT}}$				Expt.
	USDB	DJ16A	N3LO	JISP16	
$4^+ \rightarrow 3^+_1$	0.1859	0.1982	0.2274	0.2108	0.1179
$4^+ \rightarrow 4^+_1$	0.2663	0.0441	0.1069	0.0839	0.2072

### B. Nuclear matrix elements and log $ft$ values

The nuclear matrix elements contain the nuclear-structure information. The Gamow-Teller matrix elements  $\mathcal{M}_{\text{GT}}$  calculated from the microscopic and USDB interactions for the allowed  $\beta^-$  decays of  $^{24}\text{Na}(4^+) \rightarrow ^{24}\text{Mg}(3^+_1, 4^+_1)$  transitions are presented in Table I with comparison to the experimental data. The experimental  $\mathcal{M}_{\text{GT}}$  value is obtained from the log  $ft$  [15] values corresponding to the axial-vector coupling constant  $g_A = 1.00$ . In the present work, we have calculated these matrix elements by using OBTDs corresponding to all microscopic and USDB interactions. After that, we compare the calculated  $\mathcal{M}_{\text{GT}}$  with the experimental data. For both allowed transitions, the calculated  $\mathcal{M}_{\text{GT}}$  values from USDB are close to the experimental data as compared to the microscopic interactions. In the case of the  $^{24}\text{Na}(4^+) \rightarrow ^{24}\text{Mg}(4^+_1)$  transition, our calculated value of  $\mathcal{M}_{\text{GT}}$  (0.0441) from DJ16A is very small in comparison with the experimental data.

The calculated log  $ft$  values of allowed  $\beta^-$  decays of  $^{24}\text{Na}(4^+) \rightarrow ^{24}\text{Mg}(3^+_1, 4^+_1)$  transitions are presented in Table II in comparison to the experimental data. For the calculation, we have used the axial-vector coupling constants  $g_A = 1.00$  and  $g_A = 1.27$ . For the transition  $4^+ \rightarrow 3^+_1$ , the calculated log  $ft$  values for  $g_A = 1.00$  are in nice agreement with the experimental values corresponding to USDB, also all other microscopic effective interactions are in a reasonable agreement. However, in the case of the  $4^+ \rightarrow 4^+_1$  transition, the calculated log  $ft$  value from DJ16A is larger in comparison with the experimental data, but those from other interactions are close to the experimental data with both  $g_A$  values.

For the second-forbidden nonunique  $\beta^-$  decays of  $^{24}\text{Na}(4^+) \rightarrow ^{24}\text{Mg}(2^+)$  and  $^{36}\text{Cl}(2^+) \rightarrow ^{36}\text{Ar}(0^+)$ , the computed NMEs from different microscopic and USDB effective interactions are presented in Table III. The relativistic matrix element  $^V\mathcal{M}_{211}^{(0)}$  is becoming identically zero due to the limitation of our  $0\hbar\omega$   $sd$ -shell calculations for harmonic-oscillator wave functions. To get the value of the  $^V\mathcal{M}_{211}^{(0)}$  matrix element nonzero we need to perform shell model calculations in the multi- $\hbar\omega$  excitations. However, here we

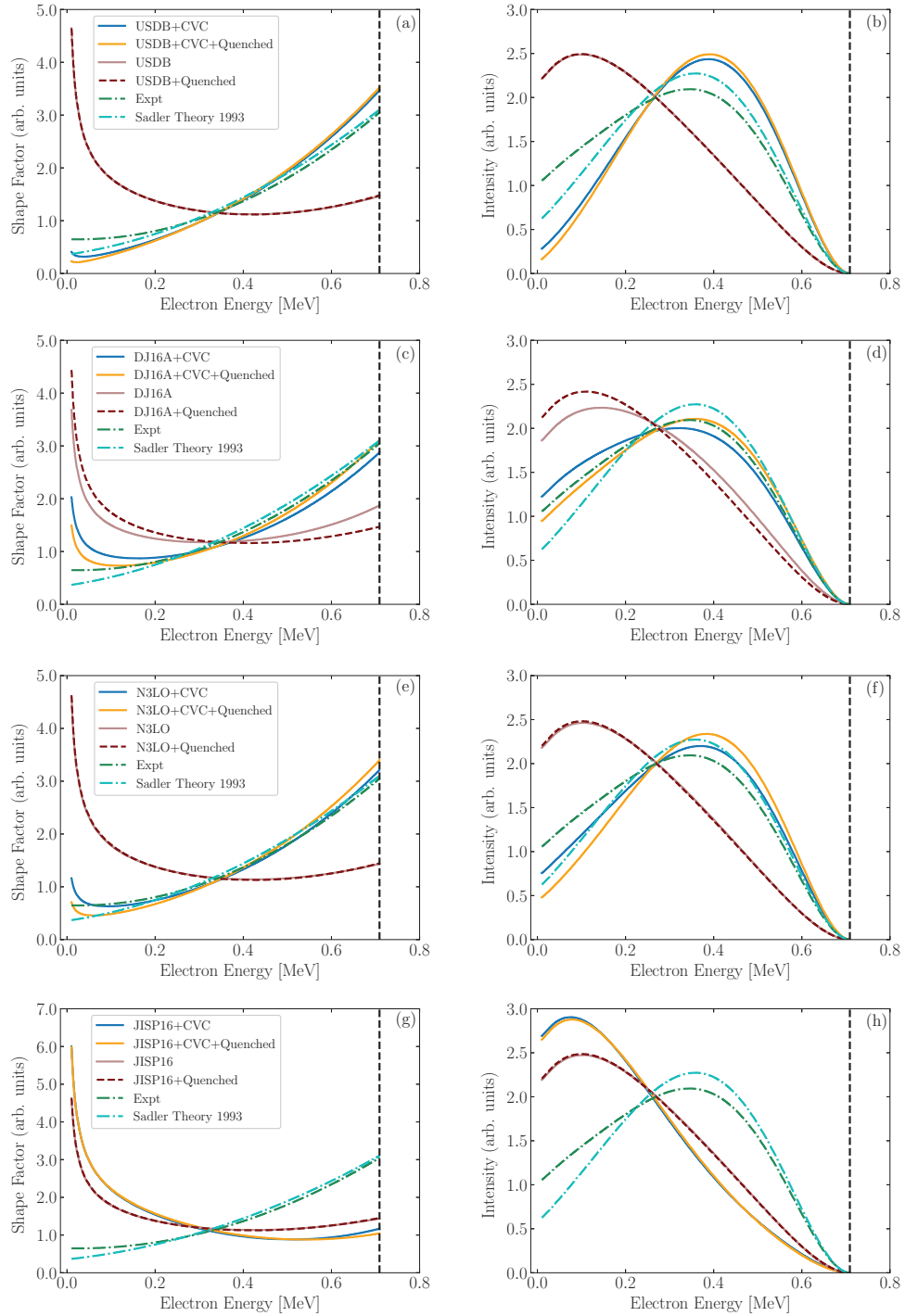


FIG. 3. Theoretical shape factors (left panels) and electron spectra (right panels) for second-forbidden  $\beta^-$  decay of  $^{36}\text{Cl}(2^+) \rightarrow ^{36}\text{Ar}(0^+)$  as functions of electron kinetic energy for different cases. The dashed vertical lines indicate the end-point energy for forbidden ( $Q_{\text{forbidden}}$ ) decay. The areas under each curve is normalized to unity.

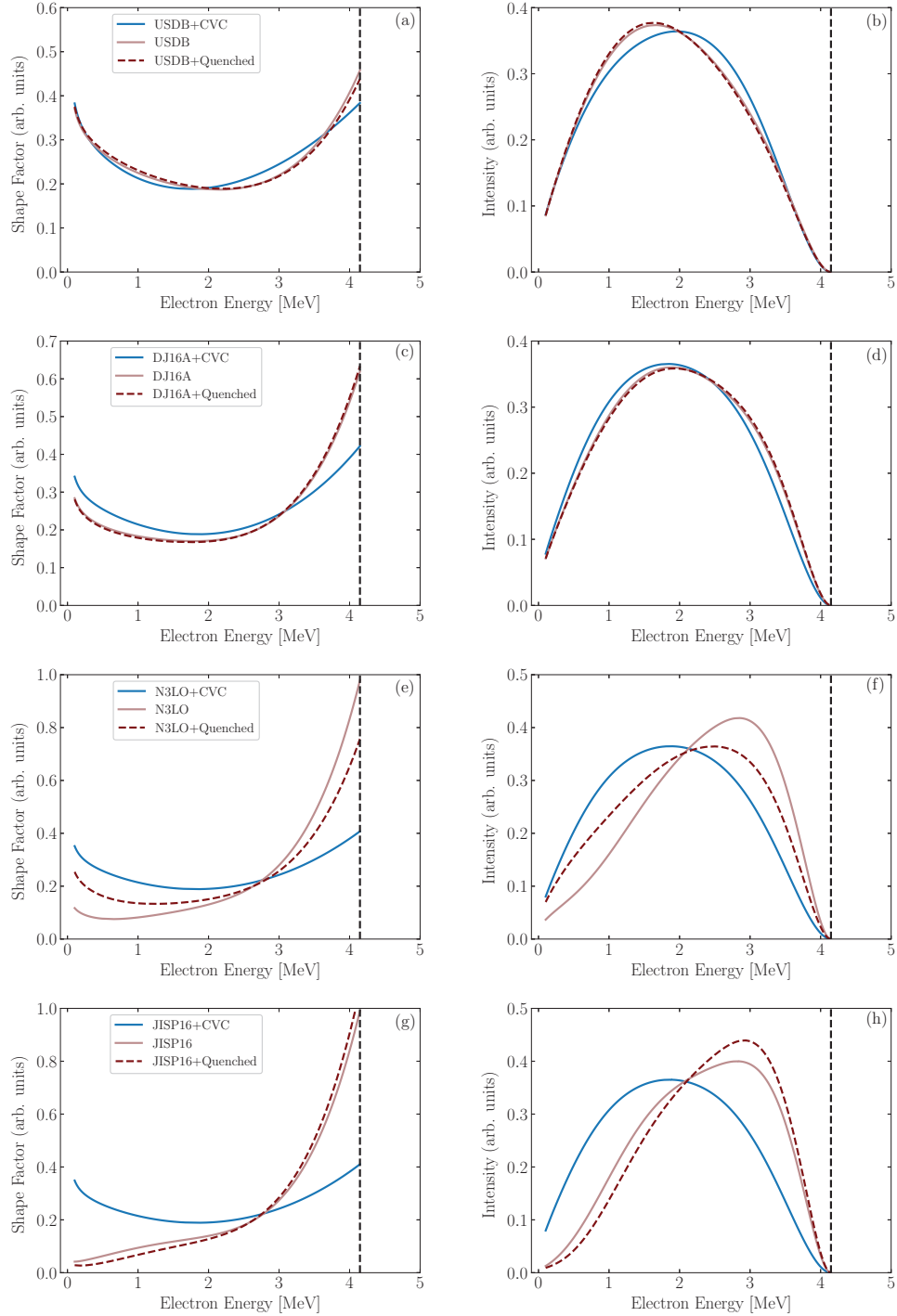


FIG. 4. Theoretical shape factors (left panels) and electron spectra (right panels) for second-forbidden  $\beta^-$  decay of  $^{24}\text{Na}(4^+) \rightarrow ^{24}\text{Mg}(2^+)$  as functions of electron kinetic energy for different cases. The dashed vertical lines indicate the end-point energy for forbidden ( $Q_{\text{forbidden}}$ ) decay. The area under each curve is normalized to unity.

TABLE II. Calculated  $\log ft$  values of the allowed  $\beta^-$  decays from g.s. ( $4^+$ ) of  $^{24}\text{Na}$  to the excited states in  $^{24}\text{Mg}$  from the microscopic and USDB effective interactions.

Transitions	$Q$ (MeV)	BR (%)	$\log ft(g_A = 1.00)$				$\log ft(g_A = 1.27)$				Expt.
			USDB	DJ16A	N3LO	JISP16	USDB	DJ16A	N3LO	JISP16	
$4^+ \rightarrow 3_1^+$	0.280	0.076	6.205	6.149	6.029	6.095	5.997	5.941	5.822	5.888	6.60(2)
$4^+ \rightarrow 4_1^+$	1.392	99.855	5.892	7.454	6.685	6.896	5.685	7.247	6.478	6.688	6.11(1)

follow a different approach to calculate the  $^V\mathcal{M}_{211}^{(0)}$  matrix element. We have used an approach based on CVC theory, since we have an experimental partial half-life, so we keep the value of coupling constants  $g_V = g_A = 1.0$  and try to reproduce the value of the experimental partial half-life by varying the matrix element  $^V\mathcal{M}_{211}^{(0)}$ . The  $^V\mathcal{M}_{211}^{(0)}$  matrix element obtained with this approach is labeled as “ $^V\mathcal{M}_{211}^{(0)}$ (CVC)” in Table III.

The axial-vector matrix elements  $^A\mathcal{M}_{221}^{(0)}$ ,  $^A\mathcal{M}_{221}^{(0)}(1, 1, 1, 1)$ ,  $^A\mathcal{M}_{221}^{(0)}(2, 1, 1, 1)$ , and  $^A\mathcal{M}_{321}^{(0)}$  could be affected by the quenching of axial-vector coupling constant  $g_A$ . The affected value of the Gamow-Teller transition matrix element by the quenching of the axial coupling constant was observed in [33]. From a recent study of the second-forbidden nonunique  $\beta^-$  decay of  $^{20}\text{F}$ , the effect of the quenching of the axial-vector coupling constant in axial-vector matrix elements is reported in Refs. [3,4]. Here, we will use the value of the axial-vector coupling constant for the two different cases:

either the bare value of  $g_A = 1.27$  or the quenched value of  $g_A = 1.00$ .

In Table IV, we presented the  $\log ft$  values for the second-forbidden nonunique  $\beta^-$  decays of  $^{24}\text{Na}$  and  $^{36}\text{Cl}$  calculated with different microscopic and phenomenological interactions in comparison with the experimental data, and the values of coupling constants are taken as  $g_A = 1.27$  and  $g_V = 1.00$  for the calculations. The results with the pure shell model are labeled as “SM,” and those constrained by experimental information are labeled as “SM + CVC.” The prediction of  $\log ft$  values with SM is far from the experimental data. However, the agreement between the calculation with “SM+CVC” and the experimental value came out to be very satisfactory.

### C. Shape factors and electron spectra

In Figs. 3 and 4, we have shown the shape factors (left panels) and  $\beta$  spectra (right panels) of the second forbidden

TABLE III. Calculated leading-order nuclear matrix elements (NMEs) of the second-forbidden nonunique  $\beta^-$  decays of  $^{24}\text{Na}$  and  $^{36}\text{Cl}$  are from microscopic and USDB interactions. The Coulomb-corrected NMEs are indicated by  $(k_e, m, n, \rho)$ , when such elements exist.

Nuclear matrix elements	$^{24}\text{Na}(4^+) \rightarrow ^{24}\text{Mg}(2^+)$			
	USDB	DJ16A	N3LO	JISP16
$^V\mathcal{M}_{211}^{(0)}$ (CVC)	0.023790±0.0001	-0.018446±0.0002	-0.020217±0.0001	-0.019636±0.0001
$^V\mathcal{M}_{220}^{(0)}$	0.431273	-0.131891	-0.237936	-0.187614
$^V\mathcal{M}_{220}^{(0)}(1, 1, 1, 1)$	0.530979	-0.123441	-0.264185	-0.203108
$^V\mathcal{M}_{220}^{(0)}(2, 1, 1, 1)$	0.509588	-0.110404	-0.247587	-0.189152
$^A\mathcal{M}_{221}^{(0)}$	-0.430287	-0.482638	-0.219655	-0.294803
$^A\mathcal{M}_{221}^{(0)}(1, 1, 1, 1)$	-0.524687	-0.577264	-0.287289	-0.370261
$^A\mathcal{M}_{221}^{(0)}(2, 1, 1, 1)$	-0.502493	-0.550486	-0.279212	-0.356859
$^A\mathcal{M}_{321}^{(0)}$	-1.459626	-0.758772	-0.067127	-0.050213
Nuclear matrix elements	$^{36}\text{Cl}(2^+) \rightarrow ^{36}\text{Ar}(0^+)$			
	USDB	DJ16A	N3LO	JISP16
$^V\mathcal{M}_{211}^{(0)}$ (CVC)	-0.029375±0.0005	-0.015943±0.0010	-0.022497±0.0008	-0.007451±0.0009
$^V\mathcal{M}_{220}^{(0)}$	-5.892542	-3.483430	-4.705624	-5.057782
$^V\mathcal{M}_{220}^{(0)}(1, 1, 1, 1)$	-7.250832	-4.357072	-5.796787	-6.225284
$^V\mathcal{M}_{220}^{(0)}(2, 1, 1, 1)$	-6.955989	-4.195245	-5.562475	-5.972497
$^A\mathcal{M}_{221}^{(0)}$	-1.249043	-2.025348	-1.716437	-1.644994
$^A\mathcal{M}_{221}^{(0)}(1, 1, 1, 1)$	-1.496326	-2.412741	-2.062063	-1.979877
$^A\mathcal{M}_{221}^{(0)}(2, 1, 1, 1)$	-1.426626	-2.297321	-1.967308	-1.889710

TABLE IV. Calculated  $\log ft$  values of the second-forbidden nonunique  $\beta^-$  decays of  $^{24}\text{Na}$  and  $^{36}\text{Cl}$  from the shell model and after constraining the matrix element  $^V\mathcal{M}_{211}^{(0)}$  from experimental data. For the  $\log ft$  calculations we have used the values of coupling constants  $g_V = 1.00$  and  $g_A = 1.27$ . The experimental data have been taken from [15].

Transitions	Type	$Q$ (MeV)	BR (%)	$\log ft(\text{SM})$				
				USDB	DJ16A	N3LO	JISP16	Expt.
$^{24}\text{Na}(4^+) \rightarrow ^{24}\text{Mg}(2^+)$	2nd nonunique forbidden	4.147	0.064	12.237	12.881	14.227	13.958	11.340(4)
$^{36}\text{Cl}(2^+) \rightarrow ^{36}\text{Ar}(0^+)$	2nd nonunique forbidden	0.710	98.1	12.635	13.978	13.120	12.976	13.321(3)
$\log ft(\text{SM+CVC})$								
Transitions	Type	$Q$ (MeV)	BR (%)	USDB	DJ16A	N3LO	JISP16	Expt.
$^{24}\text{Na}(4^+) \rightarrow ^{24}\text{Mg}(2^+)$	2nd nonunique forbidden	4.147	0.064	11.367	11.331	11.346	11.342	11.340(4)
$^{36}\text{Cl}(2^+) \rightarrow ^{36}\text{Ar}(0^+)$	2nd nonunique forbidden	0.710	98.1	13.221	13.108	13.153	13.555	13.321(3)

nonunique  $\beta^-$  decays of  $^{36}\text{Cl}$  and  $^{24}\text{Na}$ . The second-forbidden nonunique  $\beta$  decay of  $^{36}\text{Cl}$  is predicted with a strong branching ratio of 98.1%, while that of  $^{24}\text{Na}$  is predicted with a weak branching ratio less than 1%. These figures represent the shape factor of Eq. (10) and  $\beta$  spectrum corresponding to the integrand of Eq. (5) as a function of electron kinetic energy for different microscopic and USDB effective interactions. For all these calculations of second-forbidden nonunique  $\beta$  decay of  $^{24}\text{Na}$  and  $^{36}\text{Cl}$ , we have used the experimentally

measured  $Q$  values 4147 and 709.547 keV, respectively. We have calculated the shape factor by including only the leading-order terms, and the value of vector coupling constant  $g_V = 1.00$  was adopted from the CVC hypothesis. We present in the figures the purely theoretical results from the shell model interactions, labeled with the name of the interaction, and those constrained from experimental information labeled with the name of the interaction and “+CVC,” for quenched ( $g_A = 1.00$ ) and bare ( $g_A = 1.27$ ) cases. The areas under both

TABLE V. The dimensionless integrated shape factors  $\tilde{C}$  for the studied transitions, and their decompositions to vector  $\tilde{C}_V$ , axial-vector  $\tilde{C}_A$ , and vector-axial-vector  $\tilde{C}_{VA}$  parts. For the calculation of total integrated shape factor  $\tilde{C}$  we have taken  $g_V = g_A = 1.0$ .

$^{24}\text{Na}(4^+) \rightarrow ^{24}\text{Mg}(2^+)(\text{SM})$				
Interactions	$\tilde{C}_V$	$\tilde{C}_A$	$\tilde{C}_{VA}$	$\tilde{C}$
USDB	$1.3982 \times 10^{-6}$	$3.6829 \times 10^{-6}$	$1.7841 \times 10^{-6}$	$6.8653 \times 10^{-6}$
DJ16A	$9.8078 \times 10^{-8}$	$1.6952 \times 10^{-6}$	$-5.1005 \times 10^{-7}$	$1.2833 \times 10^{-6}$
N3LO	$3.7996 \times 10^{-7}$	$2.2572 \times 10^{-7}$	$-5.0839 \times 10^{-7}$	$9.7291 \times 10^{-8}$
JISP16	$2.2998 \times 10^{-7}$	$3.7051 \times 10^{-7}$	$-5.0759 \times 10^{-7}$	$9.2903 \times 10^{-8}$
$^{24}\text{Na}(4^+) \rightarrow ^{24}\text{Mg}(2^+)(\text{SM+CVC})$				
Interactions	$\tilde{C}_V$	$\tilde{C}_A$	$\tilde{C}_{VA}$	$\tilde{C}$
USDB	$8.3097 \times 10^{-5}$	$3.6829 \times 10^{-6}$	$-1.3924 \times 10^{-5}$	$7.2856 \times 10^{-5}$
DJ16A	$5.8298 \times 10^{-5}$	$1.6952 \times 10^{-6}$	$1.2868 \times 10^{-5}$	$7.2861 \times 10^{-5}$
N3LO	$6.5792 \times 10^{-5}$	$2.2572 \times 10^{-7}$	$6.8432 \times 10^{-6}$	$7.2861 \times 10^{-5}$
JISP16	$6.3828 \times 10^{-5}$	$3.7051 \times 10^{-7}$	$8.6647 \times 10^{-6}$	$7.2864 \times 10^{-5}$
$^{36}\text{Cl}(2^+) \rightarrow ^{36}\text{Ar}(0^+)(\text{SM})$				
Interactions	$\tilde{C}_V$	$\tilde{C}_A$	$\tilde{C}_{VA}$	$\tilde{C}$
USDB	$6.0691 \times 10^{-9}$	$3.1198 \times 10^{-10}$	$-2.7292 \times 10^{-9}$	$3.6519 \times 10^{-9}$
DJ16A	$2.1890 \times 10^{-9}$	$8.1048 \times 10^{-10}$	$-2.6419 \times 10^{-9}$	$3.5761 \times 10^{-10}$
N3LO	$3.8787 \times 10^{-9}$	$5.9273 \times 10^{-10}$	$-3.0074 \times 10^{-9}$	$1.4641 \times 10^{-9}$
JISP16	$4.4736 \times 10^{-9}$	$5.4657 \times 10^{-10}$	$-3.1016 \times 10^{-9}$	$1.9186 \times 10^{-9}$
$^{36}\text{Cl}(2^+) \rightarrow ^{36}\text{Ar}(0^+)(\text{SM+CVC})$				
Interactions	$\tilde{C}_V$	$\tilde{C}_A$	$\tilde{C}_{VA}$	$\tilde{C}$
USDB	$4.0126 \times 10^{-10}$	$3.1198 \times 10^{-10}$	$-7.7968 \times 10^{-11}$	$6.3528 \times 10^{-10}$
DJ16A	$1.4791 \times 10^{-10}$	$8.1048 \times 10^{-10}$	$-3.2311 \times 10^{-10}$	$6.3528 \times 10^{-10}$
N3LO	$2.5097 \times 10^{-10}$	$5.9273 \times 10^{-10}$	$-2.0843 \times 10^{-10}$	$6.3527 \times 10^{-10}$
JISP16	$2.2999 \times 10^{-9}$	$5.4657 \times 10^{-10}$	$-2.2112 \times 10^{-9}$	$6.3528 \times 10^{-10}$

the theoretical and experimental curves are normalized to unity.

For the shape factor and  $\beta$  spectrum of  $^{36}\text{Cl}$ , we have done a comparison with the available experimental data due to Rotzinger *et al.* [34] and with the theoretical results of Sadler *et al.* [14]. In the case of  $^{36}\text{Cl}$ , the shape factor calculated with the matrix element  $^V\mathcal{M}_{211}^{(0)} = 0$  yields a poor agreement in comparison to the experimental shape factor. After constraining this matrix element with the experimental half-life, the shape factor and electron spectra are consistent with the experimental data. The electron spectra from “DJ16A+CVC+Quenched” are perfectly matched with the experimental electron spectra. This means that the shape factor and electron spectra strongly depend on the matrix element  $^V\mathcal{M}_{211}^{(0)}$ . But in the case of the JISP16 interaction, we have not obtained a good number of this matrix element from the experimental half-life method. We have obtained the value of the matrix element  $^V\mathcal{M}_{211}^{(0)} = -0.007451 \pm 0.0009$  for the JISP16 interaction; it is too small as compared to other interactions.

In Fig. 4, we have presented the shape factor and  $\beta$  spectrum of  $^{24}\text{Na}$  from a pure shell model calculation with quenched and unquenched cases. In the pure shell model calculations, the shape-factor and  $\beta$ -spectrum curves depend strongly on the quenching value of  $g_A$ . After CVC constraining the matrix element  $^V\mathcal{M}_{211}^{(0)}$ , we find that the shape factor and  $\beta$  spectrum are independent of the value of  $g_A$ . So, we have presented the curve for “SM+CVC” only for the bare  $g_A$  value.

For comparison, there are no experimental data available for shape factor and electron spectra corresponding to the second-forbidden nonunique  $\beta^-$  decay of  $^{24}\text{Na}$ . Thus, our theoretical results might be quite useful to compare with a future experimental measurement.

#### D. Decomposition of the integrated shape factor

In Table V, we present the integrated shape factor  $\tilde{C}$  and its decomposition to vector  $\tilde{C}_V$ , axial-vector  $\tilde{C}_A$ , and mixed vector–axial-vector  $\tilde{C}_{VA}$  components, for the involved transitions using different effective interactions. Hence, we have calculated the value of  $\tilde{C}$  and its components with the pure shell model, labeled “SM,” and after constraining the matrix element  $^V\mathcal{M}_{211}^{(0)}$  from experimental information, labeled “SM+CVC.” For all the studied decays transition, the sign of vector  $\tilde{C}_V$  and axial-vector  $\tilde{C}_A$  components is positive from SM and SM+CVC, but the sign of the mixed axial-vector  $\tilde{C}_{VA}$  component varies. From the pure SM for  $^{24}\text{Na}$ , the axial-vector component  $\tilde{C}_A$  is dominant in the USDB and DJ16A interactions. For N3LO and JISP16 interactions, the mixed component  $\tilde{C}_{VA}$  is roughly the sum of vector and axial-vector components and negative in sign. In SM+CVC, the vector component  $\tilde{C}_V$  is dominant for all interactions. The mixed component  $\tilde{C}_{VA}$  is negative for USDB, while positive for other interactions. In case of  $^{36}\text{Cl}$ , the vector component  $\tilde{C}_V$  is dominant for all the interactions in the case of the pure SM. After applying CVC theory, the vector part is dominant only in USDB and JISP16 interactions and for the other two interactions the axial-vector part is large as compared to the

other two components. The signs of the mixed components  $\tilde{C}_{VA}$  are negative in both cases SM and SM+CVC for all interactions.

#### IV. CONCLUSIONS

In this article we have calculated  $\log ft$  values, shape factors, and electron spectra for the second-forbidden nonunique  $\beta^-$  transitions of  $^{24}\text{Na}(4^+) \rightarrow ^{24}\text{Mg}(2^+)$  and  $^{36}\text{Cl}(2^+) \rightarrow ^{36}\text{Ar}(0^+)$  using the three microscopic effective interactions (DJ16A, N3LO, and JISP16) obtained from the NCSM wave functions via the OLS transformation. Also, for comparison, we have used the more popular phenomenological effective USDB interaction.

The low-lying energy spectra of the involved mother and daughter nuclei in  $\beta^-$  decay corresponding to different *ab initio* and phenomenological effective interactions are compared with the available experimental data. The obtained wave functions have been used for further calculations. To calculate the  $\log ft$  values, shape factors and electron spectra, we have constrained the relativistic matrix element  $^V\mathcal{M}_{211}^{(0)}$  in the *sd* model space using experimental information. This matrix element plays an important role in the shape factors and electron spectra. The calculated  $\log ft$  values are compared with experimental data. In the case of the JISP16 interaction, we could not obtain a proper value of this matrix element. In our calculation, we have used two different values of  $g_A$ , either the bare value of  $g_A = 1.27$  or the quenched value of  $g_A = 1.00$ . For the allowed  $\beta$  decay of  $^{24}\text{Na}$ , the  $\log ft$  values are in reasonable agreement with the experimental data. In the case of second-forbidden nonunique  $\beta$  decay, we have calculated  $\log ft$  values corresponding to  $g_A = 1.27$  and compared them with the experimental data. Before applying CVC theory the electron spectra of  $^{24}\text{Na}$  depend significantly on the effective value of  $g_A$ , while after applying CVC they have become independent. In the case of  $^{36}\text{Cl}$ , the dependency of electron spectra on  $g_A$  is opposite from the case of  $^{24}\text{Na}$  for USDB, N3LO, and JISP16 interactions, but in the case of the DJ16A interaction the electron spectra strongly depend on  $g_A$  before and after applying CVC theory. In the case of  $^{36}\text{Cl}$ , the experimental data are available for shape factors and electron spectra. So we have compared our theoretical results with the experimental data to check the role of matrix element  $^V\mathcal{M}_{211}^{(0)}$ . But in the case of  $^{24}\text{Na}$ , there are no experimental data available for shape factors and electron spectra. Thus, our calculated results could be quite useful for comparison with future experimental data. Also, we have decomposed the integrated shape function  $\tilde{C}$  into vector  $\tilde{C}_V$ , axial-vector  $\tilde{C}_A$ , and vector–axial-vector  $\tilde{C}_{VA}$  components to see the individual effects of these components.

#### ACKNOWLEDGMENTS

A.K. would like to thank the Ministry of Human Resource Development (MHRD), Government of India, for financial support for his thesis work. P.C.S. acknowledges a research grant from SERB (India), CRG/2019/000556. We would like to thank X. Mougeot for providing the experimental shape factor data of  $^{36}\text{Cl}$ .

- [1] K. Langanke and G. Martínez-Pinedo, Nuclear weak-interaction processes in stars, *Rev. Mod. Phys.* **75**, 819 (2003).
- [2] B. Singh, J. Rodriguez, S. Wong, and J. Tuli, Review of  $\log ft$  values in  $\beta$  decay, *Nucl. Data Sheets* **84**, 487 (1998).
- [3] O. S. Kirsebom *et al.*, Measurement of the  $2^+ \rightarrow 0^+$  ground-state transition in the  $\beta$  decay of  $^{20}\text{F}$ , *Phys. Rev. C* **100**, 065805 (2019).
- [4] O. S. Kirsebom *et al.*, Discovery of an Exceptionally Strong  $\beta$ -Decay Transition of  $^{20}\text{F}$  and Implications for the Fate of Intermediate-Mass Stars, *Phys. Rev. Lett.* **123**, 262701 (2019).
- [5] T. Suzuki, S. Zha, S.-C. Leung, and K. Nomoto, Electron-capture Rates in  $^{20}\text{Ne}$  for a forbidden transition to the ground state of  $^{20}\text{F}$  relevant to final evolution of high-density O-Ne-Mg cores, *Astrophys. J.* **881**, 64 (2019).
- [6] H. Ejiri, J. Suhonen, and K. Zuber, Neutrino-nuclear responses for astro-neutrinos, single beta decays and double beta decays, *Phys. Rep.* **797**, 1 (2019).
- [7] M. Haaranen, P. C. Srivastava, J. Suhonen, and K. Zuber,  $\beta$  decay half-life of  $^{50}\text{V}$  calculated by the shell model, *Phys. Rev. C* **90**, 044314 (2014).
- [8] M. Haaranen, P. C. Srivastava, and J. Suhonen, Forbidden nonunique  $\beta$  decays and effective values of weak coupling constants, *Phys. Rev. C* **93**, 034308 (2016).
- [9] M. Haaranen, J. Kotila, and J. Suhonen, Spectrum-shape method and the next-to-leading-order terms of the  $\beta$ -decay shape factor, *Phys. Rev. C* **95**, 024327 (2017).
- [10] A. Kumar, P. C. Srivastava, and T. Suzuki, Shell model results for nuclear  $\beta^-$ -decay properties of  $sd$ -shell nuclei, *Prog. Theor. Exp. Phys.* **2020**, 033D01 (2020).
- [11] V. Kumar, P. C. Srivastava, and H. Li, Nuclear  $\beta^-$ -decay half-lives for  $fp$  and  $fp_g$  shell nuclei, *J. Phys. G: Nucl. Part. Phys.* **43**, 105104 (2016).
- [12] A. Saxena, P. C. Srivastava, and T. Suzuki, *Ab initio* calculations of Gamow-Teller strengths in the  $sd$  shell, *Phys. Rev. C* **97**, 024310 (2018).
- [13] V. Kumar and P. C. Srivastava, Shell model description of Gamow-Teller strengths in  $pf$ -shell nuclei, *Eur. Phys. J. A* **52**, 181 (2016).
- [14] R. Sadler and H. Behrens, Second-forbidden beta-decay and the effect of  $(V + A)$ - and  $S$ -interaction admixtures:  $^{36}\text{Cl}$ , *Z. Phys. A* **346**, 25 (1993).
- [15] National Nuclear Data Center (NNDC), ENSDF database, 2020, <https://www.nndc.bnl.gov/ensdf/>.
- [16] H. Behrens and W. Bühring, *Electron Radial Wave Functions and Nuclear Beta-Decay* (Clarendon, Oxford, 1982).
- [17] H. F. Schopper, *Weak Interaction and Nuclear Beta Decay* (North-Holland, Amsterdam, 1966).
- [18] M. T. Mustonen, M. Aunola, and J. Suhonen, Theoretical description of the fourth-forbidden non-unique  $\beta$  decays of  $^{113}\text{Cd}$  and  $^{115}\text{In}$ , *Phys. Rev. C* **73**, 054301 (2006); **76**, 019901(E) (2007).
- [19] E. Ydrefors, M. T. Mustonen, and J. Suhonen, MQPM description of the structure and beta decays of the odd  $A = 95, 97$  Mo and Tc isotopes, *Nucl. Phys. A* **842**, 33 (2010).
- [20] J. Suhonen, *From Nucleons to Nucleus: Concept of Microscopic Nuclear Theory* (Springer, Berlin, 2007).
- [21] J. Kostensalo, M. Haaranen, and J. Suhonen, Electron spectra in forbidden  $\beta$  decays and the quenching of the weak axial-vector coupling constant  $g_A$ , *Phys. Rev. C* **95**, 044313 (2017).
- [22] J. Kostensalo and J. Suhonen,  $g_A$ -driven shapes of electron spectra of forbidden  $\beta$  decays in the nuclear shell model, *Phys. Rev. C* **96**, 024317 (2017).
- [23] J. Suhonen, Value of the axial-vector coupling strength in  $\beta$  and  $\beta\beta$  decays: A review, *Front. Phys.* **5**, 55 (2017).
- [24] N. A. Smirnova, B. R. Barrett, Y. Kim, I. J. Shin, A. M. Shirokov, E. Dikmen, P. Maris, and J. P. Vary, Effective interactions in the  $sd$  shell, *Phys. Rev. C* **100**, 054329 (2019).
- [25] E. Dikmen, A. F. Lisetskiy, B. R. Barrett, P. Maris, A. M. Shirokov, and J. P. Vary, *Ab initio* effective interactions for  $sd$ -shell valence nucleons, *Phys. Rev. C* **91**, 064301 (2015).
- [26] S. Okubo, Diagonalization of Hamiltonian and Tamm-Dancoff equation, *Prog. Theor. Phys.* **12**, 603 (1954).
- [27] K. Suzuki and S. Y. Lee, Convergent theory for effective interaction in nuclei, *Prog. Theor. Phys.* **64**, 2091 (1980).
- [28] K. Suzuki, Construction of Hermitian effective interaction in nuclei: General relation between Hermitian and non-Hermitian forms, *Prog. Theor. Phys.* **68**, 246 (1982).
- [29] B. A. Brown and W. A. Richter, New “USD” Hamiltonians for the  $sd$  shell, *Phys. Rev. C* **74**, 034315 (2006).
- [30] A. M. Shirokov, I. J. Shin, Y. Kim, M. Sosenkina, P. Maris, and J. P. Vary, N3LO  $NN$  interaction adjusted to light nuclei in *ab initio* approach, *Phys. Lett. B* **761**, 87 (2016).
- [31] B. A. Brown and W. D. M. Rae, The shell-model code NuShellX@MSU, *Nucl. Data Sheets* **120**, 115 (2014).
- [32] E. U. Condon and G. Shortley, *The Theory of Atomic Spectra* (Cambridge University Press, Cambridge, 1951).
- [33] I. S. Towner, Quenching of spin matrix elements in nuclei, *Phys. Rep.* **155**, 263 (1987).
- [34] H. Rotzinger, M. Linck, A. Burck, M. Rodrigues, M. Loidl, E. Leblanc, L. Fleischmann, A. Fleischmann, and C. Enss, Beta spectrometry with magnetic calorimeters, *J. Low. Temp. Phys.* **151**, 1087 (2008).



## XIV

### MEASUREMENT OF THE SPECTRAL SHAPE OF THE $\beta$ - DECAY OF $^{137}\text{Xe}$ TO THE GROUND STATE OF $^{137}\text{Cs}$ IN EXO-200 AND COMPARISON WITH THEORY

by

S. Al Kharusi et al. 2020

Physical Review Letters, 124 (23), 232502.  
DOI: 10.1103/PhysRevLett.124.232502

Reproduced with kind permission by American Physical Society.

**Measurement of the Spectral Shape of the  $\beta$ -Decay of  $^{137}\text{Xe}$  to the Ground State of  $^{137}\text{Cs}$  in EXO-200 and Comparison with Theory**

S. Al Kharusi,<sup>1</sup> G. Anton,<sup>2</sup> I. Badhrees,<sup>3,‡</sup> P. S. Barbeau,<sup>4</sup> D. Beck,<sup>5</sup> V. Belov,<sup>6</sup> T. Bhatta,<sup>7</sup> M. Breidenbach,<sup>8</sup> T. Brunner,<sup>1,9</sup> G. F. Cao,<sup>10</sup> W. R. Cen,<sup>10</sup> C. Chambers,<sup>1</sup> B. Cleveland,<sup>11,§</sup> M. Coon,<sup>5</sup> A. Craycraft,<sup>12</sup> T. Daniels,<sup>13</sup> L. Darroch,<sup>1</sup> S. J. Daugherty,<sup>14,||</sup> J. Davis,<sup>8</sup> S. Delaquis,<sup>8,\*</sup> A. Der Mesrobian-Kabakian,<sup>11</sup> R. DeVoe,<sup>15</sup> J. Dilling,<sup>9</sup> A. Dolgolenko,<sup>6</sup> M. J. Dolinski,<sup>16</sup> J. Echevers,<sup>5</sup> W. Fairbank, Jr.,<sup>12</sup> D. Fairbank,<sup>12</sup> J. Farine,<sup>11</sup> S. Feyzbakhsh,<sup>17</sup> P. Fierlinger,<sup>18</sup> D. Fudenberg,<sup>15,¶</sup> P. Gautam,<sup>16</sup> R. Gornea,<sup>3,9</sup> G. Gratta,<sup>15</sup> C. Hall,<sup>19</sup> E. V. Hansen,<sup>16,\*\*</sup> J. Hoessl,<sup>2</sup> P. Hufschmidt,<sup>2</sup> M. Hughes,<sup>20</sup> A. Iverson,<sup>12</sup> A. Jamil,<sup>21</sup> C. Jessiman,<sup>3</sup> M. J. Jewell,<sup>15</sup> A. Johnson,<sup>8</sup> A. Karelin,<sup>6</sup> L. J. Kaufman,<sup>8,††</sup> T. Koffas,<sup>3</sup> J. Kostensalo,<sup>22</sup> R. Krücken,<sup>9</sup> A. Kuchenkov,<sup>6</sup> K. S. Kumar,<sup>17</sup> Y. Lan,<sup>9</sup> A. Larson,<sup>7</sup> B. G. Lenardo,<sup>15</sup> D. S. Leonard,<sup>23</sup> G. S. Li,<sup>15</sup> S. Li,<sup>5</sup> Z. Li,<sup>21</sup> C. Licciardi,<sup>11</sup> Y. H. Lin,<sup>16,||</sup> R. MacLellan,<sup>7</sup> T. McElroy,<sup>1</sup> T. Michel,<sup>2</sup> B. Mong,<sup>8</sup> D. C. Moore,<sup>21</sup> K. Murray,<sup>1</sup> P. Nakarmi,<sup>20</sup> O. Njoya,<sup>24</sup> O. Nusair,<sup>20</sup> A. Odian,<sup>8</sup> I. Ostrovskiy,<sup>20,‡</sup> A. Piepke,<sup>20</sup> A. Pocar,<sup>17</sup> F. Retière,<sup>9</sup> A. L. Robinson,<sup>11</sup> P. C. Rowson,<sup>8</sup> D. Ruddell,<sup>13</sup> J. Runge,<sup>4</sup> S. Schmidt,<sup>2</sup> D. Sinclair,<sup>3,9</sup> K. Skarpaas,<sup>8</sup> A. K. Soma,<sup>20,‡‡</sup> V. Stekhanov,<sup>6</sup> J. Suhonen,<sup>22</sup> M. Tarka,<sup>17</sup> S. Thibado,<sup>17</sup> J. Todd,<sup>12</sup> T. Tolba,<sup>10,§§</sup> T. I. Totev,<sup>1</sup> R. Tsang,<sup>20</sup> B. Veenstra,<sup>3</sup> V. Veeraraghavan,<sup>20</sup> P. Vogel,<sup>25</sup> J.-L. Vuilleumier,<sup>26</sup> M. Wagenpfeil,<sup>2</sup> J. Watkins,<sup>3</sup> M. Weber,<sup>15,|||</sup> L. J. Wen,<sup>10</sup> U. Wichoski,<sup>11</sup> G. Wrede,<sup>2</sup> S. X. Wu,<sup>15</sup> Q. Xia,<sup>21</sup> D. R. Yahne,<sup>12</sup> L. Yang,<sup>27</sup> Y.-R. Yen,<sup>16,¶¶</sup> O. Ya. Zeldovich,<sup>6</sup> and T. Ziegler<sup>2</sup>

(EXO-200 Collaboration)

<sup>1</sup>Physics Department, McGill University, Montreal, Quebec H3A 2T8, Canada

<sup>2</sup>Erlangen Centre for Astroparticle Physics (ECAP), Friedrich-Alexander University Erlangen-Nürnberg, Erlangen 91058, Germany

<sup>3</sup>Physics Department, Carleton University, Ottawa, Ontario K1S 5B6, Canada

<sup>4</sup>Department of Physics, Duke University, and Triangle Universities Nuclear Laboratory (TUNL), Durham, North Carolina 27708, USA

<sup>5</sup>Physics Department, University of Illinois, Urbana-Champaign, Illinois 61801, USA

<sup>6</sup>Institute for Theoretical and Experimental Physics named by A.I. Alikhanov of National Research Centre “Kurchatov Institute”, Moscow 117218, Russia

<sup>7</sup>Department of Physics, University of South Dakota, Vermillion, South Dakota 57069, USA

<sup>8</sup>SLAC National Accelerator Laboratory, Menlo Park, California 94025, USA

<sup>9</sup>TRIUMF, Vancouver, British Columbia V6T 2A3, Canada

<sup>10</sup>Institute of High Energy Physics, Beijing 100049, China

<sup>11</sup>Department of Physics, Laurentian University, Sudbury, Ontario P3E 2C6, Canada

<sup>12</sup>Physics Department, Colorado State University, Fort Collins, Colorado 80523, USA

<sup>13</sup>Department of Physics and Physical Oceanography, University of North Carolina at Wilmington, Wilmington, North Carolina 28403, USA

<sup>14</sup>Physics Department and CEEM, Indiana University, Bloomington, Indiana 47405, USA

<sup>15</sup>Physics Department, Stanford University, Stanford, California 94305, USA

<sup>16</sup>Department of Physics, Drexel University, Philadelphia, Pennsylvania 19104, USA

<sup>17</sup>Amherst Center for Fundamental Interactions and Physics Department, University of Massachusetts, Amherst, Massachusetts 01003, USA

<sup>18</sup>Technische Universität München, Physikdepartment and Excellence Cluster Universe, Garching 80805, Germany

<sup>19</sup>Physics Department, University of Maryland, College Park, Maryland 20742, USA

<sup>20</sup>Department of Physics and Astronomy, University of Alabama, Tuscaloosa, Alabama 35487, USA

<sup>21</sup>Wright Laboratory, Department of Physics, Yale University, New Haven, Connecticut 06511, USA

<sup>22</sup>University of Jyväskylä, Department of Physics, P.O. Box 35 (YFL), Jyväskylä FI-40014, Finland

<sup>23</sup>IBS Center for Underground Physics, Daejeon 34126, Korea

<sup>24</sup>Department of Physics and Astronomy, Stony Brook University, SUNY, Stony Brook, New York 11794, USA

<sup>25</sup>Kellogg Lab, Caltech, Pasadena, California 91125, USA

<sup>26</sup>LHEP, Albert Einstein Center, University of Bern, Bern CH-3012, Switzerland

<sup>27</sup>Department of Physics, University of California San Diego, La Jolla, California 92093, USA



(Received 3 February 2020; revised manuscript received 17 April 2020; accepted 7 May 2020; published 12 June 2020)

We report on a comparison between the theoretically predicted and experimentally measured spectra of the first-forbidden nonunique  $\beta$ -decay transition  $^{137}\text{Xe}(7/2^-) \rightarrow ^{137}\text{Cs}(7/2^+)$ . The experimental data were

acquired by the EXO-200 experiment during a deployment of an AmBe neutron source. The ultralow background environment of EXO-200, together with dedicated source deployment and analysis procedures, allowed for collection of a pure sample of the decays, with an estimated signal to background ratio of more than 99 to 1 in the energy range from 1075 to 4175 keV. In addition to providing a rare and accurate measurement of the first-forbidden nonunique  $\beta$ -decay shape, this work constitutes a novel test of the calculated electron spectral shapes in the context of the reactor antineutrino anomaly and spectral bump.

DOI: 10.1103/PhysRevLett.124.232502

*Introduction.*—The discrepancies between measured and predicted antineutrino fluxes from nuclear reactors constitute the so-called reactor antineutrino anomaly [1,2]. In addition, an event excess (“bump”) against predicted spectra between 4 and 7 MeV of antineutrino energy has been observed by the RENO [3], Double Chooz [4], and Daya Bay [5] antineutrino oscillation experiments. The spectral bump was apparently present but not recognized in the much earlier Goesgen experiment [6]. Predicting the reactor antineutrino flux is difficult due to the uncertainties related to the treatment of the  $\beta$  decays of the numerous fission fragments [7,8]. One particular problem is the description of the forbidden  $\beta$ -decay transitions whose spectra are translated to antineutrino spectra at energies relevant for the measurement of the total flux and the spectral bump [9]. It has been noted that many first-forbidden  $\beta$ -decay transitions, like the presently discussed one, in the medium-mass  $A = 89$ –143 nuclei play a key role in reactor antineutrino spectra [9,10]. Only a handful of electron spectra corresponding to  $J^+ \leftrightarrow J^-$   $\beta$  transitions in this region has been measured and with a rather poor precision [11,12]. According to [9,10], the  $\beta$  spectra for the  $J^+ \leftrightarrow J^-$  transitions, relevant for solving the reactor anomaly and spectral bump, deviate noticeably from the allowed shape, the deviation being approximately a quadratic function of the electron kinetic energy (see, e.g., Ref. [10], Fig. 3, top panel). This is the case also for the  $\beta$  decay of  $^{137}\text{Xe}$  (see Fig. 2, lower panel), making this decay an important test case of the computed spectral shapes. In the case of  $^{137}\text{Xe}$ , there is a measurement [13] that proposes a scheme for the decay of  $^{137}\text{Xe}$  to the ground state (the GS decay) and first excited state (the ES decay) of  $^{137}\text{Cs}$ , but we could not find measurements or calculations of the corresponding  $\beta$ -spectrum shapes. In the present work, we perform the  $\beta$ -spectrum-shape measurement and calculation for the decay to the ground state. Comparison with experiment confirms that the calculated shape of the  $^{137}\text{Xe}$  decay is correct, and thus there is hope that the effects of the first-forbidden  $\beta$  decays lead to mitigation of the reactor anomaly and a possible explanation of the origins of the spectral bump, as proposed by Hayen *et al.* [9,10].

The problem of many of the electron spectra of the first-forbidden  $\beta$ -decay transitions is connected to the uncertainty of the effective value of the weak axial coupling  $g_A$  [14] and the enhancement of the axial charge nuclear matrix element (NME) by meson exchange currents [15].

Recently, a sustained effort has gone into clarifying these two burning issues [16]. Related to this, we point out that the effective values of  $g_A$  are more like effective corrections to specific nuclear theory frameworks than fundamental corrections to the weak axial coupling [17]. For some decays, the spectral shape depends on the effective value of  $g_A$  and, to some extent, on the mesonic enhancement [14–16]. The uncertainties related to these parameters are reflected as theoretical uncertainties in the predicted antineutrino spectra. Fortunately, the majority of the shapes of electron spectra are not much affected by the values of these quantities. In order to test the accuracy of the theory framework used to compute the electron spectra related to the reactor antineutrino problem, one needs (1) a measured electron spectral shape of a forbidden  $\beta$ -decay transition in the nuclear mass region relevant for the reactor antineutrino problem that has (2) a nontrivial shape and that is (3) independent of both  $g_A$  and the mesonic enhancement.

These three requirements are met by the GS decay, that is by the first-forbidden nonunique  $\beta$ -decay transition  $^{137}\text{Xe}(7/2^-) \rightarrow ^{137}\text{Cs}(7/2^+\text{g.s.})$ . The condition (1) is accounted for by the experimental spectral shape extracted in the present work. The condition (2) is satisfied by the complex spectral shape containing a pseudoscalar part with two NMEs, a pseudovector part with three NMEs, and a pseudotensor part with one NME [15,16]. Furthermore, our present calculations, based on the formalism of [18] and on its recent derivative [19], show that requirement (3) is also satisfied to a high level of precision.

*Theoretical description of the forbidden  $\beta$  shape.*—For the theoretical description of the first-forbidden  $\beta^-$  decay, we adopt the expansion of Behrens and Bühring [18]. NMEs up to the next-to-leading order are included in the calculations [19].

The nuclear structure calculations were done using the shell model code NUSHELLX@MSU [20] in a model space spanned by the proton orbitals  $0g_{7/2}$ ,  $1d_{5/2}$ ,  $1d_{3/2}$ ,  $2s_{1/2}$ , and  $0h_{11/2}$  and the neutron orbitals  $0h_{9/2}$ ,  $1f_{7/2}$ ,  $1f_{5/2}$ ,  $2p_{3/2}$ ,  $2p_{1/2}$ , and  $0i_{13/2}$  with the effective Hamiltonian jj56pnb [21]. This interaction has previously been used to study the mesonic exchange effects on and  $g_A$  dependence of the electron spectra of  $A \approx 135$  nuclei [15], as well as to predict the  $\beta$  shapes of the first-forbidden decays contributing to the cumulative  $\beta$  spectra from nuclear reactors [9,10]. While  $^{137}\text{Xe}$  is not one of the major contributors itself, neighboring nuclei such as  $^{136,137,138}\text{I}$  and  $^{139,140}\text{Xe}$

are [22]. The GS decay turns out to be one of the spectra with negligible shape dependence on the adopted value of  $g_A$  or the magnitude of the mesonic enhancement effects on the axial charge matrix element. This is the case since the involved four axial vector NMEs dominantly contribute to the spectral shape and thus  $g_A$  simply gives the overall scaling of the electron spectrum and, in turn, of the half-life. This  $g_A$  dominance is clearly visible in Fig. 2, where the  $g_A$ -dependent contribution (blue dots) is compared to the full spectral shape (blue dotted line). The shape factor  $C(E)$  (ratio of the corrected spectrum to that corresponding to an allowed decay) is plotted in the bottom frame of the figure. This transition is a perfect test case for the accuracy and validity of the calculations of the  $\beta$  spectra in the context of the reactor antineutrino anomaly [9,10]. This is particularly important since the calculations of Hayen *et al.* [9,10] propose corrections to the traditional Huber-Mueller model [1,23] that explain, at least partially, the anomaly and spectral bump.

In contrast with the GS decay, the spectral shape of the ES decay to the first excited state of  $^{137}\text{Cs}$  (ES decay) does depend on the value of  $g_A$  and could, in principle, be used to constrain its value. However, the accompanying emission of a deexcitation  $\gamma$  makes accurate measurement of the ES decay's  $\beta$ -spectrum shape in EXO-200 challenging. Since both the motivation and analysis approach are substantially different for the GS and ES measurements, we consider the ES decay outside the scope of this work and only focus on the GS decay.

*Experimental details and results.*—The EXO-200 detector is a cylindrical time projection chamber (TPC). It is filled with liquid xenon (LXe) consisting of 80.6% of the isotope  $^{136}\text{Xe}$  and 19.1% of  $^{134}\text{Xe}$ , with the remaining balance composed of other isotopes. The LXe is housed in a cylindrical copper vessel of  $\sim 40$  cm diameter and  $\sim 44$  cm length. The vessel is surrounded by  $\sim 50$  cm of HFE [24], a hydrogen-rich heat transfer fluid maintained inside a vacuum-insulated copper cryostat. Further shielding is provided by at least 25 cm of lead in all directions. A small diameter copper tube runs from the outside of the lead shield through the HFE and wraps around the outside of the TPC vessel. The tube allows one to insert miniature radioactive calibration sources and place them close to the active volume of the detector. Energy depositions in the TPC produce ionization charge and scintillation light. The charge and light signals are reconstructed to provide energy and position of events. In a given event, charge deposits, or clusters, that are separated by  $\sim 1$  cm can be individually reconstructed. The event is then classified as single site (SS) or multisite (MS), depending on the number of spatially distinct reconstructed clusters. More details about the EXO-200 design and performance are available in [25,26]. The reconstruction, Monte Carlo simulation (MC), and analysis approaches are described in [27,28]. EXO-200 is designed to minimize radioactive backgrounds. Its data

rate above 1000 keV is dominated by the two-neutrino double  $\beta$  decay of  $^{136}\text{Xe}$  [29].

The experimental data used in this work were collected during the AmBe neutron source calibration campaign carried out in December 2018.  $^{137}\text{Xe}$  is produced by neutron capture on  $^{136}\text{Xe}$  and decays to  $^{137}\text{Cs}$  with the half-life of  $3.818 \pm 0.013$  min [30]. In  $\sim 67\%$  of cases [31],  $^{137}\text{Xe}$  decays to the ground state of  $^{137}\text{Cs}$ . In  $\sim 31\%$  of cases,  $^{137}\text{Xe}$  decays to a  $5/2^+$  excited state of  $^{137}\text{Cs}$ , which deexcites by emission of a 455.5 keV  $\gamma$ -ray. The neutrons were produced by the neutron source positioned at the midplane of the TPC, 3 cm outside the LXe volume. The source contains  $\sim 65$   $\mu\text{Ci}$  of  $^{241}\text{Am}$  in the form of a carrier-free  $^{241}\text{AmO}_2$  powder mixed with beryllium metal powder. The mixture is contained in a 1.2 mm diameter tungsten capsule, which is in turn contained inside a 2.0 mm diameter stainless steel capsule that is welded shut by electron beam welding. The estimated neutron activity of the source is  $\sim 90$  Bq. More details about the source construction and characterization can be found in [32]. In  $\sim 60\%$  of the cases [33], the neutron emission from the source is accompanied by a 4439.8 keV  $\gamma$  ray. The source is positioned several centimeters outside of the TPC during the calibrations, which leads to some neutrons being captured in HFE by hydrogen nuclei. The capture is followed by the emission of a 2224.6 keV  $\gamma$  ray. Additional  $\gamma$  radioactivity is expected from neutron inelastic scattering in HFE. While advantageous for the energy calibration, the  $\gamma$  rays produced when the AmBe source is deployed close to the TPC would constitute a major background for the  $^{137}\text{Xe}$   $\beta$ -decay measurement. To avoid this, a special deployment procedure was used. The deployment sequence consisted of repeated “ $^{136}\text{Xe}$  activation— $^{137}\text{Xe}$  decay” cycles. During the decay phases, the source was retracted outside of the lead shield, ceasing the associated  $\gamma$  radioactivity. The length of the periods was chosen to maximize the number of detected  $^{137}\text{Xe}$  decays. Figure 1 shows the rate of reconstructed events in EXO-200 during one of the decay periods when the source is retracted. The drop (rise) of the rate at the end (beginning) of the

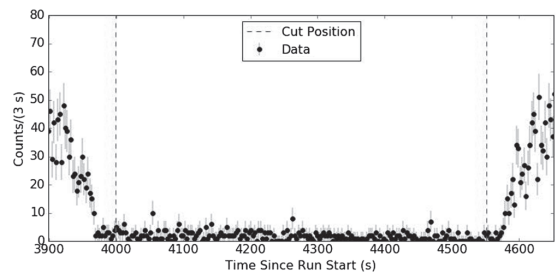


FIG. 1. Reconstructed event rate during the AmBe source calibration. The vertical lines show the cuts that select  $^{137}\text{Xe}$  decays.

activation periods is clearly seen. The red lines indicate the placement of the cuts to select the  $^{137}\text{Xe}$  decay period. A total of 60 such periods is selected during the campaign. The decay phase is defined as a period when the event rate is less than 1.33 Hz. The timing cuts are placed at +30 (−30) s from each decay period’s start (end). The integrated livetime is 8.73 hours.

The fiducial volume cuts are relaxed slightly, as compared to Ref. [28]. This increases the fiducial mass by  $\sim 5\%$ , while still retaining the good agreement between shapes of energy distributions in data and MC simulation. The relaxed cuts admit a background increase that is negligible for this study.

When  $^{137}\text{Xe}$  decays to the ground state of  $^{137}\text{Cs}$ , only the  $\beta$  particle is emitted and detected. Electrons of  $O(\text{MeV})$  energy are reconstructed predominantly as SS events in the detector. On the other hand, when the decay proceeds to the  $5/2^+$  excited state (ES decay), both the  $\beta$  and the deexcitation  $\gamma$  deposit energy and are reconstructed as an MS event in most cases. Therefore, the  $^{137}\text{Xe}$  GS decay spectrum can be examined in EXO-200 by looking at the energy distribution of the selected SS events. However, several reconstruction and physics effects introduce non-negligible differences between the theoretical GS spectrum and the spectrum of the reconstructed SS events. To take these effects into account, the MC of the AmBe source is first used to track the neutrons up to the  $^{136}\text{Xe}$  atoms on which they are captured.  $^{137}\text{Xe}$  decays, both GS and ES, are then generated from the capture position distributions. The  $\beta$  energy is sampled from the theoretical  $\beta$  spectrum. The decay products ( $\beta$  and deexcitation  $\gamma$ ) are tracked, and their energy depositions are simulated and reconstructed to produce the expected SS spectrum. This spectrum, along with the theoretical one, are shown in Fig. 2. At the lowest energy, one can see the expected effect of the charge reconstruction threshold, leading to the MC spectrum having a lower intensity than the theoretical spectrum. While the SS spectrum is dominated by the GS decays, a residual peak at 455.5 keV is expected due to ES decays that occur outside of the sensitive volume. For such events, the  $\beta$  cluster of an ES decay is lost, while the deexcitation  $\gamma$  ray has a chance to travel to the fiducial region and get reconstructed as a single cluster. At higher energies, the intensity of the MC SS spectrum is lower than the theoretical spectrum, due to reconstruction effects and the production of Bremsstrahlung photons by the  $\beta$  particles, which leads to some GS decays being reconstructed as MS events. Finally, the slightly higher apparent end point in the MC spectrum is expected due to the finite energy resolution.

The detector’s energy scale is constrained using the total of seven mono-energetic  $\gamma$  lines obtained in EXO-200 using radioactive calibration sources: 455.5 (AmBe), 661.7 ( $^{137}\text{Cs}$ ), 1173.2 ( $^{60}\text{Co}$ ), 1332.5 ( $^{60}\text{Co}$ ), 2224.6 (AmBe), 2614.5 ( $^{228}\text{Th}$ ), and 4439.8 keV (AmBe). The mean

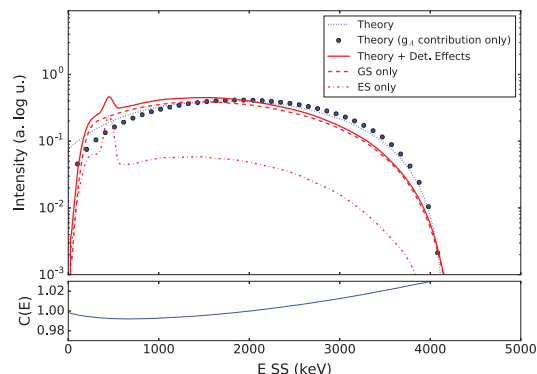


FIG. 2. (Top frame) Theoretical GS spectrum (blue dotted line) and reconstructed MC SS spectrum (red solid line). The theoretical GS spectrum shape is the same for all reasonable  $g_A$  and mesonic enhancements within the line width. The  $g_A$ -dependent contribution to the theoretical spectrum is also shown as blue dots. Individual contributions of GS and ES decays to the reconstructed spectrum are also shown as red dashed and dash-dotted lines, respectively. (Bottom frame) Shape factor,  $C(E)$ .

position of the full absorption peaks in the uncalibrated energy spectra is found using a fit by a linear combination of the Gaussian and error functions. The latter function is an *ad hoc* way to account for the shoulder to the left of the peaks, composed of Compton scattering events, multisite full absorption events with one or more small charge clusters missing, and other events. The calibration runs collected closest in time to the AmBe calibration campaign are used. The same fiducial cuts are used for the calibration events as for the  $^{137}\text{Xe}$  dataset. The SS events are selected for all calibration lines, with the exception of the 455.5 keV  $^{137}\text{Cs}$  deexcitation line. Since in that case the deexcitation  $\gamma$  is accompanied by a  $\beta$  decay, the two-cluster MS events within the timing cuts are first selected. The energy distribution of the smaller of the two charge clusters is then plotted for events in which the larger of the two charge clusters has energy  $\sim 3\sigma$  above 455.5 keV (560 keV). Figure 3 shows the resulting spectrum. It is not possible to

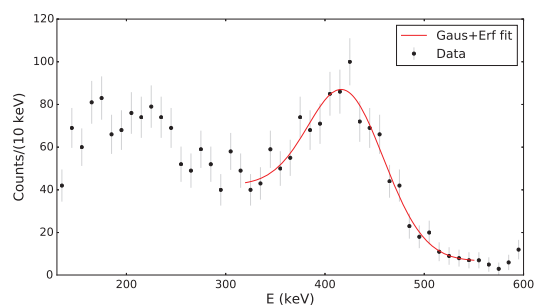


FIG. 3. Selected  $^{137}\text{Cs}$  deexcitation  $\gamma$  events. The Gaussian + Erf fit to the uncalibrated charge energy is shown as the red line.

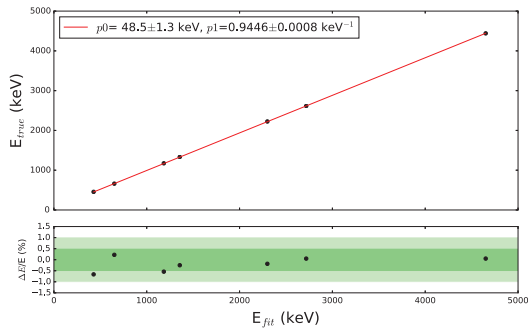


FIG. 4. SS data energy calibration. Red line is the linear fit. Best-fit parameters are also shown. The errors are statistical.

discern contributions of individual clusters to the total detected scintillation light. So the reconstructed energy in this work is based on charge signals only. The energy calibration approach used in this work extends the constrained energy range in both directions, as compared to previous analyses, at the expense of a worse energy resolution. After the mean positions of all  $\gamma$  lines are found, they are plotted versus the true energies and fit by a linear function. Figure 4 shows the resulting SS data energy calibration that is used in this analysis. The residuals are typically within  $\pm 0.5\%$ , not exceeding  $\pm 1\%$ .

Based on MC of the AmBe source, the main expected backgrounds in the selected SS spectrum are  $^{135}\text{Xe}$  and  $^{64}\text{Cu}$ .  $^{135}\text{Xe}$  is produced by capture of the AmBe neutrons on  $^{134}\text{Xe}$ , which constitutes  $\sim 19\%$  of the xenon target in EXO-200.  $^{135}\text{Xe}$  undergoes a  $\beta$  decay with a half-life of 9.14 hours and has a Q value of 1051 keV.  $^{64}\text{Cu}$  is produced in the copper vessel (and other construction elements) and undergoes  $\beta^+$  or electron capture decay with a half-life of 12.7 hours. Only a single 511 keV positron annihilation  $\gamma$  ray is expected to be seen in the SS spectrum. In  $\sim 0.5\%$  of cases,  $^{64}\text{Cu}$  electron captures to an excited state of  $^{64}\text{Ni}$  that deexcites by a 1345.8 keV  $\gamma$  ray, which can also produce an SS event. The expected SS spectra of  $^{135}\text{Xe}$  and  $^{64}\text{Cu}$  are generated by MC analogously to the case of  $^{137}\text{Xe}$ . The three spectral shapes are then fit to the calibrated charge energy spectrum of the selected SS events allowing the normalization of each of the three components to float. Figure 5 shows the selected SS events and the results of the fit. The good agreement between the best fit and the data shapes supports the expectation that  $^{64}\text{Cu}$  and  $^{135}\text{Xe}$  are the main activation backgrounds.

An SS low energy cut of 1075 keV is chosen to remove the  $^{135}\text{Xe}$  and most of the  $^{64}\text{Cu}$  events. The high energy cut is set to 4175 keV, based on the Q value of  $^{137}\text{Xe}$  GS decay. Based on the fit, the residual background contribution of  $^{64}\text{Cu}$  and  $^{135}\text{Xe}$  to the selected energy range is 22.7(5) and 0.50(2) events, respectively. Two known background contributions to the AmBe dataset are two-neutrino double  $\beta$

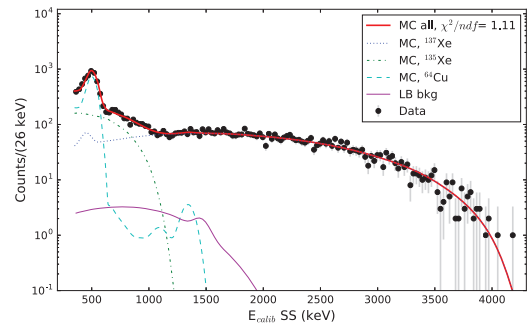


FIG. 5. Calibrated SS energy spectrum of events passing the selection cuts (black points). Blue dotted, green dashed, and cyan dash-dotted lines correspond to MC spectra of  $^{137}\text{Xe}$ ,  $^{135}\text{Xe}$ , and  $^{64}\text{Cu}$ , respectively. Thick red line corresponds to the sum of the three best-fit components. Thin magenta line corresponds to the LB backgrounds, described in the text. The reduced  $\chi^2$  of the fit is shown in the legend.

and  $^{40}\text{K}$  decays, whose rates are constrained by the EXO-200 “low background data” (LB) [28]. Taking into account the livetime and the correction for the slightly larger fiducial volume used in this analysis, one expects 43 two-neutrino double  $\beta$  and 7.8  $^{40}\text{K}$  events, or  $\sim 1.1\%$  of all the SS events in the selected energy range. Other LB components are expected to contribute less than one event total. The rate of the LB events is known to  $\sim 10\%$  relative uncertainty. The expected LB events are removed from the dataset by subtracting their MC spectra, normalized to the corresponding number of expected events. The remaining dataset contains 4526 events. For a qualitative check of the purity of the selected dataset, the time difference between each selected event and the start time of the corresponding decay period is histogrammed and fit by an exponential function (Fig. 6). The best-fit half-life value,  $3.81 \pm 0.15$  min, is in good agreement with the known half-life of  $^{137}\text{Xe}$  of  $3.818 \pm 0.013$  min [30].

Figure 7 shows the comparison between the observed and expected GS spectra of the  $^{137}\text{Xe}$  events. The comparison range is from 1075 to 4175 keV. The calibrated

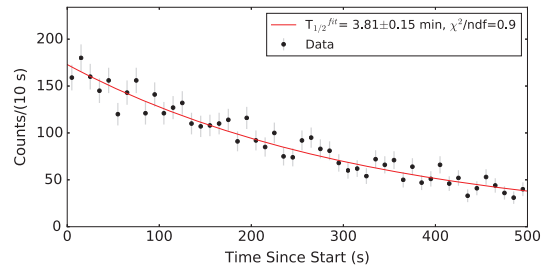


FIG. 6. Time distribution of selected SS events (black) with energies between 1075 and 4175 keV. The exponential fit is shown as red solid line.

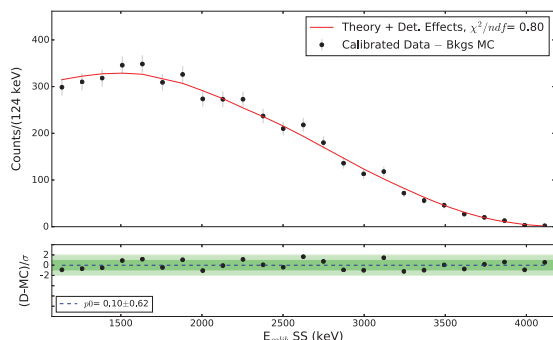


FIG. 7. (Top frame) Best fit to the selected, calibrated, background-subtracted SS data events. The data points are shown in black. The theoretical spectrum (after passing through MC) is shown in red. (Bottom frame) Residual differences between the data and best-fit curve, normalized by the statistical errors, are shown in black. The constant fit to the residuals is shown by dashed blue line.  $p0$  corresponds to the constant term of the fit.

charge energy spectrum of the selected SS data events, with the expected residual background contributions subtracted, is shown in black on the top frame of the figure. It is fit with the simulated shape based on the theoretical calculation (red). The only parameter floating in the fit is the total normalization. The reduced  $\chi^2$  of the fit (also shown) suggests a good agreement between the data and expectation. The normalized residuals are shown on the bottom frame of the figure. All residuals are within  $\pm 2\sigma$  statistical error. The residuals are fit by a constant (dashed blue line) trend line, with the best-fit parameter shown. The residuals show no statistically significant energy dependence.

Anything that can introduce an energy-dependent discrepancy between the data and MC can systematically affect the comparison shown on Fig. 7. Given the amount of the available statistics, we are sensitive to potential systematics effects on the level of a few percent or more. The data energy calibration is constrained to the subpercent level. The Gaussian + Erf fit model itself may be a source of systematics when extracting the peaks' mean positions. This effect was studied by EXO-200 and is expected to introduce a  $\sim 3$  keV bias, which is subdominant to the calibration residuals (Fig. 4). The residual background contamination in the selected SS energy range contributes  $\leq 1\%$  of events and is known to  $O(10)\%$  relative uncertainty, suggesting only a fraction of percent residual effect. Potential imperfections of the MC and reconstruction can systematically affect the comparison only if they lead to an energy-dependent difference of the SS fraction or of the overall SS spectral shape in the data and MC. Based on the latest published comparison of data and MC in EXO-200 (Fig. 1 in Ref. [28]), the energy-dependent deviation is expected to be small compared to the statistical errors in Fig. 7.

*Discussion and conclusion.*—We calculate the  $^{137}\text{Xe}$  GS spectrum and find that it has no significant dependence on

the adopted value of  $g_A$  or the magnitude of the mesonic enhancement effects on the axial charge matrix element. This makes this transition an ideal tool to validate the accuracy of the  $\beta$ -spectra calculations in the context of the reactor antineutrino anomaly. We perform a precise measurement of this first-forbidden nonunique  $\beta$ -decay shape using the data collected during an AmBe source deployment in EXO-200. A good agreement between the predicted and observed spectra is found. Therefore, this work provides both a rare measurement of the first-forbidden nonunique  $\beta$ -decay shape and a novel test related to the calculated electron spectral shapes of  $\beta$  decays that contribute strongly to the antineutrino flux from nuclear reactors. The hope is that this test justifies the calculated spectral shapes of [9,10], thus implying that the spectral bump and the flux anomaly can be explained, at least partly, by the exact spectral shapes of the abundant first-forbidden nonunique  $\beta$  decays of the fission fragments in nuclear reactors.

EXO-200 is supported by DOE and NSF in the United States, NSERC in Canada, IBS in Korea, RFBR (18-02-00550) in Russia, DFG in Germany, and CAS and ISTCP in China. EXO-200 data analysis and simulation uses resources of the National Energy Research Scientific Computing Center (NERSC). This work has been partially supported by the Academy of Finland under the Academy Project No. 318043. J.K. acknowledges the financial support from the Jenny and Antti Wihuri Foundation. We gratefully acknowledge the KARMEN collaboration for supplying the cosmic ray veto detectors, and the WIPP for their hospitality.

\*Deceased.

†Corresponding author.

iostrovskiy@ua.edu

‡Permanent address: King Abdulaziz City for Science and Technology, Riyadh, Saudi Arabia.

§Also at SNOLAB, Sudbury, Ontario, Canada.

|| Present address: SNOLAB, Sudbury, Ontario, Canada.

¶ Present address: Qventus, 295 Bernardo Ave., Suite 200, Mountain View, California 94043, USA.

\*\* Present address: Department of Physics at the University of California, Berkeley, California 94720, USA.

†† Also at Physics Department and CEEM, Indiana University, Bloomington, Indiana, USA.

‡‡ Present address: Department of Physics, Drexel University, Philadelphia, Pennsylvania 19104, USA.

§§ Present address: University of Hamburg, Institut für Experimentalphysik, Luruper Chaussee 149, 22761 Hamburg, Germany.

||| Present address: Descartes Labs, 100 North Guadalupe, Santa Fe, New Mexico 87501, USA.

¶¶ Present address: Carnegie Mellon University, Pittsburgh, Pennsylvania 15213, USA.

[1] T. A. Mueller *et al.*, *Phys. Rev. C* **83**, 054615 (2011).

- [2] F. P. An *et al.* (Daya Bay Collaboration), *Phys. Rev. Lett.* **118**, 251801 (2017).
- [3] J. K. Ahn *et al.* (RENO Collaboration), *Phys. Rev. Lett.* **108**, 191802 (2012).
- [4] Y. Abe *et al.* (Double Chooz Collaboration), *J. High Energy Phys.* **10** (2014) 086.
- [5] F. P. An *et al.* (Daya Bay Collaboration), *Phys. Rev. Lett.* **116**, 061801 (2016).
- [6] V. Zacek, G. Zacek, P. Vogel, and J. L. Vuilleumier, arXiv:1807.01810.
- [7] A. C. Hayes, J. L. Friar, G. T. Garvey, G. Jungman, and G. Jonkmans, *Phys. Rev. Lett.* **112**, 202501 (2014).
- [8] A. A. Sonzogni, E. A. McCutchan, and A. C. Hayes, *Phys. Rev. Lett.* **119**, 112501 (2017).
- [9] L. Hayen, J. Kostensalo, N. Severijns, and J. Suhonen, *Phys. Rev. C* **99**, 031301(R) (2019).
- [10] L. Hayen, J. Kostensalo, N. Severijns, and J. Suhonen, *Phys. Rev. C* **100**, 054323 (2019).
- [11] H. Daniel, *Rev. Mod. Phys.* **40**, 659 (1968).
- [12] H. M. W. Booiij, E. A. Van Hoek, H. Van Der Molen, W. F. Slot, and J. Blok, *Nucl. Phys.* **A160**, 337 (1971).
- [13] R. J. Onega and W. W. Pratt, *Phys. Rev.* **136**, B365 (1964).
- [14] J. T. Suhonen, *Front. Phys.* **5**, 55 (2017).
- [15] J. Kostensalo and J. Suhonen, *Phys. Lett. B* **781**, 480 (2018).
- [16] H. Ejiri, J. Suhonen, and K. Zuber, *Phys. Rep.* **797**, 1 (2019).
- [17] P. Gysbers, G. Hagen, J. D. Holt, G. R. Jansen, T. D. Morris, P. Navrátil, T. F. Papenbrock, S. Quaglioni, A. Schwenk, S. R. Stroberg, and K. A. Wendt, *Nat. Phys.* **15**, 428 (2019).
- [18] H. Behrens and W. Bühring, *Electron Radial Wave Functions and Nuclear Beta Decay* (Clarendon, Oxford, 1982).
- [19] M. Haaranen, J. Kotila, and J. Suhonen, *Phys. Rev. C* **95**, 024327 (2017).
- [20] B. Brown and W. Rae, *Nucl. Data Sheets* **120**, 115 (2014).
- [21] B. Brown (to be published).
- [22] M. Chadwick *et al.*, *Nucl. Data Sheets* **112**, 2887 (2011), Special Issue on ENDF/B-VII.1 Library.
- [23] P. Huber, *Phys. Rev. C* **84**, 024617 (2011).
- [24] 3M HFE-7000, [https://www.3m.com/3M/en\\_US/company-us/all-3m-products/~/3M-Novec-7000-Engineered-Fluid/?N=5002385+3290667267&rt=rud](https://www.3m.com/3M/en_US/company-us/all-3m-products/~/3M-Novec-7000-Engineered-Fluid/?N=5002385+3290667267&rt=rud).
- [25] M. Auger *et al.*, *J. Instrum.* **7**, P05010 (2012).
- [26] EXO-200 Collaboration (to be published).
- [27] J. B. Albert *et al.* (EXO-200 Collaboration), *Phys. Rev. C* **89**, 015502 (2014).
- [28] G. Anton *et al.* (EXO-200 Collaboration), *Phys. Rev. Lett.* **123**, 161802 (2019).
- [29] N. Ackerman *et al.* (EXO-200 Collaboration), *Phys. Rev. Lett.* **107**, 212501 (2011).
- [30] E. Browne and J. Tuli, *Nucl. Data Sheets* **108**, 2173 (2007).
- [31] B. C. Rasco *et al.*, *Phys. Rev. C* **95**, 054328 (2017).
- [32] I. Ostrovskiy, Ph.D. thesis, 2012, copyright—Database copyright ProQuest LLC; ProQuest does not claim copyright in the individual underlying works; Last updated—2019-10-19.
- [33] Z. Liu, J. Chen, P. Zhu, Y. Li, and G. Zhang, *Appl. Radiat. Isot.* **65**, 1318 (2007).